Journal of Applied Mechanics

Published Bimonthly by ASME

VOLUME 72 • NUMBER 2 • MARCH 2005

TECHNICAL PAPERS

BRIEF NOTES

(Contents continued on inside back cover)

Transactions of the ASME, Journal of Applied Mechanics (ISSN 0021-8936) is published bimonthly (Jan., Mar., May, July, Sept., Nov.) The American Society of Mechanical Engineers, Three Park Avenue, New York, NY 10016. Periodicals postage paid at New York, NY and additional mailing office. POSTMASTER: Send address changes to Transactions of the ASME, Journal of Applied Mechanics, c/o THE AMERICAN SOCIETY OF MECHANICAL ENGINEERS, 22 Law Drive, Box 2300, Fairfield, NJ 07007-2300.
CHANGES OF ADDRESS must be received at Society headquarters seven weeks before they are to be effective. Please send old label and new address.
STATEMENT from By-Laws. The Society shall not be responsible for statements or opinions advanced in papers or . . . printed in its publications (B7.1. Para. 3).

Journal of Applied Mechanics Volume 72, Number 2 MARCH 2005

DISCUSSION

ANNOUNCEMENTS AND SPECIAL NOTES

C. Liu[1]
Technical Staff Member,
MST-8, Materials Science and Technology Division,
Los Alamos National Laboratory,
Los Alamos, NM 87545
e-mail: cliu@lanl.gov

H. Lu
Associate Professor,
School of Mechanical and Aerospace Engineering,
Oklahoma State University,
Stillwater, OK 74078
e-mail: hongbin@okstate.edu

Y. Huang
Professor,
Department of Mechanical and Industrial Engineering,
University of Illinois at Urbana-Champaign,
Urbana, IL 61801
e-mail: huang9@uiuc.edu

Dynamic Steady-State Stress Field in a Web During Slitting

Based on a dynamic fracture mechanics analysis, the stress field in a continuous film (called a web) during slitting (or cutting) is investigated. For a homogeneous, isotropic and linearly elastic web, the steady-state dynamic stress field surrounding the slitter blade can be related to the interacting traction between the moving web and the blade, and to the far-field tension that is parallel to the slitting direction. The interaction between the moving web and the blade also includes friction that is considered to be a Coulomb type. By solving an integral equation, the normal traction between the web and the blade can be expressed as a function of the blade profile and the web speed. Numerical calculations are performed for an ideal razor blade with the wedge shape. The analysis presented in this study indicates that the contact between the moving web and the blade does not start at the tip of the blade but rather starts at some distance behind the blade tip. Moreover, it is found that the distance from the point where the web begins to separate to the point where the blade and the web start to have contact, is controlled by the toughness of the web material and also by the web speed. Some characteristic nature of the dynamic stress field surrounding the slitter blade is investigated based on the dynamic fracture mechanics analysis results. [DOI: 10.1115/1.1831298]

1 Introduction

A web is a thin, continuous, and flexible material such as a plastic film. Slitting, or equivalently cutting, of a web is a process that converts a web into narrower webs. Usually, this is the final process that requires high slit-edge quality. While only high quality final products such as photographic films and video tapes are available on the market, there is a tremendous amount of products being thrown away or recycled because of the poor slit-edge quality that attributes to improper slitting conditions or improper cutting tool, or slitters. To reduce the material waste and to improve the quality control of the slit-edge require a better understanding of the mechanics underlying the slitting processes.

Most publications on web slitting in the open literature are restricted to qualitative investigations; quantitative study is very limited. The identification of appropriate controlling parameters of slitting process relies heavily on experience and empirical methods such as trial and error. Among the few relevant quantitative investigations, Meehan and Burns [1] measured the cutting force and determined the isochromatic stress lines of a shear slitter blade in a polycarbonate sheet; Kasuga et al. [2] investigated the shearing process of ductile materials; Arcona and Dow [3] determined the relation between the cutting force and the cutting speed for plastic films; Bollen [4] studied the process of shear cutting of PET film; Bax [5] investigated the slitting energy rate and blade forces; Zheng and Wierzbicki [6] derived a closed-form solution for the cutting force for a steady-state wedge cutting process.

Web slitting can be considered primarily as a process of a controlled crack propagation in the web material. A crack is initiated by the cutting tool, or equivalently slitter blade, and is propagating in the web under the guidance of the slitter blade. Razor slitting can be considered primarily as an opening mode problem in the framework of fracture mechanics, while shear slitting may be considered primarily as an antiplane shear mode problem. Near the crack tip, there exists a high stress zone, where excessive inelastic deformation might occur. Damages, such as microvoids, most likely initiate and coalesce to form visible cracks for some web materials under certain slitting conditions. Part of the damage such as voids and cracks will remain in the wake of the main crack, i.e., the slit edge, and cause deterioration in the slit quality. The defective edges that contain debris and slivers, will also generate slit dust. Therefore, understanding the stress and strain distribution in a slitting web near the blade, their relation to the slit edge defects, and their effects on slit quality, dust formation, web winding quality following slitting etc., is essential for quality control in slitting processes.

In this paper, a general representation of the stress and strain distribution in a web during razor slitting is derived for an isotropic, homogeneous, and linearly elastic material based on dynamic fracture mechanics analysis. The solution approach is appropriate for a slitter blade of arbitrary shape with symmetry. For an ideal razor blade with the wedge profile, the stress solution is presented, and the contact condition between the moving web and the slitting blade is investigated. The solution is used to investigate the dependence of the size of yield zone on web speed.

2 Deformation Field Surrounding the Slitter

In this section, the deformation field surrounding the slitter in a moving web is obtained based on the dynamic fracture mechanics analysis. Due to the nature of the web material, the deformation is considered to be two dimensional. We also assume that the web material is homogeneous, isotropic, and elastic. First, the general formulation regarding the web slitting process is discussed. Then, the special case of concentrated tractions on the crack surface is considered. Finally, using the scheme of superposition, the stress field in the web surrounding the slitter is constructed.

2.1 Mathematical Formulation. The web slitting process is shown schematically in Fig. 1. A web is moving at a constant velocity v. A stationary slitting blade separate the moving web into two pieces. In the web plane, a Cartesian coordinate system (X_1,X_2) is chosen and it moves with the web at the speed of v. The X_1 axis is parallel to but pointing against the web moving direction.

For two-dimensional planar deformation, we may consider the two displacement potentials, $\Phi(X_1,X_2,t)$ and $\Psi(X_1,X_2,t)$, in the Cartesian system (X_1,X_2). With respect to the undeformed field, the two nonzero in-plane displacement components can be expressed through

[1]To whom correspondence should be addressed.

Contributed by the Applied Mechanics Division of THE AMERICAN SOCIETY OF MECHANICAL ENGINEERS for publication in the ASME JOURNAL OF APPLIED MECHANICS. Manuscript received by the Applied Mechanics Division, October 27, 1999; final revision, June 17, 2004. Editor: R. M. McMeeking.

$$u_\alpha = \frac{\partial \Phi(X_1, X_2, t)}{\partial X_\alpha} + e_{\alpha\beta} \frac{\partial \Psi(X_1, X_2, t)}{\partial X_\beta}, \quad \alpha = 1,2, \tag{1}$$

where the summation convention has been used. Notation $e_{\alpha\beta}$ is the two-dimensional alternator defined by

$$e_{12} = -e_{21} = 1, \quad e_{11} = e_{22} = 0.$$

The components of stress for a homogeneous, isotropic, and linearly elastic material that we consider, can be expressed through the displacement potentials as

$$\left.\begin{aligned}
\sigma_{11} &= \mu\left(\frac{c_l^2}{c_s^2}\cdot\frac{\partial^2\Phi(X_1,X_2,t)}{\partial X_\alpha \partial X_\alpha} - 2\frac{\partial^2\Phi(X_1,X_2,t)}{\partial X_2^2} + 2\frac{\partial^2\Psi(X_1,X_2,t)}{\partial X_1 \partial X_2}\right)\\
\sigma_{22} &= \mu\left(\frac{c_l^2}{c_s^2}\cdot\frac{\partial^2\Phi(X_1,X_2,t)}{\partial X_\alpha \partial X_\alpha} - 2\frac{\partial^2\Phi(X_1,X_2,t)}{\partial X_1^2} - 2\frac{\partial^2\Psi(X_1,X_2,t)}{\partial X_1 \partial X_2}\right)\\
\sigma_{12} &= \mu\left(2\frac{\partial^2\Phi(X_1,X_2,t)}{\partial X_1 \partial X_2} + \frac{\partial^2\Psi(X_1,X_2,t)}{\partial X_2^2} - \frac{\partial^2\Psi(X_1,X_2,t)}{\partial X_1^2}\right)
\end{aligned}\right\}, \tag{2}$$

where c_l and c_s are, respectively, the dilatational and shear wave speeds of the elastic material. They can be expressed, in terms of the shear modulus μ, Poisson's ratio ν, and the mass density ρ, as

$$c_l = \left(\frac{\kappa+1}{\kappa-1}\cdot\frac{\mu}{\rho}\right)^{1/2}, \quad c_s = \left(\frac{\mu}{\rho}\right)^{1/2}, \tag{3}$$

where $\kappa = 3-4\nu$ for plane strain deformation and $\kappa = (3-\nu)/(1+\nu)$ for plane stress deformation, respectively. In the absence of the body force density, equations of motion are given by

$$\frac{\partial \sigma_{\alpha\beta}}{\partial X_\beta} = \rho \frac{\partial^2 u_\alpha}{\partial t^2}, \quad \alpha = 1,2. \tag{4}$$

By using the constitutive relation (2), the equations of motion (4) can be rewritten in terms of the displacement potentials, $\Phi(X_1, X_2, t)$ and $\Psi(X_1, X_2, t)$, as

$$\frac{\partial^2\Phi(X_1,X_2,t)}{\partial X_\alpha \partial X_\alpha} - \frac{1}{c_l^2}\cdot\frac{\partial^2\Phi(X_1,X_2,t)}{\partial t^2} = 0, \tag{5a}$$

$$\frac{\partial^2\Psi(X_1,X_2,t)}{\partial X_\alpha \partial X_\alpha} - \frac{1}{c_s^2}\cdot\frac{\partial^2\Psi(X_1,X_2,t)}{\partial t^2} = 0. \tag{5b}$$

Suppose that the slitting process has started for quite some time, and the deformation surrounding the slitter has reached steady state. In other words, for an observer sitting at the slitter, the surrounding field does not change with time. Introduce a coordinate system (x_1, x_2) with the origin located at the point where the web starts to separate and with the x_1-axis pointing against the web moving direction. Then the relation between the two coordinate systems (X_1, X_2) and (x_1, x_2) is a simple translation:

$$x_1 = X_1 - vt, \quad x_2 = X_2.$$

Here we have assumed that at the moment of $t=0$, the two systems coincide. If we view the material system (X_1, X_2) as stationary, then the web slitting process can be considered as one that a straight crack propagates with a constant velocity v under the load applied by the slitter which is also traveling with the same speed.

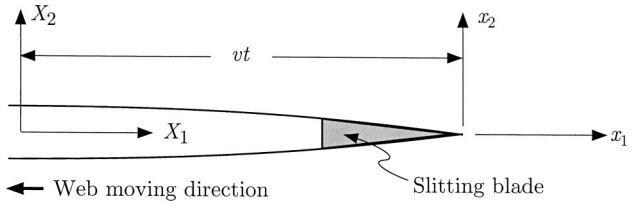

Fig. 1 Schematics of the web slitting process

In the "moving" coordinate system, the equation of motion (5) becomes

$$\phi_{,11}(x_1,x_2) + \frac{1}{\alpha_l^2}\phi_{,22}(x_1,x_2) = 0,$$

$$\psi_{,11}(x_1,x_2) + \frac{1}{\alpha_s^2}\psi_{,22}(x_1,x_2) = 0, \tag{6}$$

where $\phi(x_1,x_2) = \Phi(x_1+vt, x_2)$ and $\psi(x_1,x_2) = \Psi(x_1+vt, x_2)$, and the steady-state condition has been used in writing Eq. (6). Meanwhile the two parameters α_l and α_s are defined by

$$\alpha_l = \left(1 - \frac{v^2}{c_l^2}\right)^{1/2}, \quad \alpha_s = \left(1 - \frac{v^2}{c_s^2}\right)^{1/2}.$$

The two equations in Eq. (6) are Laplace's equations in the corresponding scaled plane $(x_1, \alpha_l x_2)$ for ϕ, and $(x_1, \alpha_s x_2)$ for ψ, respectively. As a result, the most general solutions for Eq. (6) can be expressed as [7]

$$\phi(x_1,x_2) = \mathrm{Re}[F(z_l)], \quad \psi(x_1,x_2) = \mathrm{Im}[G(z_s)], \tag{7}$$

where the complex variables z_l and z_s are given by

$$z_l = x_1 + i\alpha_l x_2, \quad z_s = x_1 + i\alpha_s x_2,$$

and $i = \sqrt{-1}$. Functions $F(z_l)$ and $G(z_s)$ are analytic everywhere in the complex z_l, or z_s planes except along the nonpositive real axis $-\infty < x_1 \leqslant 0$ occupied by the crack. In terms of the analytic functions $F(z_l)$ and $G(z_s)$, the displacement and stress components, in the (x_1, x_2) system, are

$$\begin{aligned}
u_1(x_1,x_2) &= \mathrm{Re}[F'(z_l) + \alpha_s G'(z_s)],\\
u_2(x_1,x_2) &= -\mathrm{Im}[\alpha_l F'(z_l) + G'(z_s)],
\end{aligned} \tag{8}$$

and

$$\left.\begin{aligned}
\sigma_{11}(x_1,x_2) &= \mu\,\mathrm{Re}[(1+2\alpha_l^2-\alpha_s^2)F''(z_l) + 2\alpha_s G''(z_s)]\\
\sigma_{22}(x_1,x_2) &= -\mu\,\mathrm{Re}[(1+\alpha_s^2)F''(z_l) + 2\alpha_s G''(z_s)]\\
\sigma_{12}(x_1,x_2) &= -\mu\,\mathrm{Im}[2\alpha_l F''(z_l) + (1+\alpha_s^2)G''(z_s)]
\end{aligned}\right\}, \tag{9}$$

where the prime represents the derivative with respect to the corresponding complex argument. From the above discussion, one can see that the whole deformation field will be determined if the two analytic functions $F(z_l)$ and $G(z_s)$ can be obtained.

2.2 Concentrated Tractions on the Crack Surface. In this section, we consider the stress field surrounding a steadily moving

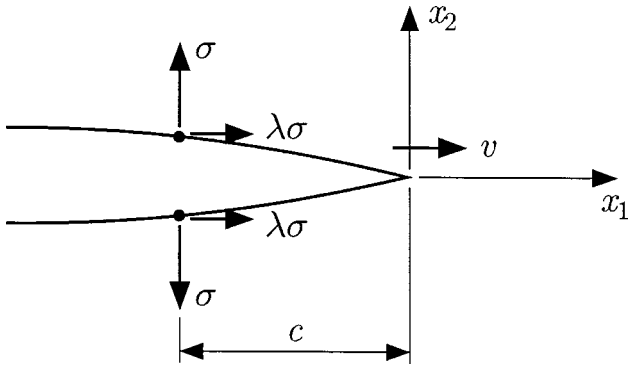

Fig. 2 Steady crack growth due to symmetrically applied concentrated tractions on the crack surface at a fixed distance, *c*, behind the crack tip

crack where concentrated tractions are applied on the crack surface. Then, the stress field surrounding the slitter can be constructed using superposition.

As shown in Fig. 2, a crack is propagating at a constant velocity, v, through an unbounded two-dimensional region. At a fixed distance, c, behind the moving crack tip, a pair of concentrated forces with the magnitude, σ, is applied to the crack surface and tends to open the crack. Meanwhile, another concentrated force, $\lambda\sigma$, is applied at the same location and is pointing to the direction of crack growth. The second concentrated force is due to friction and the Coulomb-type of contact condition is assumed with λ to be the friction coefficient. Therefore, the boundary conditions are described by

$$\left.\begin{aligned}\sigma_{22}(x_1,0^{\pm}) &= -\sigma\delta(x_1+c)\\ \sigma_{12}(x_1,0^{\pm}) &= \mp\lambda\sigma\delta(x_1+c)\end{aligned}\right\}, \quad \text{for } -\infty<x_1<0, \tag{10}$$

where $\delta(\cdot)$ is the Dirac's delta function. Far away from the crack tip, or at infinity, the stress field is such that

$$\sigma_{11}=\sigma_0, \quad \sigma_{22}=0, \ \sigma_{12}=0, \quad \text{as } (x_1^2+x_2^2)^{1/2}\to\infty, \tag{11}$$

where σ_0 characterizes the remote tension along the x_1 direction. One can see that the deformation field is symmetric with respect to the x_1 axis. As a result, the two analytic functions, $F(z_l)$ and $G(z_s)$ introduced in the previous section, have to satisfy the following restrictions:

$$\overline{F}(z_l)=F(z_l), \quad \overline{G}(z_s)=G(z_s), \tag{12}$$

where the overline stands for the complex conjugate, and therefore, we only need to consider the upper half of the (x_1,x_2) plane.

The problem of a steady growing crack subjected to concentrated shear traction on the crack surface has been discussed by Freund [7]. Following similar procedure, the two analytic functions, $F(z_l)$ and $G(z_s)$, can be obtained as

$$\left.\begin{aligned}F''(z_l) &= \frac{1+\alpha_s^2}{\pi D(v)}\cdot\frac{\sigma}{\mu}\cdot\frac{\sqrt{c}}{\sqrt{z_l}(z_l+c)}-\frac{2\alpha_s}{\pi D(v)}\cdot\frac{\lambda\sigma}{\mu}\cdot\frac{1}{z_l+c}+\frac{1}{2(\alpha_l^2-\alpha_s^2)}\cdot\frac{\sigma_0}{\mu}\\ G''(z_s) &= -\frac{2\alpha_l}{\pi D(v)}\cdot\frac{\sigma}{\mu}\cdot\frac{\sqrt{c}}{\sqrt{z_s}(z_s+c)}+\frac{1+\alpha_s^2}{\pi D(v)}\cdot\frac{\lambda\sigma}{\mu}\cdot\frac{1}{z_s+c}-\frac{1+\alpha_s^2}{4\alpha_s(\alpha_l^2-\alpha_s^2)}\cdot\frac{\sigma_0}{\mu}\end{aligned}\right\}, \tag{13}$$

where

$$D(v)=4\alpha_l\alpha_s-(1+\alpha_s^2)^2.$$

Note, that $D(v)=0$ when $v=c_R$, where c_R is the Rayleigh wave speed of the elastic material. Therefore, we exclude situation where the crack propagates with the Rayleigh wave speed c_R. The stress field surrounding the moving crack can be obtained by combining Eqs. (13) and (9).

According to the theory of linearly elastic fracture mechanics, the dynamic mode-I stress intensity factor at the moving crack tip, K_I, is defined by

$$K_I=\lim_{x_1\to 0^+}\sqrt{2\pi x_1}\,\sigma_{22}(x_1,0). \tag{14}$$

From Eqs. (9) and (13), we have

$$K_I=\sigma\sqrt{\frac{2}{\pi c}}. \tag{15}$$

One can see that the dynamic stress intensity factor, K_I, does not explicitly depend on the crack-tip speed, v.

2.3 Stress Field Surrounding the Slitter. Now, consider that the crack surface is subjected to a distributed normal traction $\sigma(x_1)$. The associated friction traction is therefore, given by $\lambda\sigma(x_1)$. Using the superposition scheme, the two analytic functions, $F(z_l)$ and $G(z_s)$, can be expressed as

$$F''(z_l)=\frac{1+\alpha_s^2}{\pi D(v)}\int_{-\infty}^{0}\frac{\sigma(s)}{\mu}\cdot\frac{\sqrt{-s}}{\sqrt{z_l}(z_l-s)}\,ds-\frac{2\lambda\alpha_s}{\pi D(v)}\times\int_{-\infty}^{0}\frac{\sigma(s)}{\mu}\cdot\frac{ds}{z_l-s}+\frac{1}{2(\alpha_l^2-\alpha_s^2)}\cdot\frac{\sigma_0}{\mu}, \tag{16a}$$

$$G''(z_s)=-\frac{2\alpha_l}{\pi D(v)}\int_{-\infty}^{0}\frac{\sigma(s)}{\mu}\cdot\frac{\sqrt{-s}}{\sqrt{z_s}(z_s-s)}\,ds+\frac{\lambda(1+\alpha_s^2)}{\pi D(v)}\int_{-\infty}^{0}\frac{\sigma(s)}{\mu}\cdot\frac{ds}{z_s-s}-\frac{1+\alpha_s^2}{4\alpha_s(\alpha_l^2-\alpha_s^2)}\cdot\frac{\sigma_0}{\mu}. \tag{16b}$$

By combining Eqs. (9) and (16), the stress field surrounding the slitter can be calculated and therefore, the deformation field can be determined. Also, by using the superposition scheme, the dynamic stress intensity factor at the crack tip, K_I, is given by

$$K_I=\sqrt{\frac{2}{\pi}}\int_{-\infty}^{0}\frac{\sigma(s)}{\sqrt{-s}}\,ds. \tag{17}$$

One can observe that for the dynamic stress intensity factor, K_I, to be finite, the normal traction $\sigma(x_1)$ has to be bounded as $x_1\to 0^-$, and $\sigma(x_1)\to|x_1|^p$ as $|x_1|\to\infty$ for some $p<-1/2$. On the other hand, if the normal traction $\sigma(x_1)$ is applied in a finite region, where the crack tip is not an end point, the normal traction $\sigma(x_1)$ has to be integrable at both end points of the region.

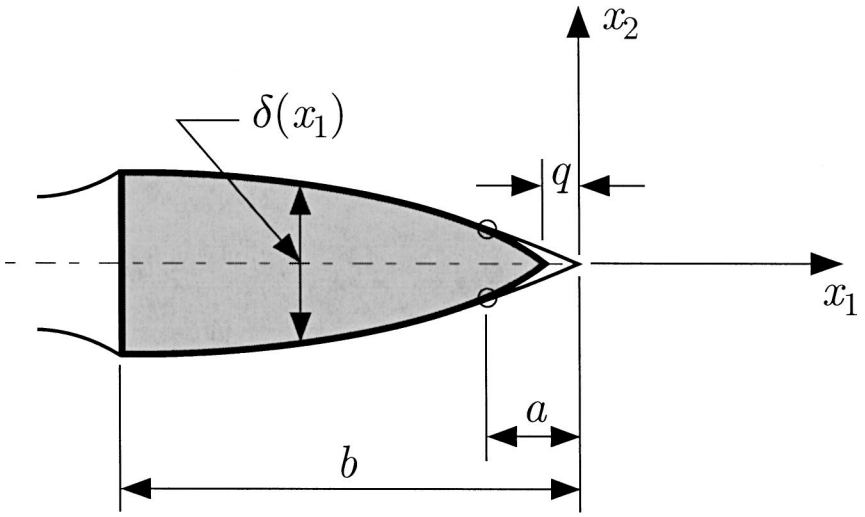

Fig. 3 Geometric profile of the slitter and contact condition

3 Interaction Between Moving Web and Slitting Blade

In the previous section, the stress field in the moving web surrounding the slitting blade, is obtained based on the dynamic fracture mechanics analysis. In determining the stress field, we have to know the function $\sigma(x_1)$, which is assumed to be prescribed along the crack surface in the analysis. With the normal traction $\sigma(x_1)$, together with the remote tensile stress, σ_0 (also called web stress), we can calculate the stress field at any point surrounding the slitting blade. However, in the web slitting process, the traction applied on the crack surface or the web edge, $\sigma(x_1)$, is the result of interaction between the slitting blade and the moving web. Intuitively, this interacting traction will depend on the moving velocity of the web and the shape of the slitting blade. In this section, we will determine the traction $\sigma(x_1)$ and investigate its properties.

Behind the crack tip, the crack opening displacement at any position x_1 is defined by

$$\delta_2(x_1)=u_2(x_1,0^+)-u_2(x_1,0^-), \quad \text{for } -\infty<x_1\leqslant 0. \tag{18}$$

With the help of Eqs. (8) and (16), one can show that

$$\delta_2'(x_1)=\frac{2\alpha_l(1-\alpha_s^2)}{D(v)}\cdot\frac{1}{\pi}\int_{-\infty}^{0}\frac{\sigma(s)}{\mu}\sqrt{\frac{-s}{-x_1}}\cdot\frac{ds}{s-x_1},$$

$$\text{for } -\infty<x_1\leqslant 0. \tag{19}$$

By using the fact that at the crack tip, $\delta_2(0)=0$, the crack opening displacement can be obtained as

$$\delta_2(x_1)=\frac{2\alpha_l(1-\alpha_s^2)}{\pi D(v)}\int_{-\infty}^{0}\frac{\sigma(s)}{\mu}\ln\left|\frac{\sqrt{-s}+\sqrt{-x_1}}{\sqrt{-s}-\sqrt{-x_1}}\right|ds,$$

$$\text{for } -\infty<x_1\leqslant 0. \tag{20}$$

Note that in the above expression, the normal opening displacement $\delta_2(x_1)$ depends only on the normal traction applied on the crack surface or web edge, $\sigma(x_1)$. The shearing traction associated with the friction coefficient λ, and the remote tensile stress σ_0, do not enter the expression for the crack opening displacement.

Consider the situation depicted in Fig. 3. Here the slitting blade has a finite length. The distance between the crack tip and the tip of the blade is q and the distance between the crack tip and the end of the blade is b. The profile of the slitting blade is characterized by the function $\delta(x_1)$. We assume that the slitting blade and the moving web keep contact in the region of $-b\leqslant x_1\leqslant -a$ where $a\geqslant q$. Therefore, when the slitting blade is perfectly aligned with the web moving direction, within the contact region, we have $\delta_2(x_1)=\delta(x_1)$. By denoting $\eta_1=-x_1/b$ and $\eta=-s/b$, from Eq. (20), one can write:

$$\int_{\alpha}^{1}\overset{*}{\sigma}(\eta)\ln\left|\frac{\sqrt{\eta}+\sqrt{\eta_1}}{\sqrt{\eta}-\sqrt{\eta_1}}\right|d\eta=\frac{\pi D(v)}{2\alpha_l(1-\alpha_s^2)}\overset{*}{\delta}(\eta_1), \quad \text{for } \alpha\leqslant\eta_1\leqslant 1, \tag{21}$$

where we have defined the following,

$$\overset{*}{\sigma}(\eta_1)=\frac{\sigma(x_1)}{\mu}, \quad \overset{*}{\delta}(\eta_1)=\frac{\delta(x_1)}{b}, \quad \alpha=\frac{a}{b}.$$

One can observe from Eq. (21) that the interacting traction between the moving web and the slitting blade, $\overset{*}{\sigma}(\eta_1)$, can be expressed in the form of

$$\overset{*}{\sigma}(\eta_1)=\frac{D(v)}{2\alpha_l(1-\alpha_s^2)}\Sigma(\eta_1), \quad \text{for } \alpha\leqslant\eta_1\leqslant 1, \tag{22}$$

which indicates that $\overset{*}{\sigma}(\eta_1)$ is composed by two parts. The first one is a function of the web speed, $D(v)/2\alpha_l(1-\alpha_s^2)$, which intrinsically also depends on the Poisson's ratio, ν. The second part, denoted by $\Sigma(\eta_1)$, does not depend on the web speed, it is only a function of the blade profile. We may refer to the first part as the speed factor and the second part as the shape factor. The variation of the speed factor as a function of the web speed is presented in Fig. 4 for different Poisson's ratios. Here we have assumed that the deformation is plane stress. One can see that the speed factor is a monotonic function of the web speed. It starts from the value of $2/(\kappa+1)$ at $v=0$ and decreases to zero when $v=c_R$, where c_R is the Rayleigh wave speed of the material.

The shape factor, or $\Sigma(\eta_1)$, is determined in the following. By substituting Eq. (22) into Eq. (21), we have

$$\frac{1}{\pi}\int_{\alpha}^{1}\Sigma(\eta)\ln\left|\frac{\sqrt{\eta}+\sqrt{\eta_1}}{\sqrt{\eta}-\sqrt{\eta_1}}\right|d\eta=\overset{*}{\delta}(\eta_1), \quad \text{for } \alpha\leqslant\eta_1\leqslant 1. \tag{23}$$

Equation (23) is an integral equation for the unknown function $\Sigma(\eta_1)$. This integral equation is of the first kind, Fredholm type, and linear. To solve Eq. (23), we differentiate both sides with respect to η_1, which leads to

$$\int_{\alpha}^{1}\frac{\sqrt{\eta}\Sigma(\eta)}{\eta-\eta_1}d\eta=\pi\sqrt{\eta_1}\overset{*}{\delta}'(\eta_1), \quad \text{for } \alpha\leqslant\eta_1\leqslant 1. \tag{24}$$

The solution to the above integral equation can be obtained as [8]

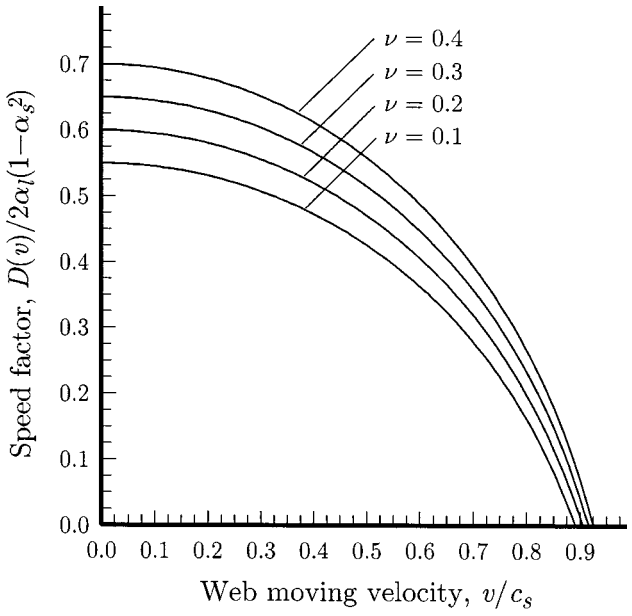

Fig. 4 Variation of the speed factor as a function of the web speed for different Poisson's ratios

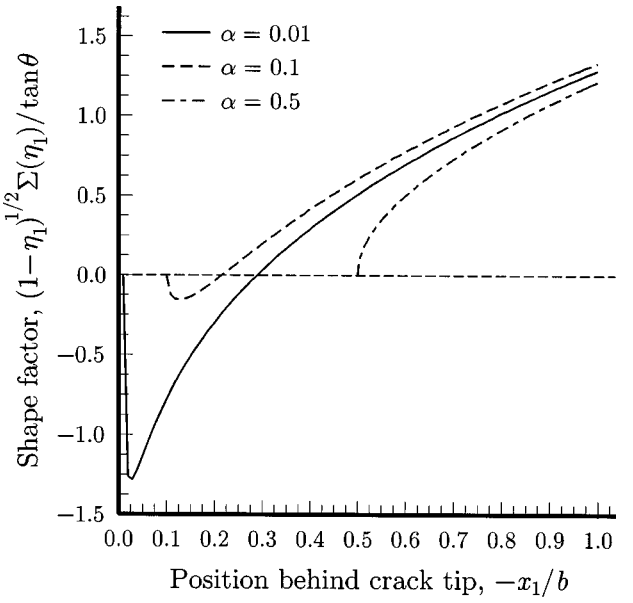

Fig. 5 Variation of the shape factor as a function of the distance behind crack tip for different values of α

$$\Sigma(\eta_1) = -\frac{1}{\pi}\int_\alpha^1 \frac{\sqrt{\eta(\eta-\alpha)(1-\eta)}}{\sqrt{\eta_1(\eta_1-\alpha)(1-\eta_1)}}\cdot\frac{\overset{*}{\delta}'(\eta)}{\eta-\eta_1}d\eta + \frac{A}{\pi\sqrt{\eta_1(\eta_1-\alpha)(1-\eta_1)}}, \quad \text{for } \alpha\leqslant\eta_1\leqslant 1, \quad (25)$$

where A is a real constant. The situation depicted in Fig. 3 has suggested that the contact traction at $\eta_1=\alpha$ has to be bounded. This requirement renders the constant A to be

$$A = \int_\alpha^1 \frac{\sqrt{\eta(1-\eta)}}{\sqrt{\eta-\alpha}}\overset{*}{\delta}'(\eta)d\eta. \quad (26)$$

Now, the function $\Sigma(\eta_1)$ can be rewritten as

$$\Sigma(\eta_1) = -\frac{1}{\pi}\sqrt{\frac{\eta_1-\alpha}{\eta_1(1-\eta_1)}}\int_\alpha^1\sqrt{\frac{\eta(1-\eta)}{\eta-\alpha}}\cdot\frac{\overset{*}{\delta}'(\eta)}{\eta-\eta_1}d\eta, \quad \text{for } \alpha\leqslant\eta_1\leqslant 1. \quad (27)$$

If we let the parameter α vanish, or the slitting blade and the moving web start to have contact right at the tip of the blade. From Fig. 3, such assumption also implies that the tip of the blade and the crack tip are coincide, or $q=0$. As a result, the expression for the function $\Sigma(\eta_1)$ becomes

$$\Sigma(\eta_1) = -\frac{1}{\pi\sqrt{1-\eta_1}}\int_0^1\frac{\sqrt{1-\eta}\overset{*}{\delta}'(\eta)}{\eta-\eta_1}d\eta, \quad \text{for } 0\leqslant\eta_1\leqslant 1. \quad (28)$$

One can show that as $\eta_1\to 0^-$, the above function $\Sigma(\eta_1)$ is unbounded. However, from Eq. (17), we have observed that the normal traction $\sigma(x_1)$ has to be bounded as $x_1\to 0^-$. Such observation indicates that in Eq. (27) we must have $\alpha\neq 0$. Therefore, the exclusion of $\alpha=0$ indicates that the contact between the moving web and the slitting blade does not start at the tip of the blade but rather starts at some distance behind the blade tip. As a matter of fact, the above conclusion is consistent with observations that during the slitting of some brittle webs, the crack tip is indeed ahead of the tip of the slitting blade.

To study the properties of the shape factor, $\Sigma(\eta_1)$, we consider an ideal shape, a wedge profile, for the slitting blade. The wedge profile can be described as

$$\delta(x_1) = 2|x_1+q|\tan\theta, \quad \text{for } -b\leqslant x_1\leqslant -q, \quad (29)$$

where 2θ is the angle of the wedge. In nondimensional form, the wedge shape in Eq. (29) can be rewritten as

$$\overset{*}{\delta}(\eta_1) = 2(\eta_1-\gamma)\tan\theta, \quad \text{for } \gamma\leqslant\eta_1\leqslant 1, \quad (30)$$

where $\gamma=q/b$ and $\gamma<\alpha$. The shape factor, $\Sigma(\eta_1)$, is expressed for slitting blade with wedge slitter as

$$\Sigma(\eta_1) = -\frac{2\tan\theta}{\pi}\sqrt{\frac{\eta_1-\alpha}{\eta_1(1-\eta_1)}}\int_\alpha^1\sqrt{\frac{\eta(1-\eta)}{\eta-\alpha}}\cdot\frac{d\eta}{\eta-\eta_1}, \quad \text{for } \alpha\leqslant\eta_1\leqslant 1. \quad (31)$$

The variation of $\sqrt{1-\eta_1}\Sigma(\eta_1)/\tan\theta$ as a function of the position behind the crack tip, is plotted in Fig. 5 for different values of the parameter α. Note that for smaller α (e.g., $\alpha=0.01$ or 0.1 in Fig. 5), as η_1 changes from α to 1, $\Sigma(\eta_1)$ starts from zero, which satisfies the requirement imposed on $\Sigma(\eta_1)$, and decreases. Then, $\Sigma(\eta_1)$ starts to increase and becomes positive. For larger α ($\alpha=0.5$ in Fig. 5), $\Sigma(\eta_1)$ becomes a monotonically increasing function. However, the interacting traction between the moving web and the slitting blade cannot be negative. Therefore, the above observation suggests that there exists a lower bound for the parameter α denoted by α_0, and we must have $\alpha\geqslant\alpha_0$. This lower bound parameter α_0 can be obtained from the following condition:

$$\left.\frac{d\Sigma(\eta_1)}{d\eta_1}\right|_{\eta_1=\alpha_0} = 0, \quad (32)$$

for any given slitting blade profile. Specifically, for blades with the wedge profile Eq. (29), a numerical estimation gives $\alpha_0=0.1739$. It is interesting to note that the limiting value α_0 does not depend on the wedge angle 2θ. However, since the analysis presented in this study is based on the infinitesimal deformation theory, the above conclusion should be understood of being true only for small angle θ.

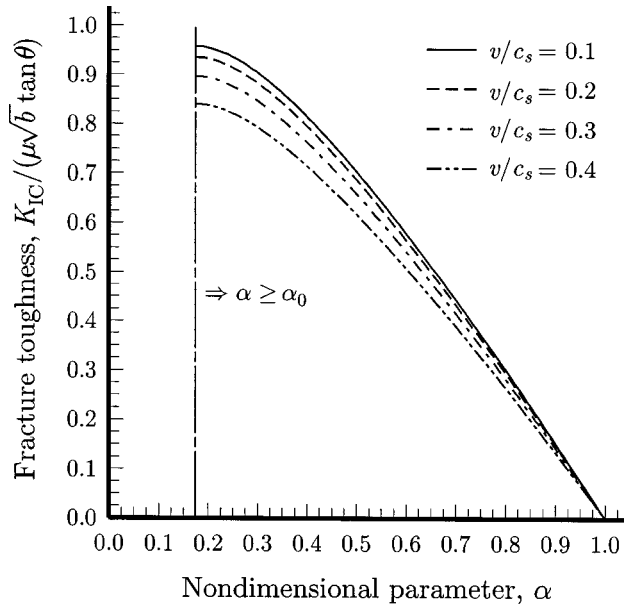

Fig. 6 Relation between the fracture toughness of the web material, K_{IC}, and the parameter α

Through the above discussions, we have shown that the interacting traction between the moving web and the slitting blade is the product of two factors, the speed factor and the shape factor. We also showed that the parameter α has to be in the range of

$$\alpha_0 \leqslant \alpha < 1, \tag{33}$$

in order for the interacting traction to be positive. Nevertheless, the constant α still remains as a free parameter and needs to be determined. Recall that the dynamic stress intensity factor at the crack tip, K_I, is given in Eq. (17). Also note that during the slitting process, the stress intensity factor, K_I, has to be equal to the fracture toughness of the web material, which is denoted by $K_{IC}(v)$. Here the notation has suggested that the fracture toughness of the web material, K_{IC}, also depends on the web speed v. In terms of the shape factor, $\Sigma(\eta_1)$, $K_{IC}(v)$ can be rewritten as

$$K_{IC}(v) = \mu\sqrt{\frac{2b}{\pi}} \cdot \frac{D(v)}{2\alpha_l(1-\alpha_s^2)} \int_\alpha^1 \frac{\Sigma(\eta)}{\sqrt{\eta}}\, d\eta. \tag{34}$$

Using the requirement Eq. (34), the parameter α is therefore determined. From Eq. (34), one can see that α will depend on the material's fracture toughness, web speed, and the shape of the blade. For slitting blades with the wedge profile Eq. (29), the relation between the fracture toughness of the web material, K_{IC}, and the parameter α is presented in Fig. 6 for several different web speeds. Here we have chosen that the Poisson's ratio $\nu = 0.25$ and the deformation is plane stress. One can see from Fig. 6 that for given wedge angle, 2θ, and web speed, v, if the toughness of the web material K_{IC} is known, the length of the contact region, characterized by $(1-\alpha)b$, can be determined by using the relation shown in Fig. 6. On the other hand, by measuring the length of contact region, or the parameter α, the fracture toughness of the web material, K_{IC}, can be determined by using the relation shown in Fig. 6, as well. Another observation from Fig. 6 is that for given wedge angle, 2θ, and web speed, v, the length of the contact region will be longer for tougher web materials.

4 Numerical Results and Discussions

In this section, some general characteristics of the dynamic steady-state stress field surrounding the blade during web slitting are studied based on the dynamic fracture mechanics analysis presented in the previous sections.

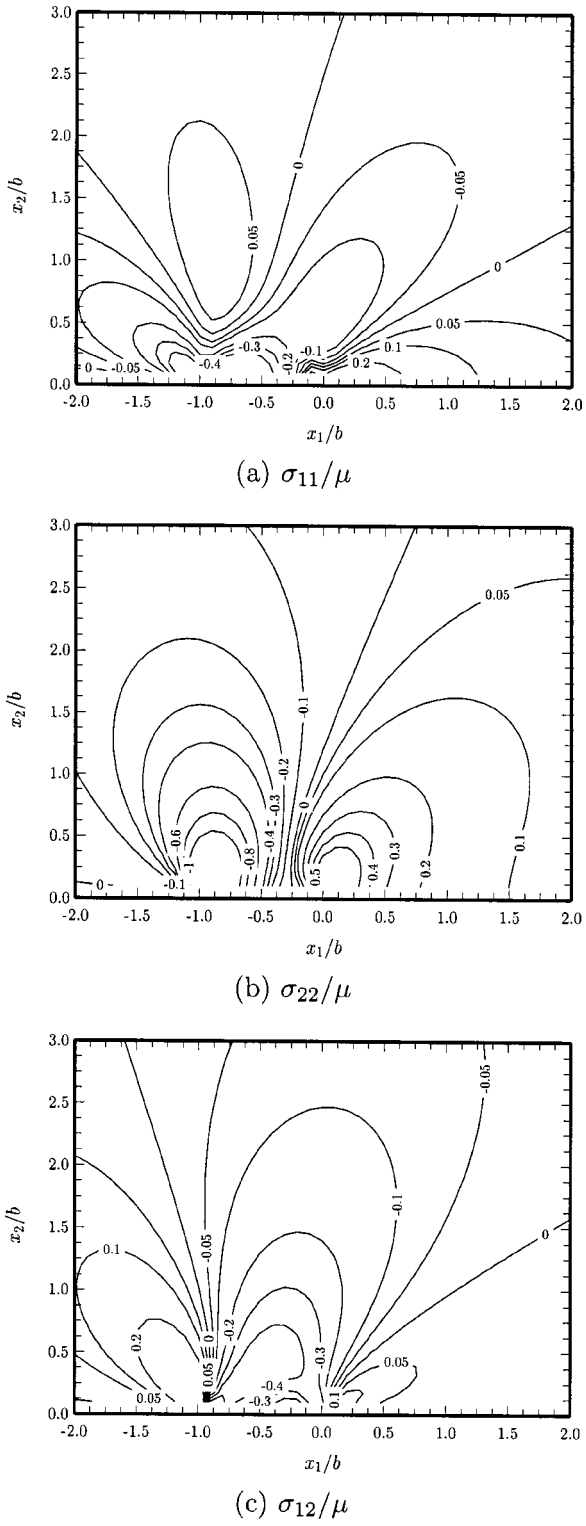

Fig. 7 Contour plots of the three stress components of the dynamic steady-state stress field surrounding the slitter

In Fig. 7, contour plots of the three components of the dynamic steady-state stress field surrounding the slitter with a wedge profile are presented. In this numerical calculation, we choose the web speed to be $v/c_s = 0.1$ where c_s is the shear wave speed of the web material with Poisson's ratio $\nu = 0.3$. The half angle of the wedge is $\theta = 5.0°$ and the friction coefficient between the moving web and the slitter is set to be $\lambda = 0.1$. We also assume that the fracture toughness of the web material is a constant and

$K_{IC}/\mu\sqrt{b}=0.075$, where μ is the shear modulus of the material and b is the distance from the crack tip to end point of the contact region as shown in Fig. 3. The remote tension is assumed to be $\sigma_0/\mu=0.008$. As shown in Fig. 6, for a given fracture toughness, the length of the contact region can be determined and from this relation we have $\alpha=0.3913$.

According to the analysis by Cotterell and Rice [9] on slightly curved and kinked stationary cracks, the sign of the T stress (the second term next to the singular term in the asymptotic expansion near the crack tip) determines the stability of the crack, where under mode-I loading, the straight crack remains stable when the T stress is compressive, i.e., $T<0$, and the straight crack becomes unstable for positive T stress, i.e., $T>0$. The unstable crack will tend to kink out of its original direction or bifurcate into several branches. On the other hand, Melin [10] suggested that the directional stability of a mode-I crack is not only controlled by the so-called T stress, but also controlled by the opening stress normal to the crack. Through a model problem, Melin [10] showed that the mode-I crack will lose its directional stability when the ratio of the T stress to the opening stress is bigger than certain value. Although directional stability remains as an unsolved problem (see [11]), the loss of stability of a mode-I crack still has some significant implications in the quality control of web slitting. This is because that after the crack becomes unstable, many micro or small cracks tend to form along the cutting edge of the web and the quality of the final product would be poor. Since the so-called T stress in mode-I type of deformation, is determined by the distribution of the σ_{11} component ahead of the crack tip, in Fig. 7(a), the contour of σ_{11}/μ is presented. One observes that ahead of the crack tip and in a wedge-shape region, the stress component σ_{11} is indeed positive. As a result, the value of the T stress is also positive. However, from the dynamic fracture mechanic analysis, the σ_{11} component ahead of the crack tip is determined by the remote tension σ_0 and the web speed v. Therefore, the web slitting quality might be controlled by adjusting these two parameters so that the T stress is controlled beneath certain threshold and this will eliminate the tendency that the crack loses its stability during slitting.

Meanwhile, from Figs. 7(a) and 7(b), we see that near the contact region between the moving web and the slitter, i.e., from $x_1=-0.3913b$ to $x_1=-b$, both σ_{11} and σ_{22} are negative. One can deduce that the two principal stresses will also be negative near the contact region. This situation might trigger the web material to buckle and this will also lead to poor quality of web cutting edges.

Finally, the contour plot of the effective stress σ_{eff} is shown in Fig. 8, where σ_{eff} is defined by

$$\sigma_{\text{eff}}=\left[\frac{1}{2}\left(\sigma_{ij}-\frac{1}{3}\sigma_{kk}\delta_{ij}\right)\left(\sigma_{ij}-\frac{1}{3}\sigma_{kk}\delta_{ij}\right)\right]^{1/2}$$
$$=\left(\frac{5}{6}\sigma_{11}^2+\frac{4}{3}\sigma_{11}\sigma_{22}+\frac{5}{6}\sigma_{22}^2+3\sigma_{12}^2\right)^{1/2}. \quad (35)$$

In writing the expression in Eq. (35), we have assumed that the deformation is plane stress. In Fig. 8, two different web speeds are considered and they are $v/c_s=0.1$ and $v/c_s=0.3$, respectively. Other parameters are the same as those shown in Fig. 7. By noting that the von Mises yield criterion can be expressed as

$$\sigma_{\text{eff}}\leqslant\tau, \quad (36)$$

where τ is the yield stress in pure shear, the contour plots shown in Fig. 8 indicate the effect of the web speed on the size of the yielding zone near the slitting blade. There are two singular points in the stress field. One is the crack tip and the other is the end of contact region. From Fig. 8, we can see that although the stress concentration at the tip of the crack will cause plastic deformation, the majority of the yielding occurring in the area surrounding the slitting blade is dominated by the contact condition, especially near the end of the contact region. Also, we can see that elevated web speed will enlarge the yielding area surrounding the slitting blade. However, this enlargement is not very significant. Nevertheless, crack-tip plasticity and plastic deformation near the end of the contact region might change the contact condition between the moving web and the slitter and this remains to be investigated further.

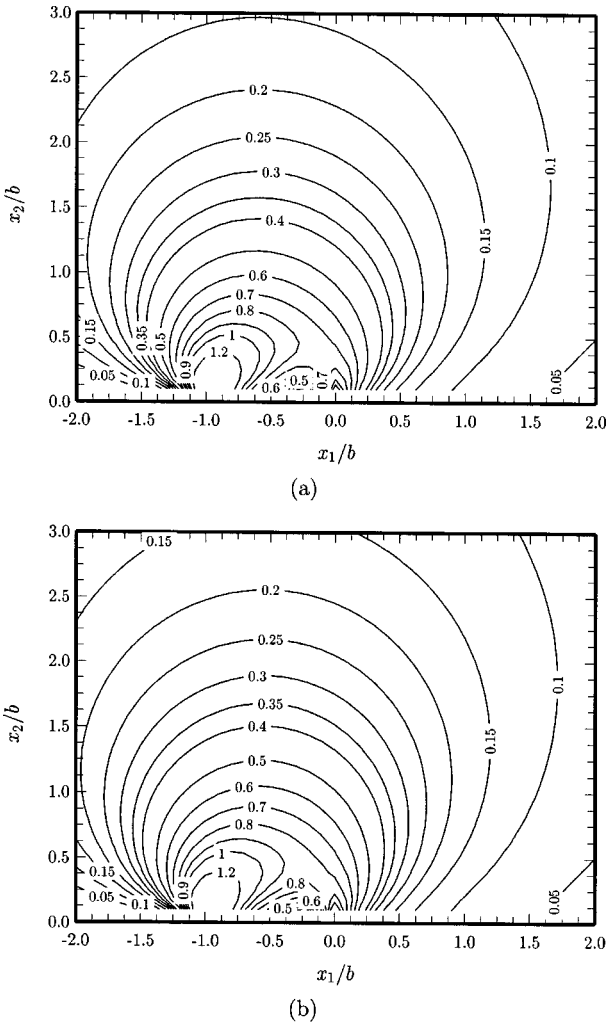

Fig. 8 Contour plots of the effective stress, σ_{eff}, for (a) $v/c_s=0.1$ and (b) $v/c_s=0.3$

5 Concluding Remarks

A stress analysis for the slitting process of a thin web material is presented in this study based on the dynamic fracture mechanics. The analysis leads to the determination of the stress and strain field for given slitter profile, web material properties, and moving velocity. It is shown that under the steady state conditions, the dynamic stress field surrounding the slitter is a function of the interacting traction and the friction between the moving web and the slitter, as well as a function of the web tension. By solving an integral equation, the normal interacting traction between the moving web and the slitter is determined as a function of the slitter profile and the web speed. For an ideal razor blade with the wedge profile, the contact condition between the moving web and the slitting blade is investigated and we found that the contact is controlled by the fracture toughness of the web material and the web speed. The fracture toughness of the web material itself might also depend on the web speed. The results presented in this paper provides the analytical foundation for studying the yielding zone

surrounding the slitting blade, thickening of the web along the slitting edge, and other phenomena that will affect the quality of web slitting.

The purpose of this work is to identify the key parameters that will contribute to the quality control during the web slitting process. The instability of the crack tip, web buckling in the region near the slitting blade, and the plastic yielding surrounding blade are believed to be the primary factors that affect the quality of the web cutting edges. In this study we are able to relate these quality-controlling factors to the mechanical conditions imposed on the web slitting process, such as the web speed and the remote tension along web moving direction, and the material parameters, including the fracture toughness of the web. The web material we considered here is assumed to be isotropic. However, the analytical method presented in this study can be extended to the situation where the web material is anisotropic. Some numerical examples are presented in this paper, but detailed parametric investigation which will lead to better design and improvement of the web slitting processes will be presented in a separate study.

Acknowledgments

The work of C.L. was supported financially by the U.S. Department of Energy, Defense Programs, Technology Transfer Initiative Program. H.L. would like to acknowledge the support under Grant No. 9697-1 from the NSF IUC/RC Research Center—Web Handling Research Center—at Oklahoma State University, the support by NSF (under CMS-9872350 and CMS-9985060), and the 3M Non-Tenured Faculty Grant. Y.H. acknowledges the support from NSF (under INT-9423964, CMS-9522147, and CMS-9983779), Motorola Foundation, and Ford Foundation.

References

[1] Meehan, R. R., and Burns, S. J., 1996, ''Mechanics of Slitting and Cutting Webs,'' Exp. Mech., **38**, pp. 103–109.
[2] Kasuga, Y., Tsutsumi, S., and Mori, T., 1977, ''On the Shearing Process of Ductile Sheet Metals (2nd Report Theoretical Analysis of the Scissors Type Shear),'' Bull. JSME, **20**, pp. 1336–1343.
[3] Arcona, C., and Dow, T. A., 1996, ''The Role of Knife Sharpness in the Slitting of Plastic Films,'' J. Mater. Sci., **31**, pp. 1327–1334.
[4] Bollen, D., Deneir, J., Aernoudt, E., and Muylle, W., 1989, ''Shear Cutting of PET Film,'' J. Mater. Sci., **24**, pp. 2957–2966.
[5] Bax, A. J., 1991, ''Characterization of Razor Slitting in Thin Sheets and Membranes,'' M.S. thesis, University of Tulsa.
[6] Zheng, Z. M., and Wierzbicki, T., 1996, ''A Theoretical Study of Steady-State Wedge Cutting Through Metal Plates,'' Int. J. Fract., **78**, pp. 45–66.
[7] Freund, L. B., 1990, *Dynamic Fracture Mechanics*, Cambridge University Press, New York.
[8] Muskhelishvili, N. I., 1954, *Some Basic Problems in the Mathematical Theory of Elasticity* (translated by J. R. M. Radok), Noordhoff, Groningen, The Netherlands.
[9] Cotterell, B., and Rice, J. R., 1980, ''Slightly Curved or Kinked Cracks,'' Int. J. Fract., **15**, pp. 155–169.
[10] Melin, S., 1992, ''Directional Instability of an Originally Straight Crack,'' Int. J. Fract., **53**, pp. 121–128.
[11] Broberg, K. B., 1999, *Cracks and Fracture*, Academic Press, London.

Hirotaka Sato[1]
e-mail: castle@wk9.so-net.ne.jp
Fracture Research Institute,
Graduate School of Engineering,
Tohoku University,
Aoba-yama 01,
Sendai 980-8579, Japan

Michihiro Kitahara
Department of Civil Engineering,
Graduate School of Engineering,
Tohoku University,
Aoba-yama 06,
Sendai 980-8579, Japan

Tetsuo Shoji
Fracture Research Institute,
Graduate School of Engineering,
Tohoku University,
Aoba-yama 01,
Sendai 980-8579, Japan

Boundary Element Analysis of Multiple Scattering Waves in High Performance Concretes

Advances in computing have allowed for the development of high performance concretes mathematically. We develop a method which combines the generalized self consistent model together with the boundary element method and the statistical averaging procedure to study the multiple scattering of plane elastic waves in concrete containing randomly distributed parallel fibers. In analysis, the concrete matrix is modeled by dispersed aggregate structure. The physical properties for a fiber-reinforced concrete are obtained numerically and shown in graphs for various microstructures at designated frequencies.
[DOI: 10.1115/1.1831299]

1 Introduction

The frequent use of the civil infrastructure under severe environments has increased the worldwide demands to develop technologies for design and maintenance of high performance concretes. The high performance concretes have possibilities to be applied by the various industries and to be developed to improve resistance to the hostile environments. In order to design, develop, and maintain the high performance concretes as new generation materials, especially fiber-reinforced concretes with the specially designed microstructures, there is a need to quantitatively describe the different classes of microstructure-physical property relationships from the viewpoints of nanoscopic, microscopic, mesoscopic, and macroscopic scales. Sato and Shindo [1,2] analyzed the scattering of in-plane compressional (P) and shear (SV) waves by a distribution of complex fibers by using the boundary element method (BEM) to control and catch the signs of the degradation. These methods neglect multiple scattering effects, and is suited to the composite materials containing dilute concentrations of fibers. In the composite materials containing dense concentrations of fibers, the problem of the propagation of multiple scattering waves has been investigated [3]. Recently, Sato and Shindo [4] studied the multiple scattering waves in a functionally graded material (FGM) and characterized the microstructures for the purpose of seeking ideally stable composite materials in any environments.

In this study, we consider the multiple scattering of plane elastic waves by a random distribution of fibers in concrete. We assume same-size fibers of identical properties, and concrete matrix which consists of mortar and small aggregates compared with the wavelength. To account for the multiple scattering at high concentrations of fibers, a method which combines the generalized self consistent model together with the boundary element method and the statistical averaging procedure is used to calculate frequency dependent phase velocities and attenuations of coherent waves. The solutions obtained are based on the plane strain assumption. In analysis, the microstructure of the concrete matrix changes with the change on the volume concentration of aggregates which are isolated from one another in the mortar. For calculating the elastic properties of the concrete matrix analytically, micromechanical model of dispersed aggregate structure is used. Numerical results for a steel fiber-reinforced concrete are obtained as a function of frequency, and the effects of multiple scattering and microstructures on the phase velocities and attenuations of the coherent waves, and the effective moduli for the steel fiber-reinforced concrete are discussed in detail.

2 Problem Statement and Analysis

We consider a random distribution of identical fibers in an infinite concrete matrix. To take into account the complex interaction among the concrete matrix and fibers, we must have a geometric model which consists of randomly distributed composite-inclusions in an infinite effective medium as shown in Fig. 1. It should be mentioned here that unknown complex wave numbers of the effective compressional (P) and shear (SV) waves in the effective medium are defined by K_p and K_{sv}, respectively. For the relevant roots, the real, and imaginary parts should be positive.

In order to study the propagations of effective P and SV waves in the composite-inclusions medium of Fig. 1, we first considered that the tentative scattered fields are assumed to be caused by a single composite inclusion. In the composite inclusion, which is embedded in the infinite effective medium with the mass density ρ^* and the effective Lamé constants λ^*, μ^* where a superscript $(*)$ denotes the effective component within the effective medium, fiber of radius a is surrounded by the concentric concrete matrix shell of outer radius b. Let λ, μ, ρ be the Lamé constants, the mass density of the concrete matrix, and λ_0, μ_0, ρ_0 those of the fiber. The geometry is depicted in Fig. 2, where (x_1, x_2, x_3) is the Cartesian coordinate system with origin at the center of the concrete matrix shell and fiber, B, D, and Ω are the domains of the effective medium, concrete matrix shell and fiber, and Γ and Γ_0 are the surfaces of the concrete matrix shell and fiber, respectively. Here, the shape variation of Γ_0 makes it possible to consider the effect of fiber shape, though Γ_0 is assumed to be circular in this study. The outer radius b of the circular concrete matrix shell, which corresponds to a spatially isotropic distribution of fibers, is related to the volume concentration of fibers c by

$$c = a^2/b^2. \tag{1}$$

The displacement components of the effective medium in the x_1 and x_2 directions are u_1^* and u_2^*, while the component u_3^* is absent because the problem is plane strain. For the same reason, derivatives with respect to x_3 are zero. The medium is in time-

[1]To whom correspondence should be addressed.

Contributed by the Applied Mechanics Division of THE AMERICAN SOCIETY OF MECHANICAL ENGINEERS for publication in the ASME JOURNAL OF APPLIED MECHANICS. Manuscript received by the Applied Mechanics Division, October 17, 2000; final revision; June 17, 2004. Associate Editor: S. Mukherjee.

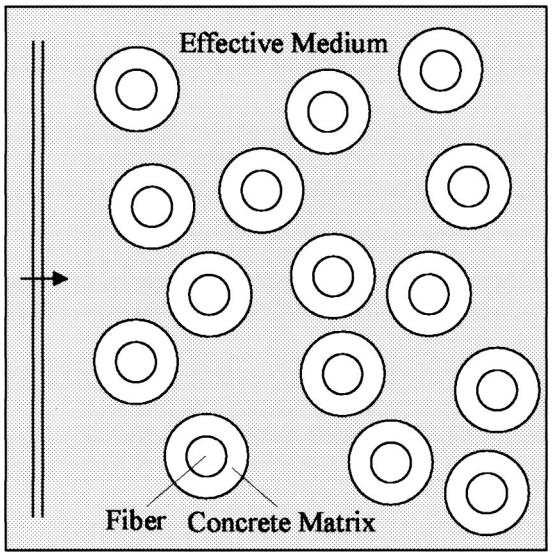

Fig. 1 Schematic diagram of composite-inclusions medium

harmonic motion, but the term $\exp(-i\omega t)$, where ω is the circular frequency and t is the time, will be omitted. Under these conditions, the stress equations of motion are given by $\sigma^*_{\beta\alpha,\beta}+\rho^*\omega^2 u^*_\alpha=0$. Here a comma denotes partial differentiation with respect to the coordinate, Greek indices can assume the values 1 and 2 only, $\sigma^*_{\beta\alpha}$ define the stress components which are related to the displacement gradients by Hooke's law, u^*_α denote the displacement components, and ρ^* is given by the average mass density as follows:

$$\rho^*=\rho(1-c)+\rho_0 c. \tag{2}$$

Then the effective Lamé constants λ^*, μ^* can be obtained from the phase velocities $\mathrm{Re}(k_p/K_p)$ and $\mathrm{Re}(k_{sv}/K_{sv})$ of the effective P and SV waves as follows:

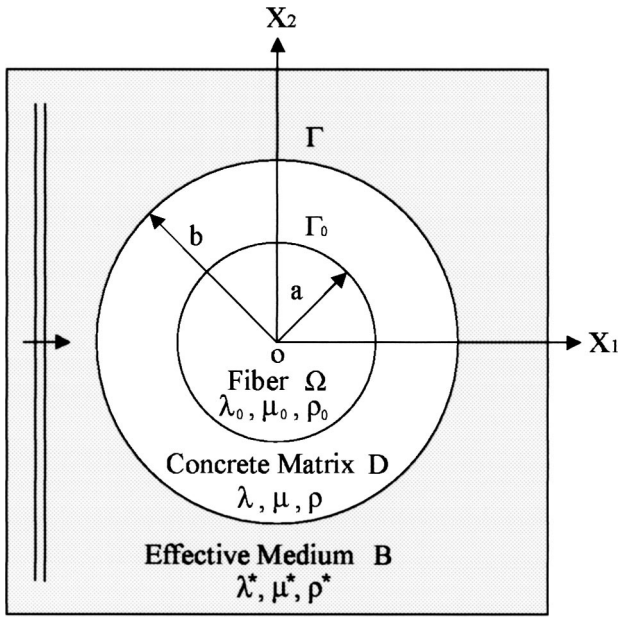

Fig. 2 Composite inclusion embedded in the effective medium and coordinate systems

$$\lambda^*+2\mu^*=(\lambda+2\mu)\left(\frac{\rho^*}{\rho}\right)\left[\mathrm{Re}\left(\frac{k_p}{K_p}\right)\right]^2, \tag{3}$$

$$\mu^*=\mu\left(\frac{\rho^*}{\rho}\right)\left[\mathrm{Re}\left(\frac{k_{sv}}{K_{sv}}\right)\right]^2, \tag{4}$$

where $k_p=\omega/c_p$ and $k_{sv}=\omega/c_{sv}$ are the wave numbers of the P and SV waves in the concrete matrix, and $c_p=[(\lambda+2\mu)/\rho]^{1/2}$ and $c_{sv}=(\mu/\rho)^{1/2}$ are the P and SV wave speeds in the concrete matrix, respectively. For the perfect bonding of fiber, the boundary conditions on Γ and Γ_0 can be written as

$$u^*_\alpha=u_\alpha, \quad t^*_\alpha+t_\alpha=0, \text{ on } \Gamma, \tag{5}$$

$$u_\alpha=u^t_\alpha, \quad t_\alpha+t^t_\alpha=0, \text{ on } \Gamma_0, \tag{6}$$

where a superscript t denotes the transmitted component within the fiber, $t^*_\alpha=\sigma^*_{\beta\alpha}n^*_\beta$, $t_\alpha=\sigma_{\beta\alpha}n_\beta$, and $t^t_\alpha=\sigma^t_{\beta\alpha}n^t_\beta$ are the traction components on the effective medium, concrete matrix shell and fiber, and n^*_β, n_β, and n^t_β are the unit outward normal components from B, D, and Ω, respectively. The boundary integral equations for the effective medium, concrete matrix shell and fiber are written as

$$c^*_{\alpha\beta}(\mathbf{x})u^*_\beta(\mathbf{x})=\int_\Gamma U^*_{\alpha\beta}(\mathbf{x},\mathbf{y})t^*_\beta(\mathbf{y})d\Gamma(\mathbf{y}) - \int_\Gamma T^*_{\alpha\beta}(\mathbf{x},\mathbf{y})u^*_\beta(\mathbf{y})d\Gamma(\mathbf{y})+u^*_0\exp(iK_p x_1)\mathbf{e}_1 + w^*_0\exp(iK_{sv}x_1)\mathbf{e}_2, \tag{7}$$

$$c_{\alpha\beta}(\mathbf{x})u_\beta(\mathbf{x})=\int_{\Gamma+\Gamma_0}U_{\alpha\beta}(\mathbf{x},\mathbf{y})t_\beta(\mathbf{y})d[\Gamma(\mathbf{y})+\Gamma_0(\mathbf{y})] - \int_{\Gamma+\Gamma_0}T_{\alpha\beta}(\mathbf{x},\mathbf{y})u_\beta(\mathbf{y})d[\Gamma(\mathbf{y})+\Gamma_0(\mathbf{y})], \tag{8}$$

$$c^t_{\alpha\beta}(\mathbf{x})u^t_\beta(\mathbf{x})=\int_{\Gamma_0}U^t_{\alpha\beta}(\mathbf{x},\mathbf{y})t^t_\beta(\mathbf{y})d\Gamma_0(\mathbf{y}) - \int_{\Gamma_0}T^t_{\alpha\beta}(\mathbf{x},\mathbf{y})u^t_\beta(\mathbf{y})d\Gamma_0(\mathbf{y}), \tag{9}$$

where $\mathbf{x}=x_1\mathbf{e}_1+x_2\mathbf{e}_2$ and $\mathbf{y}=y_1\mathbf{e}_1+y_2\mathbf{e}_2$ are the field and source points, $\mathbf{e}_1$ and $\mathbf{e}_2$ are the unit base vectors in the x_1 and x_2 directions, u^*_0 and w^*_0 are the amplitudes of the incident effective P and SV waves, the coefficients of $c^*_{\alpha\beta}$, $c_{\alpha\beta}$ and $c^t_{\alpha\beta}$ depend on the local geometries of Γ and Γ_0 at $\mathbf{x}$, and $U^*_{\alpha\beta}$, $T^*_{\alpha\beta}$, $U_{\alpha\beta}$, $T_{\alpha\beta}$, $U^t_{\alpha\beta}$, and $T^t_{\alpha\beta}$ are the fundamental solutions for displacement and traction in the effective medium, concrete matrix shell and fiber, respectively, given in Appendix A. Thus the tentative scattered fields at a large distance from a single composite inclusion is determined by Eqs. (5)–(9) and

$$u^{*s}_\alpha\sim u^*_0A^*_\alpha(K_p,\hat{\mathbf{x}})\sqrt{\frac{2}{\pi K_p|\mathbf{x}|}}\exp\left[i\left(K_p|\mathbf{x}|-\frac{\pi}{4}\right)\right] + w^*_0B^*_\alpha(K_{sv},\hat{\mathbf{x}})\sqrt{\frac{2}{\pi K_{sv}|\mathbf{x}|}}\exp\left[i\left(K_{sv}|\mathbf{x}|-\frac{\pi}{4}\right)\right], \tag{10}$$

where $\hat{\mathbf{x}}$ is a unit vector in the direction of observation, and the tentative far-field scattering amplitudes are

$$A^*_\alpha(K_p,\hat{\mathbf{x}})=\frac{1}{u^*_0}\int_\Gamma[C^{*p}_{\alpha\beta}(\hat{\mathbf{x}})t^*_\beta(\mathbf{y})+K_pD^{*p}_{\alpha\beta\gamma}(\hat{\mathbf{x}})n^*_\gamma(\mathbf{y})u^*_\beta(\mathbf{y})] \times\exp(-iK_p\hat{\mathbf{x}}\cdot\mathbf{y})d\Gamma(\mathbf{y}), \tag{11}$$

$$B^*_\alpha(K_{sv},\hat{\mathbf{x}})=\frac{1}{w^*_0}\int_\Gamma[C^{*sv}_{\alpha\beta}(\hat{\mathbf{x}})t^*_\beta(\mathbf{y})+K_{sv}D^{*sv}_{\alpha\beta\gamma}(\hat{\mathbf{x}})n^*_\gamma(\mathbf{y})u^*_\beta(\mathbf{y})]\times\exp(-iK_{sv}\hat{\mathbf{x}}\cdot\mathbf{y})d\Gamma(\mathbf{y}),\tag{12}$$

and Eqs. (*B*1)–(*B*4).

Now the statistical averaging procedure is used to obtain equations for determining the effective P and SV waves in terms of the tentative scattered fields from a single composite inclusion. It should be clarified here that the composite-inclusions medium of Fig. 1 represents the infinite concrete matrix containing randomly distributed fibers by c of Eq. (1), if the composite inclusions fill the effective medium space of Fig. 1 completely; that is, $c_b=n_b\pi b^2=1.0$, where c_b is the volume concentration of composite inclusions and n_b is the number of composite inclusions per unit area in the effective medium. This corresponds to the composite-cylinders model in [5]. It can be supposed that both the effective medium of Fig. 2 and the composite-inclusions medium ($c_b=1.0$) represent the infinite concrete matrix containing randomly distributed fibers. And the effective P and SV waves propagating through the effective medium of Fig. 2 should be the same as those propagating through the composite-inclusions medium ($c_b=1.0$), though we cannot prove that the effective medium of Fig. 2 is rigorously equivalent to the composite-inclusions medium ($c_b=1.0$). Thus, the problem, for which we present solutions, is that of obtaining relationships between the effective P and SV waves through those two mediums. To obtain the relationships, the statistical averaging procedure developed by Waterman and Truell [6] is applied to averaging waves over a random distribution of identical composite inclusions in the infinite effective medium of Fig. 1 in terms of the tentative far-field scattering amplitudes due to a single composite inclusion of Fig. 2. Combining K_p, K_{sv} of those two mediums in the x_1 direction, with the statistical averaging procedure, gives the following equations to be satisfied:

$$K_p^2=\left[K_p-\frac{2in_bA^*_1(K_p,\mathbf{e}_1)}{K_p}\right]^2-\left[\frac{2in_bA^*_1(K_p,-\mathbf{e}_1)}{K_p}\right]^2,\tag{13}$$

$$K_{sv}^2=\left[K_{sv}-\frac{2in_bB^*_2(K_{sv},\mathbf{e}_1)}{K_{sv}}\right]^2-\left[\frac{2in_bB^*_2(K_{sv},-\mathbf{e}_1)}{K_{sv}}\right]^2,\tag{14}$$

with

$$n_b=\frac{1}{\pi b^2}=\frac{c}{\pi a^2}.\tag{15}$$

Equations (13) and (14) are final forms for the determination of the complex wave numbers K_p and K_{sv} which are reasonable results at high concentrations and frequencies. It can be said that the solutions K_p, K_{sv} found with Eqs. (13) and (14) are equal to results of Fig. 2 guessed under the conditions:

$$A^*_1(K_p,\mathbf{e}_1)=0,\quad B^*_2(K_{sv},\mathbf{e}_1)=0,$$
$$A^*_1(K_p,-\mathbf{e}_1)=0,\quad B^*_2(K_{sv},-\mathbf{e}_1)=0.\tag{16}$$

For any of $\hat{\mathbf{x}}$ direction but the x_1 direction, the equations, with the statistical averaging procedure, are also given by

$$0=[0-2in_bA^*(K_p,\hat{\mathbf{x}})]^2-[2in_bA^*(K_p,-\hat{\mathbf{x}})]^2,\tag{17}$$

$$0=[0-2in_bB^*(K_{sv},\hat{\mathbf{x}})]^2-[2in_bB^*(K_{sv},-\hat{\mathbf{x}})]^2,\quad(\hat{\mathbf{x}}\neq\pm\mathbf{e}_1),\tag{18}$$

where

$$A^*(K_p,\hat{\mathbf{x}})\hat{x}_1\mathbf{e}_1+A^*(K_p,\hat{\mathbf{x}})\hat{x}_2\mathbf{e}_2=A^*_1(K_p,\hat{\mathbf{x}})\mathbf{e}_1+A^*_2(K_p,\hat{\mathbf{x}})\mathbf{e}_2$$

and

$$-B^*(K_{sv},\hat{\mathbf{x}})\hat{x}_2\mathbf{e}_1+B^*(K_{sv},\hat{\mathbf{x}})\hat{x}_1\mathbf{e}_2=B^*_1(K_{sv},\hat{\mathbf{x}})\mathbf{e}_1+B^*_2(K_{sv},\hat{\mathbf{x}})\mathbf{e}_2,$$

because no effective P and SV waves but $u^*_0\exp(iK_px_1)\mathbf{e}_1$ and $w^*_0\exp(iK_{sv}x_1)\mathbf{e}_2$ defined in Eq. (7) exist in the effective medium. Considering Eqs. (17), (18) and the composite-inclusion geometry, the tentative far-field scattering amplitudes have to be

$$A^*_\alpha(K_p,\hat{\mathbf{x}})=0,\quad B^*_\alpha(K_{sv},\hat{\mathbf{x}})=0,\quad(\hat{\mathbf{x}}\neq\pm\mathbf{e}_1).\tag{19}$$

Thus the tentative scattered fields of Eq. (10) are vanished due to $A^*_\alpha(K_p,\hat{\mathbf{x}})=0$ and $B^*_\alpha(K_{sv},\hat{\mathbf{x}})=0$ in any of $\hat{\mathbf{x}}$ direction. That is, the composite inclusion is equivalent to the effective medium.

It should be mentioned that we need to solve Eqs. (13) and (14) by using the iterative numerical scheme, because these equations can not be solved analytically. In carrying through the calculation by iteration, K_p and K_{sv} are expressed by K^p_j and K^{sv}_j ($j=0,1,2,\ldots$), respectively. Let sequences of K^p_j and K^{sv}_j be defined by

$$(K^p_{j+1})^2=\left[K^p_j-\frac{2in_bA^*_1(K^p_j,\mathbf{e}_1)}{K^p_j}\right]^2-\left[\frac{2in_bA^*_1(K^p_j,-\mathbf{e}_1)}{K^p_j}\right]^2,\tag{20}$$

$$(K^{sv}_{j+1})^2=\left[K^{sv}_j-\frac{2in_bB^*_2(K^{sv}_j,\mathbf{e}_1)}{K^{sv}_j}\right]^2-\left[\frac{2in_bB^*_2(K^{sv}_j,-\mathbf{e}_1)}{K^{sv}_j}\right]^2,\quad(j=0,1,2,\ldots),\tag{21}$$

with the tentative initial values of K^p_0 and K^{sv}_0. Then,

$$K_p=\lim_{j\to\infty}K^p_j,\quad K_{sv}=\lim_{j\to\infty}K^{sv}_j,\tag{22}$$

exist and are solutions of Eqs. (13) and (14), because the calculation is to make the effective medium be equivalent to the composite inclusion by averaging, i.e.,

$$\lim_{j\to\infty}A^*_1(K^p_j,\mathbf{e}_1)=0,$$
$$\lim_{j\to\infty}B^*_2(K^{sv}_j,\mathbf{e}_1)=0,$$
$$\lim_{j\to\infty}A^*_1(K^p_j,-\mathbf{e}_1)=0,$$
$$\lim_{j\to\infty}B^*_2(K^{sv}_j,-\mathbf{e}_1)=0,$$

which satisfy Eq. (16).

3 Numerical Results and Discussions

To examine the effects of multiple scattering and microstructures on the physical properties of the fiber-reinforced concrete, the unknown complex wave numbers of the effective P and SV waves have been computed. The values of K_p and K_{sv}, as determined above, are obviously complex. The phase velocities of the effective P and SV waves are $\mathrm{Re}(k_p/K_p)$ and $\mathrm{Re}(k_{sv}/K_{sv})$. Their corresponding attenuations are $\mathrm{Im}(K_p/k_p)$ and $\mathrm{Im}(K_{sv}/k_{sv})$, respectively. The considered fiber was steel, and concrete matrices were mortar without aggregates (Case I), mortar with limestone aggregates (Case II) and mortar with ingot iron aggregates (Case III). Limestone and ingot iron aggregates are corresponding to the normal weight and heavy weight aggregates, respectively. The size of aggregates is assumed to be sufficiently small compared to that of fibers and the wavelength, so there is no wave scattering by a distribution of aggregates. The constituent properties are given in Table 1, where λ_{mor}, μ_{mor}, ρ_{mor} are the Lamé constants, the mass density of the mortar, and λ_{agg}, μ_{agg}, ρ_{agg} those of the aggregates.

For calculating the elastic properties of the concrete matrix, a micromechanical model is used consisting of one lumped three-

Table 1 Material properties of steel, mortar, limestone, and ingot iron

Steel fiber	ρ_0 (t/m^3) 7.8	μ_0 (GPa) 78.13	$\lambda_0+2\mu_0$ (GPa) 255.7
Mortar	ρ_{mor} (t/m^3) 1.4	μ_{mor} (GPa) 11.08	$\lambda_{mor}+2\mu_{mor}$ (GPa) 29.56
Limestone aggregate	ρ_{agg} (t/m^3) 2.6	μ_{agg} (GPa) 24.38	$\lambda_{agg}+2\mu_{agg}$ (GPa) 65.00
Ingot iron aggregate	ρ_{agg} (t/m^3) 7.2	μ_{agg} (GPa) 37.25	$\lambda_{agg}+2\mu_{agg}$ (GPa) 138.3

dimensional aggregate and continuous mortar as shown in Fig. 3. Changing the volume concentration of aggregates, a number of profiles can be examined with this model. The Lamé constants λ and μ of the concrete matrix are considered to vary as

$$\lambda = \frac{E\nu}{(1+\nu)(1-2\nu)}, \tag{23}$$

$$\mu = \frac{E}{2(1+\nu)}, \tag{24}$$

where E and ν are the Young's modulus and Poisson's ratio of the concrete matrix. The composition dependent maximum Young's modulus and Poisson's ratio of the concrete matrix are obtained, in accordance with the rule of mixture like [7], as

$$E = \left[\frac{1-\zeta}{E_{mor}} + \frac{\zeta}{E_{mor}(1-\zeta^2)+E_{agg}\zeta^2}\right]^{-1}, \tag{25}$$

$$\nu = \frac{\nu_{mor}[nm+(n+m-1)(1+\zeta)\zeta](1-\zeta)+\nu_{agg}(n+m-1)\zeta^3}{[n+(m-1)\zeta][m-(m-1)\zeta]}, \tag{26}$$

where

$$n = \zeta^2 + \frac{E_{agg}}{E_{mor}}(1-\zeta^2), \quad m = (1-\zeta^2) + \frac{E_{agg}}{E_{mor}}\zeta^2, \tag{27}$$

$$V_{agg} = \zeta^3, \quad \zeta = \frac{l}{L}, \tag{28}$$

and V_{agg} is the volume concentration of aggregates in the mortar, E_{agg} and E_{mor} are the Young's moduli of the aggregate and mortar,

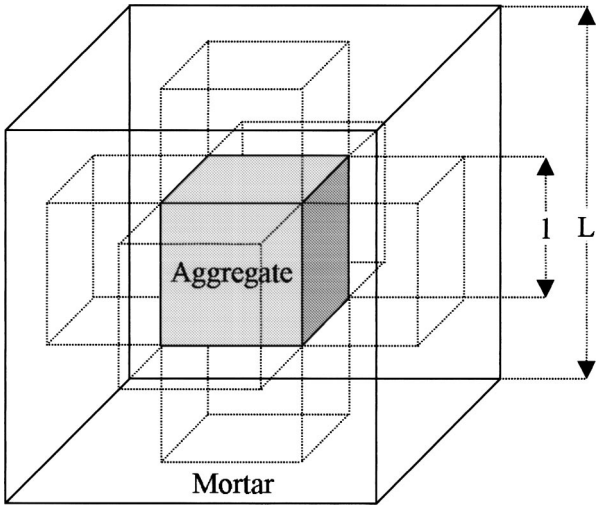

Fig. 3 Micromechanical model of concrete matrix

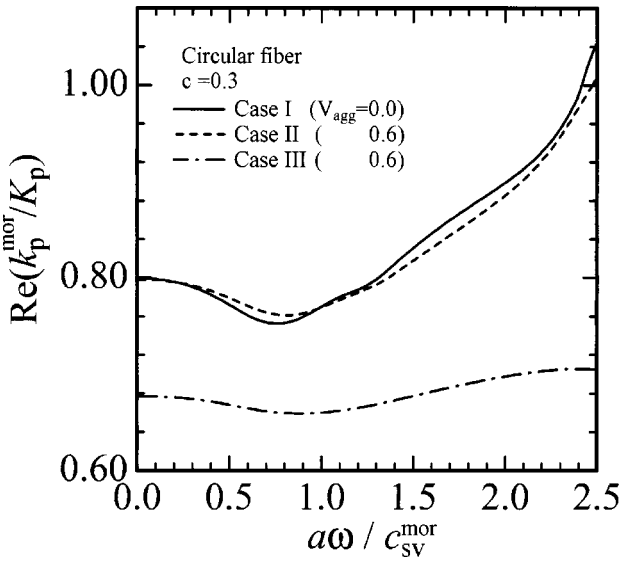

Fig. 4 Effect of concrete matrix on phase velocity versus frequency for P wave

and ν_{agg} and ν_{mor} are Poisson's ratios of the aggregate and mortar. The composition dependent minimum Young's modulus and Poisson's ratio are also given by

$$E = E_{mor}(1-\zeta^2) + \frac{E_{mor}E_{agg}\zeta^2}{E_{mor}\zeta + E_{agg}(1-\zeta)}, \tag{29}$$

$$\nu = \frac{\nu_{mor}[nm(1+\zeta)+(n+m-1)\zeta^2](1-\zeta)+\nu_{agg}(n+m-1)\zeta^3}{nm}, \tag{30}$$

where

$$n = \zeta + \frac{E_{agg}}{E_{mor}}(1-\zeta), \quad m = (1-\zeta) + \frac{E_{agg}}{E_{mor}}\zeta. \tag{31}$$

Values of E and ν calculated with Eqs. (25)–(28) are always larger than those calculated with Eqs. (29)–(31). It may be taken that Eqs. (25)–(28) give upper, and Eqs. (29)–(31) lower estimates of the Young's modulus and Poisson's ratio of the concrete matrix. After this, we use Eqs. (29)–(31) to get the elastic properties of the concrete matrix. The density of the concrete matrix is given by

$$\rho = \rho_{mor}(1-V_{agg}) + \rho_{agg}V_{agg}. \tag{32}$$

Figures 4 and 5 show the variations of the phase velocities $\mathrm{Re}(k_p^{mor}/K_p)$ and $\mathrm{Re}(k_{sv}^{mor}/K_{sv})$ of the effective P and SV waves with the frequency $a\omega/c_{sv}^{mor}$ for Cases I ($V_{agg}=0.0$), II, III ($V_{agg}=0.6$), and $c=0.3$, where $k_p^{mor}=\omega/c_p^{mor}$ and $k_{sv}^{mor}=\omega/c_{sv}^{mor}$ are the wave numbers of the P and SV waves in the mortar, and $c_p^{mor}=[(\lambda_{mor}+2\mu_{mor})/\rho_{mor}]^{1/2}$ and $c_{sv}^{mor}=(\mu_{mor}/\rho_{mor})^{1/2}$ are the P and SV wave speeds in the mortar. Up to approximately $a\omega/c_{sv}^{mor}=1.5$, the variations of the phase velocities are not so remarkable. For higher frequencies, the discrepancies of the phase velocities for Cases I, II, and III appear as the frequency is increased in the calculated range.

Figures 6 and 7 show the variations of the attenuations $\mathrm{Im}(K_p/k_p^{mor})$ and $\mathrm{Im}(K_{sv}/k_{sv}^{mor})$ of the effective P and SV waves with the frequency $a\omega/c_{sv}^{mor}$ for Cases I ($V_{agg}=0.0$), II, III ($V_{agg}=0.6$), and $c=0.3$. It is found that the attenuations increase with the frequency and reach the maximum values around $a\omega/c_{sv}^{mor}=1.2$–1.6. The maximum value for Case I is higher than those for Cases II and III. The abilities of damping are dependent on the aggregates when the volume concentrations of fibers are equal in the concretes, because the aggregates change the wave speeds in

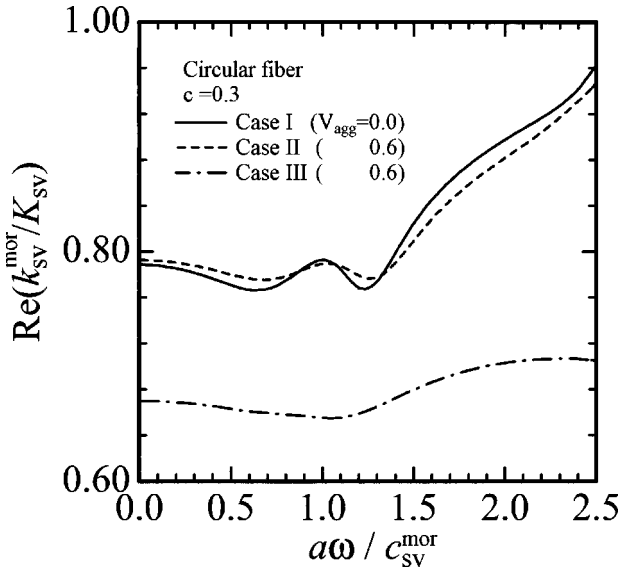

Fig. 5 Effect of concrete matrix on phase velocity versus frequency for SV wave

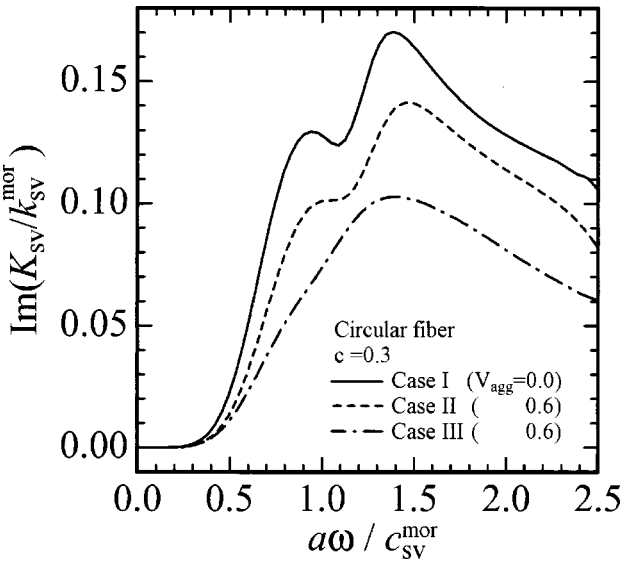

Fig. 7 Effect of concrete matrix on attenuation versus frequency for SV wave

the concrete matrix and the chance of wave scattering by fibers. The characteristics of the attenuations that are most sensitive to the microstructures may be the best to be utilized in determining the conditions of the fiber-reinforced concretes nondestructively.

Figures 8 and 9 show the variations of the effective in-plane bulk $k^*=\lambda^*+\mu^*$ and shear μ^* moduli with the frequency $a\omega/c_{sv}^{mor}$ for Cases I ($V_{agg}=0.0$), II, III ($V_{agg}=0.6$), and $c=0.3$. The changes of the elastic moduli are relatively small at lower frequencies. For Case III, the elastic moduli do not also tend to change extensively at higher frequencies compared with Cases I and II. However, after passing around $a\omega/c_{sv}^{mor}=1.5$, the elastic moduli for Cases I and II are increased and exceed those for Case III dramatically as the frequency is increased. It should also be emphasized that the results of the effective in-plane bulk modulus calculated from the present theory converge to those obtained from the Eshelby method [8] (Eq. (*C*1)) and the composite cylinder assemblage (CCA) model [5] (Eq. (*C*5)) as $a\omega/c_{sv}^{mor}\rightarrow 0.0$. Again the convergence in the effective in-plane shear moduli for the static limit calculated from the present theory and the Eshelby method [8] (Eq. (*C*2)) is good. Thus, the dynamic elastic moduli of the steel-fiber-reinforced concretes have the unique characters. These concretes can be used safely under the dynamic conditions at higher frequencies calculated. But it is desirable to be analyzed carefully at lower frequencies for the safe use of the concretes.

Figure 10 shows the variation of the phase velocity $\mathrm{Re}(k_p^{mor}/K_p)$ of the effective P wave with the volume concentration of fibers c for $a\omega/c_{sv}^{mor}=1.0$ and Cases I ($V_{agg}=0.0$), II, III ($V_{agg}=0.6$). The phase velocity decreases with the change in the aggregate at $c=0.0$, because the elastic properties of the concrete matrix are altered by the combination of constituents. The multiple scattering effect appeares as the volume concentration of fibers is increased. Unlike the previous case of $c=0.0$, the phase velocity indicates complex trend with increasing volume concentration of fibers. Figure 11 shows the variation of the attenuation $\mathrm{Im}(K_p/k_p^{mor})$.

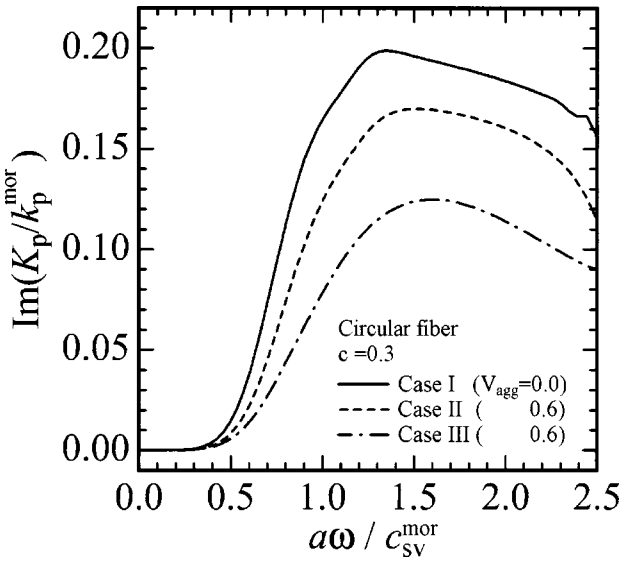

Fig. 6 Effect of concrete matrix on attenuation versus frequency for P wave

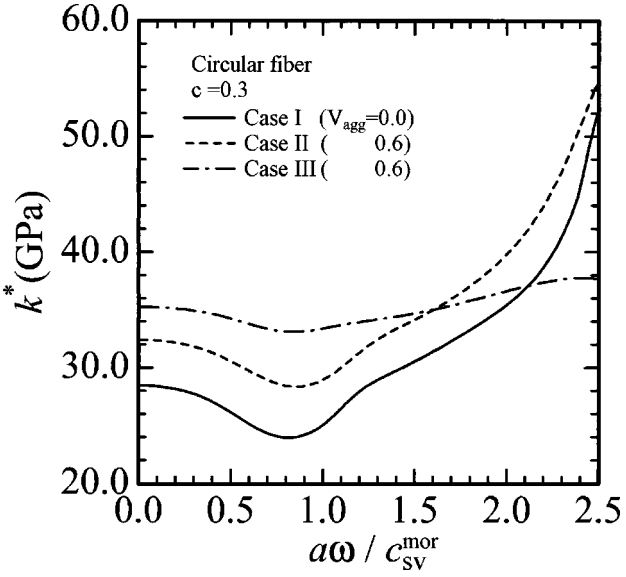

Fig. 8 Effect of concrete matrix on in-plane bulk modulus versus frequency

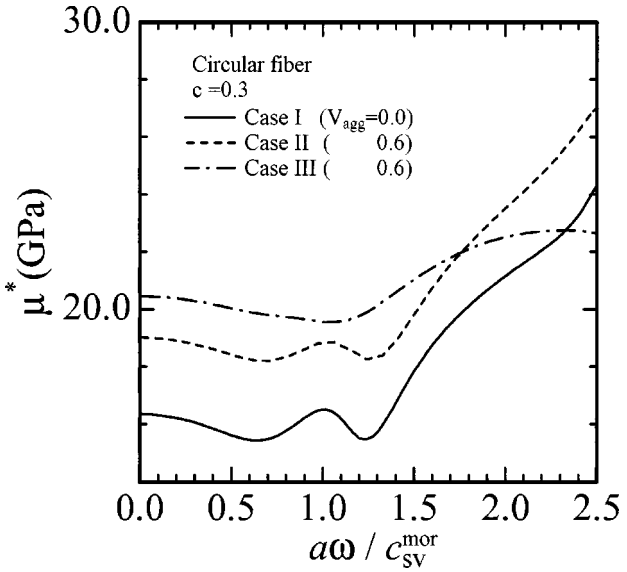

Fig. 9 Effect of concrete matrix on in-plane shear modulus versus frequency

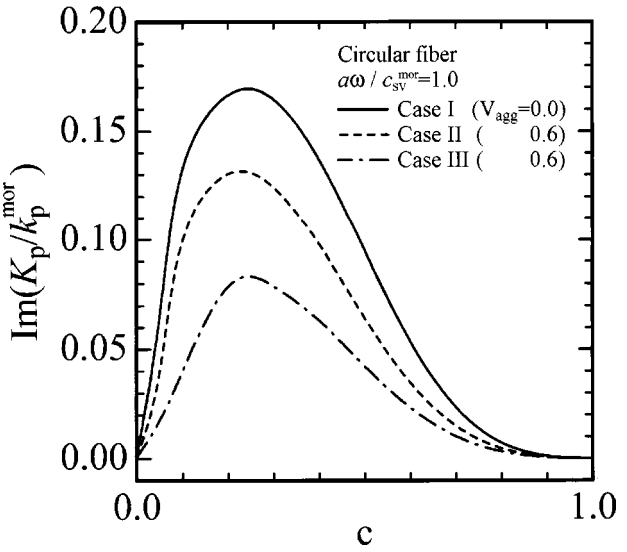

Fig. 11 Effect of concrete matrix on attenuation versus concentration for P wave

When $c=0.0$, no significant effect of the aggregates on attenuation is found compared with the phase velocity. The attenuation increases rapidly with the volume concentration of fibers at low volume concentrations and then decreases slowly to zero as the volume concentration of fibers increases to one because of the multiple scattering effect. The maximum attenuation of the effective P wave for Case I is higher than the other Cases. Thus the damping properties of waves in concretes can be controlled by the volume concentrations of fibers and aggregates.

4 Conclusions

The development of high performance concretes is important for the safe use of high-cost concrete structures. We have developed the method that can analyze the physical properties of fiber-reinforced concretes. In this method, the fiber-reinforced concrete, which is also expressed by the effective medium, can be considered as the whole world formed by identical fibers through a concrete matrix, while the composite inclusion can be regarded as the individual world formed by one fiber which has relation with the whole world through the concrete matrix. And, the equivalence of those two worlds is the essential principle to make the medium exist. Therefore, for the existence of a certain phenomenon, i.e., a certain coherent wave propagation, in the whole world, the individual world must be equivalent to the whole world. On the contrary, the variety of individual world and the principle of equivalence can materialize a variety of whole worlds and phenomena. This method can shed some new light on the creation of the fiber-reinforced concretes with the desired complex microstructures on the one hand, and predict the nanoscopic, microscopic, mesoscopic and macroscopic relations of the microstructures on the other hand. The effect of multiple scattering caused by the combination of fiber and small aggregate in the composite inclusion can, for example, really vary the phase velocities, attenuations of the coherent waves in the fiber-reinforced concretes, and the effective elastic moduli, and depend on the frequency. Fiber is the most important constituent which causes the multiple wave scattering in the fiber-reinforced concretes. It is effective to consider the small aggregate, in support of the development of nanotechnology, for changing the wave speed in the concrete matrix without the occurrence of wave scattering from the aggregate. Also, the physical properties show relatively constant trends at lower frequencies, as similarly found in undamaged composite materials [1,2,4], in spite of complex changes of the microstructures. These results provide significant information to design the ideal fiber-reinforced concretes that yield not only desirable strengths but also performances that are often not available in nature. Thus the present study can provide an appropriate methodology for such analyses to be made.

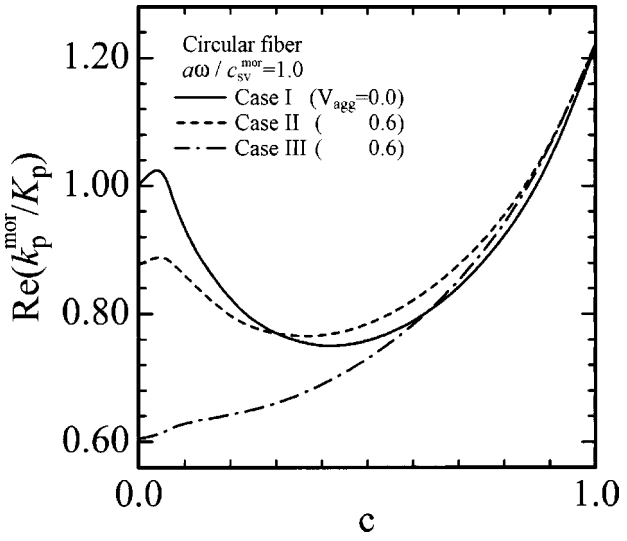

Fig. 10 Effect of concrete matrix on phase velocity versus concentration for P wave

Appendix A

The fundamental solutions of the effective medium have the following forms:

$$U^*_{\alpha\beta}(\mathbf{x},\mathbf{y}) = \frac{iK^2_{sv}}{4\rho^*\omega^2}\left(\eta^*\delta_{\alpha\beta} - \kappa^* r_{,\alpha} r_{,\beta}\right), \qquad (A1)$$

$$T^*_{\alpha\beta}(\mathbf{x},\mathbf{y})=\frac{i}{4}\left[\left(\frac{d\eta^*}{dr}-\frac{\kappa^*}{r}\right)\left(\delta_{\alpha\beta}\frac{\partial r}{\partial n^*}+n^*_\alpha r_{,\beta}\right)\right.$$
$$-2\frac{\kappa^*}{r}\left(n^*_\beta r_{,\alpha}-2r_{,\alpha}r_{,\beta}\frac{\partial r}{\partial n^*}\right)-2\frac{d\kappa^*}{dr}r_{,\alpha}r_{,\beta}\frac{\partial r}{\partial n^*}$$
$$\left.-\left\{2-\left(\frac{K_{sv}}{K_p}\right)^2\right\}\left(\frac{d\eta^*}{dr}-\frac{d\kappa^*}{dr}-\frac{\kappa^*}{r}\right)r_{,\alpha}n^*_\beta\right], \quad (A2)$$

where

$$\eta^*=H_0(K_{sv}r)-\frac{1}{K_{sv}r}\left\{H_1(K_{sv}r)-\frac{K_p}{K_{sv}}H_1(K_pr)\right\}, \quad (A3)$$

$$\kappa^*=-H_2(K_{sv}r)+\left(\frac{K_p}{K_{sv}}\right)^2H_2(K_pr). \quad (A4)$$

In the above, $\delta_{\alpha\beta}$ is the Kronecker delta, $r=|\mathbf{x}-\mathbf{y}|$, $\partial/\partial n^*$ denotes the directional differentiation along the unit outward normal vector $\mathbf{n}^*$ to Γ, and $H_l(\,)$ is the lth order Hankel function of the first kind. It is also necessary to express η^* and κ^* by the static and regular parts for sufficiently small K_pr and $K_{sv}r$ to cancel the higher order singularities. The fundamental solutions $U_{\alpha\beta}$ and $T_{\alpha\beta}$ are defined by Eqs. (*A*1)–(*A*4), but with the k_p, k_{sv} of the concrete matrix, and the unit outward normal vector $\mathbf{n}$. $U^t_{\alpha\beta}$ and $T^t_{\alpha\beta}$ are also obtained by replacing K_p, K_{sv}, $\mathbf{n}^*$ by k^t_p, k^t_{sv}, $\mathbf{n}^t$ in Eqs. (*A*1)–(*A*4). $k^t_p=\omega/c^t_p$ and $k^t_{sv}=\omega/c^t_{sv}$ are the wave numbers of the P and SV waves in the fiber, and $c^t_p=[(\lambda_0+2\mu_0)/\rho_0]^{1/2}$ and $c^t_{sv}=(\mu_0/\rho_0)^{1/2}$ are the P and SV wave speeds in the fiber, respectively.

Appendix B

$C^{*p}_{\alpha\beta}$, $D^{*p}_{\alpha\beta\gamma}$, $C^{*sv}_{\alpha\beta}$ and $D^{*sv}_{\alpha\beta\gamma}$ in Eqs. (11) and (12) are

$$C^{*p}_{\alpha\beta}(\hat{\mathbf{x}})=\frac{iK_p^2}{4\rho^*\omega^2}\hat{x}_\alpha\hat{x}_\beta, \quad (B1)$$

$$C^{*sv}_{\alpha\beta}(\hat{\mathbf{x}})=\frac{iK_{sv}^2}{4\rho^*\omega^2}(\delta_{\alpha\beta}-\hat{x}_\alpha\hat{x}_\beta), \quad (B2)$$

$$D^{*p}_{\alpha\beta\gamma}(\hat{\mathbf{x}})=\frac{1}{4}\hat{x}_\alpha\left\{\left[1-2\left(\frac{K_p}{K_{sv}}\right)^2\right]\delta_{\beta\gamma}+2\left(\frac{K_p}{K_{sv}}\right)^2\hat{x}_\beta\hat{x}_\gamma\right\}, \quad (B3)$$

$$D^{*sv}_{\alpha\beta\gamma}(\hat{\mathbf{x}})=\frac{1}{4}(\delta_{\alpha\beta}\hat{x}_\gamma+\delta_{\alpha\gamma}\hat{x}_\beta-2\hat{x}_\alpha\hat{x}_\beta\hat{x}_\gamma). \quad (B4)$$

Appendix C

Using the Eshelby method, we obtain the effective in-plane bulk modulus k^* and shear modulus μ^* as [8]

$$k^*=(1-c)k+ck_0+c(1-c)\frac{(k_0-k)(1/k_0-1/k)}{(1-c)/k+c/k_0+\mu/kk_0}, \quad (C1)$$

$$\mu^*=(1-c)\mu+c\mu_0$$
$$+c(1-c)\frac{(\mu_0-\mu)(1/\mu_0-1/\mu)}{(1-c)/\mu+c/\mu_0+(k/\mu_0)/(k+2\mu)}, \quad (C2)$$

where $k=\lambda+\mu$, $k_0=\lambda_0+\mu_0$ are the in-plane bulk moduli of the concrete matrix and fiber.

Making use of the law of mixture, we also have

$$k^*=\frac{E^*}{2(1+\nu^*)(1-2\nu^*)}, \quad (C3)$$

$$\mu^*=\frac{E^*}{2(1+\nu^*)}, \quad (C4)$$

where E^* and ν^* are the Young's modulus and Poisson's ratio of the effective medium in the form

$$E^*=\frac{2(1+\nu_0)(1+\nu)\mu_0\mu}{(1+\nu_0)\mu_0(1-c)+(1+\nu)\mu c},$$

$$\nu^*=\nu(1-c)+\nu_0c.$$

Using the composite cylinder assemblage (CCA) model [5], we also obtain the effective in-plane bulk modulus k^* in the form

$$k^*=k+\frac{c(k_0-k)(k+\mu)}{k_0+\mu-c(k_0-\mu)}. \quad (C5)$$

The generalized self consistent model [9] yields an expression for the effective in-plane shear modulus over the entire volume concentration range. Their result is the quadratic equation

$$A\left(\frac{\mu^*}{\mu}\right)+2B\left(\frac{\mu^*}{\mu}\right)+C=0, \quad (C6)$$

where

$$A=3c(1-c)^2\left(\frac{\mu_0}{\mu}-1\right)\left(\frac{\mu_0}{\mu}+\eta_0\right)+\left[\frac{\mu_0}{\mu}\eta+\eta_0\eta\right.$$
$$\left.-\left(\frac{\mu_0}{\mu}\eta-\eta_0\right)c^3\right]\left[\eta c\left(\frac{\mu_0}{\mu}-1\right)-\left(\frac{\mu_0}{\mu}\eta+1\right)\right],$$

$$B=-3c(1-c)^2\left(\frac{\mu_0}{\mu}-1\right)\left(\frac{\mu_0}{\mu}+\eta_0\right)+\frac{1}{2}\left[\frac{\mu_0}{\mu}\eta+\left(\frac{\mu_0}{\mu}-1\right)c+1\right]$$
$$\times\left[\left(\frac{\mu_0}{\mu}-1\right)\left(\frac{\mu_0}{\mu}+\eta_0\right)-2\left(\frac{\mu_0}{\mu}\eta-\eta_0\right)c^3\right]$$
$$+\frac{c}{2}(\eta+1)\left(\frac{\mu_0}{\mu}-1\right)\left[\frac{\mu_0}{\mu}+\eta_0+\left(\frac{\mu_0}{\mu}\eta-\eta_0\right)c^3\right],$$

$$C=3c(1-c)^2\left(\frac{\mu_0}{\mu}-1\right)\left(\frac{\mu_0}{\mu}+\eta_0\right)$$
$$+\left[\frac{\mu_0}{\mu}\eta+\left(\frac{\mu_0}{\mu}-1\right)c+1\right]\left[\frac{\mu_0}{\mu}+\eta_0+\left(\frac{\mu_0}{\mu}\eta-\eta_0\right)c^3\right],$$

$$\eta=3-4\nu,$$

$$\eta_0=3-4\nu_0.$$

References

[1] Sato, H., and Shindo, Y., 2002, "Scattering of Compressional and Shear Waves by a Polygonal Inclusion," Mech. Adv. Mater. Struct., **9**, pp. 81–94.

[2] Sato, H., and Shindo, Y., 2002, "Influence of Microstructure on Scattering of Plane Elastic Waves by a Distribution of Partially Debonded Elliptical Inclusions," Mech. Mater., **34**, pp. 401–409.

[3] Yang, R. B., and Mal, A. K., 1994, "Multiple Scattering of Elastic Waves in a Fiber-Reinforced Composite," J. Mech. Phys. Solids, **42**, pp. 1945–1968.

[4] Sato, H., and Shindo, Y., 2001, "Multiple Scattering of Plane Elastic Waves in a Fiber-Reinforced Composite Medium With Graded Interfacial Layers," Int. J. Solids Struct., **38**, pp. 2549–2571.

[5] Hashin, Z., and Rosen, R. W., 1964, "The Elastic Moduli of Fiber-Reinforced Materials," ASME J. Appl. Mech., **31**, pp. 223–232.

[6] Waterman, P. C., and Truell, R., 1961, "Multiple Scattering of Elastic Waves," J. Mech. Phys, **2**, pp. 512–537.

[7] Tuchinskii, L. I., 1983, "Elastic Constants of Pseudoalloys With a Skeletal Structure," Poroshk. Metall. (Kiev), **247**, pp. 85–92.

[8] Wakashima, K., 1976, "Macroscopic Mechanical Properties of Composite Materials. II. Elastic Moduli and Thermal Expansion Coefficients," Jpn. Soc. Composite Mater., **2**, pp. 161–167 (in Japanese).

[9] Christensen, R. M., and Lo, K. H., 1979, "Solutions for Effective Shear Properties in Three Phase Sphere and Cylinder Models," J. Mech. Phys. Solids, **27**, pp. 315–330.

Foundation of Correlation Parameters for Eliminating Pulse Shape Effects on Dynamic Plastic Response of Structures

Q. M. Li
School of Mechanical,
Aerospace and Civil Engineering,
Pariser Building,
The University of Manchester,
P. O. Box 88, Sackville Street,
Manchester M60 1QD, UK

Norman Jones[1]
Impact Research Centre,
Department of Engineering (Mechanical),
University of Liverpool,
Liverpool L69 3GH, UK

The theoretical foundation of Youngdahl's correlation parameters, which have been used to eliminate pulse shape effects in the dynamic plastic response of two-dimensional structural members, is studied in the present paper with the aid of bounds obtained for a rigid-plastic material. It is shown that Youngdahl's empirical estimate for the structural response time is, in general, a lower bound on the actual response time. A lower bound expression is obtained for the maximum final displacement of a two-dimensional structural member when subjected to an axisymmetrically loaded transverse time-dependent pulse, which depends only on Youngdahl's correlation parameters, and offers a theoretical foundation for the validity of Youngdahl's correlation parameter method.
[DOI: 10.1115/1.1839183]

1 Introduction

The impact and blast pulse loading shapes are difficult to repeat in both laboratory and practical conditions, and, therefore, it is necessary to understand the importance of loading shape effects on the response of structures under various pulse loads. Symonds [1] proposed that the peak load and loading impulse could be used to represent an impact or blast loading pulse. Abrahamson and Lindberg [2] used the peak load and loading impulse to define a critical loading curve for structural failure. A similar method known as the pressure-impulse diagram, or P-I diagram, has been used in protective construction design to resist blast loading [3]. When the applied loading intensity is much larger than the load to cause yielding, the peak load and loading impulse could be considered as two representative parameters for a pulse loading. However, this simplification, otherwise, may introduce a large error, as shown by Hodge [4].

Two correlation parameters have been proposed by Youngdahl [5,6] to eliminate pulse shape effects on the dynamic plastic response of two-dimensional structural members, i.e.,

$$I_e = \int_{t_y}^{t_f} P(t)dt \tag{1}$$

and

$$P_e = \frac{I_e}{2t_{mean}}, \tag{2}$$

where t_y is the time when the structural plastic response starts, t_f is the time when the structural response ceases, and

$$t_{mean} = \frac{1}{I_e}\int_{t_y}^{t_f}(t-t_y)P(t)dt. \tag{3}$$

Youngdahl's correlation parameters have been widely used as effective loading parameters to eliminate the pulse shape effects in the dynamic plastic response of structures [7,8]. This method was proposed originally for the plastic bending response of several structural members. Later studies have shown that Youngdahl's correlation parameter method is valid when transverse shear force plays an important role [9–11] and when the interaction between a structure and the damping medium exists [12].

Although Youngdahl's correlation parameter method has been used successfully for many cases, there is no general theoretical foundation to support this empirically proposed correlation method. In the present paper, bounds will be used to provide a theoretical foundation for the validity of Youngdahl's correlation parameter method.

2 Bounds and Basic Principles

An upper bound on the final displacement, a lower bound on the structural response time and a lower bound on the maximum final displacement have been developed for dynamically loaded, rigid-plastic continua. These theorems can be used to estimate the overall response characteristics of dynamically loaded, two-dimensional structural members, such as beams, circular plates and cylindrical shells.

The bounds are obtained using the principle of virtual velocities, d'Alembert's principle and Drucker's postulate for material stability. Martin [13,14] obtained an upper bound on the final displacement and a lower bound on the structural response time for impulsively loaded, rigid-plastic continua, which were extended in [15] to the cases when a time-dependent surface traction is considered. Reference [16] extended these bounds to cater for large deformation effects.

A lower bound on the maximum final displacement of a rigid-plastic continuum was obtained in [17] for the impulsive loading case, and clarified in [18,19]. This lower bound theorem was extended in [20] to include time-dependent surface tractions, and was investigated in [21] to give a more concise and less restrictive expression.

Good agreements between these upper and lower bounds, the mode approximation [22] and exact solutions on the central deflection of a simply-supported rigid-plastic beam were obtained in [20]. Reference [23] also reviewed the development of the bound

[1]To whom correspondence should be addressed.

Contributed by the Applied Mechanics Division of THE AMERICAN SOCIETY OF MECHANICAL ENGINEERS for publication in the ASME JOURNAL OF APPLIED MECHANICS. Manuscript received by the Applied Mechanics Division, February 13, 2001; final revision, August 10, 2004. Associate Editor: B. M. Moran. Discussion on the paper should be addressed to the Editor, Prof. Robert M. McMeeking, Journal of Applied Mechanics, Department of Mechanical and Environmental Engineering, University of California—Santa Barbara, Santa Barbara, CA 93106-5070, and will be accepted until four months after final publication in the paper itself in the ASME JOURNAL OF APPLIED MECHANICS.

methods and discussed their accuracy for estimating the bending response of dynamically loaded, rigid, perfectly plastic structural elements.

Bound theorems were used in [7] to estimate the maximum final displacements of simply supported beams, circular plates and cylindrical shells when transverse shear effects are important. These provided excellent estimates of the response duration and maximum final displacements of rigid, perfectly plastic theoretical analyses for impulsively loaded structural members. Similar conclusions were supported by works on fully clamped beams, circular plates and cylindrical shells [9–11].

Generalized stresses and strains, which have been defined in many textbooks (e.g., [24]), are used in the following analyses for two-dimensional structural members, such as beams, plates and shells. Q_j and q_j $(j=1,\ldots,n)$ in the present paper represent generalized stresses and strains, and u_j and ν_j $(j=1,\ldots,m)$ are generalized displacements and velocities. If a virtual velocity field, $\dot{u}_j^c$, is defined by a set of kinematically admissible velocities, and $\dot{q}_j^c$ are the associated components of the strain rate field, then the rate of the total internal energy dissipation for the given virtual velocity field $\dot{u}_j^c$ is

$$D(Q_j,\dot{u}_j^c)=\int_S Q_j\dot{q}_j^c\,dS, \tag{4}$$

and the corresponding total external energy dissipation rate is

$$\dot{E}(\dot{u}_j^c)=\int_L c_j\dot{u}_j^c\,dL+\int_S(F_j-\mu\dot{\nu}_j)\dot{u}_j^c\,dS, \tag{5}$$

where L is the boundary surrounding the area S. c_j are the generalized forces at the boundary L, which are work conjugate to the generalized displacements u_j. F_j are the external pressure loads acting on the area, which may include the gravitational force μg, where g is the acceleration of gravity, $\mu=\rho H$, H is the structural thickness, and ρ is the material density.

The principle of virtual velocity requires that

$$D(Q_j,\dot{u}_j^c)=\dot{E}(\dot{u}_j^c), \tag{6}$$

which leads to

$$\int_L c_j\dot{u}_j^c\,dL+\int_S(F_j-\mu\dot{\nu}_j)\dot{u}_j^c\,dS=\int_S Q_j\dot{q}_j^c\,dS. \tag{7}$$

If Eq. (7) is satisfied, the generalized stress field, Q_j, on S, the surface tractions, c_j, on L, and the external forces and inertia forces, $F_j-\mu\dot{\nu}_j$, on S, are in equilibrium. Drucker's postulate for material stability may be expressed in the form of generalized stresses and strains [25].

$$(Q_j-Q_j^*)\dot{q}_j\geqslant 0, \tag{8}$$

where, Q_j^* is any state of generalized stresses satisfying $\phi(Q_j^*)\leqslant 0$ with $\phi=0$ as the loading surface function; $\dot{q}_j$ is the generalized strain rate field corresponding to the generalized stress field, Q_j, in a stable material defined by Drucker's postulate.

In the following analyses, the external surface pressure load is divided into two parts

$$F_j=P_j+f_j, \tag{9}$$

where f_j is a time-independent field force, such as gravity, and P_j is a time-dependent external pressure pulse acting on a structural member.

3 Lower Bound on Response Time

By using Eq. (8), Eq. (7) with $Q_j=Q_j^*$, may be written as,

$$\int_L c_j\dot{u}_j^c\,dL+\int_S(F_j-\mu\dot{\nu}_j)\dot{u}_j^c\,dS=\int_S Q_j^*\dot{q}_j^c\,dS\leqslant\int_S Q_j^c\dot{q}_j^c\,dS, \tag{10}$$

where, Q_j^c is associated with $\dot{q}_i^c$ through Drucker's postulate of material stability. $\dot{u}_j^c$ is any postulated time-independent kinematically admissible velocity field, and therefore, the corresponding quantities $\dot{q}_j^c$ and Q_j^c are also time-independent.

Integrating Eq. (10) from time $t=0$, when plastic deformations start, to the time $t=t_f$, when plastic deformations cease, gives

$$t_f\geqslant t_f^*=\frac{\int_L I_j^a\dot{u}_j^c\,dL+\int_S I_j^b\dot{u}_j^c\,dS+\int_S\mu\nu_j^0\dot{u}_j^c\,dS}{D(Q_j^c,\dot{u}_j^c)-\int_S f_j\dot{u}_j^c\,dS} \tag{11}$$

in which

$$D(Q_j^c,\dot{u}_j^c)=\int_S Q_j^c\dot{q}_j^c\,dS,$$

$$I_j^a=\int_0^{t_f}c_j\,dt \quad \text{and} \quad I_j^b=\int_0^{t_f}P_j\,dt$$

are the total energy dissipation rate of the postulated virtual velocity field, the total external impulse on the boundary, L, and the total external impulse in the interior area, S, of the two-dimensional structural member,[2] respectively. ν_j^0 is the initial velocity field of the structural member.

An alternative way of obtaining a lower bound on the structural response time is to consider the rate of work done by a set of statically admissible loadings [13,21],[3] c_j^s, $F_j^s=P_j^s+f_j$ and their corresponding generalized stresses, Q_j^s, on the postulated virtual velocity field, $\dot{u}_j^c$. Equation (7) may then be written as

$$\int_L c_j^s\dot{u}_j^c\,dL+\int_S F_j^s\dot{u}_j^c\,dS=\int_S Q_j^s\dot{q}_j^c\,dS \tag{12}$$

in which, $\dot{u}_j^c$ and $\dot{q}_j^c$ as well as their associated generalized stresses, Q_j^c, are time-independent. Now, consider the stress state as the statically admissible loads approach the static collapse forces (c_j^* and F_j^*) for the postulated virtual deformation mode. In regions where $\|\dot{q}_j^c\|>0$, $\lim(Q_j^s)=Q_j^c, c_j^s\to c_j^*, F_j^s\to F_j^*$; here, $\|\ \|$ denotes the natural norm of the tensor, Eq. (12) gives

$$\int_L c_j^*\dot{u}_j^c\,dL+\int_S F_j^*\dot{u}_j^c\,dS=\int_S Q_j^c\dot{q}_j^c\,dS \tag{13}$$

which, when using Eqs. (9) and (10), leads to the inequality

$$\int_L c_j^*\dot{u}_j^c\,dL+\int_S P_j^*\dot{u}_j^c\,dS\geqslant\int_L c_j\dot{u}_j^c\,dL+\int_S P_j\dot{u}_j^c\,dS-\int_S\mu\dot{\nu}_j\dot{u}_j^c\,dS \tag{14}$$

when $f_j^*=f_j$. Integrating Eq. (14) from $t=0$ to $t=t_f$ gives

$$t_f\geqslant t_f^*=\frac{\int_L I_j^a\dot{u}_j^c\,dL+\int_S I_j^b\dot{u}_j^c\,dS+\int_S\mu\nu_j^0\dot{u}_j^c\,dS}{\int_L c_j^*\dot{u}_j^c\,dL+\int_S P_j^*\dot{u}_j^c\,dS}, \tag{15}$$

which is identical to Eq. (11) because the assumed time-independent velocity field, $\dot{u}_j^c$, and the associated static collapse forces, c_j^* and F_j^*, have the same stress field in the region where $\|\dot{q}_i^c\|>0$ [21], so that Eq. (13) becomes

[2]For short intensive pulse loading, the structural response time, t_f, is usually longer than the loading time.

[3]We treat all problems in the same gravity field, therefore, $f_j^s=f_j$.

$$\int_L c_j^* \dot{u}_j^c \, dL + \int_S P_j^* \dot{u}_j^c \, dS = D(Q_j^c, \dot{u}_j^c) - \int_S f_j \dot{u}_j^c \, dS.$$

Usually, the gravitational force can be neglected when compared with the impact loading, so that Eq. (11) or Eq. (15) may be written as

$$t_f \geqslant t_f^* = \frac{\int_L I_j^a \dot{u}_j^c \, dL + \int_S I_j^b \dot{u}_j^c \, dS + \int_S \mu \nu_j^0 \dot{u}_j^c \, dS}{D(Q_j^c, \dot{u}_j^c)}. \quad (16)$$

From investigations on the bending response of structural elements, Youngdahl [5] suggested that the structural response duration may be approximated by

$$I_e \approx P_y (t_f - t_y), \quad (17)$$

in which I_e is the impulse associated with the pressure loading $P(t)$, as defined by Eq. (1); t_y is the time when the structural plastic response starts[4] and P_y is the static plastic bending collapse load. It is well known that this approximation, although proposed empirically, often predicts response times which agree with the exact analytical predictions for structural bending responses. Analytical results for beams, circular plates and cylindrical shells [9–11] have shown that this approximation is still applicable when transverse shear effects are considered. Therefore, P_y may be understood in general as a static plastic collapse load.

Now, Eq. (17) is rewritten as

$$t_f \approx \frac{I_e}{P_y} \quad (18)$$

when $t_y = 0$, and we shall prove that I_e / P_y is also a lower bound on the response time.

The response time from Eq. (15) satisfies

$$t_f \geqslant t_f^* = \frac{\int_S (I_j^b + \mu \nu_j^0) \dot{u}_j^c \, dS}{\int_S P_j^* \dot{u}_j^c \, dS} \quad (19)$$

when the virtual velocity field, $\dot{u}_j^c$, on L vanishes.

For the dynamic plastic response of structural members, such as beams, circular plates, and cylindrical shells, when subjected to an axisymmetrically and uniformly distributed pressure pulse loading together with an initial velocity, the two-dimensional integration in Eq. (19) may be reduced to a one-dimensional integration, i.e.,

$$t_f \geqslant t_f^* = \frac{\int_x I \dot{w}^c \, dx}{\int_x P_y \dot{w}^c \, dx} \quad (20)$$

where, x should be replaced by r for circular plates, and I is the total impulse of the external pressure force together with the initial momentum of the structural element; P_y is the static collapse loading for the assumed virtual transverse velocity field, $\dot{w}^c$.

Therefore,

$$t_f \geqslant t_f^* = \frac{I}{P_y} \quad (21)$$

because P_y and I are independent of spatial coordinate, x.

Equation (21) may be considered as a theoretical basis for Youngdahl's approximation. Furthermore, Eq. (21) suggests that Youngdahl's approximation may be written as

$$I = I_e + I_0 = P_y t_f^* \quad (22a)$$

or

$$t_f \geqslant t_f^* = \frac{I_e + I_0}{P_y}, \quad (22b)$$

where, $I_0 = \mu \nu_0$ and ν_0 is a uniformly distributed initial transverse velocity. Equation (22*b*) with $I_0 = 0$, is the same as Eq. (18), which is Youngdahl's estimate for the final response time.

When the distribution of the pressure pulse is dependent on the spatial coordinate, x, the lower bound on the response time will be influenced by the selected $\dot{w}^c$ field.

4 Lower Bound on Maximum Final Displacement

Integrating Eq. (10) from $t = 0$ to $t = t_f^*$ leads to

$$\int_L \left(\int_0^{t_f^*} c_j \dot{u}_j^c \, dt \right) dL + \int_S \left(\int_0^{t_f^*} P_j \dot{u}_j^c \, dt \right) dS - \int_S \left(\int_0^{t_f^*} \mu \dot{\nu}_j \dot{u}_j^c \, dt \right) dS \leqslant \int_S \left(\int_0^{t_f^*} Q_j^c \dot{q}_j^c \, dt \right) dS \quad (23)$$

when neglecting the gravitational force f_j, and where, t_f^* is determined by the equality in Eq. (16). Now, $\dot{u}_j^c$ is assumed to be time dependent with the form

$$\dot{u}_j^c = \dot{U}_j^c(x_k) T(t), \quad (24)$$

where, the mode $\dot{U}_j^c(x_k)$ is time independent and satisfies the kinematic boundary conditions, x_k is a coordinate, and $T(t)$ is a time-dependent amplitude. For infinitesimal deformations, the generalized strain rate field $\dot{q}_j^c$ and dissipation function, $D(Q_j^c, \dot{u}_j^c)$, are also separable, i.e.,

$$\dot{q}_j^c = T(t) \dot{E}_j^c \quad (25a)$$

where $\dot{E}_j^c$ is associated with $\dot{U}_j^c$, and

$$D(Q_j^c, \dot{u}_j^c) = D(\dot{U}_j^c) T(t), \quad (25b)$$

in which,

$$D(\dot{U}_j^c) = \int_S Q_j^c \dot{E}_j^c \, dS. \quad (26)$$

Furthermore, $T(t)$ is assumed to take the form

$$T(t) = 1 - \frac{t}{t_f^*}, \quad \text{for } 0 \leqslant t \leqslant t_f^*$$

and

$$T(t) = 0, \quad \text{for } t > t_f^*. \quad (27)$$

Now, Eq. (23) may be expressed as

$$\int_L I_j^a(t_f^*) \dot{U}_j^c \, dL + \int_S I_j^b(t_f^*) \dot{U}_j^c \, dS - \int_L \frac{\overline{c}_j(t_f^*) \dot{U}_j^c}{t_f^*} dL - \int_S \frac{\overline{P}_j(t_f^*) \dot{U}_j^c}{t_f^*} dS + \int_S \mu \nu_j^0 \dot{U}_j^c \, dS - \frac{1}{t_f^*} \int_S \mu u_j(t_f^*) \dot{U}_j^c \, dS \leqslant \frac{1}{2} D(\dot{U}_j^c) t_f^* \quad (28)$$

in which, $\nu_j = \dot{u}_j$, $\nu_j^0 = \nu_j|_{t=0}$, and

$$I_j^a(t) = \int_0^t c_j(t) dt, \quad (29a)$$

$$I_j^b(t) = \int_0^t P_j(t) dt, \quad (29b)$$

[4] Without losing generality, t_y is assumed to be zero in this paper, which means that response time is measured from the start of plastic deformation.

$$\overline{c_j}(t)=\int_0^t tc_j(t)dt \tag{29c}$$

and

$$\overline{P_j}(t)=\int_0^t tP_j(t)dt. \tag{29d}$$

Equation (28) may be rewritten as

$$\int_S \mu u_j(t_f^*)\dot{U}_j^c\,dS \geqslant t_f^*\left(\int_L I_j^a(t_f^*)\dot{U}_j^c\,dL+\int_S I_j^b(t_f^*)\dot{U}_j^c\,dS+\int_S \mu\nu_j^0\dot{U}_j^c\,dS-\int_L \frac{\overline{c_j}(t_f^*)\dot{U}_j^c}{t_f^*}dL-\int_S \frac{\overline{P_j}(t_f^*)\dot{U}_j^c}{t_f^*}dS-\frac{D(\dot{U}_j^c)t_f^*}{2}\right) \tag{30}$$

Generally speaking, the assumed time-dependent velocity fields in Eq. (16) may differ from $\dot{U}_j^c(x_k)$ in Eq. (24), which means that t_f^* may be determined from another postulated time-independent velocity field. It was suggested in [21,23] that the same time-independent velocity field is used to determine t_f^*. Therefore, from Eq. (16), Eq. (30) may be expressed in the form

$$\frac{1}{t_f^*}\int_S \mu u_j(t_f^*)\dot{U}_j^c\,dS \geqslant \int_L I_j^a(t_f^*)\dot{U}_j^c\,dL+\int_S I_j^b(t_f^*)\dot{U}_j^c\,dS+\int_S \frac{1}{2}\mu\nu_j^0\dot{U}_j^c\,dS-\int_L \frac{\overline{c_j}(t_f^*)\dot{U}_j^c}{t_f^*}dL-\int_S \frac{\overline{P_j}(t_f^*)\dot{U}_j^c}{t_f^*}dS-\frac{1}{2}\int_L I_j^a(t_f)\dot{U}_j^c\,dL-\frac{1}{2}\int_S I_j^b(t_f)\dot{U}_j^c\,dS, \tag{31}$$

which is slightly different from the results obtained in [21,23] which ignore the difference between t_f^* and t_f.

It is necessary to choose $\dot{U}_j^c$ in Eq. (31) in order to obtain the maximum lower bound of the final displacement. This is an extreme value problem of functions. It was found in [23] that the accuracy of the bounds depends on the difference between the stresses associated with assumed velocity fields and the actual stress distribution in a continuum.

Furthermore, we should determine which quantity is in fact being bounded. References [20,21,23] treated the three components of $\dot{U}_j^c$ separately by using $(\dot{U}_1^c,0,0)$, $(0,\dot{U}_2^c,0)$, and $(0,0,\dot{U}_3^c)$. From Eq. (31) and the above assumed form of $\dot{U}_j^c$, we can obtain the lower bounds for each maximum component, but they are not the lower bounds for each component of the maximum final displacement in a medium. In fact, the existing method limits the application range of the lower bound theorem. An alternative procedure is used here to obtain a lower bound for the maximum final displacement at a point or small region in a continuum. If the direction of the maximum final displacement and its location are known, the direction of $\dot{U}_j^c$ at this point may be chosen to be the same as the direction of the maximum final displacement. Now, by using the mean value theorem for an integral, Eq. (31) predicts

$$\|\delta_j^f\| \geqslant \|\delta_j\| \geqslant \frac{t_f^* G(\dot{U}_j^c,t_f^*,t_f)}{\int_S \mu\|\dot{U}_j^c\|dS}, \tag{32}$$

where, $\|\delta_j^f\|=\max\{\|u_j(x_k,t_f)\|,x_k\in S\}$, $\|\delta_j\|=\max\{\|u_j(x_k,t_f^*)\|,x_k\in S\}$, and

$$G(\dot{U}_j^c,t_f^*,t_f)=\text{right side of Eq. (31)}. \tag{33}$$

If the components of $\dot{U}_j^c$ are taken as zero except within a particular region, the lower bound on the maximum final displacement within S is obtained from Eq. (32).

5 Elimination of Pulse Shape Effects on Lower Bound

For structural elements, such as beams, circular plates, and cylindrical shells when subjected to an axisymmetric transverse dynamic loading, the lower bound on the maximum final transverse displacement discussed in Sec. 4 may be simplified as

$$w^f \geqslant \frac{t_f^*}{2\int_x \gamma\mu\dot{w}^c\,dx}\left(\int_x 2\gamma I^b(t_f^*)\dot{w}^c\,dx-\int_x \gamma I^b(t_f)\dot{w}^c\,dx+\int_x \gamma\mu\nu^0\dot{w}^c\,dx-2\int_x \frac{\gamma\overline{P}(t_f^*)\dot{w}^c}{t_f^*}dx\right) \tag{34}$$

where $\dot{w}^c$ is the kinematically admissible transverse velocity, where

$$\gamma=b \quad \text{for beams}$$
$$\gamma=2\pi x \quad \text{for circular plates} \tag{35}$$

and

$$\gamma=2\pi R \quad \text{for cylindrical shells}$$

in which b is the width of a beam and R is the mean radius of a thin cylindrical shell.

It was shown in Sec. 3 that Youngdahl's suggestion [5], $t_f^* \approx t_f$, is based on a lower bound of the structural response time. In this case, $I^b(t_f^*)\approx I^b(t_f)$ and $\overline{P}(t_f^*)\approx\overline{P}(t_f)$, and therefore, Eq. (34) reduces to

$$w^f \geqslant \frac{t_f}{2\int_x \gamma\mu\dot{w}^c\,dx}\left(\int_x \gamma I^b(t_f)\dot{w}^c\,dx+\int_x \gamma\mu\nu^0\dot{w}^c\,dx-2\int_x \frac{\gamma\overline{P}(t_f)\dot{w}^c}{t_f}dx\right), \tag{36}$$

where I^b, $\overline{P}$ are given by Eqs. (29*b*) and (29*d*), and t_f is estimated from Eq. (22*b*). When $t_y=0$, then I^b, $\overline{P}$ and t_f in Eq. (36) can be expressed as functions of I_e and P_e defined by Youngdahl [5,6], which have the following form

$$I_e=\int_0^{t_f} P(t)dt \tag{37a}$$

and

$$P_e=\frac{I_e^2}{2\int_0^{t_f} tP(t)dt} \tag{37b}$$

according to Eqs. (1)–(3). Therefore, a lower bound for the final deflection at a selected location depends only on I_e, P_e, and the distribution of the initial velocity field as well as the selected kinematically admissible velocity field, $\dot{w}^c$, which offers a theoretical foundation of Youngdahl's empirical suggestions that two correlation parameters can represent a general uniformally distributed pulse pressure loading.

If the initial velocity field is also uniformly distributed, Eq. (36) can be further simplified into

$$w^f \geqslant \frac{t_f}{2\mu}\left(I^b(t_f)+I_0-\frac{2\overline{P}(t_f)}{t_f}\right),$$

or

$$w^f \geqslant \frac{(I_e+I_0)^2}{2\mu P_y}\left[1-\frac{I_e^2 P_y}{P_e(I_e+I_0)^2}\right] \tag{38}$$

When there is no initial velocity distribution, i.e., $I_0=0$, then Eq. (38) can be expressed in the following form

$$w^f \geqslant I_e^2 G(P_e) \tag{39}$$

The equality of Eq. (39) has been observed in many cases [5,6,8,9–12,24]. A recent study based on an elastic-plastic SDOF model also shows the validity of this general dependence of the final deflection on the two correlation parameters, I_e and P_e [26].

6 Conclusions

Youngdahl's correlation parameter method for eliminating the influence of the loading shape on the dynamic plastic response of structures was examined in the present paper by using some bound theorems that have been developed for rigid, perfectly plastic continua. In particular, bounds on the final displacement and the structural response time were presented for two-dimensional rigid-plastic structural members, which include the effects of an initial velocity field and a time-dependent surface traction as well as body forces. It is shown that the bound theorems supply a theoretical basis for Youngdahl's empirical correlation parameter method for estimating the structural response of various structural members. A lower bound on the maximum final displacement obtained when using Youngdahl's correlation parameters is insensitive to the pulse loading shapes for structural elements subjected to axisymmetrically loaded pressure pulses.

Nomenclature

c_j = generalized force applied on boundary L
D = rate of the internal energy dissipation, defined by Eq. (4)
$\dot{E}$ = rate of the external energy dissipation, defined by Eq. (5)
f_j = field force, such as gravitational force, expressed as a pressure for two-dimensional structural members
F_j = total external pressure load
H = thickness of a structural member
I = I_e+I_0
I_0 = μv_0
I_e = correlation parameter defined by Eq. (1)
I_j^a, I_j^b = defined by Eq. (11)
$I_j^a(t)$, $I_j^b(t)$ = defined by Eqs. (29*a*,*b*)
L = boundary of a two-dimensional structural member represented by the occupied area S
$P(t)$ = pressure pulse loading history
P_e = correlation parameter defined by Eq. (2)
P_j = external pressure pulse loading, defined by Eq. (9)
q_j = generalized strains
$\dot{q}_j^c$ = generalized strain rate field associated with $\dot{u}_j^c$
Q_j = generalized stresses
r = radial coordinate for a circular plate
S = the occupied area of a two-dimensional structural member
t = time
t_{mean} = defined by Eq. (3)
t_f = time when structural response ceases
t_f^* = defined as the right hand side of inequality (11)
t_y = time when structural plastic response starts
u_j = generalized displacement
$\dot{u}_j^c$ = kinematically admissible velocity field
v_0 = initial transverse velocity of the structural member
v_j = generalized velocity
w = transverse displacement
w^f = final transverse displacement
x = longitudinal coordinate for beams and cylindrical shells or radial coordinate for circular plates
μ = ρH
ρ = density

Superscript

c = kinematically admissible
s = statically admissible

References

[1] Symonds, P. S., 1953, "Dynamic Load Characteristics in Plastic Bending of Beams," ASME J. Appl. Mech., **20**, pp. 475–481.
[2] Abrahamson, G. R., and Lindberg, H. E., 1976, "Peak Load—Impulse Characterization of Critical Pulse Loads in Structural Dynamics," Nucl. Eng. Des., **37**, pp. 35–46.
[3] Mays, G. C., and Smith, P. D., 1995, *Blast Effects on Buildings—Design of Buildings to Optimize Resistance to Blast Loading*, Thomas Telford, London.
[4] Hodge, Jr., P. G., 1956, "The Influence of Blast Characteristics on the Final Deformation of Circular Cylindrical Shells," ASME J. Appl. Mech., **23**, pp. 617–624.
[5] Youngdahl, C. K., 1970, "Correlation Parameters for Eliminating the Effect of Pulse Shape on Dynamic Plastic Deformation," ASME J. Appl. Mech., **37**, pp. 744–752.
[6] Youngdahl, C. K., 1971, "Influence of Pulse Shape on the Final Plastic Deformation of a Circular Plate," Int. J. Solids Struct., **7**, pp. 1127–1142.
[7] Jones, N., 1985, "Bounds on the Dynamic Plastic Behavior of Structures Including Transverse Shear Effects," Int. J. Impact Eng., **3**, pp. 273–291.
[8] Zhu, G., Huang, Y. G., Yu, T. X., and Wang, R., 1986, "Estimation of the Plastic Structural Response Under Impact," Int. J. Impact Eng., **4**, pp. 271–282.
[9] Li, Q. M., and Jones, N., 1994, "Blast Loading of Fully Clamped Circular Plates With Transverse Shear Effects," Int. J. Solids Struct., **31**, pp. 1861–1876.
[10] Li, Q. M., and Jones, N., 1995, "Blast Loading of Fully Clamped Beams With Transverse Shear Effects," Mech. Struct. Mach., **23**, pp. 59–86.
[11] Li, Q. M., and Jones, N., 1995, "Blast Loading of a "Short" Cylindrical Shell With Transverse Shear Effects," Int. J. Impact Eng., **16**, pp. 331–353.
[12] Li, Q. M., and Shu, X. F., 1992, "Elimination of Loading Shape Effects on Blast Loading Beams in Damping Medium," *Proc. of the 2nd Int. Symposium on Intense Dynamic Loading and Its Effects*, Chengdu, pp. 480–483.
[13] Martin, J. B., 1964, "Impulsive Loading Theorems for Rigid-Plastic Continua," ASCE J. Eng. Mech. Div., **90**, pp. 27–42.
[14] Martin, J. B., 1965, "A Displacement Bound Principle for Inelastic Continua Subjected to Certain Classes of Dynamic Loading," ASME J. Appl. Mech., **32**, pp. 1–6.
[15] Robinson, D. N., 1970, "A Displacement Bound Principle for Elastic-Plastic Structures Subjected to Blast Loading," J. Mech. Phys. Solids, **18**, pp. 65–80.
[16] Ploch, J., and Wierzbicki, T., 1981, "Bounds for Large Plastic Deformations of Dynamically Loaded Continua and Structures," Int. J. Solids Struct., **17**, pp. 183–195.
[17] Morales, W. J., and Nevill, Jr., G. E., 1970, "Lower Bounds on Deformations of Dynamically Loaded Rigid-Plastic Continua," AIAA J., **8**, pp. 2043–2046.
[18] Wierzbicki, T., 1971, "Improved Lower Bound Theorem for Impulsively Loaded Continua," Arch. Mech., **23**, pp. 423–425.
[19] Wierzbicki, T., 1972, "Comment on Lower Bounds on Deformations of Dynamically Loaded Rigid-Plastic Continua," AIAA J., **10**, pp. 363–364.
[20] Morales, W. J., 1972, "Displacement Bounds for Blast Loaded Structures," ASCE J. Eng. Mech. Div., **98**, pp. 965–974.
[21] Stronge, W. J., 1983, "Lower Bound on Deformation for Dynamically Loaded Rigid-Plastic Structures," Int. J. Solids Struct., **19**, 1049–1063.
[22] Kaliszky, S., 1970, "Approximate Solutions for Impulsively Loaded Inelastic Structures and Continua," Int. J. Non-Linear Mech., **5**, pp. 143–158.
[23] Stronge, W. J., 1985, "Accuracy of Bounds of Plastic Deformation for Dynamically Loaded Plates and Shells," Int. J. Mech. Sci., **27**, pp. 97–104.
[24] Jones, N., 1989, *Structural Impact*, Cambridge University Press, Cambridge (paperback edition, 1997).
[25] Martin, J. B., 1975, *Plasticity: Fundamentals and General Results*, MIT Press, Cambridge.
[26] Li, Q. M., and Meng, H., 2002, "Pulse Loading Shape Effects on Pressure-Impulse Diagram of Elastic-Plastic Structures," Int. J. Mech. Sci., **44**, pp. 1985–1998.

A Second Look at the Higher-Order Theory for Periodic Multiphase Materials

Yogesh Bansal

Marek-Jerzy Pindera[1]
e-mail: mp3g@Virginia.edu

Civil Engineering Department,
University of Virginia,
Charlottesville, VA 22904-4742

In this communication, we present a reformulation, based on the local/global stiffness matrix approach, of the recently developed higher-order theory for periodic multiphase materials, Aboudi et al. ["Linear Thermoelastic Higher-Order Theory for Periodic Multiphase Materials," J. Appl. Mech., **68***(5), pp. 697–707]. This reformulation reveals that the higher-order theory employs an approximate, and standard, elasticity approach to the solution of the unit cell problem of periodic multiphase materials based on direct volume-averaging of the local field equations and satisfaction of the local continuity conditions in a surface-averge sense. This contrasts with the original formulation in which different moments of the local equilibrium equations were employed, suggesting that the theory is a variant of a micropolar, continuum-based model. The reformulation simplifies the derivation of the global system of equations governing the unit cell response, whose size is substantially reduced through elimination of redundant continuity equations employed in the original formulation, allowing one to test the theory's predictive capability in most demanding situations. Herein, we do so by estimating the elastic moduli of periodic composites characterized by repeating unit cells obtained by rotation of an infinite square fiber array through an angle about the fiber axis. Such unit cells possess no planes of material symmetry in the rotated coordinate system, and may contain a few or many fibers, depending on the rotation angle, which the reformulated theory can easily accommodate. The excellent agreement with the corresponding results obtained from the standard transformation equations confirms the new model's previously untested predictive capability for a class of periodic composites characterized by nonstandard, multi-inclusion repeating unit cells lacking planes of material symmetry. Comparison of the effective moduli and local stress fields with the corresponding results obtained from the original Generalized Method of Cells, which the higher-order theory supersedes, confirms the need for this new model, and dramatically highlights the original model's shortcomings for a certain class of unidirectional composites.* [DOI: 10.1115/1.1831294]

1 Introduction

The higher-order theory for periodic multiphase materials is a recently developed micromechanics model for the response of multiphase materials with arbitrary periodic microstructures, Aboudi et al. [1–3]. The model's analytical framework is based on the homogenization theory for periodic materials (cf. Kalamkarov and Kolpakov [4]), but the method of solution for the local displacement and stress fields within the repeating unit cell characterizing the material's periodic microstructure utilizes concepts previously employed in constructing the higher-order theory for functionally graded materials (FGMs) [5]. The use of the adjective *higher-order* in the model's name refers to the higher-order displacement field representation within the subvolumes of the unit cell's discretized microstructure relative to that used in the Generalized Method of Cells (GMC) micromechanics model, Paley and Aboudi [6], which the new model supersedes. The linear displacement field approximation employed in the construction of GMC, together with the manner of satisfying the local equilibrium and continuity conditions, results in the absence of so-called shear coupling which provides the required bridge between macroscopically applied normal (shear) stresses and the resulting microscopic shear (normal) stresses. This shear coupling is a natural consequence of the second-order displacement field approximation within the unit cell's subvolumes employed in the construction of the higher-order theory, and dramatically improves the accuracy of estimating the local stress fields relative to GMC. In light of the similarities involving unit cell discretization and satisfaction of the field and continuity equations employed in both models, the higher-order theory recently has been renamed the High-Fidelity Generalized Method of Cells or HFGMC.

HFGMC's capability of accurately capturing local stress and inelastic strain fields has been demonstrated for simple periodic microstructures characterized by orthogonal planes of material symmetry through exact analytical and numerical solutions [1–3]. In addition, limited data has been generated for unidirectional composites with locally irregular microstructures (Pindera et al. [7]). It is for such composites that the power of this new high-fidelity model becomes evident due to the importance of shear coupling in the presence of locally irregular microstructures as demonstrated by the above study, further highlighting the differences between the two models' predictive capabilities.

In the original formulation of HFGMC, a two-level discretization of the repeating unit cell's microstructure was employed, involving division into generic cells that were further subdivided into four subcells in the case of periodic materials with continuous reinforcement along a common direction (Fig. 1). This two-level discretization process unnecessarily complicated the satisfaction of the stress equilibrium equations within individual subcells, accomplished in a circuitous manner by satisfying the different moments of the local equilibrium equations in a volumetric sense.

[1]To whom correspondence should be addressed.

Contributed by the Applied Mechanics Division of THE AMERICAN SOCIETY OF MECHANICAL ENGINEERS for publication in the ASME JOURNAL OF APPLIED MECHANICS. Manuscript received by the Applied Mechanics Division, March 18, 2003; final revision, July 26, 2004. Associate Editor: D. Kouris. Discussion on the paper should be addressed to the Editor, Prof. Robert M. McMeeking, Journal of Applied Mechanics, Department of Mechanical and Environmental Engineering, University of California—Santa Barbara, Santa Barbara, CA 93106-5070, and will be accepted until four months after final publication in the paper itself in the ASME JOURNAL OF APPLIED MECHANICS.

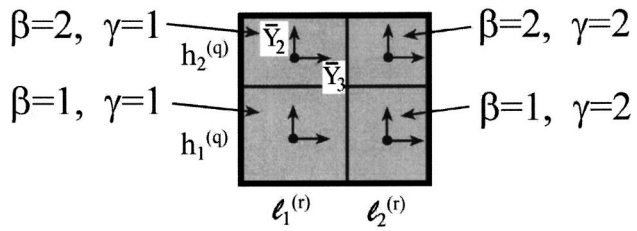

Fig. 1 A generic cell (q,r) with four subcells (β,γ) employed in the two-level discretization of the unit cell in the original higher-order theory for multiphase periodic materials, presently known as HFGMC. Adapted from Fig. 2 in Aboudi et al. [1].

These manipulations, in turn, suggested that the higher-order theory is a variant of a micropolar, micromechanics-based continuum theory, which is not the case. The satisfaction of the surface-averaged traction continuity conditions between adjacent generic cells was also complicated by the two-level unit cell discretization.

The objective of the present communication is twofold. First, we demonstrate that the underlying framework of HFGMC is based on an approximate, and quite standard, elasticity approach involving direct volume-averaging of the subcell stress equilibrium equations in conjunction with the imposition of displacement and traction continuity conditions in a surface-average sense across adjacent subcell faces. This is accomplished by first simplifying the unit cell volume discretization using solely subcells as the fundamental building blocks of a periodic material's microstructure (Fig. 2). This simplification makes it possible to reformulate the theoretical framework of HFGMC using the local/global stiffness matrix approach originally proposed by Bufler [8] for the elastic analysis of isotropic layered media, and extended by Pindera [9] to layered anisotropic composites. The reformulation is based on the construction of a local stiffness matrix relating the surface-averaged displacements to the corresponding surface-averaged tractions of the subcell, with the surface-averaged displacements becoming the fundamental unknown quantities. This construction also highlights the often unrecognized difference between HFGMC and a finite-element approach to the solution of the corresponding unit cell problem. Subsequent assembly of the individual stiffness matrices into the global stiffness matrix, which governs the response of the entire unit cell, eliminates redundant subcell continuity equations, thereby producing a significant reduction in the overall system of equations relative to the original formulation. The same approach had been employed by Bansal and Pindera [10] in reformulating the original higher-order theory for FGMs.

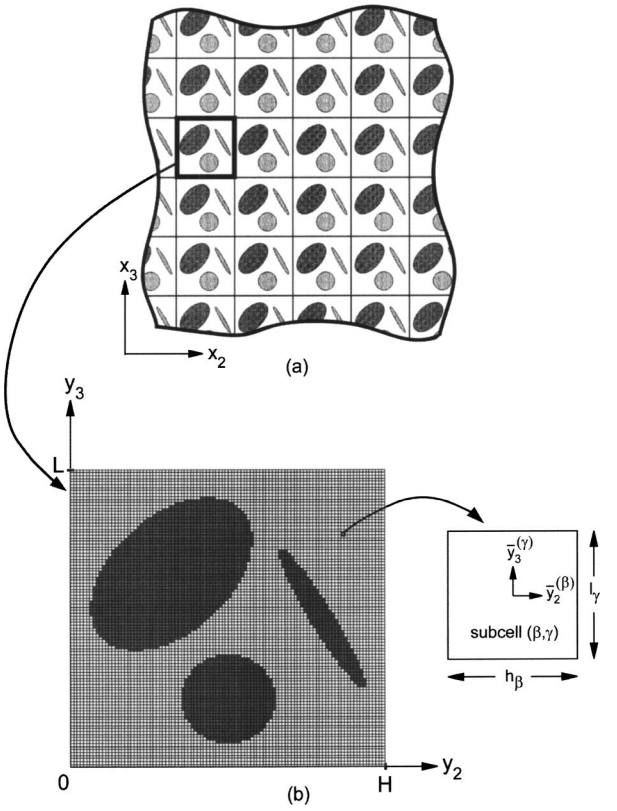

Fig. 2 (a) A continuously reinforced multiphase composite with a periodic microstructure in the x_2-x_3 plane constructed with repeating unit cells. (b) Discretization of the repeating unit cell into subcells employed in the reformulation of HFGMC.

The reformulation of HFGMC makes it possible to efficiently investigate the response of highly discretized unit cells which mimic realistic material microstructures. This, in turn, facilitates testing of the method's predictive capability in most demanding settings. The second objective, therefore, addresses this issue. In particular, given the past experience, it is expected that the intrinsic shear-coupling feature of HFGMC will play a key role in correctly capturing the elastic moduli of unidirectional composites characterized by unit cells that lack orthogonal planes of material symmetry. This may occur due to the rotation of a regular array of continuous fibers about the fiber axis, rather than locally irregular (albeit periodic) microstructures that had been previously investigated without comparison to a known standard [7]. Therefore, HFGMC is employed herein to determine the effective moduli and local stress fields in unidirectional composites characterized by a repeating unit cell with a square fiber array loaded by average stresses that do not coincide with the orthogonal planes of material symmetry due to the above-mentioned rotation. The unit cell for a particular rotation angle typically may contain a large number of fibers (in contrast with just one for the square array in the principal material coordinate system), which makes the reformulated HFGMC particularly well suited due to large number of rectangular subcells required to model realistic geometric details (such as circular fibers, for instance). The considered unit cell discretizations cannot be readily handled using the original formulation.

The predictions of the reformulated HFGMC model for the elastic moduli of two types of unidirectional composites as a function of the rotation angle are compared with the results obtained from the transformation equations for an orthotropic material rotated by an angle about the fiber axis. Such rotation produces an elastic stiffness or compliance matrix that represents a monoclinic material with just one plane of material symmetry (the plane perpendicular to the fiber axis) in the rotated coordinate system. This provides a critical test on the self-consistency of the newly developed HFGMC model previously untested in this manner. To the authors' knowledge, such test has not been attempted previously using other micromechanics models. The two types of unidirectional composites contain the same fiber volume fraction but radically different fiber/matrix moduli ratios representative of a glass/epoxy system and a porous aluminum matrix. Comparison with the corresponding GMC predictions are also provided to further justify the development of the new model by highlighting the original model's limitations for certain classes of composites.

2 Theoretical Framework

The theoretical framework of the original version of HFGMC has been described in detail by Aboudi et al. [1–3], and thus only a brief synthesis will be provided herein in order to make it possible to follow the efficient reformulation's derivation. The high-fidelity model combines concepts from the homogenization theory

and the higher-order theory for functionally graded materials. The homogenization theory is employed to construct the correct form of the displacement field representation in the discretized domains of the repeating unit cell which represents the periodic material's microstructure; to identify the governing field equations for the local problem of the repeating unit cell; and to construct appropriate boundary conditions. The construction of the displacement field is based on a two-scale expansion of the form

$$u_i(\mathbf{x},\mathbf{y}) = u_{0i}(\mathbf{x},\mathbf{y}) + \delta u_{1i}(\mathbf{x},\mathbf{y}) + \delta^2 u_{2i}(\mathbf{x},\mathbf{y}) + \cdots \tag{1}$$

where $\mathbf{x}=(x_1,x_2,x_3)$ are the global or macroscopic coordinates, $\mathbf{y}=(y_1,y_2,y_3)$ are the local or microscopic coordinates defined with respect to the repeating unit cell, and the different order terms characterized by the powers of δ are $\mathbf{y}$-periodic. The size of the unit cell characterized by the parameter δ is small relative to the overall material dimensions such that $y_i = x_i/\delta$. Thus a unit displacement at the local scale corresponds to a displacement of order δ on the global scale.

The above displacement field representation, together with the relation $y_i = x_i/\delta$ between the two spatial scales, leads to the following strain field decomposition for periodic materials given in terms of the average and fluctuating strains $\overline{\epsilon}_{ij}(\mathbf{x})$ and $\epsilon'_{ij}(\mathbf{x},\mathbf{y})$, respectively:

$$\epsilon_{ij} = \overline{\epsilon}_{ij}(\mathbf{x}) + \epsilon'_{ij}(\mathbf{x},\mathbf{y}) + \mathbf{O}(\delta) \tag{2}$$

The average and fluctuating (local) strains are derived from the corresponding displacement components $\overline{u}_i$ and u'_i, as

$$\overline{\epsilon}_{ij}(\mathbf{x}) = \frac{1}{2}\left(\frac{\partial \overline{u}_i}{\partial x_j} + \frac{\partial \overline{u}_j}{\partial x_i}\right), \quad \epsilon'_{ij}(\mathbf{x},\mathbf{y}) = \frac{1}{2}\left(\frac{\partial u'_i}{\partial y_j} + \frac{\partial u'_j}{\partial y_i}\right) \tag{3}$$

The above strain decomposition makes it possible to express the displacement field in the form

$$u_i(\mathbf{x},\mathbf{y}) = \overline{\epsilon}_{ij} x_j + u'_i + \mathbf{O}(\delta^2) \tag{4}$$

where $\overline{\epsilon}_{ij}$ are the known or applied macroscopic strains. This form is employed in constructing an approximate displacement field for the solution of the cell problem.

For specified values of the average strains $\overline{\epsilon}_{ij}$, the fluctuating displacements u'_i must satisfy: the local stress equilibrium equations within the individual subvolumes into which the repeating unit cell is discretized in a manner that mimics the actual microstructure of the periodic multiphase material; the traction and displacement continuity conditions between the individual subvolumes; and the periodic boundary conditions prescribed at the boundaries of the repeating unit cell. The solution methodology for the chosen approximation of u'_i, which follows the higher-order theory for FGMs, is based on volume-averaging of the local stress equilibrium equations in the individual subvolumes, and surface-averaging of the traction and displacement continuity conditions at the interfaces separating the individual subvolumes, as well as the periodic boundary conditions. Herein, this is carried out efficiently using the local/global stiffness matrix approach described next.

3 Efficient Reformulation of the Cell Problem

The local analysis is performed on the repeating unit cell representative of a periodic material's microstructure in the x_2–x_3 plane [Fig. 2(a)], with continuous reinforcement along the x_1 axis. The periodic microstructure is made up of any number of phases arbitrarily distributed within the unit cell so as to produce fully anisotropic behavior in the x_2–x_3 plane. The unit cell is appropriately discretized into subcells, designated by (β,γ), so as to mimic the material's periodic microstructure, as shown in Fig. 2(b) for the unit cell highlighted in Fig. 2(a). In this case, 100×100 equally dimensioned subcells were used to capture the three reinforcement shapes with sufficient fidelity, noting that such refinement would be computationally prohibitive in the original formulation. The indices $\beta=1,\ldots,N_\beta$ and $\gamma=1,\ldots,N_\gamma$, which span the unit cell along the local y_2 and y_3 axes, identify the (β,γ) subcell in the y_2–y_3 plane. The subcell dimensions along the y_2 and y_3 axes are h_β and l_γ, respectively, such that

$$H = \sum_{\beta=1}^{N_\beta} h_\beta \quad \text{and} \quad L = \sum_{\gamma=1}^{N_\gamma} l_\gamma$$

where H and L are the overall unit cell dimensions along these axes.

Following the displacement field representation within the unit cell of a periodic material given by Eq. (4), the displacement field in each (β,γ) subcell is written as follows:

$$u_i^{(\beta,\gamma)} = \overline{\epsilon}_{ij} x_j + u_i'^{(\beta,\gamma)} \tag{5}$$

Given the continuous reinforcement along the x_1 axis, the fluctuating components $u_i'^{(\beta,\gamma)}$ of the displacement field that arise due to the heterogeneity of the medium are functions of the local coordinates $(\overline{y}_2^{(\beta)}, \overline{y}_3^{(\gamma)})$ attached to the subcell's center [Fig. 2(b)]. These fluctuating components are approximated in each (β,γ) subcell by the same second-order, Legendre-type polynomial expansion in the local coordinates as that employed in the original formulation

$$\begin{aligned} u_i'^{(\beta,\gamma)} = {} & W_{i(00)}^{(\beta,\gamma)} + \overline{y}_2^{(\beta)} W_{i(10)}^{(\beta,\gamma)} + \overline{y}_3^{(\gamma)} W_{i(01)}^{(\beta,\gamma)} \\ & + \frac{1}{2}\left(3\overline{y}_2^{(\beta)2} - \frac{h_\beta^2}{4}\right) W_{i(20)}^{(\beta,\gamma)} + \frac{1}{2}\left(3\overline{y}_3^{(\gamma)2} - \frac{l_\gamma^2}{4}\right) W_{i(02)}^{(\beta,\gamma)} \end{aligned} \tag{6}$$

where $i=1,2,3$ and $W_{i(mn)}^{(\beta,\gamma)}$ are the unknown microvariables associated with each subcell. Using the above fluctuating field representation in the strain–displacement relations,

$$\epsilon_{ij}^{(\beta,\gamma)} = \overline{\epsilon}_{ij} + \frac{1}{2}\left(\frac{\partial u_i'^{(\beta,\gamma)}}{\partial \overline{y}_j^{(\cdot)}} + \frac{\partial u_j'^{(\beta,\gamma)}}{\partial \overline{y}_i^{(\cdot)}}\right) \tag{7}$$

the strain components in each (β,γ) subcell are obtained in the form

$$\begin{aligned} \epsilon_{11}^{(\beta,\gamma)} &= \overline{\epsilon}_{11} \\ \epsilon_{22}^{(\beta,\gamma)} &= \overline{\epsilon}_{22} + W_{2(10)}^{(\beta,\gamma)} + 3\overline{y}_2^{(\beta)} W_{2(20)}^{(\beta,\gamma)} \\ \epsilon_{33}^{(\beta,\gamma)} &= \overline{\epsilon}_{33} + W_{3(01)}^{(\beta,\gamma)} + 3\overline{y}_3^{(\gamma)} W_{3(02)}^{(\beta,\gamma)} \\ \epsilon_{12}^{(\beta,\gamma)} &= \overline{\epsilon}_{12} + \frac{1}{2}\left[W_{1(10)}^{(\beta,\gamma)} + 3\overline{y}_2^{(\beta)} W_{1(20)}^{(\beta,\gamma)}\right] \\ \epsilon_{13}^{(\beta,\gamma)} &= \overline{\epsilon}_{13} + \frac{1}{2}\left[W_{1(01)}^{(\beta,\gamma)} + 3\overline{y}_3^{(\gamma)} W_{1(02)}^{(\beta,\gamma)}\right] \\ \epsilon_{23}^{(\beta,\gamma)} &= \overline{\epsilon}_{23} + \frac{1}{2}\left[W_{2(01)}^{(\beta,\gamma)} + 3\overline{y}_3^{(\gamma)} W_{2(02)}^{(\beta,\gamma)} + W_{3(10)}^{(\beta,\gamma)} + 3\overline{y}_2^{(\beta)} W_{3(20)}^{(\beta,\gamma)}\right] \end{aligned} \tag{8}$$

The subcell stress components are then expressed in terms of the unknown microvariables $W_{i(mn)}^{(\beta,\gamma)}$ and the applied macroscopic strains $\overline{\epsilon}_{ij}$ using the above relations in the Hooke's law

$$\sigma_{ij}^{(\beta,\gamma)} = C_{ijkl}^{(\beta,\gamma)} \epsilon_{kl}^{(\beta,\gamma)} \tag{9}$$

For orthotropic subcells considered herein, the stiffness tensor $\mathbf{C}^{(\beta,\gamma)}$ is characterized by nine independent elements in the principal material coordinate system formed by the intersections of three orthogonal planes of material symmetry coincident with the subcell faces.

In the original formulation, the unknown microvariables $W_{i(mn)}^{(\beta,\gamma)}$ were determined by satisfying different moments of the local stress equilibrium equations in a volumetric sense, and the displacement and traction continuity conditions between subcells and generic cells, together with the periodic boundary conditions, in a surface-averaged sense. In the reformulation, the surface-averaged

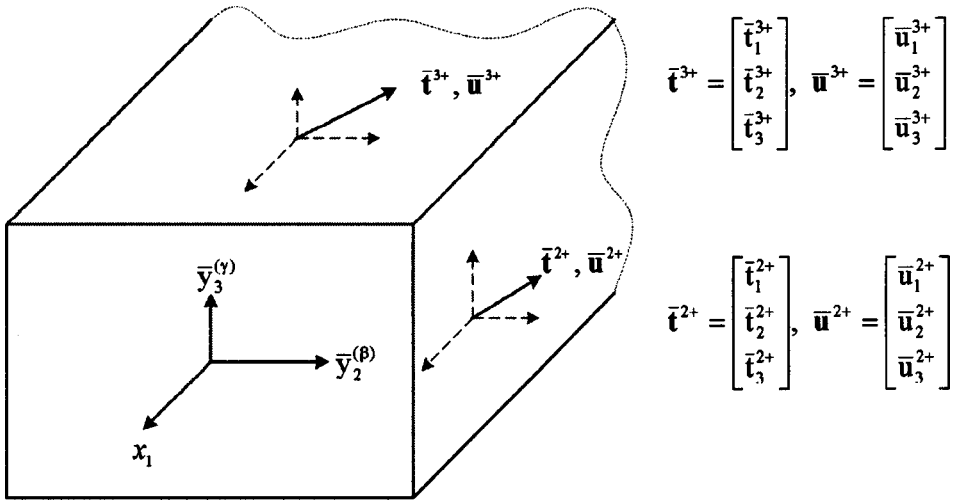

Fig. 3 A view of a subcell illustrating the convention employed in designating the surface-averaged displacement and traction components employed in the reformulation of HFGMC

fluctuating displacements are the fundamental unknowns that are related to the surface-averaged tractions through a local subcell matrix constructed in the manner described below.

3.1 Local Stiffness Matrix. We begin the construction of the local stiffness matrix for a (β,γ) subcell by defining the required two sets of surface-averaged quantities. First, the tractions at the subcell's outer faces are expressed in terms of stresses through Cauchy's relations

$$t_i^{\mathbf{n}^{(\beta,\gamma)}} = \sigma_{ji}^{(\beta,\gamma)} n_j^{(\beta,\gamma)} \tag{10}$$

where $\mathbf{n}^{(\beta,\gamma)}$ is the unit normal to a given face of the (β,γ) subcell. The corresponding surface-averaged traction components are defined in the standard manner

$$\overline{t}_i^{2\pm(\beta,\gamma)} = \frac{1}{l_\gamma} \int_{-l_\gamma/2}^{l_\gamma/2} t_i^{\mathbf{n}^{(\beta,\gamma)}} \left(\pm \frac{h_\beta}{2}, \overline{y}_3^{(\gamma)} \right) d\overline{y}_3^{(\gamma)} \tag{11}$$

$$\overline{t}_i^{3\pm(\beta,\gamma)} = \frac{1}{h_\beta} \int_{-h_\beta/2}^{h_\beta/2} t_i^{\mathbf{n}^{(\beta,\gamma)}} \left(\overline{y}_2^{(\beta)}, \pm \frac{l_\gamma}{2} \right) d\overline{y}_2^{(\beta)}, \quad i = 1,2,3 \tag{12}$$

where the superscript $j\pm(j=2,3)$ denotes the direction of the normal to the positive $(+)$ or negative $(-)$ face of the (β,γ) subcell (Fig. 3). Similarly, the surface-averaged fluctuating displacement components are determined from

$$\overline{u}_i'^{2\pm(\beta,\gamma)} = \frac{1}{l_\gamma} \int_{-l_\gamma/2}^{l_\gamma/2} u_i'^{(\beta,\gamma)} \left(\pm \frac{h_\beta}{2}, \overline{y}_3^{(\gamma)} \right) d\overline{y}_3^{(\gamma)} \tag{13}$$

$$\overline{u}_i'^{3\pm(\beta,\gamma)} = \frac{1}{h_\beta} \int_{-h_\beta/2}^{h_\beta/2} u_i'^{(\beta,\gamma)} \left(\overline{y}_2^{(\beta)}, \pm \frac{l_\gamma}{2} \right) d\overline{y}_2^{(\beta)}, \quad i = 1,2,3 \tag{14}$$

where $\overline{u}_i'^{j\pm(\beta,\gamma)}$ is the fluctuating surface-averaged displacement in the ith direction evaluated on the face of the (β,γ) subcell with normal in the $\pm j$th direction (Fig. 3).

The displacement field approximation at the subcell level given by Eq. (6) contains a total of 15 unknown $W_{i(mn)}^{(\beta,\gamma)}$ microvariables in each subcell. Since a total of 12 surface-averaged displacements must be related to 12 surface-averaged tractions through the local stiffness matrix for each (β,γ) subcell, three additional equations are required in order to express all 15 unknown microvariables in terms of the surface-averaged displacements. These three equations are obtained by satisfying the stress equilibrium equations in each subcell in a volumetric sense. It is convenient to express the local stress equilibrium equations in terms of the surface integrals of traction components as these yield direct relations for the various surface-averaged tractions used in the reformulation

$$\int_{S_{(\beta,\gamma)}} t_i^{\mathbf{n}^{(\beta,\gamma)}} dS = 0, \quad i = 1,2,3 \tag{15}$$

It is clear that the reformulation eliminates the need to consider the first and second moments of these equations, simplifying the volume-averaging procedure of the equilibrium equations to the zeroth moments, thereby revealing HFGMC to be a direct volume-averaging technique.

The above three sets of equations form the kernel of the reformulated HFGMC's theoretical framework and set the stage for the construction of the local stiffness matrix for the (β,γ) subcell. We proceed to do this by first defining the axial (out-of-plane) and transverse (in-plane) surface-averaged traction, displacement, and microvariable vectors for the (β,γ) subcell as follows:

$$\begin{aligned}
\overline{\mathbf{t}}_{\text{axial}}^{(\beta,\gamma)} &= [(\overline{t}_1^{2+}, \overline{t}_1^{2-}, \overline{t}_1^{3+}, \overline{t}_1^{3-})^{(\beta,\gamma)}]^{\mathrm{T}} \\
\overline{\mathbf{u}}_{\text{axial}}'^{(\beta,\gamma)} &= [(\overline{u}_1'^{2+}, \overline{u}_1'^{2-}, \overline{u}_1'^{3+}, \overline{u}_1'^{3-})^{(\beta,\gamma)}]^{\mathrm{T}} \\
\mathbf{W}_{\text{axial}}^{(\beta,\gamma)} &= [(W_{1(10)}, W_{1(20)}, W_{1(01)}, W_{1(02)})^{(\beta,\gamma)}]^{\mathrm{T}}
\end{aligned} \tag{16}$$

$$\begin{aligned}
\overline{\mathbf{t}}_{\text{trans}}^{(\beta,\gamma)} &= [(\overline{t}_2^{2+}, \overline{t}_2^{2-}, \overline{t}_3^{2+}, \overline{t}_3^{2-}, \overline{t}_2^{3+}, \overline{t}_2^{3-}, \overline{t}_3^{3+}, \overline{t}_3^{3-})^{(\beta,\gamma)}]^{\mathrm{T}} \\
\overline{\mathbf{u}}_{\text{trans}}'^{(\beta,\gamma)} &= [(\overline{u}_2'^{2+}, \overline{u}_2'^{2-}, \overline{u}_3'^{2+}, \overline{u}_3'^{2-}, \overline{u}_2'^{3+}, \overline{u}_2'^{3-}, \overline{u}_3'^{3+}, \\
&\quad \overline{u}_3'^{3-})^{(\beta,\gamma)}]^{\mathrm{T}} \\
\mathbf{W}_{\text{trans}}^{(\beta,\gamma)} &= [(W_{2(10)}, W_{2(20)}, W_{3(10)}, W_{3(20)}, W_{2(01)}, W_{2(02)}, \\
&\quad W_{3(01)}, W_{3(02)})^{(\beta,\gamma)}]^{\mathrm{T}}
\end{aligned} \tag{17}$$

where the superscript T denotes the transpose. We note that the microvariable vectors $\mathbf{W}_{\text{axial}}^{(\beta,\gamma)}$ and $\mathbf{W}_{\text{trans}}^{(\beta,\gamma)}$ contain only the first- and second-order quantities $W_{i(mn)}^{(\beta,\gamma)}$. Then, substituting Eqs. (8)–(10) into Eqs. (11) and (12), performing the required integration, and assembling the resulting equations in matrix form, we obtain two uncoupled relations for the axial and transverse quantities

$$\overline{\mathbf{t}}_{\text{axial}}^{(\beta,\gamma)} = \mathbf{C}_{\text{axial}}^{(\beta,\gamma)} \mathbf{W}_{\text{axial}}^{(\beta,\gamma)} + \overline{\mathbf{C}}_{\text{axial}}^{(\beta,\gamma)} \overline{\boldsymbol{\epsilon}}_{\text{axial}} \tag{18}$$

$$\overline{\mathbf{t}}_{\text{trans}}^{(\beta,\gamma)} = \mathbf{C}_{\text{trans}}^{(\beta,\gamma)} \mathbf{W}_{\text{trans}}^{(\beta,\gamma)} + \overline{\mathbf{C}}_{\text{trans}}^{(\beta,\gamma)} \overline{\boldsymbol{\epsilon}}_{\text{trans}} \tag{19}$$

where

$$\mathbf{C}_{\text{axial}}^{(\beta,\gamma)} = \begin{bmatrix} C_{66} & \frac{3h_\beta}{2} C_{66} & 0 & 0 \\ -C_{66} & \frac{3h_\beta}{2} C_{66} & 0 & 0 \\ 0 & 0 & C_{55} & \frac{3l_\gamma}{2} C_{55} \\ 0 & 0 & -C_{55} & \frac{3l_\gamma}{2} C_{55} \end{bmatrix}^{(\beta,\gamma)} \quad \overline{\mathbf{C}}_{\text{axial}}^{(\beta,\gamma)} = \begin{bmatrix} 2C_{66} & 0 \\ -2C_{66} & 0 \\ 0 & 2C_{55} \\ 0 & -2C_{55} \end{bmatrix}^{(\beta,\gamma)}$$

$$\mathbf{C}_{\text{trans}}^{(\beta,\gamma)} = \begin{bmatrix} C_{22} & \frac{3h_\beta}{2} C_{22} & 0 & 0 & 0 & 0 & C_{23} & 0 \\ -C_{22} & \frac{3h_\beta}{2} C_{22} & 0 & 0 & 0 & 0 & -C_{23} & 0 \\ 0 & 0 & C_{44} & \frac{3h_\beta}{2} C_{44} & C_{44} & 0 & 0 & 0 \\ 0 & 0 & -C_{44} & \frac{3h_\beta}{2} C_{44} & -C_{44} & 0 & 0 & 0 \\ 0 & 0 & C_{44} & 0 & C_{44} & \frac{3l_\gamma}{2} C_{44} & 0 & 0 \\ 0 & 0 & -C_{44} & 0 & -C_{44} & \frac{3l_\gamma}{2} C_{44} & 0 & 0 \\ C_{23} & 0 & 0 & 0 & 0 & 0 & C_{33} & \frac{3l_\gamma}{2} C_{33} \\ -C_{23} & 0 & 0 & 0 & 0 & 0 & -C_{33} & \frac{3l_\gamma}{2} C_{33} \end{bmatrix}^{(\beta,\gamma)}$$

$$\overline{\mathbf{C}}_{\text{trans}}^{(\beta,\gamma)} = \begin{bmatrix} C_{12} & C_{22} & C_{23} & 0 \\ -C_{12} & -C_{22} & -C_{23} & 0 \\ 0 & 0 & 0 & 2C_{44} \\ 0 & 0 & 0 & -2C_{44} \\ 0 & 0 & 0 & 2C_{44} \\ 0 & 0 & 0 & -2C_{44} \\ C_{13} & C_{23} & C_{33} & 0 \\ -C_{13} & -C_{23} & -C_{33} & 0 \end{bmatrix}^{(\beta,\gamma)}$$

and $\overline{\boldsymbol{\epsilon}}_{\text{axial}} = [\overline{\epsilon}_{12}, \overline{\epsilon}_{13}]^{\text{T}}$ and $\overline{\boldsymbol{\epsilon}}_{\text{trans}} = [\overline{\epsilon}_{11}, \overline{\epsilon}_{22}, \overline{\epsilon}_{33}, \overline{\epsilon}_{23}]^{\text{T}}$.

The first-order, $W_{i(10)}^{(\beta,\gamma)}$, $W_{i(01)}^{(\beta,\gamma)}$, and second-order, $W_{i(20)}^{(\beta,\gamma)}$, $W_{i(02)}^{(\beta,\gamma)}$, microvariables in Eqs. (18) and (19) are subsequently expressed in terms of the fluctuating surface-averaged displacements $\overline{\mathbf{u}}'^{(\beta,\gamma)}$ and the zeroth-order microvariables $W_{i(00)}^{(\beta,\gamma)}$ by employing Eqs. (6) in Eqs. (13) and (14), performing the averaging procedure, and some additional algebraic manipulations,

$$\begin{bmatrix} W_{1(10)} \\ W_{1(20)} \\ W_{1(01)} \\ W_{1(02)} \end{bmatrix}^{(\beta,\gamma)} = \begin{bmatrix} \frac{1}{h_\beta} & -\frac{1}{h_\beta} & 0 & 0 \\ \frac{2}{h_\beta^2} & \frac{2}{h_\beta^2} & 0 & 0 \\ 0 & 0 & \frac{1}{l_\gamma} & -\frac{1}{l_\gamma} \\ 0 & 0 & \frac{2}{l_\gamma^2} & \frac{2}{l_\gamma^2} \end{bmatrix} \begin{bmatrix} \overline{u}_1'^{2+} \\ \overline{u}_1'^{2-} \\ \overline{u}_1'^{3+} \\ \overline{u}_1'^{3-} \end{bmatrix}^{(\beta,\gamma)} - \begin{bmatrix} 0 \\ \frac{4}{h_\beta^2} \\ 0 \\ \frac{4}{l_\gamma^2} \end{bmatrix} W_{1(00)}^{(\beta,\gamma)} \tag{20}$$

$$\begin{bmatrix} W_{2(10)} \\ W_{2(20)} \\ W_{3(10)} \\ W_{3(20)} \end{bmatrix}^{(\beta,\gamma)} = \begin{bmatrix} \frac{1}{h_\beta} & -\frac{1}{h_\beta} & 0 & 0 \\ \frac{2}{h_\beta^2} & \frac{2}{h_\beta^2} & 0 & 0 \\ 0 & 0 & \frac{1}{h_\beta} & -\frac{1}{h_\beta} \\ 0 & 0 & \frac{2}{h_\beta^2} & \frac{2}{h_\beta^2} \end{bmatrix} \begin{bmatrix} \overline{u}_2'^{2+} \\ \overline{u}_2'^{2-} \\ \overline{u}_3'^{2+} \\ \overline{u}_3'^{2-} \end{bmatrix}^{(\beta,\gamma)} - \begin{bmatrix} 0 & 0 \\ \frac{4}{h_\beta^2} & 0 \\ 0 & 0 \\ 0 & \frac{4}{h_\beta^2} \end{bmatrix} \begin{bmatrix} W_{2(00)} \\ W_{3(00)} \end{bmatrix}^{(\beta,\gamma)} \tag{21}$$

$$\begin{bmatrix} W_{2(01)} \\ W_{2(02)} \\ W_{3(01)} \\ W_{3(02)} \end{bmatrix}^{(\beta,\gamma)} = \begin{bmatrix} \frac{1}{l_\gamma} & -\frac{1}{l_\gamma} & 0 & 0 \\ \frac{2}{l_\gamma^2} & \frac{2}{l_\gamma^2} & 0 & 0 \\ 0 & 0 & \frac{1}{l_\gamma} & -\frac{1}{l_\gamma} \\ 0 & 0 & \frac{2}{l_\gamma^2} & \frac{2}{l_\gamma^2} \end{bmatrix} \begin{bmatrix} \overline{u}_2'^{3+} \\ \overline{u}_2'^{3-} \\ \overline{u}_3'^{3+} \\ \overline{u}_3'^{3-} \end{bmatrix}^{(\beta,\gamma)} - \begin{bmatrix} 0 & 0 \\ \frac{4}{l_\gamma^2} & 0 \\ 0 & 0 \\ 0 & \frac{4}{l_\gamma^2} \end{bmatrix} \begin{bmatrix} W_{2(00)} \\ W_{3(00)} \end{bmatrix}^{(\beta,\gamma)} \tag{22}$$

The zeroth-order microvariables are then expressed in terms of the fluctuating surface-averaged displacements by employing Eqs. (18) and (19) in conjunction with Eqs. (20)–(22) in the three equilibrium equations expressed in terms of surface-averaged tractions that are obtained from Eqs. (15). Performing the required integration and simplifying yields

$$W_{1(00)}^{(\beta,\gamma)} = \frac{C_{66}^{(\beta,\gamma)}}{2\overline{C}_{11}^{(\beta,\gamma)}} (\overline{u}_1'^{2+} + \overline{u}_1'^{2-})^{(\beta,\gamma)} + \frac{h_\beta^2 C_{55}^{(\beta,\gamma)}}{2l_\gamma^2 \overline{C}_{11}^{(\beta,\gamma)}} (\overline{u}_1'^{3+} + \overline{u}_1'^{3-})^{(\beta,\gamma)} \tag{23}$$

$$W_{2(00)}^{(\beta,\gamma)} = \frac{C_{22}^{(\beta,\gamma)}}{2\overline{C}_{22}^{(\beta,\gamma)}} (\overline{u}_2'^{2+} + \overline{u}_2'^{2-})^{(\beta,\gamma)} + \frac{h_\beta^2 C_{44}^{(\beta,\gamma)}}{2l_\gamma^2 \overline{C}_{22}^{(\beta,\gamma)}} (\overline{u}_2'^{3+} + \overline{u}_2'^{3-})^{(\beta,\gamma)} \tag{24}$$

$$W_{3(00)}^{(\beta,\gamma)} = \frac{C_{33}^{(\beta,\gamma)}}{2\overline{C}_{33}^{(\beta,\gamma)}} (\overline{u}_3'^{3+} + \overline{u}_3'^{3-})^{(\beta,\gamma)} + \frac{l_\gamma^2 C_{44}^{(\beta,\gamma)}}{2h_\beta^2 \overline{C}_{33}^{(\beta,\gamma)}} (\overline{u}_3'^{2+} + \overline{u}_3'^{2-})^{(\beta,\gamma)} \tag{25}$$

where

$$\overline{C}_{11}^{(\beta,\gamma)} = C_{66}^{(\beta,\gamma)} + \frac{h_\beta^2}{l_\gamma^2} C_{55}^{(\beta,\gamma)}, \quad \overline{C}_{22}^{(\beta,\gamma)} = C_{22}^{(\beta,\gamma)} + \frac{h_\beta^2}{l_\gamma^2} C_{44}^{(\beta,\gamma)},$$

$$\overline{C}_{33}^{(\beta,\gamma)} = C_{33}^{(\beta,\gamma)} + \frac{l_\gamma^2}{h_\beta^2} C_{44}^{(\beta,\gamma)}$$

The above relations allow one to express the surface-averaged tractions given by Eqs. (18) and (19) exclusively in terms of the fluctuating surface-averaged displacements and the applied macroscopic strains. The axial and transverse surface-averaged tractions $\overline{t}_1^{j\pm(\beta,\gamma)}$ $(j=2,3)$ and $\overline{t}_i^{j\pm(\beta,\gamma)}$ $(i,j=2,3)$ are related to the corresponding fluctuating surface-averaged displacements $\overline{u}_1'^{j\pm(\beta,\gamma)}$ $(j=2,3)$ and $\overline{u}_i'^{j\pm(\beta,\gamma)}$ $(i,j=2,3)$ through the local stiffness matrices $\mathbf{L}^{(\beta,\gamma)}$ and $\mathbf{K}^{(\beta,\gamma)}$ as shown below:

$$\overline{\mathbf{t}}_{\text{axial}}^{(\beta,\gamma)} = \mathbf{L}^{(\beta,\gamma)} \overline{\mathbf{u}}_{\text{axial}}^{(\beta,\gamma)} + \overline{\mathbf{C}}_{\text{axial}}^{(\beta,\gamma)} \overline{\boldsymbol{\epsilon}}_{\text{axial}} \tag{26}$$

$$\overline{\mathbf{t}}_{\text{trans}}^{(\beta,\gamma)} = \mathbf{K}^{(\beta,\gamma)} \overline{\mathbf{u}}_{\text{trans}}^{(\beta,\gamma)} + \overline{\mathbf{C}}_{\text{trans}}^{(\beta,\gamma)} \overline{\boldsymbol{\epsilon}}_{\text{trans}} \tag{27}$$

where the elements of the local stiffness matrices are given explicitly in terms of the mechanical properties and subcell dimensions in the Appendix.

The above construction clarifies the differences between the present approach and a finite-element-based solution of the unit cell problem. In particular, surface-averaged rather than nodal quantities are employed in the construction of the $\mathbf{L}^{(\beta,\gamma)}$ and $\mathbf{K}^{(\beta,\gamma)}$ local stiffness matrices, and subcell equilibrium in the large is enforced directly instead of a variational principle.

3.2 Global Stiffness Matrix. The local stiffness matrices are used to construct the global stiffness matrix by first applying interfacial traction and displacement continuity conditions, and then periodic boundary conditions, all imposed in a surface-averaged sense across adjacent subcell interfaces and boundary subcells. At the βth interface separating (β,γ) and $(\beta+1,\gamma)$ subcells, the three fluctuating surface-averaged displacements on either side of the interface must be equal. The same holds true at the γth interface separating (β,γ) and $(\beta,\gamma+1)$ subcells. These continuity conditions are enforced by setting the corresponding displacement components to common unknown quantities as shown below:

$$\overline{u}_i'^{2+(\beta,\gamma)} = \overline{u}_i'^{2-(\beta+1,\gamma)} = \overline{u}_i'^{2(\beta+1,\gamma)} \tag{28}$$

$$\overline{u}_i'^{3+(\beta,\gamma)} = \overline{u}_i'^{3-(\beta,\gamma+1)} = \overline{u}_i'^{3(\beta,\gamma+1)}, \quad i=1,2,3 \tag{29}$$

The above equations hold true at $\beta=1,\ldots,N_\beta-1$ and $\gamma=1,\ldots,N_\gamma-1$ subcell interfaces, respectively. This gives rise to $3(N_\beta-1)N_\gamma+3(N_\gamma-1)N_\beta$ unknown interfacial surface-averaged displacements within the unit cell. The remaining $6(N_\beta+N_\gamma)$ surface-averaged displacements at the external boundaries of the unit cell

$$\overline{u}_i'^{2(1,\gamma)}, \ \overline{u}_i'^{2(N_\beta+1,\gamma)}, \ \overline{u}_i'^{3(\beta,1)}, \ \overline{u}_i'^{3(\beta,N_\gamma+1)}, \quad i=1,2,3 \tag{30}$$

are related to the corresponding surface-averaged boundary tractions. These surface-averaged boundary quantities are related through the periodic boundary conditions which will be incorporated into the global stiffness matrix in the last step.

Proceeding in a similar manner, the traction continuity conditions (or the interfacial equilibrium conditions) at the βth and γth interfaces are ensured by

$$\overline{t}_i^{2+(\beta,\gamma)} + \overline{t}_i^{2-(\beta+1,\gamma)} = 0 \tag{31}$$

$$\overline{t}_i^{3+(\beta,\gamma)} + \overline{t}_i^{3-(\beta,\gamma+1)} = 0, \quad i=1,2,3 \tag{32}$$

The above two sets of equations are written in terms of the common interfacial surface-averaged displacements $\overline{u}_1'^{2(\cdot,\cdot)}$, $\overline{u}_1'^{3(\cdot,\cdot)}$,

$\overline{u}_2'^{2(\cdot,\cdot)}$, $\overline{u}_2'^{3(\cdot,\cdot)}$, $\overline{u}_3'^{2(\cdot,\cdot)}$, $\overline{u}_3'^{3(\cdot,\cdot)}$ using Eqs. (26) and (27) and the displacement continuity conditions given by Eqs. (28) and (29). For $i=1$ we have

$$L_{12}^{(\beta,\gamma)}\overline{u}_1'^{2(\beta,\gamma)}+(L_{11}^{(\beta,\gamma)}+L_{22}^{(\beta+1,\gamma)})\overline{u}_1'^{2(\beta+1,\gamma)}+L_{21}^{(\beta+1,\gamma)}\overline{u}_1'^{2(\beta+2,\gamma)}+L_{14}^{(\beta,\gamma)}\overline{u}_1'^{3(\beta,\gamma)}+L_{13}^{(\beta,\gamma)}\overline{u}_1'^{3(\beta,\gamma+1)}+L_{24}^{(\beta+1,\gamma)}\overline{u}_1'^{3(\beta+1,\gamma)}+L_{23}^{(\beta+1,\gamma)}\overline{u}_1'^{3(\beta+1,\gamma+1)}=2(C_{66}^{(\beta,\gamma)}-C_{66}^{(\beta+1,\gamma)})\overline{\epsilon}_{12} \tag{33}$$

$$L_{32}^{(\beta,\gamma)}\overline{u}_1'^{2(\beta,\gamma)}+L_{31}^{(\beta,\gamma)}\overline{u}_1'^{2(\beta+1,\gamma)}+L_{42}^{(\beta,\gamma+1)}\overline{u}_1'^{2(\beta,\gamma+1)}+L_{41}^{(\beta,\gamma+1)}\overline{u}_1'^{2(\beta+1,\gamma+1)}+L_{34}^{(\beta,\gamma)}\overline{u}_1'^{3(\beta,\gamma)}+(L_{33}^{(\beta,\gamma)}+L_{44}^{(\beta,\gamma+1)})\overline{u}_1'^{3(\beta,\gamma+1)}+L_{43}^{(\beta,\gamma+1)}\overline{u}_1'^{3(\beta,\gamma+2)}=2(C_{55}^{(\beta,\gamma)}-C_{55}^{(\beta,\gamma+1)})\overline{\epsilon}_{13} \tag{34}$$

while for $i=2$, 3, Eqs. (31) and (32) become

$$K_{12}^{(\beta,\gamma)}\overline{u}_2'^{2(\beta,\gamma)}+(K_{11}^{(\beta,\gamma)}+K_{22}^{(\beta+1,\gamma)})\overline{u}_2'^{2(\beta+1,\gamma)}+K_{21}^{(\beta+1,\gamma)}\overline{u}_2'^{2(\beta+2,\gamma)}+K_{16}^{(\beta,\gamma)}\overline{u}_2'^{3(\beta,\gamma)}+K_{15}^{(\beta,\gamma)}\overline{u}_2'^{3(\beta,\gamma+1)}+K_{26}^{(\beta+1,\gamma)}\overline{u}_2'^{3(\beta+1,\gamma)}+K_{25}^{(\beta+1,\gamma)}\overline{u}_2'^{3(\beta+1,\gamma+1)}+K_{18}^{(\beta,\gamma)}\overline{u}_3'^{3(\beta,\gamma)}+K_{17}^{(\beta,\gamma)}\overline{u}_3'^{3(\beta,\gamma+1)}+K_{28}^{(\beta+1,\gamma)}\overline{u}_3'^{3(\beta+1,\gamma)}+K_{27}^{(\beta+1,\gamma)}\overline{u}_3'^{3(\beta+1,\gamma+1)}=(C_{12}^{(\beta,\gamma)}-C_{12}^{(\beta+1,\gamma)})\overline{\epsilon}_{11}+(C_{22}^{(\beta,\gamma)}-C_{22}^{(\beta+1,\gamma)})\overline{\epsilon}_{22}+(C_{23}^{(\beta,\gamma)}-C_{23}^{(\beta+1,\gamma)})\overline{\epsilon}_{33} \tag{35}$$

$$K_{34}^{(\beta,\gamma)}\overline{u}_3'^{2(\beta,\gamma)}+(K_{33}^{(\beta,\gamma)}+K_{44}^{(\beta+1,\gamma)})\overline{u}_3'^{2(\beta+1,\gamma)}+K_{43}^{(\beta+1,\gamma)}\overline{u}_3'^{2(\beta+2,\gamma)}+K_{36}^{(\beta,\gamma)}\overline{u}_2'^{3(\beta,\gamma)}+K_{46}^{(\beta+1,\gamma)}\overline{u}_2'^{3(\beta+1,\gamma)}+K_{35}^{(\beta,\gamma)}\overline{u}_2'^{3(\beta,\gamma+1)}+K_{45}^{(\beta+1,\gamma)}\overline{u}_2'^{3(\beta+1,\gamma+1)}+K_{38}^{(\beta,\gamma)}\overline{u}_3'^{3(\beta,\gamma)}+K_{48}^{(\beta+1,\gamma)}\overline{u}_3'^{3(\beta+1,\gamma)}+K_{37}^{(\beta,\gamma)}\overline{u}_3'^{3(\beta,\gamma+1)}+K_{47}^{(\beta+1,\gamma)}\overline{u}_3'^{3(\beta+1,\gamma+1)}=2(C_{44}^{(\beta,\gamma)}-C_{44}^{(\beta+1,\gamma)})\overline{\epsilon}_{23} \tag{36}$$

$$K_{52}^{(\beta,\gamma)}\overline{u}_2'^{2(\beta,\gamma)}+K_{51}^{(\beta,\gamma)}\overline{u}_2'^{2(\beta+1,\gamma)}+K_{62}^{(\beta,\gamma+1)}\overline{u}_2'^{2(\beta,\gamma+1)}+K_{61}^{(\beta,\gamma+1)}\overline{u}_2'^{2(\beta+1,\gamma+1)}+K_{54}^{(\beta,\gamma)}\overline{u}_3'^{2(\beta,\gamma)}+K_{53}^{(\beta,\gamma)}\overline{u}_3'^{2(\beta+1,\gamma)}+K_{64}^{(\beta,\gamma+1)}\overline{u}_3'^{2(\beta,\gamma+1)}+K_{63}^{(\beta,\gamma+1)}\overline{u}_3'^{2(\beta+1,\gamma+1)}+K_{56}^{(\beta,\gamma)}\overline{u}_2'^{3(\beta,\gamma)}+(K_{55}^{(\beta,\gamma)}+K_{66}^{(\beta,\gamma+1)})\overline{u}_2'^{3(\beta,\gamma+1)}+K_{65}^{(\beta,\gamma+1)}\overline{u}_2'^{3(\beta,\gamma+2)}=2(C_{44}^{(\beta,\gamma)}-C_{44}^{(\beta,\gamma+1)})\overline{\epsilon}_{23} \tag{37}$$

$$K_{72}^{(\beta,\gamma)}\overline{u}_2'^{2(\beta,\gamma)}+K_{71}^{(\beta,\gamma)}\overline{u}_2'^{2(\beta+1,\gamma)}+K_{82}^{(\beta,\gamma+1)}\overline{u}_2'^{2(\beta,\gamma+1)}+K_{81}^{(\beta,\gamma+1)}\overline{u}_2'^{2(\beta+1,\gamma+1)}+K_{74}^{(\beta,\gamma)}\overline{u}_3'^{2(\beta,\gamma)}+K_{73}^{(\beta,\gamma)}\overline{u}_3'^{2(\beta+1,\gamma)}+K_{84}^{(\beta,\gamma+1)}\overline{u}_3'^{2(\beta,\gamma+1)}+K_{83}^{(\beta,\gamma+1)}\overline{u}_3'^{2(\beta+1,\gamma+1)}+K_{78}^{(\beta,\gamma)}\overline{u}_3'^{3(\beta,\gamma)}+(K_{77}^{(\beta,\gamma)}+K_{88}^{(\beta,\gamma+1)})\overline{u}_3'^{3(\beta,\gamma+1)}+K_{87}^{(\beta,\gamma+1)}\overline{u}_3'^{3(\beta,\gamma+2)}=(C_{13}^{(\beta,\gamma)}-C_{13}^{(\beta,\gamma+1)})\overline{\epsilon}_{11}+(C_{23}^{(\beta,\gamma)}-C_{23}^{(\beta,\gamma+1)})\overline{\epsilon}_{22}+(C_{33}^{(\beta,\gamma)}-C_{33}^{(\beta,\gamma+1)})\overline{\epsilon}_{33} \tag{38}$$

Equations (33)–(38) provide us with a total of $3(N_\beta-1)N_\gamma+3(N_\gamma-1)N_\beta$ equations in terms of the common interfacial surface-averaged displacements and the surface-averaged displacements at the external boundaries of the unit cell. The axial and transverse surface-averaged displacements appear separately in the first and second set of these equations, respectively. Hence, they are assembled into two global stiffness matrices in the manner described next.

Assembly and Structure of the Global Stiffness Matrices. We initially assemble the global stiffness matrices by assuming that the unit cell's boundary is subjected to prescribed surface-averaged tractions. The assembly thus includes the boundary cells $(1,\gamma)$, (N_β,γ) and $(\beta,1)$, (β,N_γ), which provide the additional $6(N_\beta+N_\gamma)$ equations involving the boundary surface-averaged tractions and displacements, in addition to the interfacial continuity conditions described above. The final systems of equations relating the axial and transverse quantities are symbolically written as

$$\begin{bmatrix}\mathbf{L}_{11} & \mathbf{L}_{12}\\ \mathbf{L}_{21} & \mathbf{L}_{22}\end{bmatrix}\begin{bmatrix}\overline{\mathbf{u}}_1'^{2}\\ \overline{\mathbf{u}}_1'^{3}\end{bmatrix}=\begin{bmatrix}\overline{\mathbf{t}}_1^{2}\\ \overline{\mathbf{t}}_1^{3}\end{bmatrix}+\begin{bmatrix}\Delta\mathbf{c}_{11} & \mathbf{0}\\ \mathbf{0} & \Delta\mathbf{c}_{22}\end{bmatrix}\begin{bmatrix}\overline{\boldsymbol{\epsilon}}_{12}\\ \overline{\boldsymbol{\epsilon}}_{13}\end{bmatrix} \tag{39}$$

$$\begin{bmatrix}\mathbf{K}_{11} & \mathbf{0} & \mathbf{K}_{13} & \mathbf{K}_{14}\\ \mathbf{0} & \mathbf{K}_{22} & \mathbf{K}_{23} & \mathbf{K}_{24}\\ \mathbf{K}_{31} & \mathbf{K}_{32} & \mathbf{K}_{33} & \mathbf{0}\\ \mathbf{K}_{41} & \mathbf{K}_{42} & \mathbf{0} & \mathbf{K}_{44}\end{bmatrix}\begin{bmatrix}\overline{\mathbf{u}}_2'^{2}\\ \overline{\mathbf{u}}_3'^{2}\\ \overline{\mathbf{u}}_2'^{3}\\ \overline{\mathbf{u}}_3'^{3}\end{bmatrix}=\begin{bmatrix}\overline{\mathbf{t}}_2^{2}\\ \overline{\mathbf{t}}_3^{2}\\ \overline{\mathbf{t}}_2^{3}\\ \overline{\mathbf{t}}_3^{3}\end{bmatrix}+\begin{bmatrix}\Delta\mathbf{C}_{11} & \Delta\mathbf{C}_{12} & \Delta\mathbf{C}_{13} & \mathbf{0}\\ \mathbf{0} & \mathbf{0} & \mathbf{0} & \Delta\mathbf{C}_{24}\\ \mathbf{0} & \mathbf{0} & \mathbf{0} & \Delta\mathbf{C}_{34}\\ \Delta\mathbf{C}_{41} & \Delta\mathbf{C}_{42} & \Delta\mathbf{C}_{43} & \mathbf{0}\end{bmatrix}\begin{bmatrix}\overline{\boldsymbol{\epsilon}}_{11}\\ \overline{\boldsymbol{\epsilon}}_{22}\\ \overline{\boldsymbol{\epsilon}}_{33}\\ \overline{\boldsymbol{\epsilon}}_{23}\end{bmatrix} \tag{40}$$

where

$$\overline{\mathbf{u}}_i'^{2}=[\overline{\mathbf{u}}_i'^{2(1)},\ldots,\overline{\mathbf{u}}_i'^{2(N_\gamma)}]$$

$$\text{with}\quad \overline{\mathbf{u}}_i'^{2(\gamma)}=[\overline{u}_i'^{2(1,\gamma)},\ldots,\overline{u}_i'^{2(N_\beta+1,\gamma)}],\quad (i=1,2,3)$$

$$\overline{\mathbf{u}}_i'^{3}=[\overline{\mathbf{u}}_i'^{3(1)},\ldots,\overline{\mathbf{u}}_i'^{3(N_\beta)}]$$

$$\text{with}\quad \overline{\mathbf{u}}_i'^{3(\beta)}=[\overline{u}_i'^{3(\beta,1)},\ldots,\overline{u}_i'^{3(\beta,N_\gamma+1)}],\quad (i=1,2,3)$$

and the structure of the surface-averaged traction vectors $\overline{\mathbf{t}}_i^{2}$ and $\overline{\mathbf{t}}_i^{3}$ is similar to the above surface-averaged interfacial displacement vectors. In this case, however, the only nonzero surface-averaged traction components are those associated with the boundary subcell external surfaces as shown below. This follows from the interfacial traction continuity conditions given by Eqs. (31) and (32).

$$\overline{\mathbf{t}}_i^{2}=[\overline{\mathbf{t}}_i^{2(1)},\ldots,\overline{\mathbf{t}}_i^{2(N_\gamma)}]$$

$$\text{with}\quad \overline{\mathbf{t}}_i^{2(\gamma)}=[\overline{t}_i^{2-(1,\gamma)},0,\ldots,0,\overline{t}_i^{2+(N_\beta+1,\gamma)}],\quad (i=1,2,3)$$

$$\overline{\mathbf{t}}_i^{3}=[\overline{\mathbf{t}}_i^{3(1)},\ldots,\overline{\mathbf{t}}_i^{3(N_\beta)}]$$

$$\text{with}\quad \overline{\mathbf{t}}_i^{3(\beta)}=[\overline{t}_i^{3-(\beta,1)},0,\ldots,0,\overline{t}_i^{3+(\beta,N_\gamma+1)}],\quad (i=1,2,3)$$

The size of the global stiffness matrix in the first system of equations, which consists of four submatrices, is $[2N_\beta N_\gamma+(N_\beta+N_\gamma)]\times[2N_\beta N_\gamma+(N_\beta+N_\gamma)]$. The global stiffness matrix in the second system of equations, whose size is $[4N_\beta N_\gamma+2(N_\beta+N_\gamma)]\times[4N_\beta N_\gamma+2(N_\beta+N_\gamma)]$, consists of twelve nonzero submatrices. The diagonal submatrices $\mathbf{L}_{ii}$ and $\mathbf{K}_{ii}$, whose structures are similar, relate the surface-averaged tractions to displacements in their respective directions and have entries concentrated along the diagonal. The off-diagonal submatrices $\mathbf{L}_{ij}$ and $\mathbf{K}_{ij}$, whose structures are also similar, represent coupling of the surface-averaged quantities in the y_2 and y_3 directions and have entries scattered throughout. The structure of the diagonal and off-diagonal submatrices in both systems of equations is the same as that in the reformulated higher-order theory for FGMs and has been described in detail by Bansal and Pindera [10].

Finally, the column submatrices $\Delta \mathbf{c}_{11}$, $\Delta \mathbf{c}_{22}$, and $\Delta \mathbf{C}_{11}, \ldots, \Delta \mathbf{C}_{43}$, which are multiplied by the macroscopic strains on the right-hand side of Eqs. (39) and (40), represent the differences in the elastic stiffness elements $C_{ij}^{(\beta\gamma)}$ between adjacent subcells in the y_2 and y_3 directions, as shown on the right hand side of the traction continuity equations given by Eqs. (33) and (34) and Eqs. (35)–(38).

Reduction of the Global Stiffness Matrices. The global stiffness matrices given in Eqs. (39) and (40) are further reduced using periodicity conditions on the surface-averaged displacements and tractions imposed on the external surfaces of the boundary subcells around the repeating unit cell. The periodicity conditions for the surface-averaged boundary displacements are

$$\overline{u}_i^{2(1,\gamma)} = \overline{u}_i^{2(N_\beta+1,\gamma)}, \quad \overline{u}_i^{3(\beta,1)} = \overline{u}_i^{3(\beta,N_\gamma+1)}, \quad (i=1,2,3) \tag{41}$$

Similarly, the periodicity conditions for the surface-averaged boundary tractions are

$$\overline{t}_i^{2(1,\gamma)} + \overline{t}_i^{2(N_\beta+1,\gamma)} = 0, \quad \overline{t}_i^{3(\beta,1)} + \overline{t}_i^{3(\beta,N_\gamma+1)} = 0, \quad (i=1,2,3) \tag{42}$$

The imposed periodicity conditions (41) and (42) eliminate the traction vectors on the right-hand sides of Eqs. (39) and (40), and provide us with the necessary $6N_\beta N_\gamma$ relations for the $6N_\beta N_\gamma$ unknown subcell surface-averaged displacements, i.e., $3(N_\beta - 1)N_\gamma + 3(N_\gamma - 1)N_\beta$ unknown common interfacial surface-averaged displacements along with $3(N_\beta + N_\gamma)$ unknown surface-averaged displacements at the external boundaries of the repeating unit cell. These relations are obtained from Eqs. (39) and (40) by combining and deleting appropriate rows and columns of the original stiffness matrices appearing in these equations.

The resulting reduced equations relate the unknown surface-averaged interfacial and boundary displacements to the applied macroscopic strains through the reduced stiffness matrices. The final reduction of these singular matrices involves constraining the corner subcell faces to eliminate rigid body motion. In view of the imposed periodicity conditions on the surface-averaged boundary displacements, constraining the external surfaces of one corner subcell and just one appropriate external surface of two corner subcells at opposite ends of the diagonal is sufficient.

3.3 Homogenized Constitutive Equations. The average strains in each subcell are related to the average macroscopic strains through Hill's strain concentration tensor [11], as

$$\overline{\boldsymbol{\epsilon}}^{(\beta,\gamma)} = \mathbb{A}^{(\beta,\gamma)} \overline{\boldsymbol{\epsilon}} \tag{43}$$

The average subcell strains are obtained by averaging Eqs. (8) over the subcell volume, yielding expressions in terms of the macroscopic strains $\overline{\boldsymbol{\epsilon}}_{ij}$ and the first-order microvariables $W_{i(mn)}^{(\beta,\gamma)}$. These microvariables are then expressed in terms of the interfacial surface-averaged displacements using Eqs. (20)–(25). The solution of the reduced systems of equations yields the interfacial and boundary surface-averaged displacements as a function of the macroscopic strains. This allows us to obtain the average strain components in each subcell in terms of the macroscopic strains. In practice, we determine the elements of the strain concentration tensor $\mathbb{A}^{(\beta,\gamma)}$ for each subcell numerically by applying one component of the macroscopic strain $\overline{\boldsymbol{\epsilon}}$ at a time. For instance, applying $\overline{\boldsymbol{\epsilon}}_{11} = 1$ and all others zero, and then solving the reduced systems of equations to obtain $\overline{\boldsymbol{\epsilon}}^{(\beta,\gamma)}$ for each subcell, we obtain the first column of the strain concentration tensor using Eq. (43). The remaining elements of the strain concentration tensor $\mathbb{A}^{(\beta,\gamma)}$ are obtained by successively applying the remaining macroscopic strain components one nonzero component at a time.

The average stress in each subcell is given by

$$\overline{\boldsymbol{\sigma}}^{(\beta,\gamma)} = \mathbf{C}^{(\beta,\gamma)} \overline{\boldsymbol{\epsilon}}^{(\beta,\gamma)} \tag{44}$$

in view of the fact that the material occupying a given (β,γ) subcell is homogeneous. Using Eq. (43) to express $\overline{\boldsymbol{\epsilon}}^{(\beta,\gamma)}$ in terms of the macroscopic strains, we obtain

$$\overline{\boldsymbol{\sigma}}^{(\beta,\gamma)} = \mathbf{C}^{(\beta,\gamma)} \mathbb{A}^{(\beta,\gamma)} \overline{\boldsymbol{\epsilon}} \tag{45}$$

Averaging the subcell stresses over the entire repeating unit cell, we then obtain the macroscopic stress in terms of the macroscopic strains for the composite in the form

$$\overline{\boldsymbol{\sigma}} = \frac{1}{HL} \sum_{\gamma=1}^{N_\gamma} \sum_{\beta=1}^{N_\beta} h_\beta l_\gamma \mathbf{C}^{(\beta,\gamma)} \mathbb{A}^{(\beta,\gamma)} \overline{\boldsymbol{\epsilon}} \tag{46}$$

which can be written in the form of a macroscopic constitutive equation for the unit cell response as follows

$$\overline{\boldsymbol{\sigma}} = \mathbf{C}^* \overline{\boldsymbol{\epsilon}} \tag{47}$$

where $\mathbf{C}^*$ represents the effective elastic stiffness matrix for the repeating unit cell and is given by

$$\mathbf{C}^* = \frac{1}{HL} \sum_{\gamma=1}^{N_\gamma} \sum_{\beta=1}^{N_\beta} h_\beta l_\gamma \mathbf{C}^{(\beta,\gamma)} \mathbb{A}^{(\beta,\gamma)} \tag{48}$$

4 Numerical Results

We test the high-fidelity model's predictive capability by determining the effective moduli of a unidirectional composite, with a square array of fibers in the x_2–x_3 plane, as a function of the rotation angle θ about the fiber axis x_1. The moduli in the rotated coordinate system are then compared with the standard transformation equations which provide the correct answer. We also generate the local stress fields within a repeating unit cell for a representative rotation angle. To highlight the advantages and need for HFGMC, the moduli as well as the local stress fields predicted by this model are compared with the corresponding GMC results. This comparison illustrates the importance of including the effects of shear coupling in heterogeneous materials.

Figure 4 shows the investigated square array of fibers with a fiber volume fraction of 0.35, extending to infinity in the x_2–x_3 plane. Both the fiber and the matrix phases are isotropic. To amplify the influence of shear coupling, we consider two cases with radically different contrasts between the fiber and matrix properties. In the first case, the matrix is an epoxy resin and the fibers are glass with typical elastic moduli that produce the Young's moduli ratio $E_f/E_m = 20$. In the second case, we consider an aluminum matrix weakened by holes which are simulated by very compliant inclusions that yield the Young's moduli ratio $E_f/E_m = 0.01$. The actual constituent moduli values are given in Table 1.

As shown in Fig. 4, five different repeating unit cells are analyzed that produce homogenized properties of the same fiber array relative to five coordinate systems generated by rotating the principal material coordinate system through an angle θ about the fiber axis. These are arranged in two rows such that the number of fibers in each repeating unit cell increases in each row from left to right. As observed, the rotation angle does not increase monotonically with increasing number of fibers. The first repeating unit cell in the first row of Fig. 4 with the circular fiber in the center, for which $\theta = 0$ deg, represents the infinite square fiber array in the principal material coordinate system in light of the fact that the orthogonal planes of material symmetry passing through the fiber center coincide with the global x_1–x_2–x_3 coordinate system. Clearly, this is the simplest unit cell. The remaining unit cells were constructed by connecting the center of a reference fiber to the center of the fiber a certain number of fibers to the right of the reference fiber and up. This specified both the rotation angle and the length of the lower inclined edge of the unit cell. Completing the square in the same manner produced the entire unit cell for the particular rotation angle. Thus the four rotation angles were obtained from the relations $\theta = \tan^{-1}\{1/4, 1/2, 3/4, 1\}$, where the de-

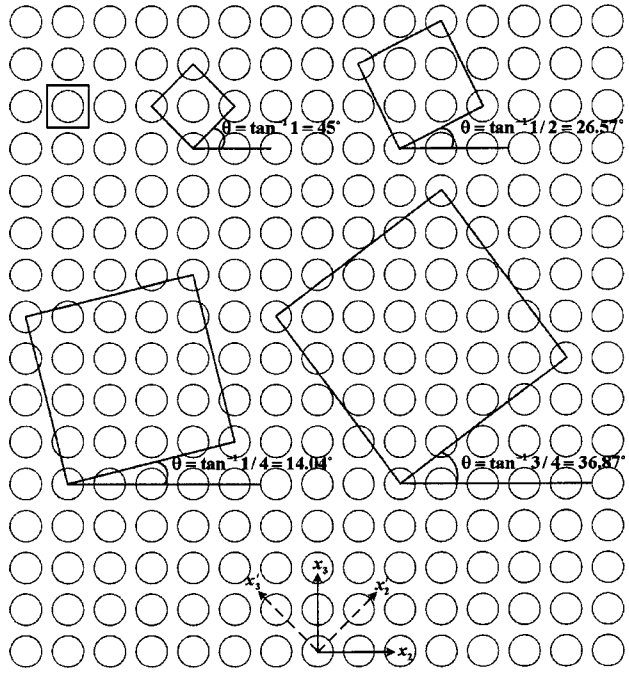

Fig. 4 A representation of an infinite array of inclusions in square packing, showing five repeating unit cells which represent the same array in different coordinate systems rotated by the indicated angles about the fiber axis

nominator represents the number of fiber distances to the right of the reference fiber, and the numerator the number of fibers up. The fiber distance is the horizontal or vertical distance between adjacent fiber centers. It is evident that the generated unit cells are the basic building blocks of the same fiber array in the five considered coordinate systems, which include the principal material system. It is also clear that three out of the five do not possess planes of material symmetry. This results in anisotropic behavior in the x_2-x_3 plane, necessitating the use of periodic boundary conditions which is an intrinsic feature of the high-fidelity model's framework.

The actual unit cells in the four rotated coordinate systems used in the calculations are shown in Fig. 5 in discretized form. Table 2 provides information on the actual microstructural discretization used for each unit cell, the number of fibers and the volume fraction of the fiber phase. We note that the fiber volume fraction within each unit cell varied slightly from the nominal fraction of 0.35 due to the use of square subcells to approximate the fiber shape. The actual number of subcells in each unit cell was dictated by the need to capture the circular fiber shape with sufficient detail given the required number of fibers and the targeted fiber volume fraction. In the case of the unit cell in the principal material coordinate system with a single fiber in the center (not shown), the repeating unit cell was discretized into 100×100 subcells in the x_2-x_3 plane. The same number was used for the repeating unit cells rotated by 26.57 deg and 45.0 deg about the x_1 axis, while 150×150 subcells were employed for the unit cells rotated by 14.04 deg and 36.87 deg.

The unit cell in the principal material coordinate system with a single fiber in the center ($\theta=0$ deg, Fig. 4) produces homogenized elastic stiffness matrix $\mathbf{C}^*$ of the form

$$\mathbf{C}^*=\begin{bmatrix} C_{11}^* & C_{12}^* & C_{13}^* & 0 & 0 & 0 \\ C_{12}^* & C_{22}^* & C_{23}^* & 0 & 0 & 0 \\ C_{13}^* & C_{23}^* & C_{33}^* & 0 & 0 & 0 \\ 0 & 0 & 0 & C_{44}^* & 0 & 0 \\ 0 & 0 & 0 & 0 & C_{55}^* & 0 \\ 0 & 0 & 0 & 0 & 0 & C_{66}^* \end{bmatrix} \tag{49}$$

where $C_{12}^*=C_{13}^*$, $C_{22}^*=C_{33}^*$, $C_{55}^*=C_{66}^*$ due to the cubic symmetry, but $C_{44}^*\neq\frac{1}{2}(C_{22}^*-C_{23}^*)$ due to the absence of isotropy in the x_2-x_3 plane. This stiffness matrix is used in the transformation equations

$$\overline{\mathbf{C}}^*(\theta)=\mathbf{T}_1\mathbf{C}^*\mathbf{T}_2^{-1} \tag{50}$$

to generate the corresponding homogenized stiffness matrix in the rotated coordinate system independently of the micromechanics-based solution for the homogenized stiffness matrix of a unit cell in the same rotated coordinate system. The transformation matrices $\mathbf{T}_1$ and $\mathbf{T}_2$ for the rotation angle θ about the x_1 axis are

$$\mathbf{T}_1=\begin{bmatrix} 1 & 0 & 0 & 0 & 0 & 0 \\ 0 & m^2 & n^2 & 2mn & 0 & 0 \\ 0 & n^2 & m^2 & -2mn & 0 & 0 \\ 0 & -mn & mn & m^2-n^2 & 0 & 0 \\ 0 & 0 & 0 & 0 & m & -n \\ 0 & 0 & 0 & 0 & n & m \end{bmatrix},$$

$$\mathbf{T}_2=\begin{bmatrix} 1 & 0 & 0 & 0 & 0 & 0 \\ 0 & m^2 & n^2 & mn & 0 & 0 \\ 0 & n^2 & m^2 & -mn & 0 & 0 \\ 0 & -2mn & 2mn & m^2-n^2 & 0 & 0 \\ 0 & 0 & 0 & 0 & m & -n \\ 0 & 0 & 0 & 0 & n & m \end{bmatrix}$$

where $m=\cos\theta$ and $n=\sin\theta$. They relate stress and engineering strain quantities in the principal coordinate system, $\boldsymbol{\sigma}$ and $\boldsymbol{\epsilon}$, to the corresponding quantities in the rotated (primed) coordinate system, $\boldsymbol{\sigma}'$ and $\boldsymbol{\epsilon}'$ (i.e., $\boldsymbol{\sigma}'=\mathbf{T}_1\boldsymbol{\sigma}$ and $\boldsymbol{\epsilon}'=\mathbf{T}_2\boldsymbol{\epsilon}$) and are used to derive Eq. (50) from Hooke's law in the principal material coordinate system. Under the above transformation, the homogenized stiffness matrix $\mathbf{C}^*(\theta)$ acquires the following form in the rotated coordinate system

Table 1 Material properties of the fiber and matrix constituents

Material	Young's modulus (MPa)	Poisson's ratio
Glass fiber	70,000	0.25
Epoxy matrix	3,500	0.35
Compliant fiber	700	0.33
Aluminum matrix	70,000	0.33

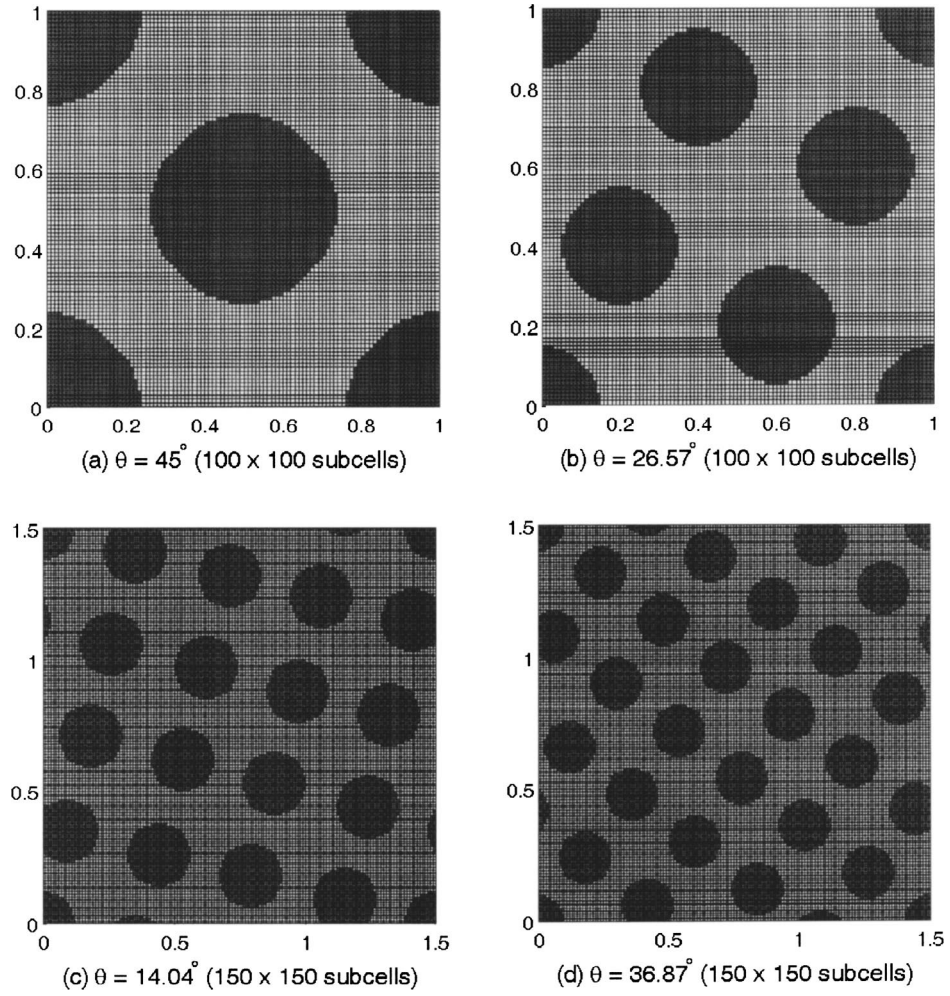

Fig. 5 Detailed volume discretizations of the four repeating unit cells in the rotated coordinate systems employed to accurately capture the geometric details within each unit cell

$$\overline{\mathbf{C}}^*(\theta)=\begin{bmatrix} \overline{C}^*_{11} & \overline{C}^*_{12} & \overline{C}^*_{13} & 0 & 0 & 0 \\ \overline{C}^*_{12} & \overline{C}^*_{22} & \overline{C}^*_{23} & \overline{C}^*_{24} & 0 & 0 \\ \overline{C}^*_{13} & \overline{C}^*_{23} & \overline{C}^*_{33} & \overline{C}^*_{34} & 0 & 0 \\ 0 & \overline{C}^*_{24} & \overline{C}^*_{34} & \overline{C}^*_{44} & 0 & 0 \\ 0 & 0 & 0 & 0 & \overline{C}^*_{55} & \overline{C}^*_{56} \\ 0 & 0 & 0 & 0 & \overline{C}^*_{56} & \overline{C}^*_{66} \end{bmatrix} \tag{51}$$

where $\overline{C}^*_{12}=\overline{C}^*_{13}$, $\overline{C}^*_{22}=\overline{C}^*_{33}$, $\overline{C}^*_{55}=\overline{C}^*_{66}$, and $\overline{C}^*_{24}=-\overline{C}^*_{34}$.

Table 2 Geometric and microstructural details of the investigated repeating unit cells

RUC rotation angle	No. of fibers	Subcell discretization	Fiber volume fraction
$\theta=\tan^{-1}(\frac{0}{1})=0$ deg	1	100×100	0.3468
$\theta=\tan^{-1}(\frac{1}{4})=14.04$ deg	17	150×150	0.3476
$\theta=\tan^{-1}(\frac{1}{2})=26.56$ deg	5	100×100	0.3440
$\theta=\tan^{-1}(\frac{3}{4})=36.87$ deg	25	150×150	0.3511
$\theta=\tan^{-1}(\frac{1}{1})=45$ deg	2	100×100	0.3504

The knowledge of the effective stiffness matrix in the rotated coordinate system makes it possible to generate the corresponding transformed compliance matrix from the inverse relationship

$$\overline{\mathbf{S}}^*(\theta)=[\overline{\mathbf{C}}^*(\theta)]^{-1} \tag{52}$$

The elements of the transformed compliance matrix $\overline{\mathbf{S}}^*(\theta)$ are then used to determine the effective engineering properties in the rotated coordinate system as follows:

$$\begin{aligned} &\overline{E}^*_{11}(\theta)=\frac{1}{\overline{S}^*_{11}}, \quad \overline{E}^*_{22}(\theta)=\frac{1}{\overline{S}^*_{22}}, \quad \overline{E}^*_{33}(\theta)=\frac{1}{\overline{S}^*_{33}} \\ &\overline{\nu}^*_{12}(\theta)=-\frac{\overline{S}^*_{12}}{\overline{S}^*_{11}}, \quad \overline{\nu}^*_{13}(\theta)=-\frac{\overline{S}^*_{13}}{\overline{S}^*_{11}}, \quad \overline{\nu}^*_{23}(\theta)=-\frac{\overline{S}^*_{23}}{\overline{S}^*_{22}} \\ &\overline{G}^*_{23}(\theta)=\frac{1}{\overline{S}^*_{44}}, \quad \overline{G}^*_{13}(\theta)=\frac{1}{\overline{S}^*_{55}}, \quad \overline{G}^*_{12}(\theta)=\frac{1}{\overline{S}^*_{66}} \\ &\overline{\eta}^*_{2,23}(\theta)=\frac{\overline{S}^*_{24}}{\overline{S}^*_{44}}, \quad \overline{\eta}^*_{3,23}(\theta)=\frac{\overline{S}^*_{34}}{\overline{S}^*_{44}}, \quad \overline{\eta}^*_{23,2}(\theta)=\frac{\overline{S}^*_{24}}{\overline{S}^*_{22}}, \\ &\overline{\eta}^*_{23,3}(\theta)=\frac{\overline{S}^*_{34}}{\overline{S}^*_{33}} \end{aligned} \tag{53}$$

where $\overline{E}^*_{ii}(\theta)$ are the three Young's moduli, $\overline{\nu}^*_{ij}(\theta)$ $(i \neq j)$ are the major Poisson's ratios, $\overline{G}^*_{ij}(\theta)$ $(i \neq j)$ are the three shear moduli, and $\overline{\eta}^*_{i,23}$, $\overline{\eta}^*_{23,i}$ are Lekhnitskii's coefficients of mutual influence of the first and second kind, respectively, Lekhnitskii [12]. These coefficients provide a measure of the extent of anisotropy in the x_2-x_3 plane introduced by the rotation angle θ about the fiber axis. The coefficients of the first kind represent ratios of transverse normal to transverse shear strains due to transverse shear loading only. Similarly, the coefficients of the second kind represent ratios of transverse shear to transverse normal strains due to transverse normal loading only.

In the following two sections, micromechanical analyses of the five repeating unit cells shown in Figs. 4 and 5 are conducted to generate the homogenized stiffness matrix elements of the two unidirectional composites in the rotated coordinate systems, which are then used to determine the corresponding compliance matrix elements from Eqs. (52), and ultimately the engineering moduli from Eqs. (53). The transformation equations, Eqs. (50), serve as the gold standard for comparison purposes. These require the knowledge of the stiffness matrix elements in the principal material coordinate system, which are obtained from the micromechanical analysis of the simple unit cell with the single fiber in the center.

4.1 Glass/Epoxy Unidirectional Composite. Figure 6 illustrates the dependence of the engineering moduli on the rotation angle θ for the glass/epoxy system with the Young's moduli ratio $E_f/E_m=20$. The predictions generated by HFGMC for the Young's and shear moduli have been normalized by the corresponding values in the principal material coordinate system (with $\theta=0$ deg), while the Poisson's ratios and the mutual influence coeffcients are presented unnormalized. The predictions of the original GMC model, which have also been normalized by the corresponding engineering moduli in the principal material coordinate system obtained from HFGMC, are included in the figure. The transformation equation predictions for the engineering moduli follow the predictions for the stiffness matrix elements (not shown, see Bansal and Pindera [13] for details). That is, while $\overline{C}^*_{11}$, $\overline{C}^*_{12}$, and $\overline{C}^*_{66}$ are insensitive to the rotation angle θ, the elements $\overline{C}^*_{22}$, $\overline{C}^*_{23}$, and $\overline{C}^*_{44}$ exhibit substantial dependence. The dependence of the coupling elements $\overline{C}^*_{24}$ and $\overline{C}^*_{34}$ on the rotation angle is also substantial, albeit the actual magnitudes are much smaller.

As observed in Fig. 6, the correlation between the HFGMC and transformation equation predictions is remarkable for the two Young's and shear moduli, and the two major Poisson's ratios. In particular, the axial Young's modulus $E^*_{11}(\theta)$ remains nearly constant for the differently oriented unit cells, as does the major Poisson's ratio $\nu^*_{12}(\theta)$ and the out-of-plane shear modulus $G^*_{12}(\theta)$, as suggested by the absence of variation of the corresponding stiffness matrix elements. The in-plane moduli, on the other hand, exhibit substantial θ dependence. While the transverse modulus $E^*_{22}(\theta)$ decreases with increasing rotation angle, the transverse Poisson's ratio $\nu^*_{23}(\theta)$ and the transverse shear modulus $G^*_{23}(\theta)$ increase. For the rotation angle $\theta=45$ deg, the decrease in the transverse Young's modulus is more than 15% of the principal material coordinate system value. For the same rotation angle, the increase in the transverse shear modulus and Poisson's ratio is more dramatic, with increases of approximately 30% and 25%, respectively. Equally remarkable is the correlation for the coefficients of mutual influence $\eta^*_{2,23}$, $\eta^*_{3,23}$, $\eta^*_{23,2}$, and $\eta^*_{23,3}$, which couple the normal and shear responses. These coefficients give a measure of the extent of anisotropy in the x_2-x_3 plane caused by the absence of material planes of symmetry.

In contrast, the GMC predictions are markedly inferior, with the exception of the Young's modulus $E^*_{11}(\theta)$. In particular, the transverse modulus $E^*_{22}(\theta)$ in the low off-axis angle range differs from the transformation and high-fidelity model predictions by over 20%. The differences in the out-of-plane shear modulus $G^*_{12}(\theta)$ are also on the order of 20% in the entire off-axis range excluding $\theta=0$ deg. An even greater difference is obtained for the transverse

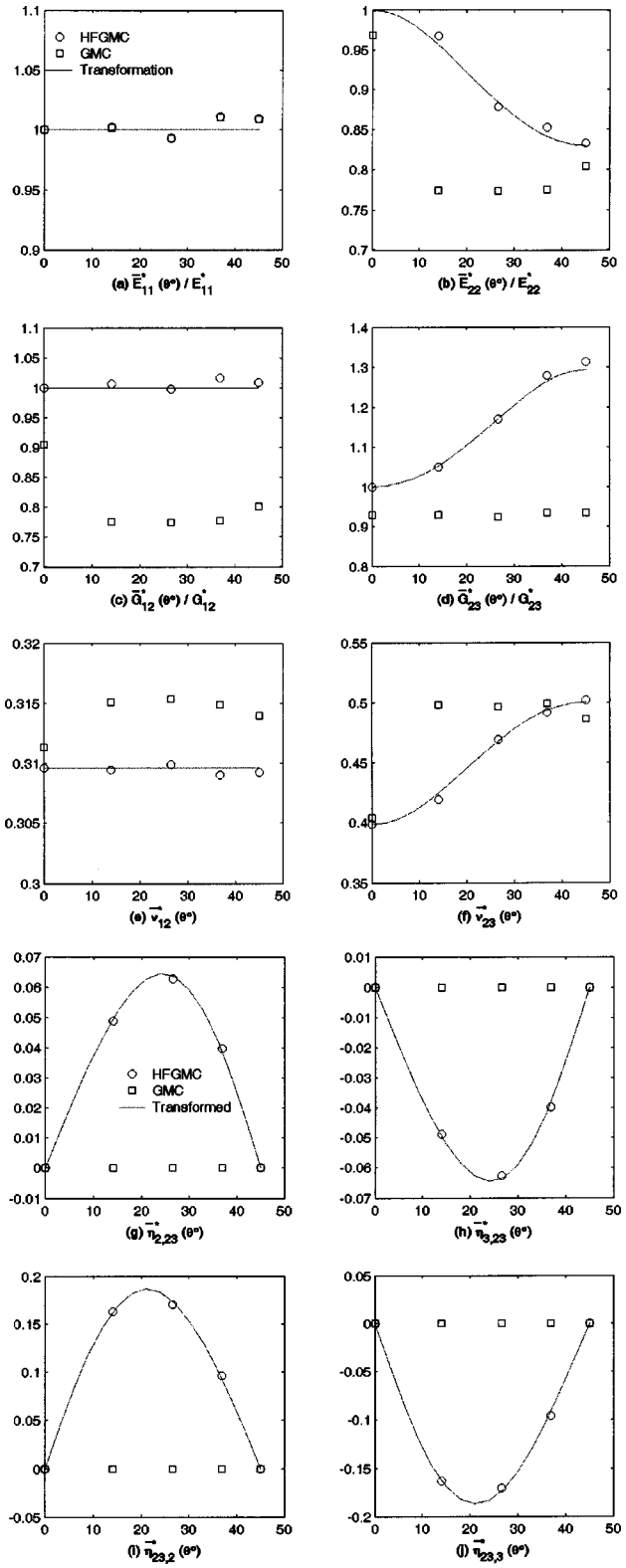

Fig. 6 Normalized engineering moduli of the glass/epoxy unidirectional composite as a function of the rotation angle θ about the fiber axis. Comparison of GMC and HFGMC predictions with the transformation equations.

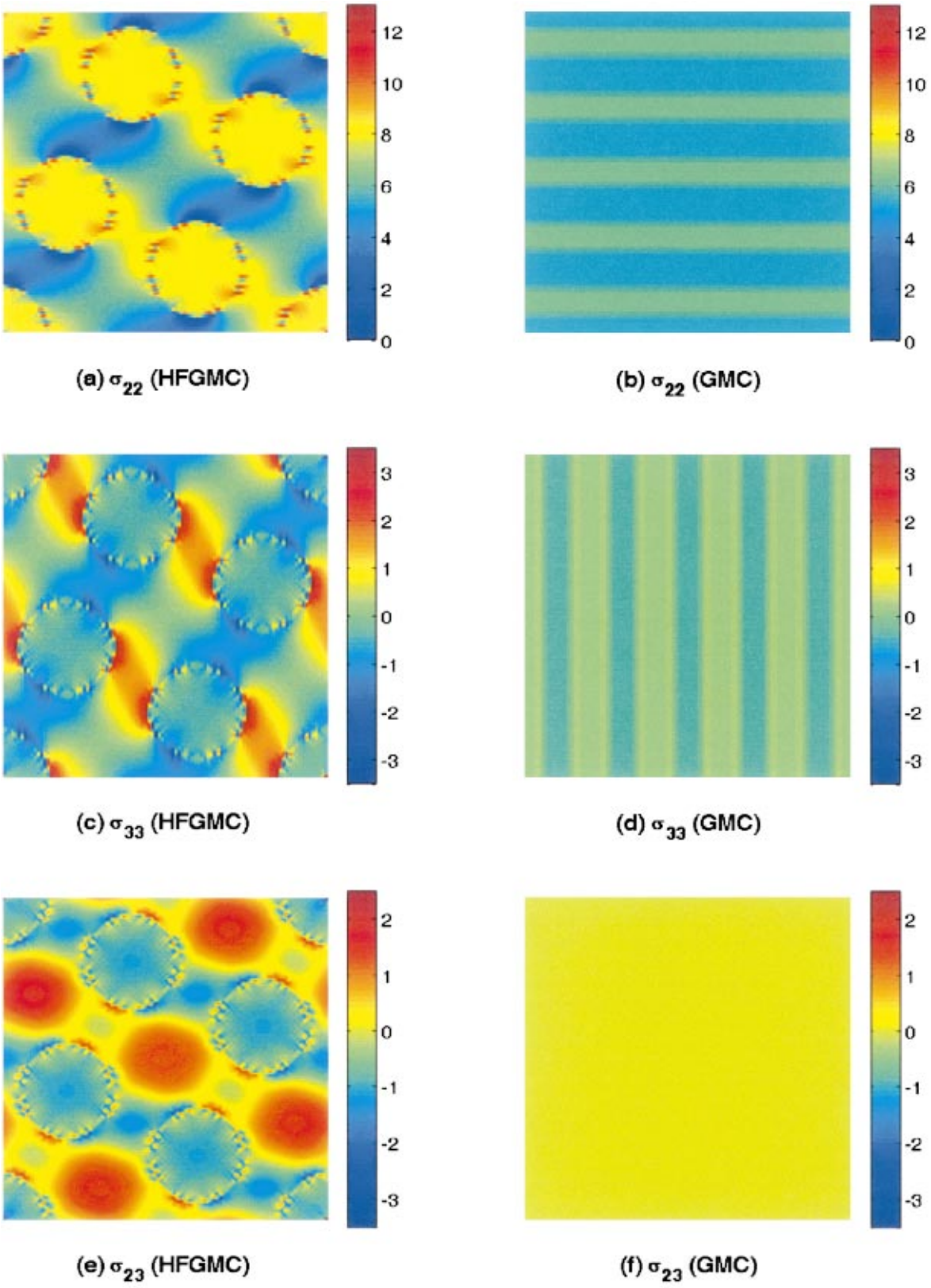

Fig. 7 ⟨Color⟩ **Comparison of σ_{22}, σ_{33}, and σ_{23} stress fields (MPa) within the unit cell of the glass/epoxy unidirectional composite rotated by 26.57 deg about the fiber axis and subjected to the average normal strain $\bar{\epsilon}_{22} = 0.1\%$: HFGMC (left column) and GMC (right column) predictions**

shear modulus $G_{23}^{*}(\theta)$ for rotation angles greater than 30 deg due to GMC's failure to predict any variation for all rotation angles. The differences between the HFGMC and GMC models are rooted in the absence of shear coupling caused by the use of a linear displacement field in the latter model, which results in constant strain and stress fields in the individual subcells. The application of traction continuity conditions in an average sense between individual subcells within each row and column of subcells renders the corresponding traction components constant with magnitudes dictated by the most compliant subcell. In the case of the transverse shear stress, this effect is further enhanced and results in a uniform shear stress throughout the entire repeating unit cell. The comparison of microscale stress fields discussed below illustrates this point more clearly.

To illustrate the influence of shear coupling, microscale stress distributions predicted by HFGMC and GMC are compared for the unit cell rotated by $\theta=26.57$ deg about the fiber axis and subjected to transverse normal and transverse shear loading. Similar results have been observed for other rotation angles, (Bansal and Pindera [13]). Figure 7 compares the microscale σ_{22}, σ_{33}, and σ_{23} stress fields for loading by the average transverse normal strain $\bar{\epsilon}_{22}=0.1\%$, with the remaining faces of the repeating unit cell traction-free in the average sense. The σ_{22} stress distribution predicted by HFGMC exhibits small departures from uniform distribution within the individual fibers, with magnitudes substantially greater than in the surrounding matrix due to the large fiber/matrix moduli mismatch. High stress concentrations are evident along certain segments of the fiber/matrix interfaces which may or may not be due to the stepwise discretization of the circular interface. This aspect requires further investigation which is beyond the scope of the present study (see Bednarcyk et al. [14] for related discussion about the mesh sensitivity of HFGMC). The σ_{33} stress distributions within the individual fibers, which are substantially smaller than the σ_{22} distributions, also exhibit small departures from uniform distributions. In the matrix phase, however, this stress component is not insignificant relative to σ_{22}. Significant σ_{33} stress concentrations are present in the matrix phase at the fiber/matrix interfaces at points along the fiber diametral planes lined up with the load axis. Significant σ_{23} stress magnitudes are also evident in oval regions surrounded by four fibers aligned with the rotated fiber rows. In contrast, the normal σ_{22} and σ_{33} stress distributions generated by GMC exhibit parallel strip patterns along the y_2 and y_3 directions, respectively. Little variation in the respective stress magnitudes is observed in the adjacent strips and the low magnitudes relative to the high-fidelity results produce a low value of the average normal stress $\bar{\sigma}_{22}$, thereby resulting in a low value of the transverse Young's modulus for this rotation angle observed in Fig. 6. Further, the transverse shear stress σ_{23} is identically zero due to the absence of shear coupling.

Figure 8 compares the microscale σ_{23} and σ_{22} stress fields for loading by the average transverse shear strain $\bar{\epsilon}_{23}=0.1\%$, with the average stresses other than $\bar{\sigma}_{23}$ set to zero. This loading case highlights the differences in the two stress distributions predicted by GMC and HFGMC models. The uniform σ_{23} stress distribution throughout the entire unit cell irrespective of location (i.e., whether the particular point lies within the hard fiber or much softer matrix phase) predicted by GMC is a direct consequence of the imposition of shear traction continuity in the surface-average sense across subcell interfaces in the y_2 and y_3 directions, given the linear displacement field approximation within each subcell. The low magnitude of this stress component relative to the HFGMC prediction produces a substantially lower value of the transverse shear modulus observed in Fig. 6. The linear displacement field approximation also uncouples the shear and normal stress fields at the local level, thereby producing vanishing σ_{22} stresses in the individual subcells. In contrast, the second-order displacement field approximation employed in HFGMC is sufficient to correctly capture the stress transfer mechanism between the two phases, enabling the fibers to carry substantially higher shear stresses, thereby producing a higher average shear stress that the repeating unit cell can support for the same applied average shear strain. This results in the higher effective transverse shear modulus seen in Fig. 6. The second-order displacement field approximation also couples the normal and shear stress fields at the local level, resulting in the observed σ_{22} stress distribution that is nearly uniform in the individual fibers and highly nonuniform in the matrix phase. The matrix σ_{22} stress nonuniformity is characterized by substantial stress concentrations at opposite locations around the fiber/matrix interface that are aligned with the diametral fiber planes coincident with the rotated fiber rows.

4.2 Aluminum Weakened by Axially Oriented Cylindrical Porosities. Figures 9 through 11 present the corresponding results for the aluminum matrix with substantially softer cylindrical inclusions. In this case, the Young's moduli ratio is $E_f/E_m=0.01$. For such a low ratio, the compliant cylindrical inclusions effectively behave as porosities.

Figure 9 illustrates the dependence of the engineering moduli on the rotation angle θ. The transformation equation predictions follow the trends presented in Fig. 6 for the glass/epoxy composite, but the variations are now greater. As before, the transformation equations predict variations only for the transverse moduli and the mutual influence coefficients. In particular, the transverse Young's modulus $\bar{E}_{22}^{*}(\theta)$ decreases by nearly 40% at the rotation angle of 45 deg relative to its value in the principal material coordinate system, compared to just a little more than 15% for the glass/epoxy system. The increase in the transverse modulus $\bar{G}_{23}^{*}(\theta)$ is almost 100%. The increase in the transverse Poisson's ratio $\bar{\nu}_{23}^{*}(\theta)$ is even more dramatic, being around 150%. These large variations with the rotation angle are captured very well by HFGMC. In contrast, the original GMC model results are completely erroneous for almost all engineering moduli at nonzero rotation angles. The exceptions are the axial Young's modulus $\bar{E}_{11}^{*}(\theta)$ and the related Poisson's ratio $\bar{\nu}_{12}^{*}$, which are predicted very accurately for all rotation angles. In the case of pure axial loading in the porosity direction, the matrix phase is continuous along this direction, and is thus effective in supporting the entire axial load without the need for stress transfer through the shear-normal coupling mechanism, while the transverse contraction which affects $\bar{\nu}_{12}^{*}$ occurs unconstrained due to porosity's presence.

The above results are explained by microscale stress distributions predicted by the two models presented in Figs. 10 and 11. As in the case of the glass/epoxy composite, these distributions have been generated for the repeating unit cell rotated by $\theta=26.57$ deg and subjected to transverse normal and transverse shear loading. Figure 10 compares the microscale σ_{22}, σ_{33} and σ_{23} stress fields in this repeating unit cell for loading by the average transverse normal strain $\bar{\epsilon}_{22}=0.1\%$. The detrimental effect of the shear coupling's absence in GMC on these stress components is clearly observed, with the σ_{22} stress field characterized by essentially uniform and very low magnitudes, and thus a low transverse Young's modulus $\bar{E}_{22}^{*}(\theta)$ seen in Fig. 9. The same holds true for the σ_{33} stress field, while the transverse shear stress σ_{23} vanishes completely. In contrast, the shear coupling effects necessary to internally support the applied transverse load are clearly evident in the HFGMC predictions for the three stress fields. Highly nonuniform distributions are observed for the three stress components in the matrix phase, characterized by significant concentrations at the porosity/matrix interfaces at specific locations as in the preceding case.

Similar trends in the stress distributions predicted by the two models are observed for loading by the average transverse shear strain $\bar{\epsilon}_{23}=0.1\%$. This is seen in Fig. 11, which compares the microscale σ_{23} and σ_{22} stress fields within the considered unit cell. As expected from the solution of the Kirsch problem for a single cylindrical cavity, large concentrations of the normal stress σ_{22} are observed at the porosity/matrix interface due to the transverse shear loading in the HFGMC predictions. These are actually

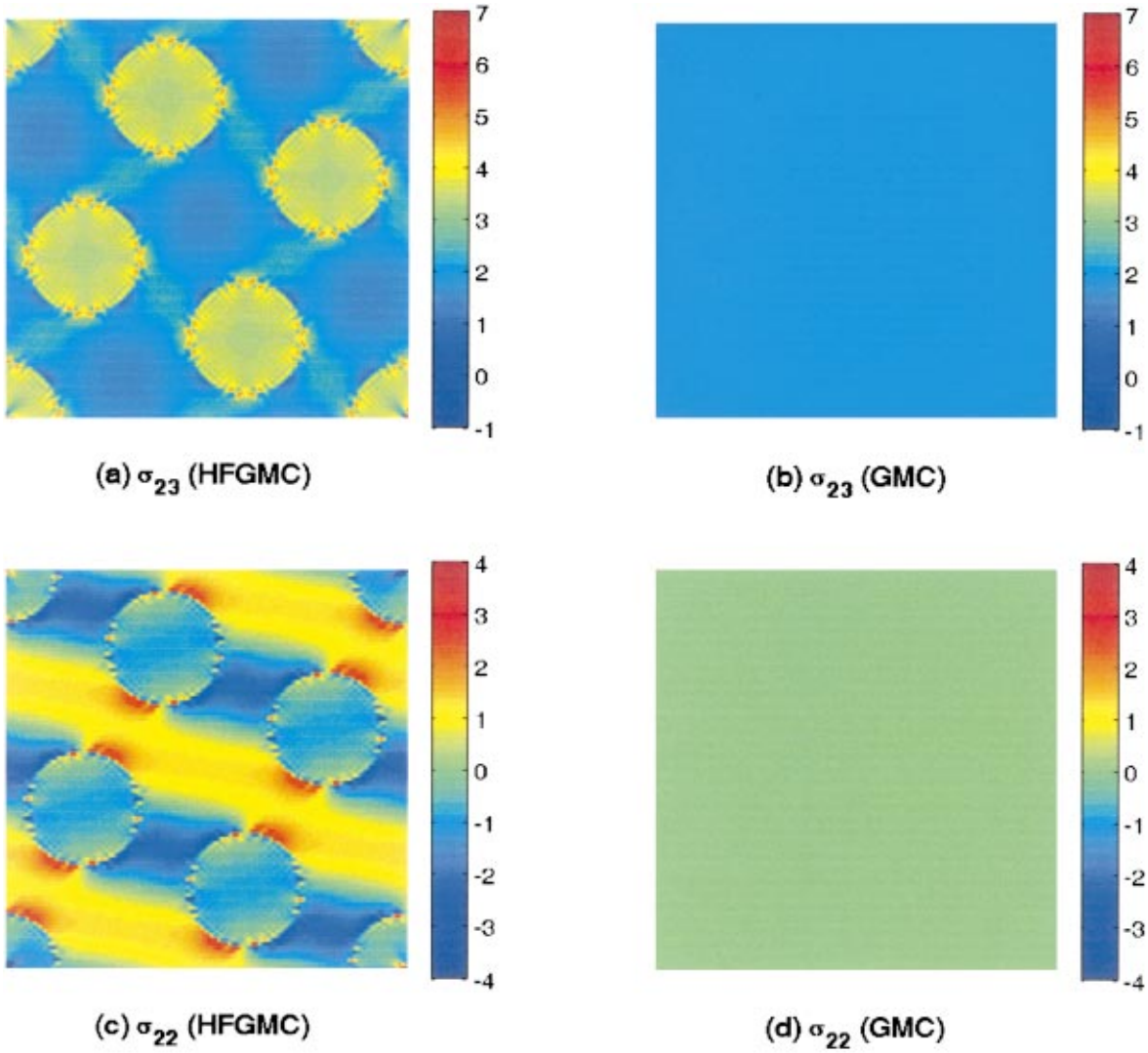

Fig. 8 ⟨Color⟩ Comparison of σ_{23} and σ_{22} stress fields (MPa) within the unit cell of the glass/epoxy unidirectional composite rotated by 26.57 deg about the fiber axis and subjected to the average shear strain $\bar{\epsilon}_{23}=0.1\%$: HFGMC (left column) and GMC (right column) predictions

higher than the corresponding transverse shear stress concentrations. The GMC model is incapable of capturing these nonuniform stress fields, and the presence of porosities results in uniform and very low magnitudes of the transverse shear stress, producing a very low value of the transverse shear modulus $G^{*}_{23}(\theta)$ seen in Fig. 9. Furthermore, the normal stress σ_{22} completely vanishes in contrast to the HFGMC result.

5 Discussion

As illustrated in the foregoing, for a unit cell without planes of material symmetry parallel to the fiber axis, the microscale stress fields predicted by the original GMC model exhibit two characteristic patterns in the plane normal to the fiber axis. The normal σ_{22} and σ_{33} stress distributions are characterized by parallel strips whose magnitude and sign depend on the applied stress orientation and the fiber/matrix Young's modulus ratio. For large ratios the patterns are visibly distinct, while for very low ratios that mimic porosities the patterns are obscured by the very low normal stress magnitudes. Similar strip patterns are observed for unit cells with a single fiber in the center, which possess two orthogonal planes of material symmetry (Pindera et al. [7] and Bednarcyk et al. [14]). In such cases, the strip patterns are wider and fewer due to the absence of overlapping fibers aligned with the load axis. In contrast, the shear stress σ_{23} distributions are uniform within the rotated unit cells as well as within unit cells in the principal material coordinate system. As discussed herein, and elsewhere, these patterns are a direct result of the absence of shear coupling and lead to inaccurate microscale stress fields, with the exception of the second invariant of the stress deviator, which is predicted sufficiently well to enable accurate modeling of the macroscopic response of unidirectional metal matrix composites (cf. Arnold et al. [15,16] and Iyer et al. [17]). As also shown for the porous aluminum case, these characteristic stress distributions produce highly inaccurate engineering moduli in the rotated coordinate system.

In order to mitigate the negative impact of the shear coupling absence, an alternative manner of determining the unit cell response, and thus the engineering moduli, in the rotated coordinate system based on the GMC model can be chosen. First, the applied normal or shear strain in the rotated coordinate system is transformed to the principal coordinate system in order to determine the response in this reference frame. The resulting strains and stresses are then transformed back to the rotated coordinate system in order to determine the elastic moduli. In fact, this is the

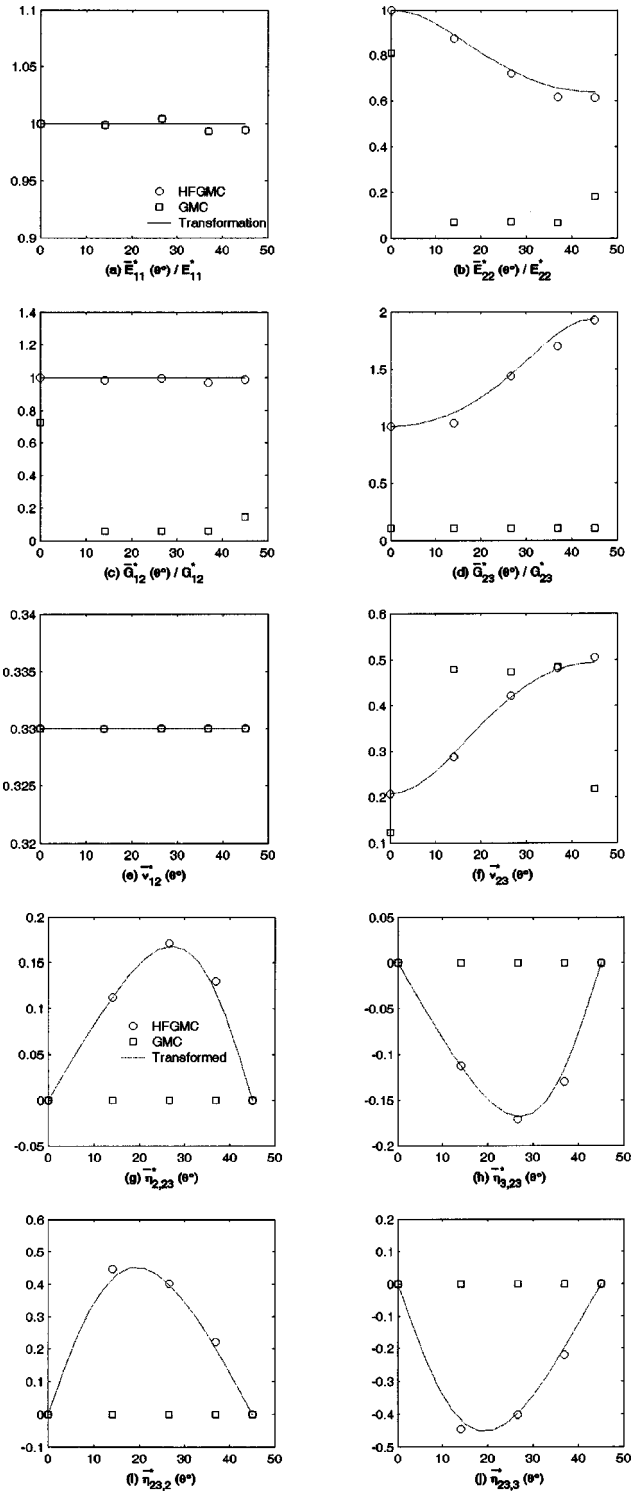

Fig. 9 Normalized engineering moduli of the aluminum matrix weakened by cylindrical porosities as a function of the rotation angle θ about the fiber axis. Comparison of HFGMC and GMC predictions with the transformation equations.

basis for the transformation equations given by Eq. (50), and should yield the same result as direct application of strains in the rotated coordinate system if the micromechanics model is self-consistent. This is clearly the case for the HFGMC model. In the case of GMC, however, the observed characteristic stress patterns indicate that this is going to be only partially successful in the presence of very compliant inclusions. In particular, transforming the applied macroscopic strain to the principal material coordinate system will not negate the fact that the transverse shear response, and thus the transverse shear modulus, will be incorrectly predicted in the presence of porosities. Specifically, the transverse shear modulus will be zero, rendering the resulting macroscopic shear stress zero. Therefore, this contribution will be absent when transforming the stresses to the rotated coordinate system, thereby producing a result that will differ from the transformation equations by an amount that depends on the rotation angle or the magnitude of the absent transverse shear stress in the principal material coordinate system. However, the dramatic differences between GMC predictions and transformation equations observed in Fig. 9 for the porous aluminum case will be reduced because the contribution of the normal stresses in the principal material coordinate system will not be completely eliminated even in the presence of porosities. This method of calculating the engineering moduli in the rotated coordinate system is in fact equivalent to the use of transformation equations based on the moduli calculated by the GMC model in the principal material coordinate system. The different results obtained from the GMC-based calculations, which depend on whether the calculations are made in the rotated or unrotated coordinate system, point to a fundamental problem that limits this model's range of applicability. This limitation has been overcome by the high-fidelity version, which can be used to accurately model the response of a wide range of periodic materials with or without planes of material symmetry in arbitrary coordinate systems.

For example, the reformulated HFGMC can now be applied with confidence to the important and rapidly growing area of micromechanics of random heterogeneous media with detailed microstructures. This can be carried out by assigning random distribution of phases within the repeating unit cell to produce a locally random but macroscopically periodic material model (cf. Baxter et al. [18], Graham-Brady et al. [19]). Alternatively, a broader class of random materials can be considered by relaxing the periodicity conditions in favor of homogeneous traction and displacement boundary conditions applied to a representative volume element, as discussed by Ostoja-Starzewski [20].

We close this section by briefly discussing the differences and similarities between the reformulated HFGMC and the finite-element approach that is often employed in analyzing the response of composite materials from micromechanics considerations under specific loadings. First, as mentioned in Sec. 3.1, the construction of the local stiffness matrix based on the employed local/global stiffness matrix reformulation clearly highlights the differences in the theoretical framework of the two methods given the fact that both are based on similar volume discretizations of a material microstructure. However, the discretization capability of the reformulated HFGMC is more limited at present since it is based strictly on rectangular subcells in contrast to the finite-element approach. Consequently, a greater number of subcells is required to model the type of microstructures investigated herein for a comparable level of geometric fidelity and local stress field accuracy. This limitation will be mitigated in the future by the development of a local stiffness matrix for trapezoidal subcells. We mention, however, that for the same volume discretization of a highly heterogeneous microstructure based on rectangular subcells, together with the same order of displacement field approximation within individual subcells or elements, the traction continuity between subcells/elements with large material property contrast is better satisfied by HFGMC relative to the displacement-based finite element formulation. This has been demonstrated by Bansal and Pindera [10] in the context of the higher-order theory for functionally graded materials which forms the basis for HFGMC. We also mention that the extent of discretization can be relaxed if the macroscopic response is the only output of interest, as demonstrated recently by Bednarcyk et al. [14] in the context of simulating the inelastic response of titanium-based composites with local damage in the form of fiber/

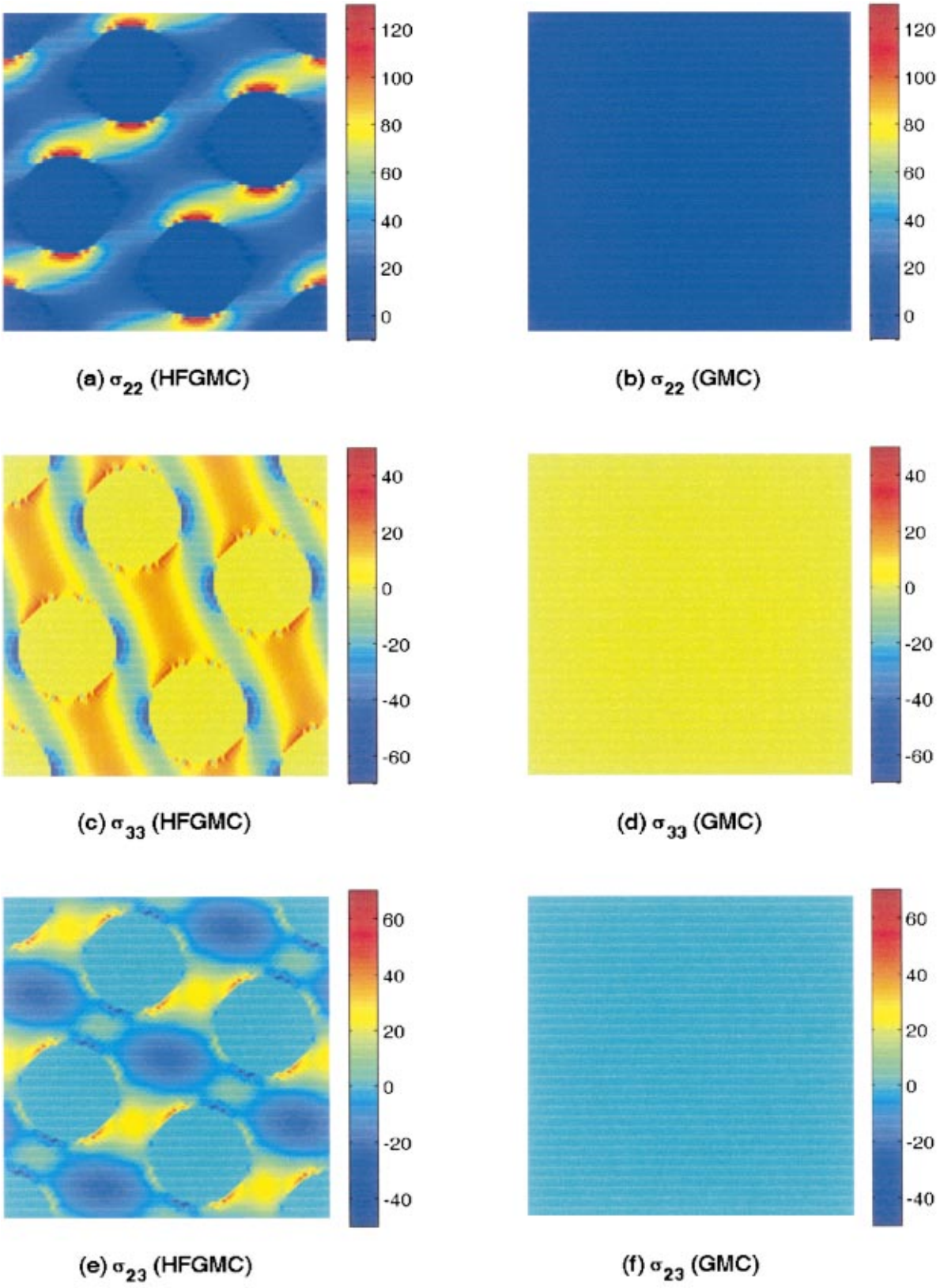

Fig. 10 ⟨Color⟩ **Comparison of σ_{22}, σ_{33}, and σ_{23} stress fields (MPa) within the unit cell of aluminum matrix with cylindrical porosities rotated by 26.57 deg about the porosity axis and subjected to the average normal strain $\bar{\epsilon}_{22}$ = 0.1%: HFGMC (left column) and GMC (right column) predictions**

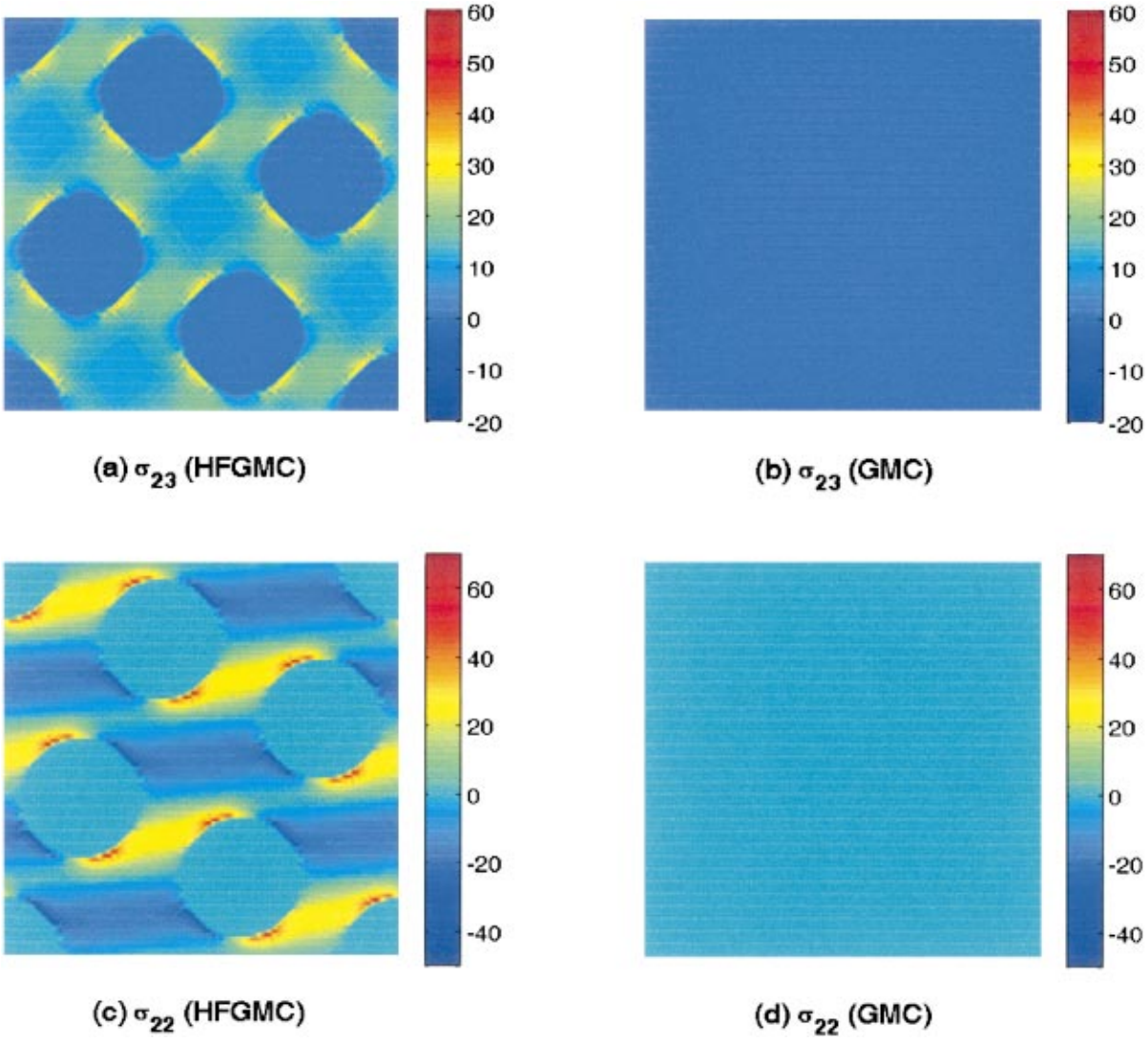

Fig. 11 ⟨Color⟩ Comparison of σ_{23} and σ_{22} stress fields (MPa) within the unit cell of aluminum matrix with cylindrical porosities rotated by 26.57 deg about the porosity axis and subjected to the average shear strain $\bar{\epsilon}_{23}=0.1\%$: HFGMC (left column) and GMC (right column) predictions

matrix debonding using the original formulation of HFGMC. The price for this, of course, is the loss of local stress field accuracy.

Further, the closed-form expression for the macroscopic constitutive equation of a homogenized material obtained from HFGMC in the form of Hooke's law [Eqs. (47) and (48)], given in terms of the repeating unit cell microstructural details and phase properties, holds for any arbitrary loading. It can thus be employed in a stand-alone manner in the development and optimization of new material systems which typically involves the application of combined external loading in arbitrary proportions, or as a subroutine in a larger structural mechanics program in the context of multiscale analysis not easily implementable using standard commercial finite-element codes. The reformulation of HFGMC presented herein simplifies the construction of the final system of equations through the closed-form expressions for the elements of the local stiffness matrix for an arbitrary subcell and a straightforward assembly procedure of the global stiffness matrix, facilitating the model's implementation and accessibility that were previously lacking. In closing, HFGMC occupies a middle ground between the highly accurate, but less robust and typically load-history specific, commercial finite-element codes and the robust and efficient, but substantially less accurate, micromechanics analytical models such as the widely used GMC.

6 Summary and Conclusions

The reformulation of the High-Fidelity Generalized Method of Cells, based on a simplified volume discretization involving only subcells as the fundamental subvolumes together with the use of the local/global stiffness matrix approach, facilitates the analysis of unit cells with complex microstructural details characteristic of realistic microstructures of multiphase materials. This is a direct result of the elimination of redundant continuity conditions present in the original formulation, which in turn produces substantial reduction in the size of the system of equations governing the unit cell response. The reformulation also reveals the high-fidelity micromechanical analysis to be an approximate elasticity technique based on the direct enforcement of subcell equilibrium equations *in the large* and the imposition of displacement and traction continuity conditions in a surface-averaged sense across interfaces between adjacent subcells. This, in turn, simplifies the derivation of the volume-averaged equilibrium equations governing the individual subcell response as well as the derivation of the traction continuity conditions.

In the present investigation, the reformulation was employed to determine the elastic moduli of a square array of stiff fibers embedded in a substantially more compliant matrix, representative of

a unidirectional glass/epoxy composite, under rotation about the fiber axis. A stiff matrix weakened by cylindrical porosities was also considered. The rotation about the fiber axis necessitates the analysis of unit cells in the rotated coordinate system, representative of the same square array, which may contain many fibers, in contrast with the single fiber within the unit cell in the principal material coordinate system. Such unit cells typically do not possess planes of material symmetry, rendering them anisotropic in the rotated coordinate system. The elastic moduli of such unit cells can also be obtained from the standard transformation equations once the effective composite properties have been calculated in the principal material coordinate system. These transformation equations can therefore be employed to validate the predictive capability of a micromechanics model that admits periodic boundary conditions required in the absence of material planes of symmetry. The effective moduli predicted by the HFGMC based on the unit cells in the rotated coordinates systems have been shown herein to correlate extremely well with the transformation equations for both material systems considered. In contrast, the predictions of the original GMC exhibited substantial departures from the transformation equations for the glass/epoxy system, which became unacceptably large for the porous aluminum. This is a direct result of the absence of shear coupling in the original method which produces erroneous results when normal/shear interaction dominates in the presence of porosities or inclusion phases that are substantially more compliant than the matrix phase. The high-fidelity version circumvents this problem, albeit at an increased computational cost which, however, is mitigated to a certain extent by the implemented reformulation. The microscale stress distributions generated by both models for different uniaxial loading situations provided additional insight supporting the predicted moduli results.

Acknowledgments

The authors gratefully acknowledge the support provided by the NASA Glenn Research Center through the NASA Grant No. NAG3-2524, and thank Dr. Arnold, the technical monitor of this grant, for the useful comments during the preparation of a related report. Constructive comments of the reviewers are also appreciated.

Appendix: Local Stiffness Matrices

Explicit expressions for the nonzero elements of the local stiffness matrix for the (β,γ) subcell, given in terms of the subcell's geometric and mechanical properties, are listed below for loading by normal and shear tractions in the y_2–y_3 plane

$$K_{11}^{(\beta,\gamma)}=K_{22}^{(\beta,\gamma)}=\frac{C_{22}^{(\beta,\gamma)}}{h_\beta}\left(4-3\,\frac{C_{22}^{(\beta,\gamma)}}{\overline{C}_{22}^{(\beta,\gamma)}}\right)$$

$$K_{12}^{(\beta,\gamma)}=K_{21}^{(\beta,\gamma)}=\frac{C_{22}^{(\beta,\gamma)}}{h_\beta}\left(2-3\,\frac{C_{22}^{(\beta,\gamma)}}{\overline{C}_{22}^{(\beta,\gamma)}}\right)$$

$$K_{15}^{(\beta,\gamma)}=K_{16}^{(\beta,\gamma)}=K_{25}^{(\beta,\gamma)}=K_{26}^{(\beta,\gamma)}=-\frac{3C_{22}^{(\beta,\gamma)}C_{44}^{(\beta,\gamma)}h_\beta}{\overline{C}_{22}^{(\beta,\gamma)}l_\gamma^2}$$

$$K_{17}^{(\beta,\gamma)}=-K_{18}^{(\beta,\gamma)}=-K_{27}^{(\beta,\gamma)}=K_{28}^{(\beta,\gamma)}=\frac{C_{23}^{(\beta,\gamma)}}{l_\gamma}$$

$$K_{33}^{(\beta,\gamma)}=K_{44}^{(\beta,\gamma)}=\frac{C_{44}^{(\beta,\gamma)}}{h_\beta}\left(4-3\,\frac{l_\gamma^2C_{44}^{(\beta,\gamma)}}{h_\beta^2\overline{C}_{33}^{(\beta,\gamma)}}\right)$$

$$K_{34}^{(\beta,\gamma)}=K_{43}^{(\beta,\gamma)}=\frac{C_{44}^{(\beta,\gamma)}}{h_\beta}\left(2-3\,\frac{l_\gamma^2C_{44}^{(\beta,\gamma)}}{h_\beta^2\overline{C}_{33}^{(\beta,\gamma)}}\right)$$

$$K_{35}^{(\beta,\gamma)}=-K_{36}^{(\beta,\gamma)}=-K_{45}^{(\beta,\gamma)}=K_{46}^{(\beta,\gamma)}=\frac{C_{44}^{(\beta,\gamma)}}{l_\gamma}$$

$$K_{37}^{(\beta,\gamma)}=K_{38}^{(\beta,\gamma)}=K_{47}^{(\beta,\gamma)}=K_{48}^{(\beta,\gamma)}=-\frac{3C_{33}^{(\beta,\gamma)}C_{44}^{(\beta,\gamma)}}{h_\beta\overline{C}_{33}^{(\beta,\gamma)}}$$

$$K_{51}^{(\beta,\gamma)}=K_{52}^{(\beta,\gamma)}=K_{61}^{(\beta,\gamma)}=K_{62}^{(\beta,\gamma)}=-\frac{3C_{22}^{(\beta,\gamma)}C_{44}^{(\beta,\gamma)}}{l_\gamma\overline{C}_{22}^{(\beta,\gamma)}}$$

$$K_{53}^{(\beta,\gamma)}=-K_{54}^{(\beta,\gamma)}=-K_{63}^{(\beta,\gamma)}=K_{64}^{(\beta,\gamma)}=\frac{C_{44}^{(\beta,\gamma)}}{h_\beta}$$

$$K_{55}^{(\beta,\gamma)}=K_{66}^{(\beta,\gamma)}=\frac{C_{44}^{(\beta,\gamma)}}{l_\gamma}\left(4-3\,\frac{h_\beta^2C_{44}^{(\beta,\gamma)}}{l_\gamma^2\overline{C}_{22}^{(\beta,\gamma)}}\right)$$

$$K_{56}^{(\beta,\gamma)}=K_{65}^{(\beta,\gamma)}=\frac{C_{44}^{(\beta,\gamma)}}{l_\gamma}\left(2-3\,\frac{h_\beta^2C_{44}^{(\beta,\gamma)}}{l_\gamma^2\overline{C}_{22}^{(\beta,\gamma)}}\right)$$

$$K_{71}^{(\beta,\gamma)}=-K_{72}^{(\beta,\gamma)}=-K_{81}^{(\beta,\gamma)}=K_{82}^{(\beta,\gamma)}=\frac{C_{23}^{(\beta,\gamma)}}{h_\beta}$$

$$K_{73}^{(\beta,\gamma)}=K_{74}^{(\beta,\gamma)}=K_{83}^{(\beta,\gamma)}=K_{84}^{(\beta,\gamma)}=-\frac{3C_{33}^{(\beta,\gamma)}C_{44}^{(\beta,\gamma)}l_\gamma}{\overline{C}_{33}^{(\beta,\gamma)}h_\beta^2}$$

$$K_{77}^{(\beta,\gamma)}=K_{88}^{(\beta,\gamma)}=\frac{C_{33}^{(\beta,\gamma)}}{l_\gamma}\left(4-3\,\frac{C_{33}^{(\beta,\gamma)}}{\overline{C}_{33}^{(\beta,\gamma)}}\right)$$

$$K_{78}^{(\beta,\gamma)}=K_{87}^{(\beta,\gamma)}=\frac{C_{33}^{(\beta,\gamma)}}{l_\gamma}\left(2-3\,\frac{C_{33}^{(\beta,\gamma)}}{\overline{C}_{33}^{(\beta,\gamma)}}\right)$$

The elements of the local stiffness matrix for loading by shear tractions in the y_1–y_2 and y_1–y_3 planes are given below

$$L_{11}^{(\beta,\gamma)}=L_{22}^{(\beta,\gamma)}=\frac{C_{66}^{(\beta,\gamma)}}{h_\beta}\left(4-3\,\frac{C_{66}^{(\beta,\gamma)}}{\overline{C}_{11}^{(\beta,\gamma)}}\right)$$

$$L_{12}^{(\beta,\gamma)}=L_{21}^{(\beta,\gamma)}=\frac{C_{66}^{(\beta,\gamma)}}{h_\beta}\left(2-3\,\frac{C_{66}^{(\beta,\gamma)}}{\overline{C}_{11}^{(\beta,\gamma)}}\right)$$

$$L_{13}^{(\beta,\gamma)}=L_{14}^{(\beta,\gamma)}=L_{23}^{(\beta,\gamma)}=L_{24}^{(\beta,\gamma)}=-\frac{3C_{55}C_{66}^{(\beta,\gamma)}h_\beta}{\overline{C}_{11}^{(\beta,\gamma)}l_\gamma^2}$$

$$L_{31}^{(\beta,\gamma)}=L_{32}^{(\beta,\gamma)}=L_{41}^{(\beta,\gamma)}=L_{42}^{(\beta,\gamma)}=-\frac{3C_{55}C_{66}^{(\beta,\gamma)}}{\overline{C}_{11}^{(\beta,\gamma)}l_\gamma}$$

$$L_{33}^{(\beta,\gamma)}=L_{44}^{(\beta,\gamma)}=\frac{C_{55}^{(\beta,\gamma)}}{l_\gamma}\left(4-3\,\frac{h_\beta^2C_{55}^{(\beta,\gamma)}}{l_\gamma^2\overline{C}_{11}^{(\beta,\gamma)}}\right)$$

$$L_{34}^{(\beta,\gamma)}=L_{43}^{(\beta,\gamma)}=\frac{C_{55}^{(\beta,\gamma)}}{l_\gamma}\left(2-3\,\frac{h_\beta^2C_{55}^{(\beta,\gamma)}}{l_\gamma^2\overline{C}_{11}^{(\beta,\gamma)}}\right)$$

References

[1] Aboudi, J., Pindera, M.-J., and Arnold, S. M., 2001, "Linear Thermoelastic Higher-Order Theory for Periodic Multiphase Materials," J. Appl. Mech., **68**, No. 5, pp. 697–707.

[2] Aboudi, J., Pindera, M.-J., and Arnold, S. M., 2002, *High-Fidelity Generalized Method of Cells for Inelastic Periodic Multiphase Materials*, NASA TM 2002-211469.

[3] Aboudi, J., Pindera, M.-J., and Arnold, S. M., 2003, "Higher-Order Theory for Periodic Multiphase Materials With Inelastic Phases," Int. J. Plast., **19**, No. 6, pp. 805–847.

[4] Kalamkarov, A. L., and Kolpakov, A. G., 1997, *Analysis, Design and Optimization of Composite Structures*, John Wiley & Sons, New York.

[5] Aboudi, J., Pindera, M.-J., and Arnold, S. M., 1999, "Higher-Order Theory for Functionally Graded Materials," Composites, Part B, **30**, No. 8, pp. 777–832.

[6] Paley, M., and Aboudi, J., 1992, ''Micromechanical Analysis of Composites by the Generalized Method of Cells,'' Mech. Mater., **14**, pp. 127–139.
[7] Pindera, M.-J., Aboudi, J., and Arnold, S. M., 2003, ''Analysis of Locally Irregular Composites Using High-Fidelity Generalized Method of Cells,'' AIAA J., **41**, No. 12, pp. 2331–2340.
[8] Bufler, H., 1971, ''Theory of Elasticity of a Multilayered Medium,'' J. Elast., **1**, pp. 125–143.
[9] Pindera, M.-J., 1991, ''Local/Global Stiffness Matrix Formulation for Composite Materials and Structures,'' Composites Eng., **1**, No. 2, pp. 69–83.
[10] Bansal, Y., and Pindera, M.-J., 2003, ''Efficient Reformulation of the Thermoelastic Higher-Order Theory for FGMs,'' J. Therm. Stresses, **26**, Nos. 11/12, pp. 1055–1092; see also: NASA CR 2002-211909.
[11] Hill, R., 1963, ''Elastic Properties of Reinforced Solids: Some Theoretical Principles,'' J. Mech. Phys. Solids, **11**, pp. 357–372.
[12] Lekhnitskii, S. G., 1981, *Theory of Elasticity of an Anisotropic Body*, Mir, Moscow.
[13] Bansal, Y., and Pindera, M.-J., 2004, ''Testing the Predictive Capability of the High-Fidelity Generalized Method of Cells Using an Efficient Reformulation,'' NASA CR 2004-213043.
[14] Bednarcyk, B. A., Arnold, S. M., Aboudi, J., and Pindera, M.-J., 2004, ''Local Field Effects in Titanium Matrix Composites Subject to Fiber-Matrix Debonding,'' Int. J. Plast., **20**, pp. 1707–1737.
[15] Arnold, S. M., Wilt, T. E., Saleeb, A. F., and Castelli, M. G., 1993, ''An Investigation of Macro and Micromechanical Approaches for a Model MMC System,'' HITEMP Review 1993: CP 19117, pp. 52.1–52.11.
[16] Arnold, S. M., Pindera, M. J., and Wilt, T. E., 1996, ''Influence of Fiber Architecture on the Inelastic Response of Metal Matrix Composites,'' Int. J. Plast., **12**, No. 4, pp. 507–545.
[17] Iyer, S. K., Lissenden, C. J., and Arnold, S. M., 2000, ''Local and Overall Flow in Composites Predicted by Micromechanics,'' Composites, Part B, **31**, pp. 327–343.
[18] Baxter, S. C., Hossain, M. I., and Graham, L. L., 2001, ''Micromechanics Based Random Material Property Fields for Particulate Reinforced Composites,'' Int. J. Solids Struct., **38**, Nos. 50/51, pp. 9209–9220.
[19] Graham-Brady, L. L., Siragy, E. F., and Baxter, S. C., 2003, ''Analysis of Heterogeneous Composites Based on Moving-Window Techniques,'' J. Eng. Mech., **129**, No. 9, pp. 1054–1064.
[20] Ostoja-Starzewski, M., 2002, ''Microstructural Randomness Versus Representative Volume Element in Thermomechanics,'' J. Appl. Mech., **69**, pp. 25–35.

An Investigaton of Minimum-Weight Dual-Material Symmetrically Loaded Wheels and Torsion Arms

Peter Dewhurst

Sriruk Srithongchai[1]

Department of Industrial and Manufacturing Engineering,
University of Rhode Island,
Kingston, RI 02881

A cylindrically symmetric layout of two opposite families of logarithmic spirals is shown to define the layout of minimum-weight, symmetrically loaded wheel structures, where different materials are used for the tension and compression members, respectively; referred to here as dual-material structures. Analytical solutions are obtained for both structure weight and deflection. The symmetric solutions are shown to form the basis for torsion arm structures, which when designed to accept the same total load, have identical weight and are subjected to identical deflections. The theoretical predictions of structure weight, deflection, and support reactions are shown to be in close agreement to the values obtained with truss designs, whose nodes are spaced along the theoretical spiral layout lines. The original Michell solution based on 45 deg equiangular spirals is shown to be in very close agreement with layout solutions designed to be kinematically compatible with the strain field required for an optimal dual-material design. [DOI: 10.1115/1.1831295]

1 Introduction

The layout of a minimum-volume spoked wheel subjected to pure torsional loading, uniformally distributed around its perimeter, is well established in the literature. Michell [1] showed that the layout lines for the spokes must follow 45 deg equiangular spirals with the opposite families of spirals crossing orthogonally and carrying equal uniaxial strain at any point in tension and compression. Following a half-century of neglect, Hemp [2] and his colleagues, Chan [3], and Chan [4], at the Cranfield College of Aeronautics in the U.K., laid down a formal mathematical basis for the investigation of Michell structures. In particular Hemp [5] showed how the requirement of a cylindrically symmetric layout, where at any radial position compression and tension spokes follow lines with the same curvature, defines the 45 deg equiangular or logarithmic-spiral solution, for a material with equal strength in tension and compression. When the spiral layout lines are translated into a wheel design the result has an undeniable elegance as illustrated in Fig. 1.

Michell's work would have been remarkable had it been confined only to materials which have the same strength in tension and compression. However, Michell developed his criterion for minimum volume in the general context of a material having different limiting stress values in tension and compression (referred to here as bi-yield materials). Rozvany [6], in a paper which recognizes Michell's role as the creator of all of the essential elements of modern optimum structural design, has shown that Michell's optimality conditions for bi-yield materials are only valid for a very restricted class of structures; namely those which are statically determinate.

Hemp [5] described a set of modified the conditions for minimum volume of bi-yield material structures, which he named ''Michell's sufficient conditions'' to maintain the attribution to Michell for his pioneering work in the field. ''Michell's sufficient conditions'' were not recognized in the literature as being fundamentally different than Michell's original conditions until the examination of the optimality criteria by Rozvany [6]. It should be mentioned that much of the progress in Michell structure design has resulted from the demonstrations independently by Hemp [2] and Prager [7], that the structural layout problem for two-dimensional Michell frameworks is identical to the determination of the layout of the slip lines in plain-strain metal deformation. Hemp [5] also established a complete analytical framework for the evaluation of volume, force distributions, and displacements of bi-yield optimum structures.

With the exception of Prager [7], all of the work described above is concerned with the design of structures for minimum volume. If a structure is manufactured from a single material then this is of course equivalent to minimum-weight design. However, if the structure tensile members are made from a different material than the compression members then the solutions for minimum volume and minimum weight are in general different. The establishment by Prager [7] of an optimality criterion for this dual-material structure design problem appears to have been completely overlooked in the literature on Michell structures. Prager's work was applied specifically to reinforced concrete structures, and for this reason the general nature of the work may not have been recognized. Srithongchai and Dewhurst [8] have shown, that for a class of statically indeterminate cantilevers, Prager's optimality criterion leads to minimum weight predictions which are slightly less than those obtained from Michell's original work.

Two of the proposed minimum-volume solutions in Michell's paper [1] are not statically determinate; namely the plane torsion wheel and the spherical torsion frame. These examples are therefore optimal only for a single material structure with equal strength in tension and compression. The main goal of the present work is to investigate the solution for minimum-weight symmetrically loaded wheels for dual-material designs. The general conditions for optimality of dual material structures are reviewed in Sec. 2. In Sec. 3, the general layout for a dual-material wheel structure is established. It is shown that, for a specific combination of radial and tangential loading, the force diagram is the precise inverse of the structure layout. The geometry of the force diagram is the mirror image of the structure layout, and the outer circle of the force diagram corresponds to the inner circle of the structure. Under these conditions the combination of structure and force diagrams allows an analytical weight solution to be obtained,

[1]Visiting Scholar from the Department of Industrial Engineering, Chulalongkorn University, Bangkok 10330, Thailand.

Contributed by the Applied Mechanics Division of THE AMERICAN SOCIETY OF MECHANICAL ENGINEERS for publication in the ASME JOURNAL OF APPLIED MECHANICS. Manuscript received by the Applied Mechanics Division, May 14, 2003; final revision, July 21, 2004. Associate Editor: K. M. Lietchi.

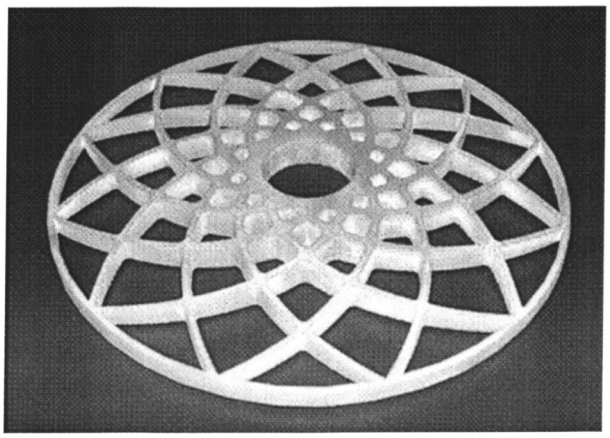

Fig. 1 Prototype pure torsion wheel manufactured by free-form laser sintering

which has remarkable similarity to Michell's original analytical solution. For completeness in Sec. 3, an analytical expression for wheel deflection is also obtained. In Sec. 4 discrete truss wheels and torsion arms are analyzed for the dual-material condition $(\sigma_T/\rho_T)/(\sigma_C/\rho_C)=3$. It is shown that in all cases the Prager solution has a smaller weight than the corresponding Michell solution, in agreement with the optimality criterion. However, the differences in all cases are remarkably small.

2 General Conditions for Optimality of Dual-Material Structures

Prager's conditions for a dual-material structural layout [7], comprising both compression and tension members, to be optimal, can be restated in a similar manner to that used by Hemp [5] for bi-yield materials as follows:

i. A virtual deformation of the space in which the structure lies must give strains of $(\sigma\varepsilon/\rho)/(\sigma_T/\rho_T)$ in all the tension members and $(\sigma\varepsilon/\rho)/(\sigma_C/\rho_C)$ in all the compression members, and no direct strain in any region of the space must have a value outside of these limits.

ii. The virtual deformation must satisfy the kinematic conditions imposed on the structure.

The proof then follows that no other structure, with limiting stress magnitudes σ_T, σ_C, and densities ρ_T, ρ_C in tension and compression, respectively, can support the same loads with a smaller weight of material. Prager [7] presented the result as just a "straightforward extension of the general theory of plastic design." Srithongchai and Dewhurst [8] laid down a direct proof of Prager's criterion using the elegant approach established by Hemp [5].

To simplify the equations which follow, σ/ρ and σ_T/ρ_T will be assumed equal, and the virtual strain magnitudes in tension and compression members respectively will be given by ε and $\lambda\varepsilon$, where $\lambda=(\sigma_T/\rho_T)/(\sigma_C/\rho_C)$.

Figure 2 illustrates the intersection of tension member *ac* and compression member *bc* with a small section *ab* of a rigid boundary. If these are subjected to principal strains ε and $\lambda\varepsilon$, then since the angle at the displaced node position c' must remain a right angle, it can readily be verified that

$$\gamma=\tan^{-1}(\lambda^{1/2}), \tag{1}$$

$$\omega=-\varepsilon\tan(\gamma), \tag{2}$$

where the negative sign in Eq. (2) denotes clockwise rotation. These boundary conditions were defined by Hemp [5] for the general case of intersection of curved structure members with a curved rigid boundary. It can also be verified that the deflection of c to c' is given by

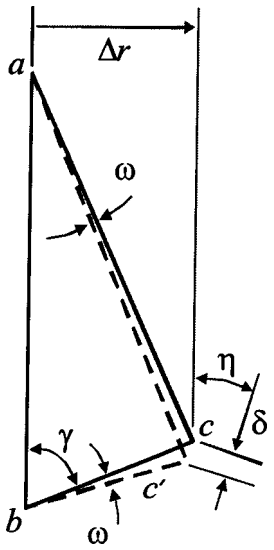

Fig. 2 Elemental truss members adjacent to boundary

$$\delta=\Delta r\varepsilon(1+\tan^2\gamma), \tag{3}$$

$$\eta=\left(2\gamma-\frac{\pi}{2}\right), \tag{4}$$

where δ is the deflection magnitude, and η the angle in Fig. 2. Interestingly, this angle value appears as a key to the determination of the analytical dual-material wheel solution in the next section.

Hemp [5] showed that, even with his more general conditions defined above, an optimum network must still satisfy the equiangular property that the angle turned through by all compression members between any pair of tension members is constant and vice versa. This is exactly the property of the lines of maximum shear in plain-strain slip-line field theory (Hill [9]). Hemp [2] identified this mathematical coincidence, and Johnson [10] took the analogy further by demonstrating that the force diagram for minimum-weight structures can be drawn in such a way as to be identical to the velocity diagram (Green [11]) in slip-line field theory. This allowed the tools which had been developed for slip-line field theory to be applied to the two-dimensional optimal structure layout problem; see for example Johnson et al. [12], Dewhurst [13], and Srithongchai et al. [14].

As a consequence of the equiangular property, and utilized extensively in the construction of slip-line fields (Hill [9]), a Michell structure layout must satisfy the geometrical property that the radii of curvature of crossing tension lines change by the distance traveled along compression lines and vice versa. At any point in a network of layout lines, this property can be represented as

$$\frac{\partial R}{\partial\beta}=-S;\quad\frac{\partial S}{\partial\alpha}=-R, \tag{5}$$

where R and S are the radii of curvature of tension and compression layout lines respectively. The negative sign in Eq. (5) occurs because the radius of curvature is counted negative for a clockwise turning layout line. Coordinates α and β define the angles turned by the tension and compression members respectively from any base point. For convenience the layout lines for tension and compression members will be referred to as α- and β-lines respectively. Coordinates α and β are both counted positive from the base point.

3 General Layout of Minimum-Weight Torsion Wheel

For the layout of a bi-yield material torsion wheel it is clear, as pointed out by Rozvany [6], that the spokes must form constant

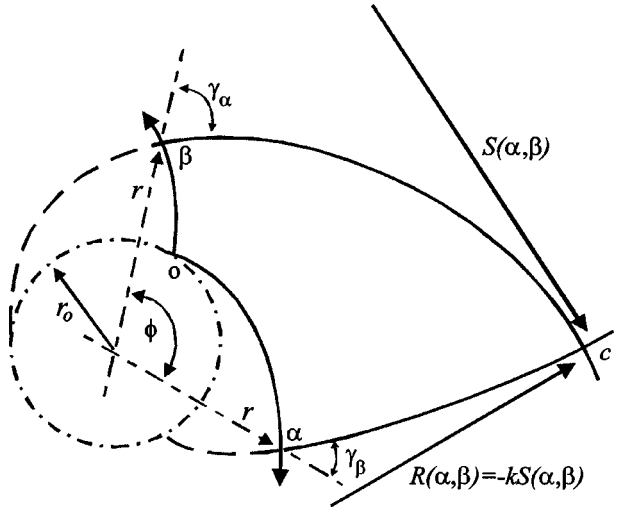

Fig. 3 Field of orthogonal logarithmic spirals

angles γ and $\pi/2-\gamma$ with the circular boundary and with any circle having the same center. It will be shown below that this condition is satisfied if the radii of curvature of the tension and compression spokes are in constant ratio throughout the structure. Assume the constant ratio has value $-k$; see Fig. 3. Equation (5) then becomes

$$\frac{\partial R}{\partial \beta}=\frac{1}{k}R;\quad \frac{\partial S}{\partial \alpha}=kS, \tag{6}$$

with general solution

$$R(\alpha,\beta)=-Ake^{k\alpha}e^{\beta/k};\quad S(\alpha,\beta)=Ae^{k\alpha}e^{\beta/k}. \tag{7}$$

These can be recognized as the radii of curvature of logarithmic spirals, with polar equations

$$r=r_0e^{k\alpha};\quad r=r_0e^{\beta/k}, \tag{8}$$

where

$$k=\cot(\gamma_\alpha), \tag{9}$$

and γ_α is the constant intersection angle of α spirals with the radial direction. The α spirals and β-spirals cross everywhere at right angles as required since $1/k=\cot(\pi/2-\gamma_\alpha)=\cot(\gamma_\beta)$, where γ_β is the constant intersection angle of β-spirals with the radial direction; see Fig. 3.

If coordinate points $(\alpha,0)$ and $(0,\beta)$, in Fig. 3, are on the same polar radius, r, then from Eqs. (8):

$$\beta=k^2\alpha, \tag{10}$$

also the polar angle ϕ, in Fig. 3, can readily be seen to be the sum of α and β,

$$\phi=\alpha+\beta. \tag{11}$$

At any point in the network $(r\,\delta\phi)^2=(R\,\delta\alpha)^2+(S\,\delta\beta)^2$, and together with Eqs. (9) and (10) this gives

$$A=r_0(1+1/k^2)^{1/2}. \tag{12}$$

Finally the radii of curvature of the individual tension and compression members starting from point 0 in Fig. 3 are given by

$$R(\alpha)=-r_0(1+k^2)^{1/2}e^{k\alpha};\quad S(\beta)=r_0(1+1/k^2)^{1/2}e^{\beta/k} \tag{13}$$

and from Eqs. (1) and (9), for a specific bi-yield material

$$k=\sqrt{(\sigma_C/\rho_C)/(\sigma_T/\rho_T)}. \tag{14}$$

If these layout lines are used to define a full wheel structure then it can be established that the corresponding force diagram comprises the same two families of logarithmic spirals. The layout diagram and the corresponding force diagram are illustrated in Figs. 4(a) and 4(b).

Consider spiral ab, in Fig. 4(a), which will be assumed to be an α-line defining the layout of a tension spoke. Curve cb is the β-line which converges to the same position b at the outer perimeter. The force diagram is drawn in such a way that its curves are everywhere orthogonal to the corresponding structure layout lines. Referring to Fig. 4(b) it can be seen that the force diagram is the geometrical inverse of the structure diagram. The inner and outer diameters of the force diagram correspond to the outer and inner diameters of the wheel respectively. Also the direction of rotation of both families of spirals has reversed. Curve $a'b'$ in the force diagram defines the distribution of force carried by the compression members at right angles to the tension member ab. Similarly $c'b'$ defines the distribution of force carried by the tension members normal to cb.

Assume the polar angle between points a and c has value ϕ, and ab, cb turn through angles θ and ψ, respectively. Arbitrary

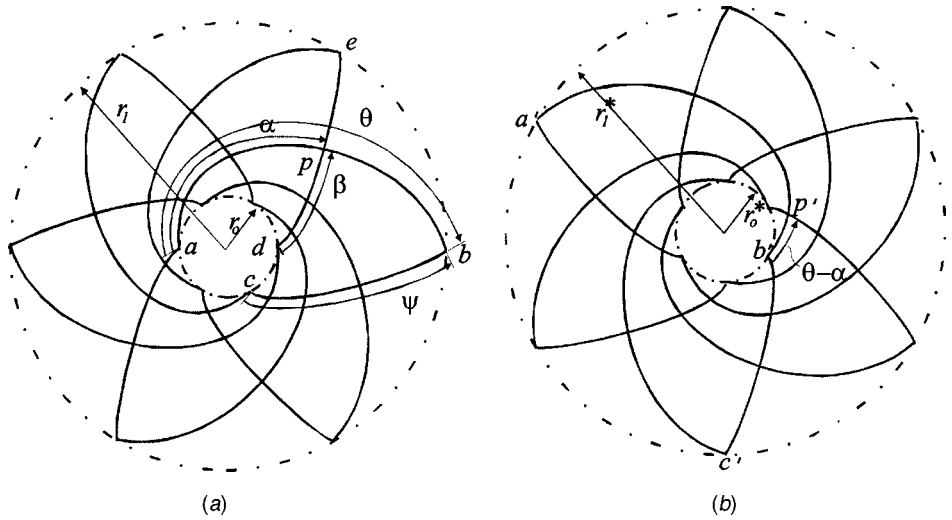

Fig. 4 (*a*) Selected layout curves for a general logarithmic spiral wheel structure, (*b*) associated force diagram

point, p, at angular position α on ab corresponds to point p' in the force diagram at angular position θ-α on curve $b'a'$.

The difference between the polar angle of corresponding points in the two diagrams can readily be shown to be

$$\eta = 2\gamma_\alpha - (\pi/2). \tag{15}$$

This defines the angle between the circumferential and radial components of loading at any point in the structure. The close geometrical similarity of layout and force diagrams for Michell structures is well documented in the literature. It seems from the present case that this similarity extends to dual-material structures, using Prager's optimality conditions.

Let the magnitude of the distributed load per unit length around the inner wheel circumference be given by f_0. From the force diagram it can be seen that total force magnitude $2\pi r_1^*$, around the outer circumference of the force diagram, will be distributed uniformally around the inner circumference of the wheel, of length $2\pi r_0$. The value of f_0 is thus given by

$$f_0 = r_1^*/r_0. \tag{16}$$

Similarly the magnitude of the distributed force per unit length around the wheel outer circumference is given by

$$f_1 = r_0^*/r_1. \tag{17}$$

Since the angle of this loading, to the circumferential direction, is the constant value given in Eq. (15), moment equilibrium about the wheel center gives

$$2\pi r_0^2 f_0 \cos(2\gamma_\alpha - \pi/2) = 2\pi r_1^2 f_1 \cos(2\gamma_\alpha - \pi/2), \tag{18}$$

substituting for f_0 and f_1, gives

$$r_1^*/r_0^* = r_1/r_0. \tag{19}$$

Since the angular sweeps of the spirals, and the ratio of the radii, are the same for both diagrams, the spirals in the force diagram must be identical but opposite logarithmic spirals to those in the structure itself; a result which is not defined by just the orthogonal relationship of the two diagrams.

Returning now to arbitrary point p in Fig. 4(a), the force acting on a narrow bundle of compression elements adjacent to layout line de in the neighborhood of p is

$$\delta f = R^*(\theta - \alpha)\,\delta\alpha, \tag{20}$$

where R^* defines the radius of curvature of spiral $b'a'$ in the force diagram. A short length of the bundle can be defined as

$$\delta l = S(\beta)\,\delta\beta, \tag{21}$$

where S defines the radius of compression spoke layout curve de.

If the maximum allowable stress in the structure compression members is given by σ_C, then the weight of this short bundle of compression elements can be given by

$$\delta W_C = \frac{\rho_C}{\sigma_C} R^*(\theta - \alpha) S(\beta)\,\delta\alpha\,\delta\beta. \tag{22}$$

To integrate this expression throughout the structure it is useful to substitute one of the spiral angles for the polar angle. Referring back to Eqs. (10) and (11), $\delta\beta$ can be represented as

$$\delta\beta = \delta\phi/(1 + 1/k^2). \tag{23}$$

Substituting for R^*, S, and $\delta\beta$, the total weight of compression elements is given by

$$W_C = \frac{\rho_C r_0 r_0^*}{\sigma_C} \int_0^{2\pi} \int_0^{\theta} \{(1+k^2)^{1/2} e^{k(\theta-\alpha)}\}\{(1 + 1/k^2)^{1/2} e^{(k^2\alpha)/k}\} d\alpha \frac{d\phi}{(1+1/k^2)}, \tag{24}$$

which integrates to the simple expression

$$W_C = \frac{2\pi\rho_C r_0 r_1^*}{\sigma_C} \ln\left(\frac{r_1}{r_0}\right). \tag{25}$$

The weight of tension members, using radii of curvature functions S^* and R can be obtained in identical fashion, and leads to the same weight solution with ρ_C/σ_C replaced by ρ_T/σ_T. It is useful to define loading parameter

$$G = 2\pi r_1 r_0^* = 2\pi r_0 r_1^*. \tag{26}$$

The total wheel weight is then

$$W = W_C + W_T = \left(\frac{\rho_C}{\sigma_C} + \frac{\rho_T}{\sigma_T}\right) G \ln\left(\frac{r_1}{r_0}\right). \tag{27}$$

This result is satisfyingly identical in form to the result obtained by Michell for the case where G represents pure torsional loading.

From Prager's condition (i) in Sec. 2, the virtual work per unit weight of the structure is $(\sigma_T/\rho_T)\varepsilon_T = (\sigma_T/\rho_T)[(\sigma\varepsilon/\rho)/(\sigma_T/\rho_T)]$ in all the tension members and $(\sigma_C/\rho_C)[(\sigma\varepsilon/\rho)/(\sigma_C/\rho_C)]$ in all the compression members; equal to $\sigma\varepsilon/\rho$ throughout the structure. Hence, if the inner radius is assumed fixed, and the outer perimeter has deflection δ_f in the direction of the applied loading, then equating virtual strain energy gives

$$2\pi r_0^* \delta_f = \sigma\varepsilon \left(\frac{1}{\sigma_C} + \frac{1}{\sigma_T}\right) G \ln\left(\frac{r_1}{r_0}\right). \tag{28}$$

Substituting for $(\sigma_T/\rho_T)/(\sigma_C/\rho_C)$ from Eqs. (9) and (14), and G from Eq. (26), Eq. (28) reduces to

$$\delta_f = \varepsilon_T(1 + \tan^2\gamma_\alpha) r_1 \ln\left(\frac{r_1}{r_0}\right), \tag{29}$$

or the equivalent expression with ε_C and γ_β.

The deflection of a Michell structure depends only on the boundary conditions, the magnitude of the strains ε_C, ε_T, and the geometry of the layout lines. Within limits, it is independent of the magnitude of the applied force or its direction, or the number or distribution of forces along the structure boundary. When the applied forces, for a given structural layout, are changed, the force diagram will change and the cross-sectional area at every region of the structure will be different for minimum weight. The cross sections will be chosen to give the limiting stress values, and so the deflections will be unchanged.

In the next section we will compare the above results, and Michell's original wheel solution, with truss designs of wheel and torsion arm structures.

4 Truss Structure Approximations

Michell structural forms are robust in the sense that discrete truss structures, whose nodes lie on the Michell layout lines, have strength and stiffness to weight ratios near the theoretical optimum values even when the node spacing is relatively large. For example, Srithongchai et al. [14] designed and manufactured an aluminum alloy test beam, with nodes positioned at 22.5 deg increments along the network of Michell layout curves. Experimental loading of the beam provided stiffness values and yield load in almost perfect agreement with the optimal values determined from the layout equations. The converse is also true. Using Prager's method [15], for optimizing trusses with a finite number of members, truss forms emerge in close agreement to Michell layouts. Figure 15, in the review paper by Rozvany et al. [16], shows an excellent example of this in the design of a 24-member cantilever truss. In this section approximate truss designs will be evaluated for a symmetrically loaded wheel structure, and for alternative layouts of a torsion arm structure.

4.1 Wheel Truss Structure. Figure 5 illustrates one quarter of a wheel structure whose nodes lie on 60 deg and 30 deg equi-

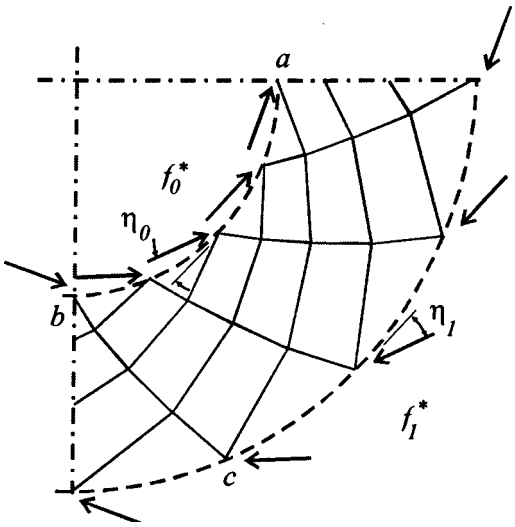

Fig. 5 Quadrant of truss wheel structure

angular spirals. The directions of the forces indicate that the 60 deg spiral spokes are the tension members, and so from Eq. (1) the structure corresponds to the optimal solution with $\gamma=\pi/3$ and $(\sigma_T/\rho_T)/(\sigma_C/\rho_C)=3$. The design comprises 16 pairs of spokes at angular spacing $\pi/8$. The inner wheel radius, r_0, is taken to be 1.0, and the outer wheel radius has been selected so that one pair of opposite spokes span one quarter of the wheel; see spokes ac and bc in Fig. 5. Using Eqs. (10), (11), and (14), $k=\sqrt{1/3}$, $\phi=\pi/2$ and the total angle turned through along the tension layout spirals, ac, is thus $3\pi/8$. The outer wheel radius, r_1, is given by

$$r_1=\exp[\sqrt{1/3}(3\pi/8)]=1.9742.$$

A force of 1000/16 units, labeled f_1^* in Fig. 5, was applied to each of the 16 nodes around the external perimeter. In each case the inclination of the force to the wheel circumference, η_1 in Fig. 5, was set equal to 30 deg corresponding to the value defined by Eq. (15). The ratio of limiting stress to density values were assumed to be $\sigma_T/\rho_T=30{,}000$, $\sigma_C/\rho_C=10{,}000$ units. The method of joints was first applied to determine the force value f in each structural member. The unit weight of each tension member was then set to the value of $f/(3\times10^4)$ and each compression member to $f/10^4$. The truss weight was calculated, by summing the product of length and unit weight for each member, to give

$$W_{\text{truss}}=\sum\ l_T f/(\sigma_T/\rho_T)+\sum\ l_C f/(\sigma_C/\rho_C).$$

Calculations are given in Table 1 for one tension spoke and one compression spoke. Using these calculated values, the total wheel truss weight is,

$$W_{\text{truss}}=(16)(84.63)/30\,000+(16)(84.32)/10\,000$$
$$=0.0451+0.1349=0.1800.$$

Table 1 Truss wheel weight calculations

Tension members			Compression members		
length, l	force, f	lf	length, l	force, f	lf
0.3693	57.23	21.14	0.2139	98.61	21.09
0.4378	48.30	21.15	0.2536	83.15	21.09
0.5190	40.77	21.16	0.3006	70.11	21.08
0.6152	34.42	21.18	0.3563	59.10	21.06
	total:	84.63		total:	84.32

For comparison, the theoretical weight from Eq. (27) is, substituting 1000 for $2\pi r_0^*$,

$$W_{\min}=\left(\frac{1}{10^4}+\frac{1}{(3)(10^4)}\right)(1000)(1.9742)\ln(1.9742)$$
$$=0.0448+0.1343=0.1791.$$

The radial and tangential deflections, u and v, respectively, of the wheel perimeter were then determined. Deflection calculations were carried out, using of the structural analysis program MASTAN2™ (2000), which operates as a toolbox in the matrix analysis program MATLAB™ (vers 5.3). Elastic modulus values for the tension and compression members were assumed to be $E_T=3\times10^6$ and $E_C=(1/3)\times10^6$; giving strain values $\varepsilon_T=0.01$ and $\varepsilon_C=0.03$ corresponding to Prager test strains. The truss deflections calculated by MASTAN2 were

$$u=-0.014\,63;\quad v=-0.053\,92.$$

These correspond to a resultant deflection of 0.055 87 at an angle of 15.18 deg to the wheel perimeter. The truss deflection in the direction of the applied load is thus

$$\delta_{f,\text{truss}}=[(0.014\,63)^2+(0.053\,92)^2]^{1/2}\cos(14.82°)$$
$$=0.054\,01.$$

For comparison, applying Eq. (29) gives theoretical deflection,

$$\delta_f=0.01[1+\tan^2(60°)]1.9742\ln(1.9742)=0.053\,71,$$

which is in remarkable agreement with the approximate truss value.

In the truss analysis, the 16 nodes on the inner circumference were constrained not to translate. The reaction forces on these nodes, labeled magnitude f_0^* at angle η_0 in Fig. 5, where calculated to be

$$f_0^*=123.54;\quad \eta_0=0.5257.$$

For comparison with the continuum model in Sec. 3, the discrete truss forces f_0^* and f_1^* are related to the continuous force distributions f_0 and f_1 by

$$f_0^*=\left(\frac{\pi}{8}r_0\right)f_0;\quad f_1^*=\left(\frac{\pi}{8}r_1\right)f_1. \tag{30}$$

Equations (15) and (19) thus give

$$f_0^*=(r_1/r_0)f_1^*=1.9742\times1000/16=123.39,$$

and

$$\eta_0=2(\pi/3)-(\pi/2)=0.5236.$$

Note, that the values of f_0^* and η_0 are not dictated by external equilibrium and so provide further validation of the theoretical model.

4.2 Torsion Arm Truss Structures. The term ''torsion arm'' is used here for brevity to describe structures which are more correctly defined as cantilevers with circular supports. Figure 6 shows a torsion arm structure corresponding to a portion of the wheel structure in the last section. The force values, f, carried by each structural member for the indicated applied tip load are given on the figure. It should be noted in passing that while the wheel structures can expand outwards without bound, a limitation exists on the design of spiral network torsion arms since the sum of the angles turned through by the outer flanges ($\alpha+\beta$ in Fig. 3) cannot be greater than 2π. Beyond this range, the optimal layout may be a combination of a tie bar and spiral net of the type described by Prager and Rozvany [17]. Such combinations may also be used to in situations where the angle of the applied tip load would be such as to put both outer flanges in tension or compression [17].

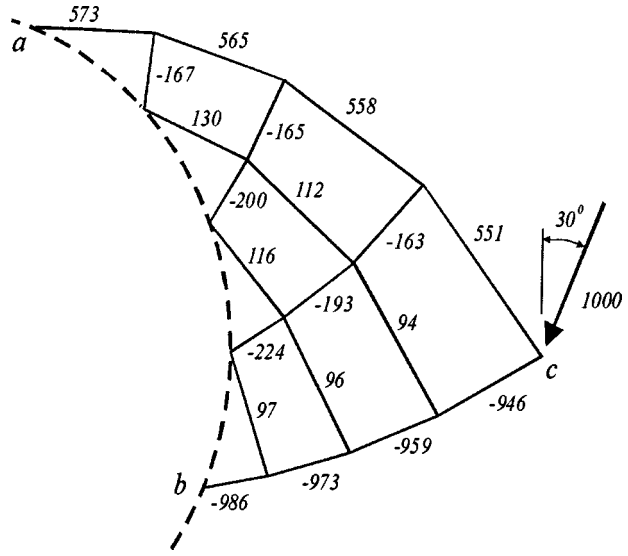

Fig. 6 Truss approximation of Prager torsion arm

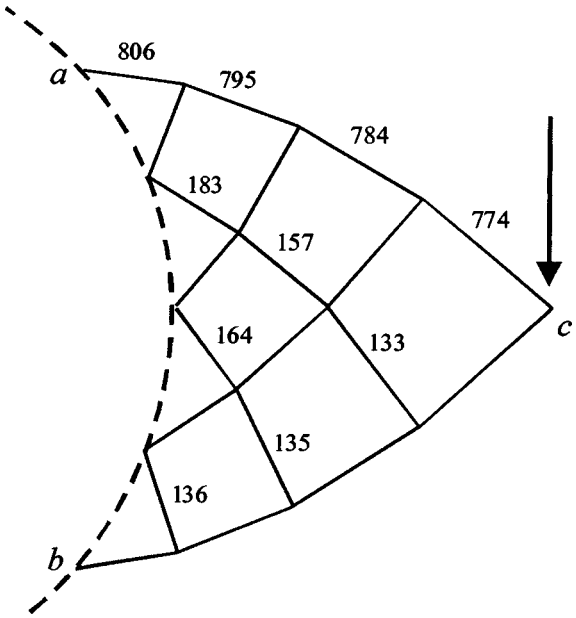

Fig. 7 Truss approximation of Michell torsion arm

The lengths of the elements in Fig. 6 can be obtained from Table 1 and so as before the truss weight can readily be shown to be

$$W_{\text{truss}} = \sum l_T f/(\sigma_T/\rho_T) + \sum l_C f/(\sigma_C/\rho_C) = 0.045 + 0.135 = 0.180,$$

exactly the same as the complete wheel weight. This is of course expected since the total loading is the same and the node deflections must be the same; see the discussion following Eq. (29). For the comparisons which follow, dimensionless weight measures, W^*, will be used, where

$$W^* = W \Big/ \left[FL\left(\frac{\rho_T}{\sigma_T} + \frac{\rho_C}{\sigma_C} \right) \right].$$

The applied load in Fig. 6 corresponds to angle $\eta = 30$ deg. The weight of the structure was recalculated for the load of 1000 units at η values of -15, 0, 15, and 45 deg. The dimensionless weight values are given in column 2 of Table 2.

For comparison, column 3 gives the dimensionless weight values for the corresponding Michell torsion arm. This structure, as shown in Fig. 7, is laid out along 45 deg spirals according to Michell's solution. To provide the same cantilever length of $L = 1.9742$, the angular sweep of the outer spirals is 38.9711 deg, and polar angle between successive spokes equal to 19.4855 deg provides four elements with equiangular spacing as shown. The lengths of successive members moving radially outwards are 0.2617, 0.3104, 0.3679, and 0.4360. The truss member forces corresponding to $\eta = 0$ are included in Fig. 7; only tensile forces are given since the compression values are identical by symmetry.

Table 2 Truss comparison of Prager and Michell dimensionless weights for $\sigma_T/\sigma_C = 3$

Load angle, η	Prager torsion arm	Michell torsion arm
−15	0.6116	0.6119
0	0.6831	0.6835
15	0.7078	0.7083
30	0.6840	0.6849
45	0.6138	0.6148

It can be seen in Table 2 that for all five loading cases the Prager solution is less than the Michell one in accordance with the optimality criterion. However, the differences are surprisingly small.

One final comparison was felt to be worthwhile; namely the weight allocation to tension and compression members for the theoretical and truss approximation cases. These are given in Table 3 below. Note that columns 2 and 3 represent different loading cases, and that Eq. (27) becomes Michell's equation when $\eta = 0$. The intention of Table 3 is thus to compare separately the Michell and Prager trusses with the theoretical minimum weight values.

5 Discussion and Conclusions

A general theoretical model has been presented for the layout of a spoked wheel or moment arm structure, which is kinematically compatible with the Prager test strains for different materials in tension and compression. Analytical predictions based on the model have been shown to be in remarkable agreement with the calculated weights, deflections, and reaction forces of approximate truss structures, whose nodes are placed on the theoretical layout lines.

An analytical solution obtained in Sec. 3 for structure weight, is applicable to a specific combination of radial and circumferential loading, and has identical mathematical form to Michell's original solution.

Comparisons of dual-material truss structures based on Michell's original layout, and on the more general layouts satisfying Prager's optimality criterion, indicate only small differences between the weights of the two structure types. However, in every case analyzed, with different tension and compression material properties, Prager's structure has lower weight than the corresponding Michell structure in accordance with Prager's optimality criterion.

Table 3 Comparison of theoretical and truss weight allocation

Dimensionless weight $(\sigma_T/\rho_T)/(\sigma_C/\rho_C) = 3$	Michell truss ($\eta = 0$)	Prager truss ($\eta = 30°$)	Theoretical values from Eq. (27)
Tension members	0.1709	0.1715	0.1700
Compression members	0.5126	0.5125	0.5101

The small difference in weight of the alternative Michell and Prager solutions allows selection to be made on the basis of other requirements. For example, the Michell truss in Fig. 7 was reanalyzed with the same 30 deg inclined loading as in the Prager truss (Fig. 6), to determine that for this case the Michell truss is just 0.13% heavier than the Prager one. However, the compression member carrying the smallest load of 163 units in the Prager design, in the same position in the Michell design carries the lightest compression load with a value of only 59 units. With similar cross-sectional shapes, the Michell design thus contains compression members having a slenderness ratio approximately three times the most slender members in the Prager design. In both trusses, in-plane global instability is initiated by buckling of those particular members with rotation of their inner joint involving the collapse of connected members. Thus the Prager layout is much more robust than the Michell one for this loading condition, and cross-sectional shape optimization to suppress buckling is more likely to be successful for the former case. For other inclinations of the applied load, the Michell layout may of course be preferable for the execution of a stable design. In other situations the selection between alternative layouts may be made on the basis of material cost. It is tempting to conclude that any pair of complimentary spiral angles can be used to obtain a whole family of structures with approximately equal efficiency. Surprisingly this is not the case. For the condition $(\sigma_T/\rho_T)/(\sigma_C/\rho_C)=3$ spiral nets other than 45/45 (Michell) or 30/60 (Prager) can lead to structure weights which are significantly heavier. It seems that Michell almost got it all perfectly right.

For cases where the densities of tension and compression members are the same, the problem reduces to that of a bi-yield material structure and minimum weight is the same condition as minimum volume. In these cases the criterion reduces to the ''sufficient conditions'' described by Hemp [5], and the structures should be referred to as Hemp trusses.

Recent work by one of the authors [18] has shown that the generalized logarithmic spiral wheel layout also satisfies the requirements of maximum stiffness, or the optimal combination of strength and stiffness per unit weight.

Acknowledgments

This material is based upon work supported by the National Science Foundation under Grant No. 0200058.

Nomenclature

α, β = arbitrary angles along tension and compression members
δ = resultant displacement or displacement in load direction
ε = arbitrary strain value
$\varepsilon_T, \varepsilon_C$ = tensile strain in all of the tensile members and compressive strain in all of the compressive members
F = externally supported loads
f = forces carried by the structural members, or forces at node points around wheel hub and outer perimeter
γ = intersection angle with support boundary
k = ratio of radius of curvature of tension and compression members
L = length between lower support point and tip point for cantilever
l = length of structural members
λ = ratio of stress divided density values
ϕ = polar angle
ρ = arbitrary weight per unit volume
ρ_T, ρ_C = weight per unit volume of tension and compression members
η = angle of applied load
r = arbitrary radial position on wheel structure
r^* = arbitrary radial position on force diagram
R, S = radii of curvature of tensile members and compression members
σ = arbitrary stress value
σ_T, σ_C = maximum allowable tensile and compressive stresses in a structure
u, v = radial and tangential displacements
W = total weight of structure
W_T, W_C = weights of tensile and compressive members
W^* = dimensionless weight of structure
θ, ψ = angular span of tensile and compressive members
ω = rotation of a structural member

References

[1] Michell, A. G. M., 1904, ''Limits of Economy of Material in Frame-Structures,'' Philos. Mag., **6**, pp. 589–597.
[2] Hemp, W. S., 1958, ''The Theory of Structural Design,'' Report No. 115, College of Aeronautics, Cranfield, UK.
[3] Chan, H. S. L., 1960, ''The Design of Michell Optimum Structures,'' Report No. 142, Cranfield College of Aeronautics, UK.
[4] Chan, H. S. Y., 1963, ''Optimum Michell Frameworks for Three Parallel Forces,'' Report No. 167, Cranfield College of Aeronautics, UK.
[5] Hemp, W. S., 1973, *Optimum Structures*, Clarendon Press, Oxford.
[6] Rozvany, G. I. N., 1996, ''Some Shortcomings in Michell's Truss Theory,'' Struct. Optim., **12**, pp. 244–250.
[7] Prager, W., 1958, ''A Problem of Optimal Design,'' Proceedings of the Union of Theoretical and Applied Mechanics, Warsaw.
[8] Srithongchai, S., and Dewhurst, P., 2003, ''Comparisons of Optimality Criteria for Minimum-Weight Dual Material Structures,'' Int. J. Mech. Sci., **45**, pp. 1781–1797.
[9] Hill, R., 1950, *The Mathematical Theory of Plasticity*, Clarendon Press, Oxford.
[10] Johnson, W., 1961, ''An Analogy Between Upper-Bound Solutions for Plane-Strain Metal Working and Minimum-Weight Two-Dimensional Frames,'' Int. J. Mech. Sci., **3**, pp. 239–246.
[11] Green, A. P., 1954, ''On the Use of Hodographs in Problems of Plane Plastic Strain,'' J. Mech. Phys. Solids, **16**, pp. 267–276.
[12] Johnson, W., Chitkara, N. R., Reid, S. R., and Collins, I. F., 1971, ''The Displacement Field and Its Significance for Certain Minimum Weight Two-Dimensional Frames Using the Analogy With Perfectly Plastic Flow in Metal Working,'' Int. J. Mech. Sci., **13**, pp. 547–561.
[13] Dewhurst, P., 2001, ''Analytical Solutions and Numerical Procedures for Minimum-Weight Michell Structures,'' J. Mech. Phys. Solids, **49**, pp. 445–467.
[14] Srithongchai, S., Demircubuk, M., and Dewhurst, P., 2003, ''A Theoretical and Experimental Investigation of a Family of Minimum-Volume Simply-Supported Beams,'' Int. J. Mech. Sci., **45**, pp. 37–55.
[15] Prager, W., 1978, ''Optimal Layout of Trusses With a Finite Number of Joints,'' J. Mech. Phys. Solids, **26**, pp. 241–250.
[16] Rozvany, X., Bendsoe, X., and Kirsch, X., 1995, ''Layout Optimization of Structures,'' Appl. Mech. Rev., **48**, pp. 41–118.
[17] Prager, W., and Rozvany, G. I. N., 1977, ''Optimization of Structural Geometry,'' in *Dynamical Systems*, edited by Bednarek, A. R. and Cesari, L., Academic Press, New York.
[18] Dewhurst, P., 2004, ''A General Optimality Criterion for Strength and Stiffness of Dual Material-Property Structures,'' Int. J. Mech. Sci., in press.

The Mechanical Response of Freestanding Circular Elastic Films Under Point and Pressure Loads

U. Komaragiri

M. R. Begley[1]
e-mail: begley@virginia.edu

J. G. Simmonds

Structural and Solid Mechanics Program,
Department of Civil Engineering,
University of Virginia, Charlottesville, VA 22904

This paper provides a comprehensive description of the mechanical response of freestanding circular elastic films subjected to point and pressure loads. Regimes of behavior, such as plate, linear membrane, and nonlinear membrane, are identified in terms of two dimensionless variables that allow the creation of a single map that indicates appropriate closed-form solutions. This map provides a theoretical framework to design experiments and interpret film behavior for all orders of magnitude of: film thickness-to-span ratio, deflection, loads, prestretch, and elastic properties. The normalization approach provides the means to quickly identify appropriate simplifications to the nonlinear governing equations, and identify applicable analytical solutions. Numerical results are used to illustrate behavior in transition regions, e.g., the transition for a given plate thickness from small to large deflections under increasing load. Critical loads, thickness and prestretch are identified which indicate when asymptotic plate or membrane solutions are accurate. Asymptotic and numerical results are presented which illustrate finite-sized regions of bending-influenced deformation near point loads and clamped edges. Theoretical predictions for the width of these regions enable us to estimate the validity of analytical strain distributions, and in turn the maximum strains in the film. These results help avoiding brittle fracture or ductile yielding of the film by identifying physical parameters that limit strains to an acceptable level. [DOI: 10.1115/1.1827246]

1 Introduction

The testing of freestanding films via transverse loading is becoming increasingly common, for many reasons, notably: (i) microfabrication techniques, such as reactive ion etching and focused ion beam milling, have greatly expanded the range of freestanding geometries that can be created, and (ii) instrumentation such as nanoindenters and atomic force microscopes have decreased the lower limits of force and displacement resolution, enabling the characterization of nanoscale films [1,2]. Furthermore, indentation of clamped films provides unique advantages, such as probing of a biaxial stress state and greater control of material creep and ratcheting [3]. The relatively simple state of deformation (in contrast to indentation of bonded films) implies that experiments can be interpreted relatively quickly in terms of simple mechanics solutions, that is, closed-form solutions for plates or membranes.

Despite the long history of plate and membrane theory development, there is no single source that can be used to identify a priori which theory (e.g., plate versus membrane) is appropriate for a given film characterized by: thickness, span, prestrain and elastic properties. Since such physical characteristics are often dictated by the application of interest rather than chosen directly, it is often not possible to conduct a test in a regime where plate (or membrane) behavior is ensured. Thus, the primary motivation of this paper is to provide maps that enable one to determine a priori whether linear plate or membrane behavior is anticipated, whether large deflection computations are necessary, the range of forces and displacements that are expected, etc.

There is a wide range of literature on the mechanics of thin films subjected to point and pressure loads; works focusing on the load-displacement relationships are summarized in Table 1. By and large, these efforts focus on obtaining asymptotic limits of behavior (e.g., bending dominated plate response) and provide relatively little guidance for identifying ranges of plate thickness, load and prestrain that allow the application of these simplifying assumptions. The work of Sheplak and Dugundji [4] is a notable exception that explicitly studies the transition between plate and membrane behavior for pressure loads.

Solutions for point-loading that include both bending and stretching (i.e., membrane behavior) are particularly sparse [5–7]—and do not exist if one includes prestrain. An important contribution of this paper is to identify the size of the bending-influenced region near point loads. For very thin films, the membrane limit wherein displacements are proportional to the cube root of load (i.e., $\delta \propto P^{1/3}$) is readily observed experimentally (e.g., pressure loads [8], point-loads [9]). However, while load-displacement relationships may be accurately captured by membrane theory, the predicted strain under point loads (e.g., an indenter tip) is singular. This creates significant problems when trying to estimate if the film will fracture or experience significant plastic deformation. The boundary layer analysis in this paper allows one to estimate the reasonableness of the analytical strain expressions, thereby giving a closer estimate to the maximum strain in the film.

The focus here is on results for point loads applied to circular, clamped thin films. Clamped is the most easily realized boundary condition in experiments, while axisymmetry reduces the number of variables needed for a comprehensive parametric study and is increasingly accessible at the micro- and nanoscales (e.g., Ref. [1]). The work presented here makes three significant and new

[1]To whom correspondence should be addressed.

Contributed by the Applied Mechanics Division of THE AMERICAN SOCIETY OF MECHANICAL ENGINEERS for publication in the ASME JOURNAL OF APPLIED MECHANICS. Manuscript received by the Applied Mechanics Division, May 23, 2003; final revision, June 17, 2004. Associate Editor: Z. Suo. Discussion on the paper should be addressed to the Editor, Prof. Robert M. McMeeking, Journal of Applied Mechanics, Department of Mechanical and Environmental Engineering, University of California—Santa Barbara, Santa Barbara, CA 93106-5070, and will be accepted until four months after final publication in the paper itself in the ASME JOURNAL OF APPLIED MECHANICS.

Table 1 Summary of literature addressing point and pressure loading of thin films

	Linear (pure bending or pretensioned membrane)	Nonlinear (bending and stretching)	
		Small rotations	Large rotations
	Theory		
Point load	7 (○/□) 11, 12 (○)		6 (○)
	4, 12 (○)	5, 7, 12, 13 (○)	None
Pressure load	7 (○/□) 7, 9 (○/□)	4, 12, 14, 15, 17, 19(○) 8, 16, 18, 28 (□)	
	Experiments		
Point load	11, 23 (○) 21, 22 (□) 20 (○)	9 (○/□)	None
Pressure load	21, 22 (□) 14, 24 (○)	8, 16, 18, 25, 26, 28(□) 9 (○/□)	None

○—circular film, □—rectangular/square film.

contributions to thin film mechanics. First, we outline a normalization procedure that clearly indicates the connection between physical variables (load, thickness, prestretch, and span) and negligible (or non-negligible) terms of the nonlinear governing equations. This enables us to succinctly state appropriate simplified forms of the governing equations for all possible scenarios, which all originate from a single set of governing equations. Second, we present maps that partition the space of physical variables into regimes where analytical solutions are accurate, and identify the ranges of physical variables for which numerical solutions are needed. Finally, we present a boundary layer analysis that enables one to estimate the physical size of bending-influenced deformation near point-loads and clamped edges. These estimates allow us to calculate when the strain distributions in the film can be reasonably computed using asymptotic analytical expressions. These contributions should greatly facilitate the design and interpretation of experiments on thin films.

To provide a comprehensive set of results for circular films, we summarize equivalent asymptotic results for pressure loading (i.e., bulge testing) in the appendix; further details of the transitions between the asymptotic limits for pressure loading are provided in Ref. [4]. One may reasonably expect that the regimes of plate and membrane behavior identified for the circular plate may be usefully extended to square plates with dimensions approximately equal to the circle radius.

2 Governing Equations

We consider an isotropic elastic circular film subjected to a transverse point/pressure load. Figure 1 shows relevant dimensions and variables used to describe the film behavior. We assume small strains, such that the deformation of the film can be described adequately by the *simplified Reissner theory* (e.g., Ref. [10]). The compatibility and equilibrium equations obtained from this theory are

$$AL_rF+2r\sin^2(\beta/2)=0 \tag{1}$$

$$D(L_r\beta+\beta-\sin\beta)-rF\sin\beta+r^2q\cos\beta=0 \tag{2}$$

where β is the angle of rotation and F is a stress variable, defined as $F\equiv rN_r$, where N_r is the conventional stress resultant in the radial direction. Hence, F has units of force. The variable q is the vertical shear stress resultant. For a downward point load of magnitude P at the center of the film, $q=P/2\pi r$; for a uniform downward pressure denoted by p, the vertical shear stress resultant is $q=pr/2$. These relationships, as well as the relationship relating bending moment to rotation, are shown schematically in Fig. 1. In Eqs. (1) and (2)

$$L_r=r^2\frac{d^2}{dr^2}+r\frac{d}{dr}-1 \tag{3}$$

is a homogenous linear differential operator, D is the bending stiffness, and A is the stretching compliance of the film defined as

$$D=\frac{Eh^3}{12(1-\upsilon^2)} \quad \text{and} \quad A=\frac{1}{Eh} \tag{4}$$

Here, E is the elastic modulus of the film, h is the film thickness and υ is the film's Poisson ratio. Detailed derivations of Eqs. (1) and (2) can be found in Ref. [10].

If we ignore, as in (1), small extensional load terms, then the extensional strains are given by

$$e_r=A(r^{-1}F\cos\beta+q\sin\beta-\upsilon F')-\varepsilon_0 \tag{5}$$

and

$$e_\theta=A[F'-\upsilon(r^{-1}F\cos\beta+q\sin\beta)]-\varepsilon_0 \tag{6}$$

where prime denotes differentiation with respect to r. ε_0 is a small positive prestrain that could be caused by several factors, including thermal expansion mismatch or residual stresses that occur during the manufacturing and processing of the film. The vertical deflection of the film (positive downward) is given by

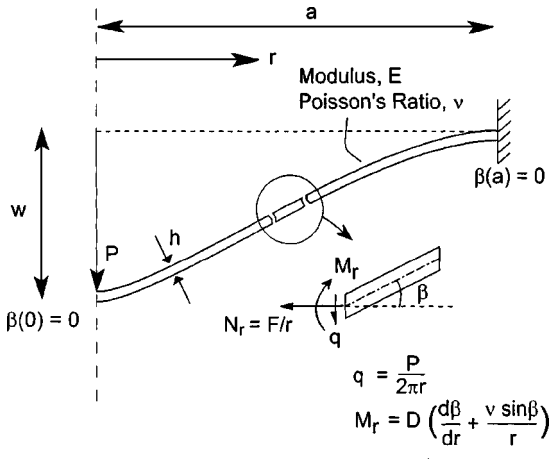

Fig. 1 Schematic illustration of the dimensions and variables used in the analysis of a thin circular film subjected to a point load

$$w(r)=\int_r^a \sin\beta(s)\,ds \tag{7}$$

where the deflection of the plate at the circular edge ($r=a$) is assumed to vanish. The boundary conditions associated with (1) and (2), for a clamped plate, are

$$\{\beta,u\}\to 0 \ \text{ as } \ r\to 0 \qquad \text{and} \qquad \beta(a)=u(a)=0 \tag{8}$$

where $u=re_\theta$ is the radial, in-plane displacement. For a simply supported plate, it is the radial moment that vanishes at the edge rather than the slope; everything else remains the same. Depending on the magnitude of the external loads, the relative thickness h/a and the magnitude of the prestrain ε_0, the solutions of the governing Eqs. (1) and (2) will exhibit different asymptotic behaviors as $h/a\to 0$, as discussed in detail in subsequent sections.

3 Regimes of Behavor and Asymptotic Solutions

The governing equations can be rewritten to highlight the relative importance of bending and stretching contributions. The purpose of the following normalization is to cast the governing equations in terms of two dimensionless parameters: α, a function of pre-stretch and film thickness, and γ, a function of load and film thickness. Using physical parameters, the relevant reduced (simplified) governing equations can be quickly identified in terms of α and γ, along with an error estimate for dropping bending or stretching terms. Thus, one may estimate the type of response for a given set of properties/loads without recourse to full numerical solutions.

Let $N\equiv\{P/2\pi, pa^2/2\}$; the understanding here and henceforth is that the first term in the braces is for point loading and the second term is for pressure loading. We use the following dimensionless variables and parameters

$$\begin{gathered} r=a\bar{r}, \quad \sigma=AN/a, \quad \varepsilon^2=\frac{AD}{a^2}=\frac{h^2}{12(1-v^2)a^2}\ll 1, \\ k=(1-v)^{-1}, \quad r^2q=aN\{\bar{r},\bar{r}^3\} \end{gathered} \tag{9a}$$

In addition, we introduce a dimensionless parameter δ to normalize the rotation and stress function, by setting

$$\beta=\varepsilon^\delta g, \quad 0\leqslant\delta, \tag{9b}$$

$$F=aEh(k\varepsilon_0\bar{r}+\varepsilon^{2\delta}f) \tag{9c}$$

where δ is set such that $f,\ g=\mathrm{O}(1)$. Note that δ is a nonphysical parameter that is chosen to highlight particular terms of Eqs. (1) and (2), as will be discussed in detail. To account for the relative influence of the prestrain ε_0 and the dimensionless load σ (whether due to a point load or a uniform pressure), we set

$$\varepsilon_0=\varepsilon^\alpha \ \text{ where } \ 0<\alpha \tag{10a}$$

and

$$\sigma=\varepsilon^\gamma \ \text{ where } \ 0\leqslant\gamma. \tag{10b}$$

Put another way, $\alpha=\log_\varepsilon\varepsilon_0$ and $\gamma=\log_\varepsilon\sigma$. It should be emphasized that since $\varepsilon\ll 1$, the logarithm function implies that (α,γ) will decrease as (ε_0,σ) increase. Thus any combination of the prestrain ε_0, external load σ and thickness-to-span ratio {i.e., $\varepsilon=[12(1-v^2)]^{-1/2}h/a$} corresponds to a point in the first quadrant of the $\alpha\gamma$ plane, as illustrated in Fig. 2.

The compatibility and normal equilibrium Eqs. (1) and (2) now take the form

$$L_{\bar{r}}f+(1/2)\bar{r}g^2\,\mathrm{sinc}^2(\varepsilon^\delta g/2)=0 \tag{11}$$

$$\begin{aligned} -\varepsilon^{2+\delta-\gamma}[L_{\bar{r}}g+(1/6)\varepsilon^{3\delta}g^3\,\mathrm{dinc}(\varepsilon^\delta g)]+\bar{r}(k\varepsilon^a\bar{r} \\ +\varepsilon^{2\delta}f)\varepsilon^{\delta-\gamma}g\,\mathrm{sinc}(\varepsilon^\delta g)=\{\bar{r},\bar{r}^3\}\cos(\varepsilon^\delta g) \end{aligned} \tag{12}$$

where

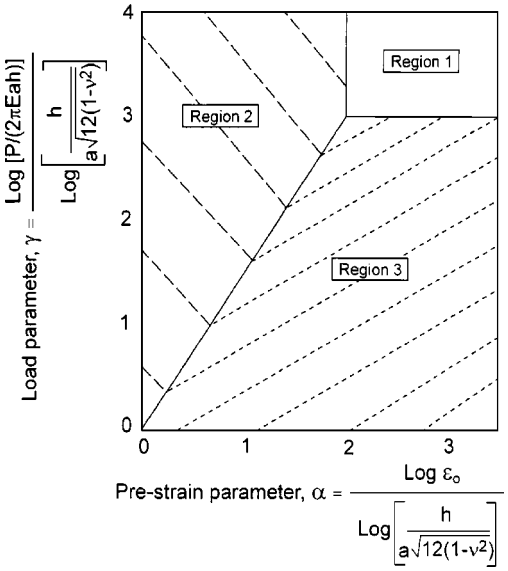

Fig. 2 Parameter space delineating between regions of plate behavior (1), linear (or pre-stretched) membrane behavior (2), and nonlinear membrane behavior (3). Note that increasing pre-stretch and load (ε_o and P) corresponds to decreasing α and γ, respectively.

$$\mathrm{sinc}\,\theta\equiv\frac{\sin\theta}{\theta}=1-\frac{\theta^2}{6}+O(\theta^4), \quad |\mathrm{sinc}\,\theta|\leqslant 1 \tag{13}$$

and

$$\mathrm{dinc}\,\theta=6\left(\frac{1-\mathrm{sinc}\,\theta}{\theta^2}\right)=1-\frac{\theta^2}{20}+O(\theta^4), \quad |\mathrm{dinc}\,\theta|\leqslant 1 \tag{14}$$

The boundary conditions are

$$\{g,\bar{r}f'-vf\}\to 0 \ \text{ as } \ \bar{r}\to 0 \tag{15a}$$

and

$$g(1)=f'(1)-vf(1)=0. \tag{15b}$$

The free parameter δ used to normalize the rotation angle β is chosen so that as $\varepsilon\to 0$, one or more terms on the left of (12) balance the $O(1)$ term on the right. This choice will depend on *given values of α and γ*, i.e., given values of ε_0, σ, and h/a. We note that if the exponents γ and δ are such that $\varepsilon^{2+\delta-\gamma}\to 0$ as $\varepsilon\to 0$ then, in general, there must be boundary (i.e., at the clamped edge, near $r=a$) or pole layers (i.e., underneath the point load, near $r=0$).

These layers represent small regions where the term $L_{\bar{r}}g$ can no longer be neglected; otherwise the boundary conditions of zero slope cannot be enforced. Neglect of the $L_{\bar{r}}g$ term corresponds to the asymptotic limit of membrane behavior wherein the load-displacement response does not depend on the bending stiffness D. While the displacements are finite (even under the point load—i.e., the pole), the rotations (and, hence, strains) at the pole are not. Inclusion of bending terms, even for extremely thin films or very large deflections—i.e., regardless of how small term the L_rg term is in Eq. (12)—creates small regions of finite rotation and finite strains. The extent of these boundary or pole regions is of critical interest when interpreting or designing experiments, since they represent regions of strain (and stress) concentration that ultimately lead to film rupture. This is discussed in detail in Secs. 5 and 6.

Before describing the quantitative details of possible simplified governing equations and their analytical solutions, it is worth discussing the qualitative implications of the earlier normalization

procedure. Knowing thickness/span ratio, prestretch, and applied load, one can calculate α and γ, subsequently calculate the coefficients of the terms in Eqs. (11) and (12), and immediately estimate their relative importance. From this, simplified governing equations can be identified that have closed-form analytical solutions.

The utility of this approach lies in the comprehensive coverage afforded by the normalization. Competition between two physical parameters (to create either the same or different effects) can be readily assessed, since all relevant physical effects (except compressive prestretch) are incorporated into α and γ. For example, when testing nanoscale films with atomic force microscopy or nanoindentation, the dominant factor governing film response—prestretch (which result in linear plate behavior) or decreasing film thickness (which results in non-linear membrane behavior)—can be estimated immediately.

The three regions in Fig. 2 correspond to classical plate or membrane solutions. Again, since $\varepsilon \ll 1$, decrease in prestretch and load correspond to increase in α and γ respectively, and vice-versa. In the extreme that α and γ are much greater than unity, stretching and prestretch effects are negligible and the film will respond according to classical plate solutions, such as those in Timoshenko and Woinosky-Krieger [7] for small deflections. This is labeled region 1 in Fig. 2. Region 2 corresponds to large values of prestretch, where membrane stretching dominates bending and one obtains classical linear membrane results. In this region, $\alpha<2$ and $\gamma>3$. Thus, both regions 1 and 2 correspond to linear load-deflection relationships, *albeit for different reasons*. Region 3 is bounded by $\alpha>2$ and $\gamma<3$; prestretch is negligible and membrane stretching dominates bending. This results in Schwerin-type solutions where $w \propto P^{1/3}$. It should be noted that closed form solutions are tractable only for a limited range in regions 2 and 3 (membrane-like behavior); the limit $\gamma \to 0$ corresponds to extremely large loads, and thus large rotations and highly nonlinear governing equations.

The boundaries between the regions reflect scenarios where the two or more of the terms in Eqs. (11) and (12) are equally important; hence, they reflect transitions between two types of response. For example, consider the case with zero prestrain and a fixed film thickness. This corresponds to $\alpha=\infty$. The response to increasing load corresponds to decreasing γ, i.e., moving down the right-hand side of Fig. 2. This scenario involves the transition from plate-like behavior at very small loads to nonlinear membrane (Schwerin) behavior at larger loads. As will be illustrated in subsections below, boundaries between regions 1 and 3 and 2 and 3 correspond to governing equations that are not amenable to analytical solutions. If one computes values for α and γ from physical parameters in a given test that lie near one of the boundaries in Fig. 2, this indicates that two effects are equally important and numerical solutions are required. By contrast, a single solution exists for regions 1 and 2 for large values of γ (i.e., small loads) and across the $\alpha=2$ boundary. This solution clearly illustrates that increasing prestretch has the same stiffening effect as increasing thickness.

3.1 Region 1: Linear Plate Theory With No Prestrain This region is defined by the inequalities $\alpha>2$, and $\gamma>3$. We choose $\delta=\gamma-2$, such that the normalized angle of rotation of the film is $g \equiv \beta/\varepsilon^{\delta}=\beta/\varepsilon^{\gamma-2}$. The governing Eqs. (11) and (12) with error terms take the form

$$L_{\bar{r}}f+(1/2)\bar{r}g^2=O(\varepsilon^{2\gamma-4}) \tag{16}$$

$$-L_{\bar{r}}g=\{\overline{r,r^3}\}+O(\varepsilon^{\alpha-2},\varepsilon^{2\gamma-6}) \tag{17}$$

Note that for $\alpha>2$ and $\gamma>3$, the error terms are of order much less than unity. The solution to the earlier equations with error terms neglected and subject to the boundary conditions (15) is

$$g(\bar{r})=-\tfrac{1}{2}\bar{r}\ln\bar{r} \tag{18a}$$

$$f(\bar{r})=\left(\frac{\bar{r}^3}{512}\right)[-8(\ln\bar{r})^2+12(\ln\bar{r})-7]+\left[\frac{9-7v}{512(1-v)}\right]\bar{r} \tag{18b}$$

In terms of the angle of rotation of a radial fiber, this is easily recognized as the plate solution that appears in various texts (e.g., Ref. [7])

$$\beta(\bar{r})=-\frac{3(1-v^2)}{\pi}\left(\frac{Pa}{Eh^3}\right)\bar{r}\ln\bar{r} \tag{19}$$

Integration of Eq. (19) yields the load-deflection relation

$$\frac{w(0)}{a}=\frac{3(1-v^2)}{4\pi}\left(\frac{Pa}{Eh^3}\right) \tag{20}$$

Thus, region 1 corresponds to classical plate theory; physically, stretching in the plane of the film is negligible compared to bending deformation. Nonlinear kinematics are also negligible: that is, loads are small enough (or thickness is large enough) to allow the assumption of small deflections. The strain distribution in the film is discussed in Sec. 6.

3.2 Region 2: Linear (Prestretched) Membrane Theory With Pole and Boundary Layers. This regime is defined by the inequalities $\alpha<2$, and $\gamma>3\alpha/2$, as shown in Fig. 2. The parameter δ is chosen to be $\gamma-\alpha$. The governing equations are (16) and

$$\underline{-\varepsilon^{2-\alpha}L_{\bar{r}}g}+k\bar{r}^2g=\{\overline{r,r^3}\}+O(\varepsilon^{2\gamma-3\alpha}) \tag{21}$$

The underlined term in Eq. (21) indicates a boundary- or pole-layer term. ''Boundary-layer'' refers to a narrow annulus near the edge of the film, while a ''pole-layer'' is a small disk at the center of the film. For point loads, singularities occur at the pole in the membrane solution when the bending term $L_{\bar{r}}g$ is neglected. Although boundary layers exist for both point and pressure loads, pole layers exist only for point loads. In general, the analysis of pole layers is more complicated than that for boundary layers. This is discussed in detail in Sec. 5.

Neglecting the underlined term in Eq. (21), the solution to Eqs. (16) and (21), subjected to the boundary conditions in (15), is

$$g(\bar{r})=\frac{\varepsilon_0}{\varepsilon^2}\frac{1}{\kappa}\left[\frac{I_1(\kappa\bar{r})}{I_1(\kappa)}\left[K_1(\kappa)-\frac{1}{\kappa}\right]-\left[K_1(\kappa\bar{r})-\frac{1}{\kappa\bar{r}}\right]\right] \tag{22a}$$

where κ is given by

$$\kappa^2=12\varepsilon_0(1+v)\left(\frac{a}{h}\right)^2 \tag{22b}$$

and I_1 and K_1 are, respectively, the modified Bessel's function of the first and second kind. Note that Eq. (22*a*) reduces to Eq. (18*a*) in the limit that the prestrain goes to zero, i.e., $\kappa \to 0$. Thus, Eq. (22*a*) represent a general solution for both regions 1 and 2. In terms of physical parameters this yields the following solution for a prestretch membrane

$$\beta(\bar{r})=\left(\frac{6Pa(1-v^2)}{\pi Eh^3}\right)\frac{1}{\kappa}\left\{\frac{I_1(\kappa\bar{r})}{I_1(\kappa)}\left[I_1(\kappa\bar{r})-\frac{1}{\kappa}\right]-\left[K_1(\kappa\bar{r})-\frac{1}{\kappa\bar{r}}\right]\right\}. \tag{23}$$

The midpoint deflection of the film must be found using Eq. (23) in a numerical evaluation of Eq. (7) with $\sin\beta$ replaced by β (an approximation consistent with the small rotations in the plate limit). This solution is identical to that presented by Hong et al. [11] and Wan et al. [12]; the prestress in the film (N) in their work is related to the prestrain (ε_0) used here by: $N=Eh\varepsilon_0/(1-v)$. Similar solutions for pressure loads are given in the Appendix.

Physically, region 2 corresponds to scenarios where: (i) the stiffness generated by prestrain is comparable (or greater than) to the bending stiffness, and (ii) loads are still small enough to avoid large deflections. It is important to note that one obtains a linear load-deflection relationship. In the region to the right of the kink in the boundary, bending stiffness dominates; to the left, prestretch is the underlying source of linear behavior. Thus, in region 2, both film thickness and prestretch must be known accurately to determine if response is bending or stretch dominated. Note that in the limit that $\kappa \to 0$, Eq. (23) asymptotes to Eq. (19).

3.3 Region 3: Nonlinear Föppl (Small Rotation) Membrane Theory With Pole and Boundary Layers. This region appears on the lower right of Fig. 2, and is defined by the inequalities $2\gamma/3<\alpha$, and $\gamma<3$. The parameter δ is chosen to be $\gamma/3$, so that the normalized angle is $g \equiv \beta/\varepsilon^{\gamma/3}$. The governing equations are (16) and

$$-\varepsilon^{2-2\gamma/3} L_{\bar{r}} g + \bar{r} f g = \{\bar{r}, \bar{r}^3\} + O(\varepsilon^{\alpha-2\gamma/3}, \varepsilon^{2\gamma/3}) \tag{24}$$

A single term particular solution to Eqs. (16) and (24) is obtained when $O(\varepsilon^{2-2\gamma/3})$ terms are neglected. This is Schwerin's classic solution [13–28]

$$g(\bar{r}) = \left(\frac{16}{9\bar{r}}\right)^{1/3}, \tag{25a}$$

and

$$f(\bar{r}) = \left(\frac{9\bar{r}}{16}\right)^{1/3}. \tag{25b}$$

In terms of physical parameters, this yields

$$\beta(r) = \left(\frac{8P}{9\pi \mathrm{Ehr}}\right)^{1/3} \tag{26a}$$

$$F(r) = \frac{P}{2\pi\beta(r)} = \frac{3}{4}\left(\frac{P^2 Ehr}{3\pi^2}\right)^{1/3} \tag{26b}$$

and

$$\frac{w(0)}{a} = \left(\frac{3P}{\pi Eah}\right)^{1/3} \tag{27}$$

It should be emphasized that this particular solution satisfies the boundary conditions only for a single value of prestretch (for a given Poisson's ratio), determined by substitution into Eq. (15). When Poisson's ratio is $v=1/3$, the particular solution meets the boundary conditions for $\varepsilon_0=0$. This fact is very often overlooked when a particular solution is obtained by combining Eqs. (16) and (24). For Poisson's ratios other than one-third and *zero prestrain*, we numerically integrated the Eqs. (16) and (24) to obtain the following approximate membrane solution for point loads

$$\frac{w(0)}{a} = f(v)\left(\frac{P}{Eah}\right)^{1/3} \tag{28}$$

where $f(v) \approx 1.0491 - 0.1462v - 0.15827v^2$. Similar membrane solutions for pressure loading of a circular film with zero prestrain are given in the appendix.

Physically, region 3 corresponds to scenarios where bending stiffness is neglible in comparison to the stiffness generated by stretching arising from large deflections. In this region, loads are large enough (or thickness small enough) that membrane behavior dominates even prestretch. For smaller loads or very large values of prestretch, deflections will be small and one returns to region 2.

3.4 Boundaries Between the Regions and Limiting Cases On the boundary between regions 1 and 2 in Fig. 2, $\alpha=2$ and $\gamma>3$. The parameter δ is chosen to be $\delta=\gamma-2$. For these cases, the governing equations are (16) and

$$-L_{\bar{r}} g + k\bar{r}^2 g = \{\bar{r}, \bar{r}^3\} + O(\varepsilon^{2\gamma-6}) \tag{29}$$

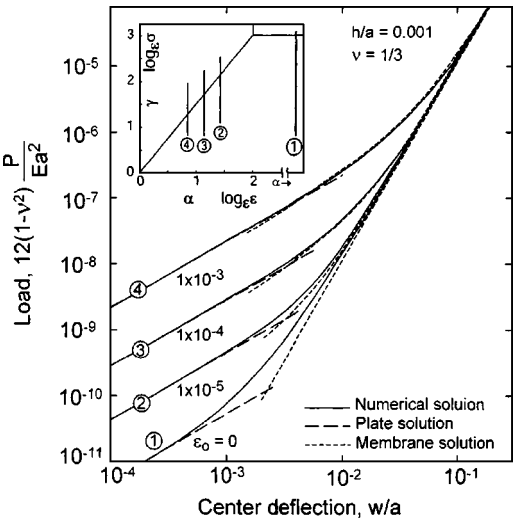

Fig. 3 Load-deflection relationships for a thin film with several values of pre-stretch; the inset depicts where these cases fall in the behavior map given as Fig. 2

This represents a specific case of Eq. (21), where the prestrain and thickness/span ratio are related by: $\varepsilon_0=\varepsilon^2=h^2/(12(1-v^2)a^2)$. Thus, along (or near) this boundary the individual roles of prestrain and thickness are difficult to determine, as one obtains linear response due to either: (i) bending dominated deformation, i.e., classic plate behavior where prestrain does not play a significant role, or (ii) stretching dominated deformation, i.e., linear membrane behavior where bending does not play a significant role. This rather straightforward result clearly illustrates that the structural stiffness of the film will be a nonunique combination of prestrain and thickness effects (since the same solution is obtained for multiple combinations of prestrain and thickness). The ability to identify these combinations without a comprehensive parameter study clears up considerable ambiguity in interpreting experiments.

The other two boundaries (between regions 2 and 3, and regions 1 and 3) yield governing equations that cannot be solved analytically, and must be integrated numerically subject to the boundary conditions outlined earlier. While one may always choose to integrate the full equations given as Eqs. (11) and (12), the simplified governing equations may prove useful for developing approximate or series solutions near these boundaries.

On the boundary between regions 2 and 3, i.e., that separating pretensioned linear membrane response from nonlinear membrane behavior, $0<\alpha<2$ and $\gamma=3\alpha/2$. We choose $\delta=\alpha/2$ to normalize the rotation. The governing equations are then (16) and

$$-\varepsilon^{2-\alpha} L_{\bar{r}} g + \bar{r}(k\bar{r}+f)g = \{\bar{r}, \bar{r}^3\} + O(\varepsilon^{\alpha}) \tag{30}$$

The transition behavior that occurs across the boundary separating regions 2–3 is considered in the next section (look ahead to Fig. 3).

The boundary between regions 1 and 3 represents the axisymmetric von Kármán equations without prestrain. On this boundary, $\alpha>2$, $\gamma=3$, and δ is simply taken as unity. The governing equations are (16) and

$$-L_{\bar{r}} g + \bar{r} f g = \{\bar{r}, \bar{r}^3\} + O(\varepsilon^{\alpha-2}, \varepsilon^2) \tag{31}$$

Alternatively, the von Kármán equations with pre-strain are appropriate at the common boundary point of regions 1, 2, and 3, where $\alpha=2$, $\gamma=3$, and $\delta=1$. In this case, the governing equations are (16) and

$$-L_{\bar{r}} g + \bar{r}(k\bar{r}+f)g = \{\bar{r}, \bar{r}^3\} + O(\varepsilon^2) \tag{32}$$

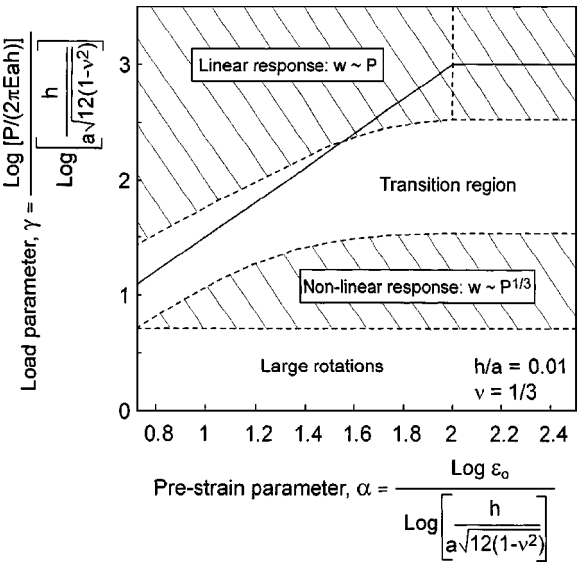

Fig. 4 Boundaries in the behavioral map determined by comparing numerical and asymptotic solutions: the shaded regions correspond to load/pre-stretch combinations for which analytical solutions have less than 10% error

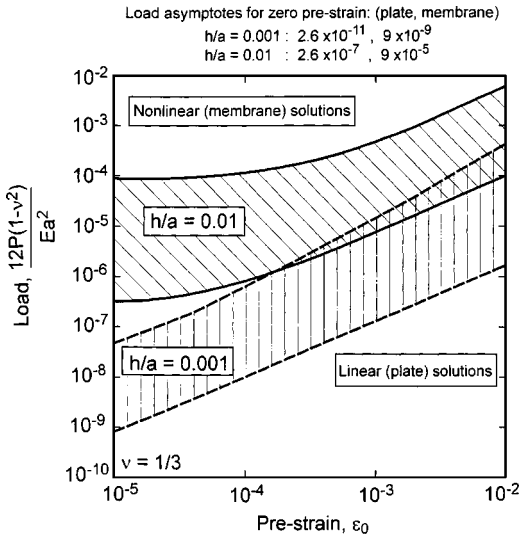

Fig. 5 Illustration of combinations of load and pre-stretch for which asymptotic solutions are accurate: the shaded region represents the plate-to-membrane transition regime where no accurate analytical solution exists

The von-Kármán plate equations are thus a subset of the simplified Reissner equations (Eqs. (1) and (2)). Note that both simplified Reissner theory and von-Kármán plate theory assume small strain behavior. But Reissner theory allows for moderate to large rotations, whereas von-Kármán plate theory is only for small rotations (i.e., when $\beta^2 \ll 1$). This is the subtle distinction between the two theories. Again, Eqs. (31) and (32) cannot be solved analytically; the coupling between g and f is such that there is no simple closed-form solution. Numerical results illustrating the solutions for these points are shown in the next section.

4 Transitions Between Regimes: Numerical Solutions

Since experiments involve a range of applied loads (and possibly film thickness or pre-strain), it is possible that a given experiment spans multiple regions in Fig. 2. In this case, numerical simulations are required to solve Eqs. (1) and (2) for the load-deflection relationship (or strains in the film), subject to the boundary conditions implied by Eqs. (5)–(8). In this section, we compare numerical solutions for load-displacement relationships with closed-form solutions valid in the asymptotic limit of large or small loads (and/or film thickness). A relaxation method was used to solve the coupled nonlinear ordinary differential equations and is briefly described in Sec. B of the Appendix.

4.1 General Cases With Finite Prestrain. We first consider the cases *with* prestrain—i.e., the entire range of behaviors illustrated in Fig. 2. Examples of transition behavior for several values of prestretch and a single film thickness are shown in Fig. 3. The load-displacement behavior goes from linear (plate) behavior at small loads to nonlinear (membrane) behavior at large loads. The behavior shown in Fig. 3 appears as a vertical line in the map given in Fig. 2 since prestretch and film thickness are held constant. This is illustrated in the inset of Fig. 3. Note again that increasing load corresponds to decreasing γ; hence, the loading direction of the line in the inset goes from top to bottom. Similarly, decreasing prestrain corresponds to increasing α such that zero prestrain corresponds to $\alpha=\infty$.

Results such as those shown in Fig. 3 can be used to construct numerical boundaries that correspond to the analytical boundaries given in Fig. 2, as shown in Fig. 4. The transition region between the linear and nonlinear response was determined by comparing numerical load-deflection curves with asymptotic solutions. The boundaries represent the combination of loads, film thickness and prestrain for which there is 10% disagreement between numerical and analytical load-displacement relationships.

Thus, the load-deflection relationship for points above the transition region will be within 10% of the linear plate or prestretched membrane solutions. (Note that both of these are obtainable from the single rotation solution given as Eq. (23).) Points below the transition region will be within 10% of the nonlinear membrane response (i.e., Schwerin solution in Eq. (27)). The line marking the bottom boundary of this nonlinear membrane region (i.e., $\gamma \approx 0.7$) is the critical load after which the rotations are no longer negligible. For larger loads, the analytical membrane solution (which is derived assuming small rotations) does not remain valid. More about this boundary is described later in this section.

Using Fig. 4, one can identify the limits of test parameters to ensure that a closed-form solution will be applicable. Naturally, one can plot similar lines representing boundaries for different film thickness, Poisson's ratio or percentage error. It is important to note that the regime where nonlinear analytical solutions (i.e., Schwerin-type approximations) are applicable does not exist for all values of h/a. The hatched area in Fig. 4 labeled "nonlinear response: $w \sim P^{1/3}$" becomes narrower as h/a increases; for $h/a \sim 0.075$, it disappears altogether. This means that as the load is increased, the response moves directly from the plate regime into the large deflection regime. This is further explained in Sec. 4.2.

4.2 Critical Loads, Prestretch, and Thickness That Indicate Asymptotic Behavior. Figures 3 and 4 represent a sampling of results for several film thickness and prestretch. A more comprehensive tabulation of the transition region for different film thickness and prestrain is shown in Figs. 5 and 6, which again represent the combinations of load, prestretch, and thickness where the numerical solutions deviate from analytical solutions. The hatched regions in Figs. 5 and 6 correspond to the transition from linear plate behavior to nonlinear membrane behavior. Below this transition region is the linear response region, where Eq. (23) can be accurately applied. Above the transition region is the nonlinear membrane region, where Eq. (27) (Schwerin's membrane solution) becomes valid.

The numerical results presented so far assume that the rotations are small compared to unity. For films that are especially thin or that are under especially large loads, it is natural to ask if the simplified axisymmetric *von Kármán* Eqs. (16) and (32) that ne-

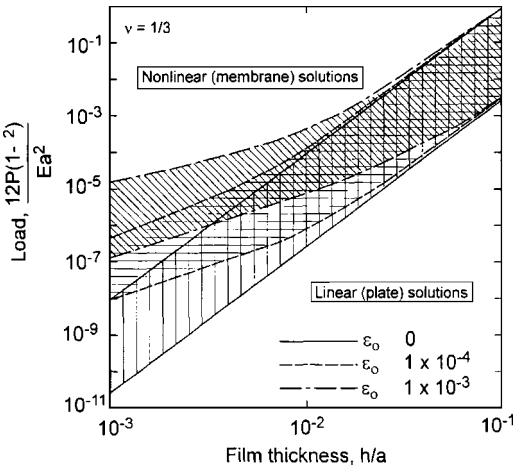

Fig. 6 Illustration of combinations of load and film thickness for which asymptotic solutions are accurate: the shaded region represents the plate-to-membrane transition regime where no accurate analytical solution exists

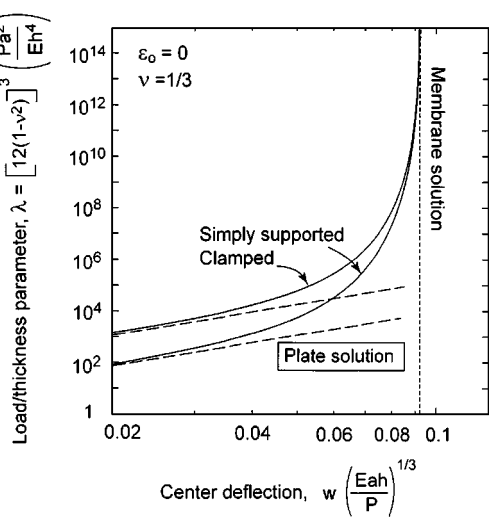

Fig. 8 Universal results for cases with several pre-stretch illustrating transition from plate to membrane behavior

glect large rotations do *not* predict the same behavior as the full *Reissner's* Eqs. (1) and (2) that allow large rotations. To establish a guideline for loads and film thickness combinations that differentiate these two results, a comparison of load-displacement curves was made between numerical solutions of (1) and (2) (i.e., large rotations), and numerical solutions of Eqs. (16) and (32), (i.e., small rotations).

Figure 7 illustrates the critical load for which the full numerical solution deviates ~10% from the simplified small rotation solution. The critical transitions between asymptotic plate and membrane solutions are shown as well. Zero prestretch is assumed, since moderate prestretch has little influence on behavior at these high loads. It can be seen that above a thickness/span ratio of about 0.075, the transition curve from small to large rotations falls below the transition curve to the analytical membrane solution. Since the analytical membrane solution is derived assuming small rotations, this means that beyond this point, the analytical membrane solution (Eq. (27)) no longer is valid. The true load deflection behavior can only be obtained by integrating the full Reissner's equations (Eqs. (1) and (2)) and not the simplified von Kármán equations (Eqs. (16) and (32)). Hence, in Fig. 7, the hatched region represents the region of validity for Schwerin's analytical solution. For $h/a=0.01$, this transition from small to large rotations is illustrated in Fig. 4 as the lower boundary at $\gamma\approx 0.7$.

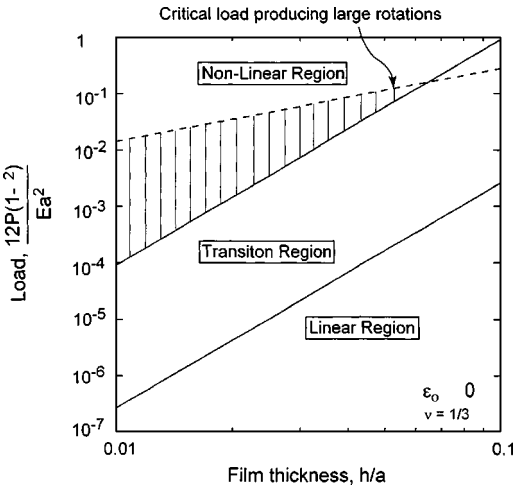

Fig. 7 Illustration of combinations of load and film thickness for which small rotation assumptions are accurate: the shaded region represents combinations where small rotation membrane analytical solutions are accurate. For $h/a\sim 0.075$, there is no accurate small rotation analytical membrane result.

4.3 Zero Prestretch. With zero prestretch, $\alpha\rightarrow\infty$ and the boundary condition (6) is homogeneous. In this case, the only possible transition in Fig. 2 is the transition from linear plate behavior (region 1) to nonlinear membrane behavior (region 3). For small rotations, a single parameter

$$\lambda = 4\pi^2\varepsilon^{2\gamma-6} = [12(1-\upsilon^2)]^3\left(\frac{Pa^2}{Eh^4}\right)^2 \tag{33}$$

can be used to account for all values of film thickness, load, and elastic properties. For large rotations, the nonlinear trigonometric terms in Eqs. (11) and (12) do not allow one to remove the parameter ε via normalization. Figure 8 plots the center-span deflection versus λ for both clamped and simply supported films. The deflection is normalized by the classical nonlinear membrane result (save a constant prefactor). As such, the results asymptote to a constant value for large loads corresponding to the membrane limit. The results for very thin films (i.e., large values of λ) are independent of the boundary conditions at the outer edge, since bending resistance becomes negligible. We again emphasize that Schwerin's one-term particular solution (Eq. (27)) is strictly only valid for zero prestretch and $\upsilon=1/3$. A similar form for zero prestretch and other Poisson's ratios, determined by fitting numerical simulations, is given by Eq. (28).

5 Asymptotic Behavior Near Point-Loads and Edges

As noted earlier, whenever the coefficient of the differential operator $L_{\bar{r}}g$ is small, then boundary and pole layers will exist. To determine the width of the boundary layer at the edge of the clamped film, we set $\bar{r}=1-\varepsilon^{\mu}\xi$, assume $\xi=O(1)$, and determine the exponent μ so that, *to lowest order*, the resulting form of (12) is free of the small parameter ε. The width of the resulting boundary layer (in the dimensionless coordinate $\bar{r}$) is $O(\varepsilon^{\mu})$. Thus, the solutions of (21), (24), and (30) will exhibit boundary layers whose respective widths are $O(\{\varepsilon^{1-\alpha/2},\varepsilon^{1-\gamma/3}\})$ and $O(\varepsilon^{1-\alpha/2})$.

To determine the width of a pole layer, we set $r=\mu\rho$ and then determine μ so that the resulting forms of (11) and (12), *to lowest order*, are free of ε. Note that, in determining pole layers, it is

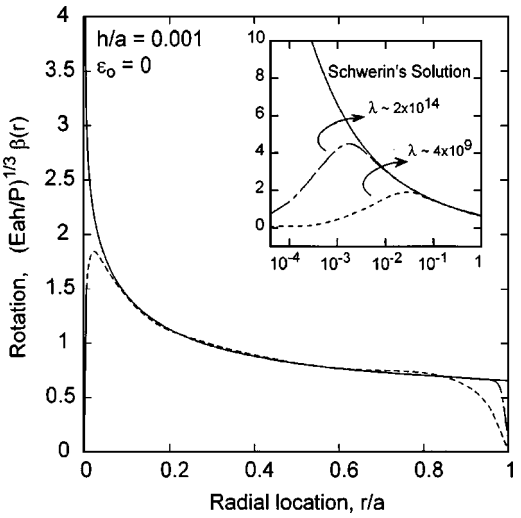

Fig. 9

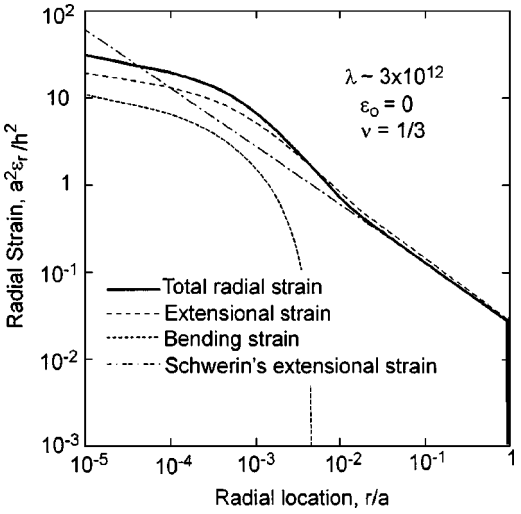

Fig. 10

essential we consider the limiting form of (12), which, since $g = O(1)$, is always $L_\rho f = 0$. Since bending, represented by the first group of g terms in (12), is important near the center of the film, the extensional strains remain finite there. This, in turn, implies that

$$f = A\rho + O(\varepsilon^{\mu}), \quad \rho = O(1) \tag{34}$$

where A is an unknown constant. Thus, in (24) and (30) the widths of the pole layers are, respectively, $O(\varepsilon^{1-\gamma/3})$ and $O(\varepsilon^{1-\alpha/2})$, whereas in (21), where the width of the pole layer does not depend on the form of f, its width is $O(\varepsilon^{1-\alpha/2})$. These boundary layers are illustrated by numerical results discussed in the next section.

6 Maximum Stresses and Strains

An important issue that arises when testing freestanding thin films is the deformation of the film beneath the load. For very thin films subjected to a transverse point load, membrane theory predicts singular yet integrable rotations that lead to a finite displacement at the center. The result is completely reasonable load-displacement behavior, yet infinite rotations (and strains) under the load point. Of course, in plate theory, there are finite-sized regions near the load point (pole layer) and the clamped edge (boundary layer) where bending is important, as described in Sec. 5.

The extent of these bending influenced regions is illustrated in Fig. 9, which shows normalized rotation distributions given as

$$\phi = \frac{\beta}{(2\pi\varepsilon^{\gamma})^{1/3}} = \left(\frac{Eah}{P}\right)^{1/3}\beta. \tag{35}$$

Results are shown for zero prestretch and different values of λ. The Schwerin membrane solution (i.e., the asymptotic limit in which $\lambda \to \infty$ or $\gamma \to 0+$) is also shown. Near the point load and outer boundary, bending influences the response and the angle of rotation goes to zero because of symmetry and clamped boundary conditions, respectively. This is more clearly observed in the inset, which depicts the same information using a log-scale to highlight the behavior near the load point. From the pole- and boundary-layer analysis in Sec. 5, the width of these asymptotic regions are of the order $O(\varepsilon^{1-\gamma/3}) = O((4\pi^2/\lambda)^{1/6})$. These theoretical estimates agree well with the numerical solution shown in Fig. 9.

Figure 10 shows the distribution of total radial strain in the film, calculated by adding bending strain in the outer fiber of the film, $(h/2)(d\beta/dr)$, to the extensional strain given as Eq. (5). Results are shown for a large value of λ, which leads to load-deflection behavior that is accurately matched by membrane solutions (which neglect bending). Localized bending deformation influences the results near the pole and close to the clamped outer edge; however, the majority of the span is dominated by stretching deformation. This is clearly illustrated by the agreement between Schwerin's analytical solution and the total and extensional strains determined via numerical solution. Hence, for large values of λ, i.e., the membrane limit, the strain away from the pole and boundary layers can be estimated using the solutions given as (26), with the result

$$\varepsilon_r = \frac{2}{3}\left(\frac{P^2}{3E^2h^2a^2\pi^2}\right)^{1/3}\bar{r}^{-2/3}. \tag{36}$$

The corresponding circumferential strain to this analytical solution is zero.

Conversely, for smaller loads or thicker films (i.e., small values of λ), extensional strains are negligible and the strain distribution is accurately given by the classical plate solution. Equations (18) and (19) yield the following for strain distribution in a plate under point loading

$$\varepsilon_r = \varepsilon_\theta = \frac{12(1-\nu^2)}{8\pi}\left(\frac{P}{Eh^2}\right)(1+\ln(\bar{r})) \tag{37}$$

Note that both asymptotic limits (linear plate theory and nonlinear membrane theory) produce strain distributions that are singular under the point load. Deformation inside the pole and boundary layers is highly localized and requires complex three-dimensional analysis to determine the strains and rotation.

The transition between bending and stretching regimes is illustrated in Fig. 11 by plotting the strain at $r/a = 0.5$ as a function of λ. The two asymptotic limits are given by Eqs. (36) (large λ) and (37) (small λ). In both limits, the total strain is slightly larger than the asymptotic predictions as it represents the sum of both bending and extensional terms. For nonzero prestrain, a reasonable estimate for the maximum strain in the film is either the pre-strain itself or the strain calculated using Eq. (37), whichever is greater.

As long as the characteristic length of the indenter is larger than the width of the pole layer (given in Sec. 5 of the paper), the earlier expressions can be used to estimate strain in the film. However, if the size of the indenter is of the order of the width of the bending dominated pole layer, the strains surrounding the contact must be determined by considering a finite contact region and then solving for the strains at the edge of the contact.

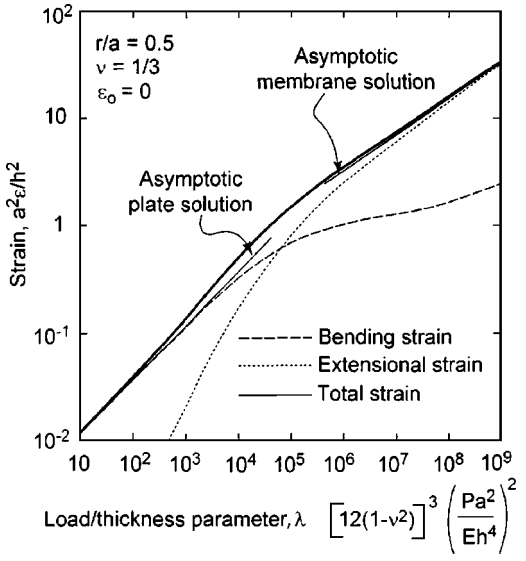

Fig. 11

7 Concluding Remarks

The solutions presented in this paper, both numerical and analytical, represent a comprehensive framework that describes the effects of prestretch, film thickness, span elastic properties, and loads on the mechanical response of freestanding circular films. These effects are captured by a single two-variable map that indicates when the nonlinear governing equations can be simplified. The map should be useful in the development and interpretation of mechanical tests that scan multiple length scales, since appropriate solutions can be identified a priori. Using a combination of these maps and numerical solutions, specific combinations of load, prestrain, and thickness have been identified for which analytical solutions are applicable.

Acknowledgments

M.R.B. and U.K. gratefully acknowledge the support of the National Science Foundation (USA) through Grants CMS No. 998451 and CMS No. 0882851.

Appendix

A Analytical Solutions for Uniform Pressure Loading

A.1 (Region 1) Linear Plate Theory With No Prestrain Solving the governing Eqs. (16) and (17) for pressure loading, one obtains

$$g(\bar{r}) = -\frac{1}{8}\bar{r}(1-\bar{r}^2) \tag{A1}$$

and

$$f(\bar{r}) = \left(\frac{\bar{r}^3}{6144}\right)[-\bar{r}^4+4\bar{r}^2-6]+\left[\frac{5-3v}{6144(1-v)}\right]\bar{r} \tag{A2}$$

In terms of the rotation variable β, the solution is given as

$$\beta(\bar{r}) = -\frac{3(1-v^2)}{4}\left(\frac{pa^3}{Eh^3}\right)[\bar{r}(1-\bar{r}^2)] \tag{A3}$$

The midpoint deflection of the plate is then obtained by integrating the earlier equation as

$$w(0) = a\int_1^0 \beta\cdot d\bar{r} = \frac{3(1-v^2)}{16}\left(\frac{pa^4}{Eh^3}\right) \tag{A4}$$

This is the classic plate solution for uniform pressure load. The expression for maximum bending strain in the film, as a function of the physical parameters and load, is given as follows

$$\varepsilon_r^{\max} = \varepsilon_\theta^{\max} = \frac{3(1-v^2)}{4}\left(\frac{Pa^2}{Eh^2}\right)@\bar{r}=1. \tag{A5}$$

A.2 (Region 2) Linear Prestretched Membrane Theory With Pole and Boundary Layers. Solution to the governing equations in this region ((16) and (21)), for pressure loading, yields

$$g(\bar{r}) = -\frac{\varepsilon_0}{\varepsilon^2}\left(\frac{1}{\kappa^2}\right)\left[\bar{r}-\frac{I_1(\kappa\bar{r})}{I_1(\kappa)}\right] \tag{A6}$$

where

$$\kappa^2 = 12\varepsilon_0(1+v)\left(\frac{a}{h}\right)^2 \tag{A7}$$

In physical terms, it can be written as

$$\beta(\bar{r}) = -\frac{6(1-v^2)}{\kappa^2}\left(\frac{pa^3}{Eh^3}\right)\left[\bar{r}-\frac{I_1(k\bar{r})}{I_1(k)}\right] \tag{A8}$$

The midpoint deflection of the film is then obtained by using (*A*8) in a numerical evaluation of Eq. (7) as

$$w(0) = a\int_1^0 \beta(\bar{r})\cdot d\bar{r} \tag{A9}$$

For zero prestrain (i.e., $\kappa\to 0$), the earlier integration will yield the classic result given in Eq. (*A*4). Equation (*A*8) is identical to the solution presented by Wan et al. [12], except that their result is presented in terms of the prestress instead of prestrain.

A.3 (Region 3) Nonlinear Föppl (Small Rotation) Membrane Theory With Pole and Boundary Layers (Without Prestrain). For pressure loading, there is no analytical closed form solution like Schwerin's solution (which is a special case in point loading where Poisson's ratio is one-third). Hence the governing membrane equations in this region (Eqs. (16) and (24)) for pressure loading have been numerically integrated and an approximate solution for midpoint deflection is obtained and given as follows

$$\frac{w(0)}{a} = g(v)\left(\frac{pa}{Eh}\right)^{1/3} \tag{A10}$$

where $g(v)\approx 0.7179-0.1706v-0.1495v^2$. Vlassak and Nix [8] discuss a similar result for pressure loading of a membrane (for no prestrain case), where the geometry of the film considered was a rectangle. In their derivation, the authors preassumed a form of displacement in the membrane, which they used to find strain energy and later used energy minimization techniques to find the unknowns in their displacement field.

A.4 (Boundary 1–2) Linear Plate With Prestrain. Solution is same as in region 2 ((*A*6)–(*A*9)), except that prestrain and thickness are related as follows

$$\varepsilon_0 = \varepsilon^2 = \frac{h^2}{12(1-v^2)a^2} \tag{A11}$$

B A Note on Numerical Integration. The governing equations in Sec. 3 of the paper constitute a two-point boundary value problem, with four variables namely f, $\dot{f}$, g, and $\dot{g}$. Based on a physical interpretation of the problem, one can assume that the solution variables are smooth functions of the radial distance, r/a. Numerical experiments with a shooting method revealed convergence problems, due to the high sensitivity of the results at the far edge (i.e., outer boundary conditions to be matched) to the initial guesses at large loads. Far greater success was achieved with a relaxation method, which involves discretizing the domain into a

finite-difference grid. The solution was guessed at each point in the mesh and successively iterated to converge (relax) to the true solution. The analytical plate solution was used to provide the initial guess for loads low enough to be in the plate limit to start the iteration. Converged solutions were then used as a starting guess for a slightly higher load. A highly refined mesh near the point-load (when relevant) and outer boundary was used to capture the singularity of the normalized rotations $[g(r)]$.

References

[1] Maner, K. C., Begley, M. R., and Oliver, W. C., 2004, ''Nanomechanical Testing and Circular Freestanding Polymer Films With Sub-Micron Thickness,'' Acta Mater., **52**, pp. 5451–5460.

[2] Espinosa, H. D., Prorok, B. C., and Fischer, M., 2003, ''A Methodology for Determining Mechanical Properties of Freestanding Thin Films and MEMS Materials,'' J. Mech. Phys. Solids, **51**, pp. 47–67.

[3] Vernon, T. J., Mackin, T. J., and Begley, M. R., 2003, ''Fatigue Testing of Polymer Membranes,'' Polym. Compos., (in press).

[4] Sheplak, M., and Dugundji, J., 1998, ''Large Deflections of Clamped Circular Plates Under Initial Tension and Transition to Membrane Behavior,'' ASME J. Appl. Mech., **65**, pp. 107–115.

[5] Frakes, J. P., and Simmonds, J. G., 1985, ''Asymptotic Solutions of the von Kármán Equations for a Circular Plate Under a Concentrated Load,'' ASME J. Appl. Mech., **52**, pp. 326–330.

[6] Junkin, II, G., and Davis, R. T., 1972, ''General Non-Linear Plate Theory Applied to a Circular Plate With Large Deflections,'' Int. J. Non-Linear Mech., **7**, pp. 503–526.

[7] Timoshenko, S., and Woinowsky-Krieger, S., 1959, *Theory of Plates and Shells*, McGraw-Hill, New York.

[8] Vlassak, J. J., and Nix, W. D., 1992, ''A New Bulge Test Technique for the Determination of Young's Modulus and Poisson's Ratio of Thin Films,'' J. Mater. Res., **7**, pp. 3242–3249.

[9] Poilane, C., Delobelle, P., Lexcellent, C., Hayashi, S., and Tobushi, H., 2000, ''Analysis of the Mechanical Behavior of Shape Memory Polymer Membranes by Nanoindentation, Bulging and Point Membrane Deflection Tests,'' Thin Solid Films, **379**, pp. 156–165.

[10] Libai, A., and Simmonds, J. G., 1998, *The Non-Linear Theory of Elastic Shells*, 2nd ed., Cambridge University Press, Cambridge.

[11] Hong, S., Weihs, T. P., Bravman, J. C., and Nix, W. D., 1990, ''Measuring Stiffnesses and Residual Stress of Silicon Nitride Thin Films,'' J. Electron. Mater., **19**, pp. 903–909.

[12] Wan, K. T., Guo, S., and Dillard, D. A., 2003, ''A Theoretical and Numerical Study of a Thin Clamped Circular Film Under an External Load in the Presence of a Tensile Residual Stress,'' Thin Solid Films, **425**, pp. 150–162.

[13] Schwerin, E., 1929, ''Uber Spannungen und Formänderungen Kreisringförmiger Membranen,'' Z. Tech. Phys. (Leipzig), **12**, pp. 651–659.

[14] Tsakalakos, T., 1981, ''Bulge Test: A Comparison of Theory and Experiment for Isotropic and Anisotropic Films,'' Thin Solid Films, **75**, pp. 293–305.

[15] Voorthuyzen, J. A., and Bergveld, P., 1984, ''The Influence of Tensile Forces on the Deflection of Circular Diaphragms in Pressure Sensors,'' Sens. Actuators, **6**, pp. 201–213.

[16] Tabata, O., Kawahata, K., Sugiyama, S., and Igarashi, I., 1989, ''Mechanical Property Measurement of Thin Films Using Load-Deflection of Composite Rectangular Membranes,'' Sens. Actuators, A, **20**, pp. 135–141.

[17] Small, M. K., and Nix, W. D., 1992, ''Analysis of the Accuracy of the Bulge Test in Determining the Mechanical Properties of Thin Films,'' J. Mater. Res., **7**, pp. 1553–1563.

[18] Ziebart, V., Paul, O., Münch, U., Schwizer, J., and Baltes, H., 1998, ''Mechanical Properties of Thin Films From the Load Deflection of Long Clamped Plates,'' J. Microelectromech. Syst., **7**, pp. 320–328.

[19] Ahmed, M., and Hashmi, M. S. J., 1998, ''Finite Element Analysis of Bulge Forming Applying Pressure and In-Plane Compressive Load,'' J. Mater. Process. Technol., **77**, pp. 95–102.

[20] Schellin, R., Hess, G., Kuhnel, W., Thielemann, C., Trost, D., Wacker, J., and Steinmann, R., 1994, ''Measurements of the Mechanical Behavior of Micromachined Silicon and Silicon-Nitride Membranes for Microphones, Pressure Sensors and Gas Flow Meters,'' Sens. Actuators, A, **41–42**, pp. 287–292.

[21] Karimi, A., Shojaei, O. R., Kruml, T., and Martin, J. L., 1997, ''Characterization of TiN Thin Films Using the Bulge Test and the Nanoindentation Technique,'' Thin Solid Films, **308–309**, pp. 334–339.

[22] Shojaei, O. R., and Karimi, A., 1998, ''Comparison of Mechanical Properties of TiN Thin Films Using Nanoindentation and Bulge Test,'' Thin Solid Films, **332**, pp. 202–208.

[23] Ju, B. F., Liu, K.-K., Ling, S.-F., and Ng, W. H., 2002, ''A Novel Technique for Characterizing Elastic Properties of Thin Biological Membrane,'' Mech. Mater., **34**, pp. 749–754.

[24] Kaenel, Y. V., Giachetto, J.-C., Stiegler, J., Drezet, J.-M., and Blank, E., 1996, ''A New Interpretation of Bulge Test Measurements Using Numerical Simulation,'' Diamond Relat. Mater., **5**, pp. 635–639.

[25] Bonnotte, E., Delobelle, P., Bornier, L., Trolard, B., and Tribillon, G., 1997, ''Two Interferometric Methods for the Mechanical Characterization of Thin Films by Bulge Tests. Application to Single Crystal of Silicon,'' J. Mater. Res., **12**, pp. 2234–2246.

[26] Jayaraman, S., Edwards, R. L., and Hemker, K. J., 1999, ''Relating Mechanical Testing and Microstructural Features of Polysilicon Thin Films,'' J. Mater. Res., **14**, pp. 688–697.

[27] Zheng, D. W., Xu, Y. H., Tsai, Y. P., Tu, K. N., Patterson, P., Zhao, B., Liu, Q.-Z., and Brongo, M., 2000, ''Mechanical Property Measurement of Thin Polymeric-Low Dielectric-Constant Films Using Bulge Testing Method,'' Appl. Phys. Lett., **76**, pp. 2008–2010.

[28] Yang, J. L., and Paul, O., 2002, ''Fracture Properties of LPCVD Silicon Nitride Thin Films From the Load-Deflection of Long Membranes,'' Sens. Actuators, A, **97–98**, pp. 520–526.

Stochastic Stability of Mechanical Systems Under Renewal Jump Process Parametric Excitation

R. Iwankiewicz
University of Witwatersrand,
Private Bag 3, WITS 2050,
Johannesburg, South Africa

S. R. K. Nielsen

J. W. Larsen

Department of Civil Engineering,
Aalborg University,
Sohngaardsholmsvej 57,
9000 Aalborg, Denmark

A dynamic system under parametric excitation in the form of a non-Erlang renewal jump process is considered. The excitation is a random train of nonoverlapping rectangular pulses with equal, deterministic heights. The time intervals between two consecutive jumps up (or down), are the sum of two independent, negative exponential distributed variables; hence, the arrival process may be termed as a generalized Erlang renewal process. The excitation process is governed by the stochastic equation driven by two independent Poisson processes, with different parameters. If the response in a single mode is investigated, the problem is governed in the state space by two stochastic equations, because the stochastic equation for the excitation process is autonomic. However, due to the parametric nature of the excitation, the nonlinear term appears at the right-hand sides of the equations. The equations become linear if the state space is augmented by the products of the original state variables and the excitation variable. Asymptotic mean and mean-square stability as well as asymptotic sample (Lyapunov) stability with probability 1 are investigated. The Lyapunov exponents have been evaluated both by the direct simulation of the stochastic equation governing the natural logarithm of the hyperspherical amplitude process and using the modification of the method wherein the time averaging of the pertinent expressions is replaced by ensemble averaging. It is found that the direct simulation is more suitable and that the asymptotic mean-square stability condition is not overly conservative. [DOI: 10.1115/1.1839591]

1 Introduction

Dynamic stability of elastic systems under parametric stochastic excitation has been a subject of research for a few decades. Most of the papers on stochastic stability that have appeared deal with the systems under Gaussian white-noise or wide-band parametric excitations. Ariaratnam [1] was one of the first authors to deal with the problem of dynamic stability of a beam-column under a Gaussian white-noise parametric stochastic loading. There exist a number of definitions of stochastic stability, e.g., Refs. [2,3]. Of special interest in connection with the problem undertaken in the present paper are papers [4,5], and [6], wherein the problems concerning more than two state variables are tackled. Ariaratnam et al. [4] investigated the stochastic stability of a two-degrees-of-freedom system resulting from the flexural–torsional stability of a narrow elastic beam subjected to stationary stochastic end couples. They used the stochastic averaging method and investigated the stochastic stability via Lyapunov exponents. Griesbaum [5] and Simon and Wedig [6] considered a similar problem governed by two coupled, white-noise-driven, equations. For four state variables, they used a hyperspherical transformation and under the ergodicity assumption they investigated the Lyapunov exponents with the aid of ensemble averaging rather than time averaging.

Much less attention has been given to non-Gaussian stochastic parametric excitations, for example, to random pulse trains. Samuels [7] was certainly one of the first authors to deal with parametric excitation in the form of a random train of impulses. Kotulski and Sobczyk [8] dealt with the moment stability of a system under a stochastic jump process excitation in the form of the random telegraph process $X(t)=(-1)^{N(t)}$, where $N(t)$ is a Poisson counting process. They derived the so-called ''correlation splitting'' formulas, which are just the differential equations governing the time evolution of the expectations $E[Y_j(t)(-1)^{N(t)}]$, where $Y_j(t)$ are the state variables of the original system. Obviously, in that formulation the time instants of the jumps up (or down) make up a usual Erlang renewal process with parameter $k=2$.

A stochastic parametric excitation considered in the present paper is a random train of nonoverlapping rectangular pulses with equal, deterministic heights. The excitation, or dynamic loading, of this kind may occur in some control systems wherein the controlling device switches the clutch on and off. Thereby, different parts of the system are coupled or decoupled, thus giving rise to sudden dynamic loading or unloading. Obviously, the dynamic loading of this kind may act as an external or a parametric excitation. The durations of pulses are assumed to be negative exponential distributed random variables and the time gaps between two consecutive pulses are also negative exponential distributed random variables, but the parameters of both distributions are different. Consequently, the pulse arrival times constitute a renewal process that may be termed as a generalized Erlang process. The excitation process is shown to be governed by the stochastic equation driven by two independent Poisson processes, with different parameters, which allows one to convert the original non-Markov problem into a Markov one.

The objective of the present paper is to investigate the asymptotic moment stability and Lyapunov asymptotic (sample) stability with probability 1. The response in a single mode is investigated; hence, the original problem is governed in the state space by two stochastic equations, because the stochastic equation for the excitation process is autonomic. However, due to the parametric nature of the excitation, two additional state variables have to be introduced in order to obtain the standard form of linear equations. It is shown that equations for mean values only form a closed set if two additional equations for second-order moments are appended. Likewise, the equations for second-order moments

Contributed by the Applied Mechanics Division of THE AMERICAN SOCIETY OF MECHANICAL ENGINEERS for publication in the ASME JOURNAL OF APPLIED MECHANICS. Manuscript received by the Applied Mechanics Division, June 27, 2003, final revision, September 13, 2004. Editor: R. M. McMeeking. Discussion on the paper should be addressed to the Editor, Prof. Robert M. McMeeking, Journal of Applied Mechanics, Department of Mechanical and Environmental Engineering, University of California-Santa Barbara, Santa Barbara, CA 393106-5070, and will be accepted until four months after final publication in the paper itself in the ASME JOURNAL OF APPLIED MECHANICS.

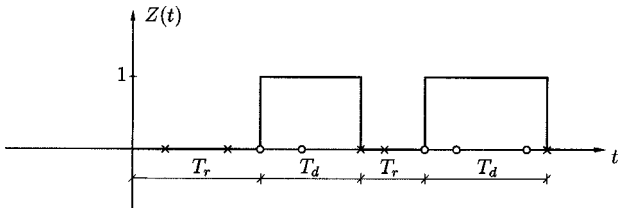

Fig. 1 A sample path of the stochastic process $Z(t)$. $\times$: N_μ-driven points, $\circ$: N_ν-driven points.

form a closed set if three additional third-order moments are taken into account. Asymptotic stability of first- and second-order ordinary moments is investigated numerically, by evaluating the largest of the real parts of all the eigenvalues. In order to investigate the asymptotic sample stability via Lyapunov exponents, the transformation of the four state variables to hyperspherical coordinates is made and two methods are used. One is the direct simulation of the stochastic equation governing the natural logarithm of the hyperspherical amplitude process and of the stochastic equations governing the angular processes. The other one is based on the ergodicity assumption, in which the time averaging of the pertinent expressions is replaced by ensemble averaging. A modification of the approach used in Refs. [5] and [6] has been developed. The numerical results show good qualitative agreement between two methods of evaluating the Lyapunov exponents. Direct simulation is, however, found to be more robust and less time consuming and therefore is more suitable for the problem. The asymptotic mean-square stability condition is, of course, more conservative than Lyapunov asymptotic (sample) stability with probability 1. It is, however, not overly conservative and may provide a good estimate of the asymptotic stochastic stability.

2 Statement of the Problem

Consider a beam-column under an axial compressive force, or a plate under in-plane compressive forces. Using a single-mode approximation, we obtain the differential equation

$$\ddot{Y}(t)+2\zeta\omega\dot{Y}(t)+\omega^2Y(t)-\beta\omega^2Z(t)Y(t)=0, \tag{1}$$

where $Z(t)$ is the dynamic compressive force, or a parametric excitation. The values $\beta=1$ and $Z(t)=\text{const.}=1$ correspond to the classical, Euler critical force for the static buckling problem.

Let us consider the stochastic excitation $Z(t)$ as a jump process, in the form of a random train of step forces of equal deterministic magnitude, with random force durations T_d and random time gaps T_r between two consecutive forces. A sample of the excitation is shown in Fig. 1.

Assume that all durations are identically, negative exponential distributed random variables T_d with the probability density

$$g_{T_d}(t)=\mu\exp(-\mu t), \quad t>0. \tag{2}$$

Likewise, all time gaps are assumed to be identical, negative exponential distributed random variables T_r with the probability density

$$g_{T_r}(t)=\nu\exp(-\nu t), \quad t>0. \tag{3}$$

The arrival times of the force pulses make up a renewal process with interarrival times $T_a=T_d+T_r$.

The excitation $Z(t)$ is governed by the stochastic equation (cf. Refs. [9,10])

$$dZ(t)=(1-Z)dN_\nu(t)-ZdN_\mu(t), \tag{4}$$

where $N_\nu(t)$ and $N_\mu(t)$ are mutually independent homogeneous Poisson processes with parameters ν and μ, respectively. The differentials in Eq. (4) are $dZ(t)=Z(t+dt)-Z(t)$, $dN_\alpha(t)=N_\alpha(t+dt)-N_\alpha(t)$, $\alpha=\mu,\nu$. At the time axis there are points driven by $N_\nu(t)$ and $N_\mu(t)$ Poisson processes. Assume that the initial condition for the $Z(t)$ variable is $Z(0)=0$. According to Eq. (4), at the first $N_\nu(t)$-driven point the variable $Z(t)$ jumps from 0 to 1, at the first subsequent $N_\mu(t)$-driven point it jumps back to 0, at the first subsequent $N_\nu(t)$-driven point it jumps again to 1, and so forth. Due to memorylessness property of the negative exponential distribution, this situation is tantamount to the sequence of alternating negative exponential distributed durations T_d and time gaps T_r [10].

Every sample function of $Z(t)$ as governed by Eq. (4) is a discontinuous function of time. Consequently, the sample functions of $\dot{Y}(t)$ are only piecewise smooth but continuous, and the sample functions of $Y(t)$ are smooth. However, every sample function of $Z(t)$ is of bounded variation over a finite time interval; hence, the existence and uniqueness of solutions of the Eq. (1) should be ensured.

Equations of motion in a state-space form are

$$d\mathbf{Y}(t)=\mathbf{c}(\mathbf{Y}(t))dt+\mathbf{b}_\nu(\mathbf{Y}(t))dN_\nu(t)+\mathbf{b}_\mu(\mathbf{Y}(t))dN_\mu(t), \tag{5}$$

where

$$\mathbf{Y}(t)=\begin{bmatrix}Y\\ \dot{Y}\\ Z\end{bmatrix}, \quad \mathbf{c}(\mathbf{Y}(t))=\begin{bmatrix}\dot{Y}\\ -\omega^2Y-2\zeta\omega\dot{Y}+\beta\omega^2YZ\\ 0\end{bmatrix}$$
$$\mathbf{b}_\nu(\mathbf{Y}(t))=\begin{bmatrix}0\\ 0\\ 1-Z\end{bmatrix}, \quad \mathbf{b}_\mu(\mathbf{Y}(t))=\begin{bmatrix}0\\ 0\\ -Z\end{bmatrix} \tag{6}$$

These equations are nonlinear due to the presence of YZ, but if the equations for $Y_{13}=YZ$ and $Y_{23}=\dot{Y}Z$ are appended, Eqs. (5) become linear and then

$$\mathbf{Y}(t)=\begin{bmatrix}Y\\ \dot{Y}\\ YZ\\ \dot{Y}Z\end{bmatrix}=\begin{bmatrix}Y_1\\ Y_2\\ Y_{13}\\ Y_{23}\end{bmatrix}, \quad \mathbf{c}(\mathbf{Y}(t))=\mathbf{A}\mathbf{Y}(t)$$

$$\mathbf{A}=\begin{bmatrix}0 & 1 & 0 & 0\\ -\omega^2 & -2\zeta\omega & \beta\omega^2 & 0\\ 0 & 0 & 0 & 1\\ 0 & 0 & \omega^2(\beta-1) & -2\zeta\omega\end{bmatrix}, \tag{7}$$

$$\mathbf{b}_\nu(\mathbf{Y}(t))=\begin{bmatrix}0\\ 0\\ Y_1-Y_{13}\\ Y_2-Y_{23}\end{bmatrix}, \quad \mathbf{b}_\mu(\mathbf{Y}(t))=\begin{bmatrix}0\\ 0\\ -Y_{13}\\ -Y_{23}\end{bmatrix}$$

It is worthwhile to note that $Y_{13}=YZ$ and $Y_{23}=\dot{Y}Z$ are also jump processes; they are equal to zero in the time intervals where $Z(t)=0$.

Stochastic equations for $Y_{13}=YZ$ and $Y_{23}=\dot{Y}Z$ have been obtained from the generalized Itô's differential rule pertinent to the problem governed by Eq. (5), which has the form (cf. Refs. [11–13])

$$dV(t,\mathbf{Y}(t))=\frac{\partial V(t,\mathbf{Y}(t))}{\partial t}dt+\sum_{j=1}^{n}\frac{\partial V(t,\mathbf{Y}(t))}{\partial Y_j}c_j(t,\mathbf{Y}(t))dt$$
$$+\sum_{\alpha=\mu,\nu}[V(t,\mathbf{Y}(t)+\mathbf{b}_\alpha(t,P(t),\mathbf{Y}(t)))$$
$$-V(t,\mathbf{X}(t))]dN_\alpha(t), \tag{8}$$

where $n=3$.

3 Moment Stability

Performing the averaging of the stochastic Eqs. (5) together with Eq. (6) does not result in a closed set of equations for the mean values due to the presence of the term YZ. However, the averaging of the stochastic Eqs. (5) together with Eqs. (7) yields the closed set of linear equations

$$\frac{d}{dt}\begin{bmatrix} m_1 \\ m_2 \\ m_{13} \\ m_{23} \end{bmatrix} = \begin{bmatrix} 0 & 1 & 0 & 0 \\ -\omega^2 & -2\zeta\omega & \beta\omega^2 & 0 \\ \nu & 0 & -(\nu+\mu) & 1 \\ 0 & \nu & \omega^2(\beta-1) & -(2\zeta\omega+\nu+\mu) \end{bmatrix} \begin{bmatrix} m_1 \\ m_2 \\ m_{13} \\ m_{23} \end{bmatrix} \tag{9}$$

where $m_1=E[Y_1]$, $m_2=E[Y_2]$, $m_{13}=E[Y_{13}]$, and $m_{23}=E[Y_{23}]$.

Likewise the set for second-order moments $m_{11}=E[Y_1^2]$, $m_{12}=E[Y_1Y_2]$, and $m_{22}=E[Y_2^2]$ is not closed. Appending the equations for $m_{113}=E[Y_1Y_{13}]$, $m_{123}=E[Y_1Y_{23}]$, and $m_{223}=E[Y_2Y_{23}]$ allows one to close the set, and the result is

$$\frac{d}{dt}\begin{bmatrix} m_{11} \\ m_{12} \\ m_{22} \\ m_{113} \\ m_{123} \\ m_{223} \end{bmatrix} = \begin{bmatrix} 0 & 2 & 0 & 0 & 0 & 0 \\ -\omega^2 & -2\zeta\omega & 1 & \beta\omega^2 & 0 & 0 \\ 0 & -2\omega^2 & -4\zeta\omega & 0 & 2\beta\omega^2 & 0 \\ \nu & 0 & 0 & -(\nu+\mu) & 2 & 0 \\ 0 & \nu & 0 & \omega^2(\beta-1) & -(2\zeta\omega+\nu+\mu) & 1 \\ 0 & 0 & \nu & 0 & 2\omega^2(\beta-1) & -(4\zeta\omega+\nu+\mu) \end{bmatrix} \begin{bmatrix} m_{11} \\ m_{12} \\ m_{22} \\ m_{113} \\ m_{123} \\ m_{223} \end{bmatrix} \tag{10}$$

First- and second-order moments are asymptotically stable if all the eigenvalues of coefficient matrices in Eqs. (9) and (10) have negative real parts. To investigate that, the well known Routh–Hurwitz criterion is usually used. Here the eigenvalues are evaluated numerically and the regions are determined where all the eigenvalues have negative real parts or not (or equivalently, where the largest of the real parts of all the eigenvalues is negative).

4 Transformation to Hyperspherical Coordinates

Let us first perform the following change of variables:

$$X_1=Y_1, \quad X_2=Y_2/\omega, \quad X_3=Y_{13}, \quad X_4=Y_{23}/\omega. \tag{11}$$

The stochastic equations are then written as

$$d\begin{bmatrix} X_1 \\ X_2 \\ X_3 \\ X_4 \end{bmatrix} = \begin{bmatrix} 0 & \omega & 0 & 0 \\ -\omega & -2\zeta\omega & \beta\omega & 0 \\ 0 & 0 & 0 & \omega \\ 0 & 0 & \omega(\beta-1) & -2\zeta\omega \end{bmatrix} \begin{bmatrix} X_1 \\ X_2 \\ X_3 \\ X_4 \end{bmatrix} dt + \begin{bmatrix} 0 & 0 \\ 0 & 0 \\ X_1-X_3 & -X_3 \\ X_2-X_4 & -X_4 \end{bmatrix} \begin{bmatrix} dN_\nu(t) \\ dN_\mu(t) \end{bmatrix} \tag{12}$$

In Lyapunov exponents approach to stochastic stability problems it is convenient to transform the original coordinates to hyperspherical ones [5,6], which are the amplitude process $A(t)$ and the angular processes $\Psi(t)$, $\Phi_1(t)$, and $\Phi_2(t)$. The advantage of such a transformation is that the equations are easier to handle, as the introduced angular processes are always bounded and the equation for the logarithm of the amplitude process may be directly integrated with respect to time.

The hyperspherical coordinates are introduced through the transformations

$$\begin{aligned} X_1(t) &= A(t)\cos\Psi(t)\cos\Phi_1(t)\cos\Phi_2(t), \\ X_2(t) &= A(t)\sin\Psi(t)\cos\Phi_1(t)\cos\Phi_2(t) \\ X_3(t) &= A(t)\sin\Phi_1(t)\cos\Phi_2(t), \\ X_4(t) &= A(t)\sin\Phi_2(t). \end{aligned} \tag{13}$$

The hyperspherical coordinates are expressed by the inverse transformations as

$$A(t)=\sqrt{X_1^2(t)+X_2^2(t)+X_3^2(t)+X_4^2(t)}, \quad 0\leqslant A(t)<\infty,$$

$$\Psi(t)=\begin{cases} \arctan\left(\dfrac{X_2(t)}{X_1(t)}\right), & X_1(t)\geqslant 0, \\ & -\dfrac{\pi}{2}<\Psi(t)<\dfrac{3\pi}{2}, \\ \arctan\left(\dfrac{X_2(t)}{X_1(t)}\right)+\pi, & X_1(t)<0, \end{cases} \tag{14}$$

$$\Phi_1(t)=\arctan\left(\frac{X_3(t)}{\sqrt{X_1^2(t)+X_2^2(t)}}\right), \quad -\frac{\pi}{2}<\Phi_1(t)<\frac{\pi}{2},$$

$$\Phi_2(t)=\arctan\left(\frac{X_4(t)}{\sqrt{X_1^2(t)+X_2^2(t)+X_3^2(t)}}\right), \quad -\frac{\pi}{2}<\Phi_2(t)<\frac{\pi}{2}.$$

With the aid of the generalized Itô's differential rule (8) the stochastic equations for the transformed variables are obtained as

$$\begin{aligned} d(\ln A(t)) &= h_1(\Psi(t),\Phi_1(t),\Phi_2(t))dt \\ &\quad + g_{1\nu}(\Psi(t),\Phi_1(t),\Phi_2(t))dN_\nu \\ &\quad + g_{1\mu}(\Psi(t),\Phi_1(t),\Phi_2(t))dN_\mu, \\ d(\Psi(t)) &= h_2(\Psi(t),\Phi_1(t),\Phi_2(t))dt \\ &\quad + g_{2\nu}(\Psi(t),\Phi_1(t),\Phi_2(t))dN_\nu \\ &\quad + g_{2\mu}(\Psi(t),\Phi_1(t),\Phi_2(t))dN_\mu, \\ d(\Phi_1(t)) &= h_3(\Psi(t),\Phi_1(t),\Phi_2(t))dt \\ &\quad + g_{3\nu}(\Psi(t),\Phi_1(t),\Phi_2(t))dN_\nu \\ &\quad + g_{3\mu}(\Psi(t),\Phi_1(t),\Phi_2(t))dN_\mu, \\ d(\Phi_2(t)) &= h_4(\Psi(t),\Phi_1(t),\Phi_2(t))dt \\ &\quad + g_{4\nu}(\Psi(t),\Phi_1(t),\Phi_2(t))dN_\nu \\ &\quad + g_{4\mu}(\Psi(t),\Phi_1(t),\Phi_2(t))dN_\mu, \end{aligned} \tag{15}$$

where the drift terms are given by

$$
\begin{aligned}
h_1 &= \cos\Phi_2(t)(-2\zeta\omega\sin^2\Psi(t)\cos^2\Phi_1(t)\cos\Phi_2(t)\\
&\quad +\beta\omega\sin\Psi(t)\sin\Phi_1(t)\cos\Phi_1(t)\cos\Phi_2(t)\\
&\quad +\beta\omega\sin\Phi_1(t)\sin\Phi_2(t))-2\zeta\omega\sin^2\Phi_2(t),\\
h_2 &= -\omega-2\zeta\omega\sin\Psi(t)\cos\Psi(t)+\beta\omega\cos\Psi(t)\tan\Phi_1(t),\\
h_3 &= 2\zeta\omega\sin^2\Psi(t)\cos\Phi_1(t)\sin\Phi_1(t)-\beta\omega\sin\Psi(t)\sin^2\Phi_1(t)\\
&\quad +\omega\cos\Phi_1(t)\tan\Phi_2(t),\\
h_4 &= 2\zeta\omega\sin^2\Psi(t)\cos^2\Phi_1(t)\cos\Phi_2(t)\sin\Phi_2(t)\\
&\quad -\beta\omega\sin\Psi(t)\cos\Phi_1(t)\sin\Phi_1(t)\cos\Phi_2(t)\sin\Phi_2(t)\\
&\quad -\omega\sin\Phi_1(t)+\beta\omega\sin\Phi_1(t)\cos^2\Phi_2(t)\\
&\quad -2\zeta\omega\cos\Phi_2(t)\sin\Phi_2(t),
\end{aligned}
\tag{16}
$$

and the ''diffusion terms'' are expressed as

$$
\begin{aligned}
g_{1\nu} &= \frac{1}{2}\ln 2+\ln(\cos\Phi_1(t)\cos\Phi_2(t)),\\
g_{1\mu} &= \ln(\cos\Phi_1(t)\cos\Phi_2(t)),\\
g_{2\nu} &= 0,\\
g_{2\mu} &= 0,\\
g_{3\nu} &= \arctan(\cos\Psi(t))-\Phi_1(t),\\
g_{3\mu} &= -\Phi_1(t),\\
g_{4\nu} &= \arctan\left(\frac{\sin\Psi(t)}{\sqrt{1+\cos^2\Psi(t)}}\right)-\Phi_2(t),\\
g_{4\mu} &= -\Phi_2(t).
\end{aligned}
\tag{17}
$$

It can be seen from the form of the drift coefficients h_i given by Eq. (16) and ''diffusion'' coefficients $g_{i\mu}, g_{i\nu}$ given by Eq. (17) that the time evolution of $\ln A(t)$ and of the angular processes $\Phi_1(t)$ and $\Phi_2(t)$ is due to drift and jumps. They are driven by the Poisson processes $N_\mu(t)$ and $N_\nu(t)$. The angular process $\Psi(t)$ is not a jump process driven by the Poisson processes, as is seen in Eqs. (15) and (17) ($g_{2\nu}=0$ and $g_{2\mu}=0$) this process develops only due to drift. However, it is a discontinuous, or a jump, process of another kind. As it follows from its definition (14) at the time instants when the displacement response $X_1(t)$ changes the sign, the process $\Psi(t)$ reveals jumps of magnitude 2π. Between these jumps, the time evolution of $\Psi(t)$ is due to drift only. The angular processes $\Phi_1(t)$ and $\Phi_2(t)$ are exactly equal to zero in the time intervals where $Z(t)=0$. This can be observed directly in Eq. (14), but it also follows from the form of the coefficients h_3, h_4 as given by (16) and from $g_{3\nu}$, $g_{3\mu}$, $g_{4\nu}$, $g_{4\mu}$, as given by Eq. (17). If the processes $\Phi_1(t)$ and $\Phi_2(t)$ start, in some time interval, from zero values, then $h_3=0$ and $h_4=0$; hence there is no drift development and these processes continue to be zero. At the first N_ν-driven point there are jump changes in both $\Phi_1(t)$ and $\Phi_2(t)$ and at the first subsequent N_μ-driven point there is a jump back to zero. The drift development is only present when $Z(t)=1$; hence, $\Phi_1(t)\neq 0$ and $\Phi_2(t)\neq 0$.

5 Lyapunov Exponents and Stability with Probability 1

A trivial solution $\mathbf{X}(t)\equiv 0$ of Eqs. (12), which are equivalent to Eq. (5) with Eq. (7), is almost surely asymptotically stable, if the largest Lyapunov exponent is negative; hence, if

$$
\lambda=\lim_{t\to\infty}\frac{1}{t}\ln\left(\frac{\|\mathbf{X}(t)\|}{\|\mathbf{X}(0)\|}\right)<0, \tag{18}
$$

where $\|\mathbf{X}(t)\|=\sqrt{X_1^2(t)+X_2^2(t)+X_3^2(t)+X_4^2(t)}$. This could be investigated numerically, by simulating the stochastic Eqs. (12). However, when the sample curve is unstable, the values of the state variables become very large, which causes some numerical problems. It is more convenient to make use of the fact that $\sqrt{X_1^2(t)+X_2^2(t)+X_3^2(t)+X_4^2(t)}=A(t)$, and we find the Lyapunov exponent is

$$
\lambda=\lim_{t\to\infty}\frac{1}{t}\ln\left(\frac{A(t)}{A(0)}\right)<0, \tag{19}
$$

simulating directly the stochastic equation for $\ln A(t)$, as given by Eq. (15). The advantage of this kind of simulation is that the only functions involved at the right-hand sides of Eqs. (15), are the angular processes $\Psi(t)$, $\Phi_1(t)$, and $\Phi_2(t)$, which are bounded [see Eq. (14)].

As the amplitude process $A(t)$ is not involved at the right-hand side of Eq. (16) for $\ln A(t)$ (cf. Refs. [5], [6]), this equation can be directly integrated with respect to time and substituted into Eq. (19), which results in a time-average integral

$$
\begin{aligned}
\lambda=\lim_{T\to\infty}\frac{1}{T}\int_0^T &(h_1(\Psi(t),\Phi_1(t),\Phi_2(t))dt+g_{1\nu}(\Phi_1(t),\Phi_2(t))dN_\nu\\
&+g_{1\mu}(\Phi_1(t),\Phi_2(t))dN_\mu)
\end{aligned}
\tag{20}
$$

Assuming ergodicity of $h_1(\Psi(t),\Phi_1(t),\Phi_2(t))$, $g_{1\nu}(\Phi_1(t),\Phi_2(t))$, and $g_{1\mu}(\Phi_1(t),\Phi_2(t))$, we can make the following replacement:

$$
\begin{aligned}
\lambda=\lim_{T\to\infty}\frac{1}{T}\int_0^T &(E[h_1(\Psi(t),\Phi_1(t),\Phi_2(t))]dt\\
&+E[g_{1\nu}(\Phi_1(t),\Phi_2(t))dN_\nu]+E[g_{1\mu}(\Phi_1(t),\Phi_2(t))dN_\mu]),
\end{aligned}
\tag{21}
$$

where $E[g_{1\nu}(\Phi_1(t),\Phi_2(t))dN_\nu]=E[g_{1\nu}(\Phi_1(t),\Phi_2(t))]\nu dt$ and $E[g_{1\mu}(\Phi_1(t),\Phi_2(t))dN_\mu]=E[g_{1\mu}(\Phi_1(t),\Phi_2(t))]\mu dt$.

Further, it is assumed that the processes $\Phi_1(t)$, $\Phi_2(t)$, and $\Psi(t)$ are stationary; hence, there exist time-invariant marginal probability densities $p(\psi,\phi_1,\phi_2)$ and $p(\phi_1,\phi_2)$. The expectations in Eqs (21) are also time-invariant, and we obtain

$$
\begin{aligned}
\lambda &= E[h_1(\Psi(t),\Phi_1(t),\Phi_2(t))]+\nu E[g_{1\nu}(\Phi_1(t),\Phi_2(t))]\\
&\quad +\mu E[g_{1\mu}(\Phi_1(t),\Phi_2(t))]\\
&= \int_{-\pi/2}^{3\pi/2}\int_{-\pi/2}^{\pi/2}\int_{-\pi/2}^{\pi/2}h_1(\psi,\phi_1,\phi_2)p(\psi,\phi_1,\phi_2)d\psi d\phi_1 d\phi_2\\
&\quad +\int_{-\pi/2}^{\pi/2}\int_{-\pi/2}^{\pi/2}(\nu g_{1\nu}(\phi_1,\phi_2)\\
&\quad +\mu g_{1\mu}(\phi_1,\phi_2))p(\phi_1,\phi_2)d\phi_1 d\phi_2.
\end{aligned}
\tag{22}
$$

It should be commented here that the time averaging may be replaced by the ensemble averaging; i.e., the time average

$$
\lim_{T\to\infty}\frac{1}{T}\int_0^T Y(t)dt \tag{23}
$$

converges to $E[Y(t)]$ with probability 1 if the process $Y(t)$ satisfies the following conditions [14]:

1. it is stationary in the strict sense,
2. $E[|Y(t)|]<\infty$,
3. almost all sample curves of $Y(t)$ are Riemann integrable on every finite interval.

The theorem may be applied to any compound function $g(Y(t))$, $g(\cdot)$ being an arbitrary Borel measurable function, if the conditions 2 and 3 are satisfied by the compound function. In the present problem the ergodicity and stationarity is assumed about

the processes $h_1(\Psi(t),\Phi_1(t),\Phi_2(t))$, $g_{1\nu}(\Phi_1(t),\Phi_2(t))$, and $g_{1\mu}(\Phi_1(t),\Phi_2(t))$ In addition, the processes $\Psi(t)$, $\Phi_1(t)$, and $\Phi_2(t)$ are assumed to be stationary. As the response process is driven by the process $Z(t)$, it is of bounded variation and so are the processes $\Psi(t)$, $\Phi_1(t)$, $\Phi_2(t)$, $h_1(\Psi(t),\Phi_1(t),\Phi_2(t))$, $g_{1\nu}(\Phi_1(t),\Phi_2(t))$, and $g_{1\mu}(\Phi_1(t),\Phi_2(t))$; hence, they satisfy condition 3 of the above theorem. Obviously condition 2 is also satisfied.

However, it is difficult to analyze the strict-sense stationarity of $\Psi(t)$, $\Phi_1(t)$, $\Phi_2(t)$, $h_1(\Psi(t),\Phi_1(t),\Phi_2(t))$, $g_{1\nu}(\Phi_1(t),\Phi_2(t))$, $g_{1\mu}(\Phi_1(t),\Phi_2(t))$, which are the complicated transformations of the response process. The stationarity assumption about these processes may be justified by the fact that the response process is driven by the process $Z(t)$, which attains stationarity after a long time interval, i.e., as $t\to\infty$, for example, its mean value is given by

$$\lim_{t\to\infty}E[Z(t)]=\lim_{t\to\infty}\frac{\nu}{\nu+\mu}(1-\exp(-(\nu+\mu)t))=\frac{\nu}{\mu+\nu}. \tag{24}$$

The probability densities $p(\psi,\phi_1,\phi_2)$ and $p(\phi_1,\phi_2)$ are evaluated from Monte Carlo simulations of the hyperspherical angular coordinate processes $\Psi(t)$, $\Phi_1(t)$, and $\Phi_2(t)$ based on Eqs. (15).

Due to the jump nature of the angular processes $\Phi_1(t)$ and $\Phi_2(t)$, and the fact that they are equal to zero during some significant time intervals, the marginal probability densities $p(\psi,\phi_1,\phi_2)$ and $p(\phi_1,\phi_2)$ are very spiky, the spikes being at $\phi_1=0$, $\phi_2=0$. This makes the numerical evaluation of the integrals (22) cumbersome. The evaluation is very much improved if those spikes are represented in the probability densities in the following way:

$$p(\psi,\phi_1,\phi_2)=P_0\delta(\phi_1)\delta(\phi_2)p(\psi)+(1-P_0)p^0(\psi,\phi_1,\phi_2), \tag{25}$$

$$p(\phi_1,\phi_2)=P_0\delta(\phi_1)\delta(\phi_2)+(1-P_0)p^0(\phi_1,\phi_2), \tag{26}$$

where $\delta(\cdots)$ is the Dirac delta, $p(\psi)$ is the marginal probability density of $\Psi(t)$, and $p^0(\psi,\phi_1,\phi_2)$, $p^0(\phi_1,\phi_2)$ are conditional probability densities $p^0(\psi,\phi_1,\phi_2)=p(\psi,\phi_1,\phi_2|\phi_1\neq0,\phi_2\neq0)$, $p^0(\phi_1,\phi_2)=p(\phi_1,\phi_2|\phi_1\neq0,\phi_2\neq0)$, whose areas are normalized to 1. The heights P_0 of the spikes are obtained by collecting the counts for which $\phi_1=0$, $\phi_2=0$.

The integrals in Eq. (22) reduce to

$$\begin{aligned}\lambda=&-2\zeta\omega P_0\int_{-\pi/2}^{3\pi/2}\sin^2\psi p(\psi)d\psi\\&+(1-P_0)\int_{-\pi/2}^{3\pi/2}\int_{-\pi/2}^{\pi/2}\int_{-\pi/2}^{\pi/2}h_1(\psi,\phi_1,\phi_2)\\&\times p^0(\psi,\phi_1,\phi_2)d\psi d\phi_1 d\phi_2+\frac{1}{2}\nu P_0\ln 2\\&+(1-P_0)\int_{-\pi/2}^{\pi/2}\int_{-\pi/2}^{\pi/2}(\nu g_{1\nu}(\phi_1,\phi_2)\\&+\mu g_{1\mu}(\phi_1,\phi_2))p^0(\phi_1,\phi_2)d\phi_1 d\phi_2.\end{aligned} \tag{27}$$

The simulation scheme for the hyperspherical angular processes governed by Eq. (15) is as follows. Between the Poisson points the Runge-Kutta scheme is used. At the first $N_\nu(t)$-driven point and at every first $N_\nu(t)$-driven point $t_{k\nu}$ subsequent to an $N_\mu(t)$-driven point, there is an increment $dN_\nu=1$; hence, according to Eqs. (15) and (17), there is a jump change in $\Phi_i(t)$ of magnitude $g_{i\nu}(\Psi(t_{k\nu}^-),\Phi_1(t_{k\nu}^-),\Phi_2(t_{k\nu}^-))$

$$\Phi_i(t_{k\nu}^+)=\Phi_i(t_{k\nu}^-)+g_{i\nu}(\Psi(t_{k\nu}^-),\Phi_1(t_{k\nu}^-),\Phi_2(t_{k\nu}^-)). \tag{28}$$

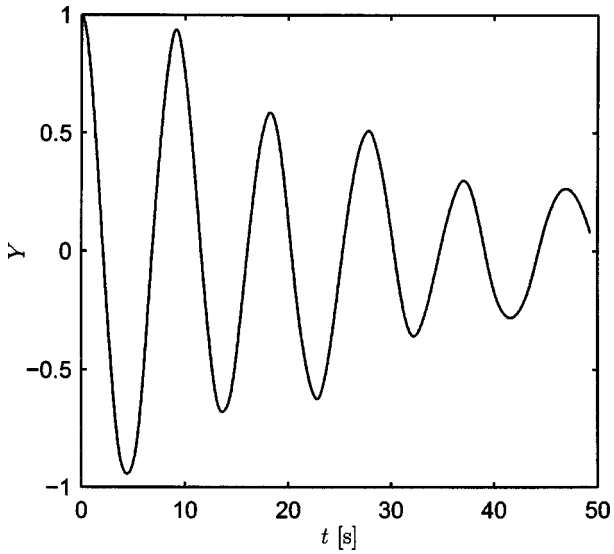

Fig. 2 Sample function of the stable displacement response $Y(t)$. Moderate durations/moderate gaps: $\mu=1.0\ \mathrm{s}^{-1}$, $\nu=1.0\ \mathrm{s}^{-1}$, $\zeta=0.05$, $\beta=0.5$, $\tau=0.5$.

At the first $N_\mu(t)$-driven point $t_{k\mu}$ subsequent to an $N_\nu(t)$-driven point, $dN_\mu=1$; hence, according to Eq. (17), there is a jump change in $\Phi_i(t)$ of magnitude $g_{i\mu}(\Psi(t_{k\nu}^-),\Phi_1(t_{k\nu}^-),\Phi_2(t_{k\nu}^-))=-\Phi_i(t_{k\nu}^-)$,

$$\Phi_i(t_{k\mu}^+)=\Phi_i(t_{k\mu}^-)+g_{i\mu}(\Psi(t_{k\mu}^-),\Phi_1(t_{k\mu}^-),\Phi_2(t_{k\mu}^-))=0. \tag{29}$$

Thus, the initial conditions $\Phi_i(t_{k\nu}^+)$ or $\Phi_i(t_{k\mu}^+)$ for the subsequent time interval starting at $t_{k\nu}^+$ or $t_{k\mu}^+$ are determined.

6 Numerical Results

As the durations and time gaps are negative-exponential distributed the mean duration is $E[T_d]=1/\mu$ and the mean time gap is $E[T_r]=1/\nu$. The mean interarrival time of the pulses equals $E[T_a]=E[T_d]+E[T_r]=1/\mu+1/\nu=(\mu+\nu)/\mu\nu$.

Computations have been performed for pulses with parameters:

$(\mu,\nu)=(0.1,0.1)$; long durations/long gaps,
$(\mu,\nu)=(1,1)$; moderate durations/moderate gaps,
$(\mu,\nu)=(10,10)$; short durations/short gaps,
$(\mu,\nu)=(0.1,10)$; long durations/short gaps.

The respective mean interarrival times are $E[T_a]=20;2;0.2;10.1$ [s].

Sample functions of the displacement response $Y(t)$ and of the velocity response $\dot{Y}(t)$ for the stable behavior, obtained for $\beta=0.5$ and for the initial conditions $Y(0)=1$ and $\dot{Y}(0)=0$ are shown in Figs. 2 and 3, respectively. It is seen that the system is performing essentially the natural vibrations.

Figure 4 shows an example phase plot of the stable response obtained for $\beta=0.5$ and for the initial conditions $Y(0)=1$ and $\dot{Y}(0)=0$. An example phase plot of the unstable response (for $\beta=1.2$) for the same initial conditions is shown in Fig. 5.

Simulated sample function of $Z(t)$ obtained for the initial condition $Z(0)=0$ is shown in Fig. 6.

The sample functions of the angular processes $\Phi_1(t)$, $\Phi_2(t)$, and $\Psi(t)$ corresponding to the sample function of $Z(t)$ shown in Fig. 6 and relevant to the stable response are shown in Figures 7–9, respectively. The behavior of $\Phi_1(t)$, $\Phi_2(t)$ is in agreement with that predicted from the governing stochastic equations (15–17). Indeed the process $\Psi(t)$ reveals jumps of magnitude 2π at the time instants separated by the intervals equal to the natural periods. This is in agreement with the fact that the system is performing essentially the natural vibrations (cf. Fig. 2), hence

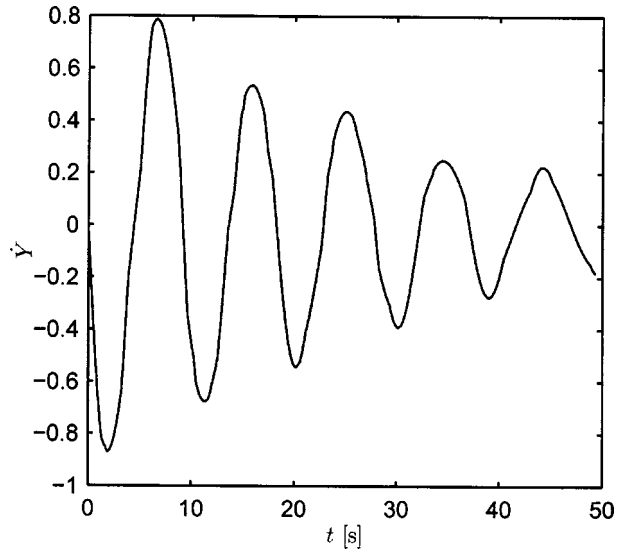

Fig. 3 Sample function of the stable velocity response $\dot{Y}(t)$. Moderate durations /moderate gaps: $\mu=1.0\ s^{-1}$, $\nu=1.0\ s^{-1}$, $\zeta=0.05$, $\beta=0.5$, $\tau=0.5$.

$X_1(t)$ changes the sign periodically. The spectrum of the sample function of $\Psi(t)$ (Fig. 10) obtained with the aid of the fast Fourier transform technique reveals the peak at the natural frequency $\omega_n=2\pi/10=0.628\ s^{-1}$ and also some finite value at $\omega=0$, which corresponds to the nonzero time average of the sample function.

Finally, Fig. 11 shows the $\ln A(t)$ for the stable response behavior.

In Figures 12–15, the stability regions are shown against the nondimensional parameter $\tau=(\mu+\nu)\omega/\mu\nu\pi$, which is the ratio of the mean interarrival time $E[T_a]$ of the pulses to half of the natural period $T_n=2\pi/\omega$ of the system. In other words, τ is a relative measure of the density of the pulse train or of its mean arrival rate. Note that the mean arrival rate (renewal density) $h_o(t)$ of the underlying renewal process is

$$h_o(t)=\frac{\mu\nu}{\nu+\mu}(1-\exp(-(\nu+\mu)t)); \tag{30}$$

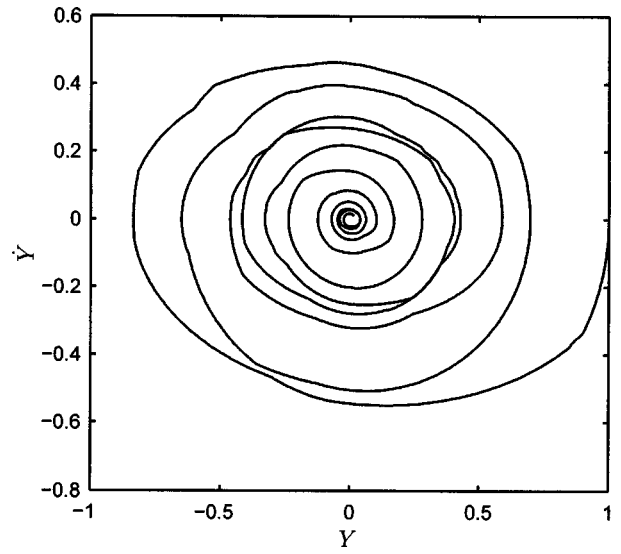

Fig. 4 Phase plot of the stable response for $\zeta=0.05$, $\mu=1.0$, $\nu=1.0$, $\beta=0.5$, $\tau=0.5$

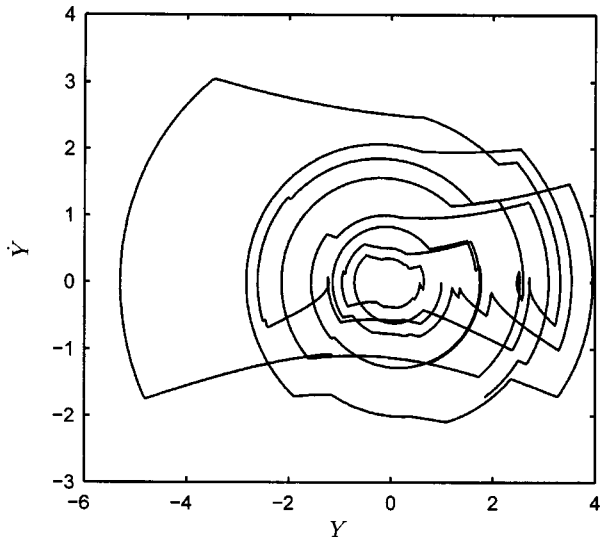

Fig. 5 Phase plot of the unstable response for $\zeta=0.05$, $\mu=1.0$, $\nu=1.0$, $\beta=1.2$, $\tau=0.5$

hence, $h_{os}=\nu\mu/(\mu+\nu)$ is the stationary (as $t\to\infty$) mean arrival rate and $h_{os}=1/E[T_a]$.

The curves in Figures 12–15 show the stability regions border lines. The stability region is below the curve. The dotted line and dashed line indicate lines of zero real parts of the eigenvalue with the largest real part, for the mean and mean-square stability, respectively. The thick solid line indicates the zero Lyapunov exponent as obtained by direct simulation of the equation for $\ln A(t)$, as given by Eq. (15). The thin solid line corresponds to the zero Lyapunov exponent as evaluated by ensemble averaging, in terms of integrals (22). The results for Lyapunov exponents obtained from both methods are qualitatively the same. It is seen that the lines of zero Lyapunov exponents lie above the lines obtained from the mean-square stability. This is certainly supported by the results shown in Fig. 12, where a very fine mesh was used for the values of τ close to zero. Such a refinement leads, however, to an excessively long computation time and has not been done in other cases.

If $\mu=\nu$, i.e., the mean durations of the pulses and mean time gaps are the same, the curves showing stability regions have very similar shape (Figs. 12–14). As the natural frequency ω of the system decreases, so does the parameter τ and the stability region increases. The curves for the moment stability have identical shapes. However the stability regions are not the same, because

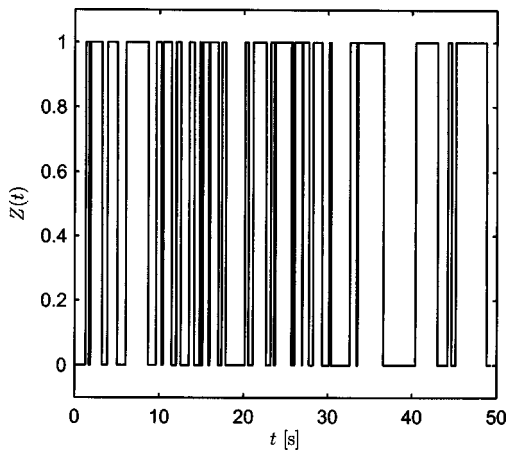

Fig. 6 Simulated sample function of $Z(t)$ for $\mu=1.0$, $\nu=1.0$

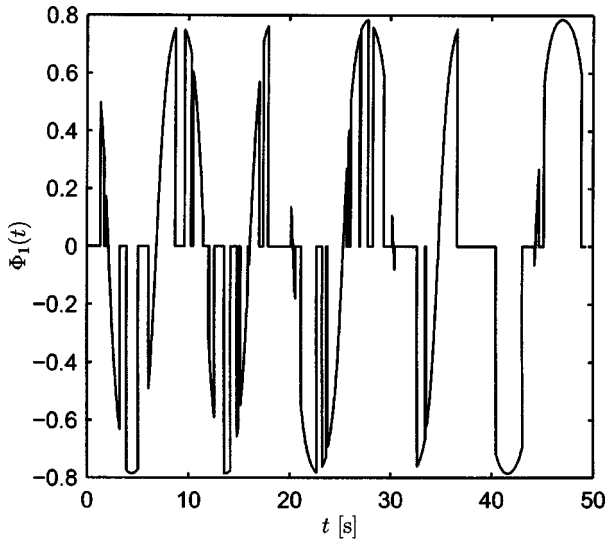

Fig. 7 Sample function of $\Phi_1(t)$ for $\zeta=0.05$, $\mu=1.0$, $\nu=1.0$, $\beta=0.5$, $\tau=0.5$

the results are shown against the relative parameter τ. When μ and ν are large, the same value τ as for small μ and ν corresponds to a higher natural frequency. For example for a pulse train with $(\mu,\nu)=(0.1,0.1)$ and $E[T_a]=20$ (Fig. 12) the natural frequency corresponding to a value $\tau=1$ equals $\pi/20$, while for $(\mu,\nu)=(1,1)$ with $E[T_a]=2$ (Fig. 13) it is $\pi/2$. It is seen that a larger stability region corresponds to $\omega=\pi/20$ in Fig. 13 than in Fig. 12. This means that as the mean interarrival time of the pulses decreases the stability region for the same oscillator increases. In other words, the stability region is larger for the pulse train with short durations and short gaps than for long durations and long gaps.

When the pulses have long mean durations and short mean gaps (Fig. 15), it corresponds to the load which is almost constant and quasistatic. The lines for mean, mean-square, and Lyapunov stability by the direct simulations coincide. The stability region is essentially the same as for the classical buckling problem, i.e., $\beta=1$ is the critical value.

Interestingly, nothing like a parametric "resonance" effect is observed when the mean interarrival time of the pulse train equals

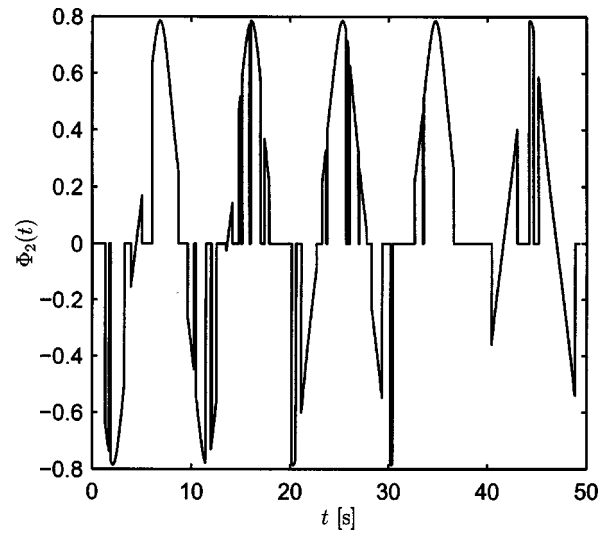

Fig. 8 Sample function of $\Phi_2(t)$ for $\zeta=0.05$, $\mu=1.0$, $\nu=1.0$, $\beta=0.5$, $\tau=0.5$

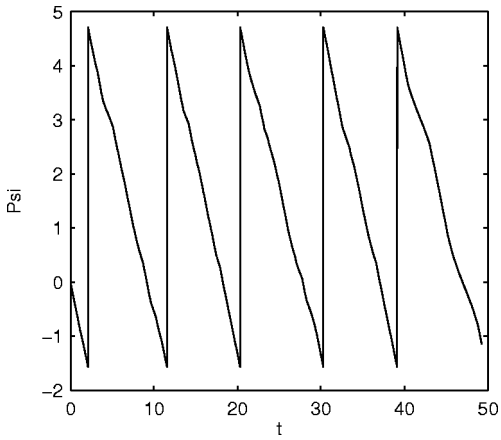

Fig. 9 Sample function of $\Psi(t)$ for $\zeta=0.05$, $\mu=1.0$, $\nu=1.0$, $\beta=0.5$, $\tau=0.5$

half of the natural period; i.e., $\tau=1$. This is so because the excitation itself as well as its mean value $E[Z(t)]$ and its mean square $E[Z^2(t)]$ are not periodic functions. The mean value and the mean square are equal and are both given by the expression (24). Likewise, if $Z(t)$ is an external excitation, nothing like a "resonance" effect is observed for the mean response when the mean interarrival time $E[T_a]=(\mu+\nu)/\mu\nu$ is equal to a natural period $T_n=2\pi/\omega$; i.e., when $\omega=2\pi\nu\mu/(\mu+\nu)$. The mean value $E[Y(t)]$ of the response of the linear oscillator to an external excitation $Z(t)$ is given by [9]

$$\mu_Y(t)=\frac{\nu}{(\nu+\mu)\omega^2}\left(1-\frac{1}{(\nu+\mu+\zeta\omega)^2+\omega_d^2}\left(\omega^2\exp(-(\nu+\mu)t)\right.\right.$$
$$-\frac{\nu+\mu}{\omega_d}(\omega_d(2\zeta\omega-(\nu+\mu))\cos\omega_d t$$
$$\left.\left.+(2\zeta^2\omega^2-\omega^2-\zeta\omega(\nu+\mu))\sin\omega_d t)\exp(-\zeta\omega t)\right)\right), \tag{31}$$

where $\omega_d=\omega\sqrt{1-\zeta^2}$ is the damped natural frequency of the oscillator. As it is seen there is no "resonance," or singularity, effect.

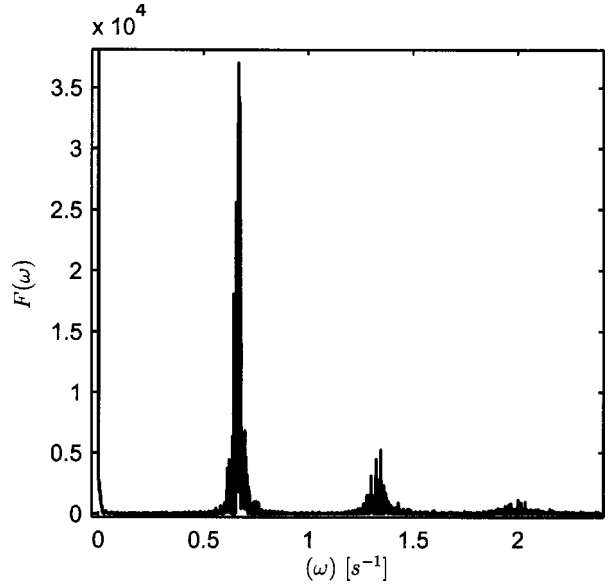

Fig. 10 Spectrum of the sample function of $\Psi(t)$ for $\zeta=0.05$, $\mu=1.0$, $\nu=1.0$, $\beta=0.5$, $\tau=0.5$

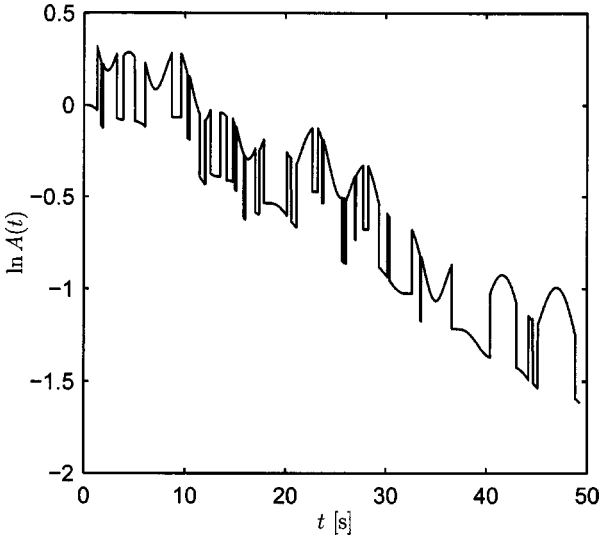

Fig. 11 Sample function of ln $A(t)$ for the stable response behavior, for $\zeta=0.05$, $\mu=1.0$, $\nu=1.0$, $\beta=0.5$, $\tau=0.5$

Regarding the computational effort, it should be commented that the direct simulation converges much faster than the time-averaging method, with a factor of 100. Further, the direct simulation is simpler to program. The main problem of the time-averaging method is to determine the probability density functions $p(\psi,\phi_1,\phi_2)$ and $p(\phi_1,\phi_2)$, which is very time consuming.

In all examined cases, the asymptotic sample stability condition reveals larger regions of stability than the asymptotic mean-square condition. This observation is in agreement with the general fact that the asymptotic moment stability is more conservative than Lyapunov asymptotic stability with probability 1 (asymptotic sample stability) [15,16]. In particular, the asymptotic mean square stability implies, for the linear systems, stability with probability one [3]. Obviously, as the ordinary moments are considered herein, the mean-square stability also implies the mean stability.

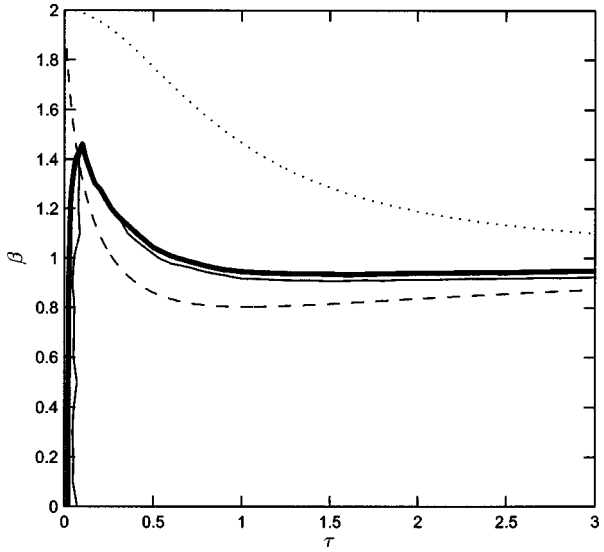

Fig. 13 Moderate durations/moderate gaps: $\mu=1.0\ s^{-1}$, $\nu=1.0\ s^{-1}$, $\zeta=0.05$. Dotted line: mean stability, dashed line: mean-square stability, thick solid line: Lyapunov exponents by direct simulations, thin solid line: Lyapunov exponents by ensemble averaging.

7 Concluding Remarks

Asymptotic stability of first- and second-order moments as well as Lyapunov asymptotic (sample) stability with probability 1 are investigated for the dynamic system under a renewal driven jump process parametric excitation. The original state vector of the system is a non-Markov process; however, the excitation process is shown to be governed by the stochastic equation driven by two independent Poisson processes, with different parameters, which allows one to convert the original non-Markov problem into a Markov one. The original state vector has been augmented by two additional equations. It has been shown that the set of equations for the mean values is closed by appending the equations for two extra second-order moments, and that the equations for second-

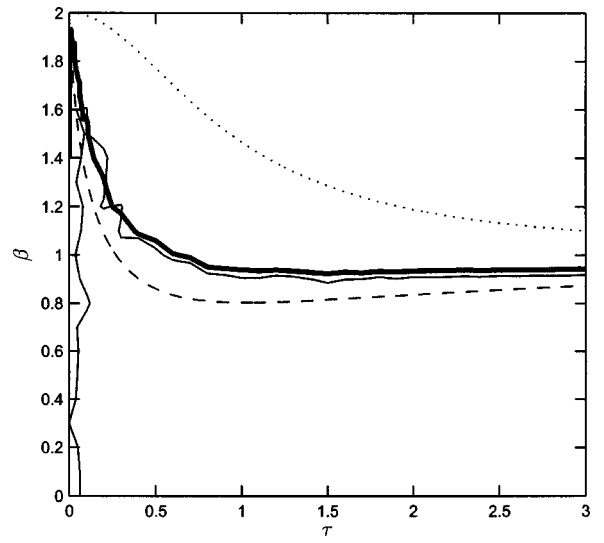

Fig. 12 Long durations/long gaps: $\mu=0.1\ s^{-1}$, $\nu=0.1\ s^{-1}$, $\zeta=0.05$. Dotted line: mean stability, dashed line: mean-square stability, thick solid line: Lyapunov exponents by direct simulations, thin solid line: Lyapunov exponents by ensemble averaging.

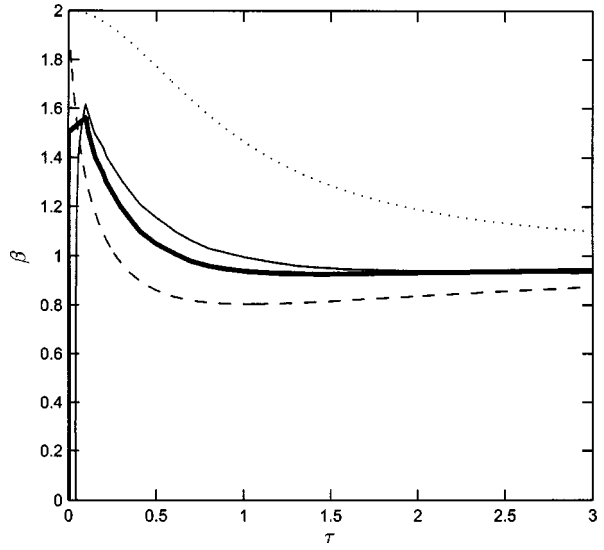

Fig. 14 Short durations/short gaps: $\mu=10\ s^{-1}$, $\nu=10\ s^{-1}$, $\zeta=0.05$. Dotted line: mean stability, dashed line: mean-square stability, thick solid line: Lyapunov exponents by direct simulations, thin solid line: Lyapunov exponents by ensemble averaging.

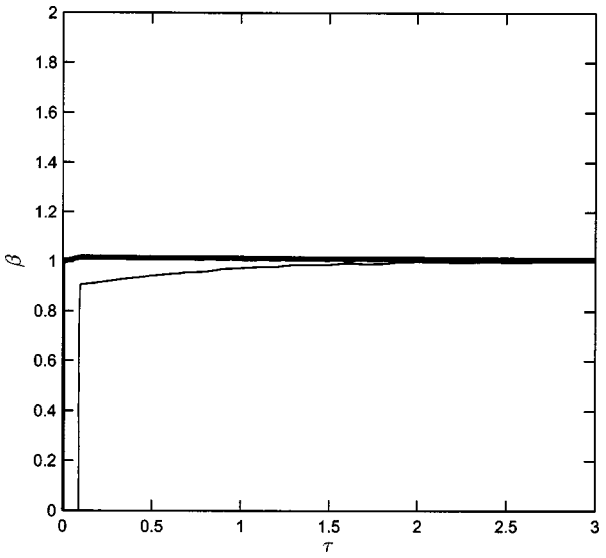

Fig. 15 Long durations/short gaps: $\mu=0.1\ s^{-1}$, $\nu=10\ s^{-1}$, $\zeta=0.05$. Dotted line: mean stability, dashed line: mean-square stability, thick solid line: Lyapunov exponents by direct simulations, thin solid line: Lyapunov exponents by ensemble averaging.

order moments form a closed set if the equations for three extra third-order moments are added. In order to investigate the asymptotic sample stability the transformation of the four state variables to hyperspherical coordinates is made. The Lyapunov exponents have been evaluated with the aid of two methods. The first one is direct simulation of the stochastic equation governing the natural logarithm of the hyperspherical amplitude process. In the second approach, based on ergodicity assumption, time averaging of the pertinent expressions is replaced by ensemble averaging and the modification of the approach used in [5] and [6] has been developed. The numerical results show good qualitative agreement between two methods of evaluating the Lyapunov exponents. Direct simulation is however more robust and less time consuming, hence it is more suitable for the problem. The asymptotic mean-square stability condition is, of course, more conservative than Lyapunov asymptotic (sample) stability with probability 1. However the asymptotic mean-square stability condition is shown not to be overly conservative and therefore provides a good estimate of the asymptotic stochastic stability.

Acknowledgments

S. R. K. Nielsen and J. W. Larsen wish to acknowledge the support from The Danish Technical Research Council within the project ''Damping Mechanisms in Dynamics of Structures and Materials.''

References

[1] Ariaratnam, S. T., 1966, ''Dynamic Stability of a Column Under Random Loading, In: *Dynamic Stability of Structures*,'' G. Herrmann, ed., Pergamon Press, New York, pp. 255–265.
[2] Kozin, F., 1969, ''A Survey of Stability of Stochastic Systems,'' Automatica, **5**, No. 1, pp. 95–112.
[3] Lin, Y. K., and Cai, G. Q., 1995, *Probabilistic Structural Dynamics. Advanced Theory and Applications*, McGraw-Hill, New York.
[4] Ariaratnam, S. T., Tam, D. S. F., and Xie, W.-C., 1991, ''Lyapunov Exponents and Stochastic Stability of Coupled Linear Systems Under White Noise Excitation,'' Probab. Eng. Mech., **6**, No. 2, pp. 51–56.
[5] Griesbaum, R., 1999, ''On the Stability of Dynamic Systems with Stochastic Parametric Excitations,'' Ph.D. thesis, University of Karlsruhe, Germany, (in German).
[6] Simon, M., and Wedig, W., 2001, ''Stochastic Stability of Elastic Structures-Quantification of Uncertainties by Lyapunov Exponents,'' in *Structural Safety and Reliability*, R. Corotis et al., eds., Swets and Zeitlinger, Amsterdam, pp. 1–7.
[7] Samuels, J. C., 1963, ''The Dynamics of Impulsively and Randomly Varying Systems,'' J. Appl. Mech., **30**, No. 1, pp. 32–42.
[8] Kotulski, Z., and Sobczyk, K., 1988, ''On the Moment Stability of Vibratory Systems with Random Impulsive Excitation,'' Arch. Mech., **40**, pp. 465–476.
[9] Iwankiewicz, R., 2002, ''Dynamic Response of Non-linear Systems to Random Trains of Non-overlapping Pulses,'' presented at *Euromech 413, Stochastic Dynamics of Non-linear Mechanical Systems*, 12–14 June 2000, Palermo, Italy) [Meccanica, **37**, No. 1, pp. 1–12].
[10] Iwankiewicz, R., 2003, ''Dynamic Systems Under Random Impulses Driven by a Generalized Erlang Renewal Process,'' *Proc. of 10th IFIP WG 7.5 Working Conference on Reliability and Optimization of Structural Systems*, March 25–27, 2002, Kansai University, Osaka, Japan, H. Furuta, M. Dogaki, and M. Sakano, eds. Balkema, pp. 103–110.
[11] Snyder, D. L., 1975, *Random Point Processes*, John Wiley, New York.
[12] Iwankiewicz, R., and Nielsen, S. R. K., 1999, ''Advanced Methods in Stochastic Dynamics of Non-linear Systems,'' *Vibration Theory*, Vol. 4, Aalborg University Press, Aalborg, Denmark, ISSN 1395-8232.
[13] Iwankiewicz, R., and Nielsen, S. R. K., 2000, ''Solution Techniques for Pulse Problems in Non-linear Stochastic Dynamics,'' Probab. Eng. Mech., **15**, No. 1, pp. 25–36.
[14] Cramér H., and Leadbetter, M. R., 1955, ''Stationary and Related Stochastic Processes,'' John Wiley, New York.
[15] Arnold, L., 1984, ''A formula connecting sample and moment stability of of linear stochastic systems,'' SIAM (Soc. Ind. Appl. Math.) J. Appl. Math., **44**, No. 4, pp. 793–802.
[16] F. Kozin and S. Sugimoto, 1977, ''Relation between Sample and Moment Stability for Linear Stochastic Differential Equations,'' *Proc. of the Conference on Stochastic Differential Equations*, D. Mason, ed., Academic Press, New York, pp. 145–162.

Investigation of the Formation and Applications of Ice Powder

D. V. Shishkin

E. S. Geskin
e-mail: gaskin@njit.edu

B. S. Goldenberg

New Jersey Institute of Technology,
Newark, NJ 07102

Water ice powder constitutes a potentially important manufacturing tool. Availability and cleanliness of this powder constitute its major advantage. It was shown that the ice particles could be used as an abrasive in the course of waterjet machining. Although the erosion potential of ice particles is inferior to that of the conventional abrasives, the environmental soundness of ice enables us to expend the use of the ice abrasive jets on food industry, medicine, precision machining, etc. The principal issue in the use of the ice abrasives is particles formation. Analysis of various technologies showed that an effective avenue in particle production is integration of the water freezing and ice decomposition. As the results, the desired flow rate of ice particles at the desired temperature and size distribution can be generated. The objective of the present paper is the experimental investigation of the production of ice particles. An experimental setup was constructed and used for particles fabrication at controlled conditions. The acquired information was applied for the analysis of the phenomena leading to the particles formation. As a result a hypothetical mechanism of the ice decomposition was suggested and validated. The experiments involving the decontamination of the electronic devices, semiconductors, fabric, leather, food products, polished metal, soft plastics, rusted auto parts, etc., were carried out in order to demonstrate the potential application of the ice blasting.
[DOI: 10.1115/1.1795223]

1 Introduction

Unique properties of the water ice determine its potential manufacturing applications. First, water ice is a readily available, inexpensive material, which, at least in principle, can be used as a green manufacturing tool. Only water, electricity, and refrigerant (if a cooling apparatus is not available) are needed for the fabrication of this tool, which can be produced ''just in time.'' Second, the use of ice tools will practically prevent pollution and eliminate workpiece contamination. Because of this, one of the most promising applications of the ice particle is cleaning technology.

Current cleaning processes are based on the use of chemicals or sand abrasive-water blasting and, thus, bring about heavy environmental pollution. The ice-air blasting constitutes a unique cleaning technology that generates practically no off-products, thus has no negative environmental impact. The use of ice blasting for such diverse operations as graffiti removal, food cleaning, car washing etc., will result in the reduction of pollution and, thus, improvement of the quality of life in urban areas. Ice blasting can effectively eliminate the consequences of chemical and biological attacks. The fine ice powder will constitute an effective medical tool.

The applications above are feasible if and only if the ice particle will be readily available for users. The objective of this study was development of a practical technology for particles production. Several technologies, including decomposition of solid ice, freezing of water droplets, and a combination of water freezing and ice decomposition, were tested. The ice decomposition was proven to be the most effective technology. The logistic of the process is straightforward and simple. The process is inexpensive and allows accurate control of particle size and temperature and, therefore, is able to address the needs of the industry.

The formation and decomposition of water ice was a subject of numerous studies, and a number of theoretical techniques were suggested for process description. The phenomenon of ice formation under normal conditions was, for example, fairly well investigated by Sanderson [1] and Hobbs [2]. However, no information is available about ice behavior in the course of integration of the solidification and decomposition. The acquisition of such information is the objective of this research. The work involved the experimental examination of the particles formation. The obtained information was used for numerical and phenomenological process description. In order to demonstrate potential ice application, the produced-powder, highly sensitive surfaces were treated.

2 Experimental Setup

The setup for investigation of the ice powder formation in the course of freezing is shown in Fig. 1. The system consists of the following functionally separated blocks:

- ice-making block, which includes the evaporator, water and cooling media precision control valves, auger, auger driver, and sealing and cooling apparatus
- ice-unloading mechanism, which includes the driver for nozzle-block traverse motion and drivers for nozzle-block springs feeder
- nozzle block, which includes parallel-situated nozzles and nozzle-supporting device

The system Fig. 1 constitutes a modified commercial icemaker of the Hoshizaki Company of America [3]. Thus the dimensions of the auger, heat exchanger, water supply port, etc., were determined by the design of the Hoshizaki Icemaker 1. The coolant 2 and water control 3 valves determined the rate of the cooling media and water supply to the system. New auger driver 4 was also incorporated into the system in order to increased the torque and prevent ice jamming. The rotation momentum of the auger 5 is provided via a gearbox 6 with gear-ratio 1:100. Cooling media was flowing through the evaporator internal channels 7.

The ice-unloading mechanism 8 coercively delivered ice particles to the abrasive port of the nozzles preventing conduits 9 and nozzle ports 10 from clogging. At the outlet of the heat exchanger, the powder was entrained by the unloading mechanism that directed it to the nozzle block 11. The nozzle block consisted of two

Contributed by the Applied Mechanics Division of THE AMERICAN SOCIETY OF MECHANICAL ENGINEERS for publication in the ASME JOURNAL OF APPLIED MECHANICS. Manuscript received by the Applied Mechanics Division, July 2, 2003; final revision, June 15, 2004. Associate Editor: D. A. Siginer. Discussion on the paper should be addressed to the Editor, Prof. Robert M. McMeeking, Journal of Applied Mechanics, Department of Mechanical and Environmental Engineering, University of California—Santa Barbara, Santa Barbara, CA 93106-5070, and will be accepted until four months after final publication of the paper itself in the ASME JOURNAL OF APPLIED MECHANICS.

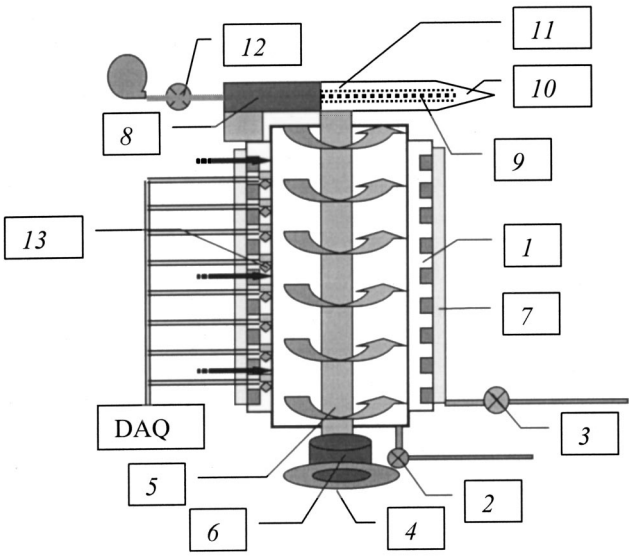

Fig. 1 Schematic of experimental setup: 1—icemaker, 2—cooling media control valve, 3—water control valve, 4—auger driver, 5—auger, 6—auger driver gearbox, 7—evaporator internal channels, 8—ice unloading mechanism, 9—conduits, 10—nozzle ports, 11—nozzle block, 12—air flow control valve, 13—sensors, DAQ—data acquisition card

air guns connected in parallel and a special nozzle-supporting device. The high-pressure air supply rate was also monitored by an air flow meter 12. The ice air jet was formed and directed to the substrate surface.

The system was also equipped with sensors 13 for monitoring the water flow rate, water temperature at the inlet, the temperature of the wall separating the water and cooling media, and the ice temperature at the exit of heat exchanger. The system was equipped with a device for rapid extraction of the auger in order to examine ice distribution during the freezing, fragmentation, and solid-state cooling (Fig. 2). A photograph of the system in operation is presented in Fig. 3.

3 Experimental Investigation of Particles Formation

Several experiments were conducted in order to determine correlation between process conditions and particles properties. The water flow rate ranges from 0 to 200 ml/min. The cooling media flow rates differed for liquid nitrogen and Galden HT-55 coolant: ~9.8 l/min for liquid nitrogen and 9.88 l/min for the Galden HT-55 cooling liquid. The temperatures of the liquid nitrogen and Galden HT-55 cooling liquid were −196°C and −72°C, respectively.

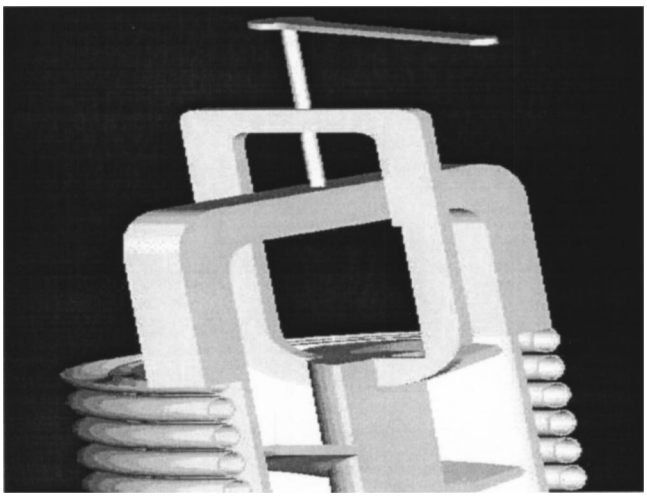

Fig. 2 Device for auger rapid extraction

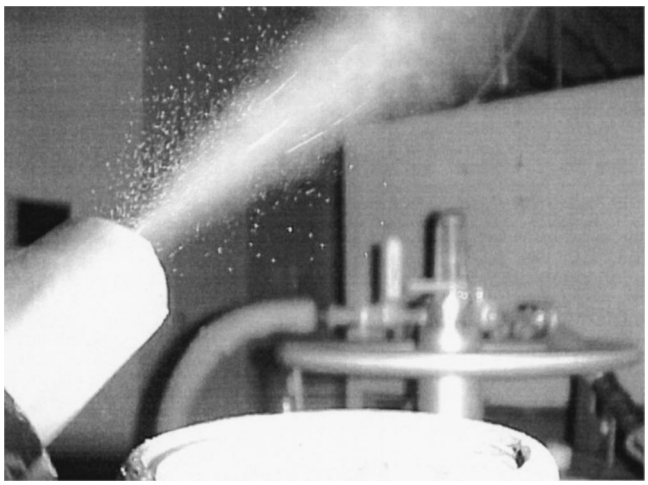

Fig. 3 System in operation

The granulometric composition of the ice abrasive as a function of water flow rate was determined using the series of digital images and the Image Tool statistical package developed by University of South Carolina. Water, cooling media types, and flow rates served as the main process control parameters. The auger was extracted from the evaporator after the fixed-cooling time periods and ice-particles formation phases were monitored and documented (Fig. 4). The ice structure was studied as well as crack and granulometric distribution along its way to the exit of the evaporator. The ice behavior under dynamically applied compressive and shear stresses and fast cooling was investigated. The visual observation of process of ice-powder formation was conducted.

The actual time of ice-plug solidification for the distinct water flow rates was established through the auger driver current-time diagram presented on Fig. 5. The ice-plug solidification and thermal expansion time is characterized by the duration of half of ascending wave on the current-time diagram. The fluctuating character of ice-powder flow at the evaporator outlet supported this conclusion. Distinct frequencies of these oscillations for different water flow rates were also observed. The frequency of ice-powder oscillation was measured and compared with the drivers' current oscillations. They did directly correspond to the ice-powder flow fluctuations. Then the conclusion could be drawn that the descending half of the current wave corresponded to the plug fragmentation.

Experimental results have shown that the granulometric composition of ice abrasive is directly related to the water flow rate (Fig. 6) as well as the ice temperature at outlet point of the evaporator (Fig. 7). The set of experiments was conducted to monitor the above dependence and incorporate it into the technology of ice abrasive production.

4 Phenomenology of Particles Formation

The nucleation of cracks under compressive stress occurs generally due to dislocation pileup at the grain boundaries and relief of stress concentration by parting along the grain boundaries. The phenomenon of crack nucleation has been well investigated for low to moderate loading conditions, and this study indicates that crack nucleation is well described by application of the delayed elastic strain criterion [1].

When ice is subjected to a stress it initially deforms in three distinct ways: it undergoes an immediate elastic strain ε_e, a tran-

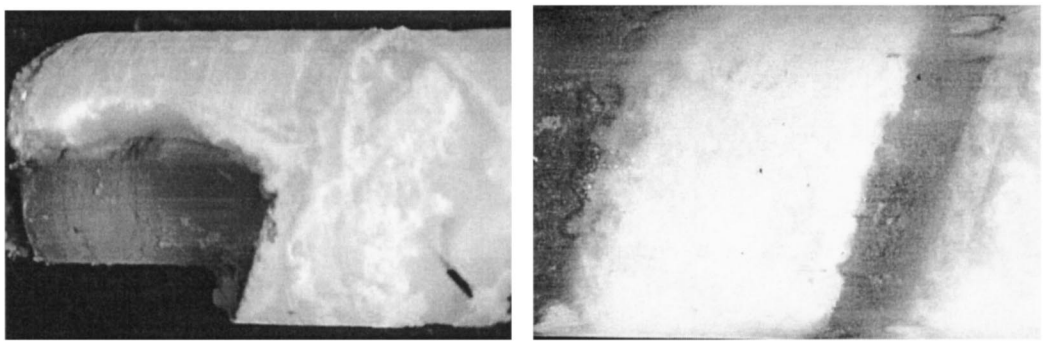

Fig. 4 Photograph of the ice-plug initial (*a*) and final (*b*) formation phases

sient time-dependent delayed elastic strain ε_d, and a time-dependent nonlinear viscous creep strain ε_v. The ''delayed elastic'' strain ε_d also is referred as primary creep and is largely recoverable on unloading; the ''viscous'' strain ε_v is referred to as the secondary creep and is permanent.

To describe this stress-strain behavior for granular ice, well-verified constitutive laws exist. Once the stage of apparently stable secondary creep has been reached and all transient creep effects have become negligible, the deformation process becomes more complex again, and a stage of tertiary creep may be entered.

For high-stresses nucleation conditions, there introduced some alternative nucleation criterion [2] that assumes that crack nucleation under compressive stress occurs simply when the lateral tensile strain induced by Poisson expansion reaches a level already defined as critical for tensile crack nucleation.

Based on the experimental results described above the hypothetical mechanism of the ice plug fragmentation was suggested (Fig. 8). According to this hypothesis, the ice nucleation initiates as soon as the liquid water meets the evaporator wall having temperature of −196°C. The initial stage of ice-plug formation is presented in Fig. 4. According to Sanderson [1], the rapid conditions of ice-plug nucleation and propagation suggested that isotropic ice polycrystalline structure has formed. Due to sufficient temperature gradient during solidification, a multilayer ice-plug pattern was formed throughout the ice plug volume and could be visually observed in Fig. 4. The supercooling and rate of heat removal at various sites of the plug determine the distribution of ice properties. At the next stage of freezing, ice undergoes the following transformations: the frozen boundary-layer thermal conductivity is sufficiently higher than that for water and the ice-plug formation process accelerated along with the generation of intensive thermal expansion stress. Ice-plug expansion imposed high pressure and shear stresses on the immovable boundaries. However, the ice plug can freely expand along the auger helical way. This phenomenon was clearly indicated by the current-time diagram and corresponds to the ascending part of the current cycle.

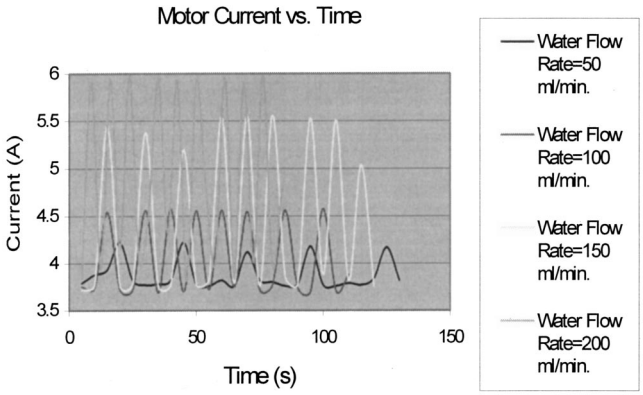

Fig. 5 Auger driver current versus time for distinct water flow rates

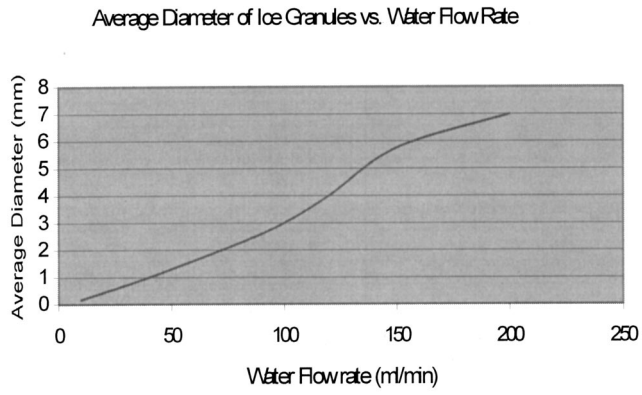

Fig. 6 Average diameter of ice granules versus water flow rate at the evaporator outlet

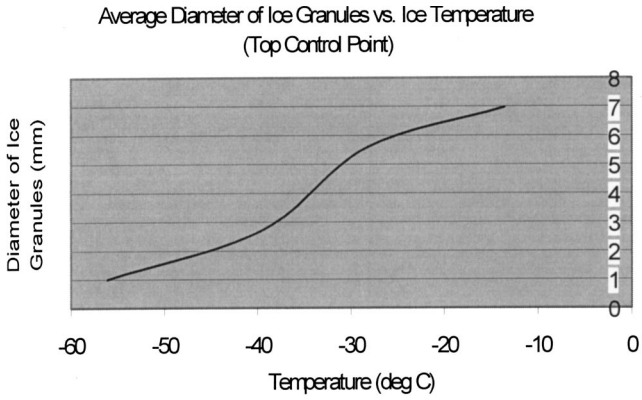

Fig. 7 Average diameter of ice granules versus ice temperature at the evaporator outlet

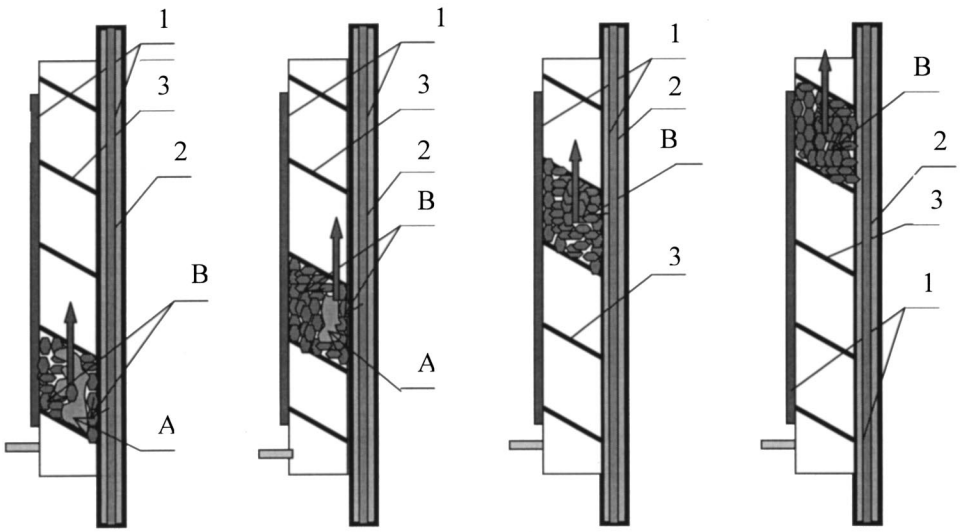

Fig. 8 Schematic of the hypothetical mechanism of ice-plug fragmentation

According to Sanderson [1], experiments conducted for moderate thermal stress conditions the ice-plug polycrystalline structure undergo the recrystallization process with tensile zone formation along the grain boundaries. It would be logical to make an assumption that under high thermal stress conditions, polycrystalline ice structure behaved similarly. Now the plug is populated with a wide variety of cracks having the length of the order of the grain size, lying at various angles clustered around the loading axis [1]. The ice-plug decomposition starts under combined thermal expansion conditions and dynamically applied stresses along with the transition of the ice plug to a brittle mode due to the ice plug core supercooling process. The tunnel and wing crack propagated along the grain boundaries were clearly observed during the extractions of ice plug.

The shearing stress of the necessary magnitude provided by auger rotation finalizes the decomposition of the plug (Fig. 9). The stage finalizes the procedure of ice-powder formation. The ice powder continued moving along the helical way toward the evaporator outlet. The supercooling process continued without any substantial changes in the granulometric composition. The development of this technology will enable producing low-cost fine powder. As the result it could be adopted by the semiconductor, electronics, and biomedical industries.

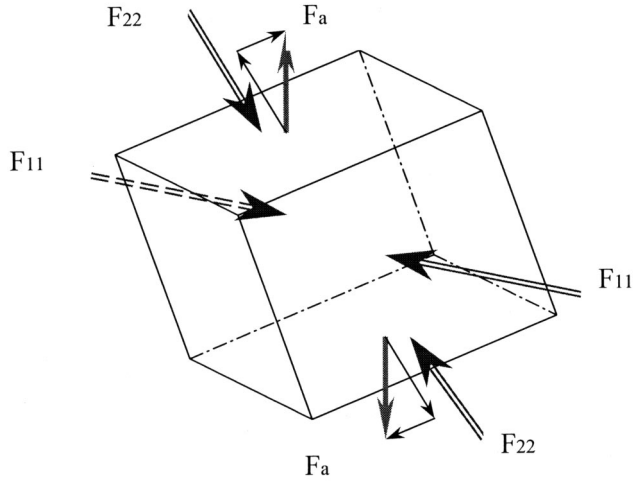

Fig. 9 Forces involved in ice-plug fragmentation: F_{11}, F_{22}—principal compressive forces, Fa—auger generated forces

5 Cleaning of Sensitive Surfaces: Case Studies

A number of experiments were carried out in order to demonstrate the potential applications of the ice particles. In the course of these experiments, ice particles were entrained in an air stream and form ice-airjet (IAJ). This jet was used for cleaning and decoating of various surfaces. The parameters of ice-airjet were in the following range: the average diameter of ice particles produced by IAJ system varies from 0.25 mm for biomedical applications to ~3 mm for the majority of electronics and industrial cleaning cases; water and ice flow rates ranged from 0 to 200 ml/min; the air pressure was 580 kPa (85 psi) with flow rate of 0.566 m^3/min; ice temperature variation before entrainment to the nozzle was from −50°C for biomedical cleaning to −80°C for the industrial cleaning cases; the standoff distance varied from 5 mm for most electronic and photonic cases to 25 mm for biomedical applications.

Different electronic devises (computers, calculators, electronic games, and watches) were disassembled, and electronic boards were contaminated by grease and metal powder. Then the boards were cleaned and reassembled. The computers, calculators, and watches worked normally. Other experiments involved degreasing, depainting and deicing of liquid crystals, polished metals, optical glass, fabric; removal emulsion from a film, etc. The biomedical applications of the IAJ were also investigated. In the course of the experiments, chicken and pork skin was treated by IAJ. The feasibility of removal of the epidermis layer without damaging the underneath-laying layers of the skin was demonstrated. Extremely fine ice abrasive of average diameter of 300 microns was used for these purposes.

The feasibility of the damage-free and pollution-free decontamination of highly sensitive surfaces was demonstrated. A generic environmentally friendly surface-processing technology is emerging as the result of the above experiments. Figure 10 represents photographs of basic types of deposit and substrates, which were treated in the course of IAJ experiments.

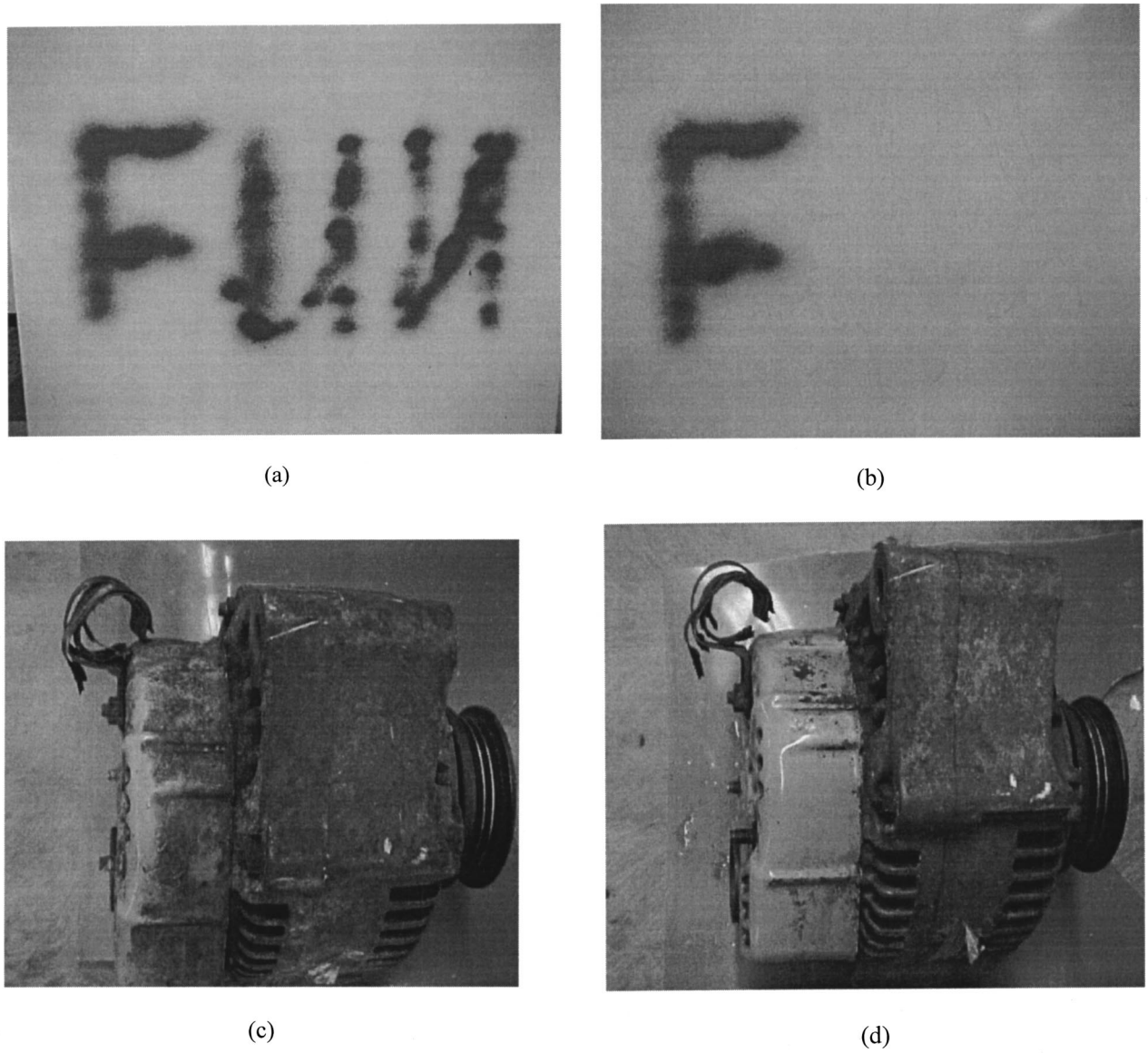

Fig. 10 Photographs of *a*) graffiti painting, *b*) graffiti painting removed with ice-airjet; c) heavily greased machined part, *c*) grease removed from the part with ice-airjet

6 Conclusion

The performed study demonstrated that ice constitutes a viable abrasive material, while a 4N Auger type heat exchanger is a competitive device for particles production. Of course, if inexpensive ice is readily available, for example in the Arctic, the crushing technology is the most advantageous. In a more general case when ice should be fabricated, the icemaker shown in Fig. 1 is a more competitive device for particles production. One of the strong advantages of this device is its feasibility to control particle size by the variation of solidification conditions. Thus, it can be used to produce ''just-in-time, just-needed'' abrasives. The modified icemaker can be also used for production of particles from materials different from water ice.

Acknowledgment

The work was supported by the NSF Grant No. DMI9900247.

References

[1] Sanderson, T. J., 1988, *Ice Mechanics: Risks to Offshore Structures*, Graham & Trotman, London, UK.
[2] Hobbs, P. V., 1974, *Ice Physics*, Clarendon Press, Oxford.
[3] Hoshizaki America, 1998, Manual, Hoshizaki America, Inc., Peachtree City, GA.

Three-Dimensional Vibration Analysis of Rectangular Plates With Mixed Boundary Conditions

D. Zhou
Department of Mechanics and Engineering Science,
Nanjing University of Science and Technology,
Nanjing 210014, People's Republic of China

Y. K. Cheung[1]
e-mail: hreccyk@hkucc.hku.hk

S. H. Lo

F. T. K. Au

Department of Civil Engineering,
The University of Hong Kong,
Pokfulam Road,
Hong Kong

Three-dimensional vibration solutions are presented for rectangular plates with mixed boundary conditions, based on the small strain linear elasticity theory. The analysis is focused on two kinds of rectangular plates, the boundaries of which are partially fixed while the others are free. One of those studied is a rectangular plate with partially fixed boundaries symmetrically arranged around four corners and the other one is a rectangular plate with partially fixed boundaries around one corner only. A global analysis approach is developed. The Ritz method is applied to derive the governing eigenvalue equation by minimizing the energy functional of the plate. The admissible functions for all displacement components are taken as a product of a characteristic boundary function and the triplicate Chebyshev polynomial series defined in the plate domain. The characteristic boundary functions are composed of a product of four components of which each corresponds to one edge of the plate. The R-function method is applied to construct the characteristic boundary function components for the edges with mixed boundary conditions. The convergence and comparison studies demonstrate the accuracy and correctness of the present method. The influence of the length of the fixed boundaries and the plate thickness on frequency parameters of square plates has been studied in detail. Some valuable results are given in the form of tables and figures, which can serve as the benchmark for the further research. [DOI: 10.1115/1.1827250]

Keywords: Eigenfrequency, Elasticity Solution, Mixed Boundary Conditions, R-Function, Ritz Method, Thick Rectangular Plate, Three-Dimensional Vibration

1 Introduction

Rectangular plates [1] have wide applications in various branches of engineering such as the floor slabs and pile caps in structural engineering, printed circuit boards and solar panels in electrical engineering, and so on. In some cases, the boundary supports of a plate may be discontinuous, and thus exert a significant influence on the mechanical properties of the structures. A number of publications on rectangular plates with mixed edge conditions can be found in the literature. Various analytical and numerical methods have been adopted in the vibration analysis. Using the superposition method, Gorman [2–4] studied, respectively, the vibration frequencies of thin and moderately thick rectangular plates with mixed edge supports such as point supports and partially clamped supports. Keer and Stahl [5] developed the dual series solutions to study the free vibration of rectangular thin plates with mixed edge conditions, which are finally reduced to the homogeneous Fredholm integral equations of the second kind. Narita [6] gave the trigonometric series-type solutions for the orthotropic rectangular thin plates with mixed boundary conditions. Torvik [7] developed a variational approach to analyze the dynamics of rectangular thin plates with mixed or discontinuous boundary conditions. Fan and Cheung [8] used the spline finite strip method to analyze the vibration of rectangular thin plates with complex edge conditions. Liew and his co-workers [9,10] studied the free vibration of isotropic and anisotropic rectangular thin plates with mixed supports by using the domain decomposition technique combining with the weighted residual method along the interconnecting boundaries of subdomains. Su and Xiang [11] presented a nondiscrete approach for vibration and buckling analysis of rectangular thin plates with mixed edge supports. Kim and Dickinson [12], and Kitipornchai et al. [13] used the Lagrangian multiplier method to study the free vibration of point-supported thin and moderately thick plates, respectively. Wei et al. [14] used the discrete singular convolution algorithm to study the natural frequencies of rectangular thin plates with mixed boundary conditions. Liew et al. [15] analyzed Mindlin rectangular plates with internal point-supports by directly adding the geometric constraints of the point-supports to the admissible functions. Moreover, the differential quadrature method [16,17] has been applied to the vibration analysis of Kirchhoff and Mindlin rectangular plates with mixed boundary conditions, respectively.

Both the classical thin plate theory and moderately thick plate theory are approximate theories by imposing some assumptions on the deformation of a plate, especially on the strain and/or stress distribution along the thickness of the plate. These assumptions reduce the dimensions of the plate problem from 3 to 2, therefore greatly simplifying the formulation and solution in both analytical and computational methods. However, they also introduce errors at the same time. The three-dimensional (3D) analysis on the basis of small-strain linear elasticity theory does not rely on any hypotheses involving the kinematics of deformation. Such analysis not only provides realistic results but also brings out physical insights, which cannot otherwise be predicted by the two-dimensional (2D) analysis.

Searching the literature, not a solution of 3D vibration for plates with mixed boundary conditions has been found. However, in the recent two decades, some attempts have been made for 3D vibration analysis of rectangular plates with uniform boundary conditions. Srinivas et al. [18] gave the exact analytical solution of rectangular plates with four simply-supported edges. Cheung and Chakrabarti [19] used the finite layer method to study the

[1]To whom correspondence should be addressed.

Contributed by the Applied Mechanics Division of THE AMERICAN SOCIETY OF MECHANICAL ENGINEERS for publication in the ASME JOURNAL OF APPLIED MECHANICS. Manuscript received by the Applied Mechanics Division, July 23, 2003; final revision, June 30, 2004. Associate Editor: N. Sri Namachchivaya. Discussion on the paper should be addressed to the Editor, Prof. Robert M. McMeeking, Journal of Applied Mechanics, Department of Mechanical and Environmental Engineering, University of California—Santa Barbara, Santa Barbara, CA 93106-5070, and will be accepted until four months after final publication in the paper itself in the ASME JOURNAL OF APPLIED MECHANICS.

vibration of thick rectangular plates with general boundary conditions. Hutchinson and Zillimer [20] and Fromme and Leissa [21] used different series solutions to analyze the 3D free vibration of a completely free parallelepiped. Malik and Bert [22] and Liew and Teo [23] used the differential quadrature method to analyze the 3D vibration of rectangular thick plates. It should be mentioned that in the 3D vibration analysis of rectangular plates, the Ritz method has demonstrated its advantages in both accuracy and computational cost. Leissa and Zhang [24] and Lim [25] used the simple algebraic polynomials and Liew et al. [26–28] used the orthogonal polynomials as admissible functions to study the 3D vibration characteristics of rectangular plates. Recently, the authors [29] used the Chebyshev polynomials [30] as the main admissible functions to analyze the 3D vibration of rectangular plates with various uniform boundary conditions. High accuracy, stable numerical computation, and rapid convergence have been observed.

In this paper, a global solution approach based on the Ritz method has been presented for the 3D vibration analysis of rectangular plates with mixed boundary conditions. The Chebyshev polynomials multiplied by a characteristic boundary function are taken as the admissible functions. The characteristic boundary function satisfies the essential geometric boundary conditions of the plates, but it takes no account of the stress boundary conditions. Since the boundary characteristic functions of the edges with mixed boundary conditions (i.e., the mixed edges) cannot be described by simple algebraic polynomials, the method given in Ref. [29] to construct boundary characteristic functions for uniform edges is not applicable to the complicated boundary conditions in the present study. Instead, the R-function method is applied to construct the characteristic boundary function components on the edges with mixed boundary conditions. Some valuable results have been obtained.

2 Modeling of the Plate

Consider a rectangular plate with partially fixed edges symmetrically disposed around four corners and the other edges free as shown in Fig. 1(*a*). It is assumed that the parts that are fixed have displacements in all three directions completely restrained. The plate has a length $2a$, a width $2b$ and a uniform thickness h. The lengths of the free boundaries at the edges $y=\pm b$ are both equal to $2a_0$. Similarly, the widths of the free boundaries at the edges $x=\pm a$ are both equal to $2b_0$. The plate geometry and dimensions are defined with respect to a Cartesian coordinate system (x,y,z), the origin of which is at the center of the plate and the axes are parallel to the edges of the plate. The corresponding displacement component at a generic point are u, v, and w in the x, y, and z directions, respectively. In the particular case of $a_0=a$ and $b_0=b$, the plate is only fixed at the four corners. It is assumed that the plate is made up of isotropic material. Considering the symmetry of boundary conditions, the vibration characteristics of the plate can be distinctly divided into eight categories. Using the symbol "A" to define the antisymmetric mode and the symbol "S" to define the symmetric mode, the vibration modes of a plate can be decomposed into categories AAA, AAS, ASA, ASS, SAA, SAS, SSA, and SSS, where the three capital letters correspond to the vibration mode in the x, y, and z directions, respectively. In such a case, only a quarter of the plate should be taken for the analysis, as shown in Fig. 1(*b*) where the shaded areas denote fixed edges with displacements in all three directions completely restrained. The geometric boundary conditions at the faces $x=0$ and $y=0$ for different categories of vibration modes are given in Table 1. Moreover, as a consequence, Fig. 1(*b*) also describes a plate partially fixed around one corner only. In such a case, the length and width of the plate are a and b, respectively, and the geometric boundary conditions at the faces $x=0$ and $y=0$ are given in Table 2.

For simplicity and convenience in mathematical formulation, the following nondimensional parameters for the plate shown in Fig. 1(*b*) are introduced

$$\xi=2x/a-1; \quad \eta=2y/b-1; \quad \zeta=2z/h \tag{1}$$

where $0\leqslant x\leqslant a$ and $0\leqslant y\leqslant b$. Using the earlier coordinate transformations, the rectangular hexahedral domain of the plate in Fig. 1(*b*) can be mapped into a cubic domain as shown in Fig. 1(*c*) where $\xi_0=2a_0/a-1$ and $\eta_0=2b_0/b-1$.

3 Basic Formulas

Based on the 3D small strain linear elasticity theory and using the dimensionless coordinates defined in Eq. (1), the maximum energy functional Π of a rectangular plate under free vibration can be written in the volume integral form as

$$\Pi=\Lambda_{\max}-T_{\max} \tag{2}$$

where

$$\Lambda_{\max}=\frac{Eh}{4\lambda(1+\nu)}\int_{-1}^{1}\int_{-1}^{1}\int_{-1}^{1}\left(\frac{\nu}{1-2\nu}\overline{\Lambda}_1+\overline{\Lambda}_2+\frac{1}{2}\overline{\Lambda}_3\right)d\zeta d\eta d\xi;$$
$$T_{\max}=\frac{\rho}{16}abh\omega^2\int_{-1}^{1}\int_{-1}^{1}\int_{-1}^{1}(U^2+V^2+W^2)d\zeta d\eta d\xi \tag{3}$$

in which E is the Young's modulus, ν is the Poisson's ratio, and ρ is the mass density per unit volume, ω denotes the natural frequency of the plate and

$$\overline{\Lambda}_1=(\overline{\varepsilon}_{\xi\xi}+\overline{\varepsilon}_{\eta\eta}+\overline{\varepsilon}_{\zeta\zeta})^2; \quad \overline{\Lambda}_2=\overline{\varepsilon}_{\xi\xi}^2+\overline{\varepsilon}_{\eta\eta}^2+\overline{\varepsilon}_{\zeta\zeta}^2;$$
$$\overline{\Lambda}_3=\overline{\varepsilon}_{\xi\eta}^2+\overline{\varepsilon}_{\xi\zeta}^2+\overline{\varepsilon}_{\eta\zeta}^2,$$
$$\overline{\varepsilon}_{\xi\xi}=\frac{\partial U}{\partial\xi}; \quad \overline{\varepsilon}_{\eta\eta}=\lambda\frac{\partial V}{\partial\eta}; \quad \overline{\varepsilon}_{\zeta\zeta}=\frac{\lambda}{\gamma}\frac{\partial W}{\partial\zeta},$$
$$\overline{\varepsilon}_{\xi\eta}=\lambda\frac{\partial U}{\partial\eta}+\frac{\partial V}{\partial\xi}; \quad \overline{\varepsilon}_{\xi\zeta}=\frac{\lambda}{\gamma}\frac{\partial U}{\partial\zeta}+\frac{\partial W}{\partial\xi}; \quad \overline{\varepsilon}_{\eta\zeta}=\frac{\lambda}{\gamma}\frac{\partial V}{\partial\zeta}+\lambda\frac{\partial W}{\partial\eta},$$
$$\lambda=a/b; \quad \gamma=h/b \tag{4}$$

In the present analysis, each of the displacement amplitude functions $U(\xi,\eta,\zeta)$, $V(\xi,\eta,\zeta)$ and $W(\xi,\eta,\zeta)$ is taken, respectively, in the form of triplicate series of Chebyshev polynomials multiplied by a characteristic boundary function which ensures that the displacement component satisfies the essential geometric boundary conditions of the plate, i.e.

$$U(\xi,\eta,\zeta)=F_u(\xi,\eta)\sum_{i=1}^{\infty}\sum_{j=1}^{\infty}\sum_{k=1}^{\infty}A_{ijk}P_i(\xi)P_j(\eta)P_k(\zeta);$$
$$V(\xi,\eta,\zeta)=F_v(\xi,\eta)\sum_{l=1}^{\infty}\sum_{m=1}^{\infty}\sum_{n=1}^{\infty}B_{lmn}P_l(\xi)P_m(\eta)P_n(\zeta);$$
$$W(\xi,\eta,\zeta)=F_w(\xi,\eta)\sum_{p=1}^{\infty}\sum_{q=1}^{\infty}\sum_{r=1}^{\infty}C_{pqr}P_p(\xi)P_q(\eta)P_r(\zeta) \tag{5}$$

where A_{ijk}, B_{lmn}, and C_{pqr} are the unknown coefficients. $P_s(\chi)$ $(s=1,2,3\ldots;\ \chi=\xi,\ \eta,\ \zeta)$ is the one-dimensional sth Chebyshev polynomial which can be written in terms of cosine functions as follows

$$P_s(\chi)=\cos[(s-1)\arccos(\chi)]; \quad (s=1,2,3,\ldots) \tag{6}$$

Note that $F_u(\xi,\eta)$, $F_v(\xi,\eta)$, and $F_w(\xi,\eta)$ are the characteristic boundary functions, respectively, corresponding to the displacements u, v, and w. They should be continuous and differentiable. However, they cannot take zero value at any point in the domain or on the boundaries except for the boundaries with given zero constraints.

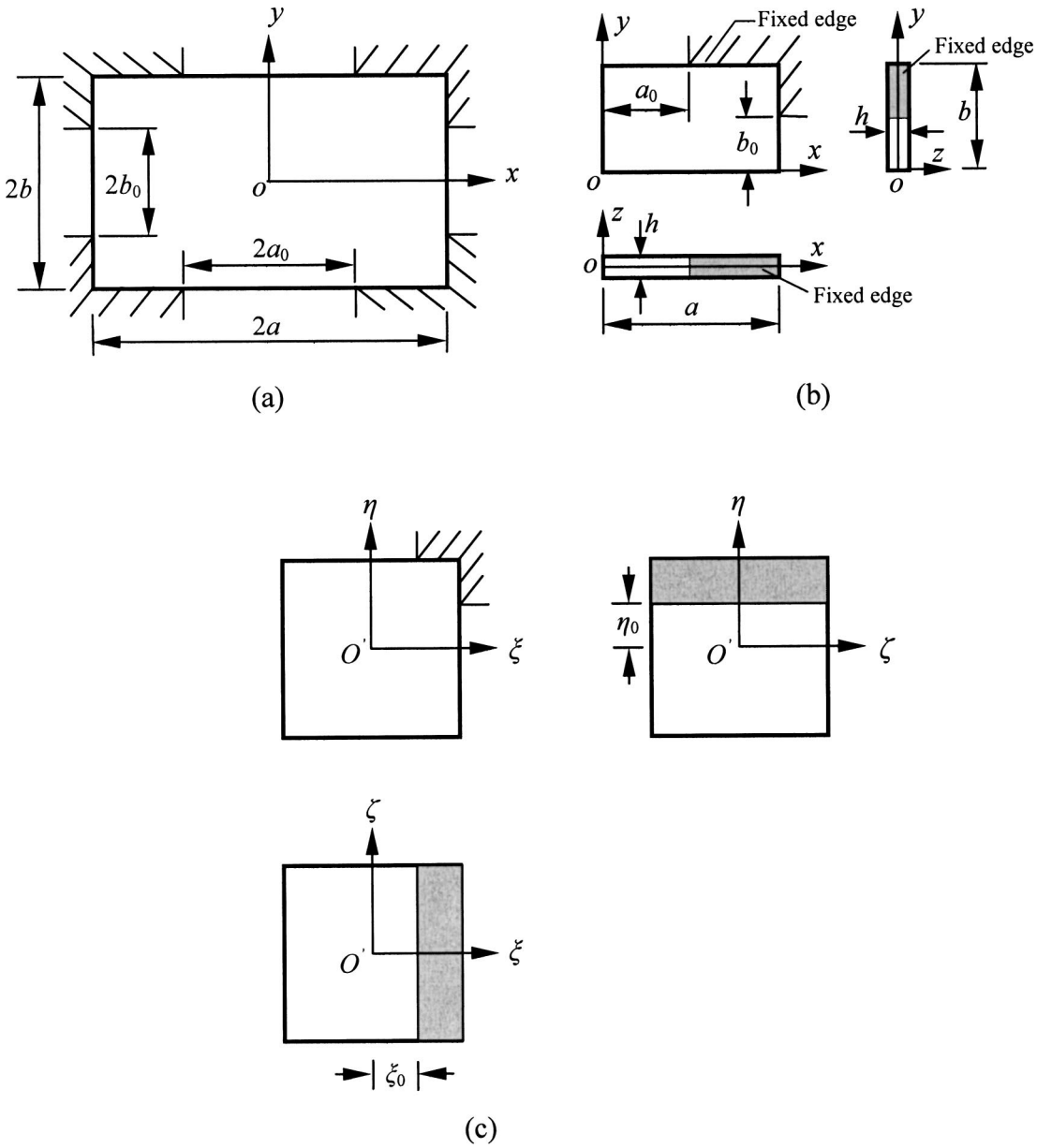

Fig. 1 A rectangular plate with mixed boundary conditions: (*a*) planform of the plate, (*b*) views of the quarter plate, (*c*) views of cubic domain after mapping

It should be mentioned that comparing to other polynomial series, the Chebyshev polynomial series [30] shows a lot of excellent properties in the approximation of functions, such as the rapid convergence and the numerical robustness. Substituting Eq. (6) into Eqs. (2)–(4) and minimizing the functional Π with respect to the coefficients of the admissible functions, i.e.

$$\frac{\partial \Pi}{\partial A_{ijk}} = 0, \quad \frac{\partial \Pi}{\partial B_{lmn}} = 0, \quad \frac{\partial \Pi}{\partial C_{pqr}} = 0$$
$$(i,j,k,l,m,n,p,q,r = 1,2,3,\ldots) \tag{7}$$

leads to the following governing eigenvalue equation in matrix form

Table 1 The geometric boundary conditions at the faces $x=0$ and $y=0$ for plates partially fixed around four corners

	Symmetric modes			Antisymmetric modes		
Boundary	u	v	w	u	v	w
$x=0$	Zero	Free	Free	Free	Zero	Zero
$y=0$	Free	Zero	Free	Zero	Free	Zero

Table 2 The geometric boundary conditions at the faces $x=0$ and $y=0$ for plates partially fixed around one corner only

Boundary condition	$x=0$			$y=0$		
	u	v	w	u	v	w
Fixed	Zero	Zero	Zero	Zero	Zero	Zero
Free	Free	Free	Free	Free	Free	Free
Hard S-S*	Free	Zero	Zero	Zero	Free	Zero
Soft S-S	Free	Free	Zero	Free	Free	Zero
Sliding	Zero	Free	Free	Free	Zero	Free

*Note: S-S means simply-supported boundary.

$$\left(\begin{bmatrix} [K_{uu}] & [K_{uv}] & [K_{uw}] \\ [K_{uv}]^T & [K_{vv}] & [K_{vw}] \\ [K_{uw}]^T & [K_{vw}]^T & [K_{ww}] \end{bmatrix} - \Delta^2 \begin{bmatrix} [M_{uu}] & 0 & 0 \\ 0 & [M_{vv}] & 0 \\ 0 & 0 & [M_{ww}] \end{bmatrix} \right) \begin{Bmatrix} \{A\} \\ \{B\} \\ \{C\} \end{Bmatrix} = \begin{Bmatrix} \{0\} \\ \{0\} \\ \{0\} \end{Bmatrix} \tag{8}$$

in which $\Delta=\omega a\sqrt{\rho/E}$, and $[K_{ij}]$ and $[M_{ii}]$ $(i,j=u,v,w)$ are the stiffness and diagonal mass submatrices, respectively. The vectors $\{A\}$, $\{B\}$, and $\{C\}$ contain the unknown coefficients A_{ijk}, B_{lmn}, and C_{pqr}. Solving Eq. (8) yields the frequency parameters Δ and the mode shape corresponding to each eigenvalue.

The vibration modes of a uniform plate can invariably be divided into two categories: flexural modes (antisymmetric ones in the thickness direction) and extensional modes (symmetric ones in the thickness direction). In Eq. (5), by taking $k=1,3,5,\ldots,$ $n=1,3,5,\ldots,$ and $r=2,4,6,\ldots$ for the symmetric modes in the ζ direction, and taking $k=2,4,6,\ldots,$ $n=2,4,6,\ldots,$ and $r=1,3,5,\ldots$ for the antisymmetric modes in the ζ direction, these two categories of modes in the thickness direction can be separately determined while maintaining the same level of accuracy.

4 Characteristic Boundary Functions

One may observe that Eq. (5) is the key to the construction of the characteristic boundary functions in the Ritz method, which are determined by the geometric boundary conditions of the plate. For fixed edges, the geometric boundary conditions are

$$U=0; \quad V=0; \quad W=0 \tag{9}$$

and for free edges, the stress boundary conditions are

$$\sigma_n=0; \quad \sigma_{\xi\zeta}=0; \quad \sigma_{\eta\zeta}=0 \tag{10}$$

where n denotes the normal direction of the edges.

The authors [29] recently used simple algebraic polynomials as characteristic boundary functions to study the 3D vibration of rectangular plates with uniform boundary conditions and obtained excellent results. However, these simple polynomials cannot model mixed boundary conditions. In the present study, the R-functions [31,32] are used to construct the characteristic boundary functions of the mixed edges. Note that the upper and lower faces of the plates are always free, and therefore there are no geometric restraints for these two faces. For the plate as shown in Fig. 1(*b*), each of the characteristic boundary functions in Eq. (5) can be written as a product of four characteristic boundary function components as follows

$$\begin{aligned} F_u(\xi,\eta)&=F_{u1}(\xi)F_{u2}(\eta)F_{u3}(\xi,\eta)F_{u4}(\xi,\eta), \\ F_v(\xi,\eta)&=F_{v1}(\xi)F_{v2}(\eta)F_{v3}(\xi,\eta)F_{v4}(\xi,\eta), \\ F_w(\xi,\eta)&=F_{w1}(\xi)F_{w2}(\eta)F_{w3}(\xi,\eta)F_{w4}(\xi,\eta) \end{aligned} \tag{11}$$

where $F_{u1}(\xi)$, $F_{v1}(\xi)$, and $F_{w1}(\xi)$ are the characteristic boundary function components at $\xi=-1$, respectively, corresponding to displacement amplitude functions $U(\xi,\eta,\zeta)$, $V(\xi,\eta,\zeta)$, and $W(\xi,\eta,\zeta)$. The characteristic boundary function components $F_{u2}(\eta)$, $F_{v2}(\eta)$, and $F_{w2}(\eta)$ are those at $\eta=-1$, respectively, corresponding to displacement amplitude functions $U(\xi,\eta,\zeta)$, $V(\xi,\eta,\zeta)$, and $W(\xi,\eta,\zeta)$. Similarly, $F_{u3}(\xi,\eta)$, $F_{v3}(\xi,\eta)$, and $F_{w3}(\xi,\eta)$ are those at $\xi=1$ while $F_{u4}(\xi,\eta)$, $F_{v4}(\xi,\eta)$, and $F_{w4}(\xi,\eta)$ are those at $\eta=1$. The characteristic boundary function components [29] at the boundaries $\xi=-1$ and $\eta=-1$ can be easily obtained because of the consistency of the boundary conditions at these two edges, which are given in Tables 3 and 4, respectively, for the two kinds of rectangular plates considered here. However, the earlier approach for uniform boundary conditions

Table 3 The characteristic boundary function components of plates partially fixed around four corners at the boundaries $\xi=-1$ and $\eta=-1$

Category of mode	Boundary $\xi=-1$			Boundary $\eta=-1$		
	$F_{u1}(\xi)$	$F_{v1}(\xi)$	$F_{w1}(\xi)$	$F_{u2}(\eta)$	$F_{v2}(\eta)$	$F_{w2}(\eta)$
A	1	$1+\xi$	1	$1+\eta$	1	1
S	$1+\xi$	1	1	1	$1+\eta$	1

Table 4 The characteristic boundary function components of plates partially fixed around one corner at the boundaries $\xi=-1$ and $\eta=-1$

Boundary condition	Boundary $\xi=-1$			Boundary $\eta=-1$		
	$F_{u1}(\xi)$	$F_{v1}(\xi)$	$F_{w1}(\xi)$	$F_{u2}(\eta)$	$F_{v2}(\eta)$	$F_{w2}(\eta)$
Fixed	$1+\xi$	$1+\xi$	$1+\xi$	$1+\eta$	$1+\eta$	$1+\eta$
Free	1	1	1	1	1	1
Hard S-S	1	$1+\xi$	$1+\xi$	$1+\eta$	1	$1+\eta$
Soft S-S	1	1	$1+\xi$	1	1	$1+\eta$
Sliding	$1+\xi$	1	1	1	$1+\eta$	1

Table 5 Convergence of the first six dimensionless frequency parameters of square plates partially fixed around one corner, $\xi_0=0$ ($a_0=a/2$) and $\eta_0=0$ ($b_0=b/2$)

h/b	$I\times J\times K$	Ω_1	Ω_2	Ω_3	Ω_4	Ω_5	Ω_6
Antisymmetric mode in the thickness direction							
0.1	8×8×2	30.70	52.18	60.67	66.48	79.32	93.75
	8×8×3	30.70	52.16	60.65	66.46	79.28	93.71
	10×10×3	30.56	51.82	60.35	65.97	78.68	93.41
	12×12×3	30.48	51.58	60.17	65.68	78.33	93.24
	14×14×3	30.44	51.44	60.05	65.52	78.13	93.16
	16×16×3	30.41	51.34	59.97	65.41	77.99	93.10
	18×18×3	30.38	51.27	59.91	65.33	77.90	93.07
0.25	6×6×3	22.51	33.45	38.46	42.94	49.65	57.57
	6×6×4	22.51	33.45	38.46	42.94	49.65	57.57
	8×8×4	22.40	33.12	38.11	42.66	49.21	57.26
	10×10×4	22.35	32.98	37.96	42.55	49.03	57.17
	12×12×4	22.32	32.89	37.86	42.48	48.93	57.12
	14×14×4	22.29	32.82	37.80	42.45	48.88	57.10
	16×16×4	22.28	32.77	37.75	42.42	48.84	57.08
Symmetric mode in the thickness direction							
0.1	8×8×2	95.28	114.4	136.8	143.4	176.4	179.0
	8×8×3	95.28	114.4	136.8	143.4	176.4	179.0
	10×10×3	94.67	113.9	136.3	143.2	175.6	178.4
	12×12×3	94.29	113.7	136.0	143.0	175.2	178.1
	14×14×3	94.07	113.5	135.8	143.0	174.8	177.8
	16×16×3	93.89	113.3	135.7	142.9	174.6	177.7
	18×18×3	93.76	113.2	135.6	142.9	174.4	177.6
0.25	6×6×3	38.69	46.30	55.16	57.74	71.16	72.02
	6×6×4	38.69	46.30	55.16	57.74	71.16	72.02
	8×8×4	38.21	45.90	54.76	57.38	70.57	71.55
	10×10×4	37.96	45.71	54.57	57.29	70.28	71.31
	12×12×4	37.82	45.60	54.46	57.23	70.08	71.18
	14×14×4	37.73	45.52	54.39	57.21	69.95	71.10
	16×16×4	37.66	45.47	54.33	57.19	69.86	71.04

does not apply to the characteristic boundary function components at the boundaries $\xi=1$ and $\eta=1$ because of the discontinuity of boundary conditions. In the present study, the basic concept of the R-functions [31] is used to construct the characteristic boundary function components at the boundaries $\zeta=1$ and $\eta=1$. The mathematical definition and demonstration of the R-functions will not be discussed in detail. Interested readers may consult the relevant monograph [32].

Using the R-conjunction operation defined by Rvachev [32], we can easily obtain that

$$F_3(\xi,\eta)=F_{u3}(\xi,\eta)=F_{v3}(\xi,\eta)=F_{w3}(\xi,\eta)=(\xi-1)\wedge(\eta-\eta_0)$$
$$=\xi-1+\eta-\eta_0-\sqrt{(\xi-1)^2+(\eta-\eta_0)^2} \tag{12}$$

$$F_4(\xi,\eta)=F_{u4}(\xi,\eta)=F_{v4}(\xi,\eta)=F_{w4}(\xi,\eta)=(\xi-\xi_0)\wedge(\eta-1)$$
$$=\xi-\xi_0+\eta-1-\sqrt{(\xi-\xi_0)^2+(\eta-1)^2} \tag{13}$$

where the symbol "$\wedge$" is the R-conjunction operator. It is obvious that

$$F_3(\xi,\eta)\begin{cases}=0, & \text{on } \eta\geqslant\eta_0,\ \xi=1\\ <0 & \text{in the plate domain}\end{cases} \tag{14}$$

$$F_4(\xi,\eta)\begin{cases}=0, & \text{on } \xi\geqslant\xi_0,\ \eta=1\\ <0 & \text{in the plate domain}\end{cases} \tag{15}$$

Using the earlier characteristic boundary function components, $F_u(\xi,\eta)$, $F_v(\xi,\eta)$, and $F_w(\xi,\eta)$ can exactly satisfy the geometric boundary conditions of the plates. It is obvious that in the present analysis, $\xi_0=-1$ (i.e., $a_0=a$) means that the plate has a completely fixed boundary at $\eta=-1$ (i.e., $y=b$) and $\eta_0=1$ (i.e., $b_0=b$) means that the plate has a completely fixed boundary at $\xi=1$ (i.e., $x=a$). The case of $\xi_0=1$ (i.e., $a_0=0$) and $\eta_0=1$ (i.e., $b_0=0$) means that the plate has a fixed point-support at the corner $\xi=1$ (i.e., $x=a$), $\eta=1$ (i.e., $y=b$).

5 Convergence Study

It is well known that the Ritz method provides the upper bound eigenvalues. However, its efficiency depends greatly on the choice of global admissible functions. These upper bound estimates could be improved by increasing the number of terms of admissible functions in the numerical computation and, hence, solution of any accuracy can be obtained theoretically. However, a practical limit to the number of terms used always exists because of the limited speed, capacity, and numerical accuracy of computers. In the three-dimensional vibration analysis of an elastic body in particular, numerical instability may occur with a great number of terms of admissible functions, especially when triplicate series are used. Therefore, the validity of a numerical method often hinges on the convergence rate, numerical stability, and accuracy of the method.

Square plates (i.e., aspect ratio $\lambda=a/b=1$) are taken for the convergence studies. The plates partially fixed around one corner have thickness ratios $h/b=0.1$, 0.25 while the plates partially fixed around four corners have thickness ratios $h/(2b)=0.1$, 0.25. In each case, two thickness-side ratios corresponding, respectively, to moderately thick and very thick plates are considered. On the edges $\xi=1$ and $\eta=1$, the length ratios of the free boundaries are $a_0/a=0.5$ (i.e., $\xi_0=0$) and $b_0/b=0.5$ (i.e., $\eta_0=0$), respectively. The Poisson's ratio $\nu=0.3$ is adopted in the present study unless stated otherwise. All the computations were performed in double precision (16 significant figures) and 24-point piecewise Gaussian quadrature was used numerically to evaluate the integrals which form the stiffness and mass matrices in Eq. (8). For simplicity, equal numbers of terms of Chebyshev polynomials were taken for the displacement amplitude functions U, V, and W in each coordinate direction, namely $I=L=P$, $J=M=Q$, and $K=N=R$. To facilitate the comparisons with 2D results, a dimensionless frequency parameter is introduced as

$$\Omega=\frac{b}{ah}\sqrt{12(1-\nu^2)}\Delta=\omega b^2\sqrt{\rho h/D} \tag{16}$$

Table 6 Convergence of the first six dimensionless frequency parameters of square plates partially fixed around four corners, $\xi_0=0$ ($a_0=a/2$) and $\eta_0=0$ ($b_0=b/2$)

$h/(2b)$	$I\times J\times K$	Ω_1	Ω_2	Ω_3	Ω_4	Ω_5	Ω_6
SSA mode							
0.1	8×8×2	5.597	13.30	16.49	27.37	30.47	39.76
	8×8×3	5.595	13.29	16.48	27.36	30.46	39.73
	10×10×3	5.561	13.18	16.36	27.29	30.37	39.64
	12×12×3	5.540	13.10	16.30	27.24	30.33	39.59
	14×14×3	5.526	13.06	16.26	27.22	30.30	39.56
	16×16×3	5.517	13.03	16.23	27.20	30.29	39.54
	18×18×3	5.510	13.00	16.21	27.19	30.28	39.53
0.25	6×6×3	4.271	8.316	10.51	17.18	18.54	22.22
	6×6×4	4.270	8.315	10.51	17.18	18.54	22.22
	8×8×4	4.232	8.193	10.40	17.12	18.44	22.12
	10×10×4	4.213	8.134	10.36	17.10	18.41	22.08
	12×12×4	4.201	8.099	10.33	17.08	18.39	22.06
	14×14×4	4.193	8.079	10.32	17.08	18.38	22.05
	16×16×4	4.188	8.065	10.31	17.07	18.37	22.04
SSS mode							
0.1	8×8×2	28.61	41.30	56.35	61.12	76.76	78.67
	8×8×3	28.61	41.30	56.35	61.11	76.75	78.67
	10×10×3	28.41	41.14	56.12	61.03	76.59	78.29
	12×12×3	28.30	41.05	55.98	60.97	76.48	78.07
	14×14×3	28.24	41.00	55.88	60.93	76.42	77.93
	16×16×3	28.20	40.97	55.80	60.91	76.37	77.84
	18×18×3	28.17	40.94	55.74	60.89	76.34	77.77
0.25	6×6×3	11.64	16.56	22.68	24.40	29.90	31.27
	6×6×4	11.64	16.56	22.68	24.40	29.90	31.27
	8×8×4	11.47	16.41	22.51	24.34	29.84	31.00
	10×10×4	11.39	16.35	22.42	24.31	29.81	30.85
	12×12×4	11.35	16.31	22.37	24.29	29.79	30.76
	14×14×4	11.32	16.29	22.33	24.28	29.78	30.70
	16×16×4	11.31	16.28	22.30	24.27	29.77	30.66

where $D=Eh^3/[12(1-\nu^2)]$ is the flexural rigidity of the plate.

Table 5 shows the convergence of the first six dimensionless frequency parameters Ω_i ($i=1,2,\ldots,6$) for the plates partially fixed around one corner and completely fixed at the edges $x=0$ and $y=0$. Similarly, Table 6 shows the convergence of the first six dimensionless frequency parameters Ω_i ($i=1,2,\ldots,6$) of the SSA and SSS modes for the plates partially fixed around four corners. In these two tables, the numbers of terms in the x and y directions both vary from 8 to 18 with increments of 2 when the thickness ratio is equal to 0.1, and from 6 to 16 with increments of 2 when the thickness ratio is equal to 0.25. The number of terms in the z direction is fixed at 3 when the thickness ratio is equal to 0.1 and at 4 when the thickness ratio is equal to 0.25. Moreover, the cases with term 8×8×2 when the thickness ratio is equal to 0.1 and term 6×6×3 when the thickness ratio equal to 0.25 are taken to investigate the effect of number of terms in the thickness direction. It is seen that the convergence trends are similar for both cases. With increasing number of terms of the admissible functions, all of the frequency parameters monotonically and steadily decrease. One can see that for plates with thickness ratio 0.1, the differences between results from terms 8×8×2 and 8×8×3 are very small, with the maximum being 0.04 only. For plates with thickness ratio 0.25, the differences between the results from terms 6×6×3 and 6×6×4 are also very small, with the maximum being 0.001 only. Moreover, for plates with thickness ratio 0.1, the maximum error between the results from terms 16×16×3 and 18×18×3 is lower than 0.14%. For plates with thickness ratio 0.25, the maximum error between the results from terms 14×14×4 and 16×16×4 is lower than 0.19%. These clearly show the convergence of the present method. In general, for thin plates, a small number of terms of Chebyshev polynomials in the thickness direction versus a large number of terms of Chebyshev polynomials in the length and width directions should be used. However, with increasing plate thickness, more terms of the Chebyshev polynomials in the thickness direction compared with those in the other directions is needed.

Apart from the Chebyshev polynomials, other polynomials such as simple algebraic polynomials and orthogonal polynomials may also be used as the main admissible functions. However, if simple algebraic polynomials are used as admissible functions, the maximum number of the terms should be carefully controlled; otherwise ill-conditioning and unstable computation may occur. This can be improved by using orthogonal polynomials instead but it will complicate the analysis. The truncation errors arising from the calculation of orthogonal polynomials by the Gram–Schmidt process may also lead to further inaccuracies. The Chebyshev polynomials possess the simplicity of simple algebraic polynomials and the efficiency of orthogonal polynomials, and can avoid the numerical instability of higher-order simple algebraic polynomials and the complication in constructing orthogonal polynomials. More detailed discussions about the excellent properties of Chebyshev polynomials in vibration analysis can be found in Ref. [33].

6 Comparison Study

The present results for partially fixed cantilevered Kirchhoff rectangular plates and Mindlin rectangular plates with point supports at four corners have been compared with available solutions. It is obvious that the solutions based on either classical thin plate theory or moderately thick plate theory only account for the antisymmetric modes in the thickness direction. Referring to the R-function given in Eq. (12) or (13), the case of $\xi_0=1$ and $\eta_0=1$ represents a concentrated support which corresponds to the clamped point support in the 2D theories. To be consistent with the available results, only zero displacement w at the point supports should be satisfied. In such a case, we should take $F_{u3}(\xi,\eta)=F_{v3}(\xi,\eta)=F_4(\xi,\eta)=F_{u4}(\xi,\eta)=F_{v4}(\xi,\eta)=F_{w4}(\xi,\eta)=1$ so that the displacements u and v are unrestrained. Table 7 gives the first six frequency parameters of rectangular plates with point supports at four corners. Two different thickness ratios $h/(2b)=0.1$, 0.2 and three different aspect ratios ($a/b=1.0,1.5,2.0$) have been considered. In the numerical computations, 14×14×3 terms of the Chebyshev polynomials in the three coordinate directions are used for plates with thickness ratio $h/(2b)=0.1$, while 12×12×4 terms are used for plates with

Table 7 Comparison of the first six frequency parameters $\bar{\Omega}=4\Omega/\pi^2$ of antisymmetric mode in the thickness direction for the rectangular plates point-supported at four corners. Note: The superscript letters are the mode types in the *x* and *y* directions, respectively.

$h/(2b)$	Method	$\bar{\Omega}_1$	$\bar{\Omega}_2$	$\bar{\Omega}_3$	$\bar{\Omega}_4$	$\bar{\Omega}_5$	$\bar{\Omega}_6$
$a/b=1.0$							
0.1	3D	0.6651^{ss}	$1.3932^{as(sa)}$	$1.3932^{as(sa)}$	1.9352^{ss}	3.2372^{aa}	3.8398^{ss}
	Mindlin[a]	0.6721	1.4156	1.4156	1.9194	3.3262	3.8908
0.2	3D	0.5734^{ss}	$1.1195^{as(sa)}$	$1.1195^{as(sa)}$	1.7697^{ss}	2.4480^{aa}	3.0537^{ss}
	Mindlin[a]	0.5932	1.1761	1.1761	1.7630	2.5904	3.1345
$a/b=1.5$							
0.1	3D	0.3893^{ss}	0.8827^{sa}	1.0430^{as}	1.4325^{ss}	2.1088^{aa}	2.8478^{ss}
	Mindlin[a]	0.3878	0.8850	1.0605	1.4376	2.1328	2.8623
0.2	3D	0.3583^{ss}	0.7551^{sa}	0.8765^{as}	1.2736^{ss}	1.7275^{aa}	2.2067^{as}
	Mindlin[a]	0.3623	0.7734	0.9132	1.2930	1.7830	2.1969
$a/b=2.0$							
0.1	3D	0.2363^{ss}	0.64855^{sa}	0.7793^{as}	1.2116^{ss}	1.4877^{aa}	1.7062^{as}
	Mindlin[a]	0.2311	0.6445	0.7824	1.2233	1.4862	1.7082
0.2	3D	0.2248^{ss}	0.5721^{sa}	0.6877^{as}	1.0528^{ss}	1.2805^{aa}	1.5329^{as}
	Mindlin[a]	0.2232	0.5769	0.7021	1.0778	1.2964	1.5431

[a]See Ref. [13].

thickness ratio $h/(2b)=0.2$. The results are compared with the Mindlin theory solutions of Kitipornchai et al. [13]. It can be seen that the present solutions are in agreement with those of the 2D Mindlin solutions. The maximum error is less than 6% (2.4480 vs 2.5904), which occurs at the fundamental frequency of AA mode for the square plate with the thickness ratio $h/(2b)=0.2$.

Table 8 gives the first six natural frequencies of each mode category for square plates with partially fixed boundaries around four corners. It is assumed that the plate has length and width $a=b=1.0$ m, Young's modulus $E=1.0$ Pa, and mass density $\rho=1.0$ kg/m^3. Two different plates are considered. One has a thickness $h=0.2$ m, and length ratios $a_0/a=0.5$ and $b_0/b=0.75$ at the partially supported edges. The other has a thickness $h=0.4$ m and length ratios $a_0/a=0.25$ and $b_0/b=0.5$ at the partially supported edges. In the numerical computation, $12\times12\times4$ terms of the Chebyshev polynomials are used. The present results are compared with those obtained by the 3D finite element (FE) analysis. The eight-node hexahedral elements of the commercial program STRAND7 [34] are used to obtain the reference finite element solutions. Altogether $20\times20\times4=1600$ cubic brick elements are used for the plate with thickness $h=0.2$ m and $20\times20\times8=3200$ cubic brick elements are used for the plate with thickness $h=0.4$ m. Good agreement has been observed in all cases. All errors between the present solutions and the finite element solutions are within 1% except for the second frequency parameter of the SS mode for the plate with thickness ratio $h/(2b)=0.1$ where the error (0.5986 vs 0.6142) is about 3%.

7 Numerical Results

From the earlier convergence and comparison studies, it has been shown that the present method can provide results with satisfactory accuracy for the 3D vibration of rectangular plates with mixed boundary conditions. In this section, some valuable results, known for the first time, are given in tabular and diagrammatic forms. Tables 9–11 give the first six frequency parameters of each mode category for square plates partially fixed around four corners. Three different thickness ratios $h/(2b)=0.05$, 0.125, 0.25 and four different length ratios of the free boundaries ($a_0/a=b_0/b=0.25,0.5,0.75,1.0$) are considered. It is clear that the case of $a_0/a=b_0/b=1.0$ represents fixed point-supports at four corners. It is seen that increasing the length of free boundaries and/or the plate thickness, all of the frequency parameters monotonically decrease and the SSA modes always provide the lowest frequency parameters for all cases. Moreover, for thin plates, the frequency parameters of the symmetric modes in the thickness direction are

Table 8 Comparison of the first six natural frequencies of each mode type for square plates with partially fixed boundaries around four corners. Note: The superscript *s* means symmetric mode in the *z* direction.

Mode	Method	ω_1	ω_2	ω_3	ω_4	ω_5	ω_6
$a_0/a=0.5$, $b_0/b=0.75$, $h/(2b)=0.1$							
AA	Present	0.9775	1.404^{s}	1.516	2.136^{s}	2.145	2.558
	3D FE	0.9857	1.393	1.521	2.137	2.154	2.562
AS	Present	0.4298	0.9064^{s}	1.045	1.606	2.044	2.286^{s}
	3D FE	0.4336	0.9062	1.043	1.617	2.058	2.270
SA	Present	0.6247	1.043	1.138^{s}	1.372	2.086	2.088^{s}
	3D FE	0.6301	1.051	1.135	1.374	2.079	2.081
SS	Present	0.2820	0.5986	0.9216	1.569^{s}	1.594	1.762
	3D FE	0.2845	0.6142	0.9331	1.593	1.639	1.753
$a_0/a=0.25$, $b_0/b=0.5$, $h/(2b)=0.2$							
AA	Present	1.764	1.807^{s}	2.548^{s}	2.729	3.162^{s}	3.371
	3D FE	1.768	1.798	2.541	2.733	3.143	3.365
AS	Present	0.9646	1.237^{s}	1.719	2.565	2.828^{s}	2.978^{s}
	3D FE	0.9711	1.235	1.775	2.565	2.817	2.973
SA	Present	1.267	1.590^{s}	2.170	2.399^{s}	2.592	3.019^{s}
	3D FE	1.275	1.591	2.184	2.383	2.608	3.013
SS	Present	0.6349	1.268	1.941	1.945^{s}	2.463	2.891
	3D FE	0.6377	1.273	1.942	1.959	2.456	2.890

Table 9 The first six frequency parameters of AAA and AAS modes for square plates ($a=b$) partially fixed around four corners

$h/(2b)$	a_0/a	Ω_1	Ω_2	Ω_3	Ω_4	Ω_5	Ω_6
AAA modes							
0.05	0.25	25.03	52.06	54.06	75.81	92.56	94.47
	0.5	22.31	39.43	48.82	54.99	67.87	83.94
	0.75	16.38	24.83	35.52	50.17	59.29	69.88
	1.0	10.42	17.42	29.41	40.89	47.96	57.91
0.125	0.25	13.42	22.78	23.61	29.08	29.87	31.45
	0.5	11.95	17.71	21.24	24.53	27.09	28.84
	0.75	9.191	13.17	17.92	23.08	24.94	27.58
	1.0	6.056	11.15	15.04	19.98	22.49	24.91
0.25	0.25	19.84	36.59	38.24	49.88	58.74	59.85
	0.5	17.67	27.86	33.91	39.31	46.75	54.74
	0.75	13.29	19.14	27.12	36.53	41.97	47.31
	1.0	8.575	14.97	22.41	30.49	36.11	41.11
AAS modes							
0.125	0.25	27.02	35.68	47.86	49.85	57.69	69.83
	0.5	21.13	32.21	39.37	43.55	46.84	58.45
	0.75	15.22	25.81	37.39	37.72	41.50	56.33
	1.0	7.995	19.60	34.34	36.46	36.93	49.30
0.25	0.25	13.56	17.86	23.97	24.98	28.91	33.76
	0.5	10.63	16.17	19.66	21.83	23.51	29.11
	0.75	7.659	13.00	18.61	18.90	20.79	27.77
	1.0	4.249	9.975	17.39	18.25	18.41	24.64

significantly higher than those of the antisymmetric modes. However, with increase in plate thickness, the rate of decrease in frequency parameters of the symmetric modes in the thickness direction is quicker than that of the antisymmetric modes.

Figures 2–5 show the first few frequency parameters versus the length ratio a_0/a of the free boundaries of square plates ($a/b=1.0$) partially fixed around a corner. It is assumed that the lengths of the two adjacent fixed boundaries around the corner are the same, i.e., $b_0=a_0$. Five different thickness ratios are considered, i.e., $h/b=0.05-0.25$, with an increment of 0.05. Figures 2–4 give the first three frequency parameters of antisymmetric modes in the thickness direction. With the decrease of plate thickness and, hence, more restraint on shear deformation, the frequency parameters of flexural modes increase and approach those obtained from the classical thin plate theory. This is easily observed in the 3D solutions shown in Figs. 2–4, where the frequency parameters increase monotonically as the plate becomes thinner and approach those of the thin plate approximated by $h/b=0.05$. Figure 5 gives the first few frequency parameters of symmetric modes in the thickness direction, i.e., the first three for $h/b=0.25$, the first two for $h/b=0.20$ and the fundamental one for $h/b=0.15$. Since the third frequency parameter for $h/b=0.20$ and the second and third frequency parameters for $h/b=0.15$ are much higher, they are omitted from the figure. Moreover, for thin plates, the frequency parameters of symmetric modes in the thickness direction belong to the higher-order ones, and therefore they are also omitted from the figure for $h/b=0.10$ and $h/b=0.05$. Note that the symmetric modes in the thickness direction cannot be predicted by the classical thin plate theory. One can also observe from Figs. 2–5 that the frequency parameters always monotonically decrease with the increase in the length ratio of the free boundaries. The increase of the length of fixed edges is equivalent to an increase in restraint stiffness and hence it always results in an increase of eigenfrequencies. Moreover, it is shown that a longer free boundary has more sensitive frequency parameters. By increasing the length ratio of the fixed boundaries, the variation of frequency parameters tends to slow down.

Table 10 The first six frequency parameters of ASA(SAA) and ASS(SAS) modes for square plates ($a=b$) partially fixed around four corners

$h/(2b)$	a_0/a	Ω_1	Ω_2	Ω_3	Ω_4	Ω_5	Ω_6
ASA (SAA) modes							
0.05	0.25	15.91	35.58	42.30	56.47	69.12	72.86
	0.5	12.05	22.73	34.43	46.20	53.54	66.70
	0.75	7.597	17.57	24.97	36.79	48.67	51.37
	1.0	4.496	13.09	19.81	28.20	40.10	46.65
0.125	0.25	13.24	26.01	30.02	38.82	46.37	48.35
	0.5	9.826	17.92	25.45	33.66	38.51	45.06
	0.75	6.433	14.58	19.68	27.67	35.99	37.41
	1.0	3.933	11.28	16.14	22.58	29.64	35.43
0.25	0.25	9.329	16.50	18.88	24.05	27.18	28.87
	0.5	6.867	12.52	16.45	21.44	23.71	26.58
	0.75	4.751	10.56	13.50	18.18	22.49	23.34
	1.0	2.985	8.448	11.55	15.58	19.29	22.41
ASS (SAS) modes							
0.125	0.25	21.65	37.95	42.96	57.02	58.91	61.28
	0.5	15.71	31.33	37.12	49.29	53.47	57.14
	0.75	11.03	26.14	32.10	45.52	47.26	49.94
	1.0	6.266	20.36	28.05	38.54	43.23	46.47
0.25	0.25	10.91	19.02	21.57	28.12	29.14	30.57
	0.5	7.923	15.71	18.58	24.45	26.59	28.50
	0.75	5.575	13.10	16.10	22.72	23.22	24.99
	1.0	3.297	10.34	14.14	19.44	21.52	22.90

Table 11 The first six frequency parameters of SSA and SSS modes for square plates ($a=b$) partially fixed around four corners

$h/(2b)$	a_0/a	Ω_1	Ω_2	Ω_3	Ω_4	Ω_5	Ω_6
SSA modes							
0.05	0.25	7.656	25.99	28.98	42.60	53.38	57.11
	0.5	5.931	15.62	19.32	31.56	35.75	49.64
	0.75	4.040	9.085	13.60	29.08	32.77	39.39
	1.0	2.284	5.475	11.14	23.05	28.61	32.73
0.125	0.25	6.834	19.77	22.13	29.90	35.18	38.82
	0.5	5.316	11.96	14.95	25.11	27.78	35.36
	0.75	3.689	7.460	11.53	23.33	25.96	29.25
	1.0	2.127	5.079	9.540	18.10	23.46	25.91
0.25	0.25	5.381	12.79	14.35	18.91	21.57	23.84
	0.5	4.213	8.134	10.36	17.10	18.41	22.08
	0.75	2.989	5.664	8.599	15.87	17.41	19.07
	1.0	1.754	4.423	7.229	12.51	16.24	17.66
SSS modes							
0.125	0.25	31.58	41.11	49.40	49.74	65.48	69.40
	0.5	22.65	32.83	44.78	48.77	61.10	62.40
	0.75	19.11	29.81	35.48	42.99	55.15	57.97
	1.0	18.22	25.36	26.66	36.96	46.78	53.88
0.25	0.25	15.94	20.52	24.69	24.83	31.62	34.67
	0.5	11.39	16.35	22.42	24.31	29.81	30.85
	0.75	9.580	14.82	17.80	21.59	27.62	28.45
	1.0	9.115	12.91	13.34	18.59	23.61	26.84

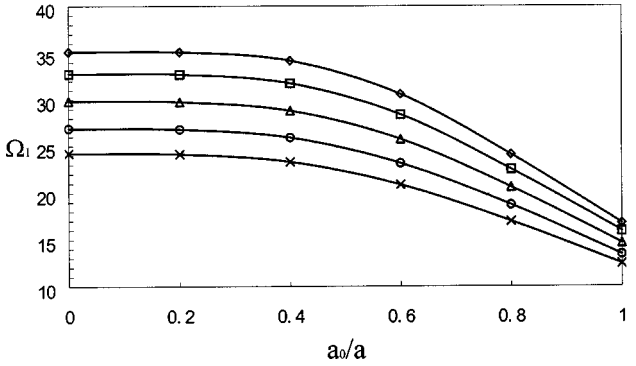

Fig. 2 Fundamental frequency parameters of antisymmetric modes in the thickness direction for square plates ($a=b$) completely fixed at two adjacent edges and partially fixed around a corner ($b_0=a_0$) with respect to the length ratio a_0/a of the free boundaries (◇ $h/b=0.05$, □ $h/b=0.1$, △ $h/b=0.15$, ○ $h/b=0.2$, × $h/b=0.25$)

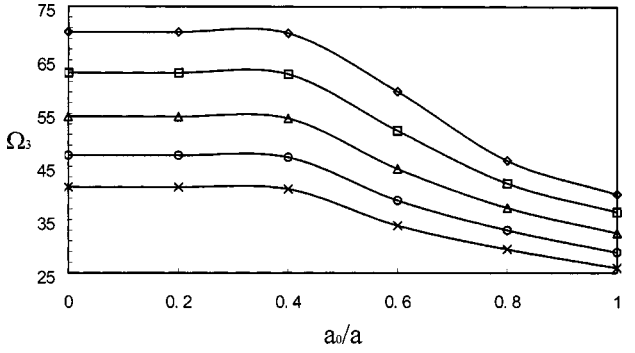

Fig. 4 The third frequency parameters of antisymmetric modes in the thickness direction for square plates ($a=b$) completely fixed at two adjacent edges and partially fixed around a corner ($b_0=a_0$) with respect to the length ratio a_0/a of the free boundaries (◇ $h/b=0.05$, □ $h/b=0.1$, △ $h/b=0.15$, ○ $h/b=0.2$, × $h/b=0.25$)

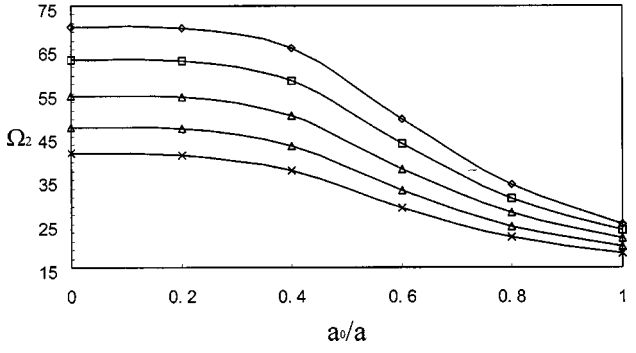

Fig. 3 The second frequency parameters of antisymmetric modes in the thickness direction for square plates ($a=b$) completely fixed at two adjacent edges and partially fixed around a corner ($b_0=a_0$) with respect to the length ratio a_0/a of the free boundaries (◇ $h/b=0.05$, □ $h/b=0.1$, △ $h/b=0.15$, ○ $h/b=0.2$, × $h/b=0.25$)

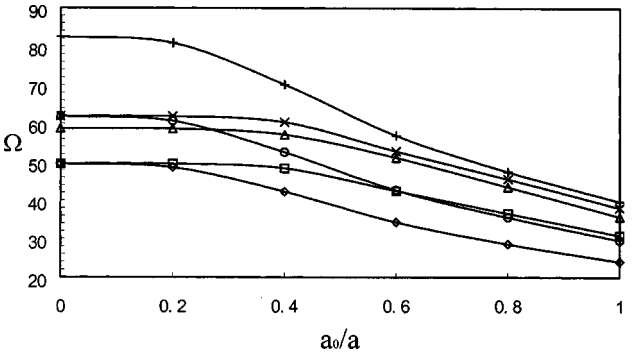

Fig. 5 Frequency parameters of symmetric modes in the thickness direction for square plates ($a=b$) fixed at two adjacent edges and partially fixed around a corner ($b_0=a_0$) with respect to the length ratio a_0/a of the free boundaries (◇ fundamental for $h/b=0.25$, □ second for $h/b=0.25$, △ third for $h/b=0.25$, ○ fundamental for $h/b=0.2$, × second for $h/b=0.2$, + fundamental for $h/b=0.15$)

8 Conclusions

In this paper, the 3D vibration characteristics of rectangular plates with mixed boundary conditions have been studied, based on the 3D elasticity. A global analysis approach has been developed based on the Ritz method. The Chebyshev polynomials are used to construct the admissible functions. The R-function method is adopted to construct the characteristic boundary function components for edges with mixed boundary conditions. The comparison of the present solutions with the Mindlin solutions and the 3D finite element solutions demonstrates the accuracy and correctness of the present method. Some valuable results known for the first time are given.

Acknowledgments

The work described in this paper was partially supported by the grant ''Three-dimensional vibration analysis of structural components using Chebyshev polynomials'' from the University Research Committee (URC) of the University of Hong Kong.

References

[1] Leissa, A. W., 1973, ''The Free Vibrations of Rectangular Plates,'' J. Sound Vib., **31**, pp. 257–293.
[2] Gorman, D. J., 1995, ''Free-Vibration of Orthotropic Cantilever Plates With Point Supports,'' J. Eng. Mech., **121**, pp. 851–857.
[3] Singhal, R. K., and Gorman, D. J., 1997, ''Free Vibration of Partially Clamped Rectangular Plates With and Without Rigid Point Supports,'' J. Sound Vib., **203**, pp. 181–192.
[4] Gorman, D. J., 1999, ''Accurate Free Vibration Analysis of Point Supported Mindlin Plates by the Superposition Method,'' J. Sound Vib., **219**, pp. 265–277.
[5] Keer, L. M., and Stahl, B., 1972, ''Eigenvalue Problems of Rectangular Plates With Mixed Edge Conditions,'' ASME J. Appl. Mech., **94**, pp. 513–520.
[6] Narita, Y., 1981, ''Application of a Series-Type Method to Vibration of Orthotropic Rectangular Plates With Mixed Boundary Conditions,'' J. Sound Vib., **77**, pp. 345–355.
[7] Torik, P. J., 1984, ''A Variational Approach to the Dynamics of Structures Having Mixed or Discontinuous Boundary Conditions,'' ASME J. Appl. Mech., **51**, pp. 831–836.
[8] Fan, S. C., and Cheung, Y. K., 1984, ''Flexural Free Vibrations of Rectangular Plates With Complex Support Conditions,'' J. Sound Vib., **93**, pp. 81–94.
[9] Liew, K. M., Hung, K. C., and Lim, M. K., 1993, ''Roles of Domain Decomposition Method in Plate Vibrations: Treatment of Mixed Discontinuous Periphery Boundaries,'' Int. J. Mech. Sci., **35**, pp. 615–632.
[10] Liew, K. M., Hung, K. C., and Lim, M. K., 1993, ''Method of Domain Decomposition in Vibrations of Mixed Edge Anisotropic Plates,'' Int. J. Solids Struct., **30**, pp. 3281–3301.
[11] Su, G. H., and Xiang, Y., 2002, ''A Non-Discrete Approach for Analysis of Plates With Multiple Subdomains,'' Eng. Struct., **24**, pp. 563–575.
[12] Kim, C. S., and Dickinson, S. M., 1987, ''Flexural Vibration of Rectangular Plates With Point Supports,'' J. Sound Vib., **115**, pp. 249–261.
[13] Kitipornchai, S., Xiang, Y., and Liew, K. M., 1994, ''Vibration Analysis of Corner Supported Mindlin Plates of Arbitrary Shape Using the Lagrange Multiplier Method,'' J. Sound Vib., **173**, pp. 457–470.
[14] Wei, G. W., Zhao, Y. B., and Xiang, Y., 2001, ''The Determination of Natural Frequencies of Rectangular Plates With Mixed Boundary Conditions by Discrete Singular Convolution,'' Int. J. Mech. Sci., **43**, pp. 1731–1746.
[15] Liew, K. M., Xiang, Y., Kitipornchai, S., and Lim, M. K., 1995, ''Vibration of Mindlin Plates on Point Supports Using Constraint Functions,'' J. Eng. Mech., **120**, pp. 499–513.
[16] Laura, P. A. A., and Gutierrez, R. H., 1994, ''Analysis of Vibrating Rectangular Plates With Non-Uniform Boundary Conditions by Using the Differential Quadrature Method,'' J. Sound Vib., **173**, pp. 702–706.
[17] Liu, F.-L., and Liew, K. M., 1999, ''Analysis of Vibrating Thick Rectangular Plates With Mixed Boundary Constraints Using Differential Quadrature Element Method,'' J. Sound Vib., **225**, pp. 915–934.
[18] Srinivas, S., Rao, C. V. J., and Rao, A. K., 1970, ''An Exact Analysis for Vibration of Simply-Supported Homogeneous and Laminated Thick Rectangular Plates,'' J. Sound Vib., **12**, pp. 187–199.
[19] Cheung, Y. K., and Chakrabarti, S., 1972, ''Free Vibration of Thick, Layered Rectangular Plates by a Finite Layer Method,'' J. Sound Vib., **21**, pp. 277–284.
[20] Hutchinson, J. R., and Zillimer, S. D., 1983, ''Vibration of a Free Rectangular Parallelepiped,'' ASME J. Appl. Mech., **50**, pp. 123–130.
[21] Fromme, A., and Leissa, A. W., 1970, ''Free Vibration of the Rectangular Parallelepiped,'' J. Acoust. Soc. Am., **48**, pp. 290–298.
[22] Malik, M., and Bert, C. W., 1998, ''Three-Dimensional Elasticity Solutions for Free Vibrations of Rectangular Plates by the Differential Quadrature Method,'' Int. J. Solids Struct., **35**, pp. 299–319.
[23] Liew, K. M., and Teo, T. M., 1999, ''Three-Dimensional Vibration Analysis of Rectangular Plates Based on Differential Quadrature Method,'' J. Sound Vib., **220**, pp. 577–599.
[24] Leissa, A. W., and Zhang, Z. D., 1983, ''On the Three-Dimensional Vibrations of the Cantilevered Rectangular Parallelepiped,'' J. Acoust. Soc. Am., **73**, pp. 2013–2021.
[25] Lim, C. W., 1999, ''Three-Dimensional Vibration Analysis of a Cantilevered Parallelepiped: Exact and Approximate Solutions,'' J. Acoust. Soc. Am., **106**, pp. 3375–3381.
[26] Liew, K. M., Hung, K. C., and Lim, M. K., 1993, ''A Continuum Three-Dimensional Vibration Analysis of Thick Rectangular Plates,'' Int. J. Solids Struct., **30**, pp. 3357–3379.
[27] Liew, K. M., Hung, K. C., and Lim, M. K., 1994, ''Three-Dimensional Vibration Analysis of Rectangular Plates: Variance of Simple Support Conditions and Influence of In-Plane Inertia,'' Int. J. Solids Struct., **31**, pp. 3233–3247.
[28] Liew, K. M., Hung, K. C., and Lim, M. K., 1995, ''Free Vibration Studies on Stress-Free Three-Dimensional Elastic Solids,'' ASME J. Appl. Mech., **62**, pp. 159–165.
[29] Zhou, D., Cheung, Y. K., Au, F. T. K., and Lo, S. H., 2002, ''Three-Dimensional Vibration Analysis of Thick Rectangular Plates Using Chebyshev Polynomial and Ritz Method,'' Int. J. Solids Struct., **39**, pp. 6339–6353.
[30] Fox, L., and Parker, I. B., 1968, *Chebyshev Polynomials in Numerical Analysis*, Oxford University Press, London.
[31] Rvachev, V. L., and Sheiko, T. I., 1995, ''R-Functions in Boundary Value Problems in Mechanics,'' Appl. Mech. Rev., **48**, pp. 151–187.
[32] Rvachev, V. L., 1982, *Theory of R-Functions and Its Some Applications* (in Russian), Nauk Dumka, Kiev.
[33] Zhou, D., 2003, ''Three-Dimensional Vibration Analysis of Structural Elements Using Chebyshev–Ritz Method,'' Ph.D. thesis, The University of Hong Kong, Hong Kong.
[34] G+D Computing Pty. Ltd., 1999, *Using STRAND7*, 1st ed., Sydney.

Vijaya Bhaskar Chalivendra
Post-doctoral Associate,
Graduate Aeronautical Laboratorires,
California Institute of Technology,
Pasadena, CA 91125
Mem. ASME

Arun Shukla[1]
Simon Ostrach Professor,
Dynamic Photomechanics Laboratory,
Department of Mechanical Engineering and
Applied Mechanics,
University of Rhode Island,
Kingston, RI 02881
e-mail: skuklaa@egr.ur.edu
Fellow ASME

Transient Elastodynamic Crack Growth in Functionally Graded Materials

A generalized elastic solution for an arbitrarily propagating transient crack in functionally graded materials (FGMs) is obtained through an asymptotic analysis. The shear modulus and mass density of the FGM are assumed to vary exponentially along the gradation direction. The out-of-plane displacement field and its gradients about the crack tip were obtained in powers of radial coordinates, with the coefficients depending on the time rates of change of crack tip speed and stress intensity factor. The effects of the transient terms on the contours of constant out-of-plane displacement are duly discussed. [DOI: 10.1115/1.1831292]

1 Introduction

With the introduction of functionally graded materials (FGMs) [1], research on various aspects of fracture of these nonhomogeneous solids has generated extensive interest. Considerable amount of analytical, numerical, and experimental work has been reported on quasistatic fracture behavior of FGMs by several researchers [2–8]. However, the dynamic fracture of FGMs has received much less attention from researchers. Atkinson and List [9] were the first to study crack propagation in materials with spatially varying elastic constants using integral transforms. Very recently, Wang and Meguid [10] performed a theoretical analysis of a finite crack propagating in an interfacial layer with spatially varying elastic properties under antiplane loading conditions. It was identified that the fracture parameters of the interfacial crack are influenced by both the local and the remote elastic properties of the media. Along with theoretical studies few numerical studies on dynamic fracture of FGMs are also reported. Using a finite-element method, Nakagaki et al. [11] addressed dynamic crack propagation in the functionally graded particle dispersed material under dynamic loading and determined the effect of gradation on crack-tip severity as it propagates in FGM. To date, very few experimental studies on dynamic fracture are available. Parameswaran and Shukla [12] investigated dynamic fracture in FGMs with discrete property variations using photoelasticity. Recently, Rousseau and Tippur [13] have experimentally investigated cracks propagating along the gradient in FGMs under impact loading using the coherent gradient sensing (CGS) technique.

For detailed experimental investigation of fracture of these materials using techniques such as photoelasticity and CGS, asymptotic expansion of crack-tip stress fields are necessary. Parameswaran and Shukla [14] obtained the first three terms in the asymptotic expansion of stress field equations for a steady-state crack propagating along the direction of gradation in FGMs and investigated the effect of different levels of nonhomogeneity on the crack-tip stress fields. Recently, Jiang and Wang [15] developed the opening and sliding displacements for a propagating crack in FGMs using Fourier transform method. In their study, the properties were assumed to vary exponentially perpendicular to the crack propagation direction. Very recently, Chalivendra et al. [16] developed the asymptotic expansion of dynamic out-of-plane displacement fields for an inclined crack propagating with constant velocity with respect to the property gradation. *In all these studies, the asymptotic expansions were developed for a constant crack velocity*. Since the properties around the crack tip in FGMs change during crack propagation, the crack growth in a FGM is likely to be transient, with the crack speed and dynamic stress intensity factor changing as a function of time. The transient phenomena would be more predominant when the crack propagates arbitrarily at an angle to the property gradation in FGMs. Freund and Rosakis [17] developed asymptotic expansion of near-tip field equations for homogeneous materials and discussed about the importance of transient terms on the accuracy of description of crack-tip fields. However, asymptotic expansion of near-tip field equations for a transient crack growth in FGMs has not yet been reported.

In this paper, through an asymptotic analysis, the transient out-of-plane displacement field and its gradients for a transient crack propagating at angle to the property gradation in FGMs are developed. The shear modulus and mass density of FGM are assumed to vary exponentially along the gradation direction. The mode mixity arising out of the inclination of property gradient to the propagating crack is accommodated in the analysis through superposition of opening and shear modes. First three terms of out-of-plane displacemnet fields are developed and the effect of transient crack growth on contours of constant out-of-plane displacements is discussed.

2 Theoretical Formulation

At a continuum level, the properties at any given point in an FGM can be assumed to be same in all directions; hence, FGMs can be treated as an isotropic nonhomogeneous solid. Spatial variation of elastic properties and inclination of property gradation direction to the propagating crack make analytical solutions to the elastodynamic equations extremely difficult. Hence, an asymptotic analysis similar to that employed by Freund [18] is used to expand the stress field around a crack propagating at an arbitrary angle to the property gradation direction.

An isotropic linear elastic FGM, containing a propagating crack at an angle to the property gradation direction in the $X-Y$ two-dimensional (2-D) plane is shown Fig. 1. The crack is propagating with varying velocity (c) as a function of time in the X direction. The shear modulus and mass density are assumed to vary exponentially in X_1 direction as given in Eq. (1) and the Poisson's ratio (ν) is assumed to be constant. The property gradation direction is at angle φ to the $Y=0$ plane.

[1]To whom correspondence should be addressed.

Contributed by the Applied Mechanics Division of THE AMERICAN SOCIETY OF MECHANICAL ENGINEERS for publication in the ASME JOURNAL OF APPLIED MECHANICS. Manuscript received by the Applied Mechanics Division, August 25, 2003; final revision, August 3, 2004. Editor: K. Ravi-Chandar. Discussion on the paper should be addressed to the Editor, Prof. Robert M. McMeeking, Journal of Applied Mechanics, Department of Mechanical and Environmental Engineering, University of California—Santa Barbara, Santa Barbara, CA 93106-5070, and will be accepted until four months after final publication in the paper itself in the ASME JOURNAL OF APPLIED MECHANICS.

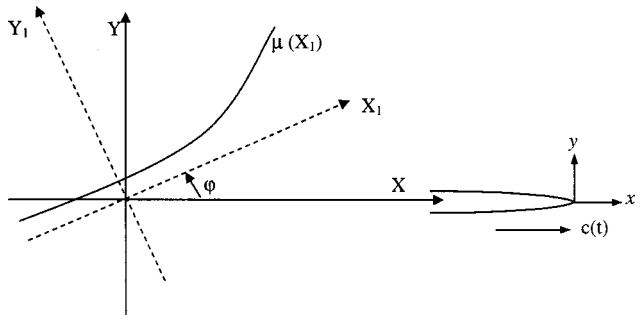

Fig. 1 Propagating crack orientation with respect to the direction of property variation in FGM

$$\mu(X_1)=\mu_0\exp(\delta X_1),\quad \rho(X_1)=\rho_0\exp(\delta X_1) \tag{1}$$

where μ_0 and ρ_0 are the shear modulus and density at the origin $(X=X_1=0)$, respectively, and δ is the nonhomogeneity parameter having dimension $(\text{Length})^{-1}$. Equation (1) can be written in terms of (X,Y) coordinates by using simple transformation as shown below.

$$\mu(X,Y)=\mu_0\exp(\alpha X+\beta Y),\quad \rho(X,Y)=\rho_0\exp(\alpha X+\beta Y) \tag{2}$$

$$\alpha=\frac{\delta}{\sqrt{1+\tan^2\varphi}},\quad \beta=\frac{\delta\tan\varphi}{\sqrt{1+\tan^2\varphi}} \tag{3}$$

It can be observed that the Lame's constant also varies exponentially, as shown in Eq. (4).

$$\lambda(X,Y)=\frac{3-\kappa}{\kappa-1}\mu_0\exp(\alpha X+\beta Y) \tag{4}$$

where $\kappa=(3-4\nu)$ for plane strain and $\kappa=(3-\nu)/(1+\nu)$ for plane stress.

Let u and v, functions of X, Y, and t, represent the displacements in the X and Y directions, respectively, with t representing the time. The Hooke's law for a plane problem can be written as

$$\begin{aligned}\sigma_{XX}&=\left(2\frac{\partial u}{\partial X}+\frac{3-\kappa}{\kappa-1}\Delta\right)\mu_0\exp(\alpha X+\beta Y)\\ \sigma_{YY}&=\left(2\frac{\partial v}{\partial Y}+\frac{3-\kappa}{\kappa-1}\Delta\right)\mu_0\exp(\alpha X+\beta Y)\\ \sigma_{XY}&=\left(\frac{\partial u}{\partial Y}+\frac{\partial v}{\partial X}\right)\mu_0\exp(\alpha X+\beta Y)\end{aligned} \tag{5}$$

in which $\Delta=\partial u/\partial X+\partial v/\partial Y$ is the dilatation and σ_{XX}, σ_{YY}, and σ_{XY} are the in-plane stress components. The equations of motion for a plane problem can be written as

$$\begin{aligned}\frac{\partial\sigma_{XX}}{\partial X}+\frac{\partial\sigma_{XY}}{\partial Y}&=\rho\frac{\partial^2 u}{\partial t^2}\\ \frac{\partial\sigma_{XY}}{\partial X}+\frac{\partial\sigma_{YY}}{\partial Y}&=\rho\frac{\partial^2 v}{\partial t^2}\end{aligned} \tag{6}$$

Substituting for the stresses and density from Eq. (5) and Eq. (1), respectively, into Eq. (6), after simplification, the equations of motion become

$$\left(\frac{3-\kappa}{\kappa-1}\right)\frac{\partial\Delta}{\partial X}+\left(\frac{\partial^2 u}{\partial Y^2}+\frac{\partial^2 v}{\partial X\partial Y}\right)+2\frac{\partial^2 u}{\partial X^2}+2\alpha\frac{\partial u}{\partial X}+\left(\frac{3-\kappa}{\kappa-1}\right)\alpha\Delta+\beta\left(\frac{\partial u}{\partial Y}+\frac{\partial v}{\partial X}\right)=\frac{\rho_0}{\mu_0}\frac{\partial^2 u}{\partial t^2} \tag{7}$$

$$\left(\frac{3-\kappa}{\kappa-1}\right)\frac{\partial\Delta}{\partial Y}+\left(\frac{\partial^2 v}{\partial X^2}+\frac{\partial^2 u}{\partial X\partial Y}\right)+2\frac{\partial^2 v}{\partial Y^2}+2\beta\frac{\partial v}{\partial Y}+\left(\frac{3-\kappa}{\kappa-1}\right)\beta\Delta+\alpha\left(\frac{\partial u}{\partial Y}+\frac{\partial v}{\partial X}\right)=\frac{\rho_0}{\mu_0}\frac{\partial^2 v}{\partial t^2} \tag{8}$$

By defining $\omega=\partial v/\partial X-\partial u/\partial Y$ as the rotation, we can write

$$\begin{aligned}\nabla^2 u&=\frac{\partial\Delta}{\partial X}-\frac{\partial\omega}{\partial Y}\\ \nabla^2 v&=\frac{\partial\Delta}{\partial Y}+\frac{\partial\omega}{\partial X}\end{aligned} \tag{9}$$

where

$$\nabla^2=\frac{\partial^2}{\partial x^2}+\frac{\partial^2}{\partial y^2}$$

Using Eq. (9), Eqs. (7) and (8) are manipulated to represent them in terms of Δ and ω only. This manipulation involves, first differentiating Eq. (7) with respect to X, differentiating Eq. (8) with respect to Y, and then adding them together. Second, Eq. (7) is differentiated with respect to Y, Eq. (8) is differentiated with respect to X, and then subtracted from the former. The resulting equations are given below.

$$\nabla^2\Delta+\alpha\frac{\partial\Delta}{\partial X}+\beta\frac{\partial\Delta}{\partial Y}-\alpha\left(\frac{\kappa-1}{\kappa+1}\right)\frac{\partial\omega}{\partial Y}+\beta\left(\frac{\kappa-1}{\kappa+1}\right)\frac{\partial\omega}{\partial X}=\left(\frac{\kappa-1}{\kappa+1}\right)\frac{\rho_0}{\mu_0}\frac{\partial^2\Delta}{\partial t^2} \tag{10}$$

$$\nabla^2\omega+\alpha\frac{\partial\omega}{\partial X}+\beta\frac{\partial\omega}{\partial Y}-\alpha\left(\frac{3-\kappa}{\kappa-1}\right)\frac{\partial\Delta}{\partial Y}+\beta\left(\frac{3-\kappa}{\kappa-1}\right)\frac{\partial\Delta}{\partial X}=\frac{\rho_0}{\mu_0}\frac{\partial^2\omega}{\partial t^2} \tag{11}$$

The above equations would reduce to the classical 2-D wave equations of dilatation and rotation by assigning α and β to zero. Due to nonhomogeneity, these equations lose their classical form and remain coupled in two fields Δ and ω, through the nonhomogeneity parameters α and β.

Using the transformations given in Eqs. (12), (13), and (14), the equations of motion (10) and (11) are further written in the crack-tip moving coordinate reference (x,y), as given in Eqs. (15) and (16).

$$x=X-ct,\quad y=Y \tag{12}$$

$$\frac{\partial^2}{\partial X^2}=\frac{\partial^2}{\partial x^2};\quad \frac{\partial^2}{\partial Y^2}=\frac{\partial^2}{\partial y^2} \tag{13}$$

$$\frac{\partial^2}{\partial t^2}=c^2\frac{\partial^2}{\partial x^2}+\frac{\partial^2}{\partial t^2}-\dot{c}\frac{\partial}{\partial x}-2c\frac{\partial^2}{\partial x\partial t} \tag{14}$$

where

$$\dot{c}=\frac{\partial c}{\partial t}$$

$$\alpha_l^2\frac{\partial^2\Delta}{\partial x^2}+\frac{\partial^2\Delta}{\partial y^2}+\alpha\frac{\partial\Delta}{\partial x}+\beta\frac{\partial\Delta}{\partial y}-\alpha\left(\frac{\kappa-1}{\kappa+1}\right)\frac{\partial\omega}{\partial y}+\beta\left(\frac{\kappa-1}{\kappa+1}\right)\frac{\partial\omega}{\partial x}+\frac{\rho_0}{\mu_0}\left(\frac{\kappa-1}{\kappa+1}\right)\left(\dot{c}\frac{\partial\Delta}{\partial x}+2c\frac{\partial^2\Delta}{\partial x\partial t}-\frac{\partial^2\Delta}{\partial t^2}\right)=0 \tag{15}$$

$$\alpha_s^2\frac{\partial^2\omega}{\partial x^2}+\frac{\partial^2\omega}{\partial y^2}+\alpha\frac{\partial\omega}{\partial x}+\beta\frac{\partial\omega}{\partial y}-\alpha\left(\frac{3-\kappa}{\kappa-1}\right)\frac{\partial\Delta}{\partial y}+\beta\left(\frac{3-\kappa}{\kappa-1}\right)\frac{\partial\Delta}{\partial x}+\frac{\rho_0}{\mu_0}\left[\dot{c}\,\frac{\partial\Delta}{\partial x}+2c\,\frac{\partial^2\Delta}{\partial x\partial t}-\frac{\partial^2\Delta}{\partial t^2}\right]=0 \tag{16}$$

where

$$\alpha_l=\left[1-\frac{\rho_0}{\mu_0}\left(\frac{\kappa-1}{\kappa+1}\right)c^2\right]^{1/2}$$

and

$$\alpha_s=\left(1-\frac{\rho_0}{\mu_0}c^2\right)^{1/2}.$$

It is assumed that for transient crack growth, the crack velocity (c) is a function of time and the fields Δ and ω depend explicitly on time in the moving coordinate reference.

2.1 Asymptotic Expansion of Crack-Tip Fields. In the asymptotic analysis, first, a new set of coordinates is introduced as defined in Eq. (17).

$$\eta_1=x/\epsilon,\quad \eta_2=y/\epsilon,\quad \text{for } 0<\epsilon<1 \tag{17}$$

ϵ is a small parameter and as ϵ approaches zero, all the points in the x–y plane except those near the crack-tip are mapped beyond the range of observation in the $\eta_1-\eta_2$ plane. Equations (15) and (16) are now written in these scaled coordinates as below.

$$\alpha_l^2\frac{\partial^2\Delta}{\partial\eta_1^2}+\frac{\partial^2\Delta}{\partial\eta_2^2}+\epsilon\left[\alpha\frac{\partial\Delta}{\partial\eta_1}+\beta\frac{\partial\Delta}{\partial\eta_2}-\alpha\left(\frac{\kappa-1}{\kappa+1}\right)\frac{\partial\omega}{\partial\eta_2}+\beta\left(\frac{\kappa-1}{\kappa+1}\right)\frac{\partial\omega}{\partial\eta_1}\right]+\frac{\rho_0}{\mu_0}\left(\frac{\kappa-1}{\kappa+1}\right)\left[\dot{c}\,\frac{\partial\Delta}{\partial\eta_1}+2c\,\frac{\partial^2\Delta}{\partial\eta_1\partial t}-\epsilon\frac{\partial^2\Delta}{\partial t^2}\right]=0 \tag{18}$$

$$\alpha_s^2\frac{\partial^2\omega}{\partial\eta_1^2}+\frac{\partial^2\omega}{\partial\eta_2^2}+\epsilon\left[\alpha\frac{\partial\omega}{\partial\eta_1}+\beta\frac{\partial\omega}{\partial\eta_2}-\alpha\left(\frac{3-\kappa}{\kappa-1}\right)\frac{\partial\Delta}{\partial\eta_2}+\beta\left(\frac{3-\kappa}{\kappa-1}\right)\frac{\partial\Delta}{\partial\eta_1}\right]+\frac{\rho_0}{\mu_0}\left[\dot{c}\,\frac{\partial\Delta}{\partial\eta_1}+2c\,\frac{\partial^2\Delta}{\partial\eta_1\partial t}-\epsilon\frac{\partial^2\Delta}{\partial t^2}\right]=0 \tag{19}$$

At this stage it is assumed that Δ and ω are represented as a power series expansion in ϵ.

$$\Delta(x,y,t)=\Delta(\epsilon\eta_1,\epsilon\eta_2,t)=\sum_{m=0}^{\infty}\epsilon^{(m-1)/2}\phi_m(\eta_1,\eta_2,t)$$
$$\omega(x,y,t)=\omega(\epsilon\eta_1,\epsilon\eta_2,t)=\sum_{m=0}^{\infty}\epsilon^{(m-1)/2}\psi_m(\eta_1,\eta_2,t) \tag{20}$$

Now, substituting power series expansions (20) into Eqs. (18) and (19) gives the following equations.

$$\sum_{m=0}^{\infty}\left\{\epsilon^{(m-1)/2}\left(\alpha_l^2\frac{\partial^2\phi_m}{\partial\eta_1^2}+\frac{\partial^2\phi_m}{\partial\eta_2^2}\right)+\epsilon^{(m+1)/2}\left[\alpha\frac{\partial\phi_m}{\partial\eta_1}+\beta\frac{\partial\phi_m}{\partial\eta_2}-\alpha\left(\frac{\kappa-1}{\kappa+1}\right)\frac{\partial\psi_m}{\partial\eta_2}+\beta\left(\frac{\kappa-1}{\kappa+1}\right)\frac{\partial\psi_m}{\partial\eta_1}\right]+\frac{\rho_0}{\mu_0}\left(\frac{\kappa-1}{\kappa+1}\right)\left(\dot{c}\,\frac{\partial\phi_m}{\partial\eta_1}+2c\,\frac{\partial^2\phi_m}{\partial\eta_1\partial t}\right)\right\}-\epsilon^{(m+3)/2}\frac{\rho_0}{\mu_0}\left(\frac{\kappa-1}{\kappa+1}\right)\frac{\partial^2\phi_m}{\partial t^2}=0 \tag{21}$$

$$\sum_{m=0}^{\infty}\left\{\epsilon^{(m-1)/2}\left(\alpha_s^2\frac{\partial^2\psi_m}{\partial\eta_1^2}+\frac{\partial^2\psi_m}{\partial\eta_2^2}\right)+\epsilon^{(m+1)/2}\left[\alpha\frac{\partial\psi_m}{\partial\eta_1}+\beta\frac{\partial\psi_m}{\partial\eta_2}-\alpha\left(\frac{3-\kappa}{\kappa-1}\right)\frac{\partial\phi_m}{\partial\eta_2}+\beta\left(\frac{3-\kappa}{\kappa+1}\right)\frac{\partial\phi_m}{\partial\eta_1}\right]+\frac{\rho_0}{\mu_0}\left(\frac{\kappa-1}{\kappa+1}\right)\left(\dot{c}\,\frac{\partial\psi_m}{\partial\eta_1}+2c\,\frac{\partial^2\psi_m}{\partial\eta_1\partial t}\right)\right\}-\epsilon^{(m+3)/2}\frac{\rho_0}{\mu_0}\left(\frac{\kappa-1}{\kappa+1}\right)\frac{\partial^2\psi_m}{\partial t^2}=0 \tag{22}$$

For Eqs. (21) and (22) to be valid, the partial differential equations corresponding to each power of $\epsilon(\epsilon^{-1/2},\epsilon^0,\epsilon^{1/2},\ldots)$ should vanish independently. This leads to the following set of partial differential equations.

For $m=0$ *and* $m=1$,

$$\alpha_l^2\frac{\partial^2\phi_m}{\partial\eta_1^2}+\frac{\partial^2\phi_m}{\partial\eta_2^2}=0 \tag{22a}$$

$$\alpha_s^2\frac{\partial^2\psi_m}{\partial\eta_1^2}+\frac{\partial^2\psi_m}{\partial\eta_2^2}=0 \tag{23}$$

For $m=2$ *and* $m=3$

$$\alpha_l^2\frac{\partial^2\phi_m}{\partial\eta_1^2}+\frac{\partial^2\phi_m}{\partial\eta_2^2}+\alpha\frac{\partial\phi_{m-2}}{\partial\eta_1}+\beta\frac{\partial\phi_{m-2}}{\partial\eta_2}-\alpha\left(\frac{\kappa-1}{\kappa+1}\right)\frac{\partial\psi_{m-2}}{\partial\eta_2}-\beta\left(\frac{\kappa-1}{\kappa+1}\right)\frac{\partial\psi_{m-2}}{\partial\eta_1}+\frac{\rho_0}{\mu_0}\left(\frac{\kappa-1}{\kappa+1}\right)\left(\dot{c}\,\frac{\partial\phi_{m-2}}{\partial\eta_1}+2c\,\frac{\partial^2\phi_{m-2}}{\partial\eta_1\partial t}\right)=0 \tag{24}$$

$$\alpha_s^2\frac{\partial^2\psi_m}{\partial\eta_1^2}+\frac{\partial^2\psi_m}{\partial\eta_2^2}+\alpha\frac{\partial\psi_{m-2}}{\partial\eta_1}+\beta\frac{\partial\psi_{m-2}}{\partial\eta_2}-\alpha\left(\frac{\kappa-1}{\kappa+1}\right)\frac{\partial\phi_{m-2}}{\partial\eta_2}-\beta\left(\frac{\kappa-1}{\kappa+1}\right)\frac{\partial\phi_{m-2}}{\partial\eta_1}+\frac{\rho_0}{\mu_0}\left(\frac{\kappa-1}{\kappa+1}\right)\left(\dot{c}\,\frac{\partial\psi_{m-2}}{\partial\eta_1}+2c\,\frac{\partial^2\psi_{m-2}}{\partial\eta_1\partial t}\right)=0 \tag{25}$$

It should be observed from the above set of equations that Eqs. (22) and (23) are similar to that for homogeneous material where as the partial differential Eqs. (24) and (25), associated with higher powers of ϵ are coupled to the differentials of the lower order functions through the nonhomogeneity parameters α and β. Equations (22) and (23) can be easily reduced to Laplace's equations in the respective complex domains $\zeta_l=\eta_1+i\alpha_l\eta_2$, $\zeta_s=\eta_1+i\alpha_s\eta_2$, $i=\sqrt{-1}$.

Since the crack is propagating at an angle to the direction of property gradation, the stress field near the crack tip is a combination of both opening and shear modes (mixed mode). For elastic solution the stress field related to opening mode and shear modes can be superposed to obtain the mixed mode solution [18]. The solutions for the Eqs. (22) and (23) are same as homogeneous material [19,20] and can be written as

$$\phi_0 = \mathrm{Re}[F_0(\zeta_l)] + \mathrm{Im}[H_0(\zeta_l)] = A_0(t)\rho_l^{-1/2}\cos\frac{\theta_l}{2} - C_0(t)\rho_l^{-1/2}\sin\frac{\theta_l}{2}$$
$$\phi_1 = A_1(t)$$
$$\psi_0 = \mathrm{Im}[G_0(\zeta_s)] + \mathrm{Re}[J_0(\zeta_s)] = -B_0(t)\rho_s^{-1/2}\sin\frac{\theta_s}{2} + D_0(t)\rho_s^{-1/2}\cos\frac{\theta_s}{2} \tag{26}$$
$$\psi_1 = D_1(t)$$

where

$$\rho_l = [\eta_1^2 + \alpha_l^2\eta_2^2]^{1/2}, \quad \tan\theta_l = \frac{\alpha_l\eta_2}{\eta_1},$$
$$\rho_s = [\eta_1^2 + \alpha_s^2\eta_2^2]^{1/2}, \quad \tan\theta_s = \frac{\alpha_s\eta_2}{\eta_1}$$

In the above Eqs. (26), A_n, B_n, C_n, and D_n are real constants that vary with time. It can also be noticed that ρ_l, θ_l, ρ_s, and θ_s are also functions of time.

Using the definitions of dynamic stress intensity factors K_{ID} and K_{IID} for opening and shear modes [19] as given in Eq. (27), the relations between $A_0(t)$, $K_{\mathrm{ID}}(t)$ and $C_0(t)$, $K_{\mathrm{IID}}(t)$ are obtained, respectively.

$$K_{\mathrm{ID}} = \lim_{\substack{x\to 0\\ y=0}} \sqrt{2\pi x}\,\sigma_{yy},$$
$$K_{\mathrm{II}} = \lim_{\substack{x\to 0\\ y=0}} \sqrt{2\pi x}\,\sigma_{xy}, \tag{27}$$

$$A_0(t) = \frac{(1+\alpha_s^2)(1-\alpha_l^2)}{4\alpha_l\alpha_s - (1+\alpha_s^2)^2}\frac{K_{\mathrm{ID}}(t)}{\mu_c\sqrt{2\pi}},$$
$$C_0(t) = \frac{2\alpha_s(1-\alpha_l^2)}{4\alpha_l\alpha_s - (1+\alpha_s^2)^2}\frac{K_{\mathrm{IID}}(t)}{\mu_c\sqrt{2\pi}} \tag{28}$$

where μ_c is the crack-tip shear modulus, $K_{\mathrm{ID}}(t)$ and $K_{\mathrm{IID}}(t)$ are the respective time-dependent mode-I and mode-II dynamic stress intensity factors.

Considering the crack face boundary conditions $\sigma_{yy}=0$ and $\sigma_{xy}=0$, we can also obtain the following relationships between $A_0(t)$, $B_0(t)$ and $C_0(t)$, $D_0(t)$, respectively:

$$B_0(t) = \frac{2\alpha_l}{1+\alpha_s^2}\frac{1-\alpha_s^2}{1-\alpha_l^2}A_0(t),$$
$$D_0(t) = -\frac{1+\alpha_s^2}{2\alpha_s}\frac{1-\alpha_s^2}{1-\alpha_l^2}C_0(t) \tag{29}$$

The solution for the Eqs. (24) and (25) corresponding to higher powers of ϵ $(m=2)$ consists of two parts—classical solution and solution due to nonhomogeneity—and these can be obtained recursively [17]. The solutions ϕ_2 and ψ_2 obtained are given below. At this stage it can be noticed that the solutions ϕ_0, ψ_0, ϕ_1, and ψ_1 automatically satisfy the compatibility equations because the solutions are same as those of homogeneous materials. Since the nonhomogeneous specific parts of ϕ_2 and ψ_2 are obtained form ϕ_0 and ψ_0, they also automatically satisfy the compatibility equations.

$$\begin{aligned}\phi_2 = {} & A_2(t)\rho_l^{1/2}\cos\frac{\theta_l}{2} + C_2(t)\rho_l^{1/2}\sin\frac{\theta_l}{2} - \frac{\alpha A_0(t)}{4\alpha_l^2}\rho_l^{1/2}\cos\frac{3\theta_l}{2} + \frac{\alpha C_0(t)}{4\alpha_l^2}\rho_l^{1/2}\sin\frac{3\theta_l}{2} - \frac{\beta A_0(t)}{4\alpha_l}\rho_l^{1/2}\sin\frac{3\theta_l}{2} - \frac{\beta C_0(t)}{4\alpha_l}\rho_l^{1/2}\cos\frac{3\theta_l}{2} \\ & + \frac{2\alpha\alpha_s}{\alpha_l^2-\alpha_s^2}\left(\frac{k-1}{k+1}\right)\left[B_0(t)\rho_s^{1/2}\cos\frac{\theta_s}{2} + D_0(t)\rho_s^{1/2}\sin\frac{\theta_s}{2}\right] + \frac{2\beta}{\alpha_l^2-\alpha_s^2}\left(\frac{k-1}{k+1}\right)\left[B_0(t)\rho_s^{1/2}\sin\frac{\theta_s}{2} - D_0(t)\rho_s^{1/2}\cos\frac{\theta_s}{2}\right] \\ & - \frac{1}{2}D_l^1[A_0(t)]\rho_l^{1/2}\cos\frac{3\theta_l}{2} - \frac{1}{2}D_l^1[C_0(t)]\rho_l^{1/2}\sin\frac{3\theta_l}{2} \\ & - \frac{1}{4}BA_l^1(t)\rho_l^{1/2}\cos\frac{3\theta_l}{2} + \frac{1}{24}BA_l^1(t)\rho_l^{1/2}\cos\frac{7\theta_l}{2} - \frac{1}{4}BC_l^1(t)\rho_l^{1/2}\sin\frac{3\theta_l}{2} - \frac{1}{24}BC_l^1(t)\rho_l^{1/2}\sin\frac{7\theta_l}{2}\end{aligned} \tag{30}$$

$$\begin{aligned}\psi_2 = {} & B_2(t)\rho_s^{1/2}\sin\frac{\theta_s}{2} + D_2(t)\rho_s^{1/2}\cos\frac{\theta_s}{2} + \frac{\alpha B_0(t)}{4\alpha_s^2}\rho_s^{1/2}\sin\frac{3\theta_s}{2} - \frac{\alpha D_0(t)}{4\alpha_s^2}\rho_s^{1/2}\cos\frac{3\theta_s}{2} - \frac{\beta B_0(t)}{4\alpha_s}\rho_s^{1/2}\cos\frac{3\theta_s}{2} - \frac{\beta D_0(t)}{4\alpha_s}\rho_s^{1/2}\sin\frac{3\theta_s}{2} \\ & + \frac{2\alpha\alpha_l}{\alpha_l^2-\alpha_s^2}\left(\frac{3-\kappa}{k-1}\right)\left[A_0(t)\rho_l^{1/2}\sin\frac{\theta_l}{2} + C_0(t)\rho_l^{1/2}\cos\frac{\theta_l}{2}\right] \\ & - \frac{2\beta}{\alpha_l^2-\alpha_s^2}\left(\frac{3-\kappa}{k-1}\right)\left[A_0(t)\rho_l^{1/2}\cos\frac{\theta_l}{2} + C_0(t)\rho_l^{1/2}\sin\frac{\theta_l}{2}\right] - \frac{1}{2}D_s^1[B_0(t)]\rho_s^{1/2}\sin\frac{3\theta_s}{2} - \frac{1}{2}D_s^1[D_0(t)]\rho_s^{1/2}\cos\frac{3\theta_s}{2} \\ & - \frac{1}{4}BB_s^1(t)\rho_s^{1/2}\sin\frac{3\theta_s}{2} + \frac{1}{24}BB_s^1(t)\rho_s^{1/2}\sin\frac{7\theta_s}{2} - \frac{1}{4}BD_s^1(t)\rho_s^{1/2}\cos\frac{3\theta_s}{2} + \frac{1}{24}BD_s^1(t)\rho_s^{1/2}\cos\frac{7\theta_s}{2}\end{aligned} \tag{31}$$

where

$$D_l^1[A_0(t)]=\frac{\rho_0}{\mu_0}\left(\frac{\kappa-1}{\kappa+1}\right)\frac{\sqrt{c(t)}}{\alpha_l^2}\frac{d}{dt}[c(t)A_0(t)],$$

$$D_l^1[C_0(t)]=\frac{\rho_0}{\mu_0}\left(\frac{\kappa-1}{\kappa+1}\right)\frac{\sqrt{c(t)}}{\alpha_l^2}\frac{d}{dt}[c(t)C_0(t)]$$

$$BA_l^1(t)=\frac{3}{2}\left(\frac{\rho_0}{\mu_0}\right)^2\left(\frac{\kappa-1}{\kappa+1}\right)^2\frac{c^2(t)}{\alpha_l^4}A_0(t)\frac{dc(t)}{dt},$$

$$BC_l^1(t)=-\frac{3}{2}\left(\frac{\rho_0}{\mu_0}\right)^2\left(\frac{\kappa-1}{\kappa+1}\right)^2\frac{c^2(t)}{\alpha_l^4}C_0(t)\frac{dc(t)}{dt}$$

$$D_s^1[B_0(t)]=-\frac{\rho_0}{\mu_0}\frac{\sqrt{c(t)}}{\alpha_s^2}\frac{d}{dt}[c(t)B_0(t)],$$

$$D_s^1[D_0(t)]=\frac{\rho_0}{\mu_0}\frac{\sqrt{c(t)}}{\alpha_s^2}\frac{d}{dt}[c(t)D_0(t)]$$

$$BB_s^1(t)=-\frac{3}{2}\left(\frac{\rho_0}{\mu_0}\right)^2\frac{c^2(t)}{\alpha_s^4}B_0(t)\frac{dc(t)}{dt},$$

$$BD_s^1(t)=\frac{3}{2}\left(\frac{\rho_0}{\mu_0}\right)^2\frac{c^2(t)}{\alpha_s^4}D_0(t)\frac{dc(t)}{dt}$$

It can be observed that the first two terms in the above Eqs. (30) and (31) are same as those for a mixed mode crack in homogeneous materials and the additional terms are the result of the material nonhomogeneity. The last six terms in the solutions (30) and (31) are transient part of the differential Eqs. (24) and (25). The equations also reveal that the two terms with coefficients $2\alpha\alpha_s/(\alpha_l^2-\alpha_s^2)$ and $2\beta/(\alpha_l^2-\alpha_s^2)$ in Eqs. (30) and (31) approach infinity as crack speed approaches zero because both α_l and α_s approach values close to 1. This irregularity, which occurs for $c<0.3c_s$, is due to the coupling between Δ and ω through the lower-order partial differentials in Eqs. (10) and (11). This irregularity was duly discussed by Parameswaran and Shukla [21] and a remedial approximation was proposed for the steady-state problem. The important details of irregularity and remedial approximation using their procedure for the transient problem are discussed below.

The solution for Eq. (24) is obtained in six parts ($\phi_2=\phi_{21}+\phi_{22}+\phi_{23}+\phi_{24}+\phi_{25}+\phi_{26}$) from the following differential equations.

$$\alpha_l^2\frac{\partial^2\phi_{21}}{\partial\eta_1^2}+\frac{\partial^2\phi_{21}}{\partial\eta_2^2}=0 \tag{32}$$

$$\alpha_l^2\frac{\partial^2\phi_{22}}{\partial\eta_1^2}+\frac{\partial^2\phi_{22}}{\partial\eta_2^2}=-\alpha\frac{\partial\phi_0}{\partial\eta_1} \tag{33}$$

$$\alpha_l^2\frac{\partial^2\phi_{23}}{\partial\eta_1^2}+\frac{\partial^2\phi_{23}}{\partial\eta_2^2}=-\beta\frac{\partial\phi_0}{\partial\eta_2} \tag{34}$$

$$\alpha_l^2\frac{\partial^2\phi_{24}}{\partial\eta_1^2}+\frac{\partial^2\phi_{24}}{\partial\eta_2^2}=\alpha\left(\frac{\kappa-1}{\kappa+1}\right)\frac{\partial\psi_0}{\partial\eta_2}=\frac{-\alpha\alpha_s}{2}\left(\frac{\kappa-1}{\kappa+1}\right)\times\left[B_0(t)\rho_s^{-3/2}\cos\frac{3\theta_s}{2}+D_0(t)\rho_s^{-3/2}\sin\frac{3\theta_s}{2}\right] \tag{35}$$

$$\alpha_l^2\frac{\partial^2\phi_{25}}{\partial\eta_1^2}+\frac{\partial^2\phi_{25}}{\partial\eta_2^2}=-\beta\left(\frac{\kappa-1}{\kappa+1}\right)\frac{\partial\psi_0}{\partial\eta_1}=\frac{-\beta}{2}\left(\frac{\kappa-1}{\kappa+1}\right)\times\left[B_0(t)\rho_s^{-3/2}\sin\frac{3\theta_s}{2}-D_0(t)\rho_s^{-3/2}\cos\frac{3\theta_s}{2}\right] \tag{36}$$

$$\alpha_l^2\frac{\partial^2\phi_{26}}{\partial\eta_1^2}+\frac{\partial^2\phi_{26}}{\partial\eta_2^2}=-\frac{\rho_0}{\mu_0}\left(\frac{\kappa-1}{\kappa+1}\right)\left(\dot{c}\frac{\partial\phi_0}{\partial\eta_1}+2c\frac{\partial^2\phi_0}{\partial\eta_1\partial t}\right) \tag{37}$$

The irregular part of the solution ϕ_2 given in Eq. (30) is associated with solutions ϕ_{24} and ϕ_{25} [the solutions of Eqs. (35) and (36)]. In order to eliminate the irregular behavior, the terms in the right-hand side of the partial differential Eqs. (35) and (36) are expanded in terms of ρ_l and θ_l. First α_s is expressed in terms of α_l through the following equations.

$$\left(\frac{\alpha_s^2}{\alpha_l^2}\right)=1-\lambda\left(\frac{c}{c_s}\right)^2 \quad \text{or} \quad \alpha_s^2=\alpha_l^2(1-\xi), \quad \xi=\lambda\left(\frac{c}{c_s}\right)^2 \tag{38}$$

Knowing the elastic constants, the parameter λ can be obtained through curve fitting. For a Poisson's ratio of 0.3, λ is 0.7. Now substituting the relation (38) in the expression for ρ_s and θ_s, we can write ρ_s and θ_s in terms of α_l as given below.

$$\rho_s=\sqrt{\eta_1^2+\alpha_1^2(1-\xi)\eta_2^2} \quad \text{and} \quad \tan\theta_s=\sqrt{1-\xi}\alpha_l\eta_2/\eta_1 \tag{39}$$

Using the above relations, the right-hand side of the Eqs. (35) and (36) are now expanded as a Taylor series in terms of the parameter ξ, resulting in the following differential equations.

$$\alpha_l^2\frac{\partial^2\phi_{24}}{\partial\eta_1^2}+\frac{\partial^2\phi_{24}}{\partial\eta_2^2}=\frac{-\alpha\alpha_s}{2}\left(\frac{\kappa-1}{\kappa+1}\right)\rho_l^{-3/2}\left\{B_0(t)\left[\left(1+\frac{3}{8}\xi\right)\cos\frac{3\theta_l}{2}-\frac{3}{8}\xi\cos\frac{7\theta_l}{2}\right]+D_0(t)\left[\left(1+\frac{3}{8}\xi\right)\sin\frac{3\theta_l}{2}-\frac{3}{8}\xi\sin\frac{7\theta_l}{2}\right]+O(\xi^2)\right\} \tag{40}$$

$$\alpha_l^2\frac{\partial^2\phi_{25}}{\partial\eta_1^2}+\frac{\partial^2\phi_{25}}{\partial\eta_2^2}=\frac{\beta}{2}\left(\frac{\kappa-1}{\kappa+1}\right)\rho_l^{-3/2}\left\{-B_0(t)\left[\left(1+\frac{3}{8}\xi\right)\sin\frac{3\theta_l}{2}-\frac{3}{8}\xi\sin\frac{7\theta_l}{2}\right]+D_0(t)\left[\left(1+\frac{3}{8}\xi\right)\cos\frac{3\theta_l}{2}-\frac{3}{8}\xi\cos\frac{7\theta_l}{2}\right]+O(\xi^2)\right\} \tag{41}$$

It was identified that ξ is very small for crack speeds, $0<c/c_s<0.3$, and therefore the higher order terms of $O(\xi^2)$ are neglected. The final solution obtained in terms ρ_l and θ_l is given in

Eqs. (42) and (43). However, for crack speeds $c>0.3c_s$, ξ is not negligible and the solutions provided in Eqs. (30) and (31) can be directly used.

$$\phi_{24}=\frac{-\alpha\alpha_s}{2}\left(\frac{\kappa-1}{\kappa+1}\right)\rho_l^{1/2}\left\{\left[1+\frac{3}{8}\left(1-\frac{\alpha_s^2}{\alpha_l^2}\right)\right]\left[\frac{-1}{2\alpha_l^2}\left(B_0(t)\cos\frac{3\theta_l}{2}+D_0(t)\sin\frac{3\theta_l}{2}\right)\right]+\left[\frac{3}{8}\left(1-\frac{\alpha_s^2}{\alpha_l^2}\right)\right]\left[\frac{1}{12\alpha_l^2}\left(B_0(t)\cos\frac{7\theta_l}{2}+D_0(t)\sin\frac{7\theta_l}{2}\right)\right]\right\} \tag{42}$$

$$\phi_{25}=\frac{\beta}{2}\left(\frac{\kappa-1}{\kappa+1}\right)\rho_l^{1/2}\left\{\left[1+\frac{3}{8}\left(1-\frac{\alpha_s^2}{\alpha_l^2}\right)\right]\left[\frac{1}{2\alpha_l^2}\left(B_0(t)\sin\frac{3\theta_l}{2}-D_0(t)\cos\frac{3\theta_l}{2}\right)\right]+\left[\frac{3}{8}\left(1-\frac{\alpha_s^2}{\alpha_l^2}\right)\right]\left[\frac{-1}{12\alpha_l^2}\left(B_0(t)\sin\frac{7\theta_l}{2}-D_0(t)\cos\frac{7\theta_l}{2}\right)\right]\right\} \tag{43}$$

A similar approach is used to correct this irregularity in Eq. (31) by representing right-hand-side terms associated with irregular differential equations in terms of ρ_s and θ_s. These changes are incorporated to obtain well-behaved solutions of ϕ_2 and ψ_2 at velocities less than the $0.3c_s$ and are given below.

$$\begin{aligned}\phi_2=&A_2(t)\rho_l^{1/2}\cos\frac{\theta_l}{2}+C_2(t)\rho_l^{1/2}\sin\frac{\theta_l}{2}-\frac{\alpha A_0(t)}{4\alpha_l^2}\rho_l^{1/2}\cos\frac{3\theta_l}{2}+\frac{\alpha C_0(t)}{4\alpha_l^2}\rho_l^{1/2}\sin\frac{3\theta_l}{2}-\frac{\beta A_0(t)}{4\alpha_l}\rho_l^{1/2}\sin\frac{3\theta_l}{2}-\frac{\beta C_0(t)}{4\alpha_l}\rho_l^{1/2}\cos\frac{3\theta_l}{2}\\&+\frac{-\alpha\alpha_s}{2}\left(\frac{\kappa-1}{\kappa+1}\right)\rho_l^{1/2}\times\left\{\left[\frac{-P}{2\alpha_l^2}\left(B_0(t)\cos\frac{3\theta_l}{2}+D_0(t)\sin\frac{3\theta_l}{2}\right)\right]+\left[\frac{R}{12\alpha_l^2}\left(B_0(t)\cos\frac{7\theta_l}{2}+D_0(t)\sin\frac{7\theta_l}{2}\right)\right]\right\}\\&+\frac{\beta}{2}\left(\frac{\kappa-1}{\kappa+1}\right)\rho_l^{1/2}\left\{\left[\frac{P}{2\alpha_l^2}\left(B_0(t)\sin\frac{3\theta_l}{2}-D_0(t)\cos\frac{3\theta_l}{2}\right)\right]+\left[\frac{-R}{12\alpha_l^2}\left(B_0(t)\sin\frac{7\theta_l}{2}-D_0(t)\cos\frac{7\theta_l}{2}\right)\right]\right\}-\frac{1}{2}D_l^1[A_0(t)]\rho_l^{1/2}\cos\frac{3\theta_l}{2}\\&-\frac{1}{2}D_l^1[C_0(t)]\rho_l^{1/2}\sin\frac{3\theta_l}{2}-\frac{1}{4}BA_l^1(t)\rho_l^{1/2}\cos\frac{3\theta_l}{2}+\frac{1}{24}BA_l^1(t)\rho_l^{1/2}\cos\frac{7\theta_l}{2}-\frac{1}{4}BC_l^1(t)\rho_l^{1/2}\sin\frac{3\theta_l}{2}-\frac{1}{24}BC_l^1(t)\rho_l^{1/2}\sin\frac{7\theta_l}{2}\end{aligned} \tag{44}$$

$$\begin{aligned}\psi_2=&B_2(t)\rho_s^{1/2}\sin\frac{\theta_s}{2}+D_2(t)\rho_s^{1/2}\cos\frac{\theta_s}{2}+\frac{\alpha B_0(t)}{4\alpha_s^2}\rho_s^{1/2}\sin\frac{3\theta_s}{2}-\frac{\alpha D_0(t)}{4\alpha_s^2}\rho_s^{1/2}\cos\frac{3\theta_s}{2}-\frac{\beta B_0(t)}{4\alpha_s}\rho_s^{1/2}\cos\frac{3\theta_s}{2}-\frac{\beta D_0(t)}{4\alpha_s}\rho_s^{1/2}\sin\frac{3\theta_s}{2}\\&-\frac{\alpha\alpha_l}{2}\left(\frac{3-\kappa}{\kappa-1}\right)\rho_s^{1/2}\left\{Q\left[\frac{-1}{2\alpha_s^2}\left(A_0(t)\sin\frac{3\theta_s}{2}+C_0(t)\cos\frac{3\theta_s}{2}\right)\right]+R\left[\frac{-1}{12\alpha_s^2}\left(A_0(t)\sin\frac{7\theta_s}{2}+C_0(t)\cos\frac{7\theta_s}{2}\right)\right]\right\}\\&+\frac{\beta}{2}\left(\frac{3-\kappa}{\kappa-1}\right)\rho_s^{1/2}\left\{Q\left[\frac{-1}{2\alpha_s^2}\left(A_0(t)\cos\frac{3\theta_s}{2}-C_0(t)\sin\frac{3\theta_s}{2}\right)\right]+R\left[\frac{-1}{12\alpha_s^2}\left(A_0(t)\cos\frac{7\theta_s}{2}-C_0(t)\sin\frac{7\theta_s}{2}\right)\right]\right\}-\frac{1}{2}D_s^1[B_0(t)]\rho_s^{1/2}\sin\frac{3\theta_s}{2}\\&-\frac{1}{2}D_s^1[D_0(t)]\rho_s^{1/2}\cos\frac{3\theta_s}{2}-\frac{1}{4}BB_s^1(t)\rho_s^{1/2}\sin\frac{3\theta_s}{2}+\frac{1}{24}BB_s^1(t)\rho_s^{1/2}\sin\frac{7\theta_s}{2}-\frac{1}{4}BD_s^1(t)\rho_s^{1/2}\cos\frac{3\theta_s}{2}+\frac{1}{24}BD_s^1(t)\rho_s^{1/2}\cos\frac{7\theta_s}{2}\end{aligned} \tag{45}$$

where

$$P=1+\frac{3}{8}\left[1-\left(\frac{\alpha_s}{\alpha_l}\right)^2\right],\quad Q=1-\frac{3}{8}\left[1-\left(\frac{\alpha_s}{\alpha_l}\right)^2\right],$$

$$R=\frac{3}{8}\left[1-\left(\frac{\alpha_s}{\alpha_l}\right)^2\right]$$

The higher order terms for $m=3$ are same as those for homogeneous material for mixed mode loading since the partial differential equations [see Eqs. (24) and (25)] reduces to scaled Laplace's equations on substituting ϕ_1 and ψ_1. The solutions ϕ_3 and ψ_3 are given below.

$$\begin{aligned}\phi_3&=A_3(t)r_l\cos\theta_l+C_3(t)r_l\sin\theta_l\\\psi_3&=B_3(t)r_s\sin\theta_s+D_3(t)r_s\cos\theta_s\end{aligned} \tag{46}$$

By satisfying crack face boundary conditions, the coefficients A_3, B_3 and C_3, D_3 can be related as

$$A_3(t)=\frac{2\alpha_s}{1-\alpha_s^2}\frac{1+\alpha_s^2}{1-\alpha_l^2}B_3(t) \tag{47}$$

$$C_3(t)=-\frac{1-\alpha_l^2}{1-\alpha_s^2}\frac{1+\alpha_s^2}{2\alpha_l}D_3(t) \tag{48}$$

Now, by substituting ϕ_0, ϕ_1, ϕ_2, and ϕ_3 in the Eq. (20), the expressions for Δ and $\partial\Delta/\partial x$ and $\partial\Delta/\partial y$ can be determined and they are given below.

$$\Delta = A_0(t) r_l^{-1/2} \cos\frac{\theta_l}{2} - C_0(t) r_l^{-1/2} \sin\frac{\theta_l}{2} + A_1(t) + A_2(t) r_l^{1/2} \cos\frac{\theta_l}{2} + C_2(t) r_l^{1/2} \sin\frac{\theta_l}{2} - \frac{\alpha A_0(t)}{4\alpha_l^2} r_l^{1/2} \cos\frac{3\theta_l}{2} + \frac{\alpha C_0(t)}{4\alpha_l^2} r_l^{1/2} \sin\frac{3\theta_l}{2}$$
$$- \frac{\beta A_0(t)}{4\alpha_l} r_l^{1/2} \sin\frac{3\theta_l}{2} - \frac{\beta C_0(t)}{4\alpha_l} r_l^{1/2} \cos\frac{3\theta_l}{2} - \frac{\alpha\alpha_s}{2}\left(\frac{\kappa-1}{\kappa+1}\right) r_l^{1/2}\left\{\left[\frac{-P}{2\alpha_l^2}\left(B_0(t)\cos\frac{3\theta_l}{2} + D_0(t)\sin\frac{3\theta_l}{2}\right)\right]\right.$$
$$\left. + \left[\frac{R}{12\alpha_l^2}\left(B_0(t)\cos\frac{7\theta_l}{2} + D_0(t)\sin\frac{7\theta_l}{2}\right)\right]\right\} + \frac{\beta}{2}\left(\frac{\kappa-1}{\kappa+1}\right) r_l^{1/2}\left\{\left[\frac{P}{2\alpha_l^2}\left(B_0(t)\sin\frac{3\theta_l}{2} - D_0(t)\cos\frac{3\theta_l}{2}\right)\right]\right.$$
$$\left. + \left[\frac{-R}{12\alpha_l^2}\left(B_0(t)\sin\frac{7\theta_l}{2} - D_0(t)\cos\frac{7\theta_l}{2}\right)\right]\right\} - \frac{1}{2} D_l^1[A_0(t)] r_l^{1/2} \cos\frac{3\theta_l}{2} - \frac{1}{2} D_l^1[C_0(t)] r_l^{1/2} \sin\frac{3\theta_l}{2} - \frac{1}{4} BA_l^1(t) r_l^{1/2} \cos\frac{3\theta_l}{2}$$
$$+ \frac{1}{24} BA_l^1(t) r_l^{1/2} \cos\frac{7\theta_l}{2} - \frac{1}{4} BC_l^1(t) r_l^{1/2} \sin\frac{3\theta_l}{2} - \frac{1}{24} BC_l^1(t) r_l^{1/2} \sin\frac{7\theta_l}{2} + A_3(t) r_l \cos\theta_l + C_3(t) r_l \sin\theta_l \tag{49}$$

$$\frac{\partial\Delta}{\partial x} = -A_0(t)\frac{r_l^{-3/2}}{2}\cos\frac{3\theta_l}{2} + C_0(t)\frac{r_l^{-3/2}}{2}\sin\frac{3\theta_l}{2} + A_2(t)\frac{r_l^{-1/2}}{2}\cos\frac{\theta_l}{2} - C_2(t)\frac{r_l^{-1/2}}{2}\sin\frac{\theta_l}{2}\left(-\frac{\alpha A_0(t)}{4\alpha_l^2} - \frac{\beta C_0(t)}{4\alpha_l}\right)\frac{r_l^{-1/2}}{2}\left(-\cos\frac{5\theta_l}{2}\right.$$
$$\left. + 2\cos\frac{\theta_l}{2}\right) + \left(\frac{\alpha C_0(t)}{4\alpha_l^2} - \frac{\beta A_0(t)}{4\alpha_l}\right)\frac{r_l^{-1/2}}{2}\left(-\sin\frac{5\theta_l}{2} + 2\sin\frac{\theta_l}{2}\right) - \frac{\alpha\alpha_s}{2}\left(\frac{\kappa-1}{\kappa+1}\right)\frac{r_l^{-1/2}}{2}\left\{\left[\frac{-P}{2\alpha_l^2}B_0(t)\left(-\cos\frac{5\theta_l}{2} + 2\cos\frac{\theta_l}{2}\right)\right]\right.$$
$$\left. + \left[\frac{-P}{2\alpha_l^2}D_0(t)\left(-\sin\frac{5\theta_l}{2} + 2\sin\frac{\theta_l}{2}\right)\right] + \left[\frac{R}{12\alpha_l^2}B_0(t)\left(-3\cos\frac{9\theta_l}{2} + 4\cos\frac{5\theta_l}{2}\right)\right] + \left[\frac{R}{12\alpha_l^2}D_0(t)\left(-3\sin\frac{9\theta_l}{2} + 4\sin\frac{5\theta_l}{2}\right)\right]\right\}$$
$$+ \frac{\beta}{2}\left(\frac{\kappa-1}{\kappa+1}\right)\frac{r_l^{-1/2}}{2}\left\{\left[\frac{P}{2\alpha_l^2}B_0(t)\left(-\sin\frac{5\theta_l}{2} + 2\sin\frac{\theta_l}{2}\right)\right] - \left[\frac{P}{2\alpha_l^2}D_0(t)\left(-\cos\frac{5\theta_l}{2} + 2\cos\frac{\theta_l}{2}\right)\right]\right.$$
$$\left. + \left[\frac{-R}{12\alpha_l^2}B_0(t)\left(-3\sin\frac{9\theta_l}{2} + 4\sin\frac{5\theta_l}{2}\right)\right]\left[\frac{-R}{12\alpha_l^2}D_0(t)\left(-3\cos\frac{9\theta_l}{2} + 4\cos\frac{5\theta_l}{2}\right)\right]\right.$$
$$- \left[\frac{1}{2}D_l^1[A_0(t)] + \frac{1}{4}BA_l^1(t)\right]\frac{r_l^{-1/2}}{2}\left(-\cos\frac{5\theta_l}{2} + 2\cos\frac{\theta_l}{2}\right) - \left[\frac{1}{2}D_l^1[C_0(t)] + \frac{1}{4}BC_l^1(t)\right]\frac{r_l^{-1/2}}{2}\left(-\sin\frac{5\theta_l}{2} + 2\sin\frac{\theta_l}{2}\right)$$
$$+ \frac{1}{24}BA_l^1(t)\frac{r_l^{-1/2}}{2}\left(-3\cos\frac{9\theta_l}{2} + 4\cos\frac{5\theta_l}{2}\right) - \frac{1}{24}BC_l^1(t)\frac{r_l^{-1/2}}{2}\left(-3\sin\frac{9\theta_l}{2} + 4\sin\frac{5\theta_l}{2}\right) + A_3(t) \tag{50}$$

$$\frac{\partial\Delta}{\partial y} = -A_0(t)\alpha_l\frac{r_l^{-3/2}}{2}\sin\frac{3\theta_l}{2} - C_0(t)\alpha_l\frac{r_l^{-3/2}}{2}\cos\frac{3\theta_l}{2} + A_2(t)\alpha_l\frac{r_l^{-1/2}}{2}\sin\frac{\theta_l}{2} + C_2(t)\alpha_l\frac{r_l^{-1/2}}{2}\cos\frac{\theta_l}{2}\left(-\frac{\alpha A_0(t)}{4\alpha_l^2} - \frac{\beta C_0(t)}{4\alpha_l}\right)\alpha_l\frac{r_l^{-1/2}}{2}$$
$$\left(-\sin\frac{5\theta_l}{2} - 2\sin\frac{\theta_l}{2}\right) + \left(\frac{\alpha C_0(t)}{4\alpha_l^2} - \frac{\beta A_0(t)}{4\alpha_l}\right)\alpha_l\frac{r_l^{-1/2}}{2}\left(\cos\frac{5\theta_l}{2} + 2\cos\frac{\theta_l}{2}\right) - \frac{\alpha\alpha_l\alpha_s}{2}\left(\frac{\kappa-1}{\kappa+1}\right)\frac{r_l^{-1/2}}{2}\left\{\left[\frac{-P}{2\alpha_l^2}B_0(t)\left(-\sin\frac{5\theta_l}{2}\right.\right.\right.$$
$$\left.\left.\left. - 2\sin\frac{\theta_l}{2}\right)\right] + \left[\frac{-P}{2\alpha_l^2}D_0(t)\left(\cos\frac{5\theta_l}{2} + 2\cos\frac{\theta_l}{2}\right)\right] + \left[\frac{R}{12\alpha_l^2}B_0(t)\left(-3\sin\frac{9\theta_l}{2} - 4\sin\frac{5\theta_l}{2}\right)\right] + \left[\frac{R}{12\alpha_l^2}D_0(t)\left(3\cos\frac{9\theta_l}{2}\right.\right.\right.$$
$$\left.\left.\left. + 4\cos\frac{5\theta_l}{2}\right)\right]\right\} + \frac{\beta\alpha_1}{2}\left(\frac{\kappa-1}{\kappa+1}\right)\frac{r_l^{-1/2}}{2}\left\{\left[\frac{P}{2\alpha_l^2}B_0(t)\left(\cos\frac{5\theta_l}{2} + 2\cos\frac{\theta_l}{2}\right)\right] - \left[\frac{P}{2\alpha_l^2}D_0(t)\left(-\sin\frac{5\theta_l}{2} - 2\sin\frac{\theta_l}{2}\right)\right]\right.$$
$$\left. + \left[\frac{-R}{12\alpha_l^2}B_0(t)\left(3\cos\frac{9\theta_l}{2} + 4\cos\frac{5\theta_l}{2}\right)\right]\left[\frac{-R}{12\alpha_l^2}D_0(t)\left(-3\sin\frac{9\theta_l}{2} - 4\sin\frac{5\theta_l}{2}\right)\right]\right.$$
$$- \left[\frac{1}{2}D_l^1[A_0(t)] + \frac{1}{4}BA_l^1(t)\right]\alpha_l\frac{r_l^{-1/2}}{2}\left(-\sin\frac{5\theta_l}{2} - 2\sin\frac{\theta_l}{2}\right) - \left[\frac{1}{2}D_l^1[C_0(t)] + \frac{1}{4}BC_l^1(t)\right]\alpha_l\frac{r_l^{-1/2}}{2}\left(\cos\frac{5\theta_l}{2} + 2\cos\frac{\theta_l}{2}\right)$$
$$+ \frac{1}{24}BA_l^1(t)\alpha_l\frac{r_l^{-1/2}}{2}\left[-3\sin\frac{9\theta_l}{2} - 4\sin\frac{5\theta_l}{2}\right] - \frac{1}{24}BC_l^1(t)\alpha_l\frac{r_l^{-1/2}}{2}\left[3\cos\frac{9\theta_l}{2} + 4\cos\frac{5\theta_l}{2}\right] + \alpha_l C_3(t) \tag{51}$$

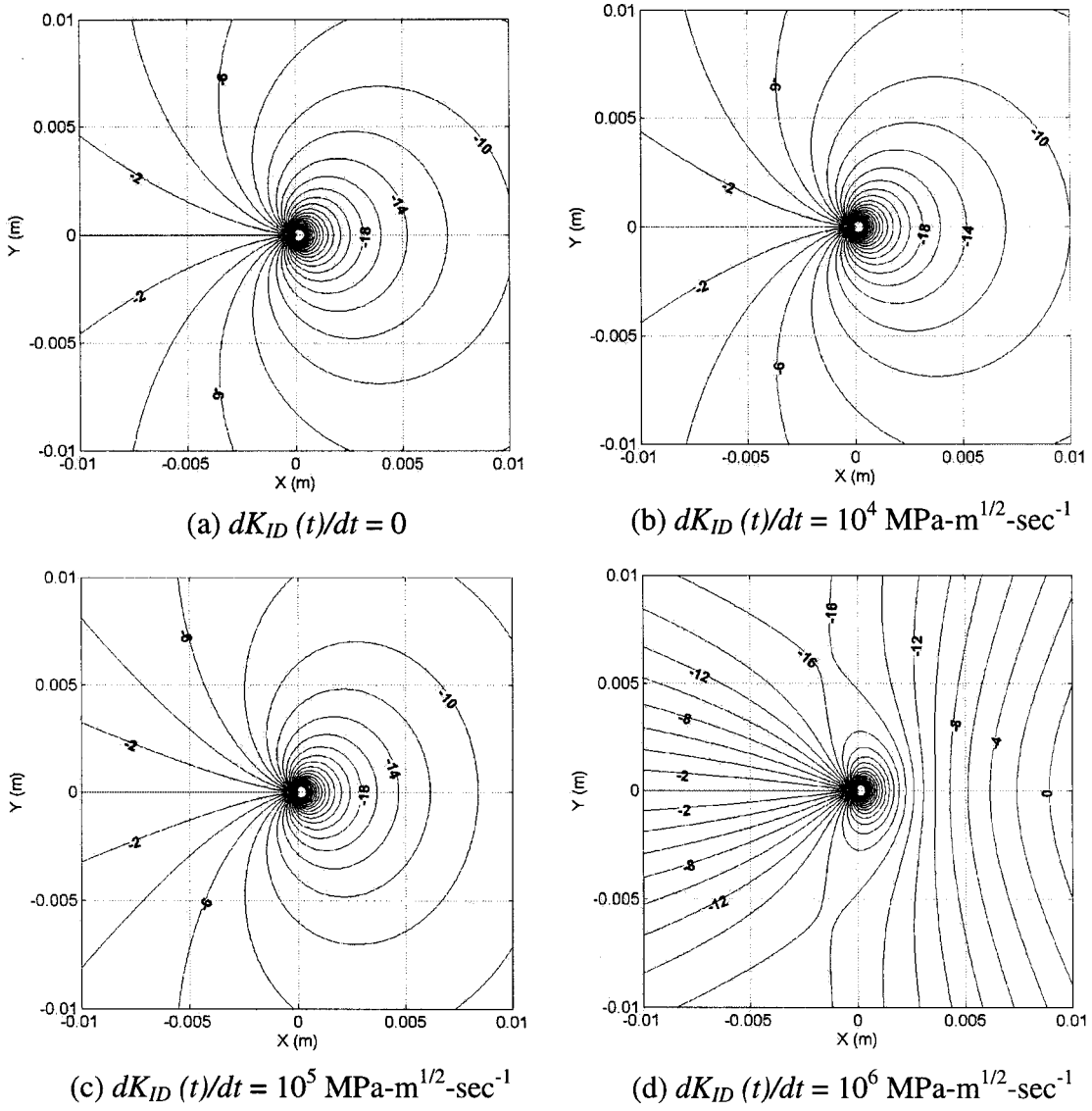

Fig. 2 Effect of rate of change of mode-I stress intensity factor on contours of constant out-of-plane displacement around the crack tip for opening mode loading in an FGM [δ=20, φ=0°, $K_{ID}(t)$=1 MPa m$^{1/2}$, $K_{IID}(t)$=0, c=300 m/s, dc/dt=0, $dK_{IID}(t)/dt$=0 and ν=0.3]

Assuming uniform strain in the out-of-plane direction for plane stress conditions, the out-of-plane displacement and their gradients can be determined by substituting Δ in Eqs. (52).

$$w = -\frac{\nu t_w}{(1-\nu)}\Delta, \quad \frac{\partial w}{\partial x} = -\frac{\nu t_w}{(1-\nu)}\frac{\partial \Delta}{\partial x}, \quad \frac{\partial w}{\partial y} = -\frac{\nu t_w}{(1-\nu)}\frac{\partial \Delta}{\partial y} \tag{52}$$

where t_w is the thickness of the specimen in the out-of-plane direction. These displacement fields and their gradients are useful in extracting the fracture parameters by analyzing full-field data around the crack tip obtained through experimental technique, CGS [22].

3 Discussion on Solutions

Equation (52) was used to study the effect of transient terms on the structure of crack-tip out-of-plane displacement fields. The contours of constant out-of-plane displacement around the crack tip were generated for both opening and mixed mode loading conditions. In an experimental investigation, the constants $A_n(t)$, $B_n(t)$, $C_n(t)$, and $D_n(t)$ of the various terms in the expansion of the out-of-plane displacements are determined from experimental data. The constants $A_0(t)$, $B_0(t)$, $C_0(t)$, and $D_0(t)$ are related to

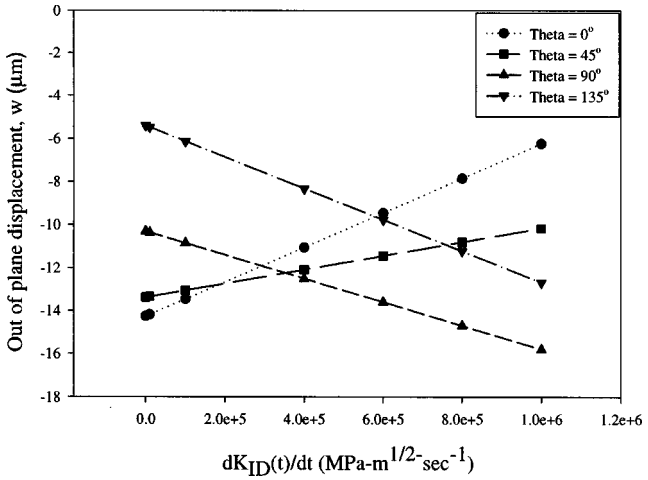

Fig. 3 Effect of transient mode-I stress intensity factor on out-of-plane displacement at various positions around the crack tip (theta is measured in a counterclockwise direction from positive *x*-axis)

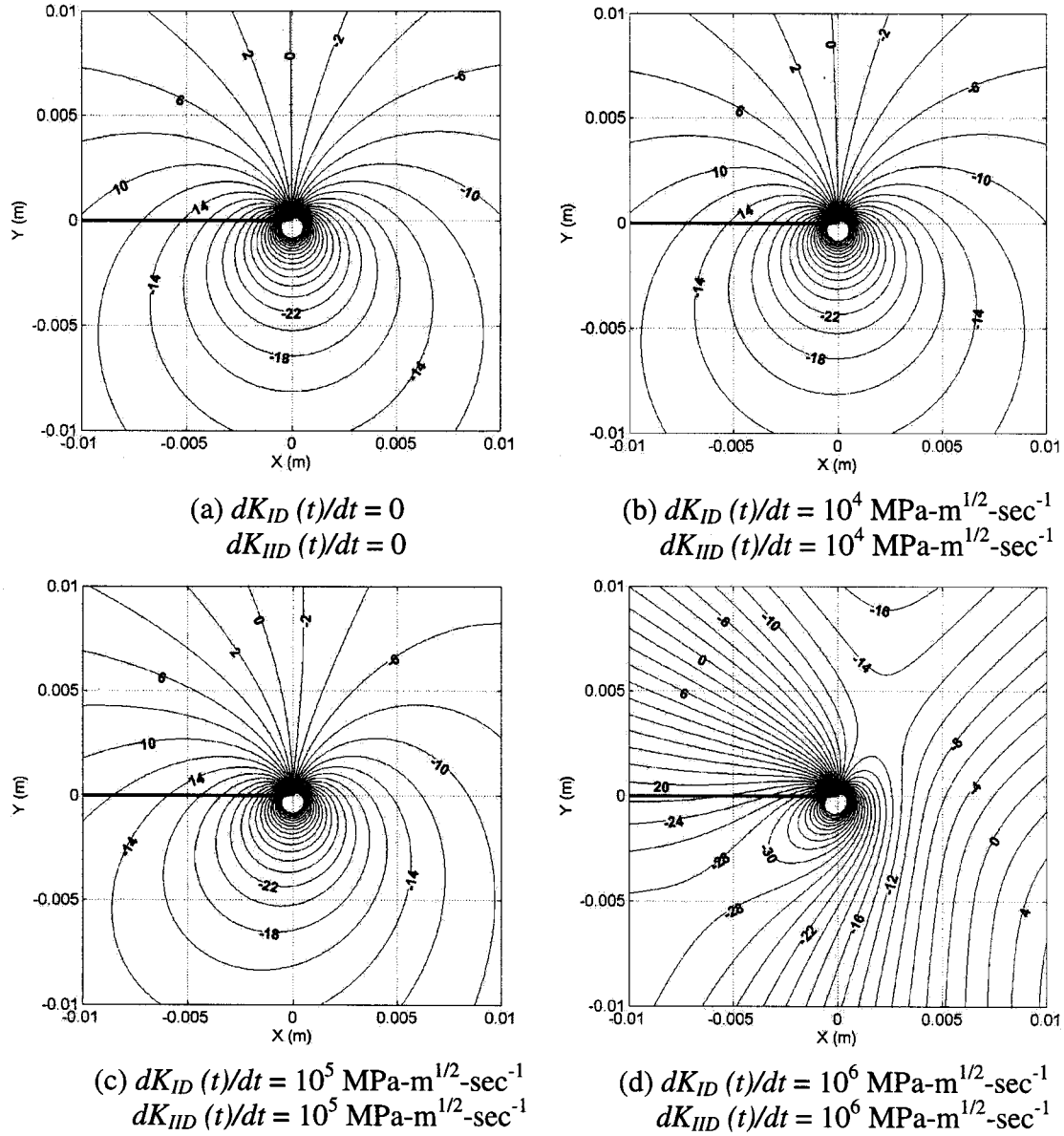

Fig. 4 Effect of rate of change of mode-I stress intensity factor and mode-II stress intensity factor on contours of constant out-of-plane displacement around the crack tip for mixed mode loading in an FGM [δ=20, φ=45°, $K_{ID}(t)$=1 MPa m$^{1/2}$, $K_{IID}(t)$=1 MPa m$^{1/2}$, c=300 m/s, dc/dt=0, and ν=0.3]

mode-I and -II stress intensity factors [$K_{ID}(t)$ and $K_{IID}(t)$ respectively] as given in Eqs. (28) and (29). The contours were drawn for a fixed value of $K_{ID}(t)$ and $K_{IID}(t)$. The remaining constants were assigned a value of zero.

The typical values of material properties and material thickness used in generating contours are as follows: Poisson's ratio (ν) =0.3, shear modulus at the crack tip (μ_c)=1 GPa, density at the crack tip (ρ_c)=2000 kg/m^3, and thickness (t)=0.01 m. Figure 2 shows the effect of rate of change of mode-I stress intensity factor [$dK_{ID}(t)/dt$] on contours of constant out-of-plane displacement (in μm) for opening mode loading around the crack tip corresponding to δ=20 and φ=0°, $K_{ID}(t)$=1.0 MPa m$^{1/2}$, $K_{IID}(t)$=0, $dK_{IID}(t)/dt$=0, c=300 m/s, and dc/dt=0. The value of $dK_{ID}(t)/dt$ was varied over six orders of magnitude. Dally and Shukla [23] showed that the rate of change of K_{ID} at crack initiation could be of the order of 10^5 MPa m$^{1/2}$ s^{-1}. The value of δ=20 corresponds to a 7.4 times increase of Young's modulus over a distance of 0.1 m along the gradient. In this figure and the figures discussed later, the crack occupies the negative x-axis and the origin is at the crack tip. It can be noticed from the figure that as the $dK_{ID}(t)/dt$ increases, the size and shape of the contours change. The contours ahead of the crack tip become compressed towards the crack tip and become elongated in the y-direction as $dK_{ID}(t)/dt$ increases. The values of out-of-plane displacement as a function of $dK_{ID}(t)/dt$ at various positions around the crack tip for radial distance of half the material thickness are shown in Fig. 3. This plot is made from the data obtained in the Fig. 2. The values of the out of plane displacement decrease by 56% along the crack line as the $dK_{ID}(t)/dt$ increases from zero to 10^6 MPa m$^{1/2}$ s^{-1}. However the out of plane displacement value decrease by only 24% for a point at angle of 45° to the positive x-axis. As the angle increase to 90°, the out of plane displacement increases by 53% for the increase of $dK_{ID}(t)/dt$ from zero to 10^6 MPa m$^{1/2}$ s^{-1}. Further increase in angle to 135°, increases the displacement values by 134% for the same increase in $dK_{ID}(t)/dt$. It can be inferred from these changes in value of

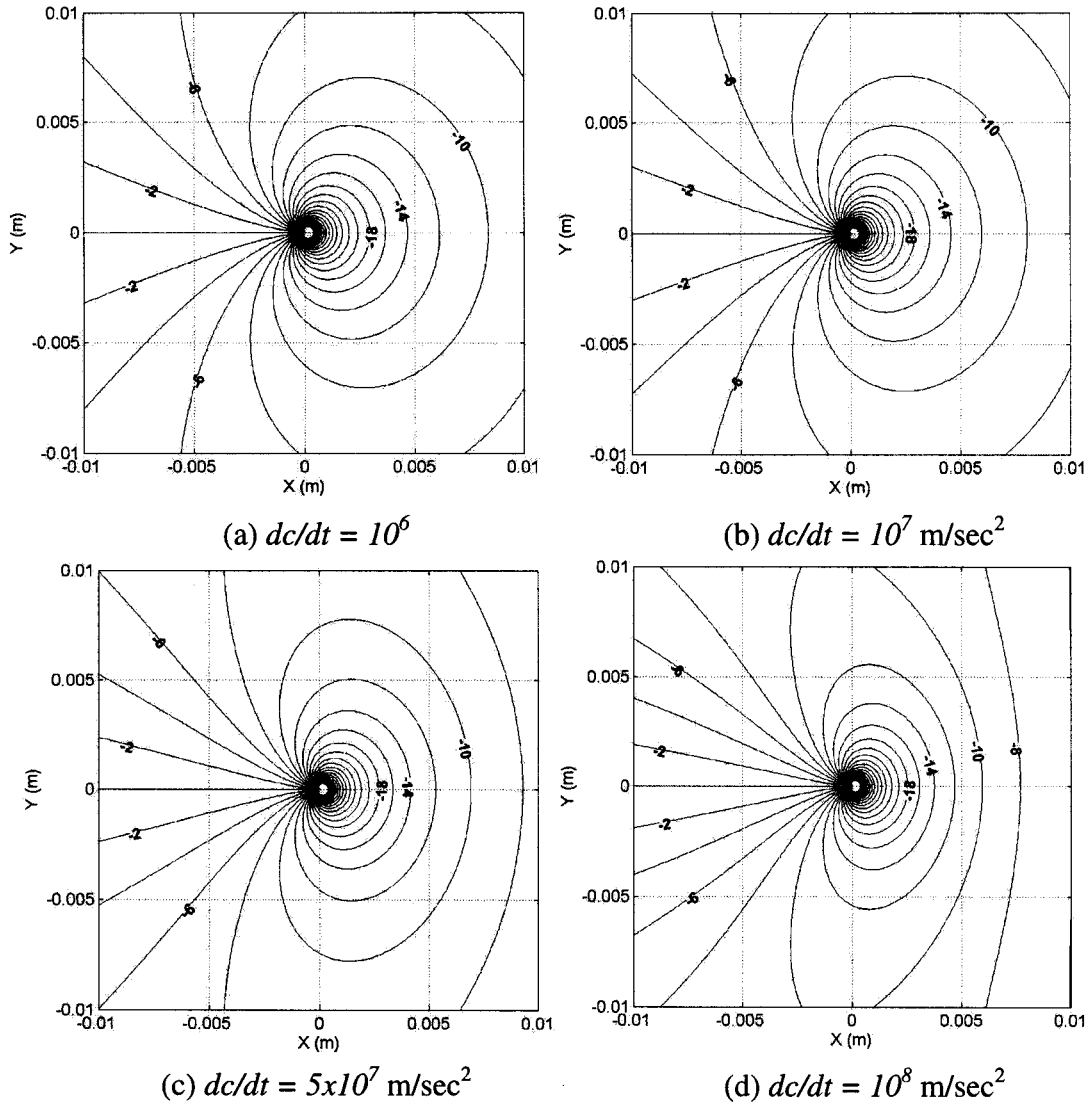

Fig. 5 Effect of crack-tip acceleration on contours of constant out-of-plane displacement around the crack tip for opening mode loading in an FGM (δ=20, φ=0°, $K_{ID}(t)$=1 MPa m$^{1/2}$, $K_{IID}(t)$=0, $dK_{ID}(t)/dt$ =10^5 MPa m$^{1/2}$ s^{-1}, $dK_{IID}(t)/dt$=0, c=300 m/s, and ν=0.3)

out-of-plane displacements around the crack tip that the transient terms have major effect on the crack-tip field for rapid change in stress intensity factor.

Figure 4 shows the effect of rate of change of mode-I stress intensity factor $[dK_{ID}(t)/dt]$ and mode-II stress intensity factor $[dK_{IID}(t)/dt]$ on contours of constant out-of-plane displacement (in μm) for mixed mode loading around the crack tip corresponding to δ=20 and φ=45°, $K_{ID}(t)=1.0$ MPa m$^{1/2}$, $K_{IID}(t)=1$ MPa m$^{1/2}$, $c=300$ m/s, and $dc/dt=0$. Similar to mode-I loading as shown in Fig. 2, in case of mixed mode loading also, the variation of $dK_{ID}(t)/dt$ and $dK_{IID}(t)/dt$ from zero to 10^6 MPa m$^{1/2}$ s^{-1} has significant effect on the size and shape of the contours. Similar to mode-I loading as shown in Fig. 3, the out-of-plane displacement values also undergo a spatial variation as the $dK_{ID}(t)/dt$ and $dK_{IID}(t)/dt$ values increase. Therefore the transient terms also have considerable effect on crack-tip field for mixed mode loading.

The effect of crack-tip acceleration on contours of constant out-of-plane displacement around the crack tip for opening mode loading, corresponding to δ=20, φ=0°, $K_{ID}(t)=1$ MPa m$^{1/2}$,

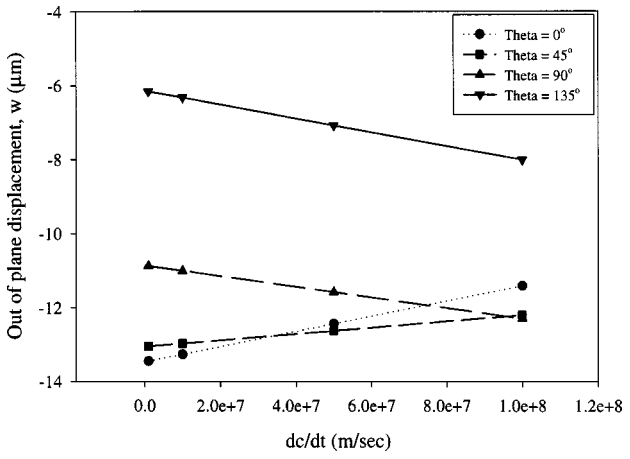

Fig. 6 Effect of acceleration on out-of-plane displacement at various positions around the crack tip (theta is measured in a counterclockwise direction from positive *x*-axis)

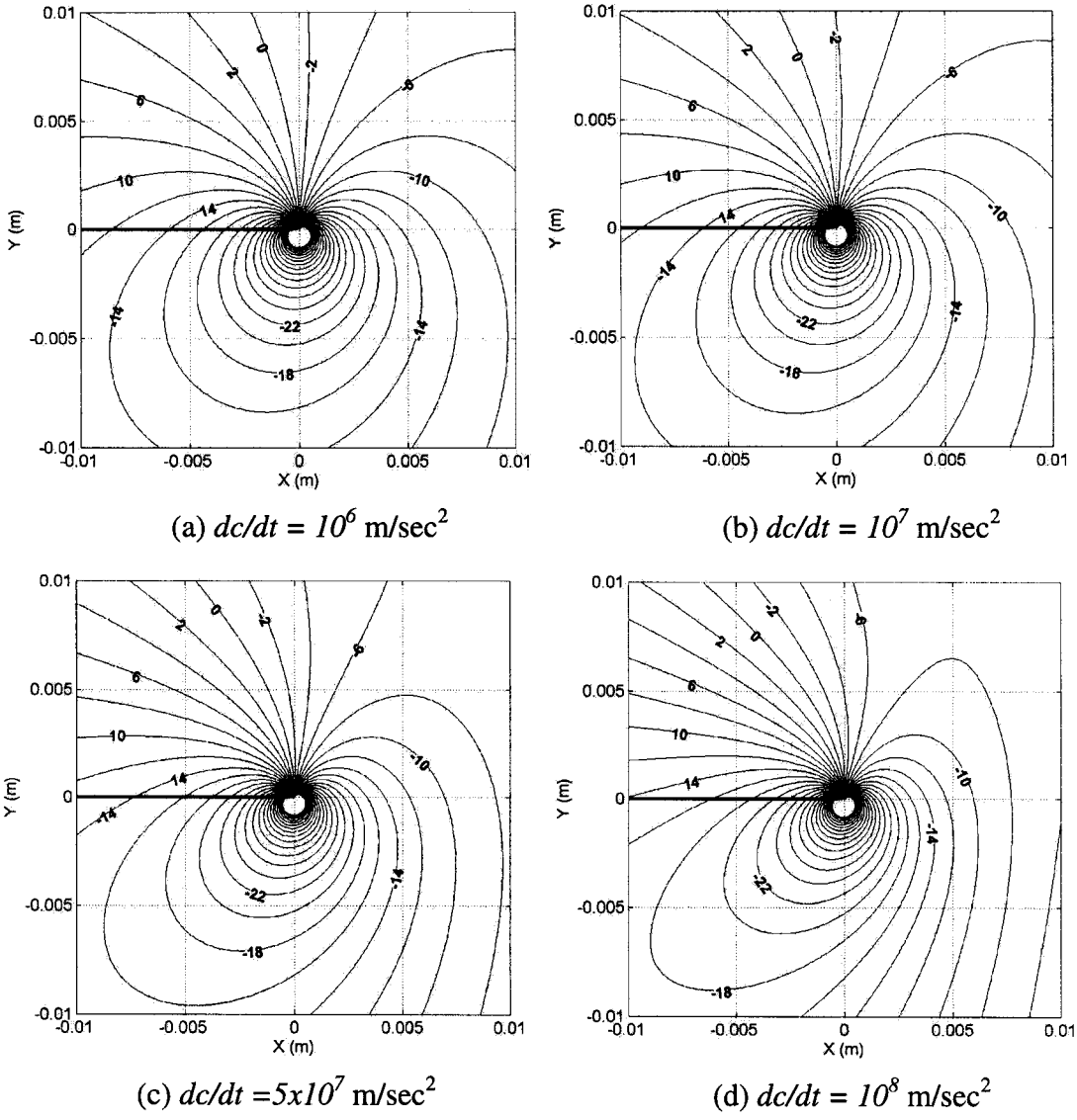

Fig. 7 Effect of crack-tip acceleration on contours of constant out-of-plane displacement around the crack tip for mixed mode loading in a FGM [δ=20, φ=45°, $K_{ID}(t)=K_{IID}(t)=1$ MPa m$^{1/2}$, $dK_{ID}(t)/dt=dK_{IID}(t)/dt=10^5$ MPa m$^{1/2}$ s^{-1}, c=300 m/s, and ν=0.3]

$dK_{ID}(t)/dt=10^5$ MPa m$^{1/2}$ s^{-1}, $K_{IID}(t)=0$, $dK_{IID}(t)/dt=0$, and $c=300$ m/s is shown in Fig. 5. The value of dc/dt was varied over eight orders of magnitude. Dally and Shukla [23] also showed that the rate of change of velocity at crack initiation could be of the order of 10^7 m/s^2. Similar to Fig. 2, the transient effect because of crack-tip acceleration also compressed the contours ahead of the crack tip as the acceleration increased. The values of out-of-plane displacement as a function of dc/dt at various positions around the crack tip for radial distance of half the plate thickness are shown in Fig. 6. This plot is made from the data obtained in the Fig. 5. The values of the out-of-plane displacement decrease by 15% along the crack line as the dc/dt increases from zero to 10^8 m/s^2. However, the out-of-plane displacement value decrease by only 6% for a point at angle of 45° to the positive x-axis for the same variation of acceleration. As the angle increases to 90°, the out-of-plane displacement increases by 13% for the increase of dc/dt from zero to 10^8 m/s^2. Further increase in angle to 135°, increases the displacement values by 30% for the same increase in dc/dt.

Figure 7 shows the effect of crack-tip acceleration on contours of constant out-of-plane displacement (in μm) around the crack tip for mixed mode loading, corresponding to δ=20 and φ=45°, $K_{ID}(t)=1.0$ MPa m$^{1/2}$, $K_{IID}(t)=1.0$ MPa m$^{1/2}$, $dK_{ID}(t)/dt=10^5$ MPa m$^{1/2}$ s^{-1}, $dK_{IID}(t)/dt=10^4$ MPa m$^{1/2}$ s^{-1}, and $c=300$ m/s. Similar to mode-I loading as shown in Fig. 5, in case of mixed mode loading also, the variation of dc/dt has considerable effect on the size and shape of the contours.

4 Concluding Remarks

Asymptotic expansion of out-of-plane displacement field and its gradients for a transient crack propagating at an angle to the property gradient were obtained. These displacement fields are required for extracting the fracture parameters by analyzing full-field data around the crack tip obtained through experimental techniques, such as CGS. Using these displacement fields, the effect of transient stress intensity factor and acceleration on synthetic contours of constant out-of-plane displacement under both opening and mixed mode loading has been shown. These contours show that the transient effects cause significant spatial variation in out-of-plane displacements around the crack tip. Therefore, in studying dynamic fracture of FGMs, it is appropriate to include the transient terms in the field equations for the situations of sudden variation of stress intensity factor or crack-tip velocity.

Acknowledgments

The financial support of the National Science Foundation (NSF), under grant No. CMS 0244330 is greatly acknowledged.

References

[1] Niino, M., Hirai, T., and Watanabe, R., 1987, ''The Functionally Gradient Materials,'' J. Jap. Soc. Comp. Mater., **13:1**, p. 257.
[2] Delale, F., and Erdogan, F., 1983, ''The Crack Problem for a Nonhomogeneous Plane,'' J. Appl. Mech., **50**, pp. 67–80.
[3] Schovanec, L., and Walton, J. R., 1988, ''On the Order of Stress Singularity for an Antiplane Shear Crack at the Interface of Two Bonded Inhomogeneous Elastic Materials,'' ASME J. Appl. Mech., **55**, pp. 234–236.
[4] Konda, N., and Erdogan, F., 1994, ''The Mixed Mode Crack Problem in a Nonhomogeneous Elastic Plane,'' Eng. Fract. Mech., **47**, pp. 533–545.
[5] Gu, P., and Asaro, R. J., 1997, ''Cracks in Functionally Graded Materials,'' Int. J. Solids Struct., **34:1**, pp. 1–17.
[6] Li, C. Y., and Weng, G. J., 2002, ''Antiplane Crack Problem in Functionally Graded Piezoelectric Materials,'' J. Appl. Mech., **69**, pp. 481–488.
[7] Rousseau, C. E., and Tippur, H. V., 2000, ''Compositionally Graded Materials With Cracks Normal to the Elastic Gradient,'' Acta Mater., **48**, pp. 4021–4033.
[8] Parameswaran, V., and Shukla, A., 2002, ''Asymptotic Stress Fields for Stationary Cracks Along the Gradient in Functionally Graded Materials,'' Trans. ASME, **69**, pp. 240–243.
[9] Atkinson, C., and List, R. D., 1978, ''Steady State Crack Propagation Into Media With Spatially Varying Elastic Properties,'' Int. J. Eng. Sci., **16**, pp. 717–730.
[10] Wang, X. D., and Meguid, S. A., 1995, ''On the Dynamic Crack Propagation in an Interface With Spatially Varying Elastic Properties,'' Int. J. Fract., **69**, pp. 87–99.
[11] Nakagaki, M., Sasaki, H., and Hagihara, S., 1995, ''A Study of Crack in Functionally Graded Materials Under Dynamic Loading,'' PVP-Dynamic Fracture, Failure and Deformations, ASME, **300**, pp. 1–6.
[12] Parameswaran, V., and Shukla, A., 1998, ''Dynamic Fracture of a Functionally Fracture in Functionally Gradient Materials,'' J. Mater. Sci., **33**, pp. 3303–3311.
[13] Rousseau, C. E., and Tippur, H. V., 2001, ''Dynamic Fracture of Compositionally Graded Materials With Cracks Along the Elastic Gradient: Experiments and Analysis,'' Mech. Mater., **33**, pp. 403–421.
[14] Parameswaran, V., and Shukla, A., 1999, ''Crack-Tip Stress Fields for Dynamic Fracture in Functionally Gradient Materials,'' Mech. Mater., **31**, pp. 579–596.
[15] Jiang, L. Y., and Wang, X. D., 2002, ''On the Dynamic Crack Propagation in an Interphase With Spatially Varying Elastic Properties Under Inplane Loading,'' Int. J. Fract., **114**, pp. 225–244.
[16] Chalivendra, V. B., Shukla, A., and Parameswaran, V., 2002, ''Dynamic Out of Plane Displacement Fields for an Inclined Crack in Graded Materials,'' J. Elast., **69**, pp. 99–119.
[17] Freund, L. B., and Rosakis, A. J., 1992, ''The Structure of the Near-Tip Field During Transient Elastodynamic Crack Growth,'' J. Am. Soc. Mass Spectrom., **40**(3), pp. 699–719.
[18] Gu, P., and Asaro, R. J., 1997, ''Cracks in Functionally Graded Materials,'' Int. J. Solids Struct., **34**(**1**), pp. 1–17.
[19] Freund, L. B., 1990, *Dynamic Fracture Mechanics*, Cambridge University Press, Cambridge, MA.
[20] G. R. Irwin, 1980, *Series Representation of the Stress Field Around Constant Speed Cracks*, University of Maryland Lecture Notes.
[21] Parameswaran, V., and Shukla, A., 2002, ''Near-Tip Out of Plane Displacement Fields for Dynamic Crack Propagation in Functionally Graded Materials,'' Mech. Res. Commun., **29**, pp. 397–406.
[22] Tippur, H. V., Krishnaswamy, S., and Rosakis, A. J., 1991, ''A Coherent Gradient Sensor for Crack Tip Measurements: Analytical and Experimental Results,'' Int. J. Fract., **40**, pp. 193–204.
[23] Dally, J. W., and Shukla, A., 1979, ''Dynamic Crack Behavior at Initiation,'' Mech. Res. Commun., **6**(4), pp. 239–244.

Damage Modeling in Random Short Glass Fiber Reinforced Composites Including Permanent Strain and Unilateral Effect

Hicham Mir
Research Professional
e-mail: mhicham@giref.ulaval.ca

Mario Fafard
Professor
e-mail: mfafard@gci.ulaval.ca

Benoît Bissonnette
e-mail: benoit.bissonnette@gci.ulaval.ca

Marie-Laure Dano
e-mail: marie-laure.dano@gmc.ulaval.ca

Department of Civil Engineering,
Université Laval,
Québec City,
Quebec G1K 7P4, Canada

This paper presents the development of a theoretical damage mechanics model applicable to random short glass fiber reinforced composites. This model is based on a macroscopic approach using internal variables together with a thermodynamic potential expressed in the stress space. Induced anisotropic damage, nonsymmetric tensile/compressive behavior (unilateral effect) and residual effects (permanent strain) are taken into account. The anisotropic damage is represented with second-order tensorial internal variables ***D****. The unilateral effect due to microcrack closure in compression is introduced by generalizing the hypothesis of the complementary elastic energy equivalence. In the case of the permanent strain, a new term related to frozen energy, which is a function of the damage variable, the stress tensor, and some materials constants to be identified, is added to the basic thermodynamic potential. Using laboratory test results, parameter identification has been performed to illustrate the applicability of the proposed model.*
[DOI: 10.1115/1.1839593]

1 Introduction

The industry of utility and recreative vehicles uses random short glass fiber reinforced composites to construct a wide variety of parts due to its light weight and the ease with which complex shapes can be achieved. For example, it is used in the manufacturing of seats for subway trains, shells for watercraft and electrical vehicles, side panels of buses, etc. To optimize those parts, both the elastic properties of the material and its behavior under heavy loads inducing progressive damage up to failure have to be characterized.

For two decades, many papers have been published on the modeling of damage mechanics using a thermodynamic approach with internal variables [1–5]. Although those models were developed using a macroscopic formulation, microscopic considerations and observations were used to justify them. The framework of the thermodynamic of irreversible processes (TIP) using internal variables is probably one of the best approaches to model damage mechanics. However, there still remain many open questions for the modeling of induced anisotropy (in particular, in the case of nonproportional loading), desactivation of damage due to microcrack closure (unilateral effect), and residual effects.

The aim of this paper is to present a theoretical damage model able to predict the behavior of glass fiber reinforced composites and the progressive degradation preceding failure. The material is made of polyester resin and short glass fibers distributed randomly in the plane of the part using a robotized technology. In Ref. [6], some results about the characterization of the tensile behavior of this material have been published. Those tests results also provided some information pertaining to the different damage mechanisms. In Refs. [7,8], detailed information related to the characterization of this material can be found. Damage is revealed by the elastic modulus decrease with progressive repeated tensile loading tests. Permanent strains have been also observed in these tests. However, loading and unloading in compression show that there is neither stiffness loss nor permanent strain due to damage, indicating that the material behavior is linear elastic. Complementary tests have been performed; they are the pseudo-biaxial tensile tests [8]. After damage has been induced in one direction, denoted 1-direction in Fig. 1, the material has been loaded in an elastic domain in some other selected direction (45 and 90 deg) in order to estimate Young's modulus, Poisson's ratio, and the shear modulus. These tests have been performed for different damage levels. Results show clearly that the transverse Young's modulus (modulus in the 2-direction) is reduced by the damage induced in the 1-direction.

This paper presents a new model based on TIP with internal variables to take into account the unilateral effect of the composite and permanent strain [9]. The data published in [7,8] and an identification procedure were used to determine the parameters of the proposed model and the tensile and shear tests were simulated.

2 Description of the Proposed Model

2.1 Modified Hypothesis of Complementary Elastic Energy Equivalence. In the case of an isotropic material, the complementary elastic energy is defined as

$$U_0^e = \frac{1}{2E}\boldsymbol{\sigma}:\boldsymbol{\sigma} - \frac{\nu}{2E}((\boldsymbol{\sigma}:\mathbf{I_2})^2 - \boldsymbol{\sigma}:\boldsymbol{\sigma}) \tag{1}$$

where $\mathbf{I_2}$ is a second-order unit tensor, $\boldsymbol{\sigma}$ is the stress tensor, E is Young's modulus, and ν is Poisson's ratio. After a tensile loading causing damage, when the material is loaded in compression, as observed on test specimens, the damage or the (smeared) cracks seem to disappear. The explanation is relatively simple. In the general case, a crack is closed (in part or totally) when a stress normal to its plane is a compressive stress. To take into account this phenomenon in the expression of complementary elastic energy of the damage material, a new hypothesis is introduced that is a modification of the hypothesis of complementary elastic energy equivalence proposed by Sidoroff [10]. It is assumed that the complementary elastic energy of the damaged material has the

Contributed by the Applied Mechanics Division of THE AMERICAN SOCIETY OF MECHANICAL ENGINEERS for publication in the ASME JOURNAL OF APPLIED MECHANICS. Manuscript received by the Applied Mechanics Division, October 30, 2003; final revision, August 12, 2004. Associate Editor: K. M. Liechti. Discussion on the paper should be addressed to the Editor, Prof. Robert M. McMeeking, Journal of Applied Mechanics, Department of Mechanics and Environmental Engineering, University of California–Santa Barbara, Santa Barbara, CA 93106-5070, and will be accepted until four months after final publication in the paper itself in the ASME JOURNAL OF APPLIED MECHANICS.

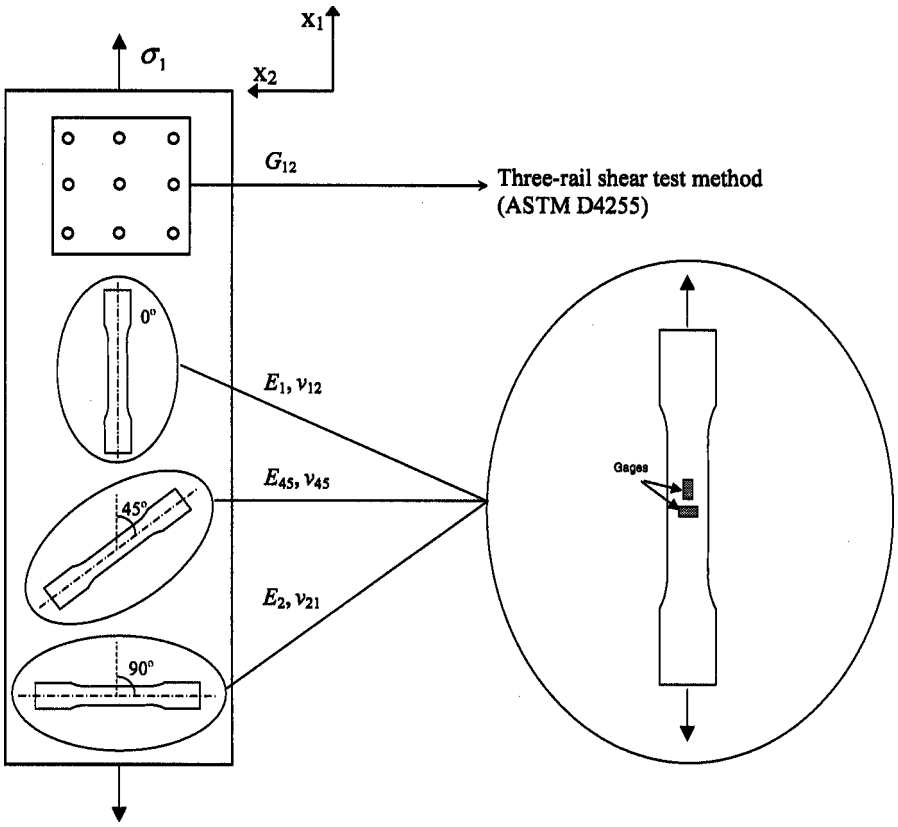

Fig. 1 Tensile testing on rectangular plates and specimens cut from it along specific directions

same form as an equivalent undamaged material by replacing the usual stress variable by an effective one, except for the energy linked to the compression that is responsible for the crack closure.

In the principal coordinate system of damage and using a classical indicial notation, the complementary elastic energy using the postulate described previously can be written as

$$U^e(\boldsymbol{\sigma},\mathbf{D}) = \frac{1}{2E}\tilde{\sigma}_{ii}^{+}\tilde{\sigma}_{ii}^{+} + \frac{1}{2E}\sigma_{ii}^{-}\sigma_{ii}^{-} + \frac{1}{2E}\tilde{\sigma}_{ij}\tilde{\sigma}_{ij}\Big|_{i\neq j} - \frac{\nu}{2E}(\tilde{\sigma}_{ii}\tilde{\sigma}_{jj} - \tilde{\sigma}_{ij}\tilde{\sigma}_{ij}) \tag{2}$$

where $\tilde{\sigma}_{ii}^{+}$ is the tensile stress (positive), and $\tilde{\sigma}_{ii}^{-}$ is the compressive stress (negative) normal to the plane of the microcrack system. In other words, the compressive stress $\boldsymbol{\sigma}^{-}$ is defined as

$$\boldsymbol{\sigma}^{-} = H(-n_i\boldsymbol{\sigma}n_i)(n_i\boldsymbol{\sigma}n_i)n_i\otimes n_i = \underline{\mathbf{P}}^{(\boldsymbol{\sigma},\mathbf{D})-}:\boldsymbol{\sigma},$$
$$\underline{\mathbf{P}}^{(\boldsymbol{\sigma},\mathbf{D})-} = H(-n_i\boldsymbol{\sigma}n_i)(n_i\otimes n_i\otimes n_i\otimes n_i) \tag{3}$$

where n_i are the principal directions of the damage and H is the Heaviside function defined by

$$H(x) = \begin{cases} 1, & x>0 \\ 0, & x<0 \end{cases} \tag{4}$$

The quantity $\underline{\mathbf{P}}^{(\sigma,D)-}$ is a fourth-order tensor corresponding to a negative projection operator. In the same way, the positive projection operator can be defined as

$$\underline{\mathbf{P}}^{(\boldsymbol{\sigma},\mathbf{D})+} = H(n_i\boldsymbol{\sigma}n_i)(n_i\otimes n_i\otimes n_i\otimes n_i) \tag{5}$$

The fourth-order damage operator $\underline{\mathbf{M}}(\mathbf{D})$ has a canonical form [11]

$$\underline{\mathbf{M}}(\mathbf{D}) = \frac{\delta_{ik}\delta_{jl}}{\sqrt{(1-D_i)(1-D_j)}}n_i\otimes n_j\otimes n_k\otimes n_l = \frac{1}{\sqrt{(1-D_i)(1-D_j)}}n_i\otimes n_j\otimes n_i\otimes n_j \tag{6}$$

where D_i is the damage eigenvalue in the principal direction i. The canonical form is used because the fourth-order tensor $\underline{\mathbf{M}}(\mathbf{D})$ is a real symmetric tensor and its second-order eigentensors associated with the real positive eigenvalues $1/\sqrt{(1-D_i)(1-D_j)}$ are $n_i\otimes n_j$.

Using Eqs. (3), (5), and (6), Eq. (2) becomes

$$U^e(\boldsymbol{\sigma},\mathbf{D}) = \frac{1}{2E}\boldsymbol{\sigma}:(\underline{\mathbf{P}}^{(\boldsymbol{\sigma},\mathbf{D})+}:\underline{\mathbf{M}}(\mathbf{D}):\underline{\mathbf{M}}(\mathbf{D}):\underline{\mathbf{P}}^{(\boldsymbol{\sigma},\mathbf{D})+}):\boldsymbol{\sigma} + \frac{1}{2E}\boldsymbol{\sigma}:(\underline{\mathbf{P}}^{(\boldsymbol{\sigma},\mathbf{D})-}:\underline{\mathbf{P}}^{(\boldsymbol{\sigma},\mathbf{D})-}):\boldsymbol{\sigma} + \frac{1}{2E}\boldsymbol{\sigma}:(\underline{\mathbf{E}}_{\mathbf{ijij}}:\underline{\mathbf{M}}(\mathbf{D}):\underline{\mathbf{M}}(\mathbf{D}):\underline{\mathbf{E}}_{\mathbf{ijij}})_{\mathbf{i}\neq\mathbf{j}}:\boldsymbol{\sigma} - \frac{\nu}{2E}[(tr(\underline{\mathbf{M}}(\mathbf{D}):\boldsymbol{\sigma}))^2 - \boldsymbol{\sigma}:(\underline{\mathbf{M}}(\mathbf{D}):\underline{\mathbf{M}}(\mathbf{D})):\boldsymbol{\sigma}] \tag{7}$$

where $\underline{\mathbf{E}}_{\mathbf{ijij}} = n_i\otimes n_j\otimes n_i\otimes n_j$. The second term of Eq. (7) can also be written as

$$\frac{1}{2E}\boldsymbol{\sigma}:(\underline{\mathbf{P}}^{(\boldsymbol{\sigma},\mathbf{D})-}:\underline{\mathbf{P}}^{(\boldsymbol{\sigma},\mathbf{D})-}):\boldsymbol{\sigma}$$

$$=\frac{1}{2E}\boldsymbol{\sigma}:(\underline{\mathbf{P}}^{(\boldsymbol{\sigma},\mathbf{D})-}:\underline{\mathbf{M}}:\underline{\mathbf{M}}:\underline{\mathbf{P}}^{(\boldsymbol{\sigma},\mathbf{D})-}):\boldsymbol{\sigma}$$

$$-\frac{1}{2E}\boldsymbol{\sigma}:[\underline{\mathbf{P}}^{(\boldsymbol{\sigma},\mathbf{D})-}:(\underline{\mathbf{M}}:\underline{\mathbf{M}}-\underline{\mathbf{I}}_4):\underline{\mathbf{P}}^{(\boldsymbol{\sigma},\mathbf{D})-}]:\boldsymbol{\sigma} \quad (8)$$

where $\underline{\mathbf{I}}_4$ is a fourth order unit tensor. Using Eq. (8), Eq. (7) becomes

$$U^e(\boldsymbol{\sigma},\mathbf{D})=\frac{1}{2E}\boldsymbol{\sigma}:(\underline{\mathbf{M}}:\underline{\mathbf{M}}):\boldsymbol{\sigma}-\frac{\nu}{2E}[(tr(\mathbf{M}:\boldsymbol{\sigma}))^2-\boldsymbol{\sigma}:(\underline{\mathbf{M}}:\underline{\mathbf{M}}):\boldsymbol{\sigma}]$$

$$-\frac{1}{2E}\boldsymbol{\sigma}:[\underline{\mathbf{P}}^{(\boldsymbol{\sigma},\mathbf{D})-}:(\underline{\mathbf{M}}:\underline{\mathbf{M}}-\underline{\mathbf{I}}_4):\underline{\mathbf{P}}^{(\boldsymbol{\sigma},\mathbf{D})-}]:\boldsymbol{\sigma} \quad (9)$$

The first two terms of Eq. (9) are identical to the one obtained by Sidoroff [10] when applying the original postulate of complementary elastic energy equivalence. The last term represents the restoration of the system rigidity due to crack closure. In that case, the microcrack system is said to become inactive. The definition corresponding to the last term of Eq. (9) is written as follows:

$$\Delta U^e(\boldsymbol{\sigma},\mathbf{D})=\frac{1}{2E}\boldsymbol{\sigma}:[\underline{\mathbf{P}}^{(\boldsymbol{\sigma},\mathbf{D})-}:(\underline{\mathbf{M}}:\underline{\mathbf{M}}-\underline{\mathbf{I}}_4):\underline{\mathbf{P}}^{(\boldsymbol{\sigma},\mathbf{D})-}]:\boldsymbol{\sigma} \quad (10)$$

Substituting Eqs. (5) and (6) in Eq. (10), one obtains

$$\Delta U^e(\boldsymbol{\sigma},\mathbf{D})=\frac{1}{2E}\boldsymbol{\sigma}:\breve{\underline{\mathbf{M}}}(\mathbf{D}):\boldsymbol{\sigma} \quad (11)$$

The fourth-order operator $\breve{\underline{\mathbf{M}}}(\mathbf{D})$ is defined as

$$\breve{\underline{\mathbf{M}}}(\mathbf{D})=H(-n_i\boldsymbol{\sigma}n_i)\frac{D_i(2-D_i)}{(1-D_i)^2}n_i\otimes n_i\otimes n_i\otimes n_i \quad (12)$$

and thus, the complementary elastic energy defined by Eq. (9) can now be written as

$$U^e(\boldsymbol{\sigma},\mathbf{D})=\frac{1}{2}\boldsymbol{\sigma}:\tilde{\underline{\mathbf{C}}}^{-1}:\boldsymbol{\sigma}-\frac{1}{2E}\boldsymbol{\sigma}:\breve{\underline{\mathbf{M}}}:\boldsymbol{\sigma} \quad (13)$$

where $\tilde{\underline{\mathbf{C}}}^{-1}=\underline{\mathbf{M}}:\underline{\mathbf{C}}^{-1}:\underline{\mathbf{M}}$ is the fourth-order elastic compliance tensor of the damaged material which could be written in the principal coordinate system of damage as

$$\tilde{\underline{\mathbf{C}}}^{-1}=\begin{bmatrix}
\frac{1}{E(1-D_1)^2} & \frac{-\nu}{E(1-D_1)(1-D_2)} & \frac{-\nu}{E(1-D_1)(1-D_3)} & 0 & 0 & 0\\
\frac{-\nu}{E(1-D_2)(1-D_1)} & \frac{1}{E(1-D_2)^2} & \frac{-\nu}{E(1-D_2)(1-D_3)} & 0 & 0 & 0\\
\frac{-\nu}{E(1-D_3)(1-D_1)} & \frac{-\nu}{E(1-D_3)(1-D_2)} & \frac{1}{E(1-D_3)^2} & 0 & 0 & 0\\
0 & 0 & 0 & \frac{1}{G(1-D_2)(1-D_3)} & 0 & 0\\
0 & 0 & 0 & 0 & \frac{1}{G(1-D_1)(1-D_3)} & 0\\
0 & 0 & 0 & 0 & 0 & \frac{1}{G(1-D_1)(1-D_2)}
\end{bmatrix} \quad (14)$$

It can be observed from Eq. (13) that if all components of the stress tensor are positive, the term $\breve{\underline{\mathbf{M}}}(\mathbf{D})$ is inactive (microcracks opening), and the classical form defined by Sidoroff [10] is obtained.

2.2 Residual Effect. When loads (tensile stress) are applied on a composite structure, cracks and thus damage are induced in the material. The level of degradation is quantified through the second-order damage tensor **D**. On the contrary, during the unloading phase, the microcracks progressively close up to a certain extent (at the end of the process, the microcracks are not necessarily entirely closed). This phenomenon has microscopic justifications related to the nature and geometry of the crack, which fall beyond the scope of this paper. Explanations of the phenomenon can be found in Refs. [4,11]. In the present paper, this residual effect (residual strain) is attributed to the state of damage, and the existence of a potential, noted U^p, which is a function of the damage tensor **D** and the stress tensor is postulated as

$$U^p(\boldsymbol{\sigma},\mathbf{D})=\boldsymbol{\sigma}:\underline{\mathbf{A}}:\mathbf{D} \quad (15)$$

where $\underline{\mathbf{A}}$ is a symmetric fourth-order tensor whose coefficients are material constants to be identified. This energy can be viewed as frozen by the microcracks. The thermodynamic potential can be rewritten as

$$U(\boldsymbol{\sigma},\mathbf{D})=\frac{1}{2}\boldsymbol{\sigma}:\tilde{\underline{\mathbf{C}}}^{-1}:\boldsymbol{\sigma}-\frac{1}{2E}\boldsymbol{\sigma}:\breve{\underline{\mathbf{M}}}:\boldsymbol{\sigma}+\boldsymbol{\sigma}:\underline{\mathbf{A}}:\mathbf{D} \quad (16)$$

2.3 State Laws

Elastic Constitutive Law. The elastic constitutive law of the damaged material is obtained by differentiating the dual potential with respect to the stress tensor. The strain is defined in two parts due the Heaviside function in the potential expression:

$$\boldsymbol{\varepsilon}=\tilde{\underline{\mathbf{C}}}^{-1}:\boldsymbol{\sigma}-\frac{1}{E}\breve{\underline{\mathbf{M}}}:\boldsymbol{\sigma}+\underline{\mathbf{A}}:\mathbf{D} \quad (17)$$

The total strain is composed of an elastic part ($\boldsymbol{\varepsilon}^e$) and a permanent part ($\boldsymbol{\varepsilon}^P$):

$$\boldsymbol{\varepsilon}^e=\left(\tilde{\underline{\mathbf{C}}}^{-1}-\frac{1}{E}\breve{\underline{\mathbf{M}}}\right):\boldsymbol{\sigma} \quad (18a)$$

$$\boldsymbol{\varepsilon}^p=\underline{\mathbf{A}}:\mathbf{D} \quad (18b)$$

The elastic compliance tensor of the damaged material taking into account the unilateral effect has the following form:

$$\tilde{\underline{\mathbf{C}}}_T^{-1} = \tilde{\underline{\mathbf{C}}}^{-1} - \frac{1}{E}\breve{\underline{\mathbf{M}}}$$

$$= \tilde{\underline{\mathbf{C}}}^{-1} - \frac{1}{E} H(-n_i \boldsymbol{\sigma} n_i) \frac{D_i(2-D_i)}{(1-D_i)^2} n_i \otimes n_i \otimes n_i \otimes n_i \quad (19)$$

In the case of a compressive stress normal to the mean surface of the microcrack system n_i, the elastic modulus $\tilde{C}_{T\ n_i n_i n_i n_i}^{-1}$ becomes

$$\tilde{C}_{T\ n_i n_i n_i n_i}^{-1} = n_i \otimes \mathrm{n_i} : \tilde{\underline{\mathbf{C}}}_{\mathrm{T}}^{-1} : n_i \otimes \mathrm{n_i}$$

$$= \frac{1}{E(1-D_i)^2} - \frac{1}{E}\frac{D_i(2-D_i)}{(1-D_i)^2} = \frac{1}{E} \quad (20)$$

This way, the elastic modulus in the direction normal to the microcrack system loaded in compression is restored. In addition, the strain–stress relation defined in Eq. (17) is continuous and the elastic compliance tensor is symmetric and positive definite. The thermodynamic model is thus physically consistent.

Associated Damage Forces. The thermodynamic force, which is known as the damage strain energy release rate, must be associated with the damage tensor. In the case wherein the principal directions of the damage should not change during loading (proportional loading), for each eigenvalue of the damage D_i, there is an associated thermodynamic force Y_i, defined as

$$Y_i = \frac{\partial U}{\partial D_i} = \boldsymbol{\sigma} : \left[\frac{1}{2} \left(\frac{\partial \underline{\mathbf{M}}}{\partial D_i} : \underline{\mathbf{C}}^{-1} : \underline{\mathbf{M}} + \underline{\mathbf{M}} : \underline{\mathbf{C}}^{-1} : \frac{\partial \underline{\mathbf{M}}}{\partial D_i} \right) \right] : \boldsymbol{\sigma}$$

$$- \boldsymbol{\sigma} : \left[H(-n_i \boldsymbol{\sigma} n_i) \frac{1}{E(1-D_i)^3} n_i \otimes n_i \otimes n_i \otimes n_i \right] : \boldsymbol{\sigma}$$

$$+ \boldsymbol{\sigma} : \underline{\mathbf{A}} : n_i \otimes n_i \quad (21a)$$

$$Y_i = \boldsymbol{\sigma} : \left[\mathrm{sym}\left(\frac{\partial \underline{\mathbf{M}}}{\partial D_i} : \underline{\mathbf{C}}^{-1} : \underline{\mathbf{M}} \right) - H(-n_i \boldsymbol{\sigma} n_i) \frac{1}{E(1-D_i)^3} n_i \right.$$

$$\left. \otimes n_i \otimes n_i \otimes n_i \right] : \boldsymbol{\sigma} + \boldsymbol{\sigma} : \underline{\mathbf{A}} : n_i \otimes n_i \quad (21b)$$

In fact, to take into account the possibility of interaction between two principal damage directions (two-dimensional (2-D) case), a correction must be done to the expression of the thermodynamic forces. A weighted sum of the two thermodynamic forces is thus used:

$$\overline{Y}_i = Y_i + b Y_j, \quad i,j = 1,2, \quad i \neq j \quad (22)$$

where the parameter b is a material constant bounded between 0 and 1.

Damage Evolution Law. The thermodynamic forces drive the evolution of the internal variable characterizing the damage up to failure. Those forces must satisfy the *Clausius–Duhem* inequality due to damage:

$$\mathbf{Y} : \dot{\mathbf{D}} \geqslant 0 \quad (23)$$

The evolution (quasi-static) law satisfying this inequality is chosen to be of the following form:

$$D_i = f(Y_i^s), \quad i = 1,2 \quad (24)$$

$$Y_i^s(t) = \max\{Y_0, \sup_{\tau \leqslant t}(\overline{Y}_i(\tau))\} \quad (25)$$

where Y_0 designates the initial damage threshold and i is one of the principal direction. The function f is a growing positive function intrinsic to the material.

3 Model Identification

To identify the parameters of the proposed model, progressive repeated tensile loading tests must be performed and followed by an estimation process using a calibrating technique. It is necessary in the course of the test to load and unload the specimen in order to estimate the damage internal variables D_1, D_2 and to measure the elastic and permanent strains ($\boldsymbol{\varepsilon}^e, \boldsymbol{\varepsilon}^p$). For further details on the experimental procedure, the reader is referred to Refs. [7,8]. Essentially, the results of the uniaxial cyclic tensile tests (Fig. 2) are used here for parameter identification purposes.

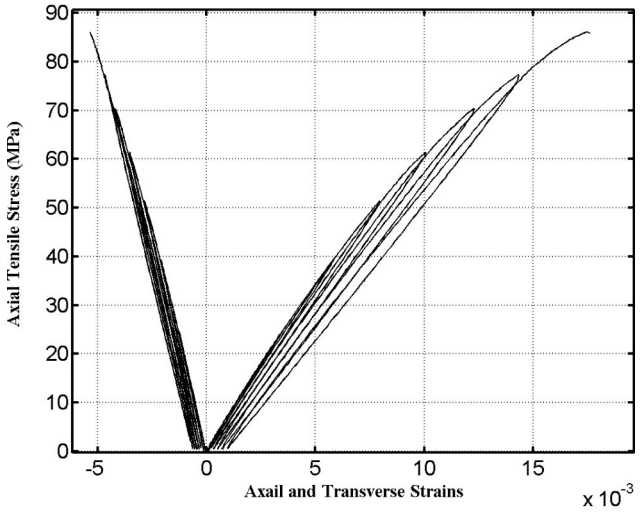

Fig. 2 Cyclic tensile stress–strain curves (Test [8])

Uniaxial tensile tests [6–8], have shown, if one neglects the permanent strain, that the following relationship between the principal damage function and the thermodynamic force is appropriate:

$$f(Y^s) = a(Y^s - Y_0) \quad (26)$$

where Y^s is the thermodynamic force defined in Eq. (25), Y_0 is the initial value at which damage begins, and a is a material parameter. These two parameters must be identified.

In the principal coordinate system of damage (2-D case), the **A** operator (Eq. (15)) is reduced to the following expression using Voigt's notation (due to symmetry of $\boldsymbol{\sigma}$, **D**, and **A**):

$$\mathbf{A} = \begin{bmatrix} \alpha & -\beta \\ -\beta & \alpha \end{bmatrix} \quad (27)$$

The residual (permanent) strains due to damage are obtained as follows (Eq. (18*b*)):

$$\begin{cases} \varepsilon_{11}^p = \alpha D_1 - \beta D_2 \\ \varepsilon_{22}^p = -\beta D_1 + \alpha D_2 \end{cases} \quad (28)$$

where α and β are unknown material parameters to be identified using loading tests results.

Equations (21) and (22) can also be simplified in the case of uniaxial loading:

$$\overline{Y}_1 = \frac{\sigma_1^2}{E(1-D_1)^3} + (\alpha - b\beta)\sigma_1,$$

$$\overline{Y}_2 = (b\alpha - \beta)\sigma_1 + b\frac{\sigma_1^2}{E(1-D_1)^3} \quad (29)$$

Table 1 summarizes the unknown parameters to be identified using an appropriate technique together with test results. In Table 2, the test results to be used for the identification are displayed. A loading/unloading test allows the estimation of the secant damage Young's modulus. The damage value can thus be estimated using Eq. (14):

$$E_1 = E(1-D_1)^2 \quad (30)$$

Table 1 Definition of the unknown parameters

Unknown parameters	a	Y_0	b	α, β
Mathematical nature	Scalar	Scalar	Scalar	Fourth-order tensor
Definition	Material coefficient necessary to estimate the damage level	Thermodynamic force beyond which damage begins	Parameter necessary to take into account cross effects in the thermodynamic force	Parameters to estimate permanent strains due to damage

and then:

$$D_1 = 1 - \sqrt{\frac{E_1}{E}} \tag{31}$$

In this unique test, it is difficult to estimate the damage parameter in the transverse direction (D_2). Information about the damaged material Poisson's ratio ν_{12} allows us to estimate its values using Eq. (14):

$$\nu_{12} = \nu \frac{1-D_1}{1-D_2} \Rightarrow D_2 = 1 - \frac{\nu}{\nu_{12}}(1-D_1) \tag{32}$$

However, in most cases, this expression may not give reliable damage values because the damaged Poisson's ratio ν_{12} measurement is not very precise. Instead, D_2 is evaluated using Eqs. (24)–(26) and (29):

$$D_2 = a(\overline{Y}_2 - Y_0) = a\left[(b\alpha - \beta)\sigma_1 + b\frac{\sigma_1^2}{E(1-D_1)^3} - Y_0\right] \tag{33}$$

Now, Eq. (28) can be used to express the permanent strain as a function of the five unknown parameters Y_0, a, b, α, and β:

$$\begin{cases} \boldsymbol{\varepsilon}_{11}^p = \alpha D_1 - \beta a(b\alpha - \beta)\sigma_1 - b\beta\dfrac{\sigma_1^2}{E(1-D_1)^3} + \beta a Y_0 \\ \varepsilon_{22}^p = -\beta D_1 + \alpha a(b\alpha - \beta)\sigma_1 + b\alpha\dfrac{\sigma_1^2}{E(1-D_1)^3} - \alpha a Y_0 \end{cases} \tag{34}$$

Parameter identification is done using a constrained optimization technique. The following equation is used as the objective function to be optimized:

Table 2 Experimental results from Ref. [7]

Maximum stress level (MPa)	Permanent axial strain ε_{11} (μm/m)	Permanent transverse strain ε_{22} (μm/m)	Damage in the direction of loading D_1
24.50	72.24	−126.7	0.0134649
39.43	240.8	−267.6	0.025708
51.41	337.1	−352.1	0.043811
61.34	550.7	−450.6	0.066579
70.27	722.4	−549.2	0.091765
77.30	987.2	−647.8	0.115231

$$ERR\_STR = \frac{\sum_{i=1}^{NC} \|(\boldsymbol{\varepsilon}_m^p - \boldsymbol{\varepsilon}_t^p)_i\|^2}{\sum_{i=1}^{NC} \|(\boldsymbol{\varepsilon}_m^p)_i\|^2} = \frac{\sum_{i=1}^{NC} [(\varepsilon_{m11}^p - \varepsilon_{t11}^p)_i^2 + (\varepsilon_{m22}^p - \varepsilon_{t22}^p)_i^2]}{\sum_{i=1}^{NC} [(\varepsilon_{m11}^p)_i^2 + (\varepsilon_{m22}^p)_i^2]} \tag{35}$$

Subject to the following constraint:

$$ERR\_EVO = \frac{\sum_{i=1}^{NC} (D_1^m - D_1^t)_i^2}{\sum_{i=1}^{NC} (D_1^m)_i^2} \leqslant Tol \tag{36}$$

where i is the cycle index, NC is the total number of cycles in axial cyclic tensile test ($=6$, Fig. 2) and ε_m^p and ε_t^p are the measured and predicted (Eq. (34)) permanent strains, respectively. D_1^m and D_1^t are the measured and predicted (using Eqs. (24)–(26) and (29)) damage variable values, respectively, in the tensile stress direction. A value of 6.9×10^{-4} was chosen for the constraint parameter Tol. The parameters have been calibrated by means of the Lagrangian operator and the Uzawa's method [12].

Table 3 gives the values obtained from the calibration procedure. The precision obtained with Eqs. (34) and (35) was 7.7×10^{-3} and 6.899×10^{-4}, respectively. Table 4 gives a comparison between the measured and the calculated values of permanent strain and damage D_1. A very good correlation between those values is observed except for the first two lines of the table corresponding to applied stresses of 24.50 and 39.43 MPa. The permanent strain and damage parameters generally have low values, particularly in the first few cycles (2 to 3 cycles, see Table 4). It is not easy to obtain reliable measured values and consequently, it may be an error source for correlation and fitting. However, in the last three cycles, the percentage differences of the expected and the measured values of strain and damage parameters are within the ranges of [−5.6%, 9.2%] and [−0.5%, 0.8%], respectively. Therefore, the proposed model with the values of parameters listed in Table 3 is applicable in representing the damage mechanics behavior of random short glass fiber reinforced composites under relatively large strain.

Table 3 Numerical values of the unknown parameters

Y_0	a	b	α	β
0.06819	0.07884	0.5878	0.010071	0.008371

Table 4 Comparison between estimated and measured values

D_1 (10^{-3})			Permanent strain ε_{11} (μm/m)			Permanent strain ε_{22} (μm/m)		
Measured	Calculated	Error %	Measured	Calculated	Error %	Measured	Calculated	Error %
13.47	10.98	18.5	72.24	135.7	−87.8	−126.7	−112.7	11.0
25.71	27.85	−8.3	240.8	258.9	−7.5	−267.6	−215.2	19.6
43.81	46.46	−6.0	337.1	417.1	−23.7	−352.1	−337.7	4.1
66.58	66.91	−0.5	550.7	581.7	−5.6	−450.6	−450.4	0.0
91.77	90.65	1.2	722.4	750.8	−3.9	−549.2	−559.6	−1.9
115.2	114.4	0.8	987.2	895.9	9.2	−647.8	−646.2	0.2

4 Numerical Simulation

4.1 Numerical Implementation. The proposed model has been implemented in the ABAQUS finite-element code using the UMAT functionality. The numerical integration is done by discretizing the loading using load increments and thus strain increments. From the mechanical state ε_n, σ_n, D_n, at time t_n, an estimation is made of the mechanical state σ_{n+1}, D_{n+1}, at time t_{n+1} corresponding to the strain increment $\Delta\varepsilon$. This local integration is done using an implicit integration algorithm and a Newton–Raphson technique to estimate the mechanical state. For this purpose, a consistent tangential matrix has been derived. The reader can find more information in Mir [9].

4.2 Simulation and Model Validation. First, to verify how consistent the identified set of parameters is, the uniaxial cyclic tensile test has been simulated using the numerical model implanted in ABAQUS. Figures 3 and 4 illustrate, respectively, the numerical cyclic tensile test results obtained from finite-element simulation and the corresponding experimental results superposed to the predicted curves. A good agreement is found. Now, to validate the model, different experimental tests [7,8] have been simulated: monotonic tensile tests, monotonic and cyclic shear tests, and tensile tests on rectangular plates and specimens cut from it (Fig. 1). In these last tests, the tensile and shear specimens were cut from the plates pre-loaded in tension to produce different degrees of damage by uniaxial tension [7,8]. Afterwards, the specimens were tested to measure their damaged-material elastic coefficients: Young's modulus and Poisson's ratio along three directions (0, 45, and 90 deg with respect to the initial loading direction) and the shear modulus (Fig. 1). The objective was to predict their evolution and degradation versus the tensile stress level.

Figure 5 illustrates the result for monotonic tensile loading. A very good agreement between numerical and test results is obtained. Monotonic and cyclic loading have been simulated in shear. Figures 6 and 7 illustrate both the numerical and the experimental results, which again are very close. References [7,8] give all the information on the test procedure.

The evolution of the degradation of the elastic properties in function of tensile stress level in three different directions (0, 45, and 90 deg) is presented in Figs. 8–10. In Figs. 8 and 9, the predicted damaged Young's modulus and Poisson's ratio can be

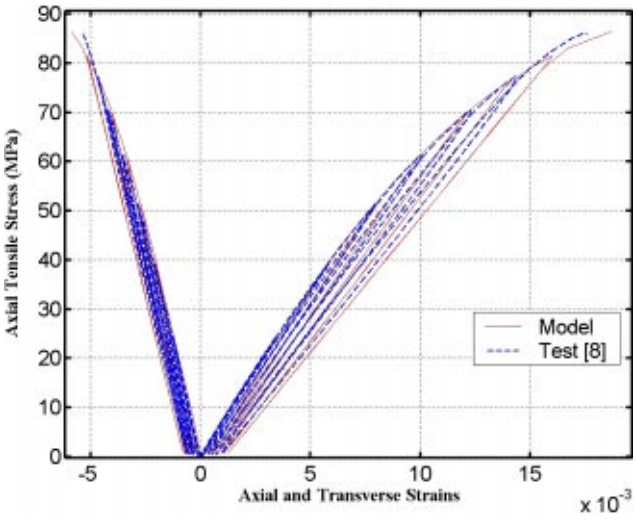

Fig. 4 Comparison of the predicted cyclic tensile stress–strain curves with corresponding experimental data

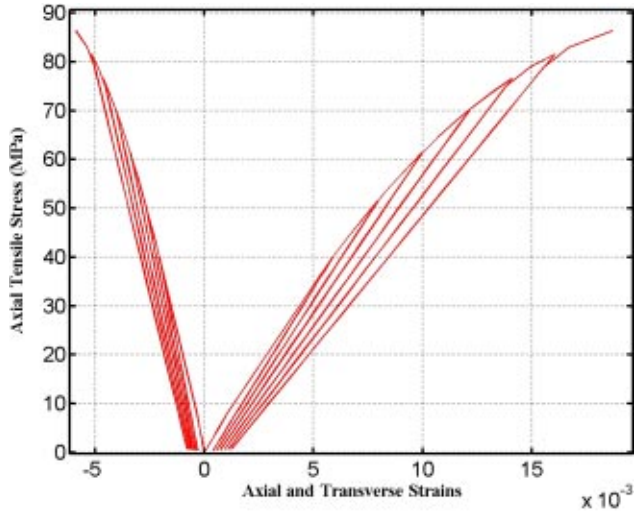

Fig. 3 Predicted cyclic tensile stress–strain curves (Model)

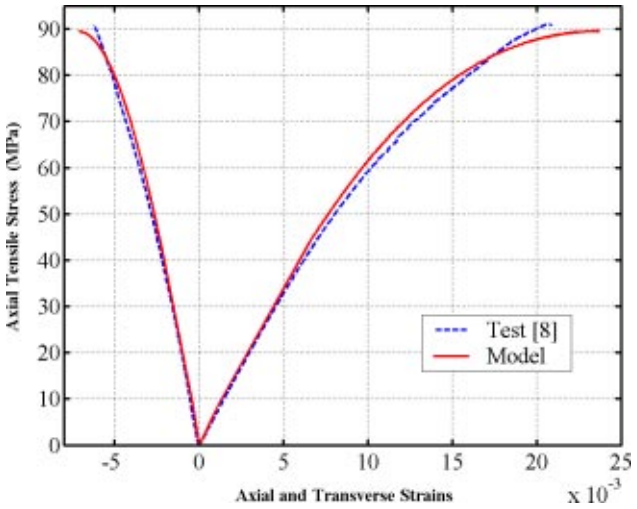

Fig. 5 Tensile stress–strain curves

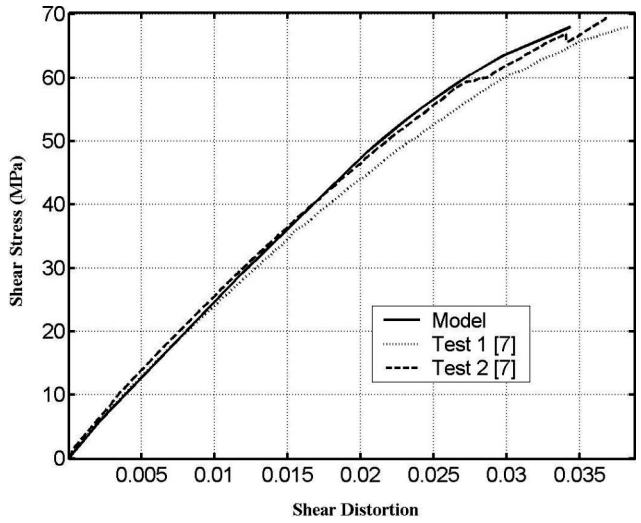

Fig. 6 Comparison of predicted shear stress–strain curves with the corresponding experimental data

compared to the test results reported by Dano et al. [8]. The prediction of Young's modulus and Poisson's ratio is relatively good in the 1- and 2-directions. In the 45 deg direction, the discrepancy is more accentuated, though the numerical prediction still remains fair.

In the case of the shear modulus presented in Fig. 10, it can be observed that the numerical results are in good agreement with the experimental data.

4.3 Simulation of a Uniaxial Tensile–Compressive Loading Test. In this simulation, we show how reversing a tensile load to compressive load restores the apparent elastic modulus (degraded by tensile load) in the direction parallel to the compressive load and how it may still cause damage evolution (cracks extension) in the transverse direction. These two directions correspond to the two principal damage directions in this load case. We denote by 1 and 2 the directions that are parallel and transverse to the loading direction, respectively.

Figure 11 illustrates the stress versus strain curve during a tensile–compressive loading test. The specimen is first loaded in tension up to 60 MPa, which induces damage and causes Young's modulus E_1 to decrease. The specimen is then, unloaded and subjected to a compressive stress. The change of slope indicates that the apparent modulus is restored when the damaged material is in compression. Figures 12(*a*) and 12(*b*) present the evolution of the applied stress and the damage variables during the tension–

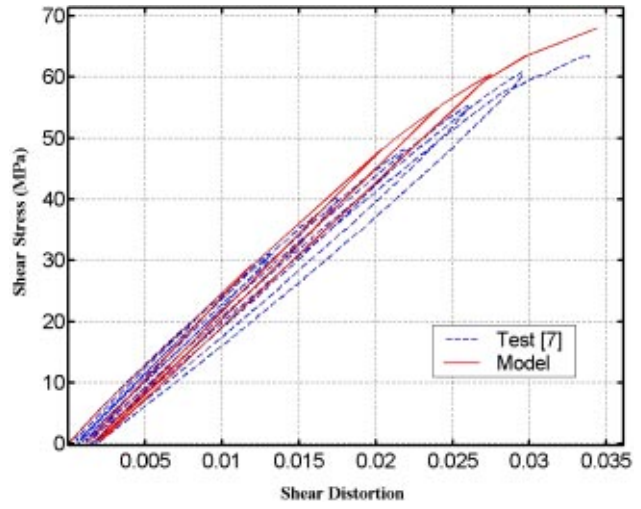

Fig. 7 Comparison of cyclic shear stress–strain curves with the corresponding experimental data

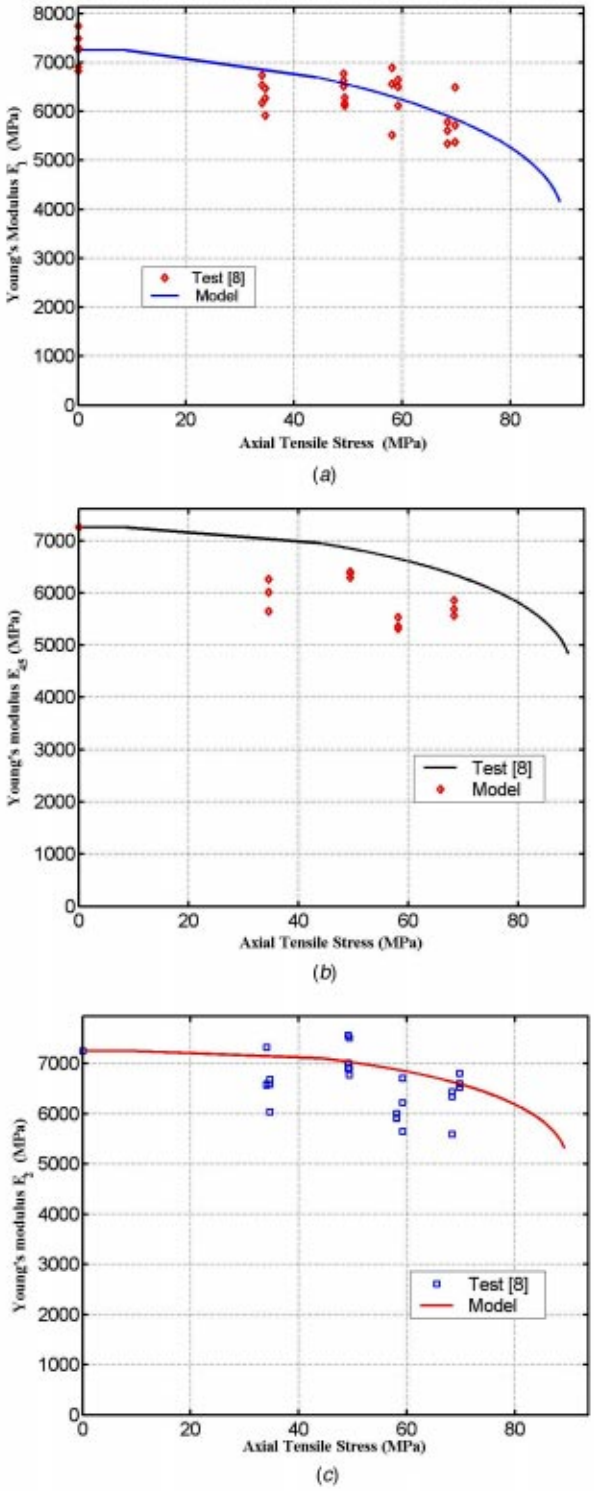

Fig. 8 (*a*) Comparison of predicted Young's modulus evolution vs stress with the corresponding experimental data ($\theta = 0$ deg). (*b*) Comparison of predicted Young's modulus evolution vs stress with the corresponding experimental data ($\theta = 45$ deg). (*c*) Comparison of predicted Young's modulus evolution vs stress with the corresponding experimental data ($\theta = 90$ deg).

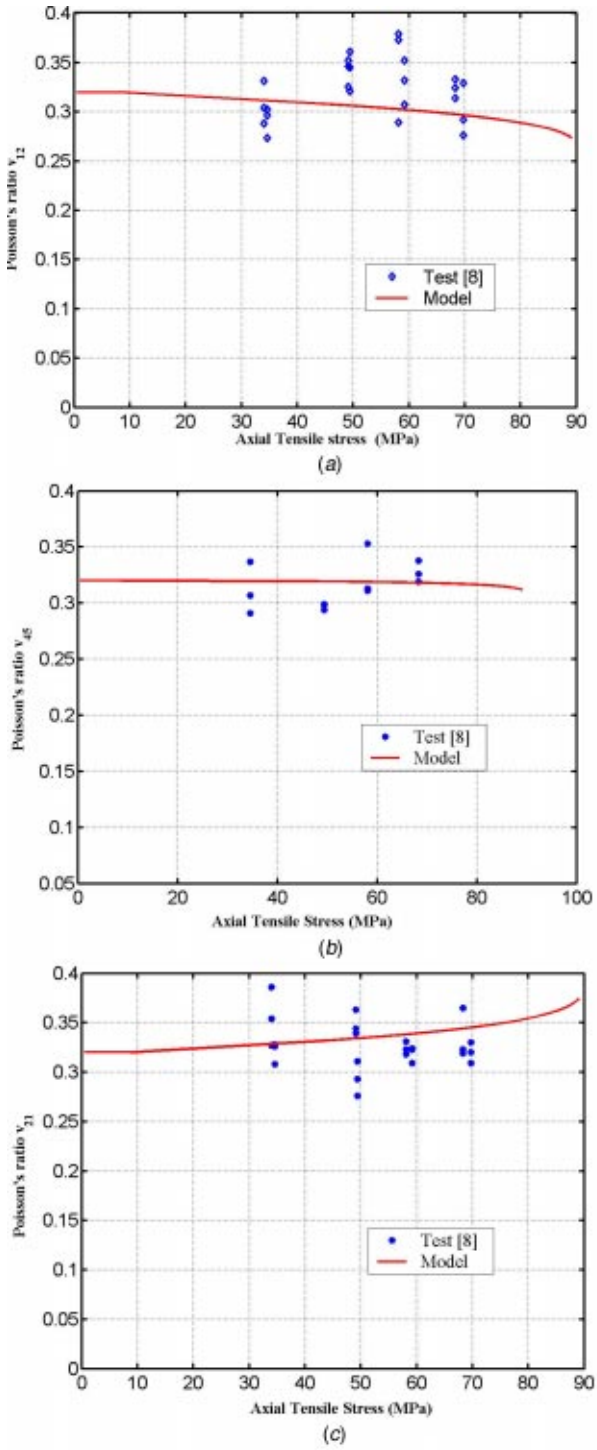

Fig. 9 (*a*) Comparison of predicted Poisson ratio evolution vs stress with the corresponding experimental data ($\theta=0$ deg). (*b*) Comparison of predicted Poisson's ratio evolution vs stress with the corresponding experimental data ($\theta=45$ deg). (*c*) Comparison of predicted Poisson's ratio evolution vs stress with the corresponding experimental data ($\theta=90$ deg).

compressive test simulation, respectively. First, up to 60 MPa, the tensile load causes material damage, and consequently, increases principal damage variables D_1 and D_2, as shown in Fig. 12(*b*). During unloading and until starting the compressive load, the damage variables stop increasing. As demonstrated by Eq. (20) and shown in Fig. 11, the compressive load restores the apparent elastic modulus in the 1-direction. However, once the compressive

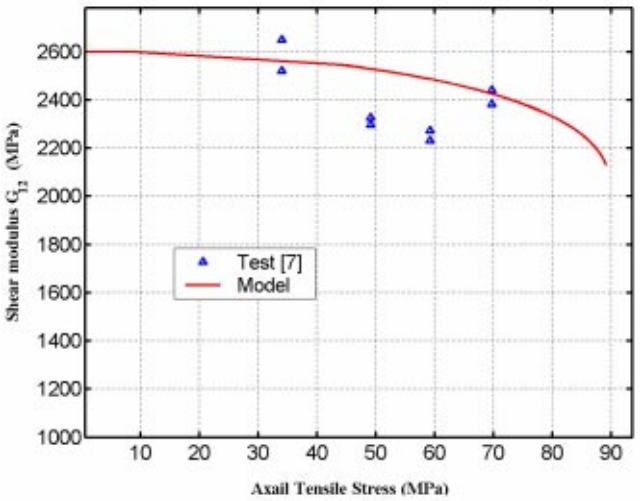

Fig. 10 Comparison of predicted Shear modulus evolution vs stress with the corresponding experimental data

stress has reached a certain level (-78 MPa), which depends on the tensile load level applied previously, the degree of damage in the 2-direction (D_2) increases again, as shown in Fig. 12(*b*). The compressive load may transmit damage and induce its evolution in the transverse direction. The cracks nucleated initially due to previous tensile load are not always perpendicular to the loading direction, but also may be along individual fiber directions and thus be inclined or parallel to the loading direction. This set of cracks becomes active under compressive load applied in the previous tensile load direction.

5 Conclusion

In this paper, a damage model for random short glass fiber reinforced composites based on the fundamental principle of thermodynamics of irreversible process was presented. The model takes into account the unilateral effect (crack closure effect) and the permanent strains after unloading (residual effect). Using tests results and an appropriate identification procedure, all unknown parameters have been identified. After implementation of the model in a finite-element code, simulations are obtained and are found to be in good agreement with experimental results. It can thus be concluded that the proposed model is appropriate to simu-

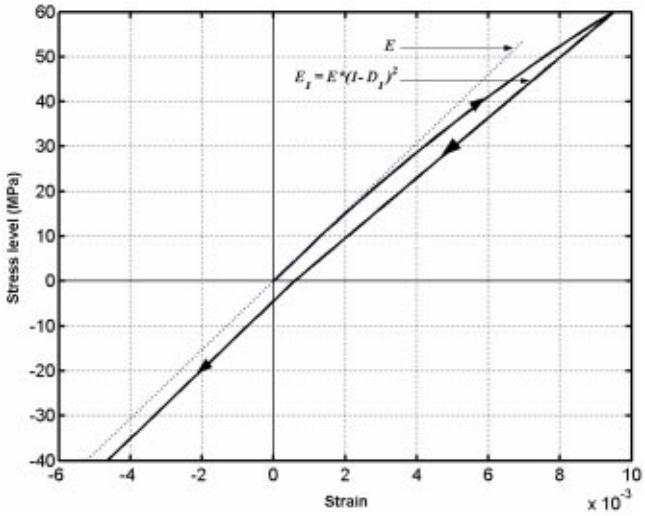

Fig. 11 Stress–strain curve in tensile–compressive load (Model)

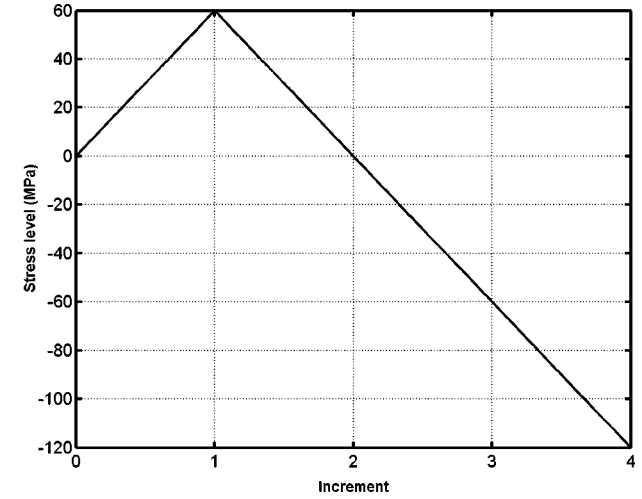

Fig. 12 Tensile–compressive load simulation: (*a*) Incremental axial stress level and (*b*) predicted damage variables evolution (Model)

late damage evolution in structures made of random short glass fiber reinforced composites in a proportional loading case. The nonproportional loading case will be treated in a future paper.

Acknowledgment

The financial support provided for this research by the Natural Sciences and Engineering Research Council of Canada, ADS Groupe Composite, Bombardier and Prevost Car, is gratefully acknowledged.

Nomenclature

$\underline{\mathbf{A}}$ = symmetric fourth-order tensor taking into account permanent strain
$\tilde{\underline{C}}^{-1}$ = fourth-order elastic compliance tensor of the damaged material
$\mathbf{D}$ = second order damage tensor
D_i = damage in the principal direction i
D_1^m = measured damage variable in the 1-direction
D_2^t = predicated damage variable in the 1-direction
E = Young's modulus of the undamaged material
E_1 = secant damage Young's modulus
ERR_STR = permanent strain relative error
ERR_EVO = damage relative error in the 1-direction
G = shear modulus of the undamaged material
$H(x)$ = Heaviside function
$\mathbf{I}_2$ = second-order unit tensor
$\underline{\mathbf{I}}_4$ = fourth-order unit tensor
$\underline{\mathbf{M}}(\mathbf{D})$ = fourth-order damage operator
$\tilde{\underline{\mathbf{M}}}(\mathbf{D})$ = fourth-order tensor to take into account the unilateral effect
$\underline{\mathbf{P}}^{(\boldsymbol{\sigma},\mathbf{D})+}$ = fourth-order tensor corresponding to a positive projection operator
$\underline{\mathbf{P}}^{(\sigma,D)-}$ = fourth-order tensor corresponding to a negative projection operator
Tol = tolerance on the evolution law of damage
U_0^e = complementary elastic energy
U^p = energy blocked by the microcracks inducing permanent strain
$\underline{Y}_i$ = thermodynamic force associated with D_i
Y_i = weighed thermodynamic force associated to D_i
Y_0 = initial damage threshold
a = material parameter
b = material constant bounded between 0 and 1
n_i = normal vector to the crack
α, β = unknown material parameters of the fourth-order tensor $\underline{\mathbf{A}}$
δ_{ik} = Kronecker delta symbol
$\boldsymbol{\varepsilon}$ = second-order strain tensor
$\boldsymbol{\varepsilon}^e$ = second-order elastic strain tensor
$\boldsymbol{\varepsilon}^p$ = second-order permanent strain tensor
$\boldsymbol{\varepsilon}_m^p$ = measured second-order permanent strain tensor
$\boldsymbol{\varepsilon}_t^p$ = predicted second-order permanent strain tensor
$\varepsilon_{11}^p, \varepsilon_{22}^p$ = permanent strain in the 1- and 2-directions
ν = Poisson's ratio of the undamaged material
ν_{12} = Poisson's ratio of damaged material
$\boldsymbol{\sigma}$ = second-order Cauchy stress tensor
$\tilde{\sigma}_{ii}^+$ = tensile stress (positive) tensor normal to the plane of the microcrack system
$\tilde{\sigma}_{ii}^-$ = compressive stress (negative) tensor normal to the plane of the microcrack system
$\otimes$ = dyadic or tensor product
$\|\cdot\|$ = Euclidean norm

References

[1] Pensée, V., and Kondo, D., 2001, "Une Analyse Micromécanique 3-D de l'Endommagement par Mésofissuration," C. R. Acad. Sci., Ser. IIb: Mec., Phys., Chim., Astron., **329**, pp. 271–276.
[2] Lu, T. J., and Chow, C. L., 1990, "On Constitutive Equations of Inelastic Solids with Anisotropic Damage," Theor. Appl. Fract. Mech., **14**, pp. 187–218.
[3] Lemaître, J., Desmorat, R., and Sauzay, M., 1999, "Loi d'Évolution de l'Endommagement Anisotrope," C. R. Acad. Sci., Ser. IIb: Mec., Phys., Chim., Astron., **327**, pp. 1231–1236.
[4] Halm, D., 1997, "Contribution à la Modélisation du Comportement Unilatéral et du Frottement Dans les Matériaux Mésofissurés," PhD thesis, École Nationale Supérieure de Mécanique et d'Aérotechnique et Faculté des Sciences Fondamentales et Appliquées, France.
[5] Kachanov, M., 1992, "Effective Elastic Properties of Cracked Solids: Critical Review of Some Basic Concepts," ASME Appl. Mech. Rev., **45**, (8), pp. 304–335.
[6] Dano, M. L., Gendron, G., and Mir, H., 2002, "Mechanics of Damage and Degradation in Random Short Glass Fiber Reinforced Composites," Journal of Thermoplastic Composite Materials, **15**, (2), pp. 169–177.
[7] Maillette, F., 2002, "Caractérisation Expérimentale d'un Matériau Composite à Fibres Courtes et Orientés Aléatoirement," Master's thesis, Dept of Civil Eng., Laval University, Quebec, Canada.
[8] Dano, M.-L., Maillette, F., Gendron, G., and Bissonnette, B., 2001, "Damage Modelling of Random Short Glass Fibre Reinforced Composites," *Proceeding of the Third Canadian Conference on Composites*, Montreal, Canada, pp. 263–270.
[9] Mir, H., 2003, "Contribution à la Modélisation de l'Endommagement des Matériaux Composites avec Fibres de Verre Courtes: Anisotropie Induite, Effets Unilatéral et Résiduel," PhD thesis, Department of Civil Engineering,

Laval University, Quebec, Canada.
[10] Sidoroff, F., 1981, ''Description of Anisotropic Damage Application to Elasticity,'' *IUTAM Colloquium, Physical Nonlinearities in Structural Analysis*, J. Hult, ed., pp. 237–244.
[11] Chen, X. F., and Chow, C. L., 1995, ''On Damage Strain Energy Release Rate Y,'' Int. J. Damage Mech., **4**, pp. 251–263.
[12] Ciarlet, P. G., 1982, *Introduction à l'Analyse Numérique Matricielle et à l'Optimization*, Masson, Paris.

Micromechanics and Homogenization of SMA-Wire-Reinforced Materials

S. Marfia

E. Sacco

University of Cassino,
Via G. Di Biasio 43,
Cassino, Frosinone 03043, Italy

The aim of the paper is to develop a micromechanical model for the evaluation of the overall constitutive behavior of a composite material obtained embedding SMA wires into an elastic matrix. A simplified thermomechanical model for the SMA inclusion, able to reproduce the superelastic as well as the shape memory effect, is proposed. It is based on two assumptions: the martensite volume fraction depends on the wire temperature and on only the normal stress acting in the fiber direction; the inelastic strain due to the phase transformations occurs along the fiber direction. The two introduced hypotheses can be justified by the fact that the normal stress in the fiber direction represents the main stress in the composite. The overall nonlinear behavior of long-fiber SMA composites is determined developing two homogenization procedures: one is based on the Eshelby dilute distribution theory, the other considers the periodicity conditions. Numerical applications are developed in order to study the thermomechanical behavior of the composite, influenced by the superelastic and shape memory effects occurring in the SMA wires. Comparisons of the results obtained adopting the two homogenization procedures are reported. The influence of the matrix stiffness and of a prestrain in the SMA wires on the overall behavior of the composites is investigated. [DOI: 10.1115/1.1839186]

1 Introduction

Smart composites, obtained including a smart material in a matrix, are very special composite materials, which exhibit a desired behavior under certain conditions. In particular, the shape memory alloys (SMA) appear very suitable for the development of smart composites. In fact, SMA are able to undergo reversible large deformations under loading/thermal cycles and to generate high values of the thermomechanical driving forces. This very special behavior of SMA is due to their native capability to undergo reversible changes of the crystallographic structure, depending on the temperature and on the state of stress. These changes can be interpreted as reversible martensitic transformations between a crystallographic more-ordered parent phase, the austenite, to a crystallographic less-ordered product phase, the martensite. In general, the austenite is stable at high temperatures and low stresses, while the martensite is stable at low temperatures and high stresses [1]. Because of their unique mechanical response, SMA have been successfully adopted as actuators and sensors in a broad set of advanced and innovative applications in aeronautical, biomedical, mechanical, and civil engineering [2].

In the last decade, great interest was aroused by the possibility to develop new, intelligent SMA composites (CSMA). New, performing materials are obtained embedding SMA wires, filaments, short fibers, particulates, or thin films into different types of matrices. Recently, SMA wires have become commercially available with diameters below 0.2 mm. These small diameters allow the direct integration of SMA wires into fiber-reinforced polymer composites without losing the structural integrity of the matrix material. The aim is to realize smart composites by a suitable distribution of SMA within the matrix material and to control the thermomechanical behavior of SMA through heating and cooling. In fact, the integration of SMA in composites offers important advantages in comparison to other actuating technologies: high reversible strains (up to 6%), high damping capacity, large reversible changes of mechanical and physical characteristics, commercial availability as thin flexible wires that can be directly embedded in a polymer matrix, and ability to generate extremely high stresses (up to 800 MPa). The main disadvantage of SMA is their reduced cooling rate which can be a limiting factor in applications that require heating and cooling of the SMA wires to generate cyclic stresses and strains.

SMA composites can be used for different potential applications, including the control of external shape, stiffness, damage, vibration, buckling, and damping properties of the structural elements. It can be emphasized that the mechanical response of the CSMA depends upon several different factors, e.g., the cure process, the prestrain level, the volume fraction, and, of course, the particular adopted materials.

Different studies of the possible use of CSMA integrated within structural elements have been developed by several researchers and published in the literature. These researches are mainly related to the following specific topics: vibration control, buckling and postbuckling effects, shape control, and micromechanics of the SMA composite material.

Birman et al. [3] proved that the use of prestrained SMA fibers embedded within a plate reduces the stresses and the deflection of laminates subjected to low-velocity impact. Hyo Jik Lee et al. [4] performed numerical simulation analyses of the thermal buckling behavior of laminated composite shells with embedded SMA wires, demonstrating that the critical buckling temperature can be increased and the thermal buckling deformation can be decreased by using the activation force of embedded SMA wire actuators. Analogously, Jung Ju Lee and Sup Choi [5] developed an analytical investigation of the thermal buckling and postbuckling behaviors of a composite beam with embedded SMA wires; the presence of SMA wires enhances the critical buckling temperature and reduces the lateral deflection for the thermal buckling. Moreover, Sup Choi et al. [6] presented the results of an experimental analysis on the active buckling control behavior of a laminated composite beam with embedded shape memory alloy wires, suggesting a simple formula for evaluating the improvement of the SMA

Contributed by the Applied Mechanics Division of THE AMERICAN SOCIETY OF MECHANICAL ENGINEERS for publication in the ASME JOURNAL OF APPLIED MECHANICS. Manuscript received by the Applied Mechanics Division, December 19, 2003; final revision; August 31, 2004. Associate Editor: D. Kouris. Discussion on the paper should be addressed to the Editor, Prof. Robert M. McMeeking, Journal of Applied Mechanics, Department of Mechanical and Environmental Engineering, University of California—Santa Barbara, Santa Barbara, CA 93106-5070, and will be accepted until four months after final publication in the paper itself in the ASME JOURNAL OF APPLIED MECHANICS.

wires in the buckling behavior. Thompson and Loughlan [7] demonstrated by numerical simulations the effectiveness of SMA fibers to reduce the out-of-plane displacement of postbuckled laminates, emphasizing that the stability of the adaptive response is very much dependent upon the laminate stacking sequence. Experimental and further numerical investigations were conducted in Ref. [8], to determine the postbuckling response of composite SMA also characterized by reduced values of actuator fraction volume. Ostachowicz et al. [9] illustrated the influence of the SMA fibers upon changes in natural frequencies and thermal buckling of a composite multilayer plate with the SMA components, developing finite-element analyses.

Micromechanical studies, devoted to the understanding and to the modeling of the constitutive behavior of SMA composite with elastic matrix, were developed. These studies can be framed in the general problem of the homogenization of composites characterized by nonlinear constitutive behavior, which is a very active research field. In this framework, rigorous bounds for the nonlinear effective properties of composites have been derived since the early 1990s; Ponte Castañeda [10], and Willis [11], among others, have developed such bounds based on the so-called ''average variational principle.'' Moreover, Suquet [12] proved that the variational procedure can be interpreted as a secant method.

More specifically, it was found for SMA composites that the interaction between the embedded SMA and the matrix was one of the critical factors in the microstructure design of the composites [13–15]. A quantitative micromechanics-based analysis on the role of microstructure and constituent properties in the overall behavior of a SMA composite was carried out in Ref. [16]. In particular, the self-consistent homogenization technique was adopted to evaluate the overall SMA composite behavior. A simplified analysis was developed, considering the internal stress and strain and their evolution as function of externally applied thermomechanical loading. Briggs and Ponte Castañeda [17] estimated the effective behavior of active composites, obtained embedding aligned SMA fibers in a linear elastic matrix, using the homogenization technique proposed by Ponte Castañeda [10].

This paper aims to establish a micromechanical-based modeling of the constitutive behavior of the SMA composites, characterized by an elastic matrix. The overall behavior of long-fiber SMA composites is determined developing suitable homogenization procedures. In particular, two homogenization procedures are proposed in this paper. The first one, based on the use of the Eshelby inclusion solution, is developed for dilute distribution composites; the homogenization technique can be very effective for SMA composites as they are usually characterized by low values of the fiber volume fraction—less than 10%. The second technique considers the problem of periodic composites, which is solved using the finite-element method (FEM). The thermomechanical behavior of the composite is governed by the martensite volume fraction of the SMA wires. In particular, it is assumed that the martensite volume fraction depends on the wire temperature and on the normal stress acting in the fiber direction. In fact, smart structural elements are designed orienting the fibers in the direction along which the actuation has to be performed, i.e., where the main stress occurs. A possible prestrain of the fibers is taken into account in the model. A backward-Euler technique is used to integrate the evolutive constitutive equations governing the SMA behavior. Finally, numerical applications are performed to investigate the thermomechanical behavior of SMA composites, and some comparisons between the results obtained by the two proposed homogenization procedures are developed.

2 Material Models for Composite SMA

The CSMA is a material obtained embedding SMA fibers into a matrix material, which is generally a composite material, such as glass or carbon epoxy plastic. In Fig. 1, the CSMA material is schematically represented, specifying the Cartesian coordinate system adopted throughout the paper. The unit cell of the composite material is indicated by V, while Ω and M represent the inclusion and the matrix, respectively.

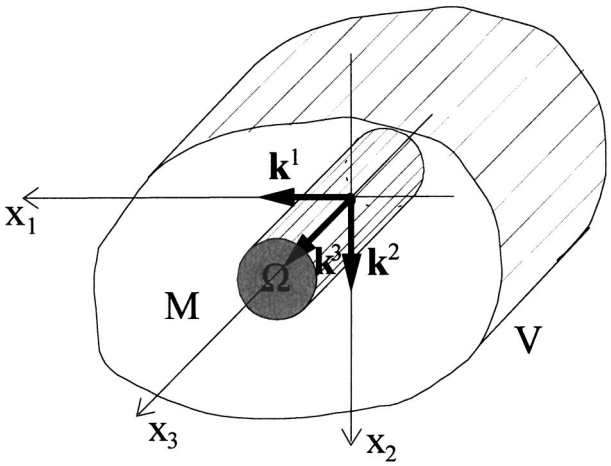

Fig. 1 SMA composite material

2.1 SMA Model. Several mathematical models able to reproduce the SMA constitutive behavior have been proposed in the literature. Boyd and Lagoudas [18] proposed a thermomechanically consistent model that takes into account the phase transformation and the martensite reorientation process. Raniecki and Lexcellent [19] developed a pseudoelastic thermodynamically consistent model. Souza et al. [20] proposed a computationally suitable three-dimensional SMA model, as illustrated also in Ref. [21].

Herein, a simple model, based on the approach proposed in Refs. [22,23], is presented; it considers the superelastic behavior, as well as the shape memory effect. Moreover, the model proposed in the following is able to reproduce the experimentally observed [24,25] asymmetric tension–compression behavior of the SMA. Only austenite–single variant martensite phase transformations are considered in the following. The austenite and the single variant martensite volume fractions are denoted as ξ_A and ξ_S, respectively. Since $\xi_A+\xi_S=1$, we have

$$\xi_A = 1-\xi_S \tag{1}$$

Hence, the single variant martensite volume fraction is chosen as an independent variable governing the phase transformations.

The elastic stress–strain relationship in the SMA inclusion Ω is defined as

$$\boldsymbol{\sigma}^{\Omega} = \mathbf{E}\,\boldsymbol{\eta}^{\Omega} \tag{2}$$

where $\boldsymbol{\sigma}^{\Omega}$ and $\boldsymbol{\eta}^{\Omega}$ are the stress and the elastic strain in the SMA inclusion, respectively, and $\mathbf{E}^{\Omega}$ is the fourth-order elastic tensor of the SMA, assumed independent of the martensite volume fraction ξ_S.

The total strain is obtained as

$$\boldsymbol{\varepsilon}^{\Omega} = \boldsymbol{\eta}^{\Omega} + (\delta+\xi_S\beta)\,\boldsymbol{\pi} + (T-T_0)\,\boldsymbol{\tau}^{\Omega} \tag{3}$$

where $\boldsymbol{\pi}=\mathbf{k}^3\otimes\mathbf{k}^3$, δ is the prestrain acting along the SMA fiber direction, β is an internal variable describing the change of martensite reorientation, and $\boldsymbol{\tau}^{\Omega}=\alpha^{\Omega}\mathbf{I}$ is the thermal strain induced by a unit temperature change, with α^{Ω} the expansion coefficient, $\mathbf{I}$ the identity tensor, T_0 the reference temperature, and T the actual temperature.

From Eq. (3) it can be noted that the inelastic strain due to the martensite transformation is assumed acting only along the fiber direction. This hypothesis, which greatly simplifies the model, can be considered justified by the fact that the SMA wires are aligned along the direction in which the actuation is desired.

A further simplifying hypothesis is introduced in the evolutionary equation of the single variant martensite fraction volume ξ_S. In fact, it is assumed that the SMA phase transformations are governed by the normal stress in the fiber direction $\mathbf{k}^3$.

The following evolutive equation, with respect to the evolution parameter t, is assumed for the internal variable β:

$$\frac{d\beta}{dt}=\begin{cases}\omega[\varepsilon_L\,\mathrm{sgn}(\sigma_{33}^{\Omega})-\beta][|\sigma_{33}^{\Omega}|-\sigma^{SS}], & \text{when } |\sigma_{33}^{\Omega}|>\sigma^{SS}\\ 0, & \text{otherwise}\end{cases} \tag{4}$$

where ε_L is the recoverable strain representing a measure of the maximum deformation obtainable aligning all the single variant martensite in one direction, with $\varepsilon_L=\varepsilon_L^{(+)}$ in tension and $\varepsilon_L=\varepsilon_L^{(-)}$ in compression, ω is a material parameter measuring the reorientation process rate, σ^{SS} is a limit stress that activates the reorientation process, with $\sigma^{SS}=\sigma^{SS(+)}$ in tension and $\sigma^{SS}=\sigma^{SS(-)}$ in compression, $|\bullet|$ is the absolute value.

The evolution of the martensite fraction ξ_S depends on the stress state and on the temperature, and it is governed by the equation

$$\frac{d\xi_S}{dt}=-(1-\xi_S)\left[\frac{1}{|\sigma_{33}^{\Omega}|-\tilde{\sigma}_f^{AS(\pm)}}\frac{d|\sigma_{33}^{\Omega}|}{dt}+\frac{1}{T-\tilde{T}_f^{AS(\pm)}}\frac{dT}{dt}\right],$$
$$\text{when } \tilde{\sigma}_s^{AS(\pm)}\leqslant|\sigma_{33}^{\Omega}|\leqslant\tilde{\sigma}_f^{AS(\pm)} \tag{5}$$

for the conversion of austenite into martensite (A→S) and by the equation

$$\frac{d\xi_S}{dt}=\xi_S\left[\frac{1}{|\sigma_{33}^{\Omega}|-\tilde{\sigma}_f^{SA(\pm)}}\frac{d|\sigma_{33}^{\Omega}|}{dt}+\frac{1}{T-\tilde{T}_f^{SA(\pm)}}\frac{dT}{dt}\right],$$
$$\text{when } \tilde{\sigma}_s^{SA(\pm)}\leqslant|\sigma_{33}^{\Omega}|\leqslant\tilde{\sigma}_f^{SA(\pm)} \tag{6}$$

for the conversion of martensite into austenite (S→A). The quantities $\tilde{\sigma}_s^{AS(+)}$, $\tilde{\sigma}_f^{AS(+)}$, $\tilde{\sigma}_s^{SA(+)}$, $\tilde{\sigma}_f^{SA(+)}$, $\tilde{\sigma}_s^{AS(-)}$, $\tilde{\sigma}_f^{AS(-)}$, $\tilde{\sigma}_s^{SA(-)}$, $\tilde{\sigma}_f^{SA(-)}$, $\tilde{T}_s^{AS(+)}$, $\tilde{T}_f^{AS(+)}$, $\tilde{T}_s^{SA(+)}$, $\tilde{T}_f^{SA(+)}$, $\tilde{T}_s^{AS(-)}$, $\tilde{T}_f^{AS(-)}$, $\tilde{T}_s^{SA(-)}$, $\tilde{T}_f^{SA(-)}$ represent the initial and final values of the stress, at a prescribed temperature, and of the temperatures, at a prescribed stress, for the transformation of austenite into martensite and for the transformation of martensite into austenite, respectively. The superscripts $(+)$ and $(-)$ indicate the cases of tension and compression, respectively.

With the help of Fig. 2, the transformation stresses and temperatures are given by the following equations:

$$\tilde{\sigma}_s^{AS(\pm)}=\langle\sigma_s^{AS(\pm)}+C^{AS(\pm)}(T-T_s^{AM})\rangle^+,$$
$$\tilde{\sigma}_f^{AS(\pm)}=\langle\sigma_f^{AS(\pm)}+C^{AS(\pm)}(T-T_s^{AM})\rangle^+$$
$$\tilde{\sigma}_s^{SA(\pm)}=\langle C^{SA(\pm)}(T-T_s^{SA})\rangle^+,\quad \tilde{\sigma}_f^{SA(\pm)}=\langle C^{SA(\pm)}(T-T_f^{SA})\rangle^+$$
$$\tilde{T}_s^{AS(\pm)}=\left\langle\frac{\sigma_{33}^{\Omega}-\sigma_s^{AS(\pm)}+C^{AS(\pm)}T_s^{AM}}{C^{AS(\pm)}}\right\rangle^+,$$
$$\tilde{T}_f^{AS(\pm)}=\left\langle\frac{\sigma_{33}^{\Omega}-\sigma_f^{AS(\pm)}+C^{AS(\pm)}T_s^{AM}}{C^{AS(\pm)}}\right\rangle^+$$
$$\tilde{T}_s^{SA(\pm)}=\left\langle\frac{\sigma_{33}^{\Omega}+C^{SA(\pm)}T_s^{SA}}{C^{SA(\pm)}}\right\rangle^+,\quad \tilde{T}_f^{SA(\pm)}=\left\langle\frac{\sigma_{33}^{\Omega}+C^{SA(\pm)}T_f^{SA}}{C^{SA(\pm)}}\right\rangle^+ \tag{7}$$

where

- C^{AS} and C^{SA} are the Clausius-Clapeyron constants for the phase transformations A→S and S→A, respectively; they are set as $C^{AS}=C^{AS(+)}$ and $C^{SA}=C^{SA(+)}$ in tension and $C^{AS}=C^{AS(-)}$ and $C^{SA}=C^{SA(-)}$ in compression;

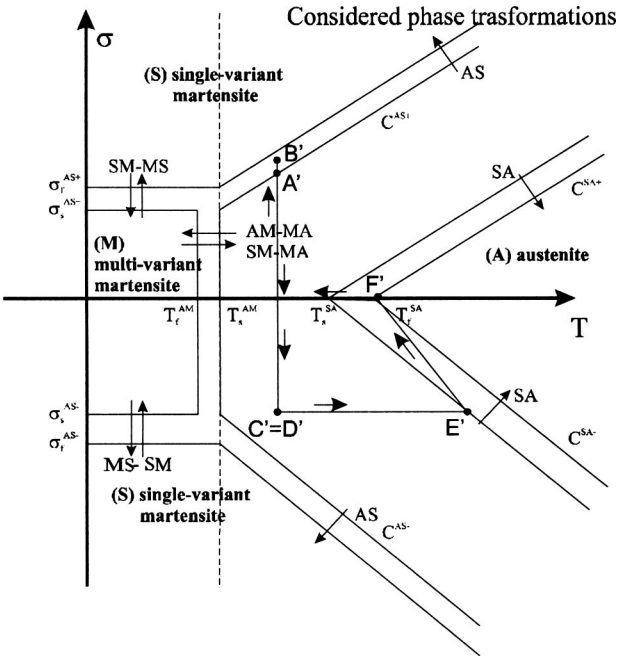

Fig. 2 Scheme of the phase transformations in uniaxial tension and compression versus temperature

- σ_s^{AS} and σ_f^{AS} are the starting and final stress for the A→S phase transformation at temperature $T=T_s^{AM}$; they are set as $\sigma_s^{AS}=\sigma_s^{AS(+)}$ and $\sigma_f^{AS}=\sigma_f^{AS(+)}$ in tension and $\sigma_s^{AS}=\sigma_s^{AS(-)}$ and $\sigma_f^{AS}=\sigma_f^{AS(-)}$ in compression;
- T_s^{SA} and T_f^{SA} are the starting and final temperature for the S→A phase transformation at stress equal to zero.

2.2 Matrix Model. A linear elastic constitutive law is considered for the matrix material M. In particular, it is assumed that

$$\boldsymbol{\sigma}^M=\mathbf{E}^M\boldsymbol{\eta}^M \tag{8}$$

where $\mathbf{E}^M$ is the fourth-order elastic tensor of the matrix and $\boldsymbol{\sigma}^M$ and $\boldsymbol{\eta}^M$ are the stress and the elastic strain in the matrix, respectively. The total strain is given by

$$\boldsymbol{\varepsilon}^M=\boldsymbol{\eta}^M+(T-T_0)\boldsymbol{\tau}^M \tag{9}$$

with $\boldsymbol{\tau}^M=\alpha^M\mathbf{I}$ the thermal strain induced by a unit temperature change and α^M the expansion coefficient of the matrix.

3 Overall CSMA Response

The average stress and strain in the composite SMA material, respectively, are defined as

$$\overline{\boldsymbol{\sigma}}=\frac{1}{V}\left(\int_{\Omega}\boldsymbol{\sigma}^{\Omega}dV+\int_M\boldsymbol{\sigma}^M dV\right)=f^{\Omega}\overline{\boldsymbol{\sigma}}^{\Omega}+f^M\overline{\boldsymbol{\sigma}}^M \tag{10}$$

$$\overline{\boldsymbol{\varepsilon}}=\frac{1}{V}\left(\int_{\Omega}\boldsymbol{\varepsilon}^{\Omega}dV+\int_M\boldsymbol{\varepsilon}^M dV\right)=f^{\Omega}\overline{\boldsymbol{\varepsilon}}^{\Omega}+f^M\overline{\boldsymbol{\varepsilon}}^M \tag{11}$$

with $f^{\Omega}=\Omega/V$ and $f^M=M/V$ the volume fractions, while $\overline{\boldsymbol{\varepsilon}}^{\Omega}$, $\overline{\boldsymbol{\sigma}}^{\Omega}$ and $\overline{\boldsymbol{\varepsilon}}^M$, $\overline{\boldsymbol{\sigma}}^M$ are the average strain and stress in the inclusion and in the matrix, respectively.

The CSMA presents a constitutive overall stress–strain relationship, which can be written in the following form:

$$\overline{\boldsymbol{\sigma}}=\overline{\mathbf{E}}\overline{\mathbf{e}} \tag{12}$$

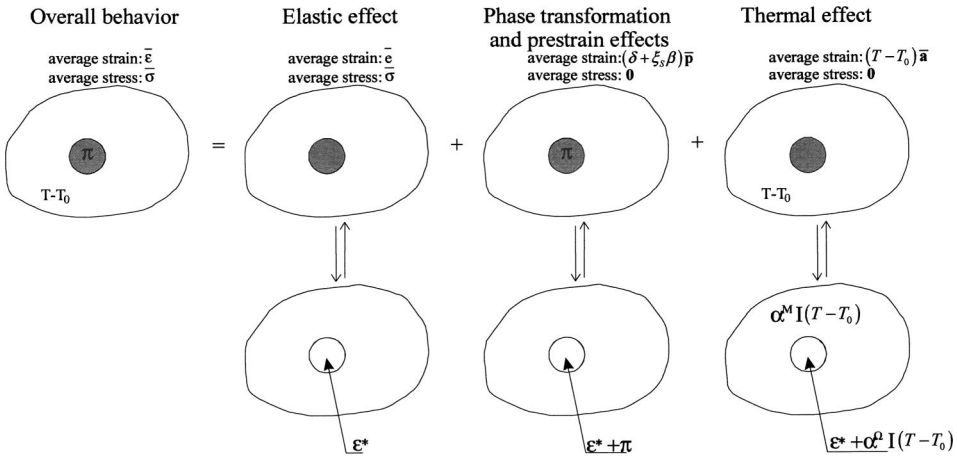

Fig. 3 Scheme of the homogenization procedure

where $\bar{\mathbf{E}}$ is the overall fourth-order elastic tensor of the CSMA and $\bar{\mathbf{e}}$ is the average elastic strain. The total average strain is obtained as

$$\bar{\boldsymbol{\varepsilon}}=\bar{\mathbf{e}}+(\delta+\xi_S\beta)\bar{\mathbf{p}}+(T-T_0)\bar{\mathbf{t}} \tag{13}$$

with $\bar{\mathbf{p}}$ the average strain tensor due to the inelastic strain $\boldsymbol{\pi}$ in the SMA inclusion and $\bar{\mathbf{t}}$ the average strain tensor due to the unit temperature change effect.

The homogenization procedure is performed in the following three phases, schematically illustrated in Fig. 3:

- homogenization of the elastic moduli to get the overall elastic tensor $\mathbf{E}$; in this phase only the average elastic strain is considered, while the inelastic deformations are not taken into account;
- determination of the overall second-order strain tensor $\bar{\mathbf{p}}$, when a constant inelastic strain $\boldsymbol{\pi}$ is present in the inclusion Ω, under the condition of null average stress;
- evaluation of the tensor $\mathbf{t}$ due to the inelastic thermal deformation, under the condition of null average stress.

In order to derive a model that is simple and in the meanwhile effective, a fundamental hypothesis can be introduced regarding the evolution of the martensite–austenite phase transformation. In fact, it is assumed that the stress governing the phase transformations is the average normal stress $\bar{\sigma}_{33}^{\Omega}$ in the SMA wire. Thus, evolutive Eqs. (4)–(6) are simply modified substituting the average stress $\bar{\sigma}_{33}^{\Omega}$ to the normal stress σ_{33}^{Ω}.

To compute the average stress in the inclusion, it is necessary to evaluate the average elastic strain $\boldsymbol{\eta}^{\Omega}$ in the inclusion, which is obtained as a linear combination of the elastic strains $\bar{\mathbf{e}}_{el}^{\Omega}$, $\bar{\mathbf{p}}_{el}^{\Omega}$, and $\bar{\mathbf{t}}_{el}^{\Omega}$, due to the overall deformations $\bar{\mathbf{e}}$, $\bar{\mathbf{p}}$, and $\bar{\mathbf{t}}$, respectively:

$$\bar{\boldsymbol{\eta}}=\bar{\mathbf{e}}_{el}^{\Omega}+(\delta+\xi_S\beta)\bar{\mathbf{p}}_{el}^{\Omega}+(T-T_0)\bar{\mathbf{t}}_{el}^{\Omega} \tag{14}$$

Summarizing, the proposed homogenization procedure is based on the two fundamental simplifying hypotheses presented above; specifically, they are

- the inelastic strain due to the martensite transformation is assumed acting only along the fiber direction;
- the stress governing the phase transformations is the average normal stress $\bar{\sigma}_{33}^{\Omega}$ in the SMA wire.

4 Dilute Distribution

Let us consider the homogenization problem of a composite characterized by a low value of the SMA volume fraction. The average strain in the cell is denoted as $\bar{\boldsymbol{\varepsilon}}$, while a prescribed strain $\boldsymbol{\gamma}$ is considered in the inclusion.

The stress and the strain tensors in the composite material can be represented in the following form [26,27]

$$\boldsymbol{\sigma}=\bar{\boldsymbol{\sigma}}+\boldsymbol{\sigma}^d, \quad \boldsymbol{\varepsilon}=\bar{\boldsymbol{\varepsilon}}+\boldsymbol{\varepsilon}^d \tag{15}$$

where $\boldsymbol{\sigma}^d$ and $\boldsymbol{\varepsilon}^d$ are the disturbances with respect to the average stress and strain tensor, respectively, due to the presence of the inclusion Ω. Moreover, the elastic strain in the inclusion is:

$$\boldsymbol{\varepsilon}_{el}^{\Omega}=\boldsymbol{\varepsilon}^{\Omega}-\boldsymbol{\gamma} \tag{16}$$

The effect of the heterogeneity of the CSMA cell, i.e., the variation of elastic moduli from the matrix to the inclusion, can be simulated introducing an eigenstrain $\boldsymbol{\varepsilon}^*$ in a homogeneous material characterized by the matrix elastic properties, as schematically shown in Fig. 3. This inelastic strain should be able to reproduce the stress state in the inclusion Ω; thus, taking into account Eqs. (15) and (16), the following classical consistency equation can be written

$$\mathbf{E}^{\Omega}(\bar{\boldsymbol{\varepsilon}}+\boldsymbol{\varepsilon}^d-\boldsymbol{\gamma})=\mathbf{E}^{M}(\bar{\boldsymbol{\varepsilon}}+\boldsymbol{\varepsilon}^d-\boldsymbol{\gamma}-\boldsymbol{\varepsilon}^*) \tag{17}$$

From Eq. (17) the strain in the inclusion is derived as

$$\boldsymbol{\varepsilon}^{\Omega}=\bar{\boldsymbol{\varepsilon}}+\boldsymbol{\varepsilon}^d=\boldsymbol{\gamma}+\mathbf{A}^{\Omega}\boldsymbol{\varepsilon}^* \tag{18}$$

with

$$\mathbf{A}^{\Omega}=(\mathbf{E}^{M}-\mathbf{E}^{\Omega})^{-1}\mathbf{E}^{M} \tag{19}$$

The solution of the Eshelby problem proves that the eigenstrain in a single ellipsoidal volume Ω leads to a constant strain $\boldsymbol{\varepsilon}^d$ in Ω, given by the algebraic equation

$$\boldsymbol{\varepsilon}^d=\mathbf{S}^{\Omega}(\boldsymbol{\varepsilon}^*+\boldsymbol{\gamma}) \tag{20}$$

where $\mathbf{S}^{\Omega}$ is the fourth-order Eshelby tensor. Substituting the Eshelby formula (20) into Eq. (18) and solving with respect to the eigenstrain $\boldsymbol{\varepsilon}^*$ yields

$$\boldsymbol{\varepsilon}^*=\mathbf{P}\bar{\boldsymbol{\varepsilon}}+\mathbf{Q}\boldsymbol{\gamma} \tag{21}$$

with

$$\mathbf{P}=(\mathbf{A}^{\Omega}-\mathbf{S}^{\Omega})^{-1}, \quad \mathbf{Q}=(\mathbf{A}^{\Omega}-\mathbf{S}^{\Omega})^{-1}(\mathbf{S}^{\Omega}-\mathbf{I}) \tag{22}$$

The total and the elastic strains in the inclusion are constant and can be evaluated from Eqs. (16), (18), and (21) as

$$\boldsymbol{\varepsilon}^{\Omega}=\bar{\boldsymbol{\varepsilon}}^{\Omega}=\boldsymbol{\gamma}+\mathbf{A}^{\Omega}(\mathbf{P}\bar{\boldsymbol{\varepsilon}}+\mathbf{Q}\boldsymbol{\gamma}), \quad \boldsymbol{\varepsilon}_{el}^{\Omega}=\bar{\boldsymbol{\varepsilon}}_{el}^{\Omega}=\mathbf{A}^{\Omega}(\mathbf{P}\bar{\boldsymbol{\varepsilon}}+\mathbf{Q}\boldsymbol{\gamma}) \tag{23}$$

4.1 Overall Elastic Tensor $\bar{\mathbf{E}}$. The average strain in the cell and the prescribed strain in the inclusion are set as

$$\bar{\boldsymbol{\varepsilon}}=\bar{\mathbf{e}}, \quad \boldsymbol{\gamma}=\mathbf{0} \tag{24}$$

From the average strain Eq. (11), we get

$$f^M\overline{\mathbf{e}}^M=\overline{\mathbf{e}}-f^\Omega\overline{\mathbf{e}}^\Omega \tag{25}$$

which, taking into account the constitutive equation of the matrix material (8), gives

$$f^M\overline{\boldsymbol{\sigma}}^M=f^M\mathbf{E}^M\overline{\mathbf{e}}^M=\mathbf{E}^M(\overline{\mathbf{e}}-f^\Omega\overline{\mathbf{e}}^\Omega) \tag{26}$$

Because of the average stress Eq. (10) and of the constitutive Eqs. (2) and (12) for the inclusion and for the composite, respectively, we get

$$f^M\overline{\boldsymbol{\sigma}}^M=\overline{\boldsymbol{\sigma}}-f^\Omega\overline{\boldsymbol{\sigma}}^\Omega=\bar{\mathbf{E}}\overline{\mathbf{e}}-f^\Omega\mathbf{E}^\Omega\overline{\mathbf{e}}^\Omega \tag{27}$$

Thus, formulas (26) and (27) give

$$(\mathbf{E}^M-\bar{\mathbf{E}})\overline{\mathbf{e}}=f^\Omega(\mathbf{E}^M-\mathbf{E}^\Omega)\overline{\mathbf{e}}^\Omega \tag{28}$$

Substitution of expressions (23) and (19) into Eq. (28) leads to the evaluation of the overall elastic tensor

$$\bar{\mathbf{E}}=\mathbf{E}^M[\mathbf{I}-f^\Omega(\mathbf{A}^\Omega-\mathbf{S}^\Omega)^{-1}] \tag{29}$$

where $\mathbf{I}$ is the fourth–order identity tensor.

The average strain in the inclusion, due to the presence of the elastic average strain $\overline{\mathbf{e}}$ in the whole cell, is elastic, and it is obtained taking into account formulas (23), as

$$\overline{\mathbf{e}}^\Omega_{el}=\overline{\mathbf{e}}^\Omega=\mathbf{A}^\Omega\mathbf{P}\overline{\mathbf{e}} \tag{30}$$

4.2 Effect of the Inelastic Strain $\boldsymbol{\pi}$. Let us consider the problem of the inclusion subjected to the inelastic strain $\boldsymbol{\pi}$, whose presence is responsible of an average strain $\overline{\mathbf{p}}$ of the whole cell. In the formulas (15)–(23), it is set as

$$\boldsymbol{\varepsilon}=\mathbf{p},\quad \boldsymbol{\gamma}=\boldsymbol{\pi} \tag{31}$$

so that the average elastic strain in the inclusion is $\overline{\mathbf{p}}^\Omega-\boldsymbol{\pi}$. Taking into account the relations (10) and (11), and the constitutive equations of the matrix and the inclusion, the average stress in the CSMA is

$$\begin{aligned}\overline{\boldsymbol{\sigma}}^p&=f^\Omega\overline{\boldsymbol{\sigma}}^{p\Omega}+f^M\overline{\boldsymbol{\sigma}}^{pM}=f^\Omega\mathbf{E}^\Omega(\overline{\mathbf{p}}^\Omega-\boldsymbol{\pi})+f^M\mathbf{E}^M\overline{\mathbf{p}}^M\\&=f^\Omega\mathbf{E}^\Omega(\overline{\mathbf{p}}^\Omega-\boldsymbol{\pi})+\mathbf{E}^M(\overline{\mathbf{p}}-f^\Omega\overline{\mathbf{p}}^\Omega)\\&=\mathbf{E}^M\overline{\mathbf{p}}+f^\Omega(\mathbf{E}^\Omega-\mathbf{E}^M)\overline{\mathbf{p}}^\Omega-f^\Omega\mathbf{E}^\Omega\boldsymbol{\pi}\end{aligned} \tag{32}$$

Substituting the first of the formulas (23) into relation (32), and setting the average stress in the cell subjected only to the inelastic strain $\boldsymbol{\pi}$ equal to zero, it results that

$$\overline{\mathbf{p}}=-f^\Omega[\mathbf{E}^M(\mathbf{I}-f^\Omega\mathbf{P})]^{-1}[(\mathbf{E}^\Omega-\mathbf{E}^M)(\mathbf{I}+\mathbf{A}^\Omega\mathbf{Q})-\mathbf{E}^\Omega]\boldsymbol{\pi} \tag{33}$$

As it is,

$$(\mathbf{E}^\Omega-\mathbf{E}^M)(\mathbf{I}+\mathbf{A}^\Omega\mathbf{Q})-\mathbf{E}^\Omega=-\mathbf{E}^M(\mathbf{I}+\mathbf{Q}) \tag{34}$$

Eq. (33) becomes

$$\overline{\mathbf{p}}=f^\Omega(f^\Omega\mathbf{P}-\mathbf{I})^{-1}(\mathbf{I}+\mathbf{Q})\boldsymbol{\pi} \tag{35}$$

so that, because of formulas (23), the total and the elastic strains in the inclusion are

$$\mathbf{p}^\Omega=\overline{\mathbf{p}}^\Omega=\boldsymbol{\pi}+\mathbf{A}^\Omega(\mathbf{P}\overline{\mathbf{p}}+\mathbf{Q}\boldsymbol{\pi}),\quad \mathbf{p}^\Omega_{el}=\overline{\mathbf{p}}^\Omega_{el}=\mathbf{A}^\Omega(\mathbf{P}\overline{\mathbf{p}}+\mathbf{Q}\boldsymbol{\pi}) \tag{36}$$

4.3 Effect of the Temperature. An average inelastic strain $\overline{\mathbf{t}}$ can be induced by thermal expansion of the CSMA, characterized by different thermal coefficients α^M and α^Ω of the matrix and the inclusion, respectively. The effect of the thermal expansion is evaluated in two steps.

• In the first step it is considered the effect of the thermal coefficient α^M in the whole cell; in this case, the strain in the cell assumes the constant value

$$\mathbf{t}^1=\overline{\mathbf{t}}^1=\alpha^M\mathbf{I} \tag{37}$$

• In the second step, the effect of the thermal coefficient $\Delta\alpha=\alpha^\Omega-\alpha^M$ in the inclusion alone is studied; this second case corresponds to the problem solved in the previous subsection. In fact, the inclusion results subjected to an inelastic strain $\Delta\alpha\,\mathbf{I}$. Taking into account formula (35), the average strain in the cell is

$$\overline{\mathbf{t}}^2=\Delta\alpha f^\Omega(f^\Omega\mathbf{P}-\mathbf{I})^{-1}(\mathbf{I}+\mathbf{Q})\mathbf{I} \tag{38}$$

As a consequence, the second-order strain tensor $\overline{\mathbf{t}}$ due to the unit temperature change effect is equal to

$$\overline{\mathbf{t}}=\overline{\mathbf{t}}^1+\overline{\mathbf{t}}^2=\alpha^M\mathbf{I}+\Delta\alpha f^\Omega(f^\Omega\mathbf{P}-\mathbf{I})^{-1}(\mathbf{I}+\mathbf{Q})\mathbf{I} \tag{39}$$

The elastic deformations of the cell due to the thermal effect is induced only by the average strain $\overline{\mathbf{t}}^2$; thus, it results that

$$\overline{\mathbf{t}}^\Omega_{el}=\mathbf{A}^\Omega(\mathbf{P}\overline{\mathbf{t}}^2+\Delta\alpha\mathbf{Q}\mathbf{I}) \tag{40}$$

5 Periodic Composite

A periodic composite is obtained by assembling an infinite number of repetitive adjacent unit cells V. In the following, parallelepiped unit cells are considered with the total dimensions along the three coordinate axes x_1, x_2, x_3 denoted by $2a_1$, $2a_2$, and $2a_3$, respectively. The x_3 axis is parallel to the SMA fiber direction, so that the repetitive unit cell is obtained considering any possible value of a_3. For periodic media, the displacement field can be represented in the form

$$\mathbf{u}(x_1,x_2,x_3)=\overline{\boldsymbol{\varepsilon}}\mathbf{x}+\hat{\mathbf{u}}(x_1,x_2,x_3) \tag{41}$$

where $\mathbf{x}$ is the position vector of the typical point of V and $\hat{\mathbf{u}}(x_1,x_2,x_3)$ is the periodic part of the displacement [28]. As consequence of formula (41), the strain tensor is given by

$$\boldsymbol{\varepsilon}(x_1,x_2,x_3)=\overline{\boldsymbol{\varepsilon}}+\hat{\boldsymbol{\varepsilon}}(x_1,x_2,x_3) \tag{42}$$

where the strain tensor $\hat{\boldsymbol{\varepsilon}}(x_1,x_2,x_3)$ is V-periodic in R^3 with null average in V.

As the thickness of the unit cell in the fiber direction can assume any value, the periodicity and continuity conditions along the x_3 direction on the displacement field results in

$$\hat{\mathbf{u}}(x_1,x_2,a_3)=\hat{\mathbf{u}}(x_1,x_2,-a_3),\quad \begin{matrix}\forall x_1\in[-a_1,a_1]\\ \forall x_2\in[-a_2,a_2]\end{matrix},\quad \forall a_3 \tag{43}$$

which leads to $\hat{u}_i(x_1,x_2,x_3)=\hat{u}_i(x_1,x_2)$. Thus, the in-plane periodicity and continuity conditions are

$$\begin{aligned}\hat{\mathbf{u}}(a_1,x_2)&=\hat{\mathbf{u}}(-a_1,x_2),\quad \forall x_2\in[-a_2,a_2]\\ \hat{\mathbf{u}}(x_1,a_2)&=\hat{\mathbf{u}}(x_1,-a_2),\quad \forall x_1\in[-a_1,a_1]\end{aligned} \tag{44}$$

The estimate of the micromechanical behavior of a periodic composite material is derived from the solution of the heterogeneous medium subjected to the mean strain state $\overline{\boldsymbol{\varepsilon}}$, under the prescribed inelastic strain $\boldsymbol{\gamma}$ in the inclusion. Hence, the elastostatic problem, governed by the following equations, is considered:

$$\begin{aligned}\mathrm{div}\,\boldsymbol{\sigma}&=\mathbf{0},\quad \text{in } V\\ \boldsymbol{\varepsilon}&=\overline{\boldsymbol{\varepsilon}}+\nabla^s\mathbf{u},\quad \text{in } V\\ \boldsymbol{\sigma}&=\mathbf{E}^M\boldsymbol{\varepsilon},\quad \text{in } M\\ \boldsymbol{\sigma}&=\mathbf{E}^\Omega(\boldsymbol{\varepsilon}-\boldsymbol{\gamma}),\quad \text{in } \Omega\end{aligned} \tag{45}$$

subjected to the boundary conditions (44). In Eqs. (45) the symbol ∇^s denotes the symmetric part of the gradient operator.

The problem defined by Eqs. (44) and (45) is solved considering two schemes. In the first scheme the representative cell is subjected only to the average strain $\overline{\boldsymbol{\varepsilon}}$ with $\boldsymbol{\gamma}=\mathbf{0}$. The strain distribution in the unit cell is obtained as

$$\boldsymbol{\varepsilon}^1(x_1,x_2,x_3)=\mathbf{R}(x_1,x_2,x_3)\overline{\boldsymbol{\varepsilon}} \tag{46}$$

where $\mathbf{R}$ is the so-called localization tensor, associated with the assumed average strain $\overline{\boldsymbol{\varepsilon}}$. The second scheme considers only the inclusion subjected to the deformation $\boldsymbol{\gamma}$ with the average strain $\overline{\boldsymbol{\varepsilon}}$ equal to zero; thus, the local strain is written in the form

$$\boldsymbol{\varepsilon}^2(x_1,x_2,x_3)=\hat{\mathbf{R}}(x_1,x_2,x_3)\boldsymbol{\gamma} \tag{47}$$

where $\hat{\mathbf{R}}$ is the localization tensor, associated to the prescribed inelastic strain $\boldsymbol{\gamma}$ in the inclusion. The elastic strains in the matrix and in the inclusion are

$$\mathbf{e}_{el}^M=\mathbf{R}\overline{\boldsymbol{\varepsilon}}+\hat{\mathbf{R}}\boldsymbol{\gamma}, \quad \mathbf{e}_{el}^\Omega=\mathbf{R}\overline{\boldsymbol{\varepsilon}}+(\hat{\mathbf{R}}-\mathbf{I})\boldsymbol{\gamma} \tag{48}$$

so that, the average stress in the periodic unit cell results in

$$\begin{aligned}\overline{\boldsymbol{\sigma}}&=\frac{1}{M}\int_M \mathbf{E}^M\boldsymbol{\varepsilon}_{el}^M dV+\frac{1}{\Omega}\int_\Omega \mathbf{E}^\Omega\boldsymbol{\varepsilon}_{el}^\Omega dV\\&=\left(\mathbf{E}^M\frac{1}{M}\int_M \mathbf{R}dV+\mathbf{E}^\Omega\frac{1}{\Omega}\int_\Omega \mathbf{R}dV\right)\overline{\boldsymbol{\varepsilon}}\\&\quad+\left[\mathbf{E}^M\frac{1}{M}\int_M \hat{\mathbf{R}}dV+\mathbf{E}^\Omega\frac{1}{\Omega}\int_\Omega(\hat{\mathbf{R}}-\mathbf{I})dV\right]\boldsymbol{\gamma}\end{aligned} \tag{49}$$

The two localization tensors $\mathbf{R}$ and $\hat{\mathbf{R}}$ can be computed using the FEM. In fact, the components of $\mathbf{R}$ are determined solving the six elastic problems, each one characterized by only one nonzero element of $\overline{\boldsymbol{\varepsilon}}$. Analogously, the component of $\hat{\mathbf{R}}$ are computed solving the six elastic problems obtained by setting to nonzero only one element of $\boldsymbol{\gamma}$.

5.1 Overall Elastic Tensor $\overline{\mathbf{E}}$. The overall elastic response of the heterogeneous composite material is determined setting

$$\overline{\boldsymbol{\varepsilon}}=\overline{\mathbf{e}}, \quad \boldsymbol{\gamma}=\mathbf{0} \tag{50}$$

In this case, the average elastic strain in the inclusion results in

$$\overline{\mathbf{e}}_{el}^\Omega=\frac{1}{\Omega}\int_\Omega \mathbf{R}dV\,\overline{\mathbf{e}} \tag{51}$$

Taking into account the positions (50), from the formula (49) it is possible to evaluate overall elastic tensor as

$$\overline{\mathbf{E}}=\mathbf{E}^M\frac{1}{M}\int_M \mathbf{R}dV+\mathbf{E}^\Omega\frac{1}{\Omega}\int_\Omega \mathbf{R}dV \tag{52}$$

5.2 Effect of the Inelastic Strain $\boldsymbol{\pi}$. Set

$$\boldsymbol{\varepsilon}=\mathbf{p}, \quad \boldsymbol{\gamma}=\boldsymbol{\pi} \tag{53}$$

Substituting positions (53) into the average stress Eq. (49), and taking into account formula (52), the condition $\overline{\boldsymbol{\sigma}}=\mathbf{0}$ gives

$$\overline{\mathbf{p}}=\mathbf{T}\boldsymbol{\pi}, \quad \text{with } \mathbf{T}=-\overline{\mathbf{E}}^{-1}\left[\mathbf{E}^M\frac{1}{M}\int_M \hat{\mathbf{R}}dV+\mathbf{E}^\Omega\frac{1}{\Omega}\int_\Omega(\hat{\mathbf{R}}-\mathbf{I})dV\right] \tag{54}$$

The average elastic strain in the inclusion is

$$\begin{aligned}\overline{\mathbf{p}}_{el}^\Omega&=\left(\frac{1}{\Omega}\int_\Omega \mathbf{R}dV\right)\overline{\mathbf{p}}+\left[\frac{1}{\Omega}\int_\Omega(\hat{\mathbf{R}}-\mathbf{I})dV\right]\boldsymbol{\pi}\\&=\frac{1}{\Omega}\left\{\left(\int_\Omega \mathbf{R}dV\right)\mathbf{T}+\left[\int_\Omega(\hat{\mathbf{R}}-\mathbf{I})dV\right]\right\}\boldsymbol{\pi}\end{aligned} \tag{55}$$

5.3 Effect of the Temperature. As in the case of dilute distribution, the effect of the thermal expansion is evaluated in two steps, the first one characterized by a constant thermal coefficient α^M in the whole cell, and the second one by a thermal coefficient $\Delta\alpha=\alpha^\Omega-\alpha^M$ in the inclusion. Following the procedure proposed in subsection 4.3 and taking into account formula (54), the average strain tensor $\overline{\mathbf{t}}$ due to the unit temperature change effect results in

$$\overline{\mathbf{t}}=(\alpha^M\mathbf{I}+\Delta\alpha\mathbf{T})\mathbf{I} \tag{56}$$

The elastic deformation of the cell due to the thermal effect is induced only by the average strain results in

$$\overline{\mathbf{t}}_{el}^\Omega=\Delta\alpha\frac{1}{\Omega}\left\{\left(\int_\Omega \mathbf{R}\,dV\right)\mathbf{T}+\left[\int_\Omega(\hat{\mathbf{R}}-\mathbf{I})dV\right]\right\}\mathbf{I} \tag{57}$$

6 Numerical Results

Two numerical procedures based on the proposed homogenization techniques are developed. The first, based on the dilute distribution homogenization presented in Sec. 4, allows us to evaluate the quantities $\mathbf{E}$, $\mathbf{A}^\Omega$, $\mathbf{P}$, $\overline{\mathbf{p}}$, $\overline{\mathbf{p}}_{el}^\Omega$, $\overline{\mathbf{t}}$, and $\overline{\mathbf{t}}_{el}^\Omega$ for composites characterized by a low value of the SMA volume fraction. It can be emphasized again that SMA composites are characterized mainly by reduced values of the volume fraction; as a consequence the Eshelby solution can lead to satisfactory solutions. For the dilute distribution technique the following components of the Eshelby tensor, suitable for a long-fiber composite, are adopted for the computations:

$$\begin{aligned}&S_{1111}^\Omega=S_{2222}^\Omega=\frac{5-4\nu}{8(1-\nu)}, \quad S_{1122}^\Omega=S_{2211}^\Omega=\frac{1-4\nu}{8(1-\nu)}\\&S_{1133}^\Omega=S_{2233}^\Omega=\frac{\nu}{2(1-\nu)}, \quad S_{1212}^\Omega=\frac{3-4\nu}{8(1-\nu)}\\&S_{1313}^\Omega=S_{2323}^\Omega=\frac{1}{4}, \quad S_{3333}^\Omega=S_{3311}^\Omega=S_{3322}^\Omega=0\end{aligned} \tag{58}$$

The second numerical procedure, developed for periodic composites, allows us to evaluate the quantities $\overline{\mathbf{E}}$, $\hat{\mathbf{R}}^\Omega$, $\overline{\mathbf{p}}$, $\overline{\mathbf{p}}_{el}^\Omega$, $\overline{\mathbf{t}}$, and $\overline{\mathbf{t}}_{el}^\Omega$, once the components of $\mathbf{R}$ and $\hat{\mathbf{R}}$ are computed, solving 12 elastostatic problems of the repetitive unit cell using the FEM; in this framework, a new suitable linear elastic finite element, described in detail in Ref. [29], is developed on the base of the kinematical hypotheses introduced in Sec. 5. A backward-Euler algorithm is used to integrate the evolutive constitutive equations of the SMA material for both the homogenization procedures.

Next, numerical applications are developed to assess the ability of the two proposed homogenization techniques to reproduce the thermo-mechanical behavior of the SMA composites and to study their superelastic and shape memory effects. Fibers of Ni-Ti alloy, embedded in a polymeric matrix characterized by low stiffness, are considered. In particular, the material properties of the elastic matrix and of the SMA are

- matrix:

$$E^M=3600 \text{ MPa} \quad \nu^M=0.305 \quad \alpha^M=0.0^\circ\text{C}^{-1}$$

- SMA fiber:

$$E^\Omega=70{,}000 \text{ MPa}, \quad \nu^\Omega=0.33, \quad \alpha^\Omega=0.00001^\circ\text{C}^{-1}$$

$$T_f^{AM}=5^\circ\text{C}, \quad T_s^{AM}=10^\circ\text{C}, \quad T_s^{SA}=30^\circ\text{C}, \quad T_f^{SA}=31^\circ\text{C}$$

$$\sigma_s^{AS(\pm)}=140 \text{ MPa}, \quad \sigma_f^{AS(\pm)}=200 \text{ MPa},$$

$$\sigma^{SS(\pm)}=30 \text{ MPa}, \quad \varepsilon_L^{(\pm)}=0.07$$

$$C^{AS(\pm)}=8.0 \text{ MPa/}^\circ\text{C}, \quad C^{SA(\pm)}=8.0 \text{ MPa/}^\circ\text{C}, \quad \omega=0.5$$

where E^M, ν^M, E^Ω, and ν^Ω are the Young modulus and the Poisson coefficient for the matrix and for the SMA, respectively.

6.1 Overall Elastic Tensor $\overline{\mathbf{E}}$. Initially, a comparison of the values of the overall elastic tensor $\overline{\mathbf{E}}$ components, obtained by the two proposed procedures, is performed for a composite characterized by the SMA volume fraction $f^\Omega=0.036$. The periodic cell problem is solved adopting a quite fine mesh characterized by 660 four-node elements.

Table 1 Elastic constants of the overall constitutive tensor, expressed in [MPa]

	$\bar{E}_{1111}=\bar{E}_{2222}$	$\bar{E}_{3333}$	$\bar{E}_{1313}=\bar{E}_{2323}$	$\bar{E}_{1122}$	$\bar{E}_{1133}=\bar{E}_{2233}$	$\bar{E}_{1212}$
Dilute composites	5153.32	7378.87	1541.94	2251.93	2267.29	1511.56 (1450.70)
Periodic composites	5165.20	7377.75	1472.78	2254.18	2271.64	1456.22 (1455.51)

As the composite material is obtained by isotropic long fibers embedded in an isotropic matrix, the constitutive tensor $\bar{\mathbf{E}}$ is transversely isotropic, so that it is characterized by five independent elastic constants.

In Table 1, the values of the average elastic moduli of the tensor $\bar{\mathbf{E}}$ obtained with the two homogenization procedures are reported. It can be emphasized that the values of the sixth elastic constant $\bar{E}_{1212}$ depends on $\bar{E}_{1111}$ and $\bar{E}_{1122}$; thus, the values of $\bar{E}_{1212}$ computed by the two procedures are given and compared with the ones determined applying the classical formula for transversely isotropic materials $\bar{E}_{1212}=(\bar{E}_{1111}-\bar{E}_{1122})/2$, reported between brackets. The values obtained using the dilute distribution and the periodic cell approaches are in good accord. This very satisfactory result is due to the reduced, but realistic, value of the inclusion fraction volume. Furthermore, the computed values of $\bar{E}_{1212}$ demonstrate the very good accuracy of the FEM solution for the periodic cell problem.

6.2 Shape Memory Effect. The shape memory effect is investigated. The volume fraction of the inclusion is $f^{\Omega}=0.1$. The following loading–unloading history is considered, setting the reference temperature $T_0=20°C$:

t [s]	0	1	2	3	4
$\bar{\varepsilon}_{33}$	0	0.025	0.0063	0.000	0.000
T[°C]	20	20	20	55	20

with the other components of the overall strain equal to zero. No initial prestrain of the SMA wires is considered.

In Fig. 4 the overall stress $\bar{\sigma}_{33}$ and the stress in the SMA $\bar{\sigma}^{\Omega}_{33}$ are plotted versus the overall strain $\bar{\varepsilon}_{33}$. The results obtained by the dilute and periodic cell homogenization techniques are in very good accord, so that only one curve has been plotted. It can be noted that the response of the composite is significantly influenced by the shape memory effects in the SMA.

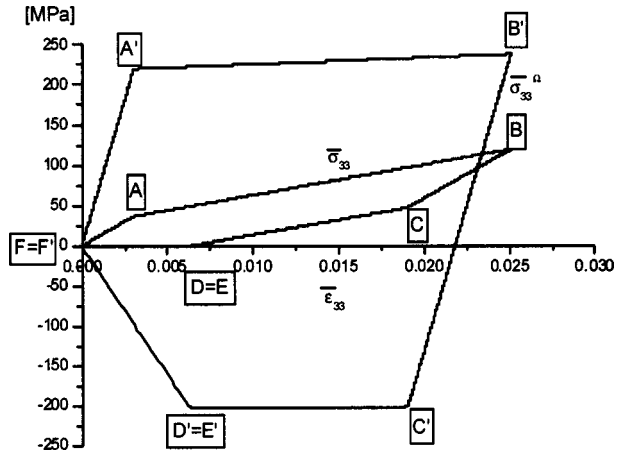

Fig. 4 Shape memory effect in the mechanical response of the SMA composite

With reference to the diagrams $\bar{\sigma}_{33}-\bar{\varepsilon}_{33}$, $\bar{\sigma}^{\Omega}_{33}-\bar{\varepsilon}_{33}$ and to Fig. 2, the mechanical response of the composite can be divided in the following steps:

- Lines AB and A′B′, A→S phase transformation in the SMA at the constant temperature T_0 until the value of the average strain $\bar{\varepsilon}_{33}=0.025$ is reached. It corresponds to a partial phase transformation with the final value of martensite volume fraction $\xi_s=0.3$.
- Lines BC and B′C′, unloading phase at constant temperature with no phase transformation.
- Lines CD and C′D′, reorientation process in the SMA fiber at a constant temperature.
- Lines DE and D′E′, increasing of the temperature until the starting of the S→A phase transformation.
- Lines EF and E′F′, S→A phase transformation controlling the value of ξ_s with $\bar{\sigma}_{33}=0$ until the strain and the stress in the SMA are equal to zero.

This last step is computed introducing a control of the martensite volume fraction in the algorithm. In particular, taking constant and equal to zero the average stress in the composite, when the S→A phase transformation occurs, the inelastic strain decreases and the stress in the SMA fibers changes. Increasing the temperature, a sudden total S→A phase transformation occurs. In order to follow the stress–temperature equilibrium path, a control on the value of the martensite volume fraction is necessary. Enforcing a gradual decrease of ξ_s, a reduction of temperature is induced, as reported in Fig. 2 with line E′F′.

6.3 SMA Volume Fraction. The superelastic mechanical response of composites characterized by different values of the SMA volume fraction is studied. In particular, comparisons between the results obtained by the two numerical procedures are carried out, considering the following loading–unloading history with no initial prestrain of the SMA wires, under constant temperature $T=T_0=60°C$:

t [s]	0	1	2
$\bar{\varepsilon}_{33}$	0	0.08	0

with all the other components of the overall strain equal to zero.

In Tables 2, 3 and 4, the values of the overall elastic modulus $\bar{\mathbf{E}}_{3333}$, the starting $\bar{\sigma}^{AS}_{33,s}$ and the final $\bar{\sigma}^{AS}_{33,f}$ transformation average stresses, for four values of the SMA volume fraction are reported.

It can be emphasized that the values of the overall elastic modulus $\bar{\mathbf{E}}_{3333}$ and of the starting and the final transformation average stress $\bar{\sigma}^{AS}_{33,s}$ and $\bar{\sigma}^{AS}_{33,f}$, computed by the two homogeniza-

Table 2 Elastic constant $\bar{E}_{3333}$ [MPa] for different values of the volume fraction

	$f^{\Omega}=0.01$	$f^{\Omega}=0.036$	$f^{\Omega}=0.05$	$f^{\Omega}=0.1$
Dilute composites	5733.84	7378.87	8557.53	11977.65
Periodic composites	5734.23	7377.75	8563.39	12000.24

Table 3 Starting transformation average stress $\bar{\sigma}^{AS}_{33,s}$ [MPa] for different values of the volume fraction

	$f^{\Omega}=0.01$	$f^{\Omega}=0.036$	$f^{\Omega}=0.05$	$f^{\Omega}=0.1$
Dilute composites	43.10	55.41	64.28	89.93
Periodic composites	43.00	55.31	64.18	89.74

Table 4 Final transformation average stress $\bar{\sigma}^{AS}_{33,f}$ [MPa] for different values of the volume fraction

	$f^{\Omega}=0.01$	$f^{\Omega}=0.036$	$f^{\Omega}=0.05$	$f^{\Omega}=0.1$
Dilute composites	381.14	386.60	390.52	401.88
Periodic composites	381.15	386.61	390.55	401.97

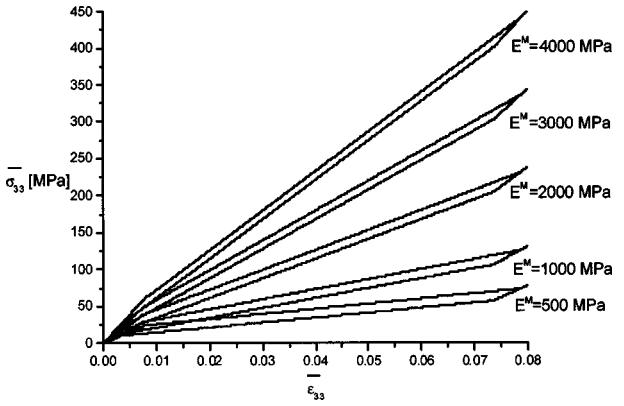

Fig. 6 Superelastic mechanical response of the SMA composites with different values of the matrix Young modulus

tion techniques, are in very good agreement for all the considered values of the inclusion volume fraction. Quite negligible differences appear only for $f^{\Omega}=0.1$, being equal to 0.19% for the elastic modulus $\bar{\mathbf{E}}_{3333}$ and to 0.22% for the starting and final transformation average stress $\bar{\sigma}^{AS}_{33,s}$ and $\bar{\sigma}^{AS}_{33,f}$. Finally, it can be concluded that the results reported in the tables can be considered in very good accord as these differences are negligible in the evaluation of the overall mechanical response of the composite.

Furthermore, the mechanical responses of composites characterized by the SMA volume fractions $f^{\Omega}=0.05$ and $f^{\Omega}=0.1$ are reported in Fig. 5, in terms of the overall stress $\bar{\sigma}_{33}$ versus the overall strain $\bar{\varepsilon}_{33}$. The results obtained by the dilute and periodic cell homogenization techniques are denoted by ''Dilute Composite'' and ''Periodic Composite,'' respectively, and reported with dashed line and dashed-dotted line, respectively. Both the A→S and S→A phase transformations occur in the SMA, and at end of the isothermal loading–unloading cycle the deformation is completely recovered. The response of the composite is significantly influenced by the superelastic effects in the SMA. As underlined above regarding the comparisons reported in Tables 2, 3, and 4, the results are in very good accord for the examined values of inclusion volume fractions.

In the same figure, a further comparison is carried out with the results obtained by the numerical homogenization technique proposed in (Marfia [29]); this latter procedure is based on nonlinear finite-element analyses performed considering the phase transformations governed by the local normal stress σ^{Ω}_{33} in the SMA wires. The results carried out by this procedure are reported in Fig. 5 with solid line and are denoted as ''Periodic Composite*.''

The results obtained for the periodic cell problem, evaluated considering the phase transformations depending on the average normal stress and the local normal stress in the fiber, are in very good accord for both the considered volume fraction values. As a consequence, it can be deduced that the simplifying assumption of governing the phase transformations by the average stress instead of the local stress is validated.

6.4 Young Modulus of the Matrix. The superelastic mechanical responses of long-fiber SMA composites characterized by different values of the matrix Young modulus are investigated for $f^{\Omega}=0.036$. The loading–unloading history under constant temperature $T=T_0=60°C$, adopted in the subsection 6.3 to study the superelastic effects, is considered. The analyses are performed using only the homogenization procedure based on Eshelby inclusion method. No prestrain is assumed in the SMA fibers.

In Fig. 6, the mechanical responses of the SMA composites, characterized by four different values of the matrix Young modulus, are represented in terms of overall stress $\bar{\sigma}_{33}$ versus the overall strain $\bar{\varepsilon}_{33}$. It can be noted that the starting $\bar{\sigma}^{AS}_{33,s}$ and the final $\bar{\sigma}^{AS}_{33,f}$ transformation average stresses increase with the stiffness of the matrix. Moreover, the overall responses, obtained embedding SMA fibers in stiffer matrices, appear less influenced by the nonlinear behavior of shape memory alloys.

6.5 Prestrain in the SMA Fibers. In the following analyses, the SMA volume fraction is set equal to 0.036. A prestrain $\delta=-0.008$ is applied to the SMA fibers before performing a loading–unloading cycle at constant temperature $T=T_0=60°C$. In particular, the following overall strain history is considered:

t [s]	0	1	2
$\bar{\varepsilon}_{33}$	0	0.075	−0.008

with the other strain components equal to zero.

The loading–unloading history induces the complete austenite–

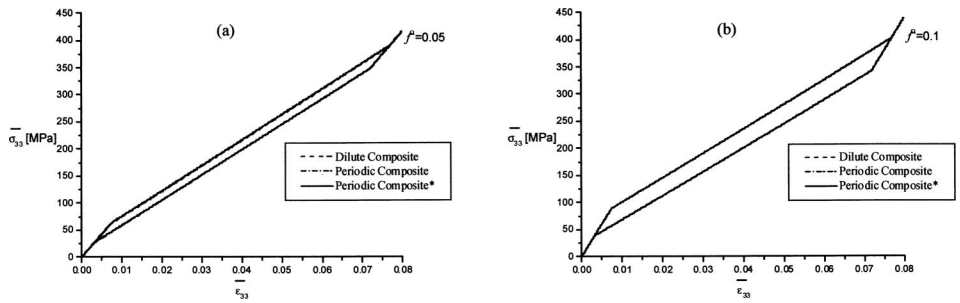

Fig. 5 Superelastic effect in the mechanical response of the SMA for composites with different values of the SMA volume fraction: (a) $f^{\Omega}=0.05$; (b) $f^{\Omega}=0.1$

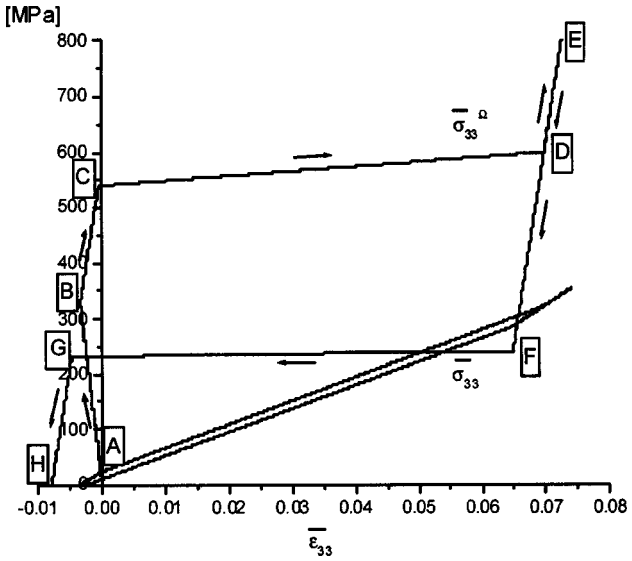

Fig. 7 Effect of a low value of the prestrain in the SMA fibers on the mechanical response of the SMA composite

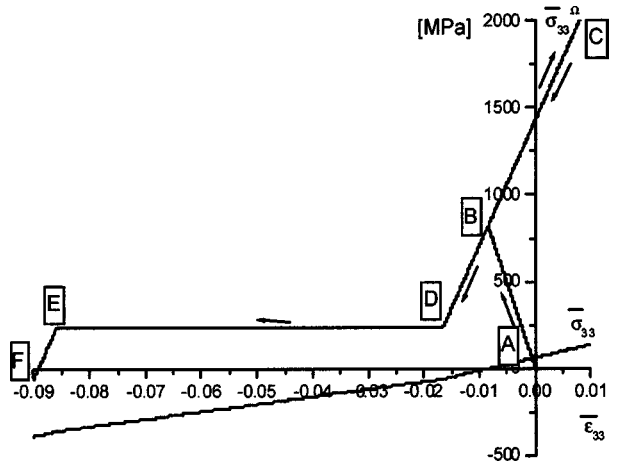

Fig. 8 Effect of a high value of the prestrain in the SMA fibers on the mechanical response of the SMA composite

martensite and martensite–austenite phase transformations in the SMA material. The analysis is performed using the homogenization technique based on the periodic cell.

In Fig. 7, the overall stress $\bar{\sigma}_{33}$ and the stress in the SMA $\bar{\sigma}^{\Omega}_{33}$ are plotted versus the overall strain $\bar{\varepsilon}_{33}$. With reference to the diagram $\bar{\sigma}^{\Omega}_{33}-\bar{\varepsilon}_{33}$, it can be noted that:

- when the prestrain is applied to the fibers (line AB), the overall stress $\bar{\sigma}_{33}$ remains equal to zero, a negative overall strain $\bar{\varepsilon}_{33}$ occurs in the composites, while the stress in the SMA fibers $\bar{\sigma}^{\Omega}_{33}$ is positive. At the end of the prestrain phase, the process of reorientation has completely occurred, while the austenite–martensite phase transformation has not started as yet;
- during the loading (line BCDE) and the unloading (line EFGH), the A→S and S→A phase transformations occur.

Comparing the results in Fig. 7 with the ones, regarding the superelastic effects without prestrain in the SMA fibers, it can be noted that the loading–unloading cycle, during which the A→S and S→A phase transformations occur in the SMA fibers, has shifted in the stress–strain space towards to lower values of the overall strain but without altering its shape.

A higher value of the prestrain equal to $\delta=-0.09$ is considered in order to achieve a complete A→S phase transformation during the prestrain; a loading–unloading history is then applied in order to obtain the martensite–austenite phase transformation at a constant temperature $T=T_0=60°\mathrm{C}$. In particular, the following overall strain history is studied:

$t\,[\mathrm{s}]$	0	1	2
$\bar{\varepsilon}_{33}$	0	0.01	−0.09

with the other strain components equal to zero.

In Fig. 8 the overall stress $\bar{\sigma}_{33}$ and the stress in the SMA $\bar{\sigma}^{\Omega}_{33}$ are plotted versus the overall strain $\bar{\varepsilon}_{33}$. With reference to the diagram $\bar{\sigma}^{\Omega}_{33}-\bar{\varepsilon}_{33}$, it can be pointed out that

- in the prestrain phase (line AB) the diagram $\bar{\sigma}^{\Omega}_{33}-\bar{\varepsilon}_{33}$ is linear, although the austenite–martensite phase transformation completely occurs;
- during the loading (line BC) the SMA composites is characterized by a linear elastic response;
- during the unloading (line CDEF), the S→A phase transformation occurs in the SMA fibers in correspondence of the plateau (line DE). Comparing this plateau with the one, obtained without prestrain, it can be pointed out that it has shifted in the stress–strain space towards to negative values of the overall strain without altering its shape.

7 Conclusions

The two proposed homogenization techniques, one based on the Eshelby inclusion solution and the other considering the periodic composites, are proved to be able to model and to reproduce the behavior of long-fiber SMA composites. The procedures are based on two reasonable assumptions: the phase transformations are governed by the average normal stress in the fibers and the inelastic strain, due to the SMA phase transformations, occurs along the fiber direction.

From the numerical results, the following considerations can be made:

- The behavior of the composites results strongly influenced by the superelastic and shape memory effects in the SMA.
- The results obtained using the proposed homogenization procedures are in very good accordance for all the considered values of the SMA volume fraction. The dilute distribution procedure is also reliable for value of the inclusion volume fraction equal to 0.1; the fiber volume fractions in SMA composites are usually very low, since a low quantity of shape memory alloy significantly influences the composite behavior.
- The simplified assumption of governing the phase transformations by the average stress instead of the local stress is validated.
- The influence of the matrix stiffness on the mechanical response of the SMA composite is investigated. It results that increasing the matrix stiffness the initial and final transformation average stresses become higher.
- The influence of a prestrain state in the SMA fibers is studied. Increasing the value of the prestrain, the average activation stress of the A→S phase transformation decrease and for a prestrain higher enough the complete phase transformation occurs with null average stress.

From a computational point of view, the procedure based on the Eshelby method is more efficient and faster than the periodic cell technique. In fact, the homogenization parameters that characterized the composites' behavior are evaluated directly in a single preanalysis, for the dilute distribution technique, and performing 12 linear elastic finite-element preanalyses that require more computational efforts, for the periodic cell.

Finally, the proposed procedures, able to determine the overall behavior for the SMA composite, can be implemented at the

Gauss point level in a finite-element code in order to perform structural analyses and to design actuators made of SMA composites able to control the displacements and vibrations of structures.

Acknowledgments

The present work has been partially developed within the joint French-Italian ''Lagrangian laboratory'' with the financial support of the Italian Ministry of Education, University and Research (MIUR) in the framework of the PRIN project.

Nomenclature

$\overline{\mathbf{E}}$ = overall fourth-order elastic tensor of the composite

$\mathbf{E}^{\Omega}$ $\mathbf{E}^{M}$ = fourth-order elastic tensor of the SMA inclusion and of the matrix

T_0 = reference temperature

T = actual temperature

$\overline{\mathbf{e}}$ = average elastic strain in the composite

$\overline{\mathbf{e}}_{el}^{\Omega}$, $\overline{\mathbf{p}}_{el}^{\Omega}$, $\overline{\mathbf{t}}_{el}^{\Omega}$ = elastic strains in the inclusion due to the overall deformations $\overline{\mathbf{e}}$, $\overline{\mathbf{p}}$, $\overline{\mathbf{t}}$

$\overline{\mathbf{p}}$ = average strain tensor due to the inelastic strain $\boldsymbol{\pi}$

$\mathbf{t}$ = average strain tensor due to the unit temperature change effect

α^{Ω} α^{M} = thermal expansion coefficient of the inclusion and of the matrix

β = internal variable describing the change of martensite reorientation

δ = prestrain acting along the SMA fiber direction

$\overline{\boldsymbol{\varepsilon}}$ = overall average total strain in the composite

$\boldsymbol{\varepsilon}^{\Omega}$ $\boldsymbol{\varepsilon}^{M}$ = total strain in the SMA inclusion and in the matrix

$\overline{\boldsymbol{\varepsilon}}^{\Omega}$ $\overline{\boldsymbol{\varepsilon}}^{M}$ = average total strain in the inclusion and in the matrix

ε_L = recoverable strain of the SMA

$\boldsymbol{\eta}^{\Omega}$ $\boldsymbol{\eta}^{M}$ = elastic strain in the SMA inclusion and in the matrix

ξ_S = single variant martensite volume fraction

$\boldsymbol{\pi}=\mathbf{k}^3\otimes\mathbf{k}^3$ = $\mathbf{k}^3$ unit vector in the fiber direction

$\overline{\boldsymbol{\sigma}}$ = average stress in the composite

$\boldsymbol{\sigma}^{\Omega}$ $\boldsymbol{\sigma}^{M}$ = stress in the SMA inclusion and in the matrix

$\overline{\boldsymbol{\sigma}}^{\Omega}$ $\overline{\boldsymbol{\sigma}}^{M}$ = average stress in the inclusion and in the matrix

σ^{SS} = limit stress that activates the reorientation process in the SMA

$\boldsymbol{\tau}^{\Omega}$ $\boldsymbol{\tau}^{M}$ = strain due to a unit temperature change in the inclusion and in the matrix

ω = material parameter measuring the reorientation process rate of the SMA

References

[1] Duerig, T. W., Melton, K. N., Stkel, D., and Wayman, C. M., (eds.), 1990, *Engineering aspects of shape-memory alloys*, Butterworth-Heinemann, Boston.

[2] Pelton, A. R., Hodgson, D., and Duerig, T. (eds.), 1994, *Proceedings of the First International Conference on Shape Memory and Superelastic Technologies*, Pacific Grove, CA.

[3] Birman, V., Chandrashekhara, K., and Sukhendu, Sain, 1996, ''An Approach to the Optimization of Shape Memory Alloy Hybrid Composite Plates Subject to Low-Velocity Impact,'' Composites, Part B, **27B**, pp. 439–446.

[4] Hyo Jik Lee, Jung Ju Lee, and Jeung Soo Huh, 1999, ''A Simulation Study on the Thermal Buckling Behavior of Laminated Composite Shells With Embedded Shape Memory Alloy (SMA) Wires,'' Compos. Struct., **47**, pp. 463–469.

[5] Jung Ju Lee and Sup Choi, 1999, ''Thermal Buckling and Postbuckling Analysis of a Laminated Composite Beam With Embedded SMA Actuators,'' Compos. Struct., **47**, pp. 695–703.

[6] Sup Choi, Jung Ju Lee, Dae Cheol Seo, and Sun Woo Choi, 1999, ''The Active Buckling Control of Laminated Composite Beams With Embedded Shape Memory Alloy Wires,'' Compos. Struct., **47**, pp. 679–686.

[7] Thompson, S. P., and Loughlan, J., 1997, ''Adaptive Post-Buckling Response of Carbon Fibre Composite Plates Employing SMA,'' Compos. Struct., **38**, pp. 667–678.

[8] Thompson, S. P., and Loughlan, J., 2000, ''The Control of the Post-Buckling Response in Thin Plates Using Smart Technology,'' Thin-Walled Struct., **36**, pp. 231–263.

[9] Ostachowicz, W., Krawczuk, M., and Zak, A., 2000, ''Dynamics and Buckling of a Multilayer Composite Plate With Embedded SMA Wires,'' Compos. Struct., **48**, pp. 163–167.

[10] Ponte Castañeda, P., 1991, ''The Effective Mechanical Properties of Nonlinear Isotropic Composites,'' J. Mech. Phys. Solids, **39**, pp. 45–71.

[11] Willis, J., 1991, ''On Methods for Bounding the Overall Properties of Nonlinear Composites,'' J. Mech. Phys. Solids, **39**, pp. 73–86.

[12] Suquet, P., 1997, ''Effective Properties of Nonlinear Composites,'' In: *CISM Lecture Notes, Vol. 377, Continuum Micromechanics*, edited by P. Suquet, Springer-Verlag, New York, pp. 197–264.

[13] Boyd, J., Lagoudas, D., and Bo, Z., 1994, ''Micromechanics of Active Composites With SMA Fibers,'' J. Eng. Mater. Technol., **116**, pp. 1337–1347.

[14] Sottos, N. R., and Kline, G. E., 1996, ''Analysis of Phase Transformation Fronts in SMA Composites,'' Proc. SPIE, **2715**, pp. 427–438.

[15] Stalmans, R., Delaey, L., and Van Humbeeck, J., 1997, ''Modelling of Adaptive Composite Materials With Embedded Shape Memory Alloy Wires,'' Mater. Res. Soc. Symp. Proc., **459**, pp. 119–130.

[16] Cherkaoui, M., Sun, Q. P., and Song, G. Q., 2000, ''Micromechanics Modeling of Composite With Ductile Matrix and Shape Memory Alloy Reinforcement,'' Int. J. Solids Struct., **37**, pp. 1577–1594.

[17] Briggs, P. J., and Ponte Castañeda, P., 2002, ''Variational Estimates for the Effective Response of Shape Memory Alloy Actuated Fiber Composites,'' J. Appl. Mech., **69**, pp. 470–480.

[18] Boyd, J., and Lagoudas, D., 1996, ''A Thermodynamical Constitutive Model for Shape-Memory Materials. Part I. The Monolithic Shape-Memory Alloy,'' Int. J. Plast., **12**, pp. 805–842.

[19] Raniecki, B., and Lexcellent, Ch., 1998, ''Thermodynamics of Isotropic Pseudoelasticity in Shape-Memory Alloys,'' Eur. J. Mech. A/Solids, **17**, pp. 185–205.

[20] Souza, A., Mamiya, E., and Zouain, N., 1998, ''Three-Dimensional Model for Solids Undergoing Stress-Induced Phase Transformation,'' Eur. J. Mech. A/Solids, **17**, pp. 789–805.

[21] Auricchio, F., and Petrini, L., 2002, ''Improvements and Algorithmical Considerations on a Recent Three-Dimensional Model Describing Stress-Induced Solid Phase Transformations,'' Int. J. Numer. Methods Eng., **55**, pp. 1255–1284.

[22] Auricchio, F., and Sacco, E., 1999, ''A Temperature-Dependent Beam for Shape-Memory Alloys: Constitutive Modelling, Finite-Element Implementation and Numerical Simulations,'' Comput. Methods Appl. Mech. Eng., **174**, pp. 171–190.

[23] Marfia, S., Sacco, E., and Reddy, J. N., 2003, ''Superelastic and Shape Memory Effects for Laminated SMA Beams,'' AIAA J., **41**, pp. 100–109.

[24] Orgéas, L., and Favier, D., 1995, ''Non-Symmetric Tension-Compression Behavior of NiTi Alloy,'' J. Phys. IV, **C8**, pp. 605–610.

[25] Gall, K., Sehitoglu, H., Chumlyakov, Y. I., and Kireeva, I. V., 1999, ''Tension-Compression Asymmetry of the Stress-Strain Response in Aged Single Crystal and Polycrystalline NiTi.'' Acta Mater., **47**, pp. 1203–1217.

[26] Mura, T., 1987, *Micromechanics of Defects in Solids*, second, revised edition, Martinus, Nijhoff, Dordrecht, The Netherlands.

[27] Nemat-Nasser, S., and Hori, M., 1999, *Micromechanics: Overall Properties of Heterogeneous Materials*, second revised edition, North-Holland/Elsevier, Amsterdam.

[28] Luciano, R., and Sacco, E., 1998, ''Variational Methods for the Homogenization of Periodic Media,'' Eur. J. Mech. A/Solids, **17**, pp. 599–617.

[29] Marfia, S., 2005, ''Micro-macro Analysis of Shape Memory Alloy Composites,'' Int. J. Solids Struct., in press.

Wei-Chau Xie
Professor,
Solid Mechanics Division,
Faculty of Engineering,
University of Waterloo,
Waterloo, ON

Monte Carlo Simulation of Moment Lyapunov Exponents

*A Monte Carlo simulation method for determining the p*th *moment Lyapunov exponents of stochastic systems, which governs the p*th *moment stability, is developed. Numerical results of two-dimensional systems under bounded noise and real noise excitations are presented to illustrate the approach.* [DOI: 10.1115/1.1839592]

1 Introduction

Stochastic differential equations are encountered in various disciplines, among which are engineering, science, and mathematics. In many engineering structures, such as buildings, bridges, heat exchangers, and aircrafts, the loadings applied, such as those arising from winds, earthquakes, or flows, often fluctuate in a random fashion. These loadings can only be described satisfactorily in probabilistic terms. The dynamic responses of these engineering structures are governed in general by n-dimensional stochastic differential equations of the form

$$\dot{X}_j = f_j(t, \mathbf{X}, \boldsymbol{\xi}), \quad j = 1,2,\ldots,n, \tag{1.1}$$

where $\mathbf{X} = \{X_1, X_2, \ldots, X_n\}^T$ is the state vector of the system and $\boldsymbol{\xi}$ is a vector of stochastic processes, such as bounded-noise, Ornstein–Uhlenbeck, or other filtered white-noise processes that characterize the randomness of the loadings.

One of the most important dynamical properties of the solution of system (1.1) is its dynamic stability. The sample or almost sure stability of system (1.1) is governed by the Lyapunov exponents defined as

$$\lambda_{\mathbf{X}} = \lim_{t\to\infty} \frac{1}{t} \log \|\mathbf{X}\|, \tag{1.2}$$

where $\|\mathbf{X}\| = (\mathbf{X}^T\mathbf{X})^{1/2}$ is the Euclidean norm. If the largest Lyapunov exponent is negative, the trivial solution of system (1.1) is stable with probability 1; otherwise, it is almost surely unstable.

The theory of Lyapunov exponents was placed on a solid mathematical footing in the celebrated *Multiplicative Ergodic Theorem* by Oseledec [1]. For the n-dimensional system (1.1), depending on the initial conditions, there are n Lyapunov exponents. Although the dynamic stability of the trivial solution of system (1.1) is governed by the largest Lyapunov exponent, there are situations in which other Lyapunov exponents are of interest. For example, when studying the localization behavior of a one-dimensional, multicoupled, randomly disordered periodic structure, the localization factor is given by the smallest positive Lyapunov exponent of the corresponding discrete dynamical system (see, e.g., Ref. [2]).

It is well known that almost all samples grow in the direction of the largest Lyapunov exponent. In order to determine the top m Lyapunov exponents, the evolution of m orthogonal basis vectors of dimension n is followed and Gram–Schmidt orthornormalization is performed after each iteration. This is the essence of the numerical algorithm proposed by Wolf et al. [3] for evaluating the Lyapunov exponents of a dynamical system.

Contributed by the Applied Mechanics Division of THE AMERICAN SOCIETY OF MECHANICAL ENGINEERS for publication in the ASME JOURNAL OF APPLIED MECHANICS. Manuscript received by the Applied Mechanics Division, January 3, 2004; final revision, September 17, 2004. Associate: N. Sri Namachchivaya. Discussion on the paper should be addressed to the Editor, Prof. Robert M. McMeeking, Journal of Applied Mechanics, Department of Mechanics and Environmental Engineering, University of California–Santa Barbara, Santa Barbara, CA 93106-5070, and will be accepted until four months after final publication in the paper itself in the ASME JOURNAL OF APPLIED MECHANICS.

On the other hand, the stability of the pth moment $\mathsf{E}[\|\mathbf{X}\|^p]$ of the solution of system (1.1) is governed by the pth moment Lyapunov exponent defined by

$$\Lambda_{\mathbf{X}}(p) = \lim_{t\to\infty} \frac{1}{t} \log \mathsf{E}[\|\mathbf{X}\|^p], \tag{1.3}$$

where $\mathsf{E}[\cdot]$ denotes the expected value. If $\Lambda_{\mathbf{X}}(p)$ is negative, then the pth moment is stable; otherwise, it is unstable.

The relationship between the sample stability and the moment stability was formulated in Ref. [4]. A systematic study of moment Lyapunov exponents is presented in Ref. [5] for linear Itô systems and in Ref. [6] for linear stochastic systems under real-noise excitations. The connection between moment Lyapunov exponents and the large deviation theory was studied in Refs. [7], [8], and [9]. A systematic presentation of the theory of random dynamical systems and a comprehensive list of references can be found in Ref. [10].

The pth moment Lyapunov exponent $\Lambda_{\mathbf{X}}(p)$ is a convex analytic function in p that passes through the origin and the slope at the origin is equal to the largest Lyapunov exponent $\lambda_{\mathbf{X}}$, i.e.,

$$\lambda_{\mathbf{X}} = \lim_{p\to 0} \frac{\Lambda_{\mathbf{X}}(p)}{p}. \tag{1.4}$$

The nontrivial zero $\delta_{\mathbf{X}}$ of $\Lambda_{\mathbf{X}}(p)$, i.e., $\Lambda_{\mathbf{X}}(\delta_{\mathbf{X}}) = 0$, is called the stability index.

To have a complete picture of the dynamical stability of a stochastic system, it is important to study both the sample and moment stability and to determine both the Lyapunov exponents and the moment Lyapunov exponents. Despite the importance of the moment Lyapunov exponents, publications are limited because of the difficulties in their actual determination. Furthermore, almost all of the research on the moment Lyapunov exponents is on the determination of approximate results of a single oscillator or two coupled oscillators under weak-noise excitations using perturbation methods. Using the analytic property of the moment Lyapunov exponents, Arnold et al. [11] obtained weak-noise expansions of the moment Lyapunov exponents of a two-dimensional system in terms of εp, where ε is a small parameter, under both white-noise and real-noise excitations. Khasminskii and Moshchuk [12] obtained an asymptotic expansion of the moment Lyapunov exponent of a two-dimensional system under white-noise parametric excitation in terms of the small fluctuation parameter ε, from which the stability index was obtained. Sri Namachchivaya and Vedula [13] obtained general asymptotic approximation of the moment Lyapunov exponent and the Lyapunov exponent for a four-dimensional system with one critical mode and another asymptotically stable mode driven by a small intensity stochastic process. Sri Namachchivaya and Van Roessel [14] studied the moment Lyapunov exponents of two coupled oscillators driven by real noise. Xie obtained weak-noise expansions of the moment Lyapunov exponent, the Lyapunov exponent, and the

stability index of a two-dimensional system under real-noise excitation [15] and bounded-noise excitation [16] in terms of the small fluctuation parameter.

Numerical determination of the pth moment Lyapunov exponents is important for at least four reasons. Firstly, numerically accurate results of the moment Lyapunov exponents are essential in assessing the validity and the ranges of applicability of the approximate analytical results. Secondly, in many engineering applications, the amplitudes of noise excitations are not small and the approximate analytical methods, such as the method of perturbation or the method of stochastic averaging, cannot be applied. Numerical approaches have to be employed to evaluate the moment Lyapunov exponents. Thirdly, for systems of large dimensions, it is very difficult, if not impossible, to obtain analytical results. Fourthly, for systems under noise excitations that cannot be described in elegant analytical forms, or if only the time series of the response of the system is known, numerical approaches have to be resorted to.

Xie [17] evaluated numerically the pth moment Lyapunov exponents of a near-nilpotent system under white-noise parametric excitation. The second-order ordinary differential eigenvalue problem governing the pth moment Lyapunov exponent is converted to a two-point boundary-value problem, which is solved numerically by the method of relaxation.

Recently, Xie and So [18] presented the first numerical approach in literature for the determination of the pth moment Lyapunov exponents of a two-dimensional system under non-white-noise, i.e., bounded-noise or real-noise, parametric excitations. The partial differential eigenvalue problems governing the pth moment Lyapunov exponents are established using the theory of stochastic dynamical systems. By expanding the eigenfunctions in double Fourier series in the bounded-noise case and in Fourier series and series involving Hermite polynomials in the real-noise case, the partial differential eigenvalue problems are transformed to linear algebraic eigenvalue problems. The resulting linear algebraic eigenvalue problems are then solved numerically using the "eigs" function in MATLAB for determining a few eigenvalues of a large sparse matrix. This numerical approach fulfills the first two and partially the third purposes mentioned above. The method is very efficient for lower dimensional systems, for which the partial differential eigenvalue problems can be easily established. For systems of larger dimensions, the conversion from partial differential eigenvalue problems to linear algebraic eigenvalue problems using series expansions of the eigenfunctions could be very involved and the dimensions of the resulting linear algebraic eigenvalue problems could be very large, which may not be handled efficiently even by using a capable algorithm for sparse matrices.

Monte Carlo simulation methods are usually more versatile, especially when the noise excitations cannot be described in such a form that can be treated easily using analytical tools. In this paper, a Monte Carlo simulation approach is presented for determining the pth moment Lyapunov exponents of stochastic systems.

2 Formulation

2.1 Determination of the pth Moment. The state vector of system (1.1) is augmented to rewrite system (1.1) as an N-dimensional system of autonomous Itô stochastic differential equations

$$\mathrm{d}Y_j = m_j(\mathbf{Y})\mathrm{d}t + \sum_{l=1}^{d} \sigma_{jl}(\mathbf{Y})\mathrm{d}W_l, \quad j=1,2,\ldots,N, \quad (2.1)$$

where $\mathbf{Y}=\{Y_1, Y_2, \ldots, Y_N\}^T$, in which $Y_j = X_j$, for $j=1,2,\ldots,n$. In the remainder of this paper, vector $\mathbf{X}$ and the vector containing the first n elements of vector $\mathbf{Y}$ are interchangeable for ease of presentation.

Since the moment Lyapunov exponent is related to the exponential rate of growth or decay of the pth moment, only the numerical approximation of the pth moment of the solution of system (1.1) or (2.1) is of interest in the Monte Carlo simulation. As a result, pathwise approximations of the solutions of the stochastic differential equations (1.1) or (2.1) are not necessary. Only a much weaker form of convergence in probability distribution is required. For the numerical solutions of the stochastic differential equations (2.1), weak Taylor approximations may be applied. To evaluate the pth moment $\mathsf{E}[\|\mathbf{X}\|^p]$, S samples of the solutions of Eqs. (2.1) are generated.

If the functions $m_j(\mathbf{Y})$ and $\sigma_{jl}(\mathbf{Y})$, $j=1,2,\ldots,N$, $l=1,2,\ldots,d$, are six times continuously differentiable, the simplified order 2.0 weak Taylor scheme of the sth realization of Eqs. (2.1) at the kth iteration with $t_k - t_{k-1} = \Delta$, where Δ is the time step of integration, is given by [19]

$$\begin{aligned} Y_{j,s}^k = {} & Y_{j,s}^{k-1} + m_{j,s}^{k-1}\cdot\Delta + \frac{1}{2}\mathcal{L}^0(m_{j,s}^{k-1})\cdot\Delta^2 \\ & + \sum_{l=1}^{d}\left\{\sigma_{jl,s}^{k-1} + \frac{1}{2}[\mathcal{L}^0(\sigma_{jl,s}^{k-1}) + \mathcal{L}^l(m_{j,s}^{k-1})]\right\}\cdot\Delta W_{l,s}^{k-1} \\ & + \frac{1}{2}\sum_{l_1=1}^{d}\sum_{l_2=1}^{d}\mathcal{L}^{l_1}(\sigma_{jl_2,s}^{k-1})(\Delta W_{l_1,s}^{k-1}\cdot\Delta W_{l_2,s}^{k-1} + V_{l_1l_2,s}^{k-1}), \\ & j=1,2,\ldots,N, \end{aligned} \quad (2.2)$$

where the subscript "s" stands for the sth sample, $s=1,2,\ldots,S$; the superscript "k" stands for the value at time t_k; and the operators $\mathcal{L}^0$, $\mathcal{L}^l$ are defined as

$$\mathcal{L}^0 = \sum_{i=1}^{N} m_i\frac{\partial}{\partial Y_i} + \frac{1}{2}\sum_{i=1}^{N}\sum_{j=1}^{N}\sum_{l=1}^{d}\sigma_{il}\sigma_{jl}\frac{\partial^2}{\partial Y_i\partial Y_j},$$

$$\mathcal{L}^l = \sum_{i=1}^{N}\sigma_{il}\frac{\partial}{\partial Y_i}, \quad l=1,2,\ldots,d,$$

in which the functions m_i and σ_{il} are evaluated at time t_{k-1} of the sth sample. In Eq. (2.2), $\Delta W_{l,s}^{k-1}$, $l=1,2,\ldots,d$, are independent random numbers satisfying the moment condition

$$\begin{aligned} & |\mathsf{E}[\Delta W]| + |\mathsf{E}[(\Delta W)^3]| + |\mathsf{E}[(\Delta W)^5]| + |\mathsf{E}[(\Delta W)^2] \\ & \quad - \Delta| + |\mathsf{E}[(\Delta W)^4] - 3\Delta^2| \leqslant C\Delta^3, \end{aligned}$$

for some constant C, in which the scripts for ΔW are dropped for simplicity of presentation. $\Delta W_{l,s}^{k-1}$ can be taken as a normally distributed random number with mean 0 and standard deviation $\sqrt{\Delta}$

$$\Delta W_{l,s}^{k-1} = n_{l,s}^{k-1}\sqrt{\Delta}, \quad (2.3)$$

where $n_{l,s}^{k-1}$ is a standard normal random number $N(0,1)$. $\Delta W_{l,s}^{k-1}$ can also be taken as a random number satisfying the following three-point distribution:

$$\mathsf{P}(\Delta W_{l,s}^{k-1} = \pm\sqrt{3\Delta}) = \tfrac{1}{6}, \quad \mathsf{P}(\Delta W_{l,s}^{k-1} = 0) = \tfrac{2}{3}. \quad (2.4)$$

$V_{l_1l_2,s}^{k-1}$ are independent random numbers with the following two-point distribution, for $l_1=1,2,\ldots,d$;

$$\begin{aligned} & \mathsf{P}(V_{l_1l_2,s}^{k-1} = \pm\Delta) = \tfrac{1}{2}, \quad \text{for} \quad l_2 = 1,2,\ldots,l_1-1, \\ & V_{l_1l_2,s}^{k-1} = -\Delta, \quad \text{for} \quad l_2 = l_1, \\ & V_{l_1l_2,s}^{k-1} = -V_{l_2l_1,s}^{k-1}, \quad \text{for} \quad l_2 = l_1+1,\ l_1+2,\ldots,d. \end{aligned} \quad (2.5)$$

For the special case when $d=1$, the order 2.0 weak Taylor scheme is, for $s=1,2,\ldots,S$,

$$Y_{j,s}^{k}=Y_{j,s}^{k-1}+m_{j,s}^{k-1}\cdot\Delta+\sigma_{j,s}^{k-1}\cdot\Delta W_{s}^{k-1}+\tfrac{1}{2}\mathcal{L}^{0}(m_{j,s}^{k-1})\cdot\Delta^{2}$$
$$+\tfrac{1}{2}\mathcal{L}^{1}(\sigma_{j,s}^{k-1})[(\Delta W_{s}^{k-1})^{2}-\Delta]$$
$$+\mathcal{L}^{0}(\sigma_{j,s}^{k-1})[\Delta W_{s}^{k-1}\cdot\Delta-\Delta Z_{s}^{k-1}]+\mathcal{L}^{1}(m_{j,s}^{k-1})\cdot\Delta Z_{s}^{k-1},$$
$$j=1,2,\ldots,N, \tag{2.6}$$

where ΔW_s^{k-1} and ΔZ_s^{k-1} are a pair of correlated normally distributed random numbers generated as

$$\Delta W_{s}^{k-1}=n_{1,s}^{k-1}\sqrt{\Delta},\quad \Delta Z_{s}^{k-1}=\frac{1}{2}\Delta^{3/2}\left(n_{1,s}^{k-1}+\frac{n_{2,s}^{k-1}}{\sqrt{3}}\right), \tag{2.7}$$

where $n_{1,s}^{k-1}$ and $n_{2,s}^{k-1}$ are two independent standard normally distributed random numbers.

Having obtained S samples of the solutions of the stochastic differential equations, the pth moment can be determined as follows:

$$\mathsf{E}[\|\mathbf{X}(t_k)\|^p]=\frac{1}{S}\sum_{s=1}^{S}\|\mathbf{X}_s^k\|^p,\quad \|\mathbf{X}_s^k\|=\sqrt{(\mathbf{X}_s^k)^T\mathbf{X}_s^k}, \tag{2.8}$$

where $X_{j,s}^k=Y_{j,s}^k$, for $j=1,2,\ldots,n$.

From Eq. (1.3), it is clearly seen that the difficulty in the Monte Carlo simulation of the pth moment Lyapunov exponent lies in the two large quantities: a large number of samples are required to evaluate the moment $\mathsf{E}[\|\mathbf{X}\|^p]$ at any time instance t, and a large time period t is needed to determine the exponential rate of growth of the pth moment. Hence, in order to be able to perform the Monte Carlo simulation efficiently, it is important that a higher order weak scheme is employed to solve the stochastic differential equations (2.1) so that a larger time step Δ can be taken to reduce the number of iterations in time.

There are order 3.0 and order 4.0 weak Taylor schemes [19]; however, they are of mainly theoretical value because of the difficulties in implementation. The extrapolation method may be applied to obtain the order 4.0 weak extrapolation [19]:

$$\mathsf{E}[\|\mathbf{X}(t_k)\|^p]=\frac{1}{21}\{32\mathsf{E}[\|\mathbf{X}^{\Delta/4}(t_k)\|^p]-12\mathsf{E}[\|\mathbf{X}^{\Delta/2}(t_k)\|^p]$$
$$+\mathsf{E}[\|\mathbf{X}^{\Delta}(t_k)\|^p]\}, \tag{2.9}$$

where $\mathbf{X}^{\Delta/4}$, $\mathbf{X}^{\Delta/2}$, and $\mathbf{X}^{\Delta}$ stand for the state vectors obtained using Eq. (2.8), in which the stochastic differential equations (2.1) are solved using the order 2.0 weak scheme (2.2) with the time steps being $\Delta/4$, $\Delta/2$, and Δ, respectively.

However, it has been found in the numerical experiments that the order 4.0 weak extrapolation (2.9) does not offer any advantages in terms of numerical efficiency and accuracy than the order 2.0 weak Taylor scheme (2.2) or (2.6) with a smaller time step Δ when studying the dynamic stability of a stochastic system. The reason is that, when the system (2.1) is unstable, a larger time step Δ may lead to the value of Eq. (2.9) to be negative at some time instances, since the solutions of the stochastic system are growing exponentially. On the other hand, if a small enough time step Δ is used, Eq. (2.9) requires the evaluation of three sets of sample realizations, at time steps Δ, $\Delta/2$, and $\Delta/4$, respectively. It has been found that it is numerically more efficient and accurate to use Eq. (2.2) or (2.6) with a small time step Δ.

2.2 Determination of the pth Moment Lyapunov Exponents. Having obtained the pth moment $\mathsf{E}[\|\mathbf{X}\|^p]$ at any time instance t using Eq. (2.8), the moment Lyapunov exponent $\Lambda_{\mathbf{X}}(p)$ can be determined using Eq. (1.3). However, since the pth moment grows or decays exponentially in time, periodic normalization of the pth moment must be applied in order to avoid numerical overflow or underflow and to correctly determine the moment Lyapunov exponent.

Take the initial condition of $\mathbf{X}_s(0)$ such that $\|\mathbf{X}_s(0)\|=1$, $s=1,2,\ldots,S$. Note that $Y_{j,s}=X_{j,s}$, for $j=1,2,\ldots,n$. Normalization of the first d elements of the state vector $\mathbf{Y}_s$ is applied after every time period $(K\Delta)$.

At the time instance $m(K\Delta)$, $m=1,2,\ldots,M$, the following ratio is determined for all values of p of interest:

$$\rho_m(p)=\frac{\mathsf{E}[\|\mathbf{X}(m(K\Delta))\|^p]}{\mathsf{E}[\|\mathbf{X}((m-1)(K\Delta))\|^p]},\quad m=1,2,\ldots,M. \tag{2.10}$$

For $s=1,2,\ldots,S$, the state vector $\mathbf{Y}_s$ is then normalized in the sense that $\|\mathbf{X}_s\|=1$ using

$$Y_{j,s}(m(K\Delta))=\frac{Y_{j,s}(m(K\Delta))}{\|\mathbf{X}_s(m(K\Delta))\|},\quad j=1,2,\ldots,n. \tag{2.11}$$

After the normalization, numerical solution of the stochastic differential equations is continued.

From Eq. (2.10), it can be easily shown that

$$\rho_1(p)\cdot\rho_2(p)\cdots\rho_M(p)=\frac{\mathsf{E}[\|\mathbf{X}(M(K\Delta))\|^p]}{\mathsf{E}[\|\mathbf{X}(0)\|^p]}$$
$$=\mathsf{E}[\|\mathbf{X}(M(K\Delta))\|^p]. \tag{2.12}$$

Using Eqs. (1.3) and (2.12), the pth moment Lyapunov exponent is given by, for all values of p of interest,

$$\Lambda_{\mathbf{X}}(p)=\frac{1}{M(K\Delta)}\log\mathsf{E}[\|\mathbf{X}(M(K\Delta))\|^p]$$
$$=\frac{1}{M(K\Delta)}\log[\rho_1(p)\cdot\rho_2(p)\cdots\rho_M(p)]$$
$$=\frac{1}{M(K\Delta)}\sum_{m=1}^{M}\log\rho_m(p),\quad \text{for large } M. \tag{2.13}$$

The purpose of using the ratios $\rho_m(p)$ is to avoid numerical data overflow or underflow because the pth moment of the system grows exponentially if it is unstable or decays exponentially if it is stable.

2.3 Monte Carlo Simulation of the pth Moment Lyapunov Exponents. The results presented in Secs. 2.1 and 2.2 are summarized in the following procedure for the Monte Carlo simulation of the pth moment Lyapunov exponent.

I. Setting the Initial Conditions
For the sth sample, $s=1,2,\ldots,S$, set the initial conditions of the first n elements of the state vector $\mathbf{Y}_s$ as

$$Y_{j,s}(0)=\frac{1}{\sqrt{n}},\quad i=1,2,\ldots,n.$$

$Y_{j,s}(0)$, $j=n+1,n+2,\ldots,N$, can be set to any values; for simplicity of implementation, they may also be set to $1/\sqrt{n}$.

II. Conducting the Monte Carlo Simulation
For time iterations $m=1,2,\ldots,M$, conduct the Monte Carlo simulation. For each increment in m, the increase in time is $K\Delta$.

1. For $k=1,2,\ldots,K$, and sample $s=1,2,\ldots,S$, perform the numerical integration of the stochastic differential equations. For each increment in k, the increment in time is Δ.
1.1. Generate $3d$ standard normally distributed random numbers to evaluate $\Delta W_{l,s}^{k-1}$, $\Delta W_{l_1,s}^{k-1}$, $\Delta W_{l_2,s}^{k-1}$, for l, l_1, $l_2=1,2,\ldots,d$, using Eq. (2.3).
1.2. Generate $\frac{1}{2}d(d-1)$ uniformly distributed random numbers in (0,1) to evaluate $V_{l_1l_2,s}^{k-1}$, for $l_1=1,2,\ldots,d$, $l_2=l_1+1,l_1+2,\ldots,d$, using Eq. (2.5).
1.3. Evaluate $\mathbf{Y}_s([(m-1)K+k]\Delta)$ in time step Δ using the iterative equation (2.2).

For the special case when d=1, the following simplified steps are taken:

1.1. Generate two standard normally distributed random numbers to evaluate ΔW_s^{k-1} and ΔZ_s^{k-1} using Eq. (2.7).

1.2. Evaluate $\mathbf{Y}_s([(m-1)K+k]\Delta)$ in time step Δ using the iterative equation (2.6).

2. For all values of p of interest and sample $s=1,2,\ldots,S$, determine the pth norms $\|\mathbf{X}_s(m(K\Delta))\|^p$ using $\|\mathbf{X}_s\| = (\mathbf{X}_s^T\mathbf{X}_s)^{1/2}$, where $X_{j,s}=Y_{j,s}$, $j=1,2,\ldots,n$.
3. Determine the pth moments $\mathsf{E}[\|\mathbf{X}(m(K\Delta))\|^p]$ using Eq. (2.8) for all values of p of interest.
4. Evaluate the ratio $\rho_m(p)$ using Eq. (2.10) for all values of p of interest.
5. Normalize the state vector $\mathbf{Y}_s(m(K\Delta))$ using Eq. (2.11).

III. Determining the pth **Moment Lyapunov Exponent**

Determine the pth moment Lyapunov exponent $\Lambda_{\mathbf{X}}(p)$ using Eq. (2.13) for all values of p of interest.

3 Numerical Results

In this section, numerical results of Monte Carlo simulation of the pth moment Lyapunov exponents of a two-dimensional system under real-noise excitation and under bounded-noise excitation are presented.

3.1 Two-Dimensional System Under Real-Noise Excitation

Consider a two-dimensional system under real-noise excitation, which is modeled by an Ornstein–Uhlenbeck process, as

$$\begin{aligned} &\frac{\mathrm{d}^2q(\tau)}{\mathrm{d}\tau^2}+2\beta\frac{\mathrm{d}q(\tau)}{\mathrm{d}\tau}+[\omega_0^2-\varepsilon_0\xi(\tau)]q(\tau)=0,\\ &\mathrm{d}\xi(\tau)=-\alpha_0\xi(\tau)\mathrm{d}\tau+\sigma_0\mathrm{d}W(\tau). \end{aligned} \tag{3.1}$$

Equations (3.1) can be written as a three-dimensional autonomous Itô stochastic system as

$$\begin{cases} \mathrm{d}Y_1=Y_2\mathrm{d}\tau,\\ \mathrm{d}Y_2=[-2\beta Y_2-(1-\varepsilon_0Y_3)Y_1]\mathrm{d}\tau,\\ \mathrm{d}Y_3=-\alpha_0Y_3\mathrm{d}\tau+\sigma_0\mathrm{d}W, \end{cases} \tag{3.2}$$

where $Y_1=q(\tau)$, $Y_2=\mathrm{d}q(\tau)/\mathrm{d}\tau$, $Y_3=\xi(\tau)$, and Y_1 and Y_2 are used to calculated the pth norm of the state vector of the system $\|\mathbf{Y}\|^p=[(Y_1)^2+(Y_2)^2]^{p/2}$.

Using Eq. (2.6), the order 2.0 weak Taylor scheme is given by

$$\begin{aligned} Y_{1,s}^k&=Y_{1,s}^{k-1}+Y_{2,s}^{k-1}\cdot\Delta+\tfrac{1}{2}R_s^{k-1}\cdot\Delta^2,\\ Y_{2,s}^k&=Y_{2,s}^{k-1}+R_s^{k-1}\cdot\Delta+\varepsilon_0\sigma_0Y_{1,s}^{k-1}\cdot\Delta Z_s^{k-1}\\ &\quad+\tfrac{1}{2}[-\omega_0^2Y_{2,s}^{k-1}-2\beta R_s^{k-1}+\varepsilon_0Y_{3,s}^{k-1}(Y_{2,s}^{k-1}-\alpha Y_{1,s}^{k-1})]\cdot\Delta^2, \end{aligned} \tag{3.3}$$

$$\begin{aligned} Y_{3,s}^k&=Y_{3,s}^{k-1}-\alpha_0Y_{3,s}^{k-1}\cdot\Delta+\sigma_0\cdot\Delta W_s^{k-1}\\ &\quad+\tfrac{1}{2}\alpha_0^2Y_{3,s}^{k-1}\cdot\Delta^2-\alpha_0\sigma_0\cdot\Delta Z_s^{k-1}, \end{aligned}$$

where

$$R_s^{k-1}=-2\beta Y_{2,s}^{k-1}-(\omega_0^2-\varepsilon_0Y_{3,s}^{k-1})Y_{1,s}^{k-1}.$$

For small values of $\varepsilon_0>0$, a sixth-order approximation of the pth moment Lyapunov exponent was obtained in Ref. [15] using a method of regular perturbation.

System (3.1) may be simplified by removing the damping using the transformation $q(\tau)=x(\tau)\mathrm{e}^{-\beta\tau}$ and applying the time scaling $t=\omega\tau$, $\omega^2=\omega_0^2-\beta^2$, to yield

$$\frac{\mathrm{d}^2x(t)}{\mathrm{d}t^2}+[1-\varepsilon\zeta(t)]x(t)=0, \tag{3.4}$$

$$\mathrm{d}\zeta(t)=-\alpha\zeta(t)\mathrm{d}t+\sigma\mathrm{d}W(t),$$

where $\varepsilon=\varepsilon_0/\omega$, $\alpha=\alpha_0/\omega$, $\sigma=\sigma_0/\sqrt{\omega}$.

Because of the transformation $q(\tau)=x(\tau)\mathrm{e}^{-\beta\tau}$, one obtains

$$\frac{\mathrm{d}q(\tau)}{\mathrm{d}\tau}=\left[\frac{\mathrm{d}x(\tau)}{\mathrm{d}\tau}-\beta x(\tau)\right]\mathrm{e}^{-\beta\tau},$$

and

$$\begin{aligned} \|\mathbf{q}(\tau)\|&=\sqrt{q^2(\tau)+\left[\frac{\mathrm{d}q(\tau)}{\mathrm{d}\tau}\right]^2}=\sqrt{x^2(\tau)+\left[\frac{\mathrm{d}x(\tau)}{\mathrm{d}\tau}-\beta x(\tau)\right]^2}\,\mathrm{e}^{-\beta\tau}\\ &=\|\mathbf{x}(\tau)\|\mathrm{e}^{-\beta\tau}, \end{aligned}$$

since the norms defined as

$$\|\mathbf{x}(\tau)\|=\sqrt{x^2(\tau)+\left[\frac{\mathrm{d}x(\tau)}{\mathrm{d}\tau}\right]^2}$$

and

$$\|\mathbf{x}(\tau)\|=\sqrt{x^2(\tau)+\left[\frac{\mathrm{d}x(\tau)}{\mathrm{d}\tau}-\beta x(\tau)\right]^2}$$

are equivalent. This leads to

$$\|\mathbf{q}(\tau)\|^p=\|\mathbf{x}(\tau)\|^p\mathrm{e}^{-p\beta\tau},$$

and

$$\Lambda_{q(\tau)}(p)=-p\beta+\Lambda_{x(\tau)}(p).$$

On the other hand, since

$$\|\mathbf{x}(t)\|=\sqrt{x^2(t)+\left[\frac{\mathrm{d}x(t)}{\mathrm{d}t}\right]^2}=\sqrt{x^2(\tau)+\frac{1}{\omega^2}\left[\frac{\mathrm{d}x(\tau)}{\mathrm{d}\tau}\right]^2},$$

and the vector norms of $\mathbf{x}(\tau)$ defined as

$$\|\mathbf{x}(\tau)\|=\sqrt{x^2(\tau)+\left[\frac{\mathrm{d}x(\tau)}{\mathrm{d}\tau}\right]^2}$$

and

$$\|\mathbf{x}(\tau)\|=\sqrt{x^2(\tau)+\frac{1}{\omega^2}\left[\frac{\mathrm{d}x(\tau)}{\mathrm{d}\tau}\right]^2}$$

are equivalent for finite ω, hence $\|\mathbf{x}(t)\|$ and $\|\mathbf{x}(\tau)\|$ are equivalent. Furthermore, since

$$\mathsf{E}[\|\mathbf{x}(t)\|^p]\sim\mathrm{e}^{\Lambda_{x(t)}(p)\cdot t}=\mathrm{e}^{\omega\Lambda_{x(t)}(p)\cdot\tau},\quad\text{as}\quad t\to\infty,$$

and

$$\mathsf{E}[\|\mathbf{x}(\tau)\|^p]\sim\mathrm{e}^{\Lambda_{x(\tau)}(p)\cdot\tau},\quad\text{as}\quad\tau\to\infty,$$

which leads to

$$\Lambda_{x(\tau)}(p)=\omega\Lambda_{x(t)}(p).$$

Therefore, the moment Lyapunov exponents of systems (3.1) and (3.4) are related by

$$\Lambda_{q(\tau)}(p)=-p\beta+\omega\Lambda_{x(t)}(p). \tag{3.5}$$

The sixth-order approximation of the pth moment Lyapunov exponent obtained in Ref. [15] is given by

$$\Lambda_{x(t)}(p)=\varepsilon^2\Lambda_2+\varepsilon^4\Lambda_4+\varepsilon^6\Lambda_6+O(\varepsilon^8), \tag{3.6}$$

where

$$\Lambda_2=\frac{p(p+2)\sigma^2}{16(\alpha^2+4)},$$

$$\Lambda_4=\frac{p(p+2)\sigma^4(\alpha^4+22\alpha^2+48)}{32\alpha(\alpha^2+1)(\alpha^2+4)^3},$$

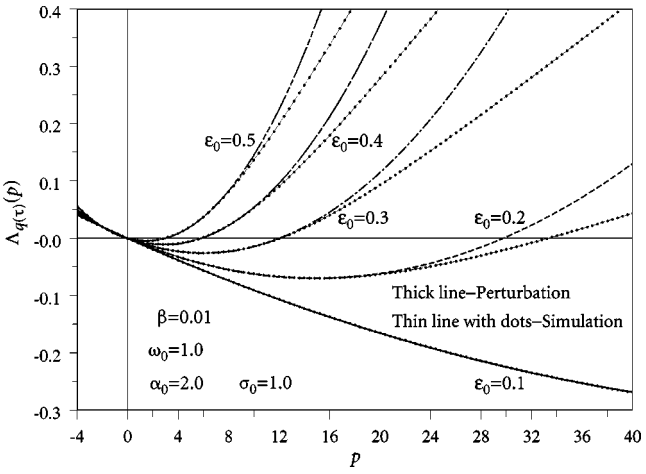

Fig. 1 Moment Lyapunov exponent $\Lambda_{q(\tau)}(p)$ under real-noise excitation, $\alpha_0=2.0$

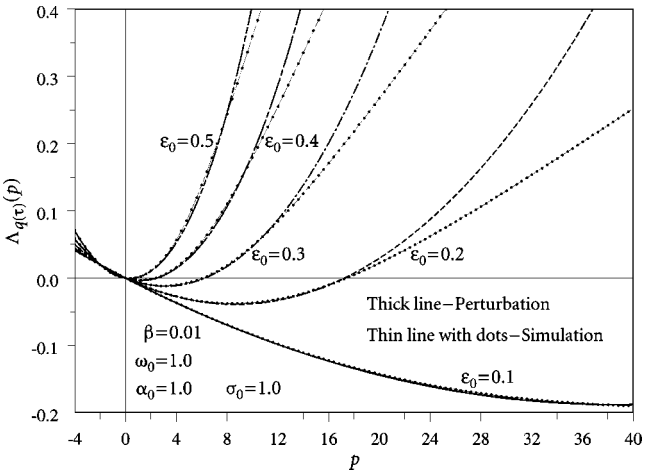

Fig. 3 Moment Lyapunov exponent $\Lambda_{q(\tau)}(p)$ under real-noise excitation, $\alpha_0=1.0$

$$\begin{aligned}\Lambda_6 = {} & p(p+2)\sigma^6[p^2(99\alpha^{14}+4274\alpha^{12}+70{,}379\alpha^{10}+499{,}596\alpha^8\\ & +15{,}47{,}568\alpha^6+2{,}119{,}232\alpha^4+1{,}267{,}200\alpha^2+262{,}144)\\ & +p(198\alpha^{14}+8548\alpha^{12}+140{,}758\alpha^{10}+999{,}192\alpha^8\\ & +3{,}095{,}136\alpha^6+4{,}238{,}464\alpha^4+2{,}534{,}400\alpha^2+524{,}288)\\ & +(-1080\alpha^{14}-42{,}960\alpha^{12}-650{,}680\alpha^{10}-3{,}903{,}840\alpha^8\\ & -2{,}981{,}760\alpha^6+27{,}553{,}280\alpha^4+60{,}641{,}280\alpha^2\\ & +31{,}457{,}280)]/[8192\alpha^2(\alpha^2+16)(9\alpha^2+4)(\alpha^2+1)^2(\alpha^2\\ & +4)^5].\end{aligned}$$

The pth moment Lyapunov exponents of system (3.1) obtained using Monte Carlo simulation and the results given by Eq. (3.6) are presented in Figs. 1 and 2 ($\alpha_0=2.0$), Figs. 3 and 4 ($\alpha_0=1.0$), and Fig. 5 ($\alpha_0=0.5$), $\beta=0.01$, $\omega_0=1.0$, $\sigma_0=1.0$, and various values of ε_0. It is seen that the approximate analytical results agree quite well with the numerical results for $\alpha_0=2.0$ and 1.0. Large discrepancy exist for $\alpha_0=0.5$.

3.2 Two-Dimensional System Under Bounded-Noise Excitation. Consider the following two-dimensional system under bounded-noise excitation:

$$\begin{aligned}&\frac{d^2q(\tau)}{d\tau^2}+2\beta\frac{dq(\tau)}{d\tau}+[\omega_0^2-\varepsilon_0\cos\xi(\tau)]q(\tau)=0,\\ &d\xi=\nu_0 d\tau+\sigma_0 dW(\tau).\end{aligned}\tag{3.7}$$

In the absence of noise, i.e., when $\sigma_0=0$, system (3.7) reduces to Mathieu's equation, a two-dimensional system under harmonic parametric excitation. It is well known that Mathieu's equation is in the primary parametric resonance when ν_0 is in the vicinity of $2\omega_0$ and in the secondary parametric resonance when ν_0 is close to ω_0.

Equations (3.7) can be converted to a three-dimensional autonomous stochastic system as

$$\begin{cases}dY_1=Y_2 d\tau,\\ dY_2=[-2\beta Y_2-(\omega_0^2-\varepsilon_0\cos Y_3)Y_1]d\tau,\\ dY_3=\nu_0 d\tau+\sigma_0 dW,\end{cases}\tag{3.8}$$

where $Y_1=q(\tau)$, $Y_2=dq(\tau)/d\tau$, and $Y_3=\xi(\tau)$. Y_1 and Y_2 are related to the state variables of the original system (3.7) and are used to calculated the pth norm $\|\mathbf{Y}\|^p=[(Y_1)^2+(Y_2)^2]^{p/2}$.

The order 2.0 weak Taylor scheme is given by, from Eq. (2.6),

$$Y_{1,s}^k=Y_{1,s}^{k-1}+Y_{2,s}^{k-1}\cdot\Delta+\frac{1}{2}R_s^{k-1}\cdot\Delta^2,$$

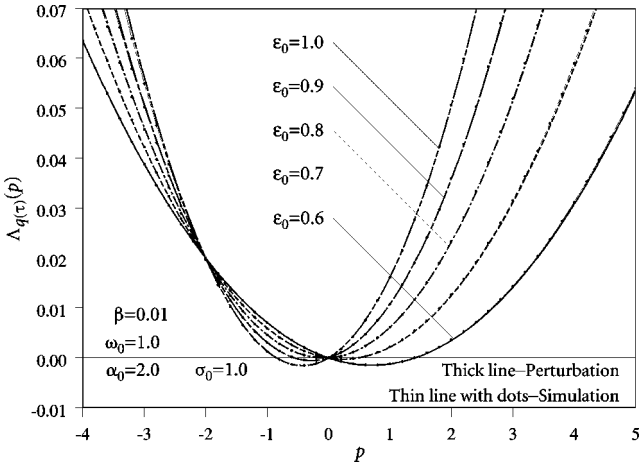

Fig. 2 Moment Lyapunov exponent $\Lambda_{q(\tau)}(p)$ under real-noise excitation, $\alpha_0=2.0$

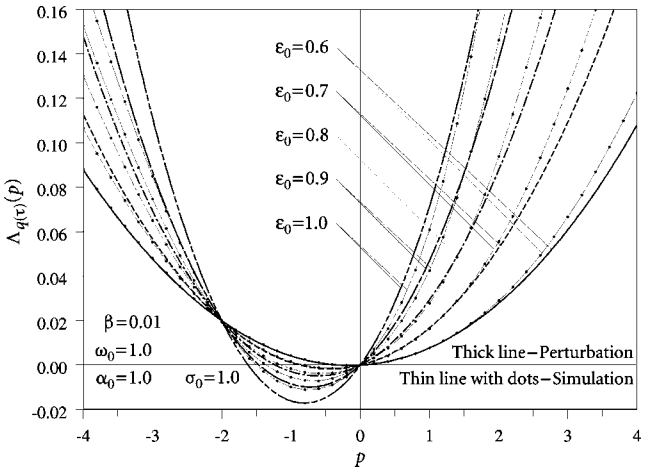

Fig. 4 Moment Lyapunov exponent $\Lambda_{q(\tau)}(p)$ under real-noise excitation, $\alpha_0=1.0$

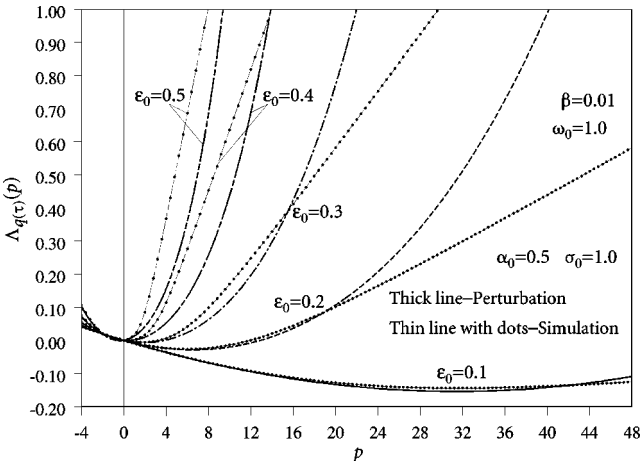

Fig. 5 Moment Lyapunov exponent $\Lambda_{q(\tau)}(p)$ under real-noise excitation, $\alpha_0=0.5$

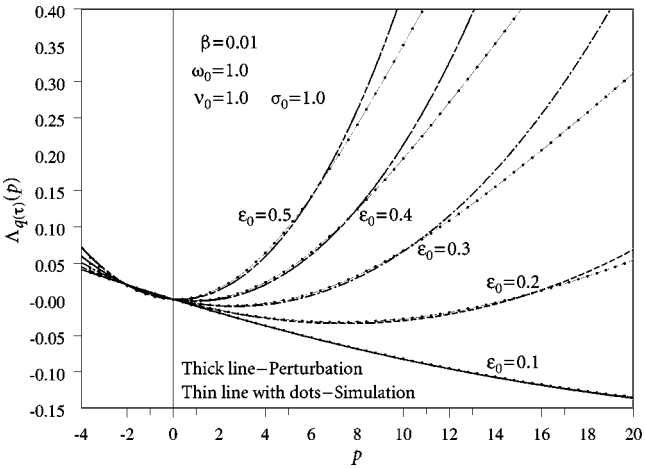

Fig. 7 Moment Lyapunov exponent $\Lambda_{q(\tau)}(p)$ under bounded-noise excitation, $\nu_0=1.0$

$$Y_{2,s}^k = Y_{2,s}^{k-1} + R_s^{k-1}\cdot\Delta - \tfrac{1}{2}[(\omega_0^2 - \varepsilon_0\cos Y_{3,s}^{k-1})Y_{2,s}^{k-1} + 2\beta R_s^{k-1} - \varepsilon_0(\nu_0\sin Y_{3,s}^{k-1} + \tfrac{1}{2}\sigma_0^2\cos Y_{3,s}^{k-1})Y_{1,s}^{k-1}]\cdot\Delta^2 - \varepsilon_0\sigma_0 Y_{1,s}^{k-1}\sin Y_{3,s}^{k-1}\cdot\Delta Z_s^{k-1}, \quad (3.9)$$

$$Y_{3,s}^k = Y_{3,s}^{k-1} + \nu_0\cdot\Delta + \sigma_0\cdot\Delta W_s^{k-1}.$$

where

$$R_s^{k-1} = -(\omega_0^2 - \varepsilon_0\cos Y_{3,s}^{k-1})Y_{1,s}^{k-1} - 2\beta Y_{2,s}^{k-1}.$$

Under weak-noise excitation, i.e., for $\varepsilon_0>0$, a fourth-order approximation of the pth moment Lyapunov exponent has been determined using a method of regular perturbation in Ref. [16]. System (3.7) can be simplified using the transformation $q(\tau)=x(\tau)e^{-\beta\tau}$ and time scaling $t=\omega\tau$, $\omega^2=\omega_0^2-\beta^2$, to yield

$$\frac{d^2x(t)}{dt^2} + [1-\varepsilon\cos\zeta(t)]x(t) = 0,$$

$$d\zeta(t) = \nu dt + \sigma dW(t), \quad (3.10)$$

where $\varepsilon=\varepsilon_0/\omega^2$, $\nu=\nu_0/\omega$, and $\sigma=\sigma_0/\sqrt{\omega}$. The moment Lyapunov exponent of system (3.7) is related to that of Eq. (3.10) by

$$\Lambda_{q(\tau)}(p) = -p\beta + \omega\Lambda_{x(t)}(p). \quad (3.11)$$

The fourth-order approximation of the pth moment Lyapunov exponent is

$$\Lambda_{x(t)}(p) = \varepsilon^2\Lambda_2 + \varepsilon^4\Lambda_4 + O(\varepsilon^6), \quad (3.12)$$

in which

$$\Lambda_2 = \frac{p(p+2)S(2)}{16},$$

where $S(2)$ is the power spectral density function $S(\omega)$ of the bounded-noise $\cos\zeta(t)$ at $\omega=2$ given by

$$S(2) = \frac{\sigma^2(4+\nu^2+\frac{1}{2}\sigma^4)}{2[(2+\nu)^2+\frac{1}{4}\sigma^4][(2-\nu)^2+\frac{1}{4}\sigma^4]}.$$

The expression for Λ_4 is quite lengthy and will not be repeated here.

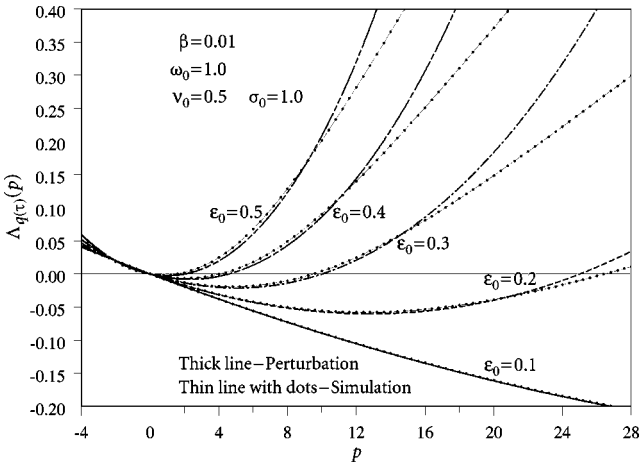

Fig. 6 Moment Lyapunov exponent $\Lambda_{q(\tau)}(p)$ under bounded-noise excitation, $\nu_0=0.5$

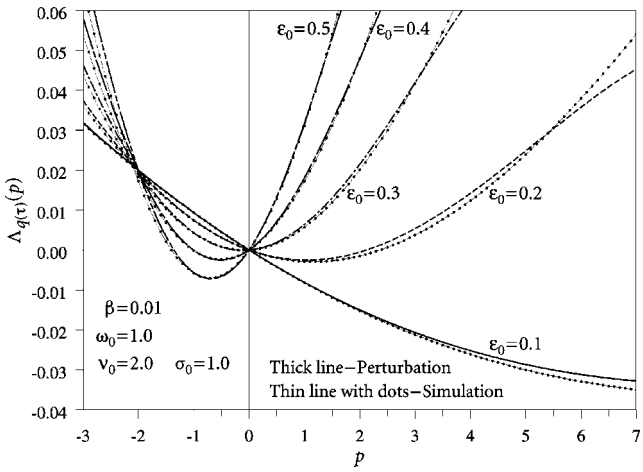

Fig. 8 Moment Lyapunov exponent $\Lambda_{q(\tau)}(p)$ under bounded-noise excitation, $\nu_0=2.0$

Numerical results of the pth moment Lyapunov exponents $\Lambda_{q(\tau)}(\tau)$ from Monte Carlo simulation, along with those given by equations (3.11) and (3.12), are plotted in Figures 6–8 for $\nu_0 = 0.5$, 1.0, and 2.0, respectively, $\beta = 0.01$, $\omega_0 = 1.0$, $\sigma_0 = 1.0$, and various values of ε_0. It is observed that the approximate analytical results agree well with the numerical results.

4 Discussion and Conclusions

In this paper, a Monte Carlo simulation procedure is developed to numerically determine the pth moment Lyapunov exponents. The procedure can be easily implemented. The approximate analytical results of the pth moment Lyapunov exponents obtained for two-dimensional systems under real-noise ([15]) or bounded-noise ([16]) excitation compare well with the numerical results for certain parameter ranges, as shown in Figures 1–8.

As mentioned earlier, the difficulties in conducting the Monte Carlo simulation of the pth moment Lyapunov exponent lie in the two large numbers: a large number of samples of the solutions of the stochastic differential equations needed for the evaluation of the pth moment $\mathsf{E}[\|\mathbf{X}\|^p]$ and a large time t required for the determination of the pth moment Lyapunov exponent $\Lambda_{\mathbf{X}}(p)$.

In this paper, S samples of solutions of the stochastic differential equations are taken to calculate the pth moment. From the Central Limit Theorem, it is well known that the estimated pth moment Lyapunov exponent is a random number, with the mean being the true value of the pth moment Lyapunov exponent and standard deviation equal to $s_p/\sqrt{S}$, where s_p is the sample standard deviation determined from the S samples. The standard deviation of the estimated pth moment Lyapunov exponent can be reduced by increasing the number of samples S.

The total time period is divided into M segments of length $(K\Delta)$, where Δ is the time step of integration. After each time segment $(K\Delta)$, the state vectors of the stochastic system are normalized. It is very important to select a suitable value of K in the simulation. If K is too small, the response of the system does not have enough time to develop and to exhibit its exponential growth or decay. If K is too large, the exponential growth or decay of the response of the system will render the vector norm of the state vector to overflow or underflow, yielding erroneous results. For different systems, it may be necessary to perform test runs to find a suitable value of K.

In the numerical examples studied in this paper, the parameters are chosen as $S = 2000$, $\Delta = 0.0005$, $K = 50{,}000$, and $M = 200$, resulting in the state vector normalization after each $t = 25$ and the total time of simulation is 5000.

Recently, Xie and So [18] presented an analytical-numerical approach for the determination of the pth moment Lyapunov exponent. For dynamic systems with certain types of stochastic excitations, such as the bounded-noise excitation, the second-order partial differential eigenvalue problem governing the pth moment Lyapunov exponent is transformed into a linear algebraic eigenvalue problem using series expansions of orthogonal functions, such as the double Fourier series expansion. The linear algebraic eigenvalue problems are then solved numerically using an algorithm for large sparse matrices, such as the ''eigs'' function in MATLAB. For two-dimensional systems with noise excitations that can be expressed in a simple analytical form, the approach has the advantages of being easy to implement, fast to execute, and having a high accuracy. Although the method can be extended to higher dimensional systems, the amount of analytical work involved and the dimension of the resulting linear algebraic eigenvalue problem increase dramatically.

The Monte Carlo simulation presented in this paper is a pure numerical method and is more general than the analytical-numerical approach [18]. The method can be easily applied for higher dimensional systems and any noise excitations, even for those with only time series available.

Acknowledgment

The research for this paper was supported, in part, by the Natural Sciences and Engineering Research Council of Canada.

References

[1] Oseledec, Y. I., 1968, ''A Multiplicative Ergodic Theorem. Lyapunov Characteristic Number for Dynamical Systems,'' Trans. Mosc. Math. Soc., **19**, pp. 197–231.
[2] Xie, W.-C., 1998, ''Buckling Mode Localization in Rib-Stiffened Plates with Randomly Misplaced Stiffeners,'' Comput. Struct., **67**, pp. 175–189.
[3] Wolf, A., Swift, J., Swinney, H., and Vastano, A., 1985, ''Determining Lyapunov Exponents from a Time Series,'' Physica D, **16**, pp. 285–317.
[4] Arnold, L., 1984, ''A Formula Connecting Sample and Moment Stability of Linear Stochastic Systems,'' SIAM (Soc. Ind. Appl. Math.) J. Appl. Math., **44**, pp. 793–802.
[5] Arnold, L., Oeljeklaus, E., and Pardoux, E., 1986, ''Almost Sure and Moment Stability for Linear Itô Equations,'' *Lyapunov Exponents* (Lecture Notes in Mathematics, 1186), L. Arnold and V. Wihstutz, eds., Springer-Verlag, Berlin, pp. 85–125.
[6] Arnold, L., Kliemann, W., and Oeljeklaus, E., 1986, ''Lyapunov Exponents of Linear Stochastic Systems,'' *Lyapunov Exponents* (Lecture Notes in Mathematics, 1186), L. Arnold and V. Wihstutz, eds., Springer-Verlag, Berlin, pp. 129–159.
[7] Baxendale, P. H., 1985, ''Moment Stability and Large Deviations for Linear Stochastic Differential Equations,'' *Proceedings of the Taniguchi Symposium on Probabilistic Methods in Mathematical Physics*, N. Ikeda, Kinokuniya, ed., Tokyo, Japan, 1985, pp. 31–54.
[8] Arnold, L., and Kliemann, W., 1987, ''Large Deviations of Linear Stochastic Differential Equations,'' *Stochastic Differential Systems* (Lecture Notes in Control and Information Sciences, 96), H. J. Englebert and W. Schmidt, eds., Springer-Verlag, Berlin, pp. 117–151.
[9] Baxendale, P., and Stroock, D., 1988, ''Large Deviations and Stochastic Flows of Diffeomorphisms,'' Probability Theory and Related Fields, **80**, pp. 169–215.
[10] Arnold, L., 1998, *Random Dynamical Systems*, Springer-Verlag, Berlin.
[11] Arnold, L., Doyle, M. M., and Sri Namachchivaya, N., 1997, ''Small Noise Expansion of Moment Lyapunov Exponents for Two-Dimensional Systems,'' Dyn. Stab. Syst., **12**, No. 3, pp. 187–211.
[12] Khasminskii, R. Z., and Moshchuk, N., 1998, ''Moment Lyapunov Exponent and Stability Index for Linear Conservative System with Small Random Perturbation,'' SIAM (Soc. Ind. Appl. Math.) J. Appl. Math., **58**, No. 1, pp. 245–256.
[13] Sri Namachchivaya, N., and Vedula, L., 2000, ''Stabilization of Linear Systems by Noise: Application to Flow Induced Oscillations,'' Dyn. Stab. Syst., **15**(2), pp. 185–208.
[14] Sri Namachchivaya, N., and Van Roessel, H. J., 2001, ''Moment Lyapunov Exponent and Stochastic Stability of Two Coupled Oscillators Driven by Real Noise,'' ASME J. Appl. Mech., **68**, No. 6, pp. 903–914.
[15] Xie, W.-C., 2001, ''Moment Lyapunov Exponents of a Two-Dimensional System under Real Noise Excitation,'' J. Sound Vib., **239**, No. 1, pp. 139–155.
[16] Xie, W.-C., 2003, ''Moment Lyapunov Exponents of a Two-Dimensional System under Bounded Noise Parametric Excitation,'' J. Sound Vib., **263**, No. 3, pp. 593–616.
[17] Xie, W.-C., 2001, ''Lyapunov Exponents and Moment Lyapunov Exponents of a Two-Dimensional Near-Nilpotent System,'' ASME J. Appl. Mech., **68**, No. 3, pp. 453–461.
[18] Xie, W.-C., and So, R. M. C., 2003, ''Numerical Determination of Moment Lyapunov Exponents of Two-Dimensional Systems,'' ASME J. Appl. Mech., accepted for publication.
[19] Kloeden, P. E., and Platen, E., 1992, *Numerical Solution of Stochastic Differential Equations*, Springer-Verlag, Berlin.

Joachim L. Grenestedt
Department of Mechanical Engineering and Mechanics,
Lehigh University,
19 Memorial Drive West,
Bethlehem, PA 18015
e-mail jog5@lehigh.edu

Mikael Danielsson
Albany International AB,
Box 510,
SE 301 80 Halmstad, Sweden
e-mail: mikael.danielsson@albint.com

Elastic-Plastic Wrinkling of Sandwich Panels With Layered Cores

Elastic-plastic wrinkling of compression loaded sandwich panels made with layered cores was studied analytically and experimentally. A core with a stiff layer near the sandwich skins can improve various properties, including wrinkling and impact strengths, with only a minor weight penalty. The 2D plane stress and plane strain bifurcation problems were solved analytically, save for a determinantal equation which was solved numerically. Experiments were performed on aluminum skin/foam core sandwich panels with different combinations of stiff and soft core materials. Good correlation between experiments and theory was obtained. [DOI: 10.1115/1.1828063]

Introduction

Polymeric foams are frequently used as core materials in load bearing sandwich structures. Many of the requirements of a sandwich core can be better fulfilled using a core material with mechanical properties varying through the thickness. For example, high stiffness and strength of a core layer next to the skins promote wrinkling and impact strength, and high chemical resistance of this core layer reduces chemical degradation of the core when the skins are attached or fabricated. Even better than having a layered core is to grade the core. Danielsson and Grenestedt [1] manufactured and tested various graded combinations of Divinycell PVC based foams, and showed that a number of benefits could be obtained.

In the present paper, wrinkling strength of a sandwich panel made with a layered foam core and aluminum skins was studied. A layered core prevents standard wrinkling formulas, such as those of Gough et al. [2] and Hoff and Mautner [3], to be used. Grenestedt and Olsson [4] solved the present problem when all materials remain linearly elastic. Their solution was in many respects similar to that of Shield et al. [5], but with a different application. At present, 2D plane stress and plane strain bifurcation analyses were performed, assuming that the face skins fulfill either J_2 flow or deformation theory, and a Ramberg-Osgood nonlinear uniaxial relation. Specimens as depicted in Fig. 1 were carefully prepared and experimentally tested to failure under uniaxial compression.

Bifurcation Analysis

The following bifurcation theory was presented by Hill [6,7] and the formalism presently used was given by Hutchinson [8]; for details and further applications these papers are recommended. An outline of the theory is provided below. The elastic wrinkling analysis of Grenestedt and Olsson [4] is here extended to include elastic-plastic material behavior.

The summation convention will be used with Latin indices ranging from 1 to 3 and Greek from 1 to 2. A finite strain Lagrangian formulation with convected coordinates is used. Covariant and contravariant components of tensors are denoted by subscripts and superscripts, respectively. The Lagrangian strain tensor is

$$\eta_{ij}=\tfrac{1}{2}(u_{i,j}+u_{j,i})+\tfrac{1}{2}u^k{}_{,i}u_{k,j} \tag{1}$$

where u_i are components of the displacement vector referred to the undeformed base vectors, and comma denotes covariant differentiation with respect to the metric in the undeformed body. With V and S denoting volume and surface, respectively, in the undeformed body, and τ^{ij} components of the symmetric Kirchhoff stress referred to base vectors in the undeformed body, the principle of virtual work is

$$\int_V \tau^{ij}\delta\eta_{ij}\,\mathrm{d}V=\int_S T^i\delta u_i\,\mathrm{d}S \tag{2}$$

where T^i are components of surface traction referred to undeformed base vectors, δ represents differentiation, and body forces have been omitted. The incremental form of the principle is

$$\int_V\{\dot{\tau}^{ij}\delta\eta_{ij}+\tau^{ij}\dot{u}^k{}_{,i}\delta u_{k,j}\}\mathrm{d}V=\int_S\dot{T}^i\delta u_i\,\mathrm{d}S \tag{3}$$

with rates of change denoted by a dot. The constitutive behavior is assumed to be of the form

$$\dot{\tau}^{ij}=L^{ijkl}\dot{\eta}_{kl}=(L_e^{ijkl}-\alpha g^{-1}m^{ij}m^{kl})\,\dot{\eta}_{kl} \tag{4}$$

where $\alpha=1$ for $m^{kl}\dot{\eta}_{kl}\geqslant 0$ and the stress is on the yield surface, and $\alpha=0$ otherwise; g is related to strain hardening and depends on the deformation history, m^{ij} are components of the unit tensor normal to the elastic domain in strain-rate space, and L_e^{ijkl} is the elastic stiffness tensor.

Dead loads are applied to the body. Assume that at some stage of the deformation, characterized by u_i^0, τ_0^{ij}, bifurcation is possible such that at least two solutions $\dot{u}_i^a$ and $\dot{u}_i^b$ exist. Let quantities with an overhead tilde denote differences between the two solutions; for example, $\tilde{u}_i=\dot{u}_i^b-\dot{u}_i^a$. Since tractions are the same for both solutions on the part of the surface of the body where tractions are prescribed, and the same holds for displacements, the following integral must vanish

$$\int_S\tilde{T}^i\tilde{u}_i\,\mathrm{d}S=\int_V\{\tilde{\tau}^{ij}\tilde{\eta}_{ij}+\tau_0^{ij}\tilde{u}^k{}_{,i}\tilde{u}_{k,j}\}\mathrm{d}V\equiv H \tag{5}$$

where H is defined by the last equality. Hill's sufficiency condition for uniqueness is obtained by introducing the moduli L_c of an

Contributed by the Applied Mechanics Division of THE AMERICAN SOCIETY OF MECHANICAL ENGINEERS for publication in the ASME JOURNAL OF APPLIED MECHANICS. Manuscript received by the Applied Mechanics Division, February 23, 2004; final revision, August 11, 2004. Associate Editor: Z. Suo. Discussion on the paper should be addressed to the Editor, Prof. Robert M. McMeeking, JOURNAL OF APPLIED MECHANICS, Department of Mechanical and Environmental Engineering, University of California—Santa Barbara, Santa Barbara, CA 93106-5070, and will be accepted until four months after final publication in the paper itself in the ASME JOURNAL OF APPLIED MECHANICS.

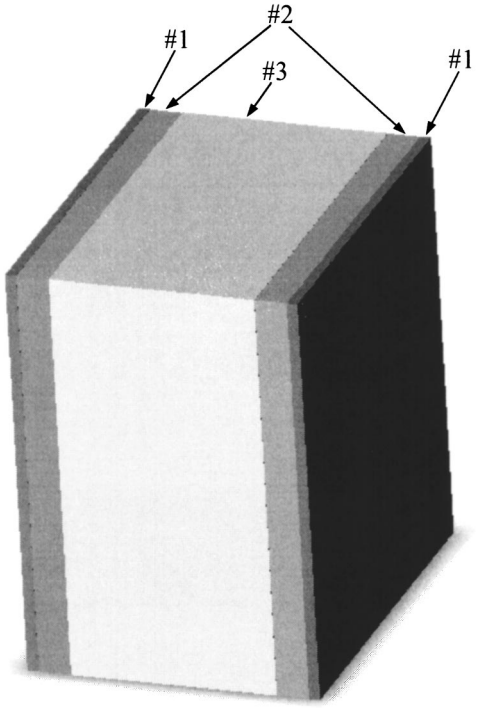

Fig. 1 Specimen under consideration, consisting of two aluminum skins (material #1, dark gray), attached to two layers of high density foam (material #2, light gray), sandwiching a low density foam (material #3, white)

elastic comparison solid such that L_c equals the moduli L obtained when $m^{kl}\dot{\eta}_{kl}>0$, independent of the actual deformation increment. Hill introduced the functional

$$F(\tilde{u})=\int_V \{L_c^{ijkl}\tilde{\eta}_{ij}\tilde{\eta}_{kl}+\tau_0^{ij}\tilde{u}^k{}_{,i}\tilde{u}_{k,j}\}\mathrm{d}V \geqslant H>0 \tag{6}$$

where the first inequality is valid for positive g and arbitrary loading, and the last inequality is the sufficiency condition for uniqueness. Assume that the first bifurcation occurs with the eigenmode $\overset{(1)}{u}_i$ such that $F(\overset{(1)}{u}_i)=0$. Minimizing the functional F leads to the eigenvalue equations

$$\overset{(1)}{\eta}_{ij}=\tfrac{1}{2}(\overset{(1)}{u}_{i,j}+\overset{(1)}{u}_{j,i})+\tfrac{1}{2}(u^0_k{}_{,j}\overset{(1)}{u}{}^k{}_{,i}+u^0_k{}_{,i}\overset{(1)}{u}{}^k{}_{,j}) \tag{7}$$

$$\overset{(1)}{\tau}{}^{ij}=L_c^{ijkl}\overset{(1)}{\eta}_{kl} \tag{8}$$

$$(\overset{(1)}{\tau}{}^{ij}+\overset{(1)}{\tau}{}^{kj}u^{0i}{}_{,k}+\tau_0^{kj}\overset{(1)}{u}{}^i{}_{,k})_{,j}=0 \tag{9}$$

$$\overset{(1)}{T}{}^i=(\overset{(1)}{\tau}{}^{ij}+\overset{(1)}{\tau}{}^{kj}u^{0i}{}_{,k}+\tau_0^{kj}\overset{(1)}{u}{}^i{}_{,k})n_j=0 \quad \text{on} \quad S_T \tag{10}$$

$$\overset{(1)}{u}_i=0 \quad \text{on} \quad S_u \tag{11}$$

For the presently considered problem, wrinkling of a flat sandwich, strains are negligible compared to 1 prior to bifurcation when, as presently assumed, moduli of skin materials are much higher than moduli of core materials, and rotations are nonpresent. Prior to bifurcation, components of Kirchhoff stress τ^{ij} then coincide with components of Cauchy stress σ^{ij}, etc. A Cartesian coordinate system will from now on be used and the distinction between covariant and contravariant components of tensors dropped. Subsequently, subscripts will be used for all tensor components. The equations above can then be simplified to

$$\overset{(1)}{\eta}_{ij}=\tfrac{1}{2}(\overset{(1)}{u}_{i,j}+\overset{(1)}{u}_{j,i}) \tag{12}$$

$$\overset{(1)}{\sigma}_{ij}=L^c_{ijkl}\overset{(1)}{\eta}_{kl} \tag{13}$$

$$\overset{(1)}{\sigma}_{ij,j}+\sigma_{kj}\overset{(1)}{u}_{i,kj}=0 \tag{14}$$

$$\overset{(1)}{T}_i=(\overset{(1)}{\sigma}_{ij}+\sigma_{kj}\overset{(1)}{u}_{i,k})n_j=0 \quad \text{on} \quad S_T \tag{15}$$

$$\overset{(1)}{u}_i=0 \quad \text{on} \quad S_u \tag{16}$$

in Cartesian coordinates[1] (the un-deformed body now equals the deformed body immediately prior to bifurcation).

Two different material models are employed, J_2 flow theory and J_2 deformation theory. For J_2 flow theory, the instantaneous moduli in Cartesian coordinates are

$$L_{ijkl}=\frac{E}{1+\nu}\left(\frac{1}{2}(\delta_{ik}\delta_{jl}+\delta_{il}\delta_{jk})+\frac{\nu}{1-2\nu}\delta_{ij}\delta_{kl}-\frac{\alpha r_1 s_{ij}s_{kl}}{1+\nu+2r_1J_2}\right) \tag{17}$$

where the stress deviator is $s_{ij}=\sigma_{ij}-\sigma_{kk}\delta_{ij}/3$ and $J_2=s_{ij}s_{ij}/2$, E is Young's modulus, and ν is Poisson's ratio; for $J_2=(J_2)_{\max}$, $\alpha=1$ if $\dot{J}_2\geqslant 0$ and $\alpha=0$ if $\dot{J}_2<0$, whereas $\alpha=0$ if $J_2<(J_2)_{\max}$. The function $r_1(J_2)$ is determined from a tensile stress-strain curve as $r_1=3[E/E_t-1]/(4J_2)$ where E_t is the tangent modulus. For J_2 deformation theory, the instantaneous moduli in Cartesian coordinates are

$$L_{ijkl}=\frac{E}{1+\nu+r_2}\left(\frac{1}{2}(\delta_{ik}\delta_{jl}+\delta_{il}\delta_{jk})+\frac{3\nu+r_2}{3(1-2\nu)}\delta_{ij}\delta_{kl}-\frac{r_2's_{ij}s_{kl}}{1+\nu+r_2+2r_2'J_2}\right) \tag{18}$$

where $r_2(J_2)=3[E/E_s-1]/2$ where E_s is the secant modulus in a tensile stress-strain curve, and $r_2'=\mathrm{d}r_2/\mathrm{d}J_2$.

In the following the material is assumed to have a Ramberg-Osgood-type uniaxial relation with

$$\frac{E\varepsilon}{\sigma_{0.7}}=\frac{\sigma}{\sigma_{0.7}}+\alpha^{RO}\left(\frac{\sigma}{\sigma_{0.7}}\right)^m \tag{19}$$

where $\sigma_{0.7}$ is the stress where the stress-strain curve intercepts a line with the slope 70% of Young's modulus, and $\alpha^{RO}=\frac{3}{7}$. This relation is plotted in Fig. 2 for 7075-T6 aluminum. The tangent and secant moduli are, respectively,

$$E_t=\frac{E}{1+\alpha^{RO}m(\sigma/\sigma_{0.7})^{m-1}} \qquad E_s=\frac{E}{1+\alpha^{RO}(\sigma/\sigma_{0.7})^{m-1}} \tag{20}$$

The functions $r_1(J_2)$ and $r_2(J_2)$ then become

$$r_1(J_2)=\frac{9\alpha^{RO}m}{4\sigma_{0.7}^{m-1}}(3J_2)^{(m-3)/2} \tag{21}$$

$$r_2(J_2)=\frac{3\alpha^{RO}}{2\sigma_{0.7}^{m-1}}(3J_2)^{(m-1)/2} \tag{22}$$

[1]Since a Cartesian coordinate system now is employed, L^c_{ijkl} is used in Eq. (13) and subsequently rather than L_c^{ijkl} as used in Eqs. (4), (6) and (8).

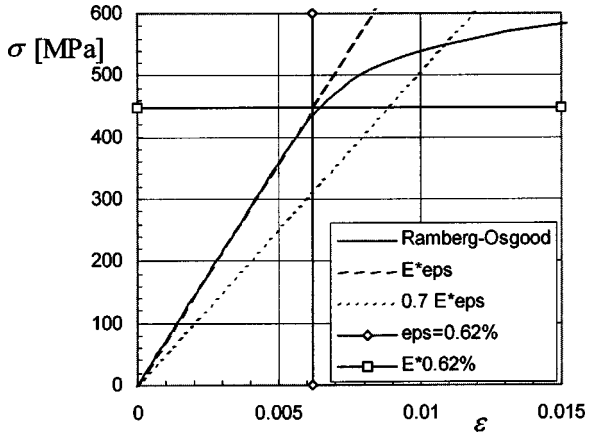

Fig. 2 Stress-strain relation of the aluminum skins according to the Ramberg-Osgood relation and the parameters in Table 1. The "yield" strain $\varepsilon=0.62\%$ is also plotted.

Pre-Bifurcation Stress State

In the plane strain case, when $\varepsilon_{13}=\varepsilon_{23}=\varepsilon_{33}=0$, the stress state prior to bifurcation is obtained by integrating the equations

$$\dot{\sigma}_{11}=\left(L_{1111}-\frac{(L_{1122})^2}{L_{2222}}\right)\dot{\varepsilon}_{11}$$
$$\dot{\sigma}_{33}=\left(L_{1133}-\frac{L_{1122}L_{2233}}{L_{2222}}\right)\dot{\varepsilon}_{11} \tag{23}$$

whereas in the plane stress case the σ_{11} stress equals σ in Eq. (19). Other stresses are zero. Presently, integration was used also in the plane stress case, integrating

$$\dot{\sigma}_{11}=\left(L_{1111}-\frac{L_{1122}(L_{1122}+L_{1133})}{L_{2222}+L_{2233}}\right)\dot{\varepsilon}_{11} \tag{24}$$

in order to obtain an estimate of integration accuracy for the plane strain case. The integration scheme presently used (Euler's explicit forward method) was accurate to five or six digits. Higher accuracy could easily be obtained using a smaller time step but it was presently not considered necessary.

Solution of the Differential Equations in Plane Strain

The partial differential equations and boundary conditions from which the bifurcation load is determined are given by Eqs. (12)–(16). A solution is presently sought in a region according to Fig. 3, consisting of three materials: a skin (#1), a finite thickness layer of core material (#2), and a semi-infinite core with a different stiffness (#3). The analytical model is not limited to a semi-infinite core sandwich per se, but is applicable to any layered structure with arbitrarily many layers of arbitrary thicknesses. However,

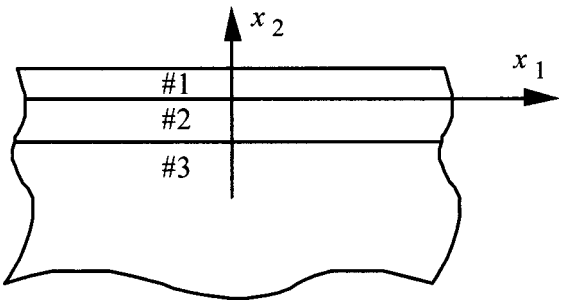

Fig. 3 Geometry of the analytically analyzed structure

with the present sandwich structure in mind, it is preferred to reduce the number of parameters by letting the core thickness increase without bounds. With this assumption some bifurcation modes, such as global (Euler-like) buckling and shear buckling, also disappear while wrinkling remains. Plane strain deformation is assumed during bifurcation, i.e., $\overset{(1)}{u}_3=0$ and $\overset{(1)}{u}_{i,3}=0$. Prior to bifurcation, the stress and deformation state will be considered to be either plane strain or plane stress. In the latter case the possible incompatibility of deformation between core and skin due to different transverse deformations is tacitly ignored (however, deformation rate compatibility is enforced during bifurcation). Before bifurcation in the former case, $\sigma_{11}\neq 0$, $\sigma_{33}\neq 0$ in general, and other $\sigma_{ij}=0$, whereas in the latter case also $\sigma_{33}=0$. The stresses will differ between the different materials but the strain η_{11} is the same. These assumptions lead to the equations

$$L^c_{\alpha\beta\gamma\delta}\overset{(1)}{u}_{\gamma,\delta\beta}+\sigma_{11}\overset{(1)}{u}_{\alpha,11}=0 \tag{25}$$

and the boundary conditions

$$\overset{(1)}{T}_i=(\sigma_{ij}+\sigma_{11}\overset{(1)}{u}_{i,1}\delta_{j1})n_j=0 \quad \text{on} \quad S_T \tag{26}$$

$$\overset{(1)}{u}_i=0 \quad \text{on} \quad S_u \tag{27}$$

and continuity of deformations and tractions between different materials. Note that $L^c_{\alpha\beta\gamma\delta}$ depends on the stress state prior to bifurcation and thus differs between the plane strain and plane stress situations. In the present setting $L^c_{\alpha\beta\gamma 3}=0$, $L^c_{\alpha 333}=0$ prior to bifurcation.

An ansatz of the form

$$\overset{(1)}{u}_1=f_1(x_2)\sin\omega x_1$$
$$\overset{(1)}{u}_2=f_2(x_2)\cos\omega x_1 \tag{28}$$

leads to two coupled ordinary differential equations for f_1 and f_2. It is assumed that the extension of the structure in the x_1-direction is such that it will always be an integer times the wave length $2\pi/\omega$. For a structure which is long compared to the wave length in the x_1-direction, this is always fulfilled with reasonable accuracy. The functions f_1 and f_2 are of the form

$$f_i=e^{\lambda x_2} \tag{29}$$

leading to the fourth degree characteristic equation

$$c_0\lambda^4+c_1\omega^2\lambda^2+c_2\omega^4=0 \tag{30}$$

where

$$c_0=-L^c_{1212}L^c_{2222}$$
$$c_1=\sigma_{11}(L^c_{1212}+L^c_{2222})+L^c_{1111}L^c_{2222}-(L^c_{1122})^2-2L^c_{1122}L^c_{1212} \tag{31}$$
$$c_2=-(\sigma_{11}+L^c_{1111})(\sigma_{11}+L^c_{1212})$$

If λ is a root to the characteristic equation, then so is $-\lambda$, and the solution is

$$f_1=A_1e^{\lambda_1x_2}+A_2e^{-\lambda_1x_2}+A_3e^{\lambda_2x_2}+A_4e^{-\lambda_2x_2}$$
$$f_2=B_1e^{\lambda_1x_2}+B_2e^{-\lambda_1x_2}+B_3e^{\lambda_2x_2}+B_4e^{-\lambda_2x_2} \tag{32}$$

for real and unique λ,

$$f_1=A_1e^{\lambda_1x_2}+A_2e^{-\lambda_1x_2}+\bar{A}_1e^{\bar{\lambda}_1x_2}+\bar{A}_2e^{-\bar{\lambda}_1x_2}$$
$$f_2=B_1e^{\lambda_1x_2}+B_2e^{-\lambda_1x_2}+\bar{B}_1e^{\bar{\lambda}_1x_2}+\bar{B}_2e^{-\bar{\lambda}_1x_2} \tag{33}$$

for complex λ, etc. Above, an overhead bar indicates a complex conjugate, A_i are constants to be determined from the boundary conditions, and B_i are related to A_i through Eq. (25). Necessary but not sufficient conditions for real λ are

$$\sigma_{11} \geq \max\left[-L^c_{1111}, -L^c_{1212}, \frac{2L^c_{1122}L^c_{1212} + (L^c_{1122})^2 - L^c_{1111}L^c_{2222}}{L^c_{1212} + L^c_{2222}} \right] \tag{34}$$

Collecting the boundary conditions leads to ten homogeneous linear equations for the A_i in the different materials ($A_2 = A_4 = 0$ in material #3 is required for finite stresses at $x_2 = -\infty$), thus a determinantal equation is obtained. The wave number ω and the strain η_{11} are parameters in this equation. The smallest η_{11} for which the determinant is zero for some ω is the wrinkling strain, η_{cr}. This was solved numerically by incrementally integrating Eq. (23) or (24) by Euler's explicit forward method, and in each increment scanning a large range of ω to find a root of the determinant. As soon as a root was found, it was bracketed in the $\omega - \eta_{11}$ space, and the solution (ω and η_{11}) was determined with at least five-digit precision using a simple bisection algorithm.

Experimental Tests and Comparison With Analytical Predictions

Symmetric sandwich specimens as depicted in Fig. 1 were manufactured and experimentally tested under uniaxial compression loads. The skins were made of $h_1 = 1.57$ mm thick 7075-T6 aluminum. This was material #1 in Fig. 1. Two different densities of Divinycell H-grade [9] expanded PVC based structural foams were used: Divinycell H100 (material #2 in Fig. 1), which is a medium density foam, and Divinycell H30 (material #3), which is the lowest density foam in the Divinycell H-grade family. The nominal densities of the foams were 100 and 36 kg/m^3, respectively. The specimens were manufactured by bonding the core layers and skins using a two component polyurethane adhesive. The skins were attached by spreading the adhesive onto the skins rather than onto the foam cores in order to not fill the cells in the foam core and thereby creating an overly stiff bond line. The joint between the H30 and H100 foam core layers was made by spreading the adhesive on the H100 foam, which has smaller cells then the H30 foam. Four different specimen configurations were made:

1. a 100 mm thick H30 core sandwiched between two $h_1 = 1.57$ mm thick aluminum skins. No H100 foam was used in this specimen, and thus $h_2 = 0$,
2. an 88 mm thick H30 core between two $h_2 = 6$ mm thick layers of H100 core, sandwiched between two $h_1 = 1.57$ mm thick aluminum skins,
3. a 76 mm thick H30 core between two $h_2 = 12$ mm thick layers of H100 core, sandwiched between two $h_1 = 1.57$ mm thick aluminum skins,
4. a 100 mm thick H100 core, sandwiched between two $h_1 = 1.57$ mm thick aluminum skins. No H30 was used in this specimen.

The total thickness of the core was $d = 100$ mm in all configurations. These specimens were believed to be sufficiently thick to be treated as infinitely thick regarding skin wrinkling. The width of the specimens was $w = 140$ mm, and the total height was 150 mm. The specimens had to be very thick also in order to not shear buckle. The shear buckling load of a specimen with a homogeneous core (a single core material) is approximately

$$F^{\text{shear}}_{cr} \approx G_c d w \tag{35}$$

where G_c is the shear modulus of the core. If the skins were linear elastic, with Young's modulus E^{skin}, then the strain in the skins at shear buckling would be

$$\varepsilon^{\text{shear}}_{cr} \approx \frac{F^{\text{shear}}_{cr}}{2h_1 w E^{\text{skin}}} \approx \frac{G_c d}{2E^{\text{skin}} h_1} \tag{36}$$

Table 1 Material data for core and skin materials. $\alpha^{RO} = \frac{3}{7}$ for the aluminum.

Material	Young's modulus E (MPa)	Poisson's ratio ν	Ramberg-Osgood stress $\sigma_{0.7}$ (MPa)	Hardening m
7075-T6 aluminum	72 000	0.3	550	13
H30 foam	32.5	0.25	⋯	⋯
H100 foam	99	0.2375	⋯	⋯

assuming that the two skins carry all load. For the H30 and H100 cores, this strain is 0.58% and 1.8%, respectively, using the properties in Table 1. These are higher than the wrinkling strains of these specimen, which are on the order of 0.4% and 0.7%, respectively; see Fig. 4. Shear buckling should thus not occur before skin wrinkling.

Wrinkling strength is known to be sensitive to geometric imperfections as well as imperfections in load introduction and therefore a major effort was made in preparing the specimens and the test procedure. Effects of initial imperfection on wrinkling in sandwich structures have been reviewed by Ley et al. [10], which is recommended for further details. A very stiff test machine was used. Each specimen was molded directly into steel shoes in the test machine in order to obtain uniform load introduction. Strains were recorded using strain gages, and loads using a calibrated load cell. Four specimens of each configuration were tested. The test specimens remained flat until they suddenly failed catastrophically. No prebuckling out-of-plane deformation was noticed. The specimens that wrinkled in the linear elastic range of the skins, i.e., configurations 1, 2, 3, failed dramatically with loud bangs and foam core fragments flying. There were large cracks in these specimens after the tests. The specimens of configuration 4 failed with a soft "thug" and no visible cracks. However, the skins developed large permanent plastic wrinkles. The results of the tests are summarized in Fig. 4, where the normalized wrinkling stress in the skin, $\sigma^{\text{skin}}_{11}/E^{\text{skin}}$, is plotted versus h_2/h_1.

In Fig. 4, the 2D analytical predictions using the theory outlined in previous sections are also plotted. The material data used for the calculations are given in Table 1. The Divinycell cores are linear elastic to strains above 1%, and thus remained elastic up through the wrinkling initiation. The aluminum was modeled with a Ramberg-Osgood constitutive relation, as depicted in Fig. 2. The yield strain of the aluminum skins is approximately 0.62%. The

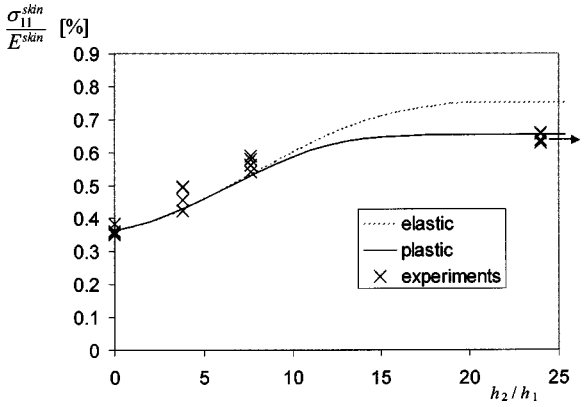

Fig. 4 Comparison between experimental and theoretical wrinkling stress for a sandwich with a layered core. Elastic analysis (dotted line), elastic-plastic analysis (solid line), and experiments (X). The experimental configuration with $h_2/h_1 = \infty$ is plotted near the right end of the graph and marked with an arrow.

results plotted in Fig. 4 were obtained assuming plane stress ($\sigma_{33}=0$) in all materials prior to wrinkling, and plane strain ($\varepsilon_{33}=0$) in all materials during wrinkling.

Both plane stress and plane strain analyses, using both flow and deformation theory, were performed. The results consistently showed that the wrinkling stresses obtained by flow theory predictions were slightly higher than those obtained by deformation theory. A discussion of this phenomenon as seen in other applications is given by Hutchinson [8]. However, for the present case, the difference between the flow and deformation theory predictions was very slight, and not even noticeable in a plot such as Fig. 4.

The analytical analyses assumed that the total core thickness was semi-infinite as in Fig. 3, whereas in the tests it was always 100 mm, and that the length of the specimens was such that the wavelength that minimizes the wrinkling strain η_{11} could be obtained. The analytical model could have been used for the finite length and finite core thickness sandwich by incorporating equations like (32) and (33) for each layer and limiting η_{11} to values compatible with the boundary conditions in the length direction. However, instead finite element (FE) bifurcation analyses were performed and the predictions compared with the analytical results. Only linear elastic material properties were used for the FE analyses. Two-dimensional (2D) FE models were made using the geometries of the experimental specimens. Three different specimen lengths were used: 150, 200 and 250 mm. Analyses were performed using either plane stress during both pre-bifurcation and bifurcation, or using plane strain during both pre-bifurcation and bifurcation. The difference in wrinkling stress between the three lengths was less than 2%. The difference in wrinkling stress between the plane stress and the plane strain cases varied between 2% and 5%, with the plane strain case always being stronger. The analytical results fell between the plane strain and the plane stress FE results for $h_2=0$ and for $h_2/h_1\to\infty$. For $h_2/h_1=6/1.57=3.82$ and $h_2/h_1=12/1.57=7.64$, the wrinkling stresses predicted by both the plane stress and the plane strain FE analyses were higher than the analytically predicted wrinkling stresses. There are a few reasons the results from the FE and the analytical analyses differ slightly: the difference in geometry (finite versus infinite thickness and length), different plane stress/strain assumptions, discretization errors in FE, etc. The difference in wrinkling stress between the analytical elastic analysis and any elastic FE analysis was less than 4%. The elastic FE analyses naturally overestimated the wrinkling stress when the skins approached the end of the linear elastic limit. This certainly occurred for the specimens with only high density (H100) core. However, also the skins in the specimens with the thick high density core layer ($h_2=12$ mm) reached stresses approaching the linear elastic limit. This can be seen in Fig. 4, where the results from the elastic analysis slightly deviate from those of the elastic-plastic analysis already at $h_2/h_1=12/1.57=7.64$.

Discussion and Conclusions

The bifurcation loads of compression loaded sandwich panels were calculated and compared to results from carefully prepared and executed experimental tests. The scatter in the experimental tests was less than what is usually encountered in compression loaded imperfection sensitive structures. We attribute this to the careful preparation of the specimens and the fact that the specimens were bonded to loading shoes inside the test machine prior to testing. The correlation between analytical elastic-plastic predictions and experimentally measured wrinkling stresses was exceptionally good for the two specimen configurations with only one foam core (either H30 or H100). For the two specimen configurations with layered foam cores, the experimental wrinkling stresses were higher than those analytically predicted ($h_2/h_1=3.82$ and $h_2/h_1=7.64$ in Fig. 4). The conjecture is that this was a result of added stiffness of the bond line between the low and high density foam cores. The bond line added a thin intermediate

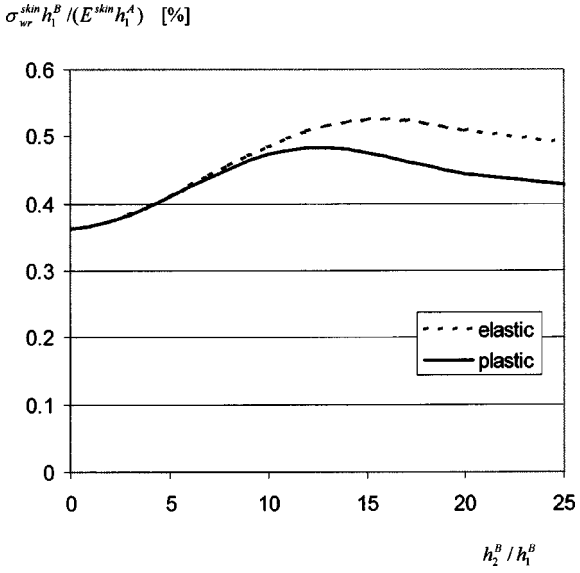

Fig. 5 Normalized load carrying capability $\sigma_{wr}^{skin}h_1^B/(E^{skin}h_1^A)$ of a sandwich with given mass and thickness, as a function of normalized thickness h_2^B/h_1^B of a layer of high density core

layer of relatively high stiffness. Any additional stiffness increases bifurcation load, a fact which is easily shown using a Rayleigh quotient. It may be mentioned that layered and graded foam cores have been produced by co-expansion, resulting in foam cores with uniform transitions between different grades and densities and no bond lines (Danielsson and Grenestedt [1]).

The advantage of a layered core over a conventional core in terms of load carrying capability before wrinkling may be demonstrated with a simple example using the data in Fig. 4. Two sandwich panels with the same total thickness and the same mass will be compared. Each sandwich has two aluminum skins and a foam core. One sandwich (configuration A) has a thicker aluminum skin (thickness h_1^A) and only H30 core, whereas the other (configuration B) has a slightly thinner aluminum skin (thickness h_1^B), an intermediate layer of H100 core (thickness h_2^B) and an H30 core in the middle. In order for the two sandwiches to have the same mass and total thickness, the skin thicknesses have to be related by

$$\frac{h_1^B}{h_1^A}=\frac{1}{1+\left(\dfrac{\rho_{\mathrm{H100}}-\rho_{\mathrm{H30}}}{\rho_{\mathrm{al}}-\rho_{\mathrm{H30}}}\right)\dfrac{h_2^B}{h_1^B}} \tag{37}$$

if the weight of a possible bond line is neglected. The load carrying capability of a sandwich is approximately equal to the wrinkling stress of the skins times the thickness of the skins. Using this approximation and the data presented in Fig. 4, the normalized load carrying capability $\sigma_{wr}^{\mathrm{skin}}h_1^B/(E^{\mathrm{skin}}h_1^A)$ is plotted versus h_2^B/h_1^B in Fig. 5 for a sandwich with constant thickness and mass. Configuration A is obtained for $h_2^B/h_1^B=0$. As can be seen in this figure, the load carrying capability of configuration B is approximately 33% higher than for configuration A, when $h_2^B/h_1^B\approx 12$ and the plastic data is used. The aluminum skins of this sandwich are 22% thinner than those of configuration A. In conclusion, without changing the total thickness or the mass of the sandwich, the load carrying capability could in this particular example be increased by more than 30% by changing from a homogeneous to a layered sandwich core.

Acknowledgments

This material is based upon work supported in part by the National Science Foundation under Grant No. 0092406 (JLG), in part by Wallenberg Stiftelsen (Incentive) (MD), and in part by the Department of Mechanical Engineering and Mechanics, Lehigh University. Dr. John W. Hutchinson and the late Dr. Bernard Budiansky are gratefully acknowledged for helpful comments. Chris Kilbourn at DIAB is gratefully acknowledged for providing the core materials.

References

[1] Danielsson, M., and Grenestedt, J. L., 1998, ''Gradient Foam Core Materials for Sandwich Structures, Preparation and Characterisation,'' Composites, Part A, **29**(8), pp. 981–988.

[2] Gough, G. S., Elam, C. F., and de Bruyne, N. A., 1940, ''The Stabilization of a Thin Sheet by a Continuous Supporting Medium,'' J. R. Aeronaut. Soc., **44**, pp. 12–43.

[3] Hoff, N. J., and Mautner, S. E., 1945, ''The Buckling of Sandwich-Type Panels,'' J. Aeronaut. Sci., **12**, pp. 285–297, eq. (103).

[4] Grenestedt, J. L., and Olsson, K.-A., 1995, ''Wrinkling of Sandwich with Layered Core or Non-Symmetric Skins,'' Proc. Third International Conference on Sandwich Construction, Southampton, UK, 12–15 September.

[5] Shield, T. W., Kim, K. S., and Shield, R. T., 1994, ''The Buckling of an Elastic Layer Bonded to an Elastic Substrate in Plane Strain,'' ASME J. Appl. Mech., **61**, pp. 231–235. *Corrections*: ASME J. Appl. Mech., **61**, pp. 796, and further, 1994, $b=\omega[1-P(1-2\nu)/(2\mu(1-\nu))]^{1/2}$ in Eq. (4).

[6] Hill, R., 1957, ''On Uniqueness and Stability in the Theory of Finite Elastic Strains,'' J. Mech. Phys. Solids, **5**, pp. 229–241.

[7] Hill, R., 1967, ''Eigenmodal Deformations in Elastic/Plastic Continua,'' J. Mech. Phys. Solids, **15**, pp. 371–386.

[8] Hutchinson, J. W., 1974, ''Plastic Buckling,'' in *Advances in Applied Mechanics*, C.-S. Yih, ed., **14**, pp. 67–144.

[9] DIAB. Divinycell H-Grade Technical Manual, 10.00. DIAB AB, Box 201, S-312 22 Laholm, Sweden (also available at www.diabgroup.com/DIAB/filecabinet.nsf/LookupFiles/H_Man_M/$file/H_Man_M.pdf)

[10] Ley, R. P., Lin, W., and Mbanefo, U., 1999, ''Facesheet Wrinkling in Sandwich Structures,'' NASA/CR-1999-208994.

Green's Functions for Holes/Cracks in Laminates With Stretching-Bending Coupling

Chyanbin Hwu
Institute of Aeronautics and Astronautics,
National Cheng Kung University,
Tainan, Taiwan, ROC
e-mail: chwu@mail.ncku.edu.tw

Consider an infinite composite laminate containing a traction-free elliptical hole subjected to concentrated forces and moments at an arbitrary point outside the hole. This problem for two-dimensional deformation has been solved analytically in the literature, while for the general unsymmetric composite laminates stretching and bending coupling may occur and due to the mathematical complexity the associated Green's functions have never been found for complete loading cases. Recently, by employing Stroh-like formalism for coupled stretching-bending analysis, the Green's functions for the infinite laminates (without holes) were obtained in closed-form. Based upon the nonhole Green's functions, through the use of analytical continuation method the Green's functions for holes are now obtained in explicit closed-form for complete loading cases and are valid for the full fields. The Green's functions for cracks are then obtained by letting the minor axis of ellipse be zero. By proper differentiation, the stress resultants and moments along the hole boundary and the stress intensity factors of cracks are also solved explicitly. Like the Green's functions for the infinite laminates, only the solutions associated with the in-plane concentrated forces $\hat{f}_1$, $\hat{f}_2$ and out-of-plane concentrated moments $\hat{m}_1$, $\hat{m}_2$ have exactly the same form as those of the corresponding two-dimensional problems. For the cases under the concentrated force $\hat{f}_3$ and torsion $\hat{m}_3$, new types of solutions are obtained.
[DOI: 10.1115/1.1839589]

1 Introduction

The problems of holes and cracks are important not only in macromechanics but also in micromechanics. From the viewpoint of macromechanics, holes are usually parts of the structure design. Due to the stress concentration induced by the existence of holes and pre-existing flaws, the cracks may initiate, propagate, and fracture. From a micromechanical viewpoint of composite materials, microcracks and voids always exist in the materials due to imperfect composite fabrication. Thus, understanding holes and cracks is of importance due to the increased utilization of composites in recent aerospace and commercial applications. Because of its importance, many analytical, numerical, and experimental studies have been published in journals and books. Among them, the study of Green's function attracts many researchers' attention because analytically it may provide solutions for arbitrary loading through superposition, and numerically it can be employed as the fundamental solutions for the boundary element method and as the kernel functions of integral equations to consider interactions between holes and cracks.

Although many Green's functions have been presented in the literature, due to mathematical infeasibility most of them are restricted to two-dimensional problems. For two-dimensional isotropic elasticity, most of the analytical solutions concerning holes and cracks can be found in the books of Muskhelishvili [1] and Savin [2]. In the case of monoclinic materials subjected to in-plane forces or out-of-plane pure bending moments, solutions can be found in the books of Lekhnitskii [3,4]. For general anisotropic materials considering the coupling of in-plane and anti-plane deformations, solutions can be found in the book of Ting [5]. In addition to the above books, which present most of the analytical solutions, there are also many papers dealing with these kinds of two-dimensional problems. However, because of anisotropy and asymmetry of lay-up, pure two-dimensional or pure bending formulation is not enough to describe the mechanical behavior of general asymmetric composite laminates. Due to mathematical complexity relatively few Green's functions have been found in closed-form for the coupled stretching-bending analysis.

To deal with the laminates with stretching-bending coupling, some complex variable formulations have been proposed in the literature such as Refs. [6–11]. By these formulations, some problems related to holes and cracks have been solved such as [12–17]. However, most of the solutions are for the case of uniform loadings. Although Chen and Shen [15] have provided Green's functions for hole problems, the loading cases they considered are not complete enough to cover all the possible loading conditions, especially the transverse forces and bending moments that play important roles in the laminate plate theory. Moreover, their solutions left a system of linear algebraic equations to be solved by numerical algorithm. This is inconvenient when we employ the Green's function as a fundamental solution of the boundary element formulation to solve more practical engineering problems.

From our recent studies [16,18], we see that without considering the transverse loading and in-plane torsion, many solutions keep the same mathematical forms as their corresponding two-dimensional problems. Thus, by simple analogy, many stretching-bending coupling problems can be solved directly from their corresponding two-dimensional problems. However, the key loading that distinguishes the in-plane problem (or axially loaded bars) from the plate bending problem (or transversely loaded beams) is the transverse loading. Therefore, inclusion of the complete loading cases such as transverse loading, in-plane loading, out-of-plane bending moment and in-plane torsion into the study of Green's function for hole problems is an important task for the present paper.

Recently, by our newly established Stroh-like formalism [11], we obtain the Green's function of the infinite composite laminates

Contributed by the Applied Mechanics Division of THE AMERICAN SOCIETY OF MECHANICAL ENGINEERS for publication in the ASME JOURNAL OF APPLIED MECHANICS. Manuscript received by the Applied Mechanics Division, March 9, 2004; final revision, August 27, 2004. Editor: R. M. McMeeking. Discussion on the paper should be addressed to the Editor, Prof. Robert M. McMeeking, Journal of Applied Mechanics, Department of Mechanical and Environmental Engineering, University of California—Santa Barbara, Santa Barbara, CA 93106-5070, and will be accepted until four months after final publication in the paper itself in the ASME JOURNAL OF APPLIED MECHANICS.

(or called nonhole problems) [18] for the complete loading cases. As in the two-dimensional problems, by the method of analytical continuation it seems that use of Green's functions for nonhole problems may help us to obtain Green's functions for hole problems. As in the Green's function for the nonhole problem [18], there are three different loading cases that should be of concern for the present problem, and two of them have different outlooks from that of two-dimensional problems. Careful derivation, such as the selection of the unperturbed functions for the method of analytical continuation, becomes important for the present study. All the works that are different from the two-dimensional mathematical routine derivations will be discussed in detail in this paper.

2 Stroh-Like Formalism for Coupled Stretching-Bending Analysis

Based upon the Kirchhoff's assumptions for thin plate, the kinematic relations, constitutive laws, and equilibrium equations for the coupled stretching-bending analysis of composite laminates can be written in tensor notation as [11]

$$\varepsilon_{ij}=\frac{1}{2}(u_{i,j}+u_{j,i}),\quad \kappa_{ij}=\frac{1}{2}(\beta_{i,j}+\beta_{j,i}),$$

$$N_{ij}=A_{ijkl}\varepsilon_{kl}+B_{ijkl}\kappa_{kl},\quad M_{ij}=B_{ijkl}\varepsilon_{kl}+D_{ijkl}\kappa_{kl}, \tag{2.1a}$$

$$N_{ij,j}=0,\quad M_{ij,ij}+q=0,\quad Q_i=M_{ij,j},\quad i,j,k,l=1,2,$$

where

$$\beta_1=-w_{,1},\quad \beta_2=-w_{,2}. \tag{2.1b}$$

In the above, the subscript comma stands for differentiation: u_1, u_2, and w are the middle surface displacements in the x_1, x_2, and x_3 directions, respectively; β_i, $i=1,2$ are the negative of the slope of the middle surface; ε_{ij} and κ_{ij} denote the midplane strain and plate curvature; N_{ij}, M_{ij}, and Q_i denote the stress resultants, bending moments, and shear forces, respectively; A_{ijkl}, B_{ijkl}, and D_{ijkl} are, respectively, the extensional, coupling, and bending stiffness tensors; q is the lateral distributed load applied on the laminates. Repeated indices imply summation.

A general solution satisfying all the basic equations stated in Eqs. (2.1) has been obtained [11] and purposely arranged in the form of a Stroh formalism [5,19] of two-dimensional anisotropic elasticity, and hence is called a *Stroh-like formalism*. With this formalism, the solution fields of displacements and stresses are expressed as [11]

$$\mathbf{u}_d=2\,\mathrm{Re}\{\mathbf{A}\mathbf{f}(z)\},\quad \boldsymbol{\phi}_d=2\,\mathrm{Re}\{\mathbf{B}\mathbf{f}(z)\}, \tag{2.2a}$$

where

$$\mathbf{u}_d=\begin{Bmatrix}\mathbf{u}\\ \boldsymbol{\beta}\end{Bmatrix},\quad \boldsymbol{\phi}_d=\begin{Bmatrix}\boldsymbol{\phi}\\ \boldsymbol{\psi}\end{Bmatrix},\quad \mathbf{u}=\begin{Bmatrix}u_1\\ u_2\end{Bmatrix},\quad \boldsymbol{\beta}=\begin{Bmatrix}\beta_1\\ \beta_2\end{Bmatrix},$$

$$\boldsymbol{\phi}=\begin{Bmatrix}\phi_1\\ \phi_2\end{Bmatrix},\quad \boldsymbol{\psi}=\begin{Bmatrix}\psi_1\\ \psi_2\end{Bmatrix}, \tag{2.2b}$$

and

$$\mathbf{f}(z)=\begin{Bmatrix}f_1(z_1)\\ f_2(z_2)\\ f_3(z_3)\\ f_4(z_4)\end{Bmatrix},\quad z_\alpha=x_1+\mu_\alpha x_2,\quad \alpha=1,2,3,4, \tag{2.2c}$$

$$\mathbf{A}=[\mathbf{a}_1\ \mathbf{a}_2\ \mathbf{a}_3\ \mathbf{a}_4],\quad \mathbf{B}=[\mathbf{b}_1\ \mathbf{b}_2\ \mathbf{b}_3\ \mathbf{b}_4]. \tag{2.2d}$$

Re stands for the real part of a complex number. In Eq. $(2.2b)_2$, ϕ_1, ϕ_2 and ψ_1, ψ_2 are the stress functions related to the stress resultants N_{ij}, shear forces Q_i, effective shear forces V_i, and bending moments M_{ij} by

$$N_{i1}=-\phi_{i,2},\quad N_{i2}=\phi_{i,1},$$

$$M_{i1}=-\psi_{i,2}-\lambda_{i1}\eta,\quad M_{i2}=\psi_{i,1}-\lambda_{i2}\eta,\quad i=1,2, \tag{2.3a}$$

$$Q_1=-\eta_{,2},\quad Q_2=\eta_{,1},\quad V_1=-\psi_{2,22},\quad V_2=\psi_{1,11},$$

where

$$\eta=\frac{1}{2}\psi_{k,k}=\frac{1}{2}(\psi_{1,1}+\psi_{2,2}), \tag{2.3b}$$

and λ_{ij} is the permutation tensor defined as

$$\lambda_{11}=\lambda_{22}=0,\quad \lambda_{12}=-\lambda_{21}=1. \tag{2.3c}$$

$f_\alpha(z_\alpha)$, $\alpha=1, 2, 3, 4$, are four holomorphic functions of complex variables z_α, which will be determined by the boundary conditions set for each particular problem. μ_α and $(\mathbf{a}_\alpha,\mathbf{b}_\alpha)$ are, respectively, the material eigenvalues and eigenvectors, which can be determined by the following eigenrelation:

$$\mathbf{N}\boldsymbol{\xi}=\mu\boldsymbol{\xi}, \tag{2.4a}$$

where $\mathbf{N}$ is a 8×8 real matrix and $\boldsymbol{\xi}$ is a 8×1 column vector defined by

$$\mathbf{N}=\begin{bmatrix}\mathbf{N}_1 & \mathbf{N}_2\\ \mathbf{N}_3 & \mathbf{N}_1^T\end{bmatrix},\quad \boldsymbol{\xi}=\begin{Bmatrix}\mathbf{a}\\ \mathbf{b}\end{Bmatrix}. \tag{2.4b}$$

The superscript T denotes the transpose of a matrix. The submatrices $\mathbf{N}_1$, $\mathbf{N}_2$ and $\mathbf{N}_3$ are the fundamental matrices of elasticity related to the extensional, coupling, and bending stiffness tensors, respectively. The detailed definitions of $\mathbf{N}_i$ for the coupled stretching-bending problems have been given in Refs. [11], [18] which are little different from those of two-dimensional problems [5]. Moreover, the explicit expressions of $\mathbf{N}_1$, $\mathbf{N}_2$ and $\mathbf{N}_3$ as well as their associated eigenvectors $\mathbf{a}$ and $\mathbf{b}$ have been found in Refs. [11], [20].

By using the relations given in Eq. (2.3), the stress resultants N_n, N_s, N_{ns}, bending moments M_n, M_s, M_{ns}, shear forces Q_n, Q_s, and effective shear forces V_n, V_s in the tangent–normal $(s-n)$ coordinate system, can be obtained directly from the stress functions as [16]

$$N_n=\mathbf{n}^T\boldsymbol{\phi}_{,s},\quad N_{ns}=\mathbf{s}^T\boldsymbol{\phi}_{,s}=-\mathbf{n}^T\boldsymbol{\phi}_{,n},\quad N_s=-\mathbf{s}^T\boldsymbol{\phi}_{,n},$$

$$M_n=\mathbf{n}^T\boldsymbol{\psi}_{,s},\quad M_{ns}=\mathbf{s}^T\boldsymbol{\psi}_{,s}-\eta=-\mathbf{n}^T\boldsymbol{\psi}_{,n}+\eta,\quad M_s=-\mathbf{s}^T\boldsymbol{\psi}_{,n}, \tag{2.5a}$$

$$Q_n=\eta_{,s},\quad Q_s=-\eta_{,n},\quad V_n=(\mathbf{s}^T\boldsymbol{\psi}_{,s})_{,s},\quad V_s=-(\mathbf{n}^T\boldsymbol{\psi}_{,n})_{,n},$$

where

$$\eta=\frac{1}{2}(\mathbf{s}^T\boldsymbol{\psi}_{,s}+\mathbf{n}^T\boldsymbol{\psi}_{,n}),$$

$$\mathbf{s}^T=(\cos\theta,\sin\theta),\quad \mathbf{n}^T=(-\sin\theta,\cos\theta). \tag{2.5b}$$

and θ is the angle directed clockwise from the positive x_1-axis to the tangential direction $\mathbf{s}$ (Fig. 1).

By using the relations (2.3), from A to B of the boundary surface the resultant forces $\tilde{t}_i$ and moments $\tilde{m}_i$ about the coordinate origin can also be expressed in terms of the stress functions as [18]

$$\tilde{t}_1=\int_A^B -N_{11}dx_2+N_{12}dx_1=\phi_1]_A^B,$$

$$\tilde{t}_2=\int_A^B -N_{12}dx_2+N_{22}dx_1=\phi_2]_A^B, \tag{2.6a}$$

$$\tilde{t}_3=\int_A^B -Q_1dx_2+Q_2dx_1=\eta]_A^B,$$

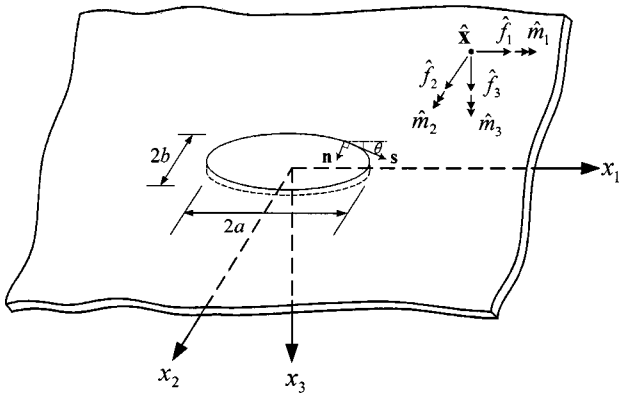

Fig. 1 An elliptic hole in laminates subjected to concentrated forces and moments

$$\tilde{m}_1=\int_A^B M_{12}dx_2-M_{22}dx_1-x_2(Q_1dx_2-Q_2dx_1)$$
$$=-(\psi_2-x_2\eta)]_A^B,$$

$$\tilde{m}_2=\int_A^B -M_{11}dx_2+M_{12}dx_1+x_1(Q_1dx_2-Q_2dx_1)$$
$$=(\psi_1-x_1\eta)]_A^B, \tag{2.6b}$$

$$\tilde{m}_3=\int_A^B x_1(-N_{12}dx_2+N_{22}dx_1)+x_2(N_{11}dx_2-N_{12}dx_1)$$
$$=(x_1\phi_2-x_2\phi_1-\Phi)]_A^B,$$

where Φ is the Airy stress function related to ϕ_i by

$$\phi_1=-\Phi_{,2}, \quad \phi_2=\Phi_{,1}. \tag{2.6c}$$

3 Green's Functions for Composite Laminates (Without Holes)

In the following sections, we will employ the method of analytical continuation to find Green's functions for hole problems. In that method, we need to know the unperturbed solutions for nonhole problems. With this concern, in this section we first consider an infinite laminate subjected to a concentrated force $\hat{\mathbf{f}}=(\hat{f}_1,\hat{f}_2,\hat{f}_3)$ and moment $\hat{\mathbf{m}}=(\hat{m}_1,\hat{m}_2,\hat{m}_3)$ at point $\hat{\mathbf{x}}=(\hat{x}_1,\hat{x}_2)$. The elasticity solution of this problem can be used as a fundamental solution of boundary element method and is generally called *Green's function*. From Eq. (2.6), we see that the relations between the resultant forces/moments and the stress functions are different for different loading directions. Therefore, for the convenience of discussion, the Green's functions are usually presented in three different loading conditions: (1) $\hat{f}_1$, $\hat{f}_2$, $\hat{m}_1$, $\hat{m}_2$; (2) $\hat{f}_3$; and (3) $\hat{m}_3$ [18,21]. From the relation (2.6) and the discussions provided in Ref. [18], the boundary conditions for each loading case can be written as

Case 1: $\hat{f}_1$, $\hat{f}_2$, $\hat{m}_1$, $\hat{m}_2$

$$\oint_C d\boldsymbol{\phi}_d=\hat{\mathbf{p}}, \quad \oint_C d\mathbf{u}_d=\mathbf{0}, \quad \hat{\mathbf{p}}=(\hat{f}_1\ \ \hat{f}_2\ \ \hat{m}_2\ -\hat{m}_1)^T. \tag{3.1a}$$

Case 2: $\hat{f}_3$

$$\oint_C d\eta=\hat{f}_3, \quad \oint_C d\psi_1=(x_1-\hat{x}_1)\hat{f}_3, \quad \oint_C d\psi_2=(x_2-\hat{x}_2)\hat{f}_3, \tag{3.1b}$$
$$\oint_C d\mathbf{u}_{d,1}=\mathbf{0}, \quad \oint_C d\mathbf{u}_{d,2}=\mathbf{0}, \quad \mathbf{i}_1^T\boldsymbol{\beta}_{,2}=\mathbf{i}_2^T\boldsymbol{\beta}_{,1}.$$

Case 3: $\hat{m}_3$

$$\oint_C d((x_1-\hat{x}_1)\phi_2-(x_2-\hat{x}_2)\phi_1-\Phi)=\hat{m}_3, \quad \oint_C dw=0,$$
$$\mathbf{n}^T\boldsymbol{\phi}_{,s}=\mathbf{n}^T\boldsymbol{\psi}_{,s}=(\mathbf{s}^T\boldsymbol{\psi}_{,s})_{,s}=0, \text{ along any arbitray surface boundary.} \tag{3.1c}$$

Through satisfaction of boundary conditions (3.1), the unknown complex function vector $\mathbf{f}(z)$ of Eq. (2.2) has been determined to be [18]

$$\text{case 1:} \quad \mathbf{f}(z)=\langle\log(z_\alpha-\hat{z}_\alpha)\rangle\mathbf{q}_1; \tag{3.2a}$$

$$\text{case 2:} \quad \mathbf{f}(z)=\langle(z_\alpha-\hat{z}_\alpha)[\log(z_\alpha-\hat{z}_\alpha)-1]\rangle\mathbf{q}_2; \tag{3.2b}$$

$$\text{case 3:} \quad \mathbf{f}(z)=\left\langle\frac{1}{z_\alpha-\hat{z}_\alpha}\right\rangle\mathbf{q}_3; \tag{3.2c}$$

where

$$\mathbf{q}_1=\frac{1}{2\pi i}\mathbf{A}^T\hat{\mathbf{p}}, \quad \mathbf{q}_2=\frac{\hat{f}_3}{2\pi i}\mathbf{A}^T\mathbf{i}_3, \quad \mathbf{q}_3=\frac{\hat{m}_3}{2\pi i}\mathbf{A}^T\mathbf{i}_2, \tag{3.2d}$$

and

$$\mathbf{i}_2=\begin{Bmatrix}0\\1\\0\\0\end{Bmatrix}, \quad \mathbf{i}_3=\begin{Bmatrix}0\\0\\1\\0\end{Bmatrix}. \tag{3.2e}$$

The angular bracket stands for the diagonal matrix whose components vary according to the subscript α, $\alpha=1, 2, 3, 4$; i.e., $\langle f_\alpha\rangle=\text{diag}[f_1,f_2,f_3,f_4]$.

4 Green's Functions for Hole Problems

Consider an infinite composite laminate containing an elliptical hole under a concentrated force and moment at point $\hat{\mathbf{x}}$ (Fig. 1). The contour of the hole boundary is represented by

$$x_1=a\cos\psi, \quad x_2=b\cos\psi, \tag{4.1}$$

where $2a$, $2b$ are the major and minor axes of the ellipse respectively, and ψ is a real parameter related to the tangent angle θ by

$$\rho\cos\theta=-a\sin\psi, \quad \rho\sin\theta=b\cos\psi, \tag{4.2a}$$

where

$$\rho^2=a^2\sin^2\psi+b^2\cos^2\psi. \tag{4.2b}$$

The force equilibrium and single-valued requirement of this problem are the same as those shown in Eq. (3.1) for each different loading case. If the hole is assumed to be traction free, the additional boundary conditions are

$$N_n=N_{ns}=M_n=V_n=0, \quad \text{along the hole boundary.} \tag{4.3}$$

Because in the Stroh-like formalism the solution fields are expressed in terms of the augmented displacement and stress function vectors ($\mathbf{u}_d$ and $\boldsymbol{\phi}_d$, respectively), in order to employ this formalism it is better to rewrite Eq. (4.3) in terms of the stress functions. With this understanding, by the relation (2.5*a*) the traction-free boundary conditions (4.3) can now be written in terms of the augmented stress function vector $\boldsymbol{\phi}_d$ as

$$\mathbf{n}^T\boldsymbol{\phi}_{,s}=\mathbf{s}^T\boldsymbol{\phi}_{,s}=\mathbf{n}^T\boldsymbol{\psi}_{,s}=(\mathbf{s}^T\boldsymbol{\psi}_{,s})_{,s}=0, \quad \text{along the hole boundary} \tag{4.4a}$$

or simply,

$$\boldsymbol{\phi}_d = \mathbf{0}, \quad \text{along the hole boundary.} \tag{4.4b}$$

Since the elliptical hole boundary in the z-plane will map to four different slanted elliptical hole boundaries in the z_α-plane, it is not convenient to solve problems with an elliptical boundary by using the argument z_α defined in Eq. (2.2c). Therefore, to treat the problems with an elliptical boundary, most of the solutions shown in the literature are expressed in terms of the transformed complex variable ζ_α, which can transform all four different slanted elliptical hole boundaries into the same hole boundary in the shape of a unit circle $|\zeta|=1$. The relation between z_α and ζ_α is

$$z_\alpha = \frac{1}{2}\left\{(a - ib\mu_\alpha)\zeta_\alpha + (a + ib\mu_\alpha)\frac{1}{\zeta_\alpha}\right\}, \quad \alpha = 1,2,3,4, \tag{4.5a}$$

or inversely,

$$\zeta_\alpha = \frac{z_\alpha + \sqrt{z_\alpha^2 - a^2 - b^2\mu_\alpha^2}}{a - ib\mu_\alpha}, \quad \alpha = 1,2,3,4. \tag{4.5b}$$

Substituting Eq. (4.1) and Eq. $(2.2c)_2$ into Eq. (4.5b), we have

$$\zeta_\alpha = \cos\psi + i\sin\psi = e^{i\psi} = \sigma, \quad \text{along the hole boundary.} \tag{4.6}$$

Using the method of analytical continuation and understanding that the unknown complex function vector $\mathbf{f}(z)$ is better expressed in terms of the arguments ζ_α, the general solution (2.2) for the present problem can now be written as

$$\mathbf{u}_d = 2\,\mathrm{Re}\{\mathbf{A}[\mathbf{f}_u(\zeta) + \mathbf{f}_p(\zeta)]\}, \quad \boldsymbol{\phi}_d = 2\,\mathrm{Re}\{\mathbf{B}[\mathbf{f}_u(\zeta) + \mathbf{f}_p(\zeta)]\}, \tag{4.7}$$

where $\mathbf{f}_u$ is the function associated with the unperturbed elastic field and $\mathbf{f}_p$ is the holomorphic function corresponding to the perturbed field of the problem and will be determined through satisfaction of the boundary conditions. To solve $\mathbf{f}_p$, we first need to have a proper choice for $\mathbf{f}_u$. If some parts of $\mathbf{f}_u$ are holomorphic outside the hole (S^+) while others are holomorphic inside the hole (S^-), we may split $\mathbf{f}_u$ into two functions $\mathbf{f}_u^+$ and $\mathbf{f}_u^-$; i.e.,

$$\mathbf{f}_u(\zeta) = \mathbf{f}_u^+(\zeta) + \mathbf{f}_u^-(\zeta), \tag{4.8}$$

where $\mathbf{f}_u^+$ is holomorphic in S^+ and $\mathbf{f}_u^-$ is holomorphic in S^-.

Employing the general solution (4.7) and the relation (4.8), the traction-free boundary condition (4.4b) now becomes

$$\mathbf{B}[\mathbf{f}_u^+(\sigma) + \mathbf{f}_u^-(\sigma) + \mathbf{f}_p(\sigma)] + \overline{\mathbf{B}}[\overline{\mathbf{f}_u^+(\sigma) + \mathbf{f}_u^-(\sigma) + \mathbf{f}_p(\sigma)}] = \mathbf{0}, \tag{4.9}$$

which can also be written as

$$\mathbf{B}\mathbf{f}_u^+(\sigma) + \mathbf{B}\mathbf{f}_p(\sigma) + \overline{\mathbf{B}\mathbf{f}_u^-(\sigma)} = -\mathbf{B}\mathbf{f}_u^-(\sigma) - \overline{\mathbf{B}\mathbf{f}_u^+(\sigma)} - \overline{\mathbf{B}\mathbf{f}_p(\sigma)}. \tag{4.10}$$

One of the important properties of holomorphic functions used in the analytical continuation method is that if $f(\zeta)$ is holomorphic outside the unit circle S^+ then $\overline{f(1/\zeta)}$ will be holomorphic inside the unit circle S^-, and vice versa. With this background, Eq. (4.10) can be rewritten as

$$\boldsymbol{\theta}(\sigma^+) = \boldsymbol{\theta}(\sigma^-), \tag{4.11a}$$

where

$$\boldsymbol{\theta}(\zeta) = \begin{cases} \mathbf{B}\mathbf{f}_u^+(\zeta) + \mathbf{B}\mathbf{f}_p(\zeta) + \overline{\mathbf{B}\mathbf{f}_u^-(1/\zeta)}, & \zeta \in S^+, \\ -\mathbf{B}\mathbf{f}_u^-(\zeta) - \overline{\mathbf{B}\mathbf{f}_u^+(1/\zeta)} - \overline{\mathbf{B}\mathbf{f}_p(1/\zeta)}, & \zeta \in S^-. \end{cases} \tag{4.11b}$$

By the holomorphic conditions discussed before this equation, we conclude that this newly defined function $\boldsymbol{\theta}(\zeta)$ will be holomorphic in S^+ and S^-, and is continuous across the unit circle. This means that $\boldsymbol{\theta}(\zeta)$ is holomorphic in the whole ζ-plane, including the points at infinity. By Liouville's theorem we have $\boldsymbol{\theta}(\zeta) \equiv$ constant. However, the constant function corresponds to rigid body motion, which may be neglected. Therefore, $\boldsymbol{\theta}(\zeta) \equiv \mathbf{0}$. With this result, Eq. $(4.11b)_1$ leads to

$$\mathbf{f}_p(\zeta) = -\mathbf{f}_u^+(\zeta) - \mathbf{B}^{-1}\overline{\mathbf{B}\mathbf{f}_u^-(1/\zeta)}. \tag{4.12}$$

Note that when employing the method of analytical continuation, the subscript α of ζ_α has been dropped in Eq. (4.12) and a replacement of ζ_1, ζ_2, ζ_3, ζ_4 should be made for each component function of $\mathbf{f}_p(\zeta)$ after the multiplication of matrices (see Appendix for detailed explanation).

The problem now becomes how to select an appropriate unperturbed solution $\mathbf{f}_u$ and split it into $\mathbf{f}_u^+$ and $\mathbf{f}_u^-$, and then use Eq. (4.12) to get $\mathbf{f}_p$. Following are the discussions based upon the Green's functions of nonhole problems provided in Sec. 3, which are presented in three different loading cases.

Case 1: $\hat{f}_1$, $\hat{f}_2$, $\hat{m}_1$, $\hat{m}_2$

In order to save the effort of considering the force equilibrium and single-valued requirement caused by the concentrated forces and moments, it is appropriate to select $\mathbf{f}_u$ to be the solution for the nonhole problems; i.e., the solution given in Eq. (3.2a). From Eq. (4.5a) we know that

$$z_\alpha - \hat{z}_\alpha = c_\alpha\{\zeta_\alpha - \hat{\zeta}_\alpha + \gamma_\alpha(\zeta_\alpha^{-1} - \hat{\zeta}_\alpha^{-1})\} = c_\alpha(\zeta_\alpha - \hat{\zeta}_\alpha)\left(1 - \frac{\gamma_\alpha}{\hat{\zeta}_\alpha\zeta_\alpha}\right), \tag{4.13a}$$

where

$$c_\alpha = \frac{1}{2}(a - ib\mu_\alpha), \quad \gamma_\alpha = \frac{a + ib\mu_\alpha}{a - ib\mu_\alpha}. \tag{4.13b}$$

In order to present $\mathbf{f}_u$ in terms of ζ_α, we substitute Eq. (4.13a) into Eq. (3.2a) and get

$$\mathbf{f}_u(\zeta) = \left\langle \log(\zeta_\alpha - \hat{\zeta}_\alpha) + \log\left(1 - \frac{\gamma_\alpha}{\hat{\zeta}_\alpha\zeta_\alpha}\right) + \log c_\alpha \right\rangle \mathbf{q}_1, \tag{4.14}$$

Knowing that $|\gamma_\alpha/(\hat{\zeta}_\alpha\zeta_\alpha)| < 1$ when $\zeta_\alpha \in S^+$ and $|\zeta_\alpha/\hat{\zeta}_\alpha| < 1$ when $\zeta_\alpha \in S^-$, we may split $\mathbf{f}_u$ of Eq. (4.14) into the following two parts:

$$\mathbf{f}_u^+(\zeta) = \left\langle \log\left(1 - \frac{\gamma_\alpha}{\hat{\zeta}_\alpha\zeta_\alpha}\right) + \log c_\alpha \right\rangle \mathbf{q}_1, \qquad \mathbf{f}_u^-(\zeta) = \langle \log(\zeta_\alpha - \hat{\zeta}_\alpha)\rangle \mathbf{q}_1. \tag{4.15}$$

Substituting Eq. (4.15) into Eq. (4.12) and understanding that the subscript of ζ_α should be dropped before the matrix multiplication (see Appendix), we get

$$\mathbf{f}_p(\zeta) = -\left\langle \log\left(1 - \frac{\gamma_\alpha}{\hat{\zeta}_\alpha\zeta}\right) + \log c_\alpha \right\rangle \mathbf{q}_1 - \mathbf{B}^{-1}\overline{\mathbf{B}}\langle \log(\zeta^{-1} - \overline{\hat{\zeta}_\alpha})\rangle \overline{\mathbf{q}}_1. \tag{4.16}$$

Using the translating technique (see Appendix), the explicit full-field solution of $\mathbf{f}_p(\zeta)$ can now be written as

$$\mathbf{f}_p(\zeta) = -\left\langle \log\left(1 - \frac{\gamma_\alpha}{\hat{\zeta}_\alpha\zeta_\alpha}\right) + \log c_\alpha \right\rangle \mathbf{q}_1 - \sum_{k=1}^{4} \langle \log(\zeta_\alpha^{-1} - \overline{\hat{\zeta}_k})\rangle \mathbf{B}^{-1}\overline{\mathbf{B}}_k \overline{\mathbf{q}}_1. \tag{4.17}$$

Adding $\mathbf{f}_u$ and $\mathbf{f}_p$ obtained in Eqs. (4.14) and (4.17) together and using $(3.2d)_1$, we have

$$\mathbf{f}(\zeta)=\mathbf{f}_u(\zeta)+\mathbf{f}_p(\zeta)=\frac{1}{2\pi i}\left\{\langle\log(\zeta_\alpha-\hat{\zeta}_\alpha)\rangle\mathbf{A}^T+\sum_{k=1}^{4}\langle\log(\zeta_\alpha^{-1}-\overline{\hat{\zeta}_k})\rangle\mathbf{B}^{-1}\overline{\mathbf{B}}\mathbf{I}_k\overline{\mathbf{A}}^T\right\}\hat{\mathbf{p}}, \tag{4.18}$$

which is exactly the same as that obtained in Refs. [5], [22], [23] for the Green's function of a hole in two-dimensional problems. In Ref. [22], the solution was found by proper selection of the function form of $\mathbf{f}(\zeta)$, which is then improved by Ting [5] using the concept of image singularities. The analytical continuation method was first introduced by Hwu and Yen [23] for general elastic inclusion problems. In Ref. [23], $\mathbf{f}_u$ was selected to be $\mathbf{f}_u^-$ of Eq. (4.15), which means that $\mathbf{f}_u^+=\mathbf{0}$. By their selection, $\mathbf{f}_p$ will be different from the one obtained in Eq. (4.17), while the final result of $\mathbf{f}=\mathbf{f}_u+\mathbf{f}_p$ still stays the same.

Note that the selections of $\mathbf{f}_u$ given in Ref. [23] and Eq. (4.14) are different only in their arguments. One is $\langle\log(\zeta_\alpha-\hat{\zeta}_\alpha)\rangle\mathbf{q}_1$, and the other is $\langle\log(z_\alpha-\hat{z}_\alpha)\rangle\mathbf{q}_1$. It appears that $\mathbf{f}_u$ can be selected directly from the nonhole problems, i.e., Eq. (4.14), or just by replacing the argument of the nonhole problems from z_α to ζ_α. However, in general, the latter way may not be correct, which should depend on the satisfaction of the force equilibrium and single-valued requirement described in Eq. (3.1). Unlike Eq. (3.2*a*), when z_α is replaced by ζ_α, the unperturbed solutions (3.2*b*) and (3.2*c*) cannot satisfy their associated boundary conditions (3.1*b*) and (3.1*c*). Therefore, in the following two cases one should be very careful about the selection of $\mathbf{f}_u$.

Case 2: $\hat{f}_3$

As stated above, $\mathbf{f}_u$ cannot be chosen to be the nonhole solution (3.2*b*) with z_α replaced by ζ_α since it does not satisfy the boundary conditions given in Eq. (3.1*b*). As in Case 1, to save the effort of considering the force equilibrium and single-valued requirement (3.1*b*), it is appropriate to select $\mathbf{f}_u$ directly from Eq. (3.2*b*) without making replacement. In order to present $\mathbf{f}_u$ in terms of ζ_α, we substitute Eq. (4.13*a*) into Eq. (3.2*b*) and get

$$\mathbf{f}_u(\zeta)=\left\langle c_\alpha(\zeta_\alpha-\hat{\zeta}_\alpha)\left(1-\frac{\gamma_\alpha}{\hat{\zeta}_\alpha\zeta_\alpha}\right)\left[\log(\zeta_\alpha-\hat{\zeta}_\alpha)+\log\left(1-\frac{\gamma_\alpha}{\hat{\zeta}_\alpha\zeta_\alpha}\right)+\log c_\alpha-1\right]\right\rangle\mathbf{q}_2. \tag{4.19}$$

Knowing that

$$\log(\zeta_\alpha-\hat{\zeta}_\alpha)=\log(-\hat{\zeta}_\alpha)-\sum_{k=1}^{\infty}\frac{1}{k}\left(\frac{\zeta_\alpha}{\hat{\zeta}_\alpha}\right)^k,\quad\text{for}\quad\left|\frac{\zeta_\alpha}{\hat{\zeta}_\alpha}\right|<1,$$
$$\log\left(1-\frac{\gamma_\alpha}{\hat{\zeta}_\alpha\zeta_\alpha}\right)=-\sum_{k=1}^{\infty}\frac{1}{k}\left(\frac{\gamma_\alpha}{\hat{\zeta}_\alpha\zeta_\alpha}\right)^k,\quad\text{for}\quad\left|\frac{\gamma_\alpha}{\hat{\zeta}_\alpha\zeta_\alpha}\right|<1, \tag{4.20}$$

and carrying out the multiplication of Eq. (4.19) into series expansion and then check the holomorphic condition of each term, we may split $\mathbf{f}_u$ of Eq. (4.19) into two functions $\mathbf{f}_u^+$ and $\mathbf{f}_u^-$ where $\mathbf{f}_u^+$ is holomorphic in S^+ (outside the hole) and $\mathbf{f}_u^-$ is holomorphic in S^- (inside the hole). They are

$$\mathbf{f}_u^+(\zeta)=\left\langle(\zeta_\alpha-\hat{\zeta}_\alpha)\left(1-\frac{\gamma_\alpha}{\hat{\zeta}_\alpha\zeta_\alpha}\right)\log\left(1-\frac{\gamma_\alpha}{\hat{\zeta}_\alpha\zeta_\alpha}\right)\right\rangle\mathbf{q}_c+\langle\gamma_\alpha(\zeta_\alpha^{-1}-\hat{\zeta}_\alpha^{-1})\rangle\mathbf{q}_c^*+\langle(\zeta_\alpha^{-1}-\hat{\zeta}_\alpha^{-1})\rangle\mathbf{q}_c^{**}, \tag{4.21a}$$

$$\mathbf{f}_u^-(\zeta)=\left\langle(\zeta_\alpha-\hat{\zeta}_\alpha)\left(1-\frac{\gamma_\alpha}{\hat{\zeta}_\alpha\zeta_\alpha}\right)\log(\zeta_\alpha-\hat{\zeta}_\alpha)\right\rangle\mathbf{q}_c+\langle(\zeta_\alpha-\hat{\zeta}_\alpha)\rangle\mathbf{q}_c^*-\langle(\zeta_\alpha^{-1}-\hat{\zeta}_\alpha^{-1})\rangle\mathbf{q}_c^{**},$$

where

$$\mathbf{q}_c=\langle c_\alpha\rangle\mathbf{q}_2,\quad\mathbf{q}_c^*=\langle c_\alpha(\log c_\alpha-1)\rangle\mathbf{q}_2,\quad\mathbf{q}_c^{**}=\langle c_\alpha\gamma_\alpha\log(-\hat{\zeta}_\alpha)\rangle\mathbf{q}_2. \tag{4.21b}$$

Substituting Eq. (4.21*a*) into Eq. (4.12) and understanding that the subscript of ζ_α should be dropped before the matrix multiplication, we get

$$\mathbf{f}_p(\zeta)=-\left\langle(\zeta-\hat{\zeta}_\alpha)\left(1-\frac{\gamma_\alpha}{\hat{\zeta}_\alpha\zeta}\right)\log\left(1-\frac{\gamma_\alpha}{\hat{\zeta}_\alpha\zeta}\right)\right\rangle\mathbf{q}_c-\langle\gamma_\alpha(\zeta^{-1}-\hat{\zeta}_\alpha^{-1})\rangle\mathbf{q}_c^*-\langle(\zeta^{-1}-\hat{\zeta}_\alpha^{-1})\rangle\mathbf{q}_c^{**}-\mathbf{B}^{-1}\overline{\mathbf{B}}\langle(\zeta^{-1}-\overline{\hat{\zeta}_\alpha})(1-\overline{\gamma}_\alpha\overline{\hat{\zeta}_\alpha^{-1}}\zeta)\log(\zeta^{-1}-\overline{\hat{\zeta}_\alpha})\rangle\overline{\mathbf{q}}_c-\mathbf{B}^{-1}\overline{\mathbf{B}}\langle(\zeta^{-1}-\overline{\hat{\zeta}_\alpha})\rangle\overline{\mathbf{q}}_c^*+\mathbf{B}^{-1}\overline{\mathbf{B}}\langle(\zeta-\overline{\hat{\zeta}_\alpha^{-1}})\rangle\overline{\mathbf{q}}_c^{**}. \tag{4.22}$$

Using the translating technique (see Appendix), the explicit full-field solution of $\mathbf{f}_p(\zeta)$ can then be written as

$$\mathbf{f}_p(\zeta)=-\left\langle(\zeta_\alpha-\hat{\zeta}_\alpha)\left(1-\frac{\gamma_\alpha}{\hat{\zeta}_\alpha\zeta_\alpha}\right)\log\left(1-\frac{\gamma_\alpha}{\hat{\zeta}_\alpha\zeta_\alpha}\right)\right\rangle\mathbf{q}_c-\langle\gamma_\alpha(\zeta_\alpha^{-1}-\hat{\zeta}_\alpha^{-1})\rangle\mathbf{q}_c^*-\langle(\zeta_\alpha^{-1}-\hat{\zeta}_\alpha^{-1})\rangle\mathbf{q}_c^{**}-\sum_{k=1}^{4}\langle(\zeta_\alpha^{-1}-\overline{\hat{\zeta}_k})(1-\overline{\gamma}_k\overline{\hat{\zeta}_k^{-1}}\zeta_\alpha)\log(\zeta_\alpha^{-1}-\overline{\hat{\zeta}_k})\rangle\mathbf{B}^{-1}\overline{\mathbf{B}}\mathbf{I}_k\overline{\mathbf{q}}_c-\sum_{k=1}^{4}\langle(\zeta_\alpha^{-1}-\overline{\hat{\zeta}_k})\rangle\mathbf{B}^{-1}\overline{\mathbf{B}}\mathbf{I}_k\overline{\mathbf{q}}_c^*+\sum_{k=1}^{4}\langle(\zeta_\alpha-\overline{\hat{\zeta}_k^{-1}})\rangle\mathbf{B}^{-1}\overline{\mathbf{B}}\mathbf{I}_k\overline{\mathbf{q}}_c^{**}. \tag{4.23}$$

Adding $\mathbf{f}_u$ and $\mathbf{f}_p$ obtained in Eqs. (4.19) and (4.23) together and using Eq. (4.13), we get

$$\mathbf{f}(\zeta)=\mathbf{f}_u(\zeta)+\mathbf{f}_p(\zeta)=\langle(z_\alpha-\hat{z}_\alpha)\log(\zeta_\alpha-\hat{\zeta}_\alpha)\rangle\mathbf{q}_2-\sum_{k=1}^{4}\langle(\zeta_\alpha^{-1}-\overline{\hat{\zeta}_k})\times(1-\overline{\gamma}_k\overline{\hat{\zeta}_k^{-1}}\zeta_\alpha)\log(\zeta_\alpha^{-1}-\overline{\hat{\zeta}_k})\rangle\mathbf{B}^{-1}\overline{\mathbf{B}}\mathbf{I}_k\langle\overline{c_\alpha}\rangle\overline{\mathbf{q}}_2+\langle(\zeta_\alpha-\hat{\zeta}_\alpha)\rangle\mathbf{q}_c^*-\sum_{k=1}^{4}\langle(\zeta_\alpha^{-1}-\overline{\hat{\zeta}_k})\rangle\mathbf{B}^{-1}\overline{\mathbf{B}}\mathbf{I}_k\overline{\mathbf{q}}_c^*-\langle(\zeta_\alpha^{-1}-\hat{\zeta}_\alpha^{-1})\rangle\mathbf{q}_c^{**}+\sum_{k=1}^{4}\langle(\zeta_\alpha-\overline{\hat{\zeta}_k^{-1}})\rangle\mathbf{B}^{-1}\overline{\mathbf{B}}\mathbf{I}_k\overline{\mathbf{q}}_c^{**}. \tag{4.24}$$

Case 3: $\hat{m}_3$

Similar to Case 2, $\mathbf{f}_u$ is selected to be the unperturbed solution (3.2*c*), in which $z_\alpha-\hat{z}_\alpha$ is related to ζ_α and $\hat{\zeta}_\alpha$ by Eq. (4.13), and hence

$$\mathbf{f}_u(\zeta)=\left\langle\frac{1}{c_\alpha(\hat{\zeta}_\alpha-\gamma_\alpha/\hat{\zeta}_\alpha)}\left\{\frac{\hat{\zeta}_\alpha}{\zeta_\alpha-\hat{\zeta}_\alpha}-\frac{\gamma_\alpha/\hat{\zeta}_\alpha}{\zeta_\alpha-\gamma_\alpha/\hat{\zeta}_\alpha}\right\}\right\rangle\mathbf{q}_3. \tag{4.25}$$

Since $\hat{\zeta}_\alpha$ and $\gamma_\alpha/\hat{\zeta}_\alpha$ are located in S^+ and S^-, respectively, $\mathbf{f}_u$ can be split into the following two parts:

$$\mathbf{f}_u^+(\zeta)=\left\langle\frac{-1}{\zeta_\alpha-\gamma_\alpha/\hat{\zeta}_\alpha}\right\rangle\mathbf{q}_3^{**},\quad\mathbf{f}_u^-(\zeta)=\left\langle\frac{1}{\zeta_\alpha-\hat{\zeta}_\alpha}\right\rangle\mathbf{q}_3^*, \tag{4.26a}$$

where

$$\mathbf{q}_3^*=\frac{\hat{\zeta}_\alpha}{c_\alpha(\hat{\zeta}_\alpha-\gamma_\alpha/\hat{\zeta}_\alpha)}\mathbf{q}_3,\quad\mathbf{q}_3^{**}=\frac{\gamma_\alpha/\hat{\zeta}_\alpha}{c_\alpha(\hat{\zeta}_\alpha-\gamma_\alpha/\hat{\zeta}_\alpha)}\mathbf{q}_3. \tag{4.26b}$$

Substituting Eq. (4.26) into Eq. (4.12) and using the translating technique described in the Appendix, the full field solution of $\mathbf{f}_p(\zeta)$ can be obtained as

$$\mathbf{f}_p(\zeta)=\left\langle \frac{1}{\zeta_\alpha-\gamma_\alpha/\hat{\zeta}_\alpha}\right\rangle \mathbf{q}_3^{**}-\sum_{k=1}^{4}\left\langle \frac{1}{\zeta_\alpha^{-1}-\overline{\hat{\zeta}_k}}\right\rangle \mathbf{B}^{-1}\overline{\mathbf{B}}\mathbf{I}_k\overline{\mathbf{q}}_3^{*}. \tag{4.27}$$

Adding $\mathbf{f}_u$ and $\mathbf{f}_p$ obtained in Eqs. (4.25) and (4.27) together we get

$$\mathbf{f}(\zeta)=\mathbf{f}_u(\zeta)+\mathbf{f}_p(\zeta)=\left\langle \frac{1}{\zeta_\alpha-\hat{\zeta}_\alpha}\right\rangle \mathbf{q}_3^{*}-\sum_{k=1}^{4}\left\langle \frac{1}{\zeta_\alpha^{-1}-\overline{\hat{\zeta}_k}}\right\rangle \mathbf{B}^{-1}\overline{\mathbf{B}}\mathbf{I}_k\overline{\mathbf{q}}_3^{*}. \tag{4.28}$$

Stress Resultants and Moments Along the Hole Boundary. In engineering applications, one is usually interested in the stress resultants and moments along the hole boundary. Since the hole considered in this paper is in the shape of an ellipse, it is better to calculate the stress resultants and bending moments in the tangent–normal $(s-n)$ coordinate instead of the Cartesian (x_1-x_2) coordinate. By the relations given in Eqs. (2.5) and $(2.2b)_2$, we know that the calculation of stress resultants and moments relies upon the calculation of the differentials $\boldsymbol{\phi}_{d,s}$ and $\boldsymbol{\phi}_{d,n}$. Moreover, due to the traction-free boundary condition prescribed in Eq. (4.4), along the hole boundary $\boldsymbol{\phi}_{d,s}$ should be zero, which will then be used as a check of our solutions.

From $(2.2a)_2$, we have

$$\boldsymbol{\phi}_{d,n}=2\,\mathrm{Re}\{\mathbf{B}\mathbf{f}_{,n}(\zeta)\}, \tag{4.29}$$

in which each term of $\mathbf{f}_{,n}(\zeta)$ can be obtained by using chain rule for differentiation, such as

$$\frac{\partial f}{\partial n}=\frac{\partial f}{\partial\zeta_\alpha}\frac{\partial\zeta_\alpha}{\partial\psi}\frac{\partial\psi}{\partial z_\alpha}\left[\frac{\partial z_\alpha}{\partial x_1}\frac{\partial x_1}{\partial n}+\frac{\partial z_\alpha}{\partial x_2}\frac{\partial x_2}{\partial n}\right]. \tag{4.30}$$

Along the hole boundary,

$$\zeta_\alpha=e^{i\psi},\quad \frac{\partial\zeta_\alpha}{\partial\psi}=ie^{i\psi},$$

$$\frac{\partial z_\alpha}{\partial\psi}=-a\sin\psi+\mu_\alpha b\cos\psi=\rho(\cos\theta+\mu_\alpha\sin\theta), \tag{4.31}$$

$$\frac{\partial x_1}{\partial n}=-\sin\theta,\quad \frac{\partial x_2}{\partial n}=\cos\theta,\quad \frac{\partial z_\alpha}{\partial x_1}=1,\quad \frac{\partial z_\alpha}{\partial x_2}=\mu_\alpha,$$

and hence,

$$\frac{\partial f}{\partial n}=\frac{ie^{i\psi}\mu_\alpha(\theta)}{\rho}\frac{\partial f}{\partial\zeta_\alpha},\quad \text{along the hole boundary,} \tag{4.32}$$

where $\mu_\alpha(\theta)$ is the generalized material eigenvalue related to μ_α by

$$\mu_\alpha(\theta)=\frac{-\sin\theta+\mu_\alpha\cos\theta}{\cos\theta+\mu_\alpha\sin\theta}. \tag{4.33}$$

By the relation (4.32), each term of $\mathbf{f}_n(\zeta)$ in Eqs. (4.18), (4.24), and (4.28) along the hole boundary can be obtained explicitly. For example,

$$\frac{\partial\log(\zeta_\alpha-\hat{\zeta}_\alpha)}{\partial n}=\frac{ie^{i\psi}}{\rho(e^{i\psi}-\hat{\zeta}_\alpha)}\mu_\alpha(\theta),\ \ldots,$$

$$\frac{\partial(\zeta_\alpha^{-1}-\overline{\hat{\zeta}_k})^{-1}}{\partial n}=\frac{ie^{i\psi}}{\rho(1-e^{i\psi}\overline{\hat{\zeta}_k})^2}\mu_\alpha(\theta),\ \ldots,\text{etc.},$$

along the hole boundary. (4.34)

Substituting these results into Eq. (4.29) and carefully performing the summation such as

$$\sum_{k=1}^{4}\mathbf{B}\left\langle \frac{\mu_\alpha(\theta)}{e^{-i\psi}-\overline{\hat{\zeta}_k}}\right\rangle \mathbf{B}^{-1}\overline{\mathbf{B}}\mathbf{I}_k\overline{\mathbf{A}}^T\hat{\mathbf{p}}$$

$$=\mathbf{B}\langle\mu_\alpha(\theta)\rangle\mathbf{B}^{-1}\overline{\mathbf{B}}\sum_{k=1}^{4}(e^{-i\psi}-\overline{\hat{\zeta}_k})^{-1}\mathbf{I}_k\overline{\mathbf{A}}^T\hat{\mathbf{p}}$$

$$=\mathbf{B}\langle\mu_\alpha(\theta)\rangle\mathbf{B}^{-1}\overline{\mathbf{B}}\langle(e^{-i\psi}-\overline{\hat{\zeta}_\alpha})^{-1}\rangle\overline{\mathbf{A}}^T\hat{\mathbf{p}} \tag{4.35}$$

we obtain

$$\boldsymbol{\phi}_{d,n}=\frac{-2}{\pi\rho}\mathbf{G}_3(\theta)\mathrm{Im}\{\mathbf{B}\langle h_i(\psi)\rangle\mathbf{A}^T\}\mathbf{p}_i,\quad i=1,2,3, \tag{4.36a}$$

where

$$h_1(\psi)=e^{i\psi}(e^{i\psi}-\hat{\zeta}_\alpha)^{-1},$$

$$h_2(\psi)=c_\alpha[e^{i\psi}\log(c_\alpha(e^{i\psi}-\hat{\zeta}_\alpha))-\gamma_\alpha e^{-i\psi}\log(1-\hat{\zeta}_\alpha^{-1}e^{i\psi})$$

$$-\gamma_\alpha\hat{\zeta}_\alpha^{-1}], \tag{4.36b}$$

$$h_3(\psi)=-\frac{e^{i\psi}\hat{\zeta}_\alpha}{c_\alpha(\hat{\zeta}_\alpha-\gamma_\alpha/\hat{\zeta}_\alpha)(e^{i\psi}-\hat{\zeta}_\alpha)^2},$$

and

$$\hat{\mathbf{p}}_1=\hat{\mathbf{p}},\quad \hat{\mathbf{p}}_2=\hat{f}_3\mathbf{i}_3,\quad \hat{\mathbf{p}}_3=\hat{m}_3\mathbf{i}_2. \tag{4.36c}$$

The subscripts $i=1$, 2, 3, denote the loading cases discussed in this paper. Note that in deriving Eq. (4.36), an identity converting complex form into real form has been used, which is

$$\mathbf{B}\langle\mu_\alpha(\theta)\rangle\mathbf{B}^{-1}=\mathbf{G}_1(\theta)+i\mathbf{G}_3(\theta), \tag{4.37}$$

where $\mathbf{G}_1(\theta)$ and $\mathbf{G}_3(\theta)$ are two real matrices defined by the generalized fundamental matrices $\mathbf{N}_i(\theta)$ and Barnett–Lothe tensors $\mathbf{S}$ and $\mathbf{L}$ as

$$\mathbf{G}_1(\theta)=\mathbf{N}_1^T(\theta)-\mathbf{N}_3(\theta)\mathbf{S}\mathbf{L}^{-1},\quad \mathbf{G}_3(\theta)=-\mathbf{N}_3(\theta)\mathbf{L}^{-1}. \tag{4.38}$$

This identity is just one of several useful identities developed in Stroh formalism for two-dimensional problems [5]. By deliberate arrangement it has been proved that these identities are still valid for Stroh-like formalism of coupled stretching-bending problems [11].

Discussion and Verification. Although the Green's functions for hole problems play important roles in stress analysis, most of the closed-form solutions presented in the literature are for two-dimensional problems. As to the holes in laminates with stretching-bending coupling, as far as I know no analytical closed-form solution has been presented in complete loading cases without leaving any unsolved coefficients. Since no other analytical solutions can be used to compare our solutions, detailed discussion and verification are necessary. When we employed the general solution (2.2), all the basic equations for the laminates with stretching-bending coupling have been satisfied. Thus, all we need to do is check the satisfaction of the boundary conditions prescribed in Eqs. (3.1*a*,*b*,*c*) and Eq. (4.4). By the method of analytical continuation, when we selected the nonhole solutions (3.2*a*,*b*,*c*) as our unperturbed solutions $\mathbf{f}_u$, the boundary conditions (3.1*a*,*b*,*c*) have been satisfied. Moreover, the perturbed solutions $\mathbf{f}_p$ obtained in Eqs. (4.17), (4.23), and (4.27) are all holomorphic in the region outside the hole, and hence will make all the contour integrals shown in Eqs. (3.1*a*,*b*,*c*) vanish and let the boundary conditions (3.1*a*,*b*,*c*) be satisfied not only by $\mathbf{f}_u$ but also

by $\mathbf{f}_u+\mathbf{f}_p$. After verifying the force equilibrium and single-valued requirement shown in Eqs. (3.1a,b,c), we now check the traction-free condition (4.4*a*).

Similar to the derivation given in Eqs. (4.30)–(4.32), the differentiation with respect to the tangential direction can be calculated by

$$\frac{\partial f}{\partial s}=\frac{ie^{i\psi}}{\rho}\frac{\partial f}{\partial \zeta_\alpha}, \quad \text{along the hole boundary.} \tag{4.39}$$

With this relation, by following the steps described in Eqs. (4.34)–(4.36), we get

$$\boldsymbol{\phi}_{d,s}=\mathbf{0}, \quad \text{along the hole boundary,} \tag{4.40}$$

which shows that the traction-free boundary conditions are also satisfied by our solutions.

In addition to the basic check of the present solutions, from the boundary conditions shown in Eq. (3.1*a*) for the first loading case, we noticed that they are identical to those of the two-dimensional problems in their mathematical form. If the mathematical forms of the general solution (2.2*a*) and the boundary conditions (3.1*a*) are all exactly the same as those of two-dimensional problems, their solutions should also be identical in their mathematical form. This can be proved by the solutions shown in Eqs. (4.18) and (4.36) for $i=1$ and those presented in Refs. [5,22,23]. For Case 1, if the force $\hat{\mathbf{p}}$ is applied on the hole surface, we may let $\hat{\zeta}_\alpha=e^{i\psi_o}$. With this value, the solution (4.36) can be further reduced to

$$\boldsymbol{\phi}_{d,n}=\frac{1}{2\pi\rho}\mathbf{G}_3(\theta)\left\{\frac{\sin(\psi-\psi_o)}{1-\cos(\psi-\psi_o)}\mathbf{I}+\mathbf{S}^T\right\}\hat{\mathbf{p}}, \tag{4.41}$$

whose mathematical form is also identical to that shown in Ref. [5] for two-dimensional problems.

5 Green's Functions for Crack Problems

An elliptic hole can be made into a crack of length $2a$ by letting the minor axis $2b$ be equal to zero. The Green's functions for crack problems can therefore be obtained from Eqs. (4.18), (4.24), and (4.28) by letting $b=0$, in which the mapped variable ζ_α becomes

$$\zeta_\alpha=\frac{1}{a}\{z_\alpha+\sqrt{z_\alpha^2-a^2}\}. \tag{5.1}$$

Substituting Eqs. (4.18), (4.24), and (4.28) with $b=0$ into Eq. $(2.2a)_2$, and using the relations (2.3) for $x_2=0$, $|x_1|>a$, we see that the stress resultants ahead of the crack tip are singular. To deal with the stress singularity, the stress intensity factors are usually defined as

$$\mathbf{K}=\begin{Bmatrix} K_{\mathrm{II}} \\ K_{\mathrm{I}} \\ K_{\mathrm{II}B} \\ K_{\mathrm{I}B} \end{Bmatrix}=\lim_{r\to 0}\sqrt{2\pi r}\begin{Bmatrix} N_{12} \\ N_{22} \\ M_{12} \\ M_{22} \end{Bmatrix}, \tag{5.2}$$

where r is the distance ahead of the crack tip. By using the relations given in Eq. (2.3), the definition (5.2) can now be rewritten in terms of the stress functions as

$$\mathbf{K}=\lim_{r\to 0}\sqrt{2\pi r}(\boldsymbol{\phi}_{d,1}-\eta\mathbf{i}_3), \quad \eta=(\mathbf{i}_3^T\boldsymbol{\phi}_{d,1}+\mathbf{i}_4^T\boldsymbol{\phi}_{d,2})/2. \tag{5.3}$$

From this relation, we know that to obtain the stress intensity factors we need to calculate $\boldsymbol{\phi}_{d,1}$ and $\boldsymbol{\phi}_{d,2}$. By the approach similar to those described in Eqs. (4.29)–(4.38), and letting $x_2=0$, $x_1>a$, $x_1-a=r$, and $r\to 0$, which will lead to $\zeta_\alpha\to 1$, we obtain

$$\lim_{r\to 0}\sqrt{2\pi r}\boldsymbol{\phi}_{d,1}=\frac{2}{\sqrt{\pi a}}\mathrm{Im}\{\mathbf{B}\langle h_i(0)\rangle\mathbf{A}^T\}\hat{\mathbf{p}}_i, \tag{5.4}$$

$$\lim_{r\to 0}\sqrt{2\pi r}\boldsymbol{\phi}_{d,2}=\frac{2}{\sqrt{\pi a}}\mathbf{G}_1(0)\mathrm{Im}\{\mathbf{B}\langle h_i(0)\rangle\mathbf{A}^T\}\hat{\mathbf{p}}_i, \quad i=1,2,3.$$

For Case 1, if the force $\hat{\mathbf{p}}$ is applied on the upper crack surface $x=c$ where $0<c<a$, the solution (5.4) can be further reduced to

$$\begin{aligned}\lim_{r\to 0}\sqrt{2\pi r}\boldsymbol{\phi}_{d,1}&=\frac{1}{2\sqrt{\pi a}}\left\{\sqrt{\frac{a+c}{a-c}}\mathbf{I}-\mathbf{S}^T\right\}\hat{\mathbf{p}},\\ \lim_{r\to 0}\sqrt{2\pi r}\boldsymbol{\phi}_{d,2}&=\frac{1}{2\sqrt{\pi a}}\mathbf{G}_1(0)\left\{\sqrt{\frac{a+c}{a-c}}\mathbf{I}-\mathbf{S}^T\right\}\hat{\mathbf{p}}.\end{aligned} \tag{5.5}$$

The mode I and mode II stress intensity factors, K_{I} and K_{II}, respectively, calculated from Eq. $(5.5)_1$ are identical to the solutions given in Refs. [22,24].

6 Conclusions

By using Stroh-like formalism and analytical continuation method, the Green's functions for holes/cracks in laminates with stretching and bending coupling are obtained in this paper. Like the Green's functions for the infinite laminates, the concentrated forces and moments will influence the mechanical behavior of the laminates in different ways when they are applied in different directions. The results show that the solutions corresponding to the in-plane concentrated forces $\hat{f}_1$, $\hat{f}_2$ and out-of-plane concentrated moments $\hat{m}_1$, $\hat{m}_2$ (Case 1) have exactly the same form as that of the corresponding two-dimensional problems. While for the cases (Cases 2 and 3) under the concentrated force $\hat{f}_3$ and torsion $\hat{m}_3$, respectively, new types of solutions are obtained explicitly. The Green's functions are expressed in complex form and are valid for the full field. By using the relations between the stress functions and stress resultants/moments, relatively simple solutions are obtained for the stress resultants and moments along the hole boundary. Furthermore, through the use of some identities developed in the literature, real form solutions are obtained for loading Case 1. Similarly, we also get the explicit solutions of the stress intensity factors for crack problems.

It should be noticed that unlike the corresponding two-dimensional problems, for the satisfaction of force equilibrium and single-valued requirement, the unperturbed solutions of Cases 2 and 3 cannot be selected from the Green's functions of nonhole problems by just replacing the function argument from z_α to ζ_α. The relation between z_α and ζ_α should be used when we change the function argument, and hence the holomorphic conditions of the complex function may also change. Thus, when we employ the analytical continuation method the unperturbed solutions should be split into two parts: one is holomorphic outside the hole and the other is holomorphic inside the hole.

Acknowledgments

The author would like to thank the National Science Council, Taiwan, R.O.C. for support through Grant No. 92-2212-E-006-132.

Appendix: Translating Technique

When we employ the method of analytical continuation, it is quite usual that a new analytical function will be introduced based upon the relation of the boundary condition. For example, the new analytical function $\boldsymbol{\theta}(\zeta)$ given in Eq. (4.11*b*) is introduced according to the relation (4.10), which comes from the traction-free boundary condition. If the function arguments ζ_α, $\alpha=1, 2, 3, 4$, have the same value on the boundary, (e.g., $\zeta_1=\zeta_2=\zeta_3=\zeta_4=\sigma$ on the hole surface), the arguments of the new analytical function can be any one of ζ_α because their introduction is based upon the boundary conditions. Therefore, when we introduce the new ana-

lytical function, it is better to represent its associated solutions by using the function vector without indicating the subscript; for example,

$$\boldsymbol{\theta}(\zeta)=\{\theta_1(\zeta)\quad\theta_2(\zeta)\quad\theta_3(\zeta)\quad\theta_4(\zeta)\}^T. \tag{A1}$$

With this understanding, the function vector $\mathbf{f}_p(\zeta)$ obtained in Eq. (4.12) also has the form of (*A*1) which is not consistent with the solution form shown in Eq. (2.2*c*) and is valid only on the boundary. To obtain the explicit full-domain solution, a mathematical operation based upon the following statement is needed: ''Once the solution of $\mathbf{f}(z)$ is obtained from the condition of analytical continuation with the understanding that the subscript of z is dropped before the matrix product, a replacement of z_1, z_2, or z_3 should be made for each component function after the multiplication of matrices.'' A technique translating the above mathematical operation was first introduced by Hwu [25] and is described below.

If a solution with the subscript of z dropped is written as

$$\mathbf{f}(z)=\mathbf{C}\langle g_\alpha(z)\rangle\mathbf{q}, \tag{A2}$$

its associated full-field solution with the form shown in Eq. (2.2*c*) can be expressed as

$$\mathbf{f}(z)=\sum_{k=1}^{4}\langle g_k(z_\alpha)\rangle\mathbf{C}\mathbf{I}_\mathbf{j}\mathbf{q}, \tag{A3}$$

where

$$\begin{aligned}\mathbf{I}_1&=\mathrm{diag}[1,0,0,0],\quad &\mathbf{I}_2&=\mathrm{diag}[0,1,0,0],\\ \mathbf{I}_3&=\mathrm{diag}[0,0,1,0],\quad &\mathbf{I}_4&=\mathrm{diag}[0,0,0,1].\end{aligned} \tag{A4}$$

References

[1] Muskhelishvili, N. I., 1954, *Some Basic Problem of the Mathematical Theory of Elasticity*, Noordhoff, Groningen pp. 339–355, 461–534.

[2] Savin, G. N., 1961, *Stress Concentration Around Holes*, Pergamon, London pp. 41–391.

[3] Lekhnitskii, S. G., 1963, *Theory of Elasticity of an Anisotropic Elastic Body*, Holden-Day Inc., San Francisco pp. 153–174.

[4] Lekhnitskii, S. G., 1968, *Anisotropic Plates*, Gordon and Breach, N.Y pp. 157–419.

[5] Ting, T. C. T., 1996, *Anisotropic Elasticity—Theory and Applications*, Oxford Science, New York pp. 371–439.

[6] Becker, W., 1991, ''A Complex Potential Method for Plate Problems With Bending Extension Coupling,'' Arch. Appl. Mech., **61**, pp. 318–326.

[7] Lu, P., and Mahrenholtz, O., 1994, ''Extension of the Stroh Formalism to an Analysis of Bending of Anisotropic Elastic Plates,'' J. Mech. Phys. Solids, **42**, No. 11, pp. 1725–1741.

[8] Cheng, Z. Q., and Reddy, J. N., 2002, ''Octet Formalism for Kirchhoff Anisotropic Plates,'' Proc. R. Soc. London, Ser. A, **458**, pp. 1499–1517.

[9] Chen, P., and Shen, Z., 2001, ''Extension of Lekhnitskii's Complex Potential Approach to Unsymmetric Composite Laminates,'' Mech. Res. Commun., **28**, No. 4, pp. 423–428.

[10] Yin, W. L., 2003, ''General Solutions of Anisotropic Laminated Plates,'' ASME J. Appl. Mech., **70**, No. 4, pp. 496–504.

[11] Hwu, C., 2003, ''Stroh-Like Formalism for the Coupled Stretching-Bending Analysis of Composite Laminates,'' Int. J. Solids Struct., **40**, No. 13–14, pp. 3681–3705.

[12] Becker, W., 1992, ''Closed-Form Analytical Solutions for a Griffith Crack in a Non-Symmetric Laminate Plate,'' Compos. Struct., **21**, pp. 49–55.

[13] Becker, W., 1993, ''Complex Method for the Elliptical Hole in an Unsymmetric Laminate,'' Arch. Appl. Mech., **63**, pp. 159–169.

[14] Zakharov, D. D., and Becker, W., 2000, ''Boundary Value Problems for Unsymmetric Laminates, Occupying a Region With Elliptic Contour,'' Compos. Struct., **49**, pp. 275–284.

[15] Chen, P., and Shen, Z., 2001, ''Green's Functions for an Unsymmetric Laminated Plate With an Elliptic Hole,'' Mech. Res. Commun., **28**, No. 5, pp. 519–524.

[16] Hsieh, M. C., and Hwu, C., 2003, ''Explicit Solutions for the Coupled Stretching-Bending Problems of Holes in Composite Laminates,'' Int. J. Solids Struct., **40**, No. 15, pp. 3913–3933.

[17] Chen, P., and Shen, Z., 2003, ''Stress Resultants and Moments Around Holes in Unsymmetrical Composite Laminates Subjected to Remote Uniform Loading,'' Mech. Res. Commun., **30**, pp. 79–86.

[18] Hwu, C., 2004, ''Green's Function for the Composite Laminates With Bending Extension Coupling,'' Compos. Struct., **63**, pp. 283–292.

[19] Stroh, A. N., 1958, ''Dislocations and Cracks in Anisotropic Elasticity,'' Philos. Mag., **7**, pp. 625–646.

[20] Hsieh, M. C., and Hwu, C., 2002, ''Explicit Expressions of the Fundamental Elasticity Matrices of Stroh-Like Formalism for Symmetric/Unsymmetric Laminates,'' Chinese Journal of Mechanics-Series A, **18**, No. 3, pp. 109–118.

[21] Becker, W., 1995, ''Concentrated Forces and Moments on Laminates With Bending Extension Coupling,'' Compos. Struct., **30**, pp. 1–11.

[22] Hwu, C., and Yen, W. J., 1991, ''Green's Functions of Two-Dimensional Anisotropic Plates Containing an Elliptic Hole,'' Int. J. Solids Struct., **27**, No. 13, pp. 1705–1719.

[23] Hwu, C., and Yen, W. J., 1993, ''On the Anisotropic Elastic Inclusions in Plane Elastostatics,'' ASME J. Appl. Mech., **60**, pp. 626–632.

[24] Wu, K. C., 1989, ''Representations of Stress Intensity Factors by Path-Independent Integrals,'' ASME J. Appl. Mech., **56**, pp. 780–785.

[25] Hwu, C., 1993, ''Explicit Solutions for the Collinear Interface Crack Problems,'' Int. J. Solids Struct., **30**, No. 3, pp. 301–312.

Analytical Solution of a Dynamic System Containing Fractional Derivative of Order One-Half by Adomian Decomposition Method

S. Saha Ray

B. P. Poddar

Institute of Management and Technology,
137, V.I.P. Road, Poddar Vihar,
Kolkata 700052, India
e-mail: santanusaharay@yahoo.com

R. K. Bera

Heritage Institute of Technology,
Chowbaga Road,
Anandapur, Kolkata 700107,
India
e-mail: rasajit@hotmail.com

*The fractional derivative has been occurring in many physical problems, such as frequency-dependent damping behavior of materials, motion of a large thin plate in a Newtonian fluid, creep and relaxation functions for viscoelastic materials, the $PI^{\lambda}D^{\mu}$ controller for the control of dynamical systems, etc. Phenomena in electromagnetics, acoustics, viscoelasticity, electrochemistry, and materials science are also described by differential equations of fractional order. The solution of the differential equation containing a fractional derivative is much involved. Instead of an application of the existing methods, an attempt has been made in the present analysis to obtain the solution of an equation in a dynamic system whose damping behavior is described by a fractional derivative of order 1/2 by the relatively new Adomian decomposition method. The results obtained by this method are then graphically represented and compared with those available in the work of Suarez and Shokooh [Suarez, L. E., and Shokooh, A., 1997, "An Eigenvector Expansion Method for the Solution of Motion Containing Fraction Derivatives," ASME J. Appl. Mech., **64**, pp. 629–635]. A good agreement of the results is observed.* [DOI: 10.1115/1.1839184]

1 Introduction

The fractional differential equations appear more and more frequently in different research areas and engineering applications. An effective and easy-to-use method for solving such equations is needed. It should be mentioned that from the viewpoint of fractional calculus applications in physics, chemistry, and engineering, it was undoubtedly the book written by K. B. Oldham and J. Spanier [1] that played an outstanding role in the development of this subject. Moreover, it was the first book that was entirely devoted to a systematic presentation of the ideas, methods, and applications of the fractional calculus.

Later there appeared several fundamental works on various aspects of the fractional calculus including extensive survey on fractional differential equations by Miller and Ross [2], I. Podlubny [3], and others. Furthermore, several references to the books by Oldham and Spanier [1], Miller and Ross [2], and Podlubny [3] show that applied scientists need first of all an easy introduction to the theory of fractional derivatives and fractional differential equations, which could help them in their initial steps to adopting the fractional calculus as a method of research.

Fractional calculus has been used to model physical and engineering processes that are found to be best described by fractional differential equations. For that reason we need a reliable and efficient technique for the solution of fractional differential equations. In this connection, it is worthwhile to mention that the recent papers on numerical solutions of fractional differential equations are available from the notable works of Diethelm, Ford, and Freed [4–8]. Recently, applications have included classes of nonlinear fractional differential equations [9] and their numerical solutions have been established by Diethelm and Ford [10].

The fractional derivative models are used for accurate modeling of those systems that require accurate modeling of damping. It has been shown that fractional derivative models describe very well the frequency-dependent damping behavior of materials and systems [11–13]. Koeller [14] considered a fractional derivative model to obtain expressions for creep and relaxation functions for viscoelastic materials. Mbodje et al. [15] presented a linear-quadratic optimal control of a rod whose damping mechanism was described in terms of fractional derivatives. Makris and Constantinou [16] presented a fractional-derivative Maxwell model for viscous dampers and validated their model using experimental results. They also presented some analytical results for a fractionally damped single-degree-of-freedom system. Techniques based on fractional derivative to model damping behavior of materials and systems have also been considered by Shen and Soong [17], Pritz [18], and Papoulia and Kelly [19].

Several methods have been proposed to find the response of a fractionally damped system. These methods include Laplace transform [12,13,20–22], Fourier transform [20,23,24] and numerical methods [25,26]. It has been seen that in the above works, the Laplace transform method requires the numerical evaluation of an improper integral and Fourier transform method also requires a numerical implementation, either via an fast Fourier transform or numerical integration. Although recently Suarez and Shokooh [27] presented an eigenvector expansion method for the solution of motion containing fractional derivatives of order 1/2, in the present analysis an attempt has been made to obtain the solution by a different method.

In this paper, we use the Adomian decomposition method [28,29] to obtain a solution for dynamic analysis of a single-degree-of-freedom spring-mass-damper system whose damping is described by a fractional derivative of order 1/2. Large classes of linear and nonlinear differential equations, both ordinary as well as partial, can be solved by the Adomian decomposition method [28–35]. A reliable modification of Adomian decomposition method has been done by Wazwaz [36]. The decomposition

Contributed by the Applied Mechanics Division of THE AMERICAN SOCIETY OF MECHANICAL ENGINEERS for publication in the ASME JOURNAL OF APPLIED MECHANICS. Manuscript received by the Applied Mechanics Division, March 12, 2004; final revision, August 23, 2004. Associate Editor: O. O'Reilly. Discussion on the paper should be addressed to the Editor, Prof. Robert M. McMeeking, Journal of Applied Mechanics, Department of Mechanical and Environmental Engineering, University of California—Santa Barbara, Santa Barbara, CA 93106-5070, and will be accepted until four months after final publication in the paper itself in the ASME JOURNAL OF APPLIED MECHANICS.

method provides an effective procedure for analytical solution of a wide and general class of dynamical systems representing real physical problems [29–32]. Recently, the implementations of the Adomian decomposition method for the solutions of generalized regularized long-wave and Korteweg–de Vries equations have been well established by the notable researchers [37–40]. This method efficiently works for initial-value or boundary-value problems and for linear or nonlinear, ordinary or partial differential equations, and even for stochastic systems. Moreover, we have the advantage of a single global method for solving ordinary or partial differential equations as well as many types of other equations. Recently, the solution of fractional differential equation has been obtained through the Adomian decomposition method by the researchers [41–45]. The application of the Adomian decomposition method for the solution of nonlinear fractional differential equations has also been established by Shawagfeh [44].

2 Mathematical Aspects

2.1 Mathematical Definition. The mathematical definition of fractional calculus has been the subject of several different approaches [1,3]. The most frequently encountered definition of an integral of fractional order is the Riemann-Liouville integral, in which the fractional order integral is defined as

$$\frac{d^{-q}f(x)}{dx^{-q}}=\frac{1}{\Gamma(q)}\int_0^x\frac{f(t)dt}{(x-t)^{1-q}} \tag{2.1.1}$$

while the definition of fractional order derivative is

$$\frac{d^{q}f(x)}{dx^{q}}=\frac{d^{n}}{dx^{n}}\left(\frac{d^{-(n-q)}f(x)}{dx^{-(n-q)}}\right)=\frac{1}{\Gamma(n-q)}\frac{d^{n}}{dx^{n}}\int_0^x\frac{f(t)dt}{(x-t)^{1-n+q}} \tag{2.1.2}$$

where q ($q>0$ *and* $q\in\mathbf{R}$) is the order of the operation and n is an integer that satisfies $n-1\leqslant q<n$.

2.2 Definition: Mittag-Leffler Function. A two-parameter function of the Mittag-Leffler type is defined by the series expansion [3]

$$E_{\alpha,\beta}(z)=\sum_{k=0}^{\infty}\frac{z^k}{\Gamma(\alpha k+\beta)},\quad(\alpha>0,\beta>0) \tag{2.2.1}$$

2.3 The Decomposition Method. Let us discuss a brief outline of the Adomian decomposition method, in general. For this, let us consider an equation in the form

$$Lu+Ru+Nu=g \tag{2.3.1}$$

where L is an easily or trivially invertible linear operator, R is the remaining linear part, and N represents a nonlinear operator.

The general solution of the given equation is decomposed into the sum

$$u=\sum_{n=0}^{\infty}u_n \tag{2.3.2}$$

where u_0 is the complete solution of $Lu=g$.

From Eq. (2.3.1), we can write

$$Lu=g-Ru-Nu$$

Because L is invertible, an equivalent expression is

$$L^{-1}Lu=L^{-1}g-L^{-1}Ru-L^{-1}Nu$$

For initial-value problems, we conveniently define L^{-1} for $L\equiv d^n/dt^n$ as the n-fold definite integration operator from 0 to t. For the operator $L\equiv d^2/dt^2$, for example, we have $L^{-1}Lu=u-u(0)-tu'(0)$, and therefore

$$u=u(0)+tu'(0)+L^{-1}g-L^{-1}Ru-L^{-1}Nu \tag{2.3.3}$$

For boundary-value problems (and, if desired, for initial-value problems as well), indefinite integrations are used and the constants are evaluated from the given conditions. Solving for u yields

$$u=A+Bt+L^{-1}g-L^{-1}Ru-L^{-1}Nu \tag{2.3.4}$$

The first three terms in Eq. (2.3.3) or (2.3.4) are identified as u_0 in the assumed decomposition $u=\Sigma_{n=0}^{\infty}u_n$. Finally, assuming Nu is analytic, we write $Nu=\Sigma_{n=0}^{\infty}A_n(u_0,u_1,u_2,\ldots,u_n)$ where A_n's are special set of polynomials obtained for the particular nonlinearity $Nu=f(u)$ and were generated by Adomian [28,29]. These A_n polynomials depend, of course, on the particular nonlinearity.

The A_n's are given as

$$A_0=f(u_0)$$

$$A_1=u_1(d/du_0)f(u_0)$$

$$A_2=u_2(d/du_0)f(u_0)+(u_1^2/2!)(d^2/du_0^2)f(u_0)$$

$$A_3=u_3(d/du_0)f(u_0)+u_1u_2(d^2/du_0^2)f(u_0)+(u_1^3/3!)\times(d^3/du_0^3)f(u_0)$$

$$\cdots$$

and can be found from the formula (for $n\geqslant 1$)

$$A_n=\sum_{\nu=1}^{n}c(\nu,n)f^{(\nu)}(u_0) \tag{2.3.5}$$

where the $c(\nu,n)$ are products (or sums of products) of ν components of u whose subscripts sum to n, divided by the factorial of the number of repeated subscripts [29].

Recently, the Adomian decomposition method is reviewed and a mathematical model of Adomian polynomials is introduced [46,47].

Therefore, the general solution becomes

$$u=u_0-L^{-1}R\sum_{n=0}^{\infty}u_n-L^{-1}Nu \tag{2.3.6}$$

$$=u_0-L^{-1}R\sum_{n=0}^{\infty}u_n-L^{-1}\sum_{n=0}^{\infty}A_n \tag{2.3.7}$$

where

$$u_0=\phi+L^{-1}g\quad\text{and}\quad L\phi=0 \tag{2.3.8}$$

so that

$$u_{n+1}=-L^{-1}Ru_n-L^{-1}A_n,\quad n\geqslant 0 \tag{2.3.9}$$

Using the known u_0, all components u_1, u_2, $\ldots$, u_n, $\ldots$, etc. are determinable by using Eq. (2.3.9). Substituting these u_0, u_1, u_2, $\ldots$, u_n, $\ldots$, etc. in Eq. (2.3.2), u is obtained.

Convergence of this method has been rigorously established by Cherruault [48], Abbaoui and Cherruault [49,50], and Himoun, Abbaoui, and Cherruault [51].

3 Fractional Dynamic Model and the Solution

To develop an analytical scheme for a fractionally damped model, let us consider a single-degree-of-freedom spring-mass-damper system whose dynamics is described by the following fractional differential equation:

$$mD_t^2x(t)+cD_t^{1/2}x(t)+kx(t)=f(t) \tag{3.1}$$

where m, c, and k represent the mass, damping, and stiffness coefficients, respectively, $f(t)$ is the externally applied force, and $D_t^{1/2}x(t)$ is the fractional derivative of order 1/2 of the displacement $x(t)$.

It is well known that selection of an appropriate set of initial conditions for fractional differential equations is a particular issue.

Lorenzo and Hartley have treated the issue of initializations in several papers wherein they formulated the problem correctly, analyzed the effect of a wrong initialization, and proposed solutions [52–54].

To follow the previous authors Suarez and Shokooh [27], in the present analysis, we will assume homogeneous initial conditions that correspond to the equilibrium state at the beginning of a dynamical process:

$$x(0)=0 \quad \text{and} \quad D_t x(t)|_{t=0}=0 \tag{3.2}$$

Homogeneous initial conditions have been taken as we are pursuing the paper of Suarez and Shokooh [27] to compare their solutions with those obtained by the Adomian decomposition method.

We adopt the Adomian decomposition method for solving Eq. (3.1) under homogeneous conditions (3.2). In the light of this method, we assume that $x(t)=x_0(t)+x_1(t)+x_2(t)+\ldots$ to be the solution of Eq. (3.1).

Now, Eq. (3.1) can be written as

$$\frac{d^2x(t)}{dt^2}+\frac{c}{m}\frac{d^{1/2}x(t)}{dt^{1/2}}+\frac{k}{m}x(t)=\frac{f(t)}{m} \tag{3.3}$$

Let us suppose that $L\equiv d^2/dt^2$, which is an easily invertible linear operator.

Now, comparing Eq. (3.3) and Eq. (2.3.1), we can observe that $d^{1/2}/dt^{1/2}$ in Eq. (3.3) represents the remaining linear operator, and the nonlinear part Nx, fortunately linear in this case, is $(k/m)x(t)$.

Therefore,

$$Nx=f(x)=\sum_{n=0}^{\infty}A_n(x_0,x_1,\ldots,x_n)=\frac{k}{m}x \tag{3.4}$$

The Adomian polynomials A_n, as discussed in subsection 2.3, become in the present case

$$A_0=f(x_0)=\frac{k}{m}x_0$$

$$A_1=x_1\frac{df(x_0)}{dx_0}=\frac{k}{m}x_1$$

$$A_2=x_2\frac{df(x_0)}{dx_0}+(x_1^2/2!)\frac{d^2f(x_0)}{dx_0^2}=\frac{k}{m}x_2$$

$$A_3=x_3\frac{df(x_0)}{dx_0}+x_1x_2\frac{d^2f(x_0)}{dx_0^2}+(x_1^3/3!)\frac{d^3f(x_0)}{dx_0^3}=\frac{k}{m}x_3$$

and so on.

Therefore, by the Adomian decomposition method, we can write

$$\begin{aligned}x(t)&=x(0)+tD_tx(t)|_{t=0}+\frac{1}{m}L^{-1}f(t)\\&\quad-L^{-1}\left(\frac{c}{m}D_t^{1/2}\left(\sum_{n=0}^{\infty}x_n(t)\right)\right)-L^{-1}\sum_{n=0}^{\infty}A_n \qquad (3.5)\\&=\frac{1}{m}L^{-1}f(t)-\frac{c}{m}L^{-1}\left(D_t^{1/2}\left(\sum_{n=0}^{\infty}x_n(t)\right)\right)\\&\quad-L^{-1}\left(\sum_{n=0}^{\infty}\frac{k}{m}x_n(t)\right) \qquad (3.6)\end{aligned}$$

This implies that

$$\begin{aligned}x(t)&=\frac{1}{m}\frac{d^{-2}}{dt^{-2}}f(t)-\frac{c}{m}\frac{d^{-3/2}}{dt^{-3/2}}\left(\sum_{n=0}^{\infty}x_n(t)\right)\\&\quad-\frac{k}{m}\frac{d^{-2}}{dt^{-2}}\left(\sum_{n=0}^{\infty}x_n(t)\right)\end{aligned} \tag{3.7}$$

where

$$x_0(t)=\frac{1}{m}\frac{d^{-2}}{dt^{-2}}f(t)$$

$$x_1(t)=-\frac{c}{m}\frac{d^{-3/2}x_0(t)}{dt^{-3/2}}-\frac{k}{m}\frac{d^{-2}x_0(t)}{dt^{-2}}$$

$$x_2(t)=-\frac{c}{m}\frac{d^{-3/2}x_1(t)}{dt^{-3/2}}-\frac{k}{m}\frac{d^{-2}x_1(t)}{dt^{-2}}$$

$$x_3(t)=-\frac{c}{m}\frac{d^{-3/2}x_2(t)}{dt^{-3/2}}-\frac{k}{m}\frac{d^{-2}x_2(t)}{dt^{-2}}$$

and so on.

Therefore, the general solution of Eq. (3.1) is

$$\begin{aligned}x(t)&=\frac{1}{m}\frac{d^{-2}}{dt^{-2}}f(t)-\frac{c}{m}\left[\frac{d^{-3/2}x_0(t)}{dt^{-3/2}}+\frac{d^{-3/2}x_1(t)}{dt^{-3/2}}+\frac{d^{-3/2}x_2(t)}{dt^{-3/2}}\right.\\&\quad\left.+\frac{d^{-3/2}x_3(t)}{dt^{-3/2}}+\cdots\right]-\frac{k}{m}\left[\frac{d^{-2}x_0(t)}{dt^{-2}}+\frac{d^{-2}x_1(t)}{dt^{-2}}\right.\\&\quad\left.+\frac{d^{-2}x_2(t)}{dt^{-2}}+\frac{d^{-2}x_3(t)}{dt^{-2}}+\cdots\right]\end{aligned} \tag{3.8}$$

4 Step Function Response

At first let us examine the response of an initially stationary oscillator subject to an excitation of the form $f(t)=Au(t)$, where $u(t)$ is the Heaviside function and A is a constant, for Eq. (3.1). We will then obtain

$$x_0(t)=\frac{1}{m}\frac{d^{-2}}{dt^{-2}}f(t)=\frac{At^2}{2m}$$

$$x_1(t)=-\frac{c}{m}\frac{d^{-3/2}x_0(t)}{dt^{-3/2}}-\frac{k}{m}\frac{d^{-2}x_0(t)}{dt^{-2}}=-\frac{cA}{m^2}\frac{t^{7/2}}{\Gamma(\frac{9}{2})}-\frac{kA}{m^2}\frac{t^4}{\Gamma(5)}$$

$$\begin{aligned}x_2(t)&=-\frac{c}{m}\frac{d^{-3/2}x_1(t)}{dt^{-3/2}}-\frac{k}{m}\frac{d^{-2}x_1(t)}{dt^{-2}}=\frac{c^2A}{m^3}\frac{t^5}{\Gamma(6)}\\&\quad+\frac{2kcA}{m^3}\frac{t^{11/2}}{\Gamma(\frac{13}{2})}+\frac{k^2A}{m^3}\frac{t^6}{\Gamma(7)}\end{aligned}$$

$$\begin{aligned}x_3(t)&=-\frac{c}{m}\frac{d^{-3/2}x_2(t)}{dt^{-3/2}}-\frac{k}{m}\frac{d^{-2}x_2(t)}{dt^{-2}}=-\frac{c^3A}{m^4}\frac{t^{13/2}}{\Gamma(\frac{15}{2})}\\&\quad-\frac{3kc^2A}{m^4}\frac{t^7}{\Gamma(8)}-\frac{3k^2Ac}{m^4}\frac{t^{15/2}}{\Gamma(\frac{17}{2})}-\frac{k^3A}{m^4}\frac{t^8}{\Gamma(9)}\end{aligned}$$

$$x_4(t)=-\frac{c}{m}\frac{d^{-3/2}x_3(t)}{dt^{-3/2}}-\frac{k}{m}\frac{d^{-2}x_3(t)}{dt^{-2}}=\frac{c^4A}{m^5}\frac{t^8}{\Gamma(9)}+\frac{4kc^3A}{m^5}\frac{t^{17/2}}{\Gamma(\frac{19}{2})}+\frac{6k^2c^2A}{m^5}\frac{t^9}{\Gamma(10)}+\frac{4k^3cA}{m^5}\frac{t^{19/2}}{\Gamma(\frac{21}{2})}+\frac{k^4A}{m^5}\frac{t^{10}}{\Gamma(11)}$$

and so on.

Therefore, the solution (3.8) becomes

$$x(t)=\frac{A}{m}\sum_{r=0}^{\infty}\frac{(-1)^r}{r!}\left(\frac{k}{m}\right)^r t^{2(r+1)}\sum_{j=0}^{\infty}\left(\frac{-c}{m}\right)^j\frac{(j+r)!t^{3j/2}}{j!\Gamma\left(\frac{3j}{2}+2r+3\right)}=\frac{A}{m}\sum_{r=0}^{\infty}\frac{(-1)^r}{r!}\left(\frac{k}{m}\right)^r t^{2(r+1)}E^{(r)}_{3/2,r/2+3}\left(\frac{-c}{m}t^{3/2}\right) \tag{4.1}$$

where $E_{\lambda,\mu}(z)$ is the Mittag-Leffler function in two parameters:

$$E^{(r)}_{\lambda,\mu}(y)\equiv\frac{d^r}{dy^r}E_{\lambda,\mu}(y)=\sum_{j=0}^{\infty}\frac{(j+r)!y^j}{j!\Gamma(\lambda j+\lambda r+\mu)},\quad (r=0,1,2,\ldots)$$

5 Impulse Response

As a second example, let us now examine the response of the oscillator to a unit impulse load $f(t)=\delta(t)$, where $\delta(t)$ is the unit impulse function. Here we will obtain

$$x_0(t)=\frac{1}{m}\frac{d^{-2}}{dt^{-2}}f(t)=\frac{t}{m}$$

$$x_1(t)=-\frac{c}{m}\frac{d^{-3/2}x_0(t)}{dt^{-3/2}}-\frac{k}{m}\frac{d^{-2}x_0(t)}{dt^{-2}}=-\frac{c}{m^2}\frac{t^{5/2}}{\Gamma(\frac{7}{2})}-\frac{k}{m^2}\frac{t^3}{\Gamma(4)}$$

$$x_2(t)=-\frac{c}{m}\frac{d^{-3/2}x_1(t)}{dt^{-3/2}}-\frac{k}{m}\frac{d^{-2}x_1(t)}{dt^{-2}}=\frac{c^2}{m^3}\frac{t^4}{\Gamma(5)}+\frac{2kc}{m^3}\frac{t^{9/2}}{\Gamma(\frac{11}{2})}+\frac{k^2}{m^3}\frac{t^5}{\Gamma(6)}$$

$$x_3(t)=-\frac{c}{m}\frac{d^{-3/2}x_2(t)}{dt^{-3/2}}-\frac{k}{m}\frac{d^{-2}x_2(t)}{dt^{-2}}=-\frac{c^3}{m^4}\frac{t^{11/2}}{\Gamma(\frac{13}{2})}-\frac{3kc^2}{m^4}\frac{t^6}{\Gamma(7)}-\frac{3k^2c}{m^4}\frac{t^{13/2}}{\Gamma(\frac{15}{2})}-\frac{k^3}{m^4}\frac{t^7}{\Gamma(8)}$$

$$x_4(t)=-\frac{c}{m}\frac{d^{-3/2}x_3(t)}{dt^{-3/2}}-\frac{k}{m}\frac{d^{-2}x_3(t)}{dt^{-2}}=\frac{c^4}{m^5}\frac{t^7}{\Gamma(8)}+\frac{4kc^3}{m^5}\frac{t^{15/2}}{\Gamma(\frac{17}{2})}+\frac{6k^2c^2}{m^5}\frac{t^8}{\Gamma(9)}+\frac{4k^3c}{m^5}\frac{t^{17/2}}{\Gamma(\frac{19}{2})}+\frac{k^4}{m^5}\frac{t^9}{\Gamma(10)}$$

and so on.

Therefore, the solution (3.8) becomes

$$x(t)=\frac{1}{m}\sum_{r=0}^{\infty}\frac{(-1)^r}{r!}\left(\frac{k}{m}\right)^r t^{2r+1}\sum_{j=0}^{\infty}\left(\frac{-c}{m}\right)^j\frac{(j+r)!t^{3j/2}}{j!\Gamma\left(\frac{3j}{2}+2r+2\right)}=\frac{1}{m}\sum_{r=0}^{\infty}\frac{(-1)^r}{r!}\left(\frac{k}{m}\right)^r t^{2r+1}E^{(r)}_{3/2,r/2+2}\left(\frac{-c}{m}t^{3/2}\right) \tag{5.1}$$

where $E_{\lambda,\mu}(z)$ is the Mittag-Leffler function in two parameters,

$$E^{(r)}_{\lambda,\mu}(y)\equiv\frac{d^r}{dy^r}E_{\lambda,\mu}(y)=\sum_{j=0}^{\infty}\frac{(j+r)!y^j}{j!\Gamma(\lambda j+\lambda r+\mu)},\quad (r=0,1,2,\ldots)$$

The solutions (4.1) and (5.1) agree with the solution obtained by Podlubny [3] using a fractional Green's function.

6 Verification of the Solutions

The fractional Green's function discussed by Podlubny [[3], Section 5.4] for the fractional differential Equation (3.1) is

$$G_3(t)=\frac{1}{m}\sum_{r=0}^{\infty}\frac{(-1)^r}{r!}\left(\frac{k}{m}\right)^r t^{2r+1}E^{(r)}_{3/2,r/2+2}\left(\frac{-c}{m}t^{3/2}\right)$$

Therefore, the solution of Eq. (3.1) under homogeneous initial conditions is

$$x(t)=\int_0^t G_3(t-\tau)f(\tau)d\tau$$

This implies that

$$x(t)=\frac{A}{m}\sum_{r=0}^{\infty}\frac{(-1)^r}{r!}\left(\frac{k}{m}\right)^r t^{2(r+1)}E^{(r)}_{3/2,r/2+3}\left(\frac{-c}{m}t^{3/2}\right),\quad \text{if } f(t)=Au(t) \tag{6.1}$$

$$=\frac{1}{m}\sum_{r=0}^{\infty}\frac{(-1)^r}{r!}\left(\frac{k}{m}\right)^r t^{2r+1}E^{(r)}_{3/2,r/2+2}\left(\frac{-c}{m}t^{3/2}\right),\quad \text{if } f(t)=\delta(t) \tag{6.2}$$

The solutions (6.1) and (6.2) are exactly identical with the solutions in Eq. (4.1) and Eq. (5.1).

7 Numerical Results and Discussions

To make a comparison of the present analysis through the Adomain decomposition method with that of other available method [27], the graphs have been drawn using MATLAB software.

In the present numerical computation, we have assumed $c/m=2\eta\omega_n^{3/2}$, $\omega_n^2=k/m$, and $m=1$, where η is the damping ratio and ω_n is the natural frequency, as is taken in [27].

It is interesting to note that the graphs obtained in our case exactly coincide with those of Suarez and Shokooh [27] in cases of Figs. 1 and 4. In the present analysis, Fig. 2 also coincides with that of Suarez and Shokooh [27], but in this case the natural frequency ω_n should be 5 rad/s, instead of 10 rad/s, as taken by Suarez and Shokooh [27].

It may be mentioned in this connection that the graph drawn in Fig. 2 of Suarez and Shokooh [27] for $\omega_n=10$ rad/s should be for $\omega_n=5$ rad/s. This is definitely a mistake to be reckoned with and should be taken into account for further study. However, the corresponding graph for $\omega_n=10$ rad/s is also drawn by us and given in Fig. 3.

Equation (5.1) has been used to calculate the impulse response functions shown in Fig. 1 for oscillators with natural frequency $\omega_n=10$ rad/s and damping ratios $\eta=0.05$, 0.5, and 1.

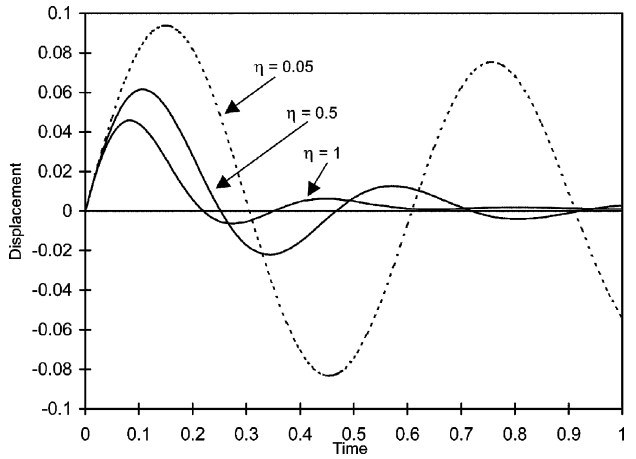

Fig. 1 Impulse response function for oscillators with natural frequency $\omega_n = 10$ rad/s and damping ratios $\eta = 0.05$, 0.5, and 1

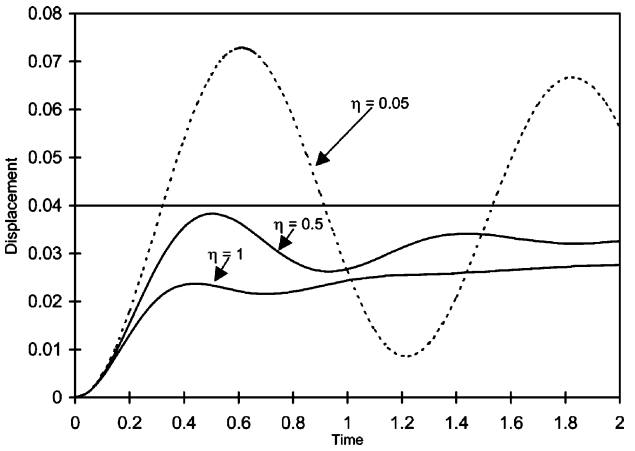

Fig. 4 Unit step response function for oscillators with natural frequency $\omega_n = 5$ rad/s and damping ratios $\eta = 0.05$, 0.5, and 1

Figure 2 shows the impulse response function for an oscillator with natural frequency $\omega_n = 5$ rad/s and damping ratios $\eta = \sqrt{\pi}$, 3, and 5, and it has been drawn with the help of Eq. (5.1).

The graph drawn in Fig. 2 of Suarez and Shokooh [27] for $\omega_n = 10$ rad/s should be for $\omega_n = 5$ rad/s., Figure 3 in the present study confirms our assertion. Figure 3 shows the impulse response function for an oscillator with natural frequency $\omega_n = 10$ rad/s and damping ratios $\eta = \sqrt{\pi}$, 3, and 5. Here, Eq. (5.1) has also been used to draw the following figure.

It can be noted that, when the damping ratio is equal to $\sqrt{\pi}$, the curves in Figs. 2 and 3 touch the axis of zero displacement. In addition, the curves in Figs. 2 and 3 tend to zero without crossing the axis of zero displacement for damping ratios greater than $\sqrt{\pi}$.

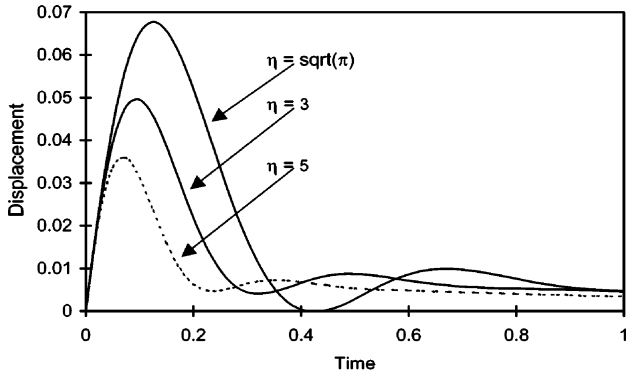

Fig. 2 Impulse response function for oscillators with natural frequency $\omega_n = 5$ rad/s and damping ratios $\eta = \text{sqrt}(\pi)$, 3, and 5

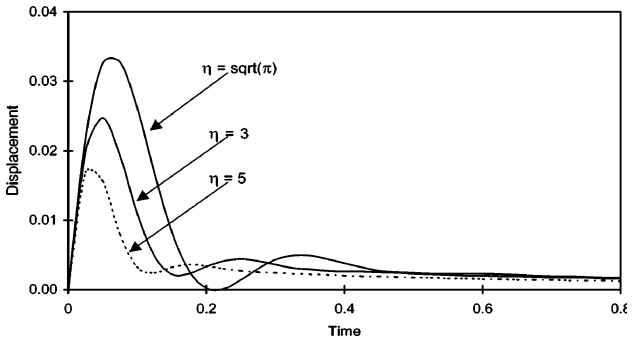

Fig. 3 Impulse response function for oscillators with natural frequency $\omega_n = 10$ rad/s and damping ratios $\eta = \text{sqrt}(\pi)$, 3, and 5

Consequently, the value $\eta = \sqrt{\pi}$ is considered as the *critical damping ratio*. Moreover, one can easily verify the validity of Fig. 3 by observing Fig. 1. From these two figures, we see that with natural frequency $\omega_n = 10$ rad/s, as damping ratio η increases from 0.05 to 5, the axis of zero displacement tends to become the asymptote of the curves. In other words, with natural frequency $\omega_n = 10$ rad/s, as damping ratio η increases, the displacement decreases and finally tends to the axis of zero displacement with the increase of time.

In the next numerical example, three oscillators with natural frequency of $\omega_n = 5$ rad/s and damping ratios $\eta = 0.05$, 0.5, and 1 are subjected to a step load magnitude $A = 1$. In this case, Eq. (4.1) has been utilized to draw Fig. 4. This figure shows the displacement response of the oscillators. It shows that the curves for $\eta = 0.5$ and 1 do not exhibit oscillations around the static equilibrium response $A/\omega_n^2 = 0.04$ and the same result was obtained by Suarez and Shokooh [27].

8 Conclusion

This present analysis exhibits the applicability of the decomposition method to solve fractional differential equation of fractional order 1/2. In this work we demonstrate that this method is well suited to solve linear fractional differential equations. The decomposition method is straightforward, without restrictive assumptions, and the components of the series solution can be easily computed using any mathematical symbolic package. Moreover, this method does not change the problem into a convenient one for the use of linear theory. It, therefore, provides more realistic series solutions that generally converge very rapidly in real physical problems. When solutions are computed numerically, the rapid convergence is obvious. Moreover, no linearization or perturbation is required. It can avoid the difficulty of finding the inverse of Laplace transform and can reduce the labor of the perturbation method. This paper presents an analytical scheme to obtain the dynamic response of a fractionally damped system. Although other methods (as already mentioned) are available in open literature, the present Adomian decomposition method justifies its efficiency and gives quite satisfactory results.

Acknowledgment

We take this opportunity to express our sincere thanks and gratitude to the learned reviewers for their valuable comments and suggestions for the improvement of the paper.

References

[1] Oldham, K. B., and Spanier, J., 1974, *The Fractional Calculus*, Academic, New York.

[2] Miller, K. S., and Ross, B., 1993, *An Introduction to the Fractional Calculus and Fractional Differential Equations*, John Wiley and Sons, New York.
[3] Podlubny, I., 1999, *Fractional Differential Equations*, Academic Press, San Diego.
[4] Diethelm, K., 1997, "An Algorithm for the Numerical Solution of Differential Equations of Fractional Order," Elec. Transact. Numer. Anal., **5**, pp. 1–6.
[5] Diethelm, K., and Freed, A. D., 1999, "The FracPECE Subroutine for the Numerical Solution of Differential Equations of Fractional Order," No. 52 in GWDG-Berichte, *Forschung und wissenschaftliches Rechnen: Beiträge zum Heinz-Billing-Preis 1998*, S. Heinzel and T. Plesser, eds., Gesellschaft für wissenschaftliche Datenverarbeitung, Göttingen, pp. 57–71.
[6] Diethelm, K., and Ford, N. J., 2002, "Analysis of Fractional Differential Equations," J. Math. Anal. Appl., **265**, pp. 229–248.
[7] Diethelm, K., Ford, N. J., and Freed, A. D., 2002, "A Predictor-Corrector Approach for the Numerical Solution of Fractional Differential Equations," Nonlinear Dyn., **29**, pp. 3–22.
[8] Diethelm, K., and Ford, N. J., 2002, "Numerical Solution of the Bagley-Torvik Equation," Bit Numer. Math., **42**(3), pp. 490–507.
[9] Diethelm, K., and Ford, A. D., 1999, "On the Solution of Nonlinear Fractional-Order Differential Equations Used in the Modeling of Viscoplasticity," *Scientific Computing in Chemical Engineering II. Computational Fluid Dynamics, Reaction Engineering, and Molecular Properties*, F. Keil, W. Mackens, H. Voß, and J. Werther, eds., Springer-Verlag, Heidelberg, pp. 217–224.
[10] Diethelm, K., and Ford, N. J., 2001, "The Numerical Solution of Linear and Nonlinear Fractional Differential Equations Involving Fractional Derivatives of Several Orders," Numerical Analysis Report No. 379, Manchester Center for Computational Mathematics, Manchester, England.
[11] Bagley, R. L., and Torvik, P. J., 1983, "A Theoretical Basis for the Application of Fractional Calculus to Viscoelasticity," J. Rheol., **27**(3), pp. 201–210.
[12] Bagley, R. L., and Torvik, P. J., 1983, "Fractional Calculus-A Different Approach to the Analysis Viscoelastically Damped Structures," AIAA J., **21**(5), pp. 741–748.
[13] Bagley, R. L., and Torvik, P. J., 1985, "Fractional Calculus in the Transient Analysis of Viscoelastically Damped Structures," AIAA J., **23**(6), pp. 918–925.
[14] Koeller, R. C., 1984, "Application of Fractional Calculus to the Theory of Viscoelasticity," ASME J. Appl. Mech., **51**, pp. 299–307.
[15] Mbodje, B., Montseny, C., Audounet, J., and Benchimol, P., 1994, "Optimal Control for Fractionally Damped Flexible Systems," *The Proceedings of the Third IEEE Conference on Control Applications*, August 24–26, The University of Strathclyde, Glasgow, pp. 1329–1333.
[16] Makris, N., and Constaninou, M. C., 1991, "Fractional Derivative Maxwell Model for Viscous Dampers," J. Struct. Eng., **117**(9), pp. 2708–2724.
[17] Shen, K. L., and Soong, T. T., 1995, "Modeling of Viscoelastic Dampers for Structural Applications," J. Eng. Mech., **121**, pp. 694–701.
[18] Pritz, T., 1996, "Analysis of Four-Parameter Fractional Derivative Model of Real Solid Materials," J. Sound Vib., **195**, pp. 103–115.
[19] Papoulia, K. D., and Kelly, J. M., 1997, "Visco-Hyperelastic Model for Filled Rubbers Used in Vibration Isolation," ASME J. Eng. Mater. Technol., **119**, pp. 292–297.
[20] Shokooh, A., and Suarez, L., 1994, "On the Fractional Derivative Modeling of Damping Materials," Technical Report presented for NASA Langley, College of Engineering, University of Puerto Rica, Mayaguez, PR.
[21] Suarez, L. E., and Shokooh, A., 1995, "Response of Systems With Damping Materials Modeled Using Fractional Calculus," ASME J. Appl. Mech. Rev., **48**(11), Part 2, pp. S118–S127.
[22] Suarez, L., Shokooh, A., and Arroyo, J., 1995, "Finite Element Analysis of Damping Materials Modeled by the Fractional Derivative Method," Technical Report presented for NASA Langley, College of Engineering, University of Puerto Rico, Mayaguez, PR.
[23] Gaul, L., Klein, P., and Kemple, S., 1989, "Impulse Response Function of an Oscillator With Fractional Derivative in Damping Description," Mech. Res. Commun., **16**(5), pp. 297–305.
[24] Gaul, L., Klein, P., and Kemple, S., 1991, "Damping Description Involving Fractional Operators," Mech. Syst. Signal Process., **5**(2), pp. 8–88.
[25] Koh, C. G., and Kelly, J. M., 1990, "Application of Fractional Derivatives to Seismic Analysis of Base-Isolated Models," Earthquake Eng. Struct. Dyn., **19**, pp. 229–241.
[26] Padovan, J., 1987, "Computational Algorithms for Finite Element Formulation Involving Fractional Operators," Comput. Mech., **2**, pp. 271–287.
[27] Suarez, L. E., and Shokooh, A., 1997, "An Eigenvector Expansion Method for the Solution of Motion Containing Fractional Derivatives," ASME J. Appl. Mech., **64**, pp. 629–635.
[28] Adomian, G., 1989, *Nonlinear Stochastic Systems Theory and Applications to Physics*, Kluwer Academic, Netherlands.
[29] Adomian, G., 1994, *Solving Frontier Problems of Physics: The Decomposition Method*, Kluwer Academic, Boston.
[30] Adomian, G., 1991, "An Analytical Solution of the Stochastic Navier-Stokes System," Found. Phys., **21**(7), pp. 831–843.
[31] Adomian, G., and Rach, R., 1991, "Linear and Nonlinear Schrödinger Equations," Found. Phys., **21**, pp. 983–991.
[32] Adomian, G., 1994, "Solution of Physical Problems by Decomposition," Comput. Math. Appl., **27**, Nos. 9/10, pp. 145–154.
[33] Adomian, G., 1998, "Solutions of Nonlinear P.D.E.," Appl. Math. Lett., **11**(3), pp. 121–123.
[34] Abbaoui, K., and Cherruault, Y., 1999, "The Decomposition Method Applied to the Cauchy Problem," Kybernetes, **28**(1), pp. 68–74.
[35] Kaya, D., and Yokus, A., 2002, "A Numerical Comparison of Partial Solutions in the Decomposition Method for Linear and Nonlinear Partial Differential Equations," Math. Comput. Simul., **60**(6), pp. 507–512.
[36] Wazwaz, A., 1999, "A Reliable Modification of Adomian Decomposition Method," Appl. Math. Comput., **102**(1), pp. 77–86.
[37] Kaya, D., and El-Sayed, S. M., 2003, "On a Generalized Fifth Order KdV Equations," Phys. Lett. A, **310**(1), pp. 44–51.
[38] Kaya, D., and El-Sayed, S. M., 2003, "An Application of the Decomposition Method for the Generalized KdV and RLW Equations," Chaos, Solitons, Fractals, , **17**(5), pp. 869–877.
[39] Kaya, D., 2003, "An Explicit and Numerical Solutions of Some Fifth-Order KdV Equation by Decomposition Method," Appl. Math. Comput., **144**(2/3), pp. 353–363.
[40] Kaya, D., 2004, "A Numerical Simulation of Solitary-Wave Solutions of the Generalized Regularized Long-Wave Equation," Appl. Math. Comput., **149**(3), pp. 833–841.
[41] George, A. J., and Chakrabarti, A., 1995, "The Adomian Method Applied to Some Extraordinary Differential Equations," Appl. Math. Lett., **8**(3), pp. 91–97.
[42] Arora, H. L., and Abdelwahid, F. I., 1993, "Solutions of Non-Integer Order Differential Equations Via the Adomian Decomposition Method," Appl. Math. Lett., **6**(1), pp. 21–23.
[43] Shawagfeh, N. T., 1999, "The Decomposition Method for Fractional Differential Equations," J. Fractional Calculus, **16**, pp. 27–33.
[44] Shawagfeh, N. T., 2002, "Analytical Approximate Solutions for Nonlinear Fractional Differential Equations," Appl. Math. Comput., **131**, pp. 517–529.
[45] Saha Ray, S., and Bera, R. K., 2004, "Solution of an Extraordinary Differential Equation by Adomian Decomposition Method," J. Appl. Math., **4**, pp. 331–338.
[46] Seng, V., Abbaoui, K., and Cherruault, Y., 1996, "Adomian's Polynomials for Nonlinear Operators," Math. Comput. Modell., **24**(1), pp. 59–65.
[47] Abdelwahid, F., 2003, "A Mathematical Model of Adomian Polynomials," Appl. Math. Comput., **141**, pp. 447–453.
[48] Cherruault, Y., 1989, "Convergence of Adomian's Method," Kybernetes, **18**(2), pp. 31–38.
[49] Abbaoui, K., and Cherruault, Y., 1994, "Convergence of Adomian's Method Applied to Differential Equations," Comput. Math. Appl., **28**(5), pp. 103–109.
[50] Abbaoui, K., and Cherruault, Y., 1995, "New Ideas for Proving Convergence of Decomposition Methods," Comput. Math. Appl., **29**, pp. 103–108.
[51] Himoun, N., Abbaoui, K., and Cherruault, Y., 1999, "New Results of Convergence of Adomian's Method," Kybernetes, **28**(4), pp. 423–429.
[52] Lorenzo, C. F., and Hartley, T. T., 1998, "Initialisation Conceptualization, and Application in the Generalized Fractional Calculus," TM 1998-208415, NASA, NASA Center for Aerospace Information, 7121 Stadard Drive, Hanover, MD 21076.
[53] Lorenzo, C. F., and Hartley, T. T., 2000, "Initialised Fractional Calculus," Int. J. Appl. Math., **3**(3), pp. 249–265.
[54] Lorenzo, C. F., and Hartley, T. T., 2001, "Initialization in Fractional Order Systems," *Proceedings of the European Control Conference*, Porto, Portugal, pp. 1471–1476.

Journal of Applied Mechanics

Brief Note

A Brief Note is a short paper that presents a specific solution of technical interest in mechanics but which does not necessarily contain new general methods or results. A Brief Note should not exceed 2500 words *or equivalent* (a typical one-column figure or table is equivalent to 250 words; a one line equation to 30 words). Brief Notes will be subject to the usual review procedures prior to publication. After approval such Notes will be published as soon as possible. The Notes should be submitted to the Editor of the JOURNAL OF APPLIED MECHANICS. Discussions on the Brief Notes should be addressed to the Editorial Department, ASME International, Three Park Avenue, New York, NY 10016-5990, or to the Editor of the JOURNAL OF APPLIED MECHANICS. Discussions on Brief Notes appearing in this issue will be accepted until two months after publication. Readers who need more time to prepare a Discussion should request an extension of the deadline from the Editorial Department.

Buckling of a Thin Circular Plate Loaded by In-Plane Gravity

Z.-Q. Cheng

J. N. Reddy[1]
Distinguished Professor
e-mail: jnreddy@shakti.tamu.edu
Fellow ASME

Department of Mechanical Engineering, Texas A&M University, College Station, TX 77843-3123

Y. Xiang
School of Engineering and Indutrial Design, University of Western Sydney, Penrith South DC, NSW 1797, Australia

[DOI: 10.1115/1.1831293]

1 Introduction

Tejeda et al. [1] presented a new exact solution in a recent publication on a plane distortion study of the next generation ion-beam projection lithographic (IPL) masks. An IPL circular mask is supported by a relatively stiff frame and held in a vertical orientation during exposure to the ion beam [2]. It is typically made of silicon of 3.0 μm in thickness and of the order of 200 mm in diameter. The problem was modeled as a clamped circular membrane loaded by in-plane gravity, and an exact plane stress solution was derived [1].

The elastic distortions due to gravitational loading are negligible in most engineering applications. However, they can be significant in next generation IPL masks used for semiconductor device fabrication. Therefore, the plane stress solution [1] is of practical importance to accurately predict the IPL deformations in order to enhance the quality of the microcircuit to be manufactured.

While gravity plays an important role for in-plane deformation, it also becomes significant for out-of-plane deformation. This is especially the case for such a thin mask with a thickness-to-diameter ratio on the order of 10^{-5}. The in-plane gravity could be large enough to induce the mask in a buckling or postbuckling state. Thus, the plane stress solution is only valid within the prebuckling range and the mask would be in an unstable state beyond it. It is the purpose of this technical note to provide the limit of buckling by modeling the mask as a thin plate and studying its bending deformation under the in-plane stresses. As will be seen, for a silicon mask with thickness of 3.0 μm, the radius must be no more than 84.459 mm to prevent the mask from being in the buckling state. This provides designers a precaution that the plane stress solution [1] is subjected to a limit of buckling and beyond this limit either the mask is in an instable state or a nonlinear postbuckling analysis will have to be performed.

2 Buckling Solution

Because the plate is symmetric in its midplane, the plane stress deformation is decoupled from the bending deformation. Therefore, we can first deal with the plane stress deformation. A stress function approach in polar coordinates was adopted in [1]. In the present study, we use an alternative displacement approach in rectangular coordinates. As will be seen, this approach appears to be more straightforward and simpler.

For the specific problem of a clamped circular plate loaded by its in-plane gravity, we use a Cartesian coordinate system with the y-axis in the vertical direction. Assume that the in-plane displacement fields are

$$u=0, \quad v=k(x^2+y^2-R^2), \tag{1}$$

where u and v are the in-plane displacements in the x and y directions, respectively, R is the radius of the plate, and k is a constant to be determined. The displacements satisfy the boundary conditions for a rigidly clamped edge; i.e., $u=v=0$ at $r\equiv\sqrt{x^2+y^2}=R$. Using the plane stress constitutive relation for an isotropic material yields

$$\sigma_{xx}^0=\frac{2\nu E}{1-\nu^2}ky, \quad \sigma_{yy}^0=\frac{2E}{1-\nu^2}ky, \quad \sigma_{xy}^0=\frac{E}{1+\nu}kx, \tag{2}$$

where E is Young's modulus and ν is the Poisson ratio. The governing equations for a thin plate, held in a vertical orientation, are

$$\frac{\partial\sigma_{xx}^0}{\partial x}+\frac{\partial\sigma_{xy}^0}{\partial y}=0, \quad \frac{\partial\sigma_{xy}^0}{\partial x}+\frac{\partial\sigma_{yy}^0}{\partial y}-\rho g=0, \tag{3}$$

[1]To whom correspondence should be addressed.

Contributed by the Applied Mechanics Division of THE AMERICAN SOCIETY OF MECHANICAL ENGINEERS for publication in the ASME JOURNAL OF APPLIED MECHANICS. Manuscript received by the ASME Applied Mechanics Division, September 27, 2001, final revision, May 10, 2004. Associate Editor: N. Triantafyllidis.

Table 1 Convergence study of the buckling factor $\lambda = \rho g h R^3/D$ for a clamped circular plate subjected to in-plane gravity (ν=0.2)

Polynomial degree, p	Buckling factor, $\lambda = \rho g h R^3/D$
1	144.391
2	121.461
3	118.729
4	111.548
5	110.239
6	110.210
7	110.078
8	110.054
9	110.054
10	110.054

where ρg is the gravitational force in the vertical direction. The unknown constant k is determined by substituting Eq. (2) into Eq. (3) as

$$k = \frac{(1-\nu^2)\rho g}{(3-\nu)E}. \tag{4}$$

Thus, we complete the solution for the plane stress problem. Our approach yields exactly the same solution as given in [1]. Incidentally, with such a approach an exact solution could also be obtained for the plane stress problem of an elliptic thin plate made of an anisotropic material.

Having obtained the plane stress distribution, the bending deformation problem is in order. This is a buckling problem of a circular plate under the gravity. As is seen from Eq. (2), the stress distribution in the midplane of the plate varies. In particular, there are both stretching and compression deformations. Such a buckling problem differs from conventional buckling cases in which a constant in-plane loading is assumed. The governing equation for the bending deformation of the plate is (see Reddy [3])

$$\frac{\partial^2 M_{xx}}{\partial x^2} + 2\frac{\partial^2 M_{xy}}{\partial x \partial y} + \frac{\partial^2 M_{yy}}{\partial y^2} + h\frac{\partial}{\partial x}\left(\sigma^0_{xx}\frac{\partial w}{\partial x} + \sigma^0_{xy}\frac{\partial w}{\partial y}\right) + h\frac{\partial}{\partial y}\left(\sigma^0_{xy}\frac{\partial w}{\partial x} + \sigma^0_{yy}\frac{\partial w}{\partial y}\right) = 0, \tag{5}$$

where

$$M_{xx} = -D\left(\frac{\partial^2 w}{\partial x^2} + \nu\frac{\partial^2 w}{\partial y^2}\right), \quad M_{yy} = -D\left(\frac{\partial^2 w}{\partial y^2} + \nu\frac{\partial^2 w}{\partial x^2}\right), \quad M_{xy} = -(1-\nu)D\frac{\partial^2 w}{\partial x \partial y}, \tag{6}$$

D is the bending stiffness

$$D = \frac{Eh^3}{12(1-\nu^2)}, \tag{7}$$

and h is the thickness of the plate. In view of Eqs. (2)–(4) and (6), Eq. (5) reduces to the following differential equation for the deflection w:

$$-D\left(\frac{\partial^2}{\partial x^2} + \frac{\partial^2}{\partial y^2}\right)^2 w + \rho g h\frac{\partial w}{\partial y} + \frac{2}{3-\nu}\rho g h\left[\nu y\frac{\partial^2 w}{\partial x^2} + y\frac{\partial^2 w}{\partial y^2} + (1-\nu)x\frac{\partial^2 w}{\partial x \partial y}\right] = 0. \tag{8}$$

We need to find the limit of the gravity load ρg under which the plane stress state is stable, and beyond which there are bifurcation points and its plane state is no longer stable. Any small transverse perturbation would cause an out-of-plane deformation of the plate beyond the limit. Thus, the first bifurcation point, which corresponds to the critical buckling mode, is of practical interest.

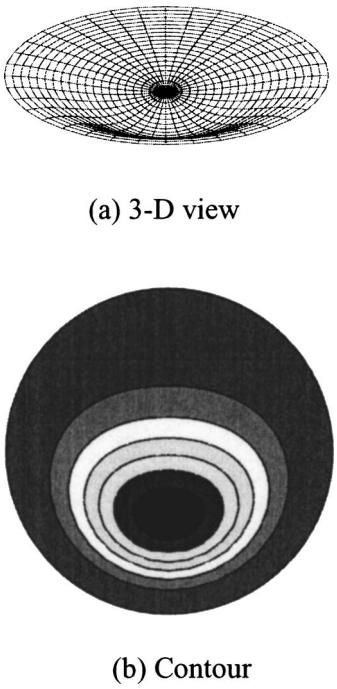

Fig. 1 The buckling modal shape for a clamped vertical circular plate subjected to gravity

Because the differential equation (8) has variable coefficients, it seems to be very difficult, if not impossible, to find an exact solution. The Ritz method is employed to solve the problem. The following strain energy is needed in the Ritz method (see Reddy [3,4] and Liew et al. [5]):

$$U = -\frac{1}{2}\int_A\left(M_{xx}\frac{\partial^2 w}{\partial x^2} + 2M_{xy}\frac{\partial^2 w}{\partial x \partial y} + M_{yy}\frac{\partial^2 w}{\partial y^2}\right)dA + \frac{h}{2}\int_A\left[\sigma^0_{xx}\left(\frac{\partial w}{\partial x}\right)^2 + 2\sigma^0_{xy}\frac{\partial w}{\partial x}\frac{\partial w}{\partial y} + \sigma^0_{yy}\left(\frac{\partial w}{\partial y}\right)^2\right]dA, \tag{9}$$

where A is the area of the plate. Assuming

$$w = (x^2+y^2-R^2)^2\sum_{q=0}^{p}\sum_{i=0}^{q} c_m x^{q-i} y^i, \tag{10}$$

and p is the degree of the two-dimensional complete polynomial used in the trial function in Eq. (10) and $m=(q+1)(q+2)/2-i$ (see [5]). The solution in the form of Eq. (10) satisfies the geometric boundary conditions $w=\partial w/\partial r=0$ for a rigidly clamped edge at $r=R$. The Ritz method requires

$$\frac{\partial U}{\partial c_i} = 0, \quad i = 1,2,\ldots,(p+1)(p+2)/2. \tag{11}$$

Using Eqs. (2), (6), and (9)–(11), we obtain an eigenvalue equation. Table 1 provides a convergence study of the Ritz method. It is seen that numerical convergence to six significant digits is reached at $p=8$.

The Ritz method requires that the trial functions $\phi_i(x,y)$ satisfy $\phi_i = \partial\phi_i/\partial x = \partial\phi_i/\partial y = 0$ for a fixed edge at $r=R$. When we construct them in terms of power series in x and y, it can be proved that such a function of the lowest-order power series in x and y (not in r) must be in quartic form, and more specifically, $(x^2+y^2-R^2)^2$. The representation shown in Eq. (10) provides a complete set of the trial functions up to additional order p, and thus provides a global minimum of the buckling load. It should be

noted that the trial function $(r-R)^2$ is the lowest order in r; however, it does not furnish a power series representation.

For a nontrivial solution of w, we obtain the critical value $\lambda_{cr} = 110.054$ for the dimensionless buckling factor $\lambda \equiv \rho g h R^3/D$. With this solution, a restriction is placed in the plane stress state. The above-mentioned exact elasticity solution [1] for the plane-stressed circular thin plate is only valid within the limit; i.e., $\lambda \leqslant \lambda_{cr}$. Figure 1 shows the first buckling mode shape of the thin circular plate subjected to in-plane gravity.

The circular thin plate is made of silicon material. The material properties correspond to the average isotropic values for ⟨100⟩ silicon [2]

$$E = 160 \text{ GPa}, \quad \nu = 0.2, \quad \rho = 2330 \text{ kg/m}^3. \tag{12}$$

As mentioned earlier in Sec. 1, the typical thickness of the silicon plate is 3.0 μm. From the condition $\lambda \leqslant \lambda_{cr}$, the radius of the circular plate must be within the range of

$$R \leqslant 84.459 \text{ mm}. \tag{13}$$

Note that the Ritz method predicts the upper bound of a real solution. The distortion of the IPL circular mask with a radius 100 mm or larger mentioned in [1] is already in either an instable plane state or a postbuckling state. In order to minimize the distortion, the mask has to be designed by reducing the radius or by providing extensional prestresses such that it is within a prebuckling range.

References

[1] Tejeda, R. O., Lovell, E. G., and Engelstad, R. L., 2000, ''In-Plane Gravity Loading of a Circular Membrane,'' J. Appl. Mech., **67**, pp. 837–839.

[2] Tejeda, R. O., Engelstad, R. L., Lovell, E. G., and Berry, I. L., 1998, ''Analysis, Design, and Optimization of Ion-Beam Lithography Masks,'' Proc. SPIE, **3331**, pp. 621–628.

[3] Reddy, J. N., 1999, *Theory and Analysis of Elastic Plates*, Taylor & Francis, Philadelphia, PA.

[4] Reddy, J. N., 1984, *Energy and Variational Methods in Applied Mechanics*, John Wiley, New York, NY.

[5] Liew, K. M., Wang, C. M., Xiang, Y., and Kitipornchai, S., 1998, *Vibration of Mindlin Plates: Programming the p-Version Ritz Method*, Elsevier, Oxford.

Connections Between Stability, Convexity of Internal Energy, and the Second Law for Compressible Newtonian Fluids

Stephen E. Bechtel
Department of Mechanical Engineering, The Ohio State University, Columbus, OH 43210

Francis J. Rooney
Bishop O'Dowd, 9500 Stearns Avenue, Oakland, CA 94605

M. Gregory Forest
Department of Mathematics, University of North Carolina, Chapel Hill, NC 27599

In this note we provide proofs of the following statements for a compressible Newtonian fluid: (i) internal energy being a convex function of entropy and specific volume is equivalent to nonnegativity of both specific heat at constant volume and isothermal bulk modulus; (ii) convexity of internal energy together with the second law of thermodynamics imply linear stability of the rest state; and (iii) linear stability of the rest state together with the second law imply convexity of internal energy. [DOI: 10.1115/1.1831297]

1 Introduction

In thermodynamics of fluids one encounters different notions of stable equilibrium. One is that internal energy is a convex function of entropy and specific volume. Another is that certain material properties must be nonnegative. A third is that all small perturbations of the rest state do not grow.

In this brief note we connect these three notions in a compressible Newtonian fluid by providing proofs that nonnegativity of specific heat at constant volume and isothermal bulk modulus is equivalent to convexity of internal energy, that the second law and convexity of internal energy together imply linear stability of the rest state, and that the second law and linear stability of the rest state together demand convexity of internal energy.

2 Governing Equations for Newtonian Fluids

The equations of conservation of mass, linear momentum, angular momentum, and energy for a continuum are, respectively,

$$\dot{\rho}+\rho\nabla\cdot\mathbf{v}=0,\quad \rho\dot{\mathbf{v}}=\nabla\cdot\mathbf{T}+\rho\mathbf{f},\quad \mathbf{T}=\mathbf{T}^{T},\quad \rho\dot{\epsilon}=\mathbf{T}\cdot\mathbf{D}+\rho r-\nabla\cdot\mathbf{q}, \tag{1}$$

where ρ is the density, $\mathbf{v}$ the velocity, $\mathbf{T}$ the Cauchy stress, $\mathbf{D}$ the symmetric part of the velocity gradient, $\mathbf{f}$ the specific body force, r the internal heat production, $\mathbf{q}$ the heat flux, and ϵ the specific internal energy, and $(\dot{})$ denotes the material time derivative. A Newtonian fluid is characterized by the constitutive equations

$$\mathbf{T}=-p\mathbf{I}+\lambda(\nabla\cdot\mathbf{v})\mathbf{I}+2\mu\mathbf{D},\quad \mathbf{q}=-k\nabla\theta, \tag{2}$$

where p is the pressure, θ the absolute temperature, λ the dilatational viscosity, μ the shear viscosity, and k the thermal conductivity. Entropy η can be defined through [1]

$$\dot{\epsilon}=p\frac{\dot{\rho}}{\rho^2}+\theta\dot{\eta}. \tag{3}$$

Contributed by the Applied Mechanics Division of THE AMERICAN SOCIETY OF MECHANICAL ENGINEERS for publication in the ASME JOURNAL OF APPLIED MECHANICS. Manuscript received by the ASME Applied Mechanics Division, March 28, 2002, final revision, June 16, 2004. Associate Editor: K. R. Rajagopal.

The material parameters λ, μ, and k may depend upon the independent thermal variable (θ or η, depending on the formulation) and independent mechanical variable (either p or ρ). Here we select ρ and η as the independent variables. In this formulation the auxiliary mechanical (p) and thermal (θ) variables are prescribed in terms of ρ, η, and ϵ through

$$p(\rho,\eta)=\rho^2\frac{\partial\epsilon}{\partial\rho},\quad \theta(\rho,\eta)=\frac{\partial\epsilon}{\partial\eta}; \tag{4}$$

Eqs. (1)–(4) determine a closed system.

We employ the second law of thermodynamics in the form of the Clausius-Duhem inequality,

$$\dot{S}=\frac{d}{dt}\int_{\mathcal{V}}\rho\eta dV\geqslant\int_{\mathcal{V}}\frac{r}{\theta}\rho dV-\int_{\partial\mathcal{V}}\frac{\mathbf{q}\cdot\mathbf{n}}{\theta}dA, \tag{5}$$

where volume $\mathcal{V}$ is arbitrary. Using Eqs. (1)–(3), this implies

$$\int_{\mathcal{V}}\frac{1}{\theta}\left[\left(\lambda+\frac{2}{3}\mu\right)(\nabla\cdot\mathbf{v})^2+2\mu\mathbf{D}_d\cdot\mathbf{D}_d+\frac{k}{\theta}|\nabla\theta|^2\right]dV\geqslant 0, \tag{6}$$

where $\mathbf{D}_d$ denotes the deviatoric part of $\mathbf{D}$. Thus the second law for Newtonian fluids is equivalent to

$$\lambda+\frac{2}{3}\mu\geqslant 0,\quad \mu\geqslant 0,\quad k\geqslant 0. \tag{7}$$

3 Equivalence of Convexity of ϵ and Stability of the Rest State

The conditions that internal energy ϵ is a convex function of entropy η and specific volume ($\tau=\rho^{-1}$) (mathematically equivalent to entropy being a concave function of internal energy and specific volume) are [2]

$$\frac{\partial^2\epsilon(\tau,\eta)}{\partial\tau^2}\geqslant 0,\quad \frac{\partial^2\epsilon(\tau,\eta)}{\partial\eta^2}\geqslant 0,$$
$$\frac{\partial^2\epsilon(\tau,\eta)}{\partial\tau^2}\frac{\partial^2\epsilon(\tau,\eta)}{\partial\eta^2}-\left(\frac{\partial^2\epsilon(\tau,\eta)}{\partial\tau\partial\eta}\right)^2\geqslant 0. \tag{8}$$

Note, that the three conditions (8) are not independent: $(8)_1$ and $(8)_3$ imply $(8)_2$, and $(8)_2$ and $(8)_3$ imply $(8)_1$.

One notion of stable thermodynamic equilibrium is in [3]: "Using the principle—often attributed to Le Chatelier—that any spontaneous change in the parameters of a system that is in stable equilibrium will give rise to processes that tend to restore the system to equilibrium," Stanley argues that specific heats and compressibilities (reciprocals of bulk moduli) must be nonnegative. Since specific heat at constant pressure is in general greater than or equal to specific heat at constant volume C_V, and the adiabatic bulk modulus is in general greater than or equal to the isothermal bulk modulus κ, these conditions for stability become

$$C_V\equiv\theta\frac{\partial\eta(\theta,\tau)}{\partial\theta}\geqslant 0,\quad \kappa\equiv-\tau\frac{\partial p(\theta,\tau)}{\partial\tau}\geqslant 0. \tag{9}$$

Using Eqs. (4), conditions $(9)_{1,2}$ are directly equivalent to conditions $(8)_{2,3}$, respectively, and from $(8)_{2,3}$ condition $(8)_1$ can be deduced. Hence, nonnegativity of C_V and κ is equivalent to internal energy being a convex function of entropy and specific volume, in the sense of satisfying conditions (8).

With the change of variables from specific volume to density, the convexity conditions Eqs. (8) are translated into

$$\frac{2\epsilon_\rho}{\rho}+\epsilon_{\rho\rho}\geqslant 0,\quad \epsilon_{\eta\eta}\geqslant 0,$$
$$\left(\frac{2\epsilon_\rho}{\rho}+\epsilon_{\rho\rho}\right)\epsilon_{\eta\eta}-\epsilon_{\rho\eta}^2\geqslant 0, \tag{10}$$

where subscripts denote partial differentiation.

We now consider an equilibrium state in the absence of a body force and internal heat supply,

$$\mathbf{v}=\mathbf{0},\quad \theta=\theta_0,\quad \rho=\rho_0,\quad p=p_0,\quad \eta=\eta_0, \tag{11}$$

where ρ_0, v_0, and η_0 are arbitrary constant solutions of Eqs. (1)–(3), and p_0, θ_0 are determined from equations of state (4) evaluated at ρ_0 and η_0. We allow an infinitesimal disturbance of this rest state,

$$\mathbf{v}=\mathbf{v}^*,\quad \theta=\theta_0+\theta^*,\quad \eta=\eta_0+\eta^*,\quad \rho=\rho_0+\rho^*,\quad p=p_0+p^*, \tag{12}$$

the starred quantities are infinitesimal variations of which only linear terms will be retained. Disturbances p^*, θ^* are deduced from ρ^*, η^* by linearization of the constitutive relations (4). The linearization of problem Eqs. (1)–(3) then consists of constant-coefficient linear partial differential equations for ρ^* and η^*, along with two linear algebraic equations for p^*, θ^*, for which Fourier analysis applies. We posit eigenfunctions for each primitive variable of the form

$$F^*(\mathbf{x},t)=\tilde{F}\exp(is\mathbf{n}\cdot\mathbf{x}-\sigma t), \tag{13}$$

where the wave vector $s\mathbf{n}$ has norm s and direction $\mathbf{n}$. The rest state Eq. (11) is linearly stable if $\mathrm{Re}(\sigma_j)\geqslant 0$ for all roots σ_j of the linearized dispersion relation at all wave numbers s, and unstable if $\mathrm{Re}(\sigma_j)<0$ for some root σ_j at some s.

The linearized disperson relation for $\sigma(s)$ is [4]

$$\left(\sigma-\frac{\mu_0}{\rho_0}s^2\right)^2\left[\sigma-\frac{\lambda_0+2\mu_0}{\rho_0}s^2+\frac{s^2\left(\sigma(\rho_0^2\epsilon_{\rho\rho}^{(0)}+2\rho_0\epsilon_\rho^{(0)})-\dfrac{k_0\rho_0}{\theta_0}s^2\Delta_0\right)}{\sigma\left(\sigma-\epsilon_{\eta\eta}^{(0)}\dfrac{k_0}{\rho_0\theta_0}s^2\right)}\right]=0, \tag{14}$$

where μ_0, λ_0, k_0, $\epsilon_{\rho\rho}^{(0)}$, $\epsilon_\rho^{(0)}$, $\epsilon_{\eta\eta}^{(0)}$, and $\epsilon_{\rho\eta}^{(0)}$ denote functions evaluated on the equilibrium state and

$$\Delta_0=\left(\epsilon_{\rho\rho}^{(0)}+2\frac{\epsilon_\rho^{(0)}}{\rho_0}\right)\epsilon_{\eta\eta}^{(0)}-(\epsilon_{\rho\eta}^{(0)})^2. \tag{15}$$

3.1 Proof That Stability of the Rest State and Consequences (7) of the Second Law Imply Convexity Conditions (10). Assume the second law holds, so that $\lambda_0+2/3\mu_0\geqslant 0$, $\mu_0\geqslant 0$, $k_0\geqslant 0$. A repeated root of dispersion relation (14) is

$$\sigma_4=\sigma_5=s^2\mu_0/\rho_0. \tag{16}$$

Note, that $\sigma_4=\sigma_5\geqslant 0$ since $\mu_0\geqslant 0$. The other three dispersion branches satisfy

$$\sigma^3-s^2\left(\frac{\lambda_0+2\mu_0}{\rho_0}+\epsilon_{\eta\eta}^{(0)}\frac{k_0}{\rho_0\theta_0}\right)\sigma^2+s^2\left(\rho_0^2\epsilon_{\rho\rho}^{(0)}+2\rho_0\epsilon_\rho^{(0)}+\frac{\lambda_0+2\mu_0}{\rho_0}\epsilon_{\eta\eta}^{(0)}\frac{k_0}{\rho_0\theta_0}s^2\right)\sigma-\frac{k_0\rho_0}{\theta_0}s^4\Delta_0=0. \tag{17}$$

Since the coefficients of this cubic equation are real, either all three roots are real or one is real and the other pair consists of complex conjugates. We label the roots of Eq. (17) by σ_1, σ_2, σ_3. We assume the rest state is stable, so that σ_1, σ_2, and σ_3 all have nonnegative real parts, and hence the product σ_1, σ_2, σ_3 is nonnegative. The constant term of Eq. (17) shows

$$\sigma_1\sigma_2\sigma_3=\frac{k_0\rho_0}{\theta_0}s^4\Delta_0. \tag{18}$$

Since $k_0\geqslant 0$, we have $\Delta_0\geqslant 0$, which is inequality $(10)_3$ evaluated at arbitrary values ρ_0 and η_0 of density and entropy.

We next consider the special perturbations given by

$$\tilde{\mathbf{f}}=(\mathbf{0},0,\tilde{\eta}), \tag{19}$$

for which the linearized problem reduces to

$$\left(\sigma-\frac{s^2k_0}{\rho_0\theta_0}\epsilon_{\eta\eta}^{(0)}\right)\tilde{\eta}=0.$$

Since we have assumed the rest state is stable for all perturbations, σ is nonnegative, so that $\epsilon_{\eta\eta}\geqslant 0$ at arbitrary values of density and entropy, which is inequality $(10)_2$. We have proved inequalities $(10)_2$ and $(10)_3$, and $(10)_2$ and $(10)_3$ imply $(10)_1$. Hence inequalities (7) and stability of the rest state demand convexity of internal energy, in the sense that conditions (10) are satisfied.

3.2 Proof That Convexity Conditions (10) Together With the Consequences (7) of the Second Law Imply Stability of the Rest State. Recall that either all three roots σ_1, σ_2, and σ_3 of the cubic Eq. (17) are real or one is real and the other pair consists of complex conjugates. Since $k_0\geqslant 0$ from inequality $(7)_3$, if we assume inequality $(10)_3$ then $\Delta_0\geqslant 0$, and from Eq. (18) at least one of the roots, say σ_1, must be real and nonnegative. We rewrite Eq. (17) in the form

$$\sigma=\frac{\sigma^2s^2\left(\dfrac{\lambda_0+2\mu_0}{\rho_0}+\epsilon_{\eta\eta}^{(0)}\dfrac{k_0}{\rho_0\theta_0}\right)+\dfrac{k_0\rho_0}{\theta_0}s^4\Delta_0}{\sigma^2+s^2\left(\rho_0^2\epsilon_{\rho\rho}^{(0)}+2\rho_0\epsilon_\rho^{(0)}+\dfrac{\lambda_0+2\mu_0}{\rho_0}\epsilon_{\eta\eta}^{(0)}\dfrac{k_0}{\rho_0\theta_0}s^2\right)}. \tag{20}$$

The coefficients on the right-hand side are all positive because of the convexity of ϵ and the second law. Hence if the remaining two roots σ_2 and σ_3 are real they must be nonnegative, and if they are complex conjugates then

$$\mathrm{Re}(\sigma_2)=\mathrm{Re}(\sigma_3)=\frac{|\sigma_2^2+C|^2}{2D}, \tag{21}$$

where

$$C=s^2\left(\rho_0^2\epsilon_{\rho\rho}^{(0)}+2\rho_0\epsilon_\rho^{(0)}+\frac{\lambda_0+2\mu_0}{\rho_0}\epsilon_{\eta\eta}^{(0)}\frac{k_0}{\rho_0\theta_0}s^2\right), \tag{22}$$

$$D=s^4(\lambda_0+2\mu_0)(\rho_0\epsilon_{\rho\rho}^{(0)}+2\epsilon_\rho^{(0)})+(\lambda_0+2\mu_0)^2\epsilon_{\eta\eta}^{(0)}\frac{k_0}{\rho_0^3\theta_0}s^6+(\lambda_0+2\mu_0)(\epsilon_{\eta\eta}^{(0)})^2\frac{k_0^2}{\rho_0^3\theta_0^2}s^6+(\epsilon_{\rho\eta}^{(0)})^2\frac{\rho_0k_0}{\theta_0}s^4,$$

and so $\mathrm{Re}(\sigma_2)=\mathrm{Re}(\sigma_3)$ is nonnegative. This completes the argument that the convexity conditions on internal energy plus the second law imply stability. Combined with the earlier result that stability plus the second law imply the convexity of ϵ, it follows that, assuming the second law, the convexity conditions on internal energy are equivalent to linear stability of the rest state.

Acknowledgments

This work was sponsored in part by the National Science Foundation under Grant Nos. CTS-9711109 and DMI-0115445.

References

[1] Batchelor, G. K., 1967, *An Introduction to Fluid Dynamics*, Cambridge University Press, Cambridge.
[2] Rockafellar, R. T., 1970, *Convex Analysis*, Princeton University Press, Princeton, NJ.
[3] Stanley, H. E., 1971, *Introduction to Phase Transistions and Critical Phenomena*, Oxford University Press, New York.
[4] Bechtel, S. E., Forest, M. G., Rooney, F. J., and Wang, Q., 2003, "Thermal Expansion Models of Viscous Fluids Based on Limits of Free Energy," Phys. Fluids, **15**, pp. 2681–2693.

Wrinkling of Circular Tubes Under Axial Compression: Effect of Anisotropy

S. Kyriakides, F. C. Bardi, and J. A. Paquette
Research Center for Mechanics of Solids, Structures & Materials, The University of Texas at Austin, WRW 110, C0600, Austin, TX 78712

[DOI: 10.1115/1.1839590]

1 Introduction

Elastic buckling of cylindrical shells under axial compression results in sudden and catastrophic failure. By contrast, for thicker shells that buckle in the plastic range, failure is preceded by a cascade of events where the first instability and failure are separated by strains of up to 5%. The first instability is uniform axisymmetric wrinkling. The wrinkle amplitude gradually grows and, in the process, the axial rigidity of the shell is reduced. For thicker shells, this eventually leads to a limit load instability beyond which failure takes the form of localized buckling that can lead to concertina folding. For thinner shells, a second bifurcation involving nonaxisymmetric deformation can precede this limit load. This buckling mode again localizes and can again result in folding.

Axisymmetric wrinkling is a classic plastic bifurcation from a uniaxial stress state with the following buckling mode:

$$\tilde{w}=a\cos\frac{\pi x}{\lambda} \quad \text{and} \quad \tilde{u}=b\sin\frac{\pi x}{\lambda}. \tag{1}$$

It can be easily shown that the critical stress (σ_C) and half-wavelength of this buckling mode (λ_C) are, respectively,

$$\sigma_C=\left[\frac{C_{11}C_{22}-C_{12}^2}{3}\right]^{1/2}\left(\frac{t}{R}\right) \quad \text{and}$$

$$\lambda_C=\pi\left[\frac{C_{11}^2}{12(C_{11}C_{22}-C_{12}^2)}\right]^{1/4}(Rt)^{1/2}, \tag{2}$$

where R and t are the radius and wall thickness of the shell respectively, and $[C_{\alpha\beta}]$ are the instantaneous moduli of the material at the bifurcation point [1]. During the last fifty years, use of the J_2 deformation theory instantaneous moduli in Eq. (2) has gained wide acceptance primarily because it yields better results than the corresponding flow theory [2].

The problem was recently revisited in order to establish the extent to which tubes can be deformed plastically before failure. Because failure follows the onset and evolution of axisymmetric wrinkling, its prediction requires establishing first accurately $\{\sigma_C,\epsilon_C,\lambda_C\}$ (see Refs. [3–5]). Experiments were conducted on super-duplex stainless steel (SAF 2507) tubes with D/t values ranging from about 23 to 52. The experiments involved buckling and failure under pure axial compression and under combined internal pressure and axial compression. In both sets of experiments, some discrepancies between the classical bifurcation predictions of Eqs. (2) and measured values of the critical states were found. The cause of the discrepancies was shown to be plastic anisotropy present in the tubes used. This brief note reports on how the discrepancy was resolved.

Contributed by the Applied Mechanics Division of THE AMERICAN SOCIETY OF MECHANICAL ENGINEERS for publication in the ASME JOURNAL OF APPLIED MECHANICS. Manuscript received by the ASME Applied Mechanics Division, April 4, 2004, final revision, September 2, 2004. Editor: R. M. McMeeking.

2 Buckling Experiments

Super-duplex SAF 2507 specimens with D/t values in the range of 23 to 52 were machined from thicker tube stock. They were turned both on the inside and outside, resulting in nearly parallel test section walls. The test section length varied between $3R$ and $5R$. Linear tapers were machined at the ends, reducing edge effects and resulting in nearly uniform stress in the test section. The specimens were compressed to failure under displacement control. The evolution of wrinkles was monitored by periodically interrupting the loading, and scanning the specimen axially using a custom surface scanner. In the case of combined loading, the specimens were pressurized to a chosen pressure and compressed to failure while holding the pressure constant. The wrinkle wavelength increases with pressure and, as a result, all pressure tests had the longer test section of $5R$.

All specimens initially deformed uniformly. At some value of strain, wrinkles became discernible on the surface of the tubes. Figure 1(a) shows stress-shortening response ($\sigma_x-\delta_x$) recorded for a tube with $D/t=26.3$ loaded under pure compression. Figure 1(b) shows a set of axial scans taken at the positions marked on the response by solid circles. Because of the discrete nature of the scans, the onset of wrinkling will be bounded between two strain values. In this case, wrinkling occurred between strains of 1.08% and 1.18% (indicated by ↓). Under continued compression, the wrinkle amplitude grew, gradually reducing the axial rigidity. The growth of the wave approximately at the midspan of the test section accelerated, indicating localization in deformation. A load maximum developed at an ''average'' strain of approximately 4.75% and a stress of 111.2 ksi (767 MPa, marked by ''^'' on the response). Following the limit load, deformation in the central wave accelerated significantly. At some stage in the process, before the limit load, deformation in the neighborhood of this wave reverted to a nonaxisymmetric mode with two lobes ($m=2$). The test was terminated at a net shortening of 6.5%.

The critical strains (bounds) from 14 experiments are plotted against D/t in Fig. 2. They range from about 1.5% for the lower D/t tubes to about 0.7% for the higher values. Some of the experiments were repeated while others were run with a longer test section (■,□) to ensure that the test section length did not influence the results. Figure 3 shows a plot of the measured half-wavelengths as a function of D/t. They vary from about $0.4R$ for the lower D/t tubes to about $0.2R$ for the high values. Upper and lower bound values are again given in the figure.

Despite the careful machining of the specimens, imperfections were unavoidable. These include small wall thickness variations around the circumference and the length, small eccentricities in the applied load, and some local hardening and surface marking from machining. Although generally small, the imperfections influenced the onset, the wavelength, and evolution of wrinkles. In addition, in the perfect case, wrinkling is a nearly tangential bifurcation, making it very difficult to establish its onset experimentally. Thus, the experiments were not repeatable, and the results in Figs. 2 and 3 exhibit some scatter, although their trend is quite clear.

The material stress–strain response is well represented by the Ramberg–Osgood fit given by

$$\epsilon=\frac{\sigma}{E}\left[1+\frac{3}{7}\left(\frac{\sigma}{\sigma_y}\right)^{n-1}\right], \tag{3}$$

where $E=28.2\times10^3$ ksi (194 GPa), $\sigma_y=83.0$ ksi (572 MPa), and $n=13$. Included in Figs. 2 and 3 are the predicted critical strains and half-wavelengths using J_2 flow and deformation theories in Eqs. (2). As expected, flow theory overpredicts the measured critical strains (and stresses) considerably. By contrast, the deformation theory results follow the trend and generally are in good agreement with the experiments. The flow theory overpredicts λ_C significantly as well, while the deformation theory predictions are closer to the measured values but are still higher by a factor of

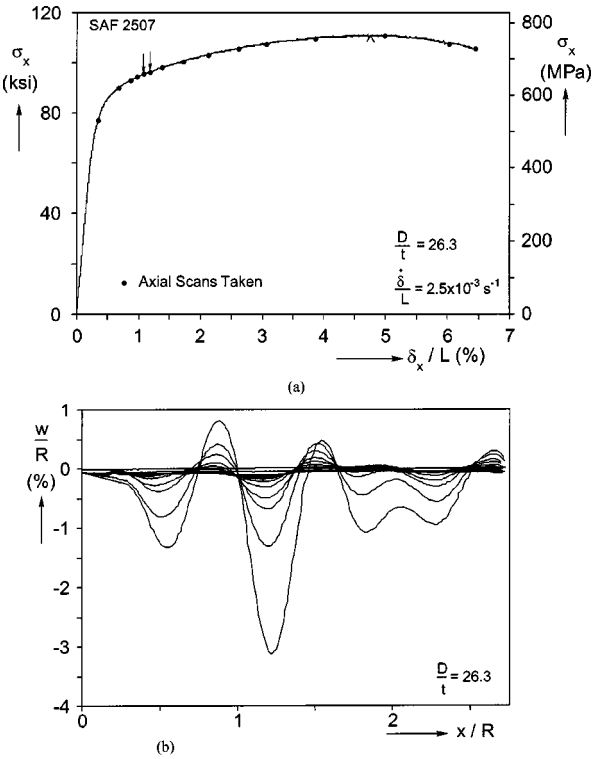

Fig. 1 (*a*) Measured tube axial stress-shortening response for pure compression. (*b*) Axial scans showing evolution of wrinkles.

about 2. Interestingly, similar overprediction of measured values of λ_C were reported in Refs. [6] and [7] for the related problem of inelastic bending of long tubes.

Because λ_C is the starting point of all postbuckling calculations, this difference is a significant problem that had to be addressed. It was found that plastic anisotropy introduced by the manufacturing process to the seamless tube stock was at least partly responsible for the discrepancy. The anisotropy was modeled through Hill's quadratic anisotropic yield function (Ref. [8]). For relatively thin-walled circular tubes, the radial stress (σ_r) can be neglected. If, in addition, the tube is under a principal state of stress (σ_x, σ_θ), Hill's yield function can be written as

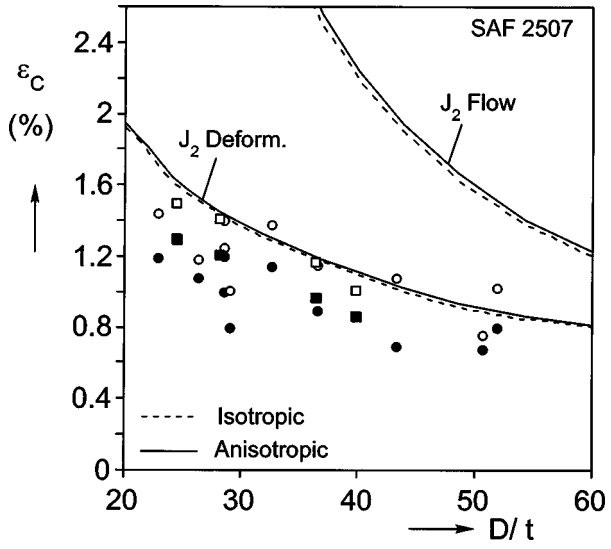

Fig. 2 Comparison of measured and predicted critical strains for pure compression

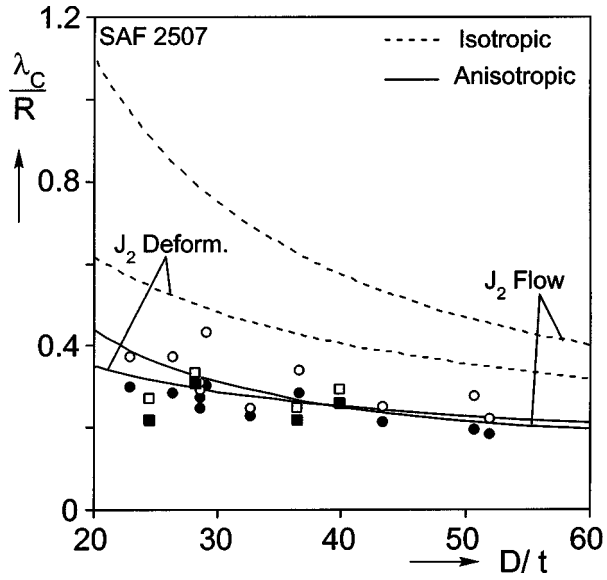

Fig. 3 Comparison of measured and predicted wrinkle half-wavelengths for pure compression

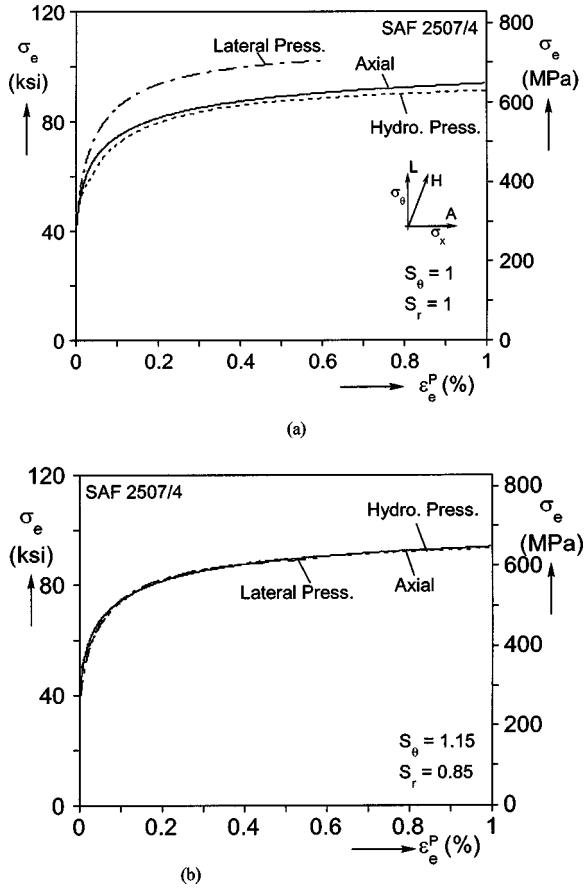

Fig. 4 (*a*) Equivalent stress–strain curves from three paths. (*b*) Equivalent stress–strain curves from three paths.

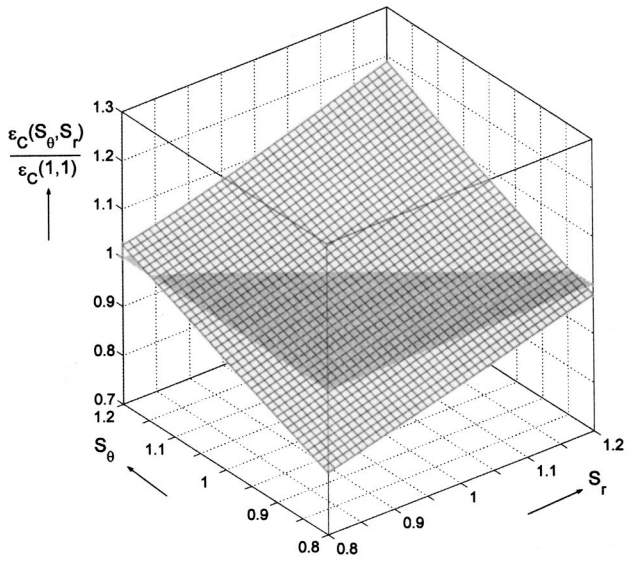

(*a*)

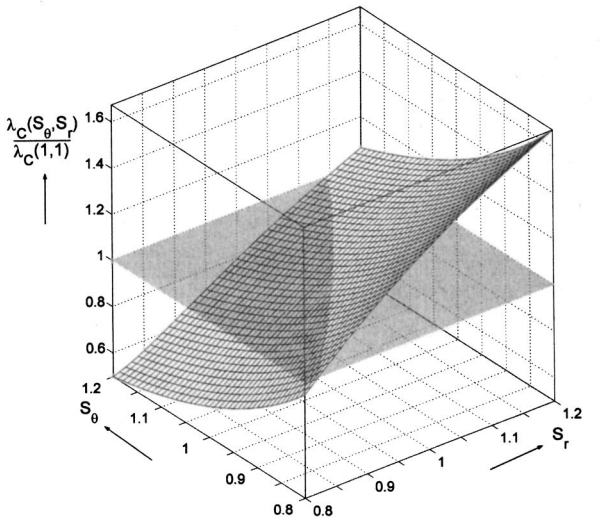

(*b*)

Fig. 5 (*a*) Critical strain as a function of anisotropy variables (D/t=26.3). (*b*) Half-wavelength as a function of anisotropy variables (D/t=26.3).

$$f=\sigma_e=\left[\sigma_x^2-\left(1+\frac{1}{S_\theta^2}-\frac{1}{S_r^2}\right)\sigma_x\sigma_\theta+\frac{1}{S_\theta^2}\sigma_\theta^2\right]^{1/2}=\sigma_{e\,\max}, \quad (4)$$

where $S_\theta=\sigma_{o\theta}/\sigma_{ox}$, $S_r=\sigma_{or}/\sigma_{ox}$, and $\{\sigma_{ox},\sigma_{or},\sigma_{o\theta}\}$ are the yield stresses in the respective directions. A work compatible measure of equivalent plastic strain increment is

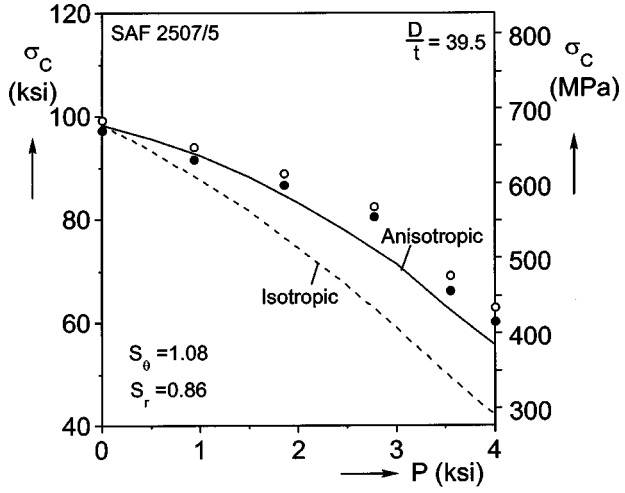

Fig. 6 Critical stress versus pressure: experiments and predictions

$$d\epsilon_e^p=\sqrt{2}\left[\frac{\frac{1}{S_\theta^2}(d\epsilon_x^p)^2+(d\epsilon_\theta^p)^2+\left(1+\frac{1}{S_\theta^2}-\frac{1}{S_r^2}\right)d\epsilon_x^p d\epsilon_\theta^p}{\frac{1}{S_\theta^2}+\frac{1}{S_r^2}-\frac{1}{2}-\frac{1}{2}\left(\frac{1}{S_\theta^2}-\frac{1}{S_r^2}\right)^2}\right]^{1/2}. \quad (5)$$

The anisotropy constants were evaluated by conducting uniaxial experiments in the axial (A) and circumferential directions (L), and a hydrostatic pressure inflation test (H) as described in Ref. [9]. Figure 4(*a*) shows a comparison of $\sigma_e-\epsilon_e^P$ for the three tests assuming the material yields isotropically. The extent to which they are different is a measure of the anisotropy. The three responses coalesce, as shown in Fig. 4(*b*), when the values $S_\theta=1.15$ and $S_r=0.85$ are used in Eqs. (4) and (5).

The strain increments are assumed to consist of an elastic part and a plastic part as follows:

$$d\epsilon_{ij}=d\epsilon_{ij}^e+d\epsilon_{ij}^p, \quad (6a)$$

where

$$d\epsilon_{ij}^e=\frac{1}{E}[(1+\nu)d\sigma_{ij}-\nu d\sigma_{kk}\delta_{ij}]. \quad (6b)$$

The plastic strain increments obey the flow rule given by

$$d\epsilon_{ij}^p=\frac{1}{H}\left(\frac{\partial f}{\partial\sigma_{mn}}d\sigma_{mn}\right)\frac{\partial f}{\partial\sigma_{ij}}. \quad (6c)$$

Specializing Eq. (6) to Eq. (4) results in

$$\begin{Bmatrix}d\epsilon_x\\ d\epsilon_\theta\end{Bmatrix}=\frac{1}{E}\begin{bmatrix}1+Q(2\sigma_x-\beta\sigma_\theta)^2, & -\nu+Q(2\sigma_x-\beta\sigma_\theta)(2\alpha\sigma_\theta-\beta\sigma_x)\\ -\nu+Q(2\sigma_x-\beta\sigma_\theta)(2\alpha\sigma_\theta-\beta\sigma_x), & 1+Q(2\alpha\sigma_\theta-\beta\sigma_x)^2\end{bmatrix}\begin{Bmatrix}d\sigma_x\\ d\sigma_\theta\end{Bmatrix} \quad (7)$$

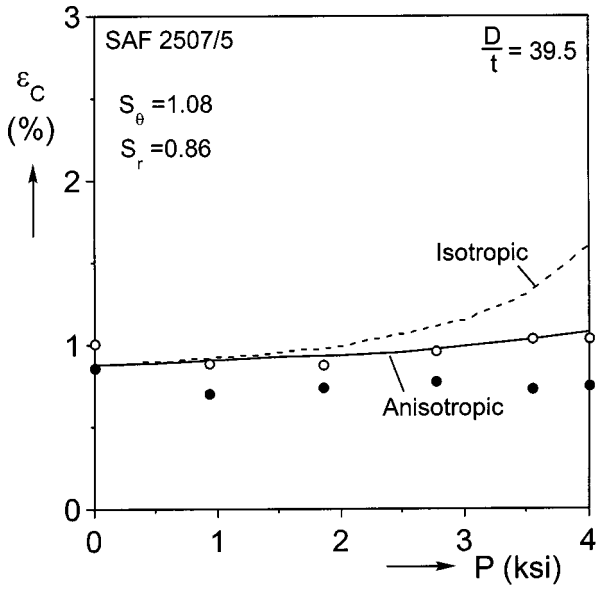

Fig. 7 Critical strain versus pressure: experiments and predictions

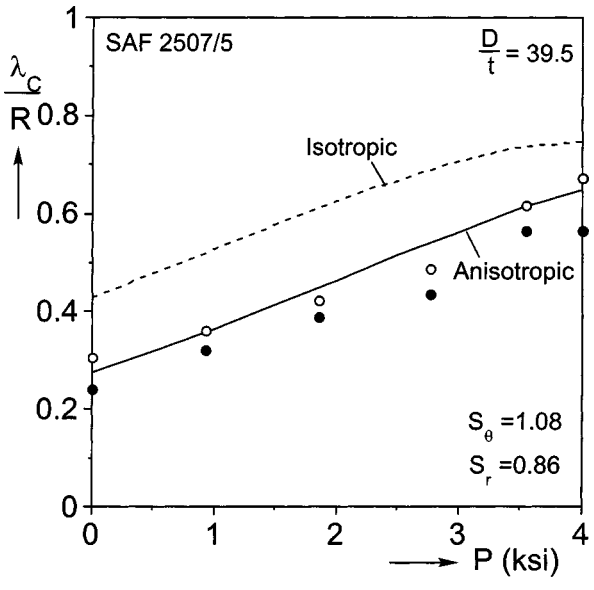

Fig. 8 Wrinkle half-wavelength versus pressure: experiments and predictions

where

$$\alpha=\frac{1}{S_\theta^2},\quad \beta=\left(1+\frac{1}{S_\theta^2}-\frac{1}{S_r^2}\right),\quad \text{and}\quad Q=\frac{1}{4\sigma_e^2}\left(\frac{E}{E_t(\sigma_e)}-1\right).$$

Deformation theory inelasticity is essentially nonlinear elasticity. The corresponding formulation to the anisotropic flow theory above is developed by assuming that there exists a complementary strain energy density function $U^c(\sigma_e)$, such that

$$\epsilon_{ij}^P=\frac{\partial U^c}{\partial \sigma_{ij}}=\frac{\partial U^c}{\partial \sigma_e}\frac{\partial \sigma_e}{\partial \sigma_{ij}}=\left(\frac{1}{E_s}-\frac{1}{E}\right)\sigma_e\frac{\partial \sigma_e}{\partial \sigma_{ij}}. \tag{8}$$

The incremental version of Eq. (8) required in bifurcation calculations is developed in the usual manner (e.g., Ref. [10]). When specialized to the two stress problems of interest here, it can be written as follows:

$$\begin{Bmatrix} d\epsilon_x \\ d\epsilon_\theta \end{Bmatrix}=\frac{1}{E_s}\begin{bmatrix} 1+q(2\sigma_x-\beta\sigma_\theta)^2, & -\hat{\nu}_s+q(2\sigma_x-\beta\sigma_\theta)(2\alpha\sigma_\theta-\beta\sigma_x) \\ -\hat{\nu}_s+q(2\sigma_x-\beta\sigma_\theta)(2\alpha\sigma_\theta-\beta\sigma_x), & \alpha+\frac{E_s}{E}(1-\alpha)+q(2\alpha\sigma_\theta-\beta\sigma_x)^2 \end{bmatrix}\begin{Bmatrix} d\sigma_x \\ d\sigma_\theta \end{Bmatrix} \tag{9}$$

where

$$q=\frac{1}{4\sigma_e^2}\left(\frac{E_s(\sigma_e)}{E_t(\sigma_e)}-1\right)\quad \text{and}\quad \hat{\nu}_s=\frac{\beta}{2}+\frac{E_s}{E}\left(\nu-\frac{\beta}{2}\right).$$

The moduli $[C_{\alpha\beta}]$ in Eqs. (2) are the inverse of the matrices in Eqs. (7) and (9). The calculations of the critical states were repeated using the anisotropic versions of $[C_{\alpha\beta}]$ with the anisotropy values given above. The results are drawn with solid lines in Figs. 2 and 3. Anisotropy has an insignificant effect on the critical stress and strain for both the flow and deformation theory predictions. By contrast, it changes significantly the wavelength of the buckling mode for both material models as illustrated in Fig. 3. Both anisotropic results now pass through the data with the deformation theory yielding the better agreement.

The broader effect of the anisotropy variables $\{S_r, S_\theta\}$ on the critical strain and wrinkle wavelength was considered and the results are plotted in Fig. 5. Interestingly, the anisotropy has the opposite effect on ϵ_C (and σ_C) than on λ_C. Thus, when $S_\theta>1$ and $S_r<1$, as was the case for our tubes, the effect on λ_C is large and on ϵ_C is small. A similar effect is seen when $S_\theta<1$ and $S_r>1$, but now the predicted wavelength is longer than that of the isotropic case. On the other hand, when both S_θ and S_r are either >1 or <1, the effect on ϵ_C is large and on λ_C is small.

Anisotropy was found to also have a significant effect on the critical states of the combined loading problem of axial compression under internal pressure. This study involves tubes of the same alloy with $D/t=39.5$ compressed at constant displacement rates at fixed values of internal pressure. The experimental procedure is similar to the one described for pure compression. The prebuckling state is now calculated using the anisotropic flow theory, while the critical states are again calculated using the incremental deformation theory moduli. In this case, the measured stress–strain response represented as piecewise linear was used in the calculations (approximately represented by the following Ramberg–Osgood fit parameters $E=28.1\times10^3$ ksi, (193.8 GPa), $\sigma_y=87.0$ ksi (600 MPa) and $n=13.5$). The anisotropy parameters were found to be $S_\theta=1.08$ and $S_r=0.86$ (mother tube different than the one used for pure compression). Figures 6–8 show plots of the measured critical values of σ_C, ϵ_C, and λ_C, respectively, as a function of internal pressure (P). Included in each are the predicted values for the isotropic and anisotropic materials. In this case, anisotropy affects the critical stress also because of the bi-

axial loading. The wrinkle wavelength increases with pressure and this is reproduced well by the anisotropic model. The critical strain is affected the least, but again, the anisotropic predictions are seen to be an improvement over those from the isotropic material.

In conclusion, it has been found that yield anisotropy can significantly affect the onset of plastic instabilities and their characteristic wavelengths. The onset of wrinkling of axial cylinders under pure compression and under combined internal pressure and compression have been shown to be predicted with accuracy using an anisotropic deformation theory based on Hill's anisotropic yield function.

References

[1] Batterman, S. C., 1965, ''Plastic Buckling of Axially Compressed Cylindrical Shells,'' AIAA J., **3**, pp. 316–325.

[2] Hutchinson, J. W., 1974, ''Plastic Buckling,'' in *Advances in Applied Mechanics*, Volume 14, C. S. Yih, ed., Academic Press, New York, pp. 67–144.

[3] Gellin, S., 1979, ''Effect of an Axisymmetric Imperfection on the Plastic Buckling of an Axially Compressed Cylindrical Shell,'' ASME J. Appl. Mech., **46**, pp. 125–131.

[4] Tvergaard, V., 1983, ''Plastic Buckling of Axially Compressed Circular Cylindrical Shells,'' Thin-Walled Struct., **1**, pp. 139–163.

[5] Yun, H. D., and Kyriakides, S., 1990, ''On the Beam and Shell Modes of Buckling of Buried Pipelines,'' Soil Dyn. Earthquake Eng., **9**, pp. 179–193.

[6] Reddy, B. D., 1979, ''An Experimental Investigation of the Plastic Buckling of Circular Cylinders in Pure Bending,'' Int. J. Solids Struct., **17**, pp. 669–683.

[7] Ju, G. T., and Kyriakides, S., 1992, ''Bifurcation and Localization Instabilities in Cylindrical Shells Under Bending: Part II Predictions,'' Int. J. Solids Struct., **29**, pp. 1143–1171.

[8] Hill, R., 1948, ''A Theory of the Yielding and Plastic Flow of Anisotropic Metals,'' Proc. R. Soc. London, Ser. A, **193**, pp. 281–297.

[9] Kyriakides, S., and Yeh, M.-K., 1988, ''Plastic Anisotropy in Drawn Metal Tubes,'' ASME J. Eng. Ind., **110**, pp. 303–307.

[10] Budiansky, B., 1959, ''A Reassessment of Deformation Theories of Plasticity,'' ASME J. Appl. Mech., **26**, pp. 259–264.

Journal of Applied Mechanics

Discussion

Discussion: "A Displacement Equivalent-Based Damage Model for Brittle Materials" (Soh, C. K., Liu, Y., Yang, Y., and Dang, Y., 2003, ASME J. Appl. Mech., 70, pp. 681–695)

N. D. Cristescu
e-mail: cristescu@ufl.edu
Graduate Research Professor, Mem. ASME
University of Florida, 231 Aero Building,
P.O. Box 116250, Gainesville, FL 32611-6250

In the article, the damage discussed is the microcracks existing in any brittle material. It is a time-independent theory. However, the authors seem not to know that I published two books: *Rock Rheology* by N. Cristescu, 1988, Kluwer Academic, 336 pp. and *Time Effects in Rock Mechanics* by N. D. Cristescu and U. Hunsche, 1998, Wiley, 342 pp. In these books are chapters on damage: in the first, ''Damage and Failure of Rocks'' and in the second, ''Damage and Creep Failure.'' The damage I have considered is based on the same idea: increase or decrease of microcracks, with the distinction that I have considered also the hydrostatic tests, which the authors disregard. For instance, in Fig. 1 (Fig. 4.25) (all figures are from the second book) one can see the initial contribution of the hydrostatic contribution on the alumina powder obtained in a three-axial test apparatus. I have considered the phenomenon to be time-dependent. Thus, if you stop everything at a certain level of stress, the strains are increasing in creep. In addition, the authors consider only elastic properties. I have considered inelastic properties with respect to developing damage. Thus, I have considered damage produced by shear. For instance, on Fig. 2 (Fig. 6.11) is shown, in an octahedral plane, various possible pure three-axial tests. A pure hydrostatic test is shown as (*b*), (*c*) is a typical true three-axial test. One can see that initially OA are the microcracks closed during the initial hydrostatic test. They are followed by a continuous increase of the microcracks. Only in the last part one is forming other microcracks and the curve is going down. Finally, curve (*d*) corresponds to a very high initial hydrostatic tests. When the stress state close to the failure curve, the failure is imminent. Departing from this curve and approaching the incompressible domain would increase the time to failure to infinity. The damage rate is defined by the evolution law

$$\dot{d}(t) = -\dot{W}_v(t) = -k_T\left\langle 1 - \frac{W(t)}{H(\sigma)}\right\rangle \frac{\partial F}{\partial \sigma}\sigma - k_S\frac{\partial S}{\partial \sigma}\sigma$$

$$\text{if } \frac{\partial F}{\partial \sigma} < 0 \quad \text{and} \quad \frac{\partial S}{\partial \sigma} < 0.$$

where $H(T) = \int_0^T \sigma(t)\dot{\epsilon}_V^I(t)dt + \int_0^T \sigma'(t):\dot{\epsilon}^{I'}(t)dt$ measures the irreversibility, $H(\sigma)$ is the yield function, $F(\sigma)$ is the viscoplastic potential for transient creep, $S(\sigma)$ is the potential for the steady-state creep, k_T *and* k_S are two viscosity constants, and $\langle A\rangle = A$ if $A > 0$ and $\langle A\rangle = 0$ if $A \leqslant 0$.

I have also considered decrease of damage, not only increase, as produced by hydrostatic or deviatory tests. It was very well checked experimentally. For instance, on Fig. 3 (Fig. 9.17) is shown the damage produced at a tunnel. The results presented concerning damage over time and the instantaneous one are quite well accepted. My approach is also used for particulate materials. Here, however, they are applied to particulate materials with a grain size 20 μm or bigger. For small particles—nanoparticles—my approach does not work for failure.

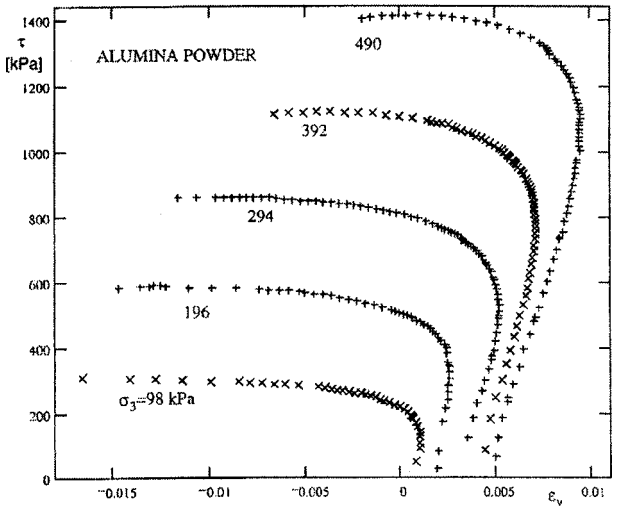

Fig. 1 (Fig. 4.25 Compressibility of alumina powder in classical triaxial tets)

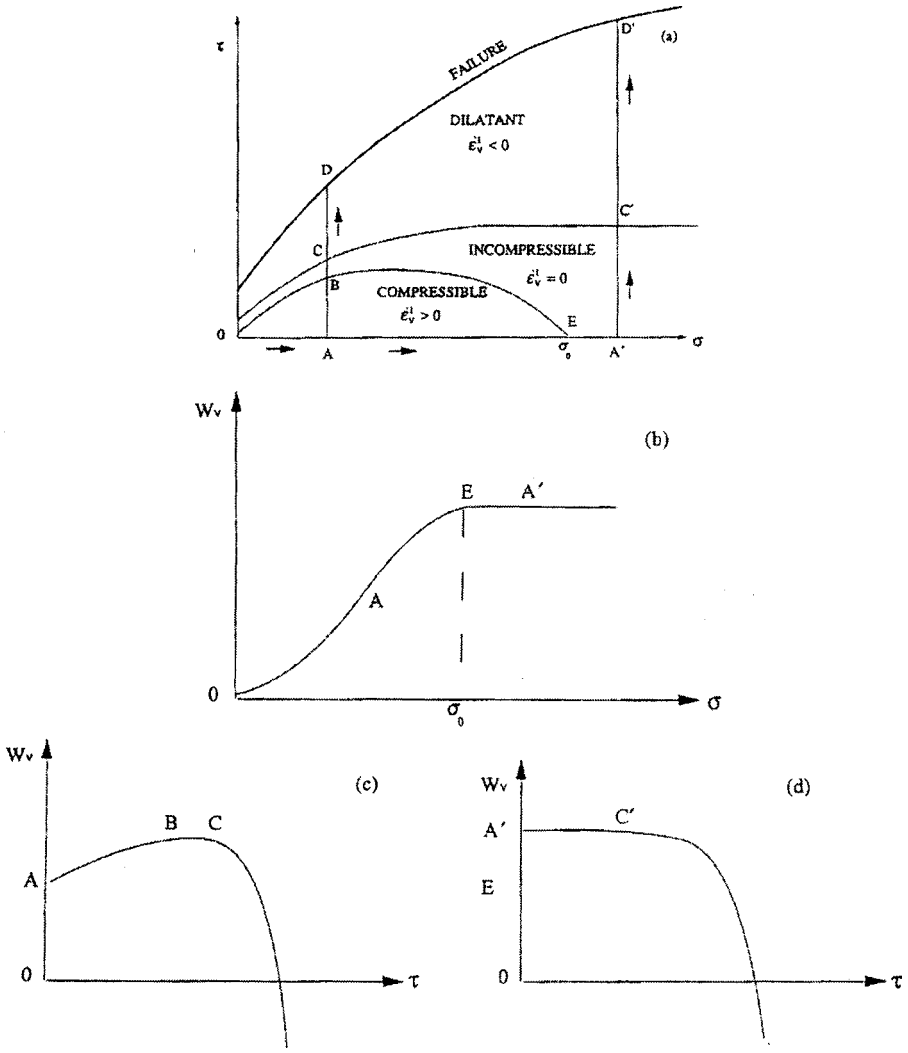

Fig. 2 (Fig. 6.11 Schematic variation of W_v during true triaxial test: (a) stress trajectories shown in constitutive plane; (b) during hydrostatic test; (c) during deviatoric test starting from small or moderate pressure; and (d) during deviatoric test starting from very high pressures above σ_0)

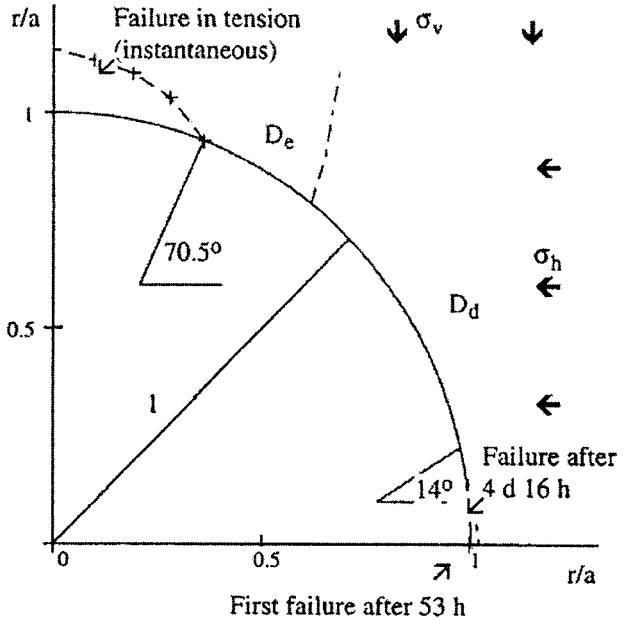

Fig. 3 (Fig. 9.17 Short term failure and creep failure for a tunnel excavated in andesite at h=900 m (Cristescu [1986]))

Closure to "A Displacement Equivalence-Based Damage Model for Brittle Materials, Part I: Theory; Part II: Verification" (2005, ASME J. Appl. Mech., 72, pp. 306–307)

Chee Kiong Soh[1]
e-mail: csohck@ntu.edu.sg
Professor

Yu Liu
e-mail: cliuy@ntu.edu.sg
Research Fellow

Yaowen Yang
e-mail: cywyang@ntu.edu.sg
Assistant Professor
School of Civil and Environmental Engineering,
Nanyang Technological University, Singapore 639798

We would like to highlight that one of the contributions of our papers [1,2] is to propose the assumption of displacement equivalence and the other contribution is to apply this assumption to derive a constitutive model for brittle materials. For simplification, the material is assumed to be ideal brittle, and hence only elastic damage is considered. We have indicated that it is a simplified model, which is invalid for the case of the material under triaxial compression and for the case of the principal directions of damage not coinciding with those of stress and strain.

The displacement equivalence-based damage model for brittle materials has been generalized for quasibrittle materials such as concrete by dealing with the above two cases, as presented in Chap. 5 of Ref. [3]. The first modification is to consider the case in which the principal directions of damage do not coincide with those of stress and strain, and the model is thus established in a randomly selected system. The effect of shear stress has been dealt with in the auxiliary system. The second modification aims to consider the plastic effect of concrete under triaxial compression. Besides the opening cracks considered in Refs. [1,2], the slipping cracks occurring in the case of triaxial compression have also been taken into account. The damage activation criterion and the additional normal strain have been modified to reflect the effect of confinement. The stiffness degradation due to hydrostatic compression has also been considered. In addition, a new damage evolution rule of concrete under triaxial compression has been developed using the experiment-based method.

According to Eqs. (4), (7), and (15) of Ref. [2], the damage is time dependent. However, in engineering applications, it is very difficult to perform dynamic analysis for specimens or structures made of brittle materials such as concrete. A time-independent constitutive model is also necessary for the case of quasistatic loading. Hence, although the damage evolution rule was defined as time dependent, it has been simplified to be time independent by assuming that the strain rate remains constant while loading.

On the other hand, we believe that the constitutive model given in Ref. [4] is derived using viscoplasticity. The total decrease of irreversible stress work due to volumetric deformation from its maximum value is defined as the damage parameter. As indicated by its authors, "the damage of the rock due to a loading history producing dilatancy is described by the constitutive equation itself, more exact by the part of the constitutive equation describing the irreversible deformation of the volume by dilatancy." To us, this definition of damage parameter is a dispensable part of their constitutive equation. Furthermore, according to the theory of continuum damage mechanics (CDM), the damage in the material is irreversible and the damage-induced dissipation is nonnegative. However, the damage parameter defined in Ref. [4] can increase and decrease, and is thus reversible. Because of these two reasons, we concluded that the model given in Ref. [4] is not based on CDM but on viscoplasticity. Hence, this is different from our model presented in Refs. [1,2] which is based on CDM.

We would like to thank Professor Cristescu for his comments on our paper.

References

[1] Soh, C. K., Liu, Y., Yang, Y. W., and Dong, Y. X., 2003, "A Displacement Equivalence-Based Damage Model for Brittles-Part 1: Theory," ASME J. Appl. Mech., **70**, pp. 681–687.
[2] Liu, Y., Soh, C. K., Dong, Y. X., and Yang, Y. W., 2003, "A Displacement Equivalence-Based Damage Model for Brittles-Part 2: Verification," ASME J. Appl. Mech., **70**, pp. 688–695.
[3] Liu, Y., 2003, *Computational Experiment of Reinforced Concrete Structural Element Using Damage Mechanics*, Ph.D. thesis, Nanyang Technological University, Singapore.
[4] Cristescu, N. D., and Hunsche, U., 1998, *Time Effect in Rock Mechanics*, Wiley, Chichester, England.

[1]To whom correspondence should be addressed.

